OXIDANTS AND REDOX SIGNALING IN INFLAMMATION

EDITED BY: Gabor Csanyi and Rikard Holmdahl
PUBLISHED IN: Frontiers in Immunology

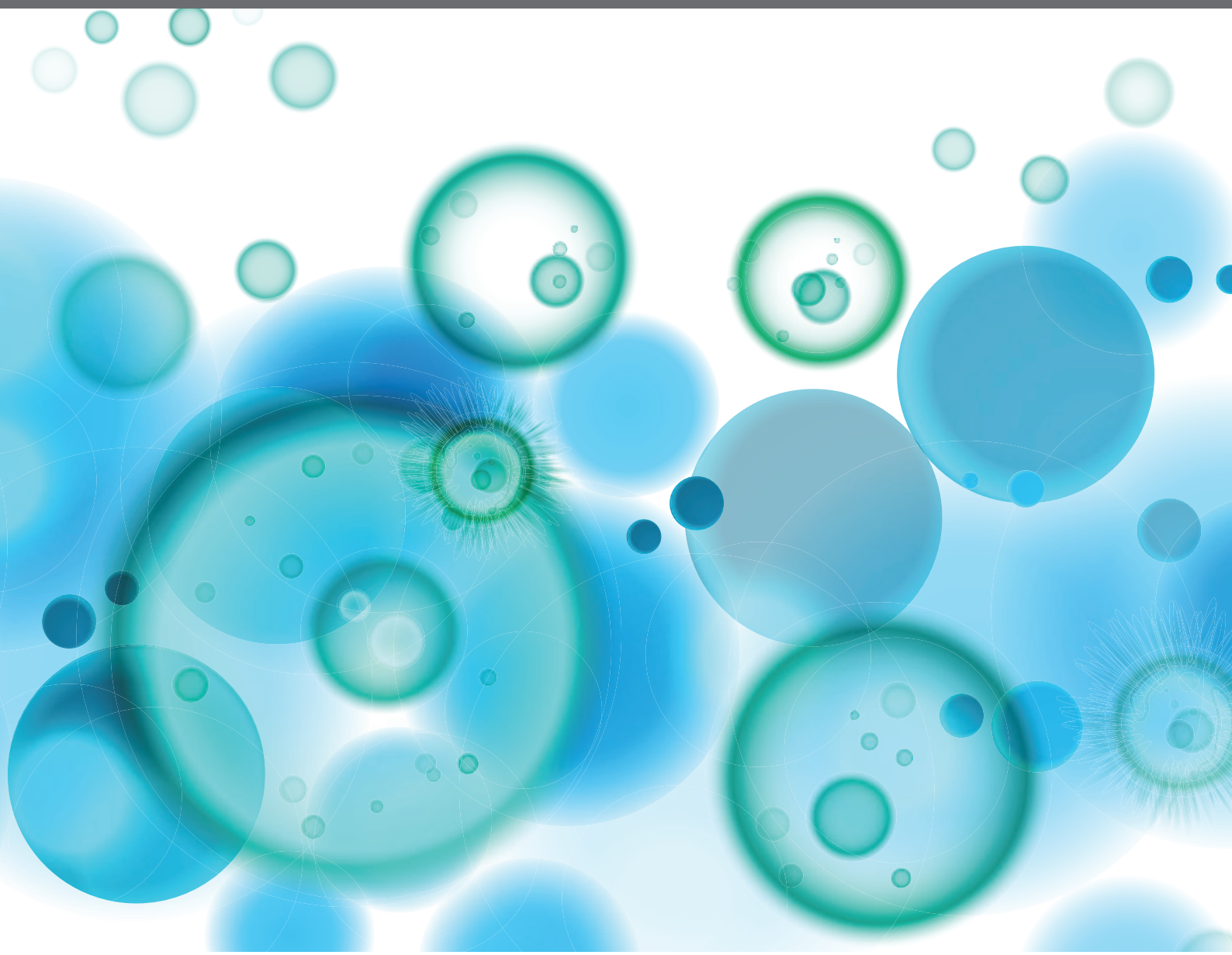

frontiers Research Topics

ISSN 1664-8714
ISBN 978-2-88945-888-2
DOI 10.3389/978-2-88945-888-2

About Frontiers

Frontiers is more than just an open-access publisher of scholarly articles: it is a pioneering approach to the world of academia, radically improving the way scholarly research is managed. The grand vision of Frontiers is a world where all people have an equal opportunity to seek, share and generate knowledge. Frontiers provides immediate and permanent online open access to all its publications, but this alone is not enough to realize our grand goals.

Frontiers Journal Series

The Frontiers Journal Series is a multi-tier and interdisciplinary set of open-access, online journals, promising a paradigm shift from the current review, selection and dissemination processes in academic publishing. All Frontiers journals are driven by researchers for researchers; therefore, they constitute a service to the scholarly community. At the same time, the Frontiers Journal Series operates on a revolutionary invention, the tiered publishing system, initially addressing specific communities of scholars, and gradually climbing up to broader public understanding, thus serving the interests of the lay society, too.

Dedication to Quality

Each Frontiers article is a landmark of the highest quality, thanks to genuinely collaborative interactions between authors and review editors, who include some of the world's best academicians. Research must be certified by peers before entering a stream of knowledge that may eventually reach the public - and shape society; therefore, Frontiers only applies the most rigorous and unbiased reviews.
Frontiers revolutionizes research publishing by freely delivering the most outstanding research, evaluated with no bias from both the academic and social point of view. By applying the most advanced information technologies, Frontiers is catapulting scholarly publishing into a new generation.

What are Frontiers Research Topics?

Frontiers Research Topics are very popular trademarks of the Frontiers Journals Series: they are collections of at least ten articles, all centered on a particular subject. With their unique mix of varied contributions from Original Research to Review Articles, Frontiers Research Topics unify the most influential researchers, the latest key findings and historical advances in a hot research area! Find out more on how to host your own Frontiers Research Topic or contribute to one as an author by contacting the Frontiers Editorial Office: researchtopics@frontiersin.org

OXIDANTS AND REDOX SIGNALING IN INFLAMMATION

Topic Editors:
Gabor Csanyi, Medical College of Georgia at Augusta University, United States
Rikard Holmdahl, Karolinska Institute, Sweden

During the last two decades, our view of the role of reactive oxygen species (ROS) in inflammatory processes has changed dramatically. ROS that are constantly produced at lower levels by living cells metabolizing oxygen contribute to normal cellular function and tissue homeostasis. ROS are produced at higher levels in inflammation and regulate the inflammatory response in specific ways. The role of ROS in inflammation is complex and primarily determined by their relative amount, chemical properties, reactivity, subcellular localization and molecular environment, specificity for their biological targets, and availability and mechanisms of antioxidant defense systems.

This eBook comprises eleven reviews and original articles that provide new findings on the role of ROS in the regulation of inflammatory processes, highlight emerging topics in redox signaling, describe new ROS detection techniques and discuss alternative therapeutic strategies to treat inflammatory disorders. The editorial that precedes the published articles briefly summarizes the main findings of each research paper. We hope that this collection of research articles contribute to a better understanding of ROS in inflammation.

Citation: Csanyi, G., Holmdahl, R., eds. (2019). Oxidants and Redox Signaling in Inflammation. Lausanne: Frontiers Media. doi: 10.3389/978-2-88945-888-2

Table of Contents

frontiers in Immunology

EDITORIAL
published: 26 March 2019
doi: 10.3389/fimmu.2019.00545

Editorial: Oxidants and Redox Signaling in Inflammation

Bhupesh Singla[1], *Rikard Holmdahl*[2,3]* *and Gabor Csanyi*[1,4]*

[1] Vascular Biology Center, Medical College of Georgia, Augusta University, Augusta, GA, United States, [2] Section for Medical Inflammation Research, Department of Medical Biochemistry and Biophysics, Karolinska Institutet, Stockholm, Sweden, [3] Center for Medical Inflammation Research, Southern Medical University, Guangzhou, China, [4] Department of Pharmacology and Toxicology, Medical College of Georgia, Augusta University, Augusta, GA, United States

Keywords: reactive oxygen species, inflammation, NADPH oxidase, NCF1, PKCδ, Nrf2, Hsp70

Editorial on the Research Topic

Oxidants and Redox Signaling in Inflammation

Inflammation is a biological response of the host to any harmful (infectious or sterile) aberration. Anti-inflammatory and pro-resolving mediators are secreted shortly after the beginning of the inflammatory response to revert destruction and repair tissues. Inadequate transition from the inflammatory phase to resolution could lead to a plethora of chronic inflammatory diseases, including atherosclerosis, cancer, chronic respiratory disorders, arthritis, inflammatory bowel disease, allergies, and Alzheimer's disease (1, 2).

During the last two decades, a shift in the view of the role of reactive oxygen species (ROS) has emerged to be viewed as critical regulators of the inflammatory process. ROS were previously viewed mainly as driving inflammation through toxic effects, based on their strong association with the inflammatory response and direct toxic effects at high concentrations (3). However, genetic evidence underlined a much broader role of ROS, as it was found that experimental animals with genetic variants leading to low ROS responsiveness have a higher risk of developing autoimmune diseases (4–6). More recently, it was shown that Ncf1 ($p47^{phox}$) and low ROS responsiveness are important factors in human autoimmune diseases. As a direct follow up of the experimental studies, a single nucleotide polymorphism in the *Ncf1* gene was recently shown to be an important genetic factor in the common autoimmune disease systemic lupus erythematosus (SLE) (6, 7).

The biological effects of ROS are complex and regulate the inflammatory response in specific ways. ROS regulate intracellular signaling by oxidizing amino acid residues, such as cysteine and lysine, oxidize lipids and nucleic acids, and under physiological conditions are kept in balance and compartmentalized by antioxidant enzymes (8, 9). Despite great progress in the field of redox biology, much remains unknown regarding the specific redox mechanisms that control the inflammatory process and mediate the pathogenesis of chronic inflammatory disorders.

This Research Topic entitled "*Oxidants and Redox Signaling in Inflammation*" focuses on the sources of ROS in inflammation, further explores how ROS interact with their downstream targets, identifies novel redox cell signaling pathways, discusses new ROS detection techniques and describe new therapeutic strategies to treat chronic inflammatory diseases. The published research articles are briefly described below.

The review article published by Reshetnikov et al. introduces the pivotal role of neutrophils and neutrophil-derived ROS in innate immune response and regulation of inflammatory responses involving cytotoxic effects, neutrophil extracellular trap formation, secretion of various proteases and antimicrobial factors. They highlight various compounds which can amplify ROS production by neutrophils both *in vitro* and *in vivo* and discuss their therapeutic potential. In addition, they summarize possible approaches to enhance ROS production to treat inflammatory, autoimmune, and bacterial diseases. The review article by Sirokmány and Geiszt provides a timely

OPEN ACCESS

Edited and reviewed by:
Pietro Ghezzi,
University of Sussex, United Kingdom

***Correspondence:**
Rikard Holmdahl
rikard.holmdahl@ki.se
Gabor Csanyi
gcsanyi@augusta.edu

Specialty section:
This article was submitted to Inflammation, a section of the journal Frontiers in Immunology

Received: *17 January 2019*
Accepted: *28 February 2019*
Published: *26 March 2019*

Citation:
Singla B, Holmdahl R and Csanyi G (2019) Editorial: Oxidants and Redox Signaling in Inflammation. Front. Immunol. 10:545. doi: 10.3389/fimmu.2019.00545

overview of heme peroxidases and their associations with H_2O_2-generating NADPH oxidases. Using human and metazoan examples, the authors describe the functional relationship and biological consequences of the tandem interaction between NADPH oxidases and heme peroxidases.

Nuclear factor erythroid 2-related factor 2 (Nrf2) is a transcription factor that provides resistance to oxidative stress and metal toxicity (10). Encountering ROS, Nrf2 binds to the antioxidant response elements located in the upstream promoter region of antioxidant genes and initiates their transcription. The first original research article in this issue by Han et al. investigated the therapeutic potential of dimethyl fumarate (DMF), an Nrf2 activator, for the treatment of acute graft-vs.-host disease (aGVHD). The authors report that DMF treatment attenuated histological damage and improved the survival of mice with aGVHD following MHC-mismatched allogeneic hematopoietic stem cell transplantation (allo-HSCT). Another study by Ohl et al. using murine models evaluated the effects of constitutive Nrf2 activation on myeloid-derived suppressor cells (MDSCs), which are known regulators of pathological immune responses due to their potent immunosuppressive effect. They demonstrated that constitutive Nrf2 activation in hematopoietic cells ($VAV^{cre}Keap^{fl/fl}$) upregulates immunosuppressive MDSCs and maintains metabolic homeostasis of these cells. In addition, mice with constitutive Nrf2 activation were resistant to lethal doses of LPS, indicating a key role of Nrf2 in the generation of tolerant MDSCs and protection against sepsis.

NADPH oxidases (Nox) are multi-subunit enzyme complexes that transfer electrons to oxygen to generate superoxide anion ($O_2^{\bullet-}$), or its dismuted form, hydrogen peroxide (H_2O_2) (11). Nox2 is dormant in quiescent cells and becomes rapidly activated upon exposure to various exogenous stimuli. Singla et al. found that activation of PKCδ and Nox2-derived ROS stimulate antigen macropinocytosis in immature dendritic cells (iDCs). Using genetically modified iDCs, they demonstrated the role of PKCδ-mediated Nox2 activation in iDC macropinocytosis, maturation and subsequent secretion of T-cell stimulatory cytokines, which are crucial for T-cell mediated immune responses. Chronic granulomatous disease (CGD) is characterized by mutations in the *CYBB* gene (encodes Nox2) and CGD patients are more susceptible to pathogenic infection due to decreased ROS generation (12). The interesting study published by Cachat et al. showed elevated levels of IgG_2 in both CGD patients and Nox2 knockout mice, increased IgG_1, IgG_{2b}, and IgG_{2c} production following immunization with ovalbumin + curdlan (dectin-1 agonist) and augmented T-cell activation in Nox2-deficient mice. Following stimulation of Nox2-deficient DCs, they found an increase in the release of Th_1 stimulating cytokines. The authors concluded that DC Nox2 plays an important role at the interface of innate and specific immunity.

Nox1 is a major source of ROS in the colon (13). Nox1 consists of the membrane-bound $p22^{phox}$ (*CYBA*) and two cytosolic subunits (NoxA1 and NoxO1). As NoxO1 lacks the autoinhibitory region (AIR) observed in Ncf1, NoxO1 is able to associate with $p22^{phox}$ constitutively, leading to $O_2^{\bullet-}$ generation in the absence of exogenous stimuli. The study by Moll et al. demonstrated that lack of NoxO1 stimulates proliferation and inhibits apoptosis of colon epithelial cells. Furthermore, NoxO1 deletion increased the severity of dextran sulfate sodium (DSS)-induced colitis and contributed to the development of azoxymethane/DSS-induced colon cancer. An original research investigation by Carvalho et al. studied DSS-induced acute and chronic colitis in wild type and Ncf1-mutant mice. They observed more severe clinical scores of colitis in mutant mice compared to controls. Interestingly, Ncf1-mutant, but not control, mice developed adenocarcinoma in the DSS-induced colitis model. The authors concluded that Ncf1-mediated ROS generation is essential to prevent the development of adenocarcinoma from chronic colitis.

Proniewski et al. employed a novel technique using immuno-spin trapping and fluorescent detection of DMPO nitrone adducts to characterize and quantify the progression of oxidative modifications in a murine model of heart failure (Tgαq*44 mice). Progressive elevation of DMPO nitrone adducts was detected in the cardiomyocytes and coronary endothelium of 10- to 16-month-old Tgαq*44 mice compared to age-matched controls.

Pneumonia is a leading cause of death in children and elder individuals worldwide (14, 15). However, the mechanisms by which pneumolysin (PLY), a toxin produced by causative bacteria, induce pulmonary permeability edema and acute lung injury are not fully understood. Li et al. have shown that Hsp70 overexpression using adenovirus-mediated gene transfer or geranylgeranylacetone (GGA) attenuate PLY-induced increase in lung microvascular endothelial cell permeability via reducing mitochondrial ROS production and cell death. These results suggest that acute upregulation of Hsp70 may be an effective therapeutic approach in the treatment of lung injury associated with pneumonia.

Finally, Widdrington et al. investigated the association between compensatory immune responses and mitochondrial function, triggered by an inflammatory stimulus in monocytes. Exposure of monocytes to LPS caused early oxidative stress (6 h), which was resolved by induction of antioxidant mechanisms and mitochondrial degradation through mitophagy.

The articles published in this Research Topic contribute to a better understanding of redox regulation of inflammatory processes. The knowledge gained from these studies may help identifying novel therapeutic targets to aid resolution and combat chronic inflammatory disorders.

AUTHOR CONTRIBUTIONS

All authors contributed to the writing and editing of the editorial and approved it for publication.

FUNDING

This work was supported by National Institutes of Health grants (R01HL139562, R01HL137087, and R00HL114648) awarded to GC and American Heart Association Postdoctoral Fellowship (17POST33661254) given to BS. It was also supported by grants from the Knut and Alice Wallenberg Foundation (KAW

2015.0063), the Swedish Association against Rheumatism (R-757331), the Swedish Research Council (2015-02662), and the Swedish Foundation for Strategic Research (RB13-0156) given to RH.

ACKNOWLEDGMENTS

The editorial team is grateful to all authors and reviewers for their contributions to this special issue.

REFERENCES

1. Weyand CM, Shen Y, Goronzy JJ. Redox-sensitive signaling in inflammatory T cells and in autoimmune disease. *Free Radic Biol Med.* (2018) 125:36–43. doi: 10.1016/j.freeradbiomed.2018.03.004
2. Hoffmann MH, Griffiths HR. The dual role of Reactive Oxygen Species in autoimmune and inflammatory diseases: evidence from preclinical models. *Free Radic Biol Med.* (2018) 125:62–71. doi: 10.1016/j.freeradbiomed.2018.03.016
3. Bedard K, Krause KH. The NOX family of ROS-generating NADPH oxidases: physiology and pathophysiology. *Physiol Rev.* (2007) 87:245–313. doi: 10.1152/physrev.00044.2005
4. Hultqvist M, Olofsson P, Holmberg J, Backstrom BT, Tordsson J, Holmdahl R. Enhanced autoimmunity, arthritis, and encephalomyelitis in mice with a reduced oxidative burst due to a mutation in the Ncf1 gene. *Proc Natl Acad Sci USA*. (2004) 101:12646–51. doi: 10.1073/pnas.0403831101
5. Olofsson P, Holmberg J, Tordsson J, Lu S, Akerstrom B, Holmdahl R. Positional identification of Ncf1 as a gene that regulates arthritis severity in rats. *Nat Genet.* (2003) 33:25–32. doi: 10.1038/ng1058
6. Olsson LM, Johansson AC, Gullstrand B, Jonsen A, Saevarsdottir S, Ronnblom L, et al. A single nucleotide polymorphism in the NCF1 gene leading to reduced oxidative burst is associated with systemic lupus erythematosus. *Ann Rheum Dis.* (2017) 76:1607–13. doi: 10.1136/annrheumdis-2017-211287
7. Zhao J, Ma J, Deng Y, Kelly JA, Kim K, Bang SY, et al. A missense variant in NCF1 is associated with susceptibility to multiple autoimmune diseases. *Nat Genet.* (2017) 49:433–7. doi: 10.1038/ng.3782
8. Rhee SG, Woo HA, Kang D. The role of peroxiredoxins in the transduction of H2O2 signals. *Antioxid Redox Signal.* (2018) 28:537–57. doi: 10.1089/ars.2017.7167
9. Woo HA, Yim SH, Shin DH, Kang D, Yu DY, Rhee SG. Inactivation of peroxiredoxin I by phosphorylation allows localized H(2)O(2) accumulation for cell signaling. *Cell.* (2010) 140:517–28. doi: 10.1016/j.cell.2010.01.009
10. Biswas M, Chan JY. Role of Nrf1 in antioxidant response element-mediated gene expression and beyond. *Toxicol Appl Pharmacol.* (2010) 244:16–20. doi: 10.1016/j.taap.2009.07.034
11. Segal AW. The function of the NADPH oxidase of phagocytes and its relationship to other NOXs in plants, invertebrates, and mammals. *Int J Biochem Cell Biol.* (2008) 40:604–18. doi: 10.1016/j.biocel.2007.10.003
12. Cachat J, Deffert C, Hugues S, Krause KH. Phagocyte NADPH oxidase and specific immunity. *Clin Sci (Lond).* (2015) 128:635–48. doi: 10.1042/CS20140635
13. Rada B, Leto TL. Oxidative innate immune defenses by Nox/Duox family NADPH oxidases. *Contrib Microbiol.* (2008) 15:164–87. doi: 10.1159/000136357
14. Rudan I, Boschi-Pinto C, Biloglav Z, Mulholland K, Campbell H. Epidemiology and etiology of childhood pneumonia. *Bull World Health Organ.* (2008) 86:408–16. doi: 10.2471/BLT.07.048769
15. Ruuskanen O, Lahti E, Jennings LC, Murdoch DR. Viral pneumonia. *Lancet.* (2011) 377:1264–75. doi: 10.1016/S0140-6736(10)61459-6

Conflict of Interest Statement: The authors declare that the research was conducted in the absence of any commercial or financial relationships that could be construed as a potential conflict of interest.

frontiers in Immunology

REVIEW
published: 13 August 2018
doi: 10.3389/fimmu.2018.01827

Chemical Tools for Targeted Amplification of Reactive Oxygen Species in Neutrophils

Viktor Reshetnikov[1], Jonas Hahn[2], Christian Maueröder[3,4], Christine Czegley[2], Luis Enrique Munoz[2], Martin Herrmann[2], Markus H. Hoffmann[2] and Andriy Mokhir[1]**

[1] Department of Chemistry and Pharmacy, Organic Chemistry II, Friedrich-Alexander-Universität Erlangen-Nürnberg, Erlangen, Germany, [2] Department of Internal Medicine 3 – Rheumatology and Immunology, University Hospital Erlangen, Friedrich-Alexander-Universität Erlangen-Nürnberg, Erlangen, Germany, [3] Cell Clearance in Health and Disease Lab, VIB Center for Inflammation Research, Ghent, Belgium, [4] Department of Biomedical Molecular Biology, Ghent university, Ghent, Belgium

A number of chemical compounds are known, which amplify the availability of reactive oxygen species (ROS) in neutrophils both *in vitro* and *in vivo*. They can be roughly classified into NADPH oxidase 2 (NOX2)-dependent and NOX2-independent reagents. NOX2 activation is triggered by protein kinase C agonists (e.g., phorbol esters, transition metal ions), redox mediators (e.g., paraquat) or formyl peptide receptor (FPR) agonists (e.g., aromatic hydrazine derivatives). NOX2-independent mechanisms are realized by reagents affecting glutathione homeostasis (e.g., L-buthionine sulfoximine), modulators of the mitochondrial respiratory chain (e.g., ionophores, inositol mimics, and agonists of peroxisome proliferator-activated receptor γ) and chemical ROS amplifiers [e.g., aminoferrocene-based prodrugs (ABPs)]. Since a number of inflammatory and autoimmune diseases, as well as cancer and bacterial infections, are triggered or enhanced by aberrant ROS production in neutrophils, it is tempting to use ROS amplifiers as drugs for the treatment of these diseases. However, since the known reagents are not cell specific, their application for treatment likely causes systemic enhancement of oxidative stress, leading to severe side effects. Cell-targeted ROS enhancement can be achieved either by using conjugates of ROS amplifiers with ligands binding to receptors expressed on neutrophils (e.g., the GPI-anchored myeloid differentiation marker Ly6G or FPR) or by designing reagents activated by neutrophil function [e.g., phagocytic activity or enzymatic activity of neutrophil elastase (NE)]. Since binding of an artificial ligand to a receptor may trigger or inhibit priming of neutrophils the latter approach has a smaller potential for severe side effects and is probably better suitable for therapy. Here, we review current approaches for the use of ROS amplifiers and discuss their applicability for treatment. As an example, we suggest a possible design of neutrophil-specific ROS amplifiers, which are based on NE-activated ABPs.

Keywords: aminoferrocenes, autoimmune disease, chronic granulomatous disease, inflammation, NADPH oxidase 2, neutrophils, reactive oxygen species, therapy

OPEN ACCESS

Edited by:
Gabor Csanyi, Augusta University, United States

Reviewed by:
Angelo A. Manfredi, Università Vita-Salute San Raffaele, Italy
John Hancock, University of the West of England, United Kingdom

****Correspondence:***
Markus H. Hoffmann
markus.hoffmann@uk-erlangen.de;
Andriy Mokhir
andriy.mokhir@fau.de

Specialty section:
This article was submitted to Inflammation, a section of the journal Frontiers in Immunology

Received: *18 April 2018*
Accepted: *24 July 2018*
Published: *13 August 2018*

Citation:
Reshetnikov V, Hahn J, Maueröder C, Czegley C, Munoz LE, Herrmann M, Hoffmann MH and Mokhir A (2018) Chemical Tools for Targeted Amplification of Reactive Oxygen Species in Neutrophils. Front. Immunol. 9:1827. doi: 10.3389/fimmu.2018.01827

INTRODUCTION

Neutrophils are formed from stem cells in the bone marrow and constitute roughly 40–75% of the leukocyte population in humans, which makes them the most abundant white blood cells. They play a key role in the response of the innate immune system toward both infectious and sterile agents. These cells possess high mobility due to their characteristic segmented nuclei that coined them the

name polymorphonuclear (PMN) cells. Therefore, neutrophils can quickly migrate from blood to the site of inflammation, where they respond with either phagocytosis of the inflammatory trigger or with degranulation, finally resulting in disintegration of pathogens. Alternatively, neutrophils release DNA-rich neutrophil extracellular traps (NETs), which entrap and neutralize infectious pathogens and sterile factors (1, 2). Additionally, neutrophils recruit macrophages, activate dendritic cells, trigger production of antibodies, and stimulate $CD4^+$ and $CD8^+$ T cells, thereby affecting the adaptive immune system (3–5). In many of these crucial processes the generation of reactive oxygen species (ROS) plays a key role, either because ROS act directly as cytotoxic agents against pathogens or as important regulators of inflammatory responses including, e.g., NET formation, secretion of various proteases, redox enzymes, and antimicrobial factors. In fully functional primed neutrophils, ROS are mainly produced by NADPH oxidase 2 (NOX2) resulting in the so-called oxidative burst. In contrast to its pro-inflammatory role during the early phase of the fight against infections, ROS can also inhibit inflammatory responses (6), e.g., by deactivation of T cells (7–10) or by degradation of inflammatory mediators in NETs (11–13) (**Figure 1**). In agreement with these functions, insufficient ROS production by neutrophils, e.g., due to NOX2 deficiency results in persistent infections but also in autoimmunity and non-resolving inflammation, as can be observed in chronic granulomatous disease (CGD) (14–17).

Despite modern clinical management, long-term outcomes in patients with CGD are still bleak, especially for those individuals with fewer than 10% neutrophils with normal oxidase activity (18, 19). Hematopoietic stem cell transplantations, as the first-line definitive therapy in CGD, are often hampered by limitations in available matched bone marrow donors and the

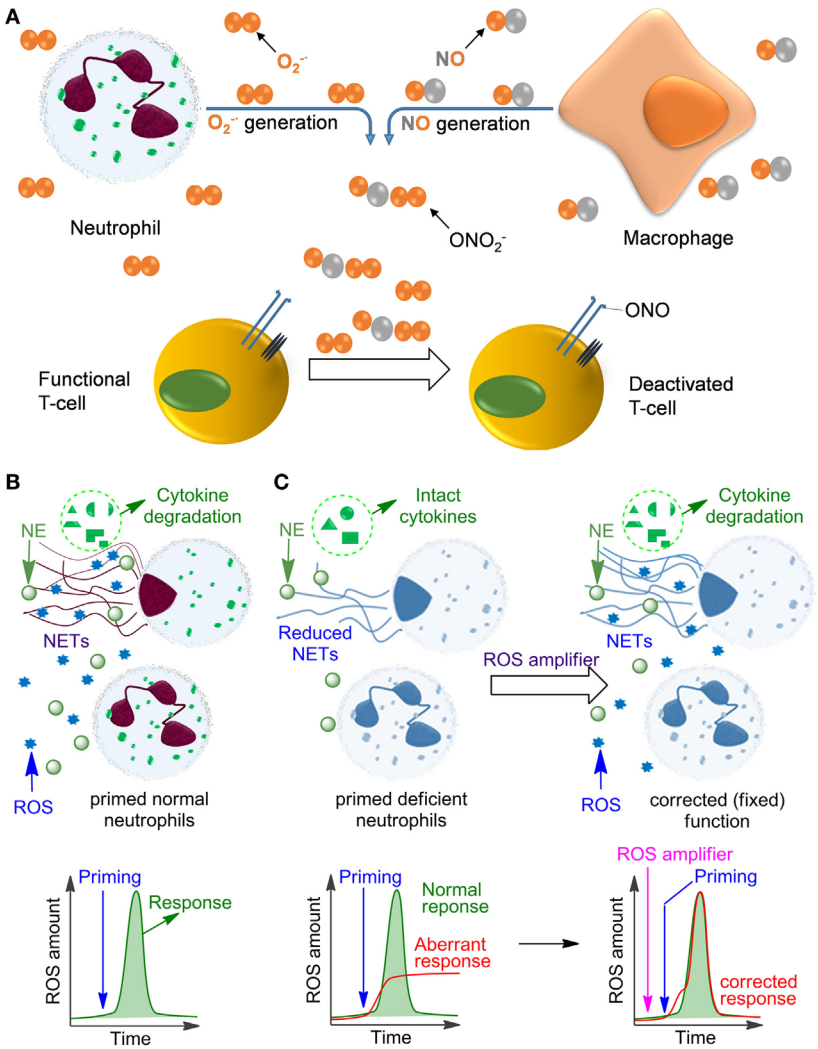

FIGURE 1 | Influence of reactive oxygen species (ROS) on immune cell function. **(A)** The mechanism of deactivation of T-cells by ROS and reactive nitrogen species produced by neutrophils and monocytes/macrophages. This process is facilitated by the proximity of macrophages and T-cells at the sites of infection due to binding of the T-cells to antigens presented on the macrophage surface. **(B)** Oxidative burst in normal primed neutrophils leading to ROS production and neutrophil extracellular trap (NET) formation. **(C)** Aberrant response of NADPH oxidase 2-deficient neutrophils (e.g., in chronic granulomatous disease) leading to low ROS and insufficient NET formation. This deficiency can be fixed by applying ROS amplifiers.

risk of graft-versus-host disease (20). In the last years, technical advantages have also paved the way for specific gene editing to restore proteins encoded by genes carrying loss-of-function mutations [reviewed in Ref. (21)]. Particularly, gene therapy using lentiviral vectors enabling specific expression in myeloid cells (22) and approaches employing the clustered regularly interspaced short palindromic repeats/Cas9 system (23) have obtained promising results.

An alternative approach would be the use of drugs that are capable to trigger ROS generation in NOX2-deficient neutrophils. Such compounds would have the potential to both stimulate the immune system and prevent chronic inflammation (24). In this review, we summarize chemical substances that reportedly can be used for stimulation of ROS production in neutrophils. We also discuss mechanisms of action as well as problems in application of these compounds as drugs and suggest possible solutions.

FORMATION OF ROS UPON PRIMING OF FUNCTIONAL NEUTROPHILS AND THEIR MUTUAL TRANSFORMATIONS IN LIVE ORGANISMS

The multienzymatic NOX2 is activated upon neutrophil priming. In the active state it is able to catalyze one-electron reduction of molecular oxygen ($^3O_2$) with the formation of a superoxide anion radical ($O_2^-\bullet$) (**Figure 2**). This reactive and, therefore, short-lived anion is one of the key precursors of other ROS in cells and the extracellular space, including hydrogen peroxide (H_2O_2), hydroxyl radicals (HO•), hypochlorous acid (HOCl) and its anion hypochlorite (ClO^-), singlet oxygen ($^1O_2$), as well as a series of reactive nitrogen species, e.g., peroxynitrite ($ONOO^-$) and carbon-centered (R•), alkoxy- (RO•) and alkylperoxy-radicals (ROO•). In aqueous solution $O_2^-\bullet$ is dismutated spontaneously with formation of H_2O_2 and $^3O_2$. This reaction is accelerated over 10^4-fold in the presence of superoxide dismutase. In contrast to $O_2^-\bullet$, H_2O_2 is a stable molecule. For example, concentrated aqueous solutions of H_2O_2 are commercially available, can be safely delivered over long distances and stored over extended time. Apart from NOX2, the protein folding machinery in the endoplasmic reticulum (ER) also causes generation of ROS (25).

H_2O_2 is able to cross the cellular membrane, e.g., *via* the aquaporin-mediated pathway (26, 27). Therefore, it is distributed over both the intracellular and extracellular space independently of its site of generation. Though H_2O_2 is itself not a toxic molecule, in the presence of electron donors, e.g., Cu^+ or Fe^{2+}, it is reduced with cleavage of the O-O bond leading to formation of the hydroxide anion HO^- and the HO• radical (Fenton reaction, **Figure 2**). HO• radicals are extremely reactive and, therefore, short-lived. They are capable of subtracting a hydrogen atom ("H") even from very stable (bio)molecules, e.g., lipids, nucleic acids, proteins that leads to formation of a variety of organic radicals (e.g., R•, RO•, and ROO•), deactivation of the biomolecules, and ultimately induction of cell death *via* different pathways, e.g., apoptosis, necrosis, or the formation of NETs. Other reactions leading to H_2O_2 elimination in cells include catalase (CA)-induced conversion of H_2O_2 to water and molecular oxygen ($^3O_2$) and glutathione peroxidase-catalyzed reduction of H_2O_2 in the presence of glutathione (GSH) with the formation of glutathione disulfide (GSSG) and water. Interestingly, H_2O_2 is accumulated in some organelles, e.g., lysosomes (LY) and the ER. This can be explained by the low catalase activity in LY (28) and the low concentration of reduced GSH in ER relatively to its concentration in cytoplasm (29).

In neutrophils, H_2O_2 is also used as a substrate of myeloperoxidase (MPO), which transforms Cl^- anions to highly reactive HOCl. At pH 7 the latter acid (pK_a~7.5) is partially dissociated, forming ClO^- anions. In the MPO-catalyzed reaction both H_2O_2 and ClO^- co-exist for some time in solution. At these conditions electronically excited form of molecular oxygen $^1O_2$ is formed with high yield (30). In contrast to highly reactive HO• and $O_2^-\bullet$, which act locally at the site of their generation, $^1O_2$ exhibits extended lifetime in aqueous solution of ~3 μs and can migrate over 100 nm after its generation (31).

Furthermore, nitric oxide (NO•), which is a rather reactive inorganic radical, is generated from L-arginine in the presence of inducible NO-synthase in activated macrophages (32) and to the lesser degree in primed neutrophils themselves (33). Since macrophages are located at the infection site in close proximity to neutrophils, NO• produced by these cells can combine with $O_2^-\bullet$ generated by neutrophils in an extremely quick reaction with the formation of highly reactive $ONOO^-$. All these species (ROS, NO•, and $ONOO^-$) chemically modify and in this way deactivate extracellular receptors of neighboring T cells or even cause their apoptosis and necrosis (8–10).

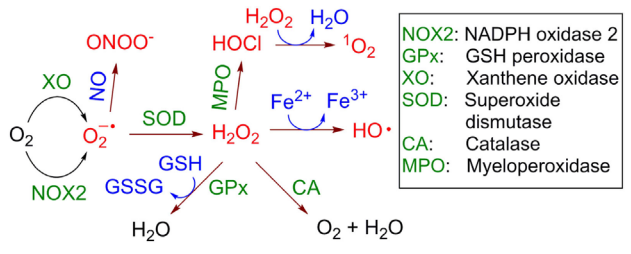

FIGURE 2 | Generation and transformation of reactive oxygen species in live cells. Reactive species are red colored.

STIMULATION OF ROS PRODUCTION IN NEUTROPHILS BY CHEMICAL COMPOUNDS

Chemical and natural compounds amplifying the ROS amount in neutrophils can be classified as NOX2-dependent modulators, which are more common, and NOX2-independent ones.

NOX2-Dependent ROS Modulators

Protein Kinase C (PKC) Agonists

After its activation within cells, PKC catalyzes phosphorylation of the $p47^{phox}$ subunit of the protein associate $p47^{phox}$/SH3/$p7^{phox}$ (**Figure 3A**). The resulting product migrates to the cellular membrane, where it is assembled due to the interaction between SH3 and $p22^{phox}$ subunits with formation of the functional NOX2

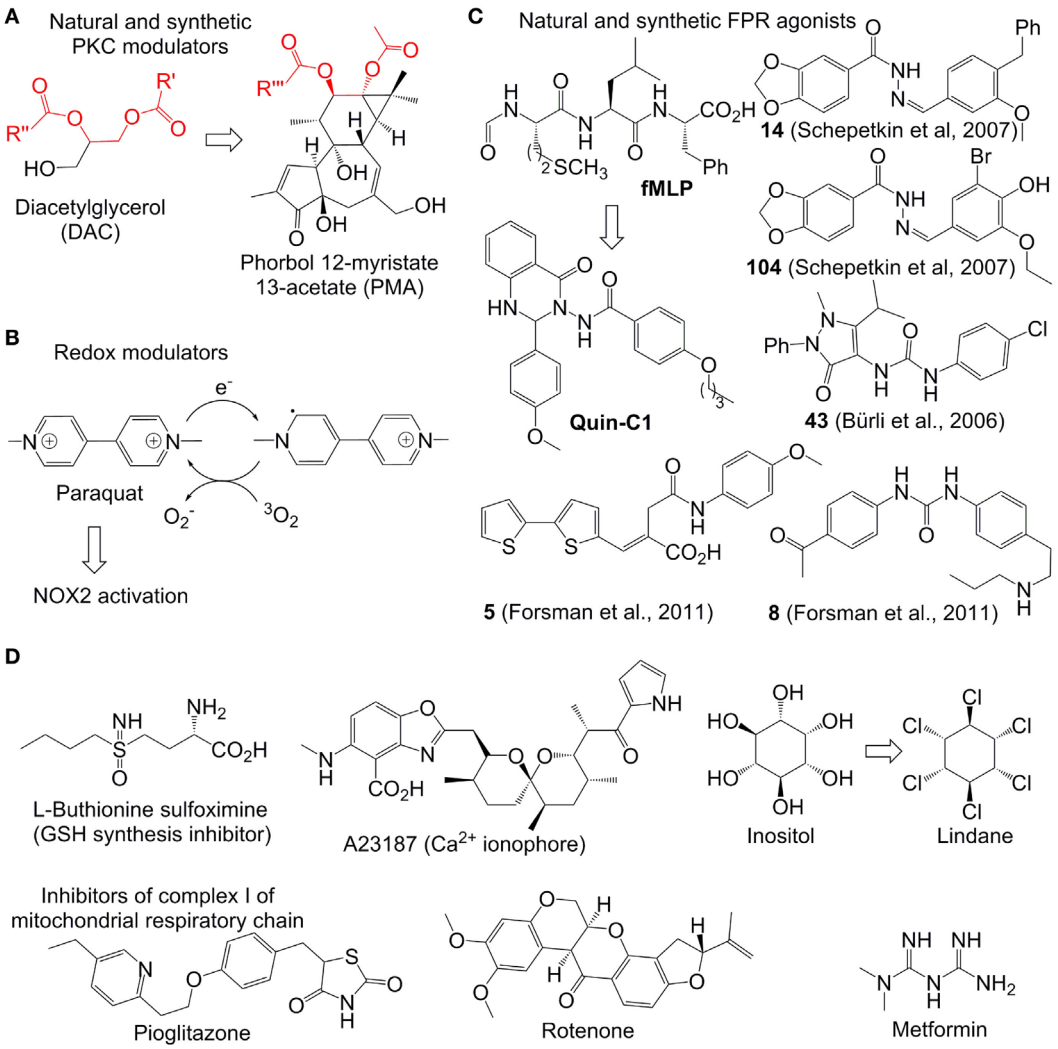

FIGURE 3 | Representative reactive oxygen species (ROS) modulators in neutrophils. **(A–C)**: NADPH oxidase 2(NOX2)-dependent modulators. Quin-C1 is an formyl peptide receptor agonist, but does not induce ROS in cells. **(D)** NOX2-independent modulators. Structurally related fragments in DAC and phorbol myristate acetate are indicated with red color.

system (34). Therefore, compounds enhancing the PKC activity (PKC agonists) are expected to stimulate NOX2 formation and correspondingly increase ROS generation. Examples of such agonists include a variety of hydrophobic phorbol esters, e.g., phorbol myristate acetate (PMA) and phorbol dibutyrate (PDB). These compounds act in this way due to their similarity to the natural activator of PKC, diacylglycerol (DAC) (**Figure 3A**). They are broadly used in immunological research. However, these esters exhibit a number of undesired side effects *in vivo*, which prevents their therapeutic applications. For example, PMA is oncogenic and can cause fever (35). The effects of phorbol esters are attenuated by diphenyleneiodonium (DPI), a commonly used unspecific covalent inhibitor of NOX2, which binds to reduced flavin adenine dinucleotide in the $gp91^{phox}$ subunit (36). These data confirm that the increased ROS production in neutrophils in response PMA is derived from the NOX2 activity.

The Ca^{2+}-ionophore A23187 (**Figure 3D**) was found to further enhance the ROS-production in PDB-treated neutrophils (37). This synergy is logical, since the increased amount of intracellular Ca^{2+}, caused by the treatment with Ca^{2+}-ionophores such as A23187 and ionomycin, is expected to further stimulate PKC. Additionally to that, it has been found that Ca^{2+} strengthens binding of phorbol esters to their receptors (37). A number of other natural and synthetic agonists of PKC, which are either analogs of phorbol esters or unrelated structures, have been reported. However, clinical application of all known agonists is limited by substantial side effects (38).

Fully inorganic PKC activators, which are known to increase ROS in neutrophils *in vitro*, include ionic salts of the soft transition metal ions Zn^{2+}, Cd^{2+}, and Ni^{2+} ions. They are usually only active at the high concentration of ≥1 mM (39, 40). The metal ion effect is strongly dependent on the presence of chelating

agents in the medium. Otherwise, the mechanism of activation is not known.

Redox Mediators

Paraquat is an intensely colored, dicationic 4,4′-bipyridinium salt (other name: methyl viologen) (**Figure 3B**). This compound is used as a broad spectrum herbicide. Its mode of action relies on its powerful electron acceptor properties. For example, in plants it accepts an electron from photosystem I with formation of a resonance-stabilized organic radical (**Figure 3B**). The latter species transfer the electron further to molecular oxygen with formation of $O_2^{-}\bullet$ followed by generation of other ROS (as described above). The toxic effects of ROS generation in plants explain the herbicidal properties of paraquat. In humans this drug is accumulated in lungs, where it catalyzes ROS production by mediation of the electron transfer to oxygen, analogously to its effect in plants, that leads to acute lung injury (41). In mammalian cells, NAPDH can potentially act as donor of electrons for paraquat (42). It has been reported that in neutrophils paraquat-induced ROS generation activates p38 MAPK and NF-kB signaling pathways thereby delaying neutrophil apoptosis. This effect is fully blocked by NOX2 inhibitors and partially blocked by PKC inhibitors confirming the involvement of the latter two enzymes in the paraquat-induced activation of neutrophils (43, 44).

Formyl Peptide Receptor (FPR) Agonists

Formyl peptide receptor is a G-protein coupled receptor expressed on the neutrophil membrane (45). Its stimulation by the bacteria-specific peptide formylmethionyl-leucyl-phenylalanine (fMLF) activates NOX2 thereby inducing ROS generation (**Figure 3C**). A number of organic molecules have been discovered, which act as fMLF mimics and, therefore, are able to stimulate ROS production in functional neutrophils. They include compounds 14, 104 (46), 43 (A) (47, 48), 5, and 10 (49). In contrast to the parent stimulant fMLF, all synthetic ligands are heterocyclic compounds. It is worth noting that many potent synthetic FPR ligands reported in the literature contain one N-N bond (**Figure 3C**). The role of this structural element still remains to be clarified.

Not all FPR agonists induce ROS production in neutrophils. One such example is the quinazolinone C derivative Quin-C1 (50, 51). Though it does not generate ROS, it induces mobilization of Ca^{2+}, chemotaxis, and secretion of beta-glucuronidase.

Other known NOX2-activators include alkanes C_nH_{2n+2} (n = 10–13) and phytol, which are active in the millimolar concentration range (24, 52) as well as a series of patented quinolinone derivatives (53).

NOX2-Independent ROS Modulators

Electron-Deficient Compounds Reactive With Sulfur- and Selen-Containing Biomolecules

A number of electron-deficient (electrophilic) chemical compounds increasing intracellular ROS amount in transformed and proliferating cells have been reported (**Figure 3D**). However, they are not necessarily applicable for modulation of ROS in neutrophils, which are terminally differentiated cells. For example, arsenic trioxide (As_2O_3, Trisenox) is a clinically approved inorganic drug for the treatment of acute promyelocytic leukemia. It is a relatively soft electrophile, which can coordinate soft nucleophilic sulfhydryl and selen-containing biomolecules in cells (54). For example, glutathione (GSH)-depleted cancer cells are especially sensitive to As_2O_3 indicating the important role of this tripeptide in As_2O_3-detoxification (55). The sulfhydryl- and selen-containing biomolecules including, e.g., GSH, glutathione reductase, and thioredoxin reductase participate in neutralization of ROS in the cells. Their deactivation by As_2O_3 usually leads to ROS increase in mammalian cells, which is believed to be one of the reasons of the anticancer activity of this drug. However, though the treatment of neutrophils with As_2O_3 causes their apoptosis, the latter is not associated with increase of the intracellular ROS amount (56). One possible explanation of this fact is the higher antioxidant capacity in neutrophils than that of $As_2O_3^{-}$ sensitive cancer cells. In particular, it has been found that even during the oxidative burst the amount of bulk antioxidants in neutrophils including GSH/GSSG, ascorbate, and vitamin E is not significantly altered (57).

Some highly potent drugs affecting homeostasis of intracellular thiols were found to induce oxidative stress also in myeloid cells. For example, L-buthionine sulfoximine (BSO, **Figure 3D**), an inhibitor of gamma-glutamyl-cysteine-synthase (γGCS) and suppressor of GSH synthesis, was found to enhance the oxidative stress in neutrophils and in cultured myeloid progenitors (58). This effect was also reproduced *in vivo* both for wild-type and X-linked CGD mice (59). Since NOX2 is not functional in the CGD mice, the BSO-induced ROS increase in the latter case should be NOX2 independent. In general, the effect of BSO and other GSH modulators on ROS production in neutrophils is substantially weaker than that in cancer cells. One possible explanation of that is the low level of GSH-dependent antioxidant enzymes in neutrophils, whose antioxidative protection seems to rely more strongly on the catalase activity (60).

Modulators of the Intracellular Concentration of Ca^{2+} ions

Ca^{2+} ions are present in high concentrations in extracellular space and in the intracellular organelle ER. Release of this metal ion into the cytoplasm triggers a number of biochemical processes including, e.g., NET-formation and mitochondrial permeability transition (61–63). Ca^{2+} transfer across the membrane can be induced by Ca^{2+} ionophores, e.g., A23187 or ionomycin. The ROS-enhancing effects of these ionophores were demonstrated for neutrophils as well as other cells (61–63). However, ROS produced by NOX2 are not essential for the effects of both ionophores, e.g., on formation of NETs (61).

Inositol Mimics

γ-Hexaclorocyclohexane (common abbreviation HCCH, other name Lindane) is a potent insecticide. It is also used for the treatment of scabies and lice infestation. However, these pharmaceutical applications have been restricted in many western countries due to pronounced side effects of Lindane, including neuro-, nephro-, and hepatotoxicity. Moreover, this compound was

classified as carcinogenic for humans (group 1). Since Lindane is structurally related to inositol, it affects the phosphatidylinositol (PI) cycle in many cells (64), including those of myeloid origin. In particular, this drug triggers ROS amplification in pulmonary alveolar macrophages that is accompanied by increase of the PI turnover and intracellular Ca^{2+} concentration (65). The modulation of ROS and intracellular Ca^{2+} by Lindane was also observed in neutrophils. Additionally, this reagent was found to stimulate degranulation, but did not act as a chemotactic agent, which distinguishes it from stimulants like PMA (66). Apart from being an inositol mimic, HCCH is a hydrophobic molecule. It seems to be aggregated in aqueous solution as evidenced by its concentration-dependent octanol-water partition coefficients ranging from logP = 3.7 at 10 mg/L to logP = 3.9 at <0.1 μg/L (67). Due to these hydrophobic properties, Lindane can interact efficiently with cellular membranes leading to reorganization of phospholipids. In such altered membranes the phospholipids are more exposed to the external factors and, therefore, prone to degradation (68). One of the products formed during this degradation process is arachidonic acid (AA). AA can stimulate ROS production at least *via* two alternative pathways. In particular, AA as well as its metabolites can potentially activate NOX2 (69). Moreover, AA inhibits complex I and III of the mitochondrial respiratory chain that causes electron leakage and generation of superoxide anion radicals as well as other ROS (70). Since NOX2 inhibitors do not attenuate the HCCH-induced ROS-modulation in neutrophils, one can conclude that the mitochondrial AA-mediated pathway predominates in the Lindane-induced oxidative stress in the cells of this type.

Effectors of Mitochondrial ROS

Thioglitazones, e.g., pioglitazone and related derivatives, are drugs exhibiting insulin-sensitizing properties (71). They are approved for the treatment of type 2 diabetes. Moreover, these compounds are known to have moderate antiproliferative and anti-inflammatory activity (72). The mechanism of action of thioglitazones relies on activation (agonist properties) of peroxisome proliferator-activated receptor γ, which is a transcription factor of the nuclear receptor family. Moreover, they are known to induce production of mitochondrial ROS both in neutrophils and other cell types (73, 74) due to inactivation of complex I of the mitochondrial respiratory chain (75). Other common inhibitors of the complex I including rotenone (a natural compound, used as insecticide and pesticide) and metformin (a synthetic compound, first-line drug for the treatment of diabetes type 2) also induce ROS generation in neutrophils (76). As expected, this effect is not NOX2-dependent. Therefore, these drugs can be used for ROS modulation in NOX2-deficient states, as it has been demonstrated for pioglitazone in $gp91^{phox-/-}$ mice (a CGD model) and *ex vivo* for primary cells from X-linked CGD patients (74).

Neutrophil-Specific ROS Modulation

It has been convincingly confirmed *in vitro* and *in vivo* in several animal models of human inflammatory and autoimmune diseases that controlled increase of ROS can be beneficial for the pathological conditions caused by insufficient NOX2 activity in neutrophils, e.g., CGD (74), RA (7, 24), and systemic lupus erythematosus (77). Therefore, it would be appealing to use ROS amplifiers for the treatment of these and related diseases. However, known drugs of this type exhibit a number of undesired side effects due to their influence on other cells than neutrophils. Therefore, for the further clinical development of ROS-enhancing therapies, drugs specific toward neutrophils and able to trigger ROS production at the desired time points, including, e.g., pathogen challenge in CGD, are desirable.

The targeting of the therapeutic agents can in principle be conducted by using approaches developed for non-invasive tracking of neutrophils *in vivo*. For example, neutrophils were successfully labeled and monitored using quantum dots conjugated to a monoclonal antibody, raised against GPI-anchored myeloid differentiation marker (Ly6G or Gr1).

Though the labeled neutrophils remained fully functional in this case (78), higher loading of the drug would be necessary for a functional therapy approach. At these conditions antibodies against Ly6G (per example clone 1A8) are known to cause neutropenia *in vivo* (79). Another known approach for neutrophil labeling in mice makes use of targeting FPR. In particular, it has been demonstrated that conjugates of non-natural peptide ligand cinnamoyl-F-(D)L-F-(D)-L-FK (cFLFLF) with either the radioactive ^{64}Cu complex (80) or the near-infrared fluorescence imaging probe Cy7 (81) can be used for neutrophil labeling and monitoring in mice: binding affinity of the Cu-conjugate to FPR was found to be ~18 nM. The weak agonistic effect of cFLFLF on FPR is not crucial in this case, since low loading of the detectable moiety is sufficient for the labeling. However, higher loading, required for functional therapy, is expected to cause unspecific neutrophil activation triggering an unwanted immune response.

Albertine and Gee (82) have reported on an alternative, receptor-independent approach for neutrophil labeling *in vivo*. In particular, they applied the hydrophobic cationic dye PKH26, which is commercially available from Merck (previously Sigma-Aldrich). Under optimized conditions this dye forms microaggregates, which are preferentially taken up by neutrophils *in vivo*. However, it has been found later on that these aggregates are also taken by other phagocytic cells, e.g., macrophages. Though at the concentrations required for labeling PKH26 is not toxic, in the presence of day light the toxicity is dramatically increased (83). Furthermore, PKH26 and related structures containing a positively charged polar head and two hydrophobic tail groups at higher concentrations, which would be required for the therapy, can potentially induce lysis of red blood cells. Thus, we conclude that all known neutrophil-targeting approaches are not ideal for therapeutic applications.

This warrants further research efforts in this field. A possible solution of the problems addressed above is the use of aminoferrocene-based prodrugs (ABP), which were originally developed for targeting cancer cells (84–91). A structure of the parent ABP is shown in **Figure 4**. Here the ferrocene fragment is a functional unit, which is covalently attached to an electron-acceptor protecting group (arylmethyloxycarbonylamino). Therefore, the molecules of this type are relatively electron-deficient and, correspondingly, do not act as electron donors both in the extracellular space and

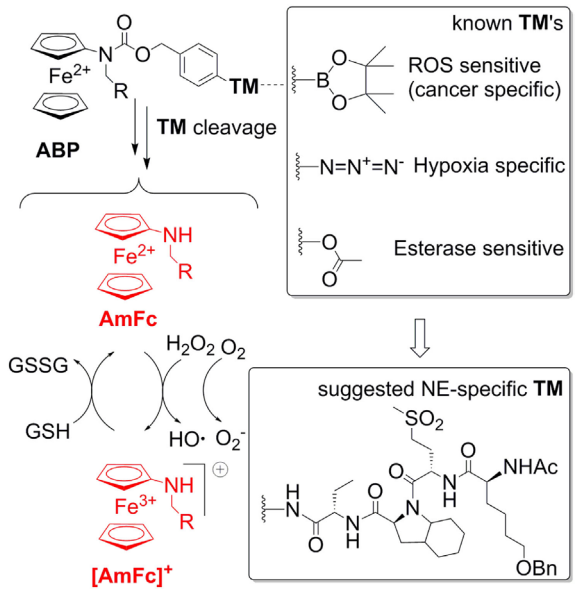

FIGURE 4 | A general structure of aminoferrocene-based prodrugs (ABPs) and the mechanisms of their activation after cleavage of the triggering moiety (TM). The NE-sepcific TM is based on the peptide reported in Ref. (92).

in cells (84). Furthermore, the ABP contains a triggering moiety (TM). Its removal leads to formation of unstable phenol or aniline derivatives, which spontaneously undergo 1,6-elimination with formation of substituted aminoferrocenes (AmFc). The AmFc derivatives are substantially more electron-rich than the parent ABPs (the redox potential $\Delta E_{1/2}$ is shifted by ca. 0.3V). Therefore, in contrast to the ABPs, they act as electron donors for endogenous H_2O_2 and $^3O_2$ leading to formation of highly reactive ROS (HO• and O_2^{-}•) as well as ferrocenium cations $[AmFc]^+$. The latter product can be reduced back to the AmFc by endogenous bulk reducing agents (GSH, ascorbate, and NADPH), thereby closing the catalytic cycle. The ABPs were found to be powerful ROS amplifiers both *in vitro* (experiments with cell cultures and primary cells) and *in vivo* (experiments with mice and rats). By the variation of the TM moiety one can potentially design any cell-specific prodrug providing the cell-specific enzymatic activity is known. For example, already validated TM's include aryl boronic acid esters (cancer cell-specific and activated under conditions of enhanced oxidative stress), arylazides (hypoxia-specific activation), and carboxylic acid ester (activation in the presence of esterases). Therefore, it is of high interest to explore the possibility of using these versatile prodrugs for design of neutrophil-specific ROS amplifiers.

Current Ideas and Future Perspectives

In pilot studies, we confirmed that a representative ABP compound, MIS43 (81), is able to enhance ROS in normal neutrophils. This effect is not inhibited by DPI, which indicates that it is not NOX2-dependent. We observed that at the selected experimental conditions MIS43 is a more potent ROS amplifier than known ones including Lindane and BSO, whereas the effect of PMA was found to be stronger (unpublished results).

To create a neutrophil-specific ROS amplifier, we suggest incorporating neutrophil elastase (NE)-specific moieties as TMs in the ABP structure (**Figure 4**). We selected NE as a neutrophil target, since it is released in the extracellular space and in phagosome and activated only upon neutrophil stimulation, whereas its activity is absent in inactive neutrophils. Moreover, it is known that NOX2-deficient neutrophils release large amounts of NE (93). Therefore, potentially such NE-specific ABPs can be used to enhance ROS specifically in NOX2-deficient neutrophils, which are relevant for CGD, RA, and lupus. As a NE-specific TM one can select a reactive fragment from the number of reported NE-specific fluorogenic substrates. For example, the non-natural tetrapeptide Ac-Nle(OBzl)-Met$(O)_2$-Oic-Abu- could be suitable. In particular, this tetrapeptide is NE-specific. Moreover, since it is an artificial structure, it is not expected to be unspecifically degraded *in vivo* (92).

AUTHOR CONTRIBUTIONS

VR helped in drafting the manuscript and the figures. JH, CM, CC, LM, MaHe, and MaHo provided scientific input to the manuscript. AM provided the first draft and finalized the manuscript.

FUNDING

MaHe and MaHo were supported by the German Research Foundation (DFG) (grant number SFB 1181-C03). MaHo further received support by the EU-project RISE-Redoxit (H2020-MSCA-RISE-2014, Project 644035). AM thanks German Research Council (DFG, grant MO 1418/7-1), Emerging Field Initiative of Friedrich-Alexander-University of Erlangen-Nuremberg (grant 3_Nat_01, "Chemistry in live cells"), and Interdisciplinary Center of Molecular Materials (ICMM, a Ph.D.-fellowship for VR) for funding this project. AM also acknowledges the partial support from the EU-project RISE-CLATHROPROBES (H2O2-MSCA-RISE-2017, Project 778245).

REFERENCES

1. Brinkmann V, Reichard U, Goosmann C, Fauler B, Uhlemann Y, Weiss DS, et al. Neutrophil extracellular traps kill bacteria. *Science* (2004) 303(5663): 1532–5. doi:10.1126/science.1092385
2. Gupta S, Kaplan MJ. The role of neutrophils and NETosis in autoimmune and renal diseases. *Nat Rev Nephrol* (2016) 12:402–13. doi:10.1038/nrneph.2016.71
3. Nathan C. Neutrophils and immunity: challenges and opportunities. *Nat Rev Immunol* (2006) 6:173–82. doi:10.1038/nri1785
4. Kalyan S, Kabelitz D. When neutrophils meet T cells: beginnings of a tumultuous relationship with underappreciated potential. *Eur J Immunol* (2014) 44:627–33. doi:10.1002/eji.201344195
5. Holmdahl R, Sareila O, Olsson LM, Bäckdahl L, Wing K. Ncf1 polymorphism reveals oxidative regulation of autoimmune chronic inflammation. *Immunol Rev* (2016) 269(1):228–47. doi:10.1111/imr.12378
6. Hoffmann MH, Griffiths HR. The dual role of ROS in autoimmune and inflammatory diseases: evidence from preclinical models. *Free Radic Biol Med* (2018). doi:10.1016/j.freeradbiomed.2018.03.016

7. Hultqvist M, Olsson LM, Gelderman KA, Holmdahl R. The protective role of ROS in autoimmune disease. *Trends Immunol* (2009) 30(5):201–8. doi:10.1016/j.it.2009.03.004
8. Gabrilovich DI, Nagaraj S. Myeloid-derived-suppressor cells as regulators of the immune system. *Nat Rev Immunol* (2009) 9(3):162–74. doi:10.1038/nri2506
9. Franchina DG, Dostert C, Brenner D. Reactive oxygen species: involvement in T cell signalling and metabolism. *Trends Immunol* (2018) 39(6):489–502. doi:10.1016/j.it.2018.01.005
10. Veglia F, Perego M, Gabrilovich D. Myeloid-derived suppressor cells coming of age. *Nat Immunol* (2018) 19:108–19. doi:10.1038/s41590-017-0022-x
11. Schauer C, Janko C, Munoz LE, Zhao Y, Kienhöfer D, Frey B, et al. Aggregated neutrophil extracellular traps limit inflammation by degrading cytokines and chemokines. *Nat Med* (2014) 20(5):511–7. doi:10.1038/nm.3547
12. Reinwald C, Schauer C, Csepregi JZ, Kienhöfer D, Weidner D, Malissen M, et al. Reply to "neutrophils are not required for resolution of acute gouty arthritis in mice". *Nat Med* (2016) 22(12):1384–6. doi:10.1038/nm.4217
13. Maueröder C, Kienhöfer D, Hahn J, Schauer C, Manger B, Schett G, et al. How neutrophil extracellular traps orchestrate the local immune response in gout. *J Mol Med* (2015) 93(7):727–34. doi:10.1007/s00109-015-1295-x
14. Segal BH, Leto TL, Gallin JI, Malech HL, Holland SM. Genetic, biochemical, and clinical features of chronic granulomatous disease. *Medicine* (2000) 79(3):170–200. doi:10.1097/00005792-200005000-00004
15. De Ravin SS, Naumann N, Cowen EW, Friend J, Hilligoss D, Marquessen M, et al. Chronic granulomatous disease as a risk factor for autoimmune disease. *J Allergy Clin Immunol* (2008) 122(6):1097–103. doi:10.1016/j.jaci.2008.07.050
16. Magnani A, Brosselin P, Beauté J, de Vergnes N, Mouy R, Debré M, et al. Inflammatory manifestations in a single-center cohort of patients with chronic granulomatous disease. *J Allergy Clin Immunol* (2014) 134(3):655–62. doi:10.1016/j.jaci.2014.04.014
17. Winkelstein JA, Marino MC, Johnston RB Jr, Boyle J, Curnutte J, Gallin JI, et al. Holland SM, Ochs H, Quie P, Buckley RH, Foster CB, Chanock SJ, Dickler H. Chronic granulomatous disease. Report on a national registry of 368 patients. *Medicine* (2000) 79(3):155–69. doi:10.1097/00005792-200005000-00003
18. Kuhns DB, Alvord WG, Heller T, Feld JJ, Pike KM, Marciano BE, et al. Residual NADPH oxidase and survival in chronic granulomatous disease. *N Engl J Med* (2010) 363(27):2600–10. doi:10.1056/NEJMoa1007097
19. Marciano BE, Zerbe CS, Falcone EL, Ding L, DeRavin SS, Daub J, et al. X-linked carriers of chronic granulomatous disease: illness, lyonization, and stability. *J Allergy Clin Immunol* (2018) 141(1):365–71. doi:10.1016/j.jaci.2017.04.035
20. Kang EM, Marciano BE, DeRavin S, Zarember KA, Holland SM, Malech HL. Chronic granulomatous disease: overview and hematopoietic stem cell transplantation. *J Allergy Clin Immunol* (2011) 127(6):1319–26. doi:10.1016/j.jaci.2011.03.028
21. Keller MD, Notarangelo LD, Malech HL. Future of care for patients with chronic granulomatous disease: gene therapy and targeted molecular medicine. *J Pediatric Infect Dis Soc* (2018) 7(Suppl_1):S40–4. doi:10.1093/jpids/piy011
22. Santilli G, Almarza E, Brendel C, Choi U, Beilin C, Blundell MP, et al. Biochemical correction of X-CGD by a novel chimeric promoter regulating high levels of transgene expression in myeloid cells. *Mol Ther* (2011) 19(1):122–32. doi:10.1038/mt.2010.226
23. De Ravin SS, Li L, Wu X, Choi U, Allen C, Koontz S, et al. CRISPR-Cas9 gene repair of hematopoietic stem cells from patients with X-linked chronic granulomatous disease. *Sci Transl Med* (2017) 9(372):eaah3480. doi:10.1126/scitranslmed.aah3480
24. Hultqvist M, Olofsson P, Geldermann KA, Holmberg J, Holmdahl R. A new arthritis therapy with oxidative burst inducers. *PLoS Med* (2006) 3(9):e348. doi:10.1371/journal.pmed.0030348
25. Chaudhari N, Talwar P, Parimisetty A, Lefebvre d'Hellencourt C, Ravanan P. A molecular web: endoplasmic reticulum stress, inflammation, and oxidative stress. *Front Cell Neurosci* (2014) 8:213. doi:10.3389/fncel.2014.00213
26. Bienert GP, Moller ALB, Kristiansen KA, Schulz A, Moller IM, Schjoerring JK, et al. Specific aquaporins facilitate the diffusion of hydrogen peroxide across membranes. *J Biol Chem* (2007) 282:1183–92. doi:10.1074/jbc.M603761200
27. Dynowski M, Schaaf G, Loque D, Moran O, Ludewig U. Plant plasma membrane water channels conduct the signalling molecule H2O2. *Biochem J* (2008) 414:53–61. doi:10.1042/BJ20080287
28. Terman A, Kurz T, Gustafsson B, Brunk UT. Lysosomal labilization. *IUBMB Life* (2006) 58(9):531–9. doi:10.1080/15216540600904885
29. Hwang C, Sinskey AJ, Lodish HF. Oxidized redox state of glutathione in the endoplasmic reticulum. *Science* (1992) 257:1496–502. doi:10.1126/science.1523409
30. Klebanoff SJ. Myeloperoxidase: friend and foe. *J Leukoc Biol* (2005) 77:598–625. doi:10.1189/jlb.1204697
31. Hatz S, Lambert JD, Ogilby PR. Measuring the lifetime of singlet oxygen in a single cell: addressing the issue of cell viability. *Photochem Photobiol Sci* (2007) 6(10):1106–16. doi:10.1039/b707313e
32. Fang FC, Vazquez-Torres A. Nitro oxide production by human macrophages: there is NO doubt about it. *Am J Physiol Lung Cell Mol Physiol* (2002) 282:941–3. doi:10.1152/ajplung.00017.2002
33. Wright CD, Mülsch A, Busse R, Osswald H. Generation of nitric oxide by human neutrophils. *Biochem Biophys Res Commun* (1989) 160(2):813–9. doi:10.1016/0006-291X(89)92506-0
34. Rastogi R, Geng X, Li F, Ding Y. NOX activation by subunit interaction and underlying mechanisms in disease. *Front Cell Neurosci* (2017) 10:301. doi:10.3389/fncel.2016.00301
35. McKernan LN, Momjian D, Kulkosky J. Protein kinase C: one pathway towards the eradication of latent HIV-1 reservoirs. *Adv Virol* (2012) 2012:805347. doi:10.1155/2012/805347
36. Ellis JA, Mayer SJ, Jones OT. The effect of the NADPH oxidase inhibitor diphenyleneiodonium on aerobic and anaerobic microbicidal activities of human neutrophils. *Biochem J* (1988) 251(3):887–91. doi:10.1042/bj2510887
37. French JK, Hurst NP, Zalewski PD, Valente L, Forbes IJ. Calcium ionophore A23187 enhances human neutrophil superoxide release, stimulated by phorbol dibutyrate, by converting phorbol ester receptors from a low- to high-affinity state. *FEBS Lett* (1987) 212(2):242–6. doi:10.1016/0014-5793(87)81353-4
38. Jiang G, Dandekar S. Targeting NF-kB signaling with protein kinase C agonists as an emerging strategy for combating HIV latency. *Aids Res Hum Retrovir* (2015) 31:4–12. doi:10.1089/aid.2014.0199
39. Freitas M, Gomes A, Porto G, Fernandes E. Nickel induces oxidative burst, NF-kB activation and interleukin-8 production in human neutrophils. *J Biol Inorg Chem* (2010) 15:1275–83. doi:10.1007/s00775-010-0685-3
40. Freitas M, Porto G, Lima JLFC, Fernandes E. Zinc activates neutrophils' oxidative burst. *Biometals* (2010) 23:31–41. doi:10.1007/s10534-009-9264-x
41. Dinis-Oliveira RJ, Sarmento A, Reis P, Amaro A, Remião F, Bastos ML, et al. Acute paraquat poisoning: report of a survival case following intake of a potential lethal dose. *Pediatr Emerg Care* (2006) 22(7):537–40. doi:10.1097/01.pec.0000223179.07633.8a
42. Bus JS, Aust SD, Gibson JE. Superoxide- and singlet oxygen-catalyzed lipid peroxidation as a possible mechanism for paraquat (methyl viologen) toxicity. *Biochem Biophys Commun* (1974) 58(3):749–55. doi:10.1016/S0006-291X(74)80481-X
43. Mitra S, Abraham E. Participation of superoxide in neutrophil activation and cytokine production. *Biochim Biophys Acta* (2006) 1762(8):732–41. doi:10.1016/j.bbadis.2006.06.011
44. Wang X, Luo F, Zhao H. Paraquat-induced reactive oxygen species inhibit neutrophil apoptosis via a p38 MAPK/NF-kB-IL-6/TNF-α positive-feedback circuit. *PLoS One* (2014) 9(4):e93837. doi:10.1371/journal.pone.0093837
45. Fu H, Karlsson J, Bylund J, Movitz C, Karlsson A, Dahlgren C. Ligand recognition and activation of formyl peptide receptors in neutrophils. *J Leukoc Biol* (2006) 79(2):247–56. doi:10.1189/jlb.0905498
46. Schepetkin IA, Kirpotina LN, Khlebnikov AI, Quinn MT. High-throughput screening for small-molecule activators of neutrophils: identification of novel N-formyl peptide receptor agonists. *Mol Pharm* (2007) 71:1061–74. doi:10.1124/mol.106.033100
47. Bürli RW, Xu H, Zou X, Muller K, Golden J, Frohn M, et al. Potent hFPRL1 (ALXR) agonists as potential anti-inflammatory agents. *Bioorg Med Chem Lett* (2006) 16:3713–8. doi:10.1016/j.bmcl.2006.04.068
48. Sogawa Y, Shimizugawa A, Ohyama T, Maeda H, Hirahara K. The pyrazolone originally reported to be a formyl peptide receptor (FPR) 2/ALX-selective agonist is instead an FPR1 and FPR2/ALX dual agonist. *J Pharmacol Sci* (2009) 111(3):317–21. doi:10.1254/jphs.09196SC
49. Forsman H, Kalderén C, Nordin A, Nordling E, Jensen AJ, Dahlgren C. Stable formyl peptide receptor agonists that activate the neutrophil NADPH-oxidase identified through screening of a compound library. *Biochem Pharmacol* (2011) 81:402–11. doi:10.1016/j.bcp.2010.11.005

50. Nanamori M, Cheng X, Mei J, Sang H, Xuan Y, Zhou C, et al. A novel nonpeptide ligand for formyl peptide receptor-like 1. *Mol Pharmacol* (2004) 66:1213–22. doi:10.1124/mol.104.004309
51. Zhou C, Zhang S, Nanamori M, Zhang Y, Liu Q, Li N, et al. Pharmacological characterization of a novel nonpeptide antagonist for formyl peptide receptor like 1. *Mol Pharmacol* (2007) 72(4):976–83. doi:10.1124/mol.107.037564
52. Olofsson P, Holmberg J, Tordsson J, Lu S, Akerström B, Holmdahl R. Positional identification of Ncf1 as a gene that regulates arthritis severity in rats. *Nat Genet* (2003) 33:25–32. doi:10.1038/ng1058
53. Wallner KF, Olofsson JP, Hultquist MK, Pelcman BH. Quinolinone derivatives for use in the treatment of an autoimmune disease and/or an inflammatory disease. *WIPO Patent* (2011) WO2012127214A1.
54. Li YM, Broome JD. Arsenic targets tubulins to induce apoptosis in myeloid leukemia cells. *Cancer Res* (1999) 59:776–80.
55. Yang CH, Kuo ML, Chen JC, Chen YC. Arsenic trioxide sensitivity is associated with low level of glutathione in cancer cells. *Br J Cancer* (1999) 81(5): 796–9. doi:10.1038/sj.bjc.6690766
56. Binet F, Cavalli H, Moisan É, Girard D. Arsenic trioxide (AT) is a novel human neutrophil pro-apoptotic agent: effects of catalase on AT-induced apoptosis, degradation of cytoskeletal proteins and de novo protein synthesis. *Br J Haematol* (2005) 132:349–58. doi:10.1111/j.1365-2141.2005.05866.x
57. Ogino T, Packer L, Maguire JJ. Neutrophil antioxidant capacity during the respiratory burst: loss of glutathione induced by chloramines. *Free Radic Biol Med* (1997) 23(3):445–52. doi:10.1016/S0891-5849(97)00115-9
58. Kwak HJ, Liu P, Bajrami B, Xu Y, Park SY, Nombela-Arrieta C, et al. Myeloid cell-derived reactive oxygen species externally regulate the proliferation of myeloid progenitors in emergency granulopoiesis. *Immunity* (2015) 42: 159–71. doi:10.1016/j.immuni.2014.12.017
59. Zhu H, Kwak H-J, Liu P, Bajrami B, Xu Y, Park S-Y, et al. Reactive oxygen species-producing myeloid cells act as a bone marrow niche for sterile inflammation-induced granulopoiesis. *J Immunol* (2017) 198:2854–64. doi:10.4049/jimmunol.1602006
60. Kinnula VL, Soini Y, Kvist-Mäkelä K, Savolainen ER, Koistinen P. Antioxidant defense mechanism in human neutrophils. *Antioxid Redox Signal* (2002) 4(1):27–34. doi:10.1089/152308602753625825
61. Kenny EF, Herzig A, Krüger R, Muth A, Mondal S, Thompson PR, et al. Diverse stimuli engage different neutrophil extracellular trap pathways. *Elife* (2017) 6:e24437. doi:10.7554/eLife.24437
62. Kajitani N, Kobuchi H, Fujita H, Yano H, Fujiwara T, Yasuda T, et al. Mechanism of A23187-induced apoptosis in HL-60 cells: dependency on mitochondrial permeability transition, but not on NADPH oxidase. *Biosci Biotechnol Biochem* (2007) 71(11):2701–11. doi:10.1271/bbb.70304
63. Lemasters JJ, Theruvath TP, Zhong Z, Nieminen AL. Mitochondrial calcium and the permeability transition in cell death. *Biochim Biophys Acta* (2009) 1787(11):1395–401. doi:10.1016/j.bbabio.2009.06.009
64. Hokin MR, Brown DF. Inhibition by gamma-hexachlorocyclohexane of acetylcholine-stimulated phosphatidylinositol (PI) synthesis in cerebral cortex slices and of phosphatidic acid-inositol transferase in cerebral cortex particular fractions. *J Neurochem* (1969) 16:475. doi:10.1111/j.1471-4159.1969.tb06846.x
65. Holian A, Marchiarullo MA, Stickle DF. Gamma-hexachlorocyclohexane activation in alveolar macrophage phosphatidylinositol cycle, calcium mobilization of O2- production. *FEBS Lett* (1984) 176(1):151–4. doi:10.1016/0014-5793(84)80930-8
66. English D, Schell M, Siakotos A, Gabig TG. Reversible activation of the neutrophil superoxide generating system by hexachlorocyclohexane: correlation with effects on a subcellular superoxide-generating fraction. *J Immunol* (1986) 137:283–90.
67. Paschke A, Schüürmann G. Concentration dependence of the octanol/water partition coefficients of the hexachlorocyclohexane isomers at 25°C. *Chem Eng Technol* (2000) 23(8):666–70. doi:10.1002/1521-4125(200008)23:8<666::AID-CEAT666>3.0.CO;2-5
68. Parries GS, Hokin-Neaverson M. Inhibition of phosphatidylinositol synthase and other membrane-associated enzymes by stereoisomers of hexachlorocyclohexane. *J Biol Chem* (1985) 260(5):2687–93.
69. Matono R, Mlyano K, Klyohara T, Sumimoto H. Arachidonic acid induces direct interaction of the p67*phox*-Rac complex with the phagocyte oxidase Nox2, leading to superoxide production. *J Biol Chem* (2014) 289(36): 24874–84. doi:10.1074/jbc.M114.581785
70. Cocco T, De Paola M, Papa S, Lorusso M. Arachidonic acid interaction with the mitochondrial electron transport chain promotes reactive oxygen species generation. *Free Radic Biol Med* (1999) 27(1–2):51–9. doi:10.1016/S0891-5849(99)00034-9
71. Yki-Järvinen H. Thiazolidinediones. *N Engl J Med* (2004) 351:1106–18. doi:10.1056/NEJMra041001
72. Feinstein DL, Spagnolo A, Akar C, Weinberg G, Murphy P, Gavrilyuk V, et al. Receptor-independent actions of PPAR thiazolidinedione agonists: is mitochondrial function the key? *Biochem Pharmacol* (2005) 70:177–88. doi:10.1016/j.bcp.2005.03.033
73. Pérez-Ortiz JM, Tranque P, Burgos M, Vaquero CF, Llopis J. Glitazones induce astroglioma cell death by releasing reactive oxygen species from mitochondria: modulation of cytotoxicity by nitric oxide. *Mol Pharm* (2007) 72(2):407–17. doi:10.1124/mol.106.032458
74. Fernandez-Boyanapalli RF, Frasch SC, Thomas SM, Malcolm KC, Nicks M, Harbeck RJ, et al. Pioglitazone restores phagocyte mitochondrial oxidants and bactericidal capacity in chronic granulomatous disease. *J Allergy Clin Immunol* (2015) 135(2):517–27.e12. doi:10.1016/j.jaci.2014.10.034
75. García-Ruiz I, Solís-Muños P, Fernández-Moreira D, Muñoz-Yagüe T, Solís-Herruzo JA. Pioglitazone leads to an inactivation and disassembly of complex I of the mitochondrial respiratory chain. *BMC Biol* (2013) 11:88. doi:10.1186/1741-7007-11-88
76. Zmijewski JW, Lorne E, Zhao X, Tsuruda Y, Sha Y, Liu G, et al. Mitochondrial respiratory complex I regulates neutrophil activation and severity of lung injury. *Am J Respir Crit Care Med* (2008) 178:168–79. doi:10.1164/rccm.200710-1602OC
77. Kienhöfer D, Hahn J, Stoof J, Csepregi JZ, Reinwald C, Urbonaviciute V, et al. Experimental lupus is aggravated in mouse strains with impaired induction of neutrophil extracellular traps. *JCI Insight* (2017) 2(10):e92920. doi:10.1172/jci.insight.92920
78. Kikushima K, Kita S, Higuchi H. A non-invasive imaging for the in vivo tracking of high-speed vesicle transport in mouse neutrophils. *Sci Rep* (2013) 3:1913. doi:10.1038/srep01913
79. Daley JM, Thomay AA, Connolly MD, Reicher JS, Albina JE. Use of Ly6G-specific monoclonal antibody to deplete neutrophils in mice. *J Leukoc Biol* (2008) 83(1):64–70. doi:10.1189/jlb.0407247
80. Locke LW, Chordia MD, Zhang Y, Kundu B, Kennedy D, Landseadel J, et al. A novel neutrophil-specific PET imaging agent: cFLFLFK-PEG-64Cu. *J Nucl Med* (2009) 50:790–7. doi:10.2967/jnumed.108.056127
81. Xiao L, Zhang Y, Berr SS, Chordia MD, Pramoonjago P, Pu L, et al. A novel near-infrared fluorescence imaging probe for in vivo neutrophil tracking. *Mol Imaging* (2012) 11(5):372–82. doi:10.2310/7290.2011.00054
82. Albertine KH, Gee MH. In vivo labeling of neutrophils using a fluorescence cell linker. *J Leuk Biol* (1996) 59:631–8. doi:10.1002/jlb.59.5.631
83. Oh DJ, Lee GM, Francis K, Palsson BO. Phototoxicity of the fluorescent membrane dyes PKH2 and PKH26 on the human hematopoietic KG1a progenitor cell line. *Cytometry* (1999) 36:312–8. doi:10.1002/(SICI)1097-0320(19990801)36:4<312::AID-CYTO5>3.0.CO;2-V
84. Hagen H, Marzenell P, Jentzsch E, Wenz F, Veldwijk MR, Mokhir A. Aminoferrocene-based prodrugs activated by reactive oxygen species. *J Med Chem* (2012) 55(2):924–34. doi:10.1021/jm2014937
85. Marzenell P, Hagen H, Sellner L, Zenz T, Grinyte R, Pavlov V, et al. Aminoferrocene-based prodrugs and their effects on human normal and cancer as well as bacterial cells. *J Med Chem* (2013) 56(17):6935–44. doi:10.1021/jm400754c
86. Schikora M, Reznikov A, Chaykovskaya L, Sachinska O, Polyakova L, Mokhir A. Activity of aminoferrocene-based prodrugs against prostate cancer. *Bioorg Med Chem Lett* (2015) 25(17):3447–50. doi:10.1016/j.bmcl.2015.07.013
87. Daum S, Chekhun V, Todor I, Lukianova N, Shvets Y, Sellner L, et al. Improved synthesis of N-benzylaminoferrocene-based prodrugs and evaluation of their toxicity and antileukemic activity. *J Med Chem* (2015) 58(4):2015–24. doi:10.1021/jm5019548
88. Kinski E, Marzenell P, Hofer W, Hagen H, Raskatov JA, Knaup KX, et al. 4-Azidobenzyl ferrocenylcarbamate as an anticancer prodrug activated at reductive conditions. *J Inorg Biochem* (2016) 160:218–24. doi:10.1016/j.jinorgbio.2016.02.023
89. Reshetnikov V, Daum S, Mokhir A. Cancer specific, intracellular, reductive activation of anticancer Pt(IV)-prodrugs. *Chem Eur J* (2017) 23(24):5678–81. doi:10.1002/chem.201701192

90. Daum S, Reshetnikov V, Sisa M, Dumych T, Lootsik MD, Bilyy R, et al. Lysosome-targeting amplifiers of reactive oxygen species as anticancer prodrugs. *Angew Chem Int Ed Engl* (2017) 56(49):15545–9. doi:10.1002/anie.201706585
91. Daum S, Babiy S, Konovalova H, Hofer W, Shtemenko A, Shtemenko N, et al. Tuning the structure of aminoferrocene-based anticancer prodrugs to prevent their aggregation in aqueous solution. *J Inorg Biochem* (2018) 178:9–17. doi:10.1016/j.jinorgbio.2017.08.038
92. Kasparkiewicz P, Poreba M, Snipas SJ, Parker H, Winterbourn CC, Salvesen GS, et al. Design of ultrasensitive probes for human neutrophil esterase through hybrid combinatorial substrate library profiling. *Proc Natl Acad Sci U S A* (2014) 111(7):2518–23. doi:10.1073/pnas.1318548111
93. Tintinger GT, Theron AJ, Steel HC, Anderson R. Accelerated calcium influx and hyperactivation of neutrophils in chronic granulomatous disease. *Clin Exp Immunol* (2001) 123:254–63. doi:10.1046/j.1365-2249.2001.01447.x

Conflict of Interest Statement: The authors declare that the research was conducted in the absence of any commercial or financial relationships that could be construed as a potential conflict of interest.

frontiers in Immunology

ORIGINAL RESEARCH
published: 20 November 2017
doi: 10.3389/fimmu.2017.01605

Inhibition of Acute Graft-versus-Host Disease with Retention of Graft-versus-Tumor Effects by Dimethyl Fumarate

Jingjing Han[1,2,3†], Shoubao Ma[1,3†], Huanle Gong[1†], Shuangzhu Liu[2,3], Lei Lei[1,2,3], Bo Hu[1,3], Yang Xu[1,2,3], Haiyan Liu[4] and Depei Wu[1,2,3]**

[1] Institute of Blood and Marrow Transplantation, Soochow University, Suzhou, China, [2] Jiangsu Institute of Hematology, The First Affiliated Hospital of Soochow University, Suzhou, China, [3] Collaborative Innovation Center of Hematology, Soochow University, Suzhou, China, [4] Immunology Programme, Department of Microbiology and Immunology, Life Sciences Institute, National University of Singapore, Singapore, Singapore

OPEN ACCESS

Edited by:
Gabor Csanyi,
Augusta University,
United States

Reviewed by:
Natasha Mireille Rogers,
University of Pittsburgh,
United States
Rui Li,
University of Pennsylvania,
United States

***Correspondence:**
Haiyan Liu
micliuh@nus.edu.sg;
Depei Wu
wudepei@medmail.com.cn

†These authors have contributed equally to this work.

Specialty section:
This article was submitted to Inflammation, a section of the journal Frontiers in Immunology

Received: 25 July 2017
Accepted: 07 November 2017
Published: 20 November 2017

Citation:
Han J, Ma S, Gong H, Liu S, Lei L, Hu B, Xu Y, Liu H and Wu D (2017) Inhibition of Acute Graft-versus-Host Disease with Retention of Graft-versus-Tumor Effects by Dimethyl Fumarate. Front. Immunol. 8:1605. doi: 10.3389/fimmu.2017.01605

Acute graft-versus-host disease (aGVHD) remains a clinical challenge and a major source of morbidity and mortality following allogeneic hematopoietic stem cell transplantation (allo-HSCT). Dimethyl fumarate (DMF), an activator of Nrf2, has been shown to have anti-inflammatory and immunomodulatory properties without significant immunosuppression. We therefore hypothesized that DMF could be potentially harnessed for the treatment of aGVHD with retention of graft-versus-tumor effect. In this study, we showed that DMF significantly inhibited alloreactive T cell responses *in vitro* in mixed lymphocyte reaction assay. Administration of DMF significantly alleviated the severity, histological damage, and the overall mortality of aGVHD in an MHC-mismatched aGVHD model. DMF administration reduced the activation and effector function of donor T cells *in vitro* and *in vivo*. In addition, DMF treatment upregulated antioxidant enzymes heme oxygenase-1 and glutathione S-transferase-α1 expressions. Furthermore, DMF treatment markedly increased the frequencies of Treg cells. Depletion of $CD25^+$ cells in DMF recipients aggravated aGVHD mortality compared with IgG control recipients. DMF could promote Treg cell differentiation in a dose dependent manner by upregulating TGF-β expression *in vitro*. Most importantly, DMF administration preserved graft-versus-leukemia effect after bone marrow transplantation. In conclusion, our findings demonstrated DMF as a promising agent for the prevention of aGVHD after allo-HSCT.

Keywords: acute graft-versus-host disease, graft-versus-leukemia, Nrf2, dimethyl fumarate, Treg cells

INTRODUCTION

Allogeneic hematopoietic stem cell transplantation (allo-HSCT) has become a potential curative treatment for malignant hematological diseases (1). However, the success of an allo-HSCT is frequently limited by life-threatening complications, such as acute graft-versus-host disease (aGVHD) (1). aGVHD is a T cell-mediated disease which is caused by alloreactive donor T cells recognizing and attacking recipient target organs, such as the liver, lungs, intestines and skin (2). Various effector T subsets, Th1, Th2, and Th17, are involved in the pathogenesis of aGVHD (3).

They particularly contribute to the initiation and development and of aGVHD, and have been considered as potential targets for the treatment and prevention of aGVHD (3). Currently, therapy of established aGVHD is still dependent on corticosteroids, despite their limited efficacy and considerable toxicity (2). Therefore, development of novel therapies will be critical for the prevention and treatment of aGVHD.

It is previously noticed that conditioning regimens including high-dose chemotherapy and radiation therapy generally result in the formation of reactive oxygen species (ROS) in allo-HSCT patients, which triggers inflammatory response and tissue injury, and plays an important role in the development of aGVHD (4–6). Therefore, appropriate control of oxidative stress, particularly ROS production, is crucial for effectively managing aGVHD. The transcription factor nuclear factor erythroid 2-related factor 2 (Nrf2) is the "master regulator" of the antioxidant response. Upon exposure to ROS, Nrf2 translocates to the nucleus, binds to antioxidant response elements (AREs) in combination with hundreds of genes located in the promoter region to confer antioxidant protective effects (7). Therefore, it is proposed that Nrf2 activation can scavenge oxygen free radicals produced by conditioning regimens of allo-HSCT, then therefore, inhibit oxidative stress damage to organs and tissues.

Dimethyl fumarate (DMF) was first proposed by a German chemist, Walter Schweckendiek, in 1959, initially for the treatment of psoriasis (8). It was then developed as an oral capsule for the treatment of adults with relapsing forms of multiple sclerosis (MS) (trade name Tecfidera) on March 27, 2013 (9). The pharmacological properties of DMF include the activation of Nrf2-dependent antioxidant response and inhibition of NF-κB pathway (10). On the one hand, DMF activates Nrf2 and induces the expression of many antioxidant defense enzymes, such as the sentinel cytoprotectant heme oxygenase-1 (HO-1), NAD(P)H quinone oxidoreductase-1, and glutathione S-transferase (GST) (11, 12). On the other hand, Nrf2 activation can simultaneously inhibit the NF-κB signaling pathway, and consequently modulate inflammatory cytokines and chemokine production, such as IL-1, IL-2, IL-6, iNOS, IFN-γ, as well as CCL2 and CXCL10 (11, 13, 14). Moreover, DMF could inhibit Th1 polarization and promote Th2 differentiation (15, 16), inhibit the maturation and function of dendritic cells (DCs), as well as the subsequent DC-mediated Th1 and Th17 cell responses (17). Furthermore, DMF also suppresses CCL2-induced chemotaxis of human monocytes (18), inhibits lipopolysaccharide (LPS) induced proinflammatory cytokine production in macrophages (19). Therefore, through a combination of Nrf2 activation and NF-κB signaling inhibition, DMF has been shown to have anti-inflammatory, anti-oxidative, and immunomodulatory properties without significant immunosuppression.

Based on the immunomodulatory effect of DMF, we hypothesize that DMF could have the potential for the treatment of aGVHD with retention of graft-versus-tumor effect after allo-HSCT. In this study, by using murine models of aGVHD and GVL, we showed that Nrf2 activation by DMF treatment significantly reduced aGVHD without impairing GVL effect. The protective role of DMF in aGVHD was associated with increased donor Tregs and reduced T cells infiltration and activation in aGVHD target organs. Our findings suggest that DMF can be used for the prevention and treatment of aGVHD.

MATERIALS AND METHODS

Mice and Leukemia Cell Line

Female C57BL/6 (H-2^b) and BALB/C (H-2^d) mice were purchased from Shanghai Laboratory Animal Center (Shanghai, China). All mice were maintained in a specific pathogen-free room at Animal Facilities of Soochow University. Experiments were carried out and approved according to the guidelines of the animal care and use committee at Soochow University. A20 lymphoma cells were purchased from American Type Culture Collection (Rockville, MD, USA). Cells were cultured at 37°C in a 5% CO_2 incubator in RPMI 1640 culture media supplemented with 10% fetal bovine serum (Biological Industries, Co., Haemek, Israel). For bioluminescent imaging, stable luciferase-expressing A20 cells (A20-luc) were generated in our laboratory.

aGVHD and GVL Models

Murine aGVHD and GVL models were induced as described previously (20, 21). Briefly, BALB/c mice were given lethally 650 cGy (one dose) total body irradiation from X-ray, irradiated BALB/c mice was transplanted with 1×10^7 C57BL/6 bone marrow cells and 5×10^6 C57BL/6 spleen cells *via* the tail vein. DMF (30 mg/kg body weight, Item No. 50744, Sigma-Aldrich, USA) was administrated to the recipient mice by gavage once daily starting from day −3 to day 3 after bone marrow transplantation (BMT). 0.8% methocel (Sigma-Aldrich Fluka, USA) at the same volume was used as vehicle control. For GVL model, 1×10^6 A20-luc cells were added to bone marrow graft as mentioned above, and injected into lethally irradiated BALB/c mice. *In vivo* bioluminescence imaging was performed as described previously (20). Briefly, mice were given an intraperitoneal injection of 200 μg firefly luciferin and then anesthetized and imaged using Xenogen, IVIS 100 Bioluminescent Imaging System (Caliper Life Sciences, Hopkinton, MA, USA). Treg depletion was performed as described previously (22, 23). Briefly, lethally irradiated BALB/c mice were transplanted with 5×10^6 TCD-BM plus 1×10^6 total spleen T cells or CD25-depleted T cells from B6 mice, DMF was administered to these recipients, with vehicle treatment as control. T cell depletion was performed by anti-Thy1.2 mAb (30H12, Biolegend, USA) and rabbit complement (24). T cell purification was performed by using mouse T cell isolation kit (catalog #19851, Stemcell technologies, Vancouver, BC, USA), CD25 depletion was performed by using mouse CD25 regulatory T cell positive selection kit (catalog #18782, Stemcell technologies, USA) according to the manufacturer's protocols. Unlabeled CD25 negative cells were collected. CD25 depletion efficiency was confirmed by FACS. The recipients were monitored daily for survival and every three days for body weight changes and clinical signs of GVHD. The severity of GVHD was assessed using a GVHD scoring system as described previously (20, 21).

Histopathologic Analysis

Fourteen days after transplantation, liver, lung, small intestine and skin were obtained from the transplanted recipients and fixed in 10% formalin. Samples were then embedded in paraffin, sectioned were stained with hematoxylin and eosin. Tissue damage was assessed based on a semiquantitative scoring system as described previously (25, 26).

Mixed Lymphocyte Reaction (MLR) and Cytotoxicity Assay

Mixed lymphocyte reaction assay was performed as described previously (27). Briefly, responder T cells were isolated from spleen of C57BL/6 mice by mouse T cell enrichment kit (StemCell Technologies, Vancouver, BC, Canada). Stimulators were DCs from BALB/c cells. BM-derived DCs were generated and expanded from BALB/c mice with GM-CSF (10 ng/ml) and IL-4 (10 ng/ml) for 7 days. DCs were pretreated with DMF or DMSO for 24 h, then washed twice with PBS. 1×10^4 DCs treated as above were irradiated (30 Gy) and cocultured with 1×10^5 allogeneic T cells in U-bottom microwell plates. 5 days later, tritiated thymidine (^{3}H-TdR, 1 mCi/well) (Shanghai Institute of Physics, Chinese Academy of Sciences) were added to the culture for 16–18 h prior to harvesting and were counted on a β-plate reader (PerkinElmer Instruments, Meriden, CT, USA). Cytokines in the supernatants were collected and measured by ELISA. In some experiments, T cells were labeled with CellTrace CFSE (5 μmol/L, Invitrogen) according to the manufacturer's protocol. The CFSE dilution was examined by flow cytometry. For *ex vivo* MLR, splenocytes from transplanted recipients 14 days after BMT were as responders, irradiated splenocytes from BALB/c mice were as stimulators. Cytotoxicity assays were performed as described previously (20). Splenocytes from transplanted recipients 14 days after BMT were used as killing cells, and their killing ability of A20 targets was measured using CytoTox 96 nonradioactive cytotoxicity assay kit (Promega, Fitchburg, WI, USA).

Cell Preparation and Flow Cytometry

The procedure for isolating single-cell suspensions from spleens has been described previously (21). Antibodies against CD3, CD4, CD8, CD11c, CD25, CD40, CD44, CD69, CD86, PD-1, PD-L1, IFN-γ, H-2k^b, H-2k^d used in this study were all purchased from BioLegend (San Diego, CA, USA). For cell surface staining, cell samples were stained with fluorescent dye-conjugated mAb for 20 min at 4°C in the presence of FcR-Block. For intracellular cytokine staining, cells were stimulated for 5 h with PMA (50 ng/ml) and ionomycin (500 ng/ml) in the presence of brefeldin A (10 μg/ml). Cells were harvested, washed, and stained with surface molecule antibodies in the presence of FcR-Block (eBioscience, San Diego, CA, USA). After the wash, cells were then fixed using CytoFix/CytoPerm buffer (BD Biosciences, USA) and stained with antibodies against intracellular cytokines or isotype control on ice for 30 min. Intracellular staining for FoxP3 was performed by using a Foxp3 staining kit (eBioscience, San Diego, CA, USA). Data were acquired on a NovoCyte Flow cytometer (ACEA Biosciences, San Diego, CA, USA) and analyzed using Flowjo software (FlowJo, Ashland, OR, USA).

ELISA

Blood samples were obtained from recipients 14 days after BMT, serum was separated by centrifugation and was stored at −80°C. Culture supernatants were collected at indicated time by centrifugation. The levels of IL-2, IL-6, IFN-γ, TNF-α, TGF-β were examined by ELISA kit according to the manufacturer's instructions (R&D system, Minneapolis, MN, USA).

Immunofluorescent Microscopy

For examining Nrf2 nuclear translocation, CD3$^+$T cells were isolated from spleen of C57BL/6 mice and activated by plate bound anti-CD3 (5 μg/ml) and anti-CD28 (1 μg/ml) in the presence of DMF or DMSO for 3 h. The cells were harvested and fixed in 4% paraformaldehyde for 15 min, then permeabilized with 0.2% Triton X100 for 10 min, and blocked with 2% BSA for 30 min. Sample were incubated overnight with an anti-Nrf2 antibody (sc-13032, Santa Cruz, CA, USA) in 0.5% BSA. After three washes with PBS, cells were stained with Alexa Fluor 488 goat antirabbit IgG (Molecular Probes, USA). Cell nuclei were stained with DAPI. The fluorescent images were captured with the Leica DMi8 confocal microscope (Leica, Wetzlar, Germany).

Real-time PCR

Total RNA were extracted with TRIzol reagent (Takara, Japan) from aGVHD targets organs according to the manufacturer's instructions. Transcription levels of Nrf2, Keap1, HO-1, GST-α1, IL-1β, IL-2, IL-6, IFN-γ genes were analyzed by real-time PCR using SYBR Green Master Mix (Applied Biosystems, Warrington, UK). The primers used were: Nrf2, Forward 5′-TAGATGACCATGAGTCGCTTGC-3′, reverse 5′-GCCAAACTTGCTCCATGTCC-3′; keap1, forward 5′-TGCCCCTGTGGTCAAAGTG-3′, reverse 5′-GGTTCGGTTACCGTCCTGC-3′; HO-1, forward 5′-AAGCCGAGAATGCTGAGTTCA-3′, reverse 5′-GCCGTGTAGATATGGTACAAGGA-3′; GST-α1, forward 5′-AAGCCCGTGCTTCACTACTTC-3′, reverse 5′-GGGCACTTGGTCAAACATCAAA-3′; β-actin, forward 5′-ATCTGGCACCACACCTTC-3′, reverse 5′-AGCCAGGTCCAGACGCA-3′. The relative expression of the gene was quantified using the comparative $2^{-\Delta\Delta Ct}$ method relative to the housekeeping gene β-actin.

ROS Detection

CD3$^+$ T cells were isolated from spleen of C57BL/6 mice and activated by plate bound anti-CD3 (5 μg/ml) and anti-CD28 (1 μg/ml) in the presence of DMF or DMSO for 12 h. ROS levels were examined by Reactive Oxygen Species Assay Kit according to the manufacturer's instructions (Beyotime, Shanghai, China). Briefly, cells were harvested and washed three times using RPMI-1640 media, 2′-7′-dichlorofluoresci1n diacetate was added at a final concentration of 10 μM to the cells. After a 20-min incubation at 37°C, cells were washed and resuspended in PBS. Data were acquired on a NovoCyte Flow cytometer and analyzed using Flowjo software.

Cell Proliferation and Apoptosis

For cell proliferation, 2×10^4 A20 cells were seeded into 96-well plates and treated with DMF or DMSO for 48 h. Then 10 μl of CCK-8 solution was added to each well and incubated for additional 2 h, the absorbance was measured at 450 nm. Cell apoptosis was evaluated using a Annexin V Apoptosis Detection Kit (eBioscience, San Diego, CA, USA) according to the manufacturer's instructions. Briefly, 48 h after DMF treatment, the cells were washed with PBS and resuspended in 500 μl binding buffer with 5 μl annexin V and 10 μl propidium iodide. Data were acquired by flow cytometry and analyzed using Flowjo software.

Statistical Analysis

Survival data were analyzed by log-rank test and Kaplan-Meier survival curves were generated using GraphPad Prism version 5 (GraphPad 6.0, San Diego, CA, USA). The data were expressed as the mean ± SD. Two-tailed Student's *t*-test was used for statistical comparison between two groups. One-way ANOVA with Dunnet's test was used for multiple comparisons. The significance levels are marked $^*P < 0.05$; $^{**}P < 0.01$; $^{***}P < 0.001$.

RESULTS

DMF Inhibits Alloreactive T Cell Responses *In Vitro*

Dimethyl fumarate has been demonstrated to potently inhibit NF-κB activity while promote Nrf2 activation. Therefore, we investigated the impact of DMF on alloreactive T cell responses in MLR assays. BMDCs from BALB/c mice were cultured with allogeneic splenic $CD3^+$T cells purified from C57BL/6 mice, in the presence of the Nrf2 activator DMF (**Figure 1A**). The results showed that DMF significantly inhibited the proliferation of alloreactive T cells in a dose-dependent manner on day 5 determined by ^{3}H-TdR and CFSE dye dilution (**Figures 1B,C**). Consistent with the T cell proliferation results, cytokine analysis showed that proinflammatory cytokines IL-2, IL-6, IFN-γ, and TNF-α production were significantly decreased in

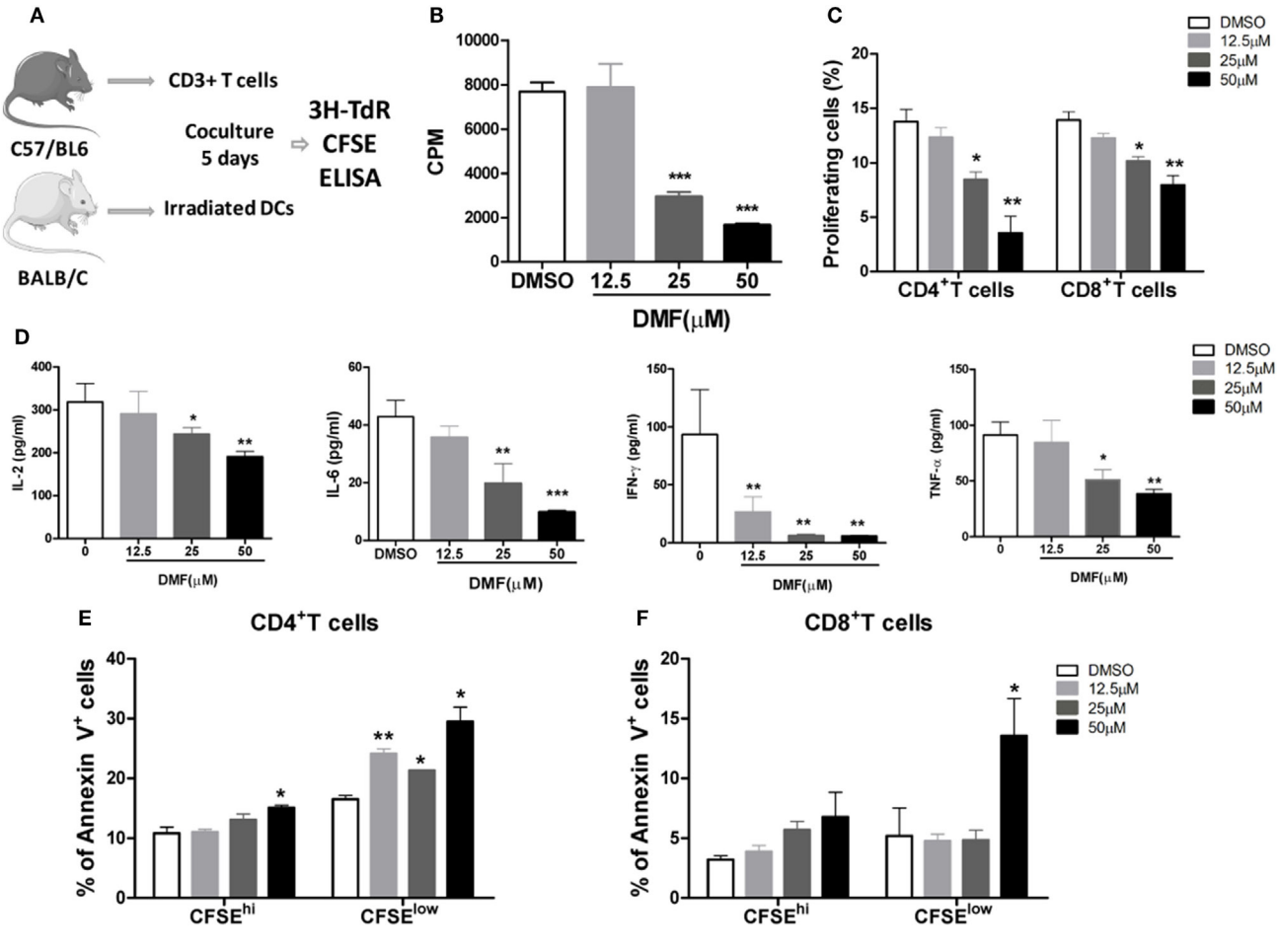

FIGURE 1 | Dimethyl fumarate (DMF) inhibits alloreactive T cell responses *in vitro*. BMDCs from BALB/c mice were cocultured with allogeneic splenic $CD3^+$ T cells purified from C57BL/6 mice, in the presence of the DMF **(A)**, 5 days later, cell proliferation was evaluated by ^{3}H-TdR **(B)** or CFSE **(C)**. The levels of proinflammatory cytokines IL-2, IL-6, IFN-γ, and TNF-α in the supernatants were examined by ELISA **(D)**. Cell apoptosis of alloreactive $CD4^+$ T cells and $CD8^+$ T cells was examined by Annexin V staining **(E,F)**. Data shown are mean ± SD. $^*P < 0.05$; $^{**}P < 0.01$; $^{***}P < 0.001$, compared with DMSO group (ANOVA with Dunnett's test).

a dose-dependent manner upon DMF treatment (**Figure 1D**). In addition, cell apoptosis assay showed that the apoptosis of alloreactive $CD4^+$ T cells were significantly increased in the presence of DMF (**Figures 1E,F**). More interesting, the apoptotic cells were mainly $CFSE^{low}$ populations. To address whether DMF has a direct effect on T cells, we performed a T cell activation assay with anti-CD3/CD28 stimulation, the result showed that DMF could significantly inhibit T cells proliferation directly (Figure S1A in Supplementary Material). Additionally, we examined the effect of DMF on antigen presenting cells (APC). We cultured bone marrow DCs and then treated with DMF. The data showed that DMF had no effect on DC maturation, however, when DCs were preactivated by LPS, DMF could reduce CD80, CD86, and CD40 expression in a dose-dependent manner (Figure S1B–D in Supplementary Material). Similar results were observed in IL-6 and TNF-α expression (Figure S1E,F in Supplementary Material). Taken together, the results demonstrated that DMF could inhibit alloreactive T responses by suppressing cell proliferation and inducing cell apoptosis *in vitro,* through both direct effects on T cells and indirect effects on DCs.

DMF Administration Alleviates aGVHD in Mice

To determine the possible role of Nrf2 activation in aGVHD, we first examined the Nrf2 expression after allo-HSCT. We observed that Nrf2 mRNA levels were significantly decreased in the spleen, liver, lung and intestine of allogeneic BMT mice compared to those of syngeneic control animals (**Figure 2A**),

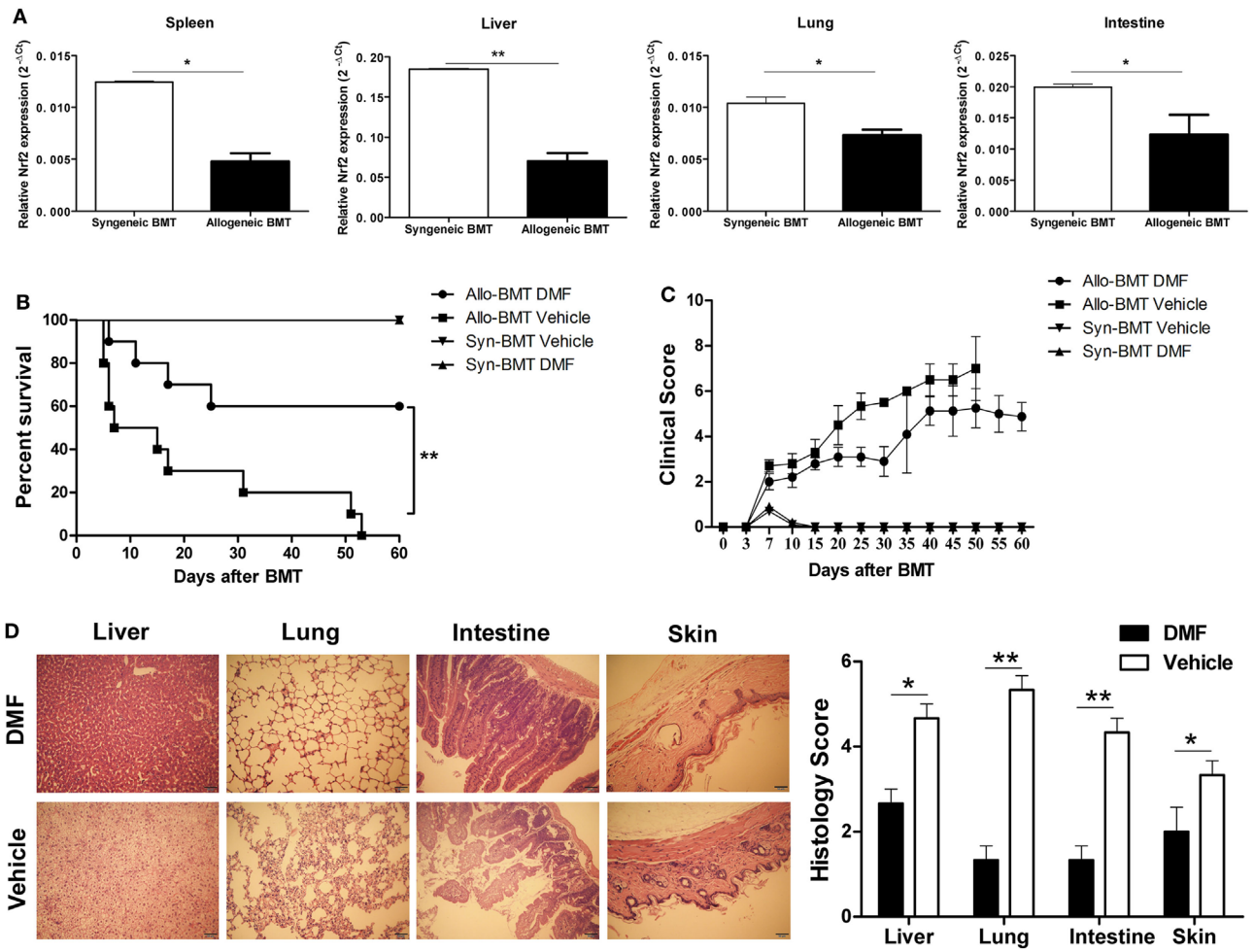

FIGURE 2 | Dimethyl fumarate (DMF) administration alleviates acute graft-versus-host disease (aGVHD) in mice. Irradiated BALB/c mice was transplanted with 1×10^7 C57BL/6 bone marrow cells and 5×10^6 C57BL/6 spleen cells (allogeneic) or 1×10^7 BALB/c bone marrow cells and 5×10^6 BALB/c spleen cells (syngeneic). The mRNA level of Nrf2 in spleen, liver, lung and intestine of allogeneic or syngeneic bone marrow transplantation (BMT) mice was examined by qRT-PCR **(A)**. DMF (30 mg/kg body weight) was administrated to the allogeneic recipient mice by gavage once daily starting from day −3 to day 3 after BMT. DMF treatment significantly prolongs survival (log rank, $P = 0.005$) **(B)** and reduced aGVHD severity **(C)** compared with vehicle control. Histological analysis revealed that there was decreased pathological damage in the liver, lung, intestine and skin of recipients receiving DMF 14 days after BMT **(D)**. Survival data were analyzed by log-rank test and Kaplan-Meier survival curves were generated using GraphPad Prism. Data shown are mean ± SD. $^*P < 0.05$; $^{**}P < 0.01$; $^{***}P < 0.001$, compared with vehicle group (Student's *t*-test).

suggesting that Nrf2 suppression could be involved in the pathogenesis of aGVHD. We then evaluated the potential impact of DMF on the aGVHD development *in vivo* by using a murine aGVHD model. As shown in **Figure 2B**, DMF treatment significantly prolonged survival (log rank, $P = 0.005$) of the hosts following allo-HSCT (**Figure 2B**). In addition, aGVHD scores were reduced in DMF-treated mice compared with vehicle control recipients (**Figure 2C**). Histological analysis revealed that there was decreased pathological damage in the liver, lung, intestine and skin of recipients receiving DMF 14 days after allo-HSCT (**Figure 2D**). Similar protective effect was observed when the dose of DMF was changed to 60 mg/kg from day −3 to day +3 post-allo-HSCT (data not shown). Moreover, DMF administration did not affect donor chimerism 14 days posttransplant (data not shown). Therefore, these data suggested that Nrf2 activation by DMF treatment *in vivo* significantly improved aGVHD outcomes as evidenced by prolonged survival and reduced aGVHD scores following allo-HSCT.

DMF Administration Reduces Activation and Effector Function of Donor T Cells and Upregulates Antioxidant Response

To investigate the potential mechanisms responsible for reduced aGVHD severity by DMF treatment, we analyzed the alloreactive T cell responses *in vivo*. On day 14 after allo-HSCT, decreased infiltration of donor $CD3^+$ T and $CD4^+$ T cells was observed in spleen of DMF-treated recipients compared with vehicle control recipients (**Figure 3A**). The *ex vivo* MLR assay further demonstrated that DMF treatment significantly reduced donor T cell alloreactivity (**Figure 3B**). In addition, both donor $CD4^+$ T and $CD8^+$ T cells had a reduced activation phenotype indicated by CD69 levels in the hosts treated with DMF (**Figure 3C**). Furthermore, purified $CD4^+$ T cells were activated *in vitro* by anti-CD3/CD28, and DMF treatment significantly inhibited T cell activation and downregulated CD69, CD44, as well as PD-1 expressions. The CD25 levels, however, were slightly upregulated by DMF treatment (**Figure 3D**). Intracellular staining revealed that the frequencies of IFN-γ-producing donor $CD4^+$ T and $CD8^+$ T cells in spleen were significantly decreased in recipients given DMF (**Figure 3E**). Analysis of serum samples on day 14 following allo-HSCT showed that the levels of proinflammatory cytokines IL-6, IFN-γ as well as TNF-α were significantly downregulated in DMF-treated recipients compared with vehicle control recipients (**Figure 3F**).

Since DMF is a potent activator of Nrf2 and can induce the Nrf2-dependent antioxidant response, we then examined the ROS production and antioxidant genes expression. We found that DMF could significantly inhibit ROS production by activated T cells in a dose-dependent manner *in vitro* (**Figure 3G**). Moreover, the Nrf2 levels and antioxidant defense enzymes HO-1 and GST-α1 expressions were upregulated in recipients treated with DMF (**Figure 3H**). We then explored the effect of DMF on nuclear translocation of Nrf2, which has been demonstrated as a major mechanism of function for DMF. We observed a dose-dependent effect of DMF on nuclear translocation of Nrf2 in the $CD3^+$ T cells by immunofluorescent staining (**Figure 3I**). Taken together, these results suggested that DMF could inhibit donor T cell alloreactivity, and production of proinflammatory cytokines, as well as upregulate antioxidant enzymes, which led to the alleviation of aGVHD severity.

DMF Inhibits aGVHD by Promoting Treg Cells

Dimethyl fumarate upregulated CD25 expression on CD4 T cells, suggesting that DMF may promote the generation of Treg cells. We examined the frequencies and absolute numbers of $CD4^+Foxp3^+$ Treg cells in spleen on day 14 after allo-HSCT. As shown in **Figures 4A,B**, the frequencies, as well as the numbers of Treg cells in spleen were significantly increased in DMF-treated compared with vehicle control recipients, suggesting that DMF could increase Treg cells *in vivo*. *In vitro* MLR assay showed that DMF promoted Treg cell differentiation in a dose-dependent manner (**Figure 4C**). To further confirm that the effect of DMF on aGVHD was partially dependent on the promotion of Treg cells, mice were injected with anti-CD25 antibody to deplete Treg cells *in vivo*. As shown in **Figure 4D**, depletion of $CD25^+$ cells in DMF recipients aggravated aGVHD mortality compared with IgG control recipients, while it had no effect on vehicle treatment recipients. TGF-β has been known to promote Treg generation, we therefore examined the TGF-β levels in serum of GVHD mice and in MLR culture supernatants. Date shown that TGF-β was increased in DMF recipients (**Figure 4E**) and upregulated upon DMF treatment *in vitro* (**Figure 4F**). Therefore, these results suggested that the protective effect of DMF treatment on aGVHD was at least partially dependent on the promotion of Treg cells.

DMF Administration Preserves GVL Effect after allo-HSCT

To evaluate the impact of DMF administration on GVL effects, aGVHD mice were challenged with A20-luc leukemia cells post-allo-HSCT. As shown in **Figure 5A**, mice transplanted with allo-BM alone plus A20-luc leukemia cells all died from leukemia within 40 days after transplant, regardless of whether DMF was administered. It has been reported that DMF could inhibit cell proliferation and induce apoptosis in a number of malignant cell lines including myeloid and lymphoid leukemia cell lines. However, the results in **Figure 5A** suggested that DMF may not directly affect A20 cell growth *in vivo*. DMF administration to mice receiving allo-BM and splenocytes, plus A20-luc showed prolonged survival compared with mice receiving vehicle control (**Figure 5B**), and low tumor burden was observed in DMF recipients as shown in bioluminescence imaging (**Figure 5C**), indicating the presence of GVL effect in DMF treated mice. The cell proliferation and apoptosis assay showed that low concentrations of DMF could not affect tumor growth and apoptosis *in vitro*, suggesting that DMF treatment inhibits A20 cell growth only at high concentrations, which may not be reached *in vivo* (**Figures 5D,E**). We also observed that donor T cells from DMF-treated recipients showed comparable, or even increased CTL killing

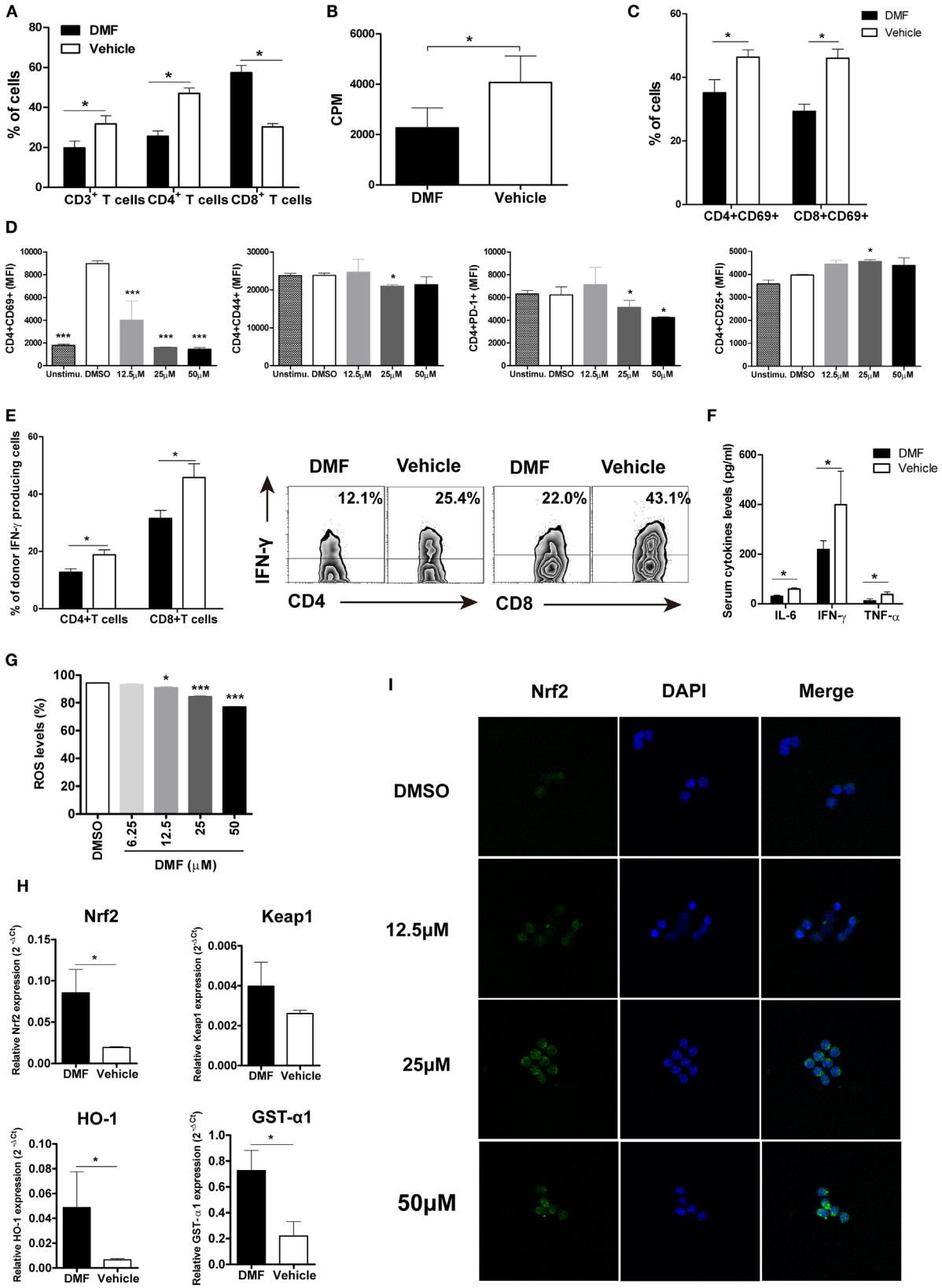

FIGURE 3 | Continued

FIGURE 3 | Continued
Dimethyl fumarate (DMF) administration reduces activation and effector function of donor T cells and upregulates antioxidant response. 14 days after bone marrow transplantation (BMT), the percentages of donor T cells in spleen were analyzed by FACS **(A)**. *Ex vivo* mixed lymphocyte reaction (MLR) was performed by coculturing splenocytes from transplanted recipients 14 days after BMT with irradiated splenocytes from BALB/c mice. Cell proliferation was evaluated by ^{3}H-TdR **(B)**. CD69 expression on CD4^{+} and CD8^{+}T cells of recipients mice 14 days after BMT was examined by FACS **(C)**. Purified CD3^{+}T cells were activated by anti-CD3/CD28 *in vitro* and treated with DMF. The activation markers CD69, CD44, CD25, and costimulatory molecule PD-1 levels were analyzed 24 h after treatment **(D)**. IFN-γ production by CD4^{+} and CD8^{+}T cells of recipients mice 14 days after BMT was examined by Intracellular staining **(E)**. Serum levels of proinflammatory cytokines IL-6, IFN-γ, and TNF-α were examined by ELISA **(F)**. Purified CD3^{+}T were activated by anti-CD3/CD28 *in vitro* and treated with DMF for 12 h, reactive oxygen species (ROS) levels were examined by Reactive Oxygen Species Assay Kit **(G)**. The Nrf2, keap 1, and antioxidant defense enzymes HO-1 and GST-α1 mRNA expressions in the spleen were examined by qRT-PCR 14 days after BMT **(H)**. **(I)** CD3^{+}T cells were isolated from spleen of C57BL/6 mice and activated by plate bound anti-CD3 (5 μg/ml) and anti-CD28 (1 μg/ml) in the presence of DMF or DMSO for 3 h. Nrf2 nuclear translocation was exmianed by immunofluorescent assay. Data shown are mean ± SD. *P < 0.05; **P < 0.01; ***P < 0.001, compared with vehicle group (Student's t-test), or DMSO group (ANOVA with Dunnett's test).

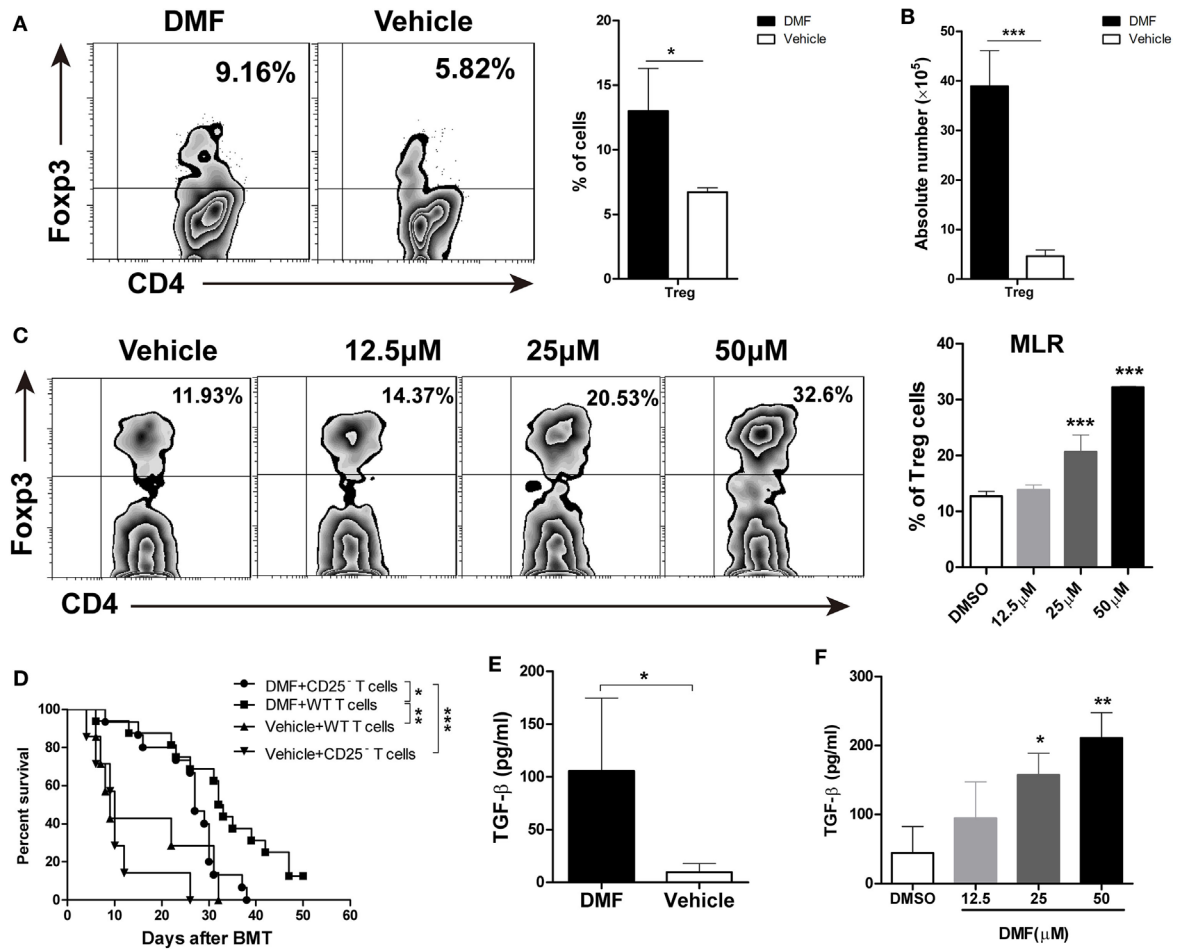

FIGURE 4 | Dimethyl fumarate (DMF) inhibits acute graft-versus-host disease (aGVHD) by promoting Treg cells *in vitro* and *in vivo*. The frequencies and absolute number of CD4^{+}Foxp3^{+} Treg cells in spleen on day 14 after bone marrow transplantation (BMT) were examined by FACS **(A,B)**. Purified CD4^{+} T were activated by anti-CD3/CD28 in the presence of TGF-β (2 ng/ml) and IL-2 (50 U/ml) to induce Treg cells development *in vitro*, The effect of DMF on Treg cells differentiation was measured by FACS 4 days after Treg polarization **(C)**. Lethally irradiated BALB/c mice were transplanted with 5 × 10^{6} TCD-BM plus 1 × 10^{6} total spleen T cells or CD25-depleted T cells from B6 mice. Depletion of CD25^{+} cells in DMF recipients aggravated aGVHD mortality compared with IgG control recipients **(D)**. TGF-β levels in serum of aGVHD mice and MLR culture supernatants were measured by qRT-PCR **(E,F)**. Survival data were analyzed by log-rank test and Kaplan-Meier survival curves were generated using GraphPad Prism. Data shown are mean ± SD. *P < 0.05; **P < 0.01; ***P < 0.001, compared with DMSO group or vehicle group (Student's t-test), or DMSO group (ANOVA with Dunnett's test).

activity against A20 leukemia cells compared to vehicle controls (**Figure 5F**). These findings further supported the observations that DMF treatment could preserve GVL effect after allo-HSCT.

DISCUSSION

Dimethyl fumarate has been shown to have potent anti-inflammatory or immunomodulatory properties without

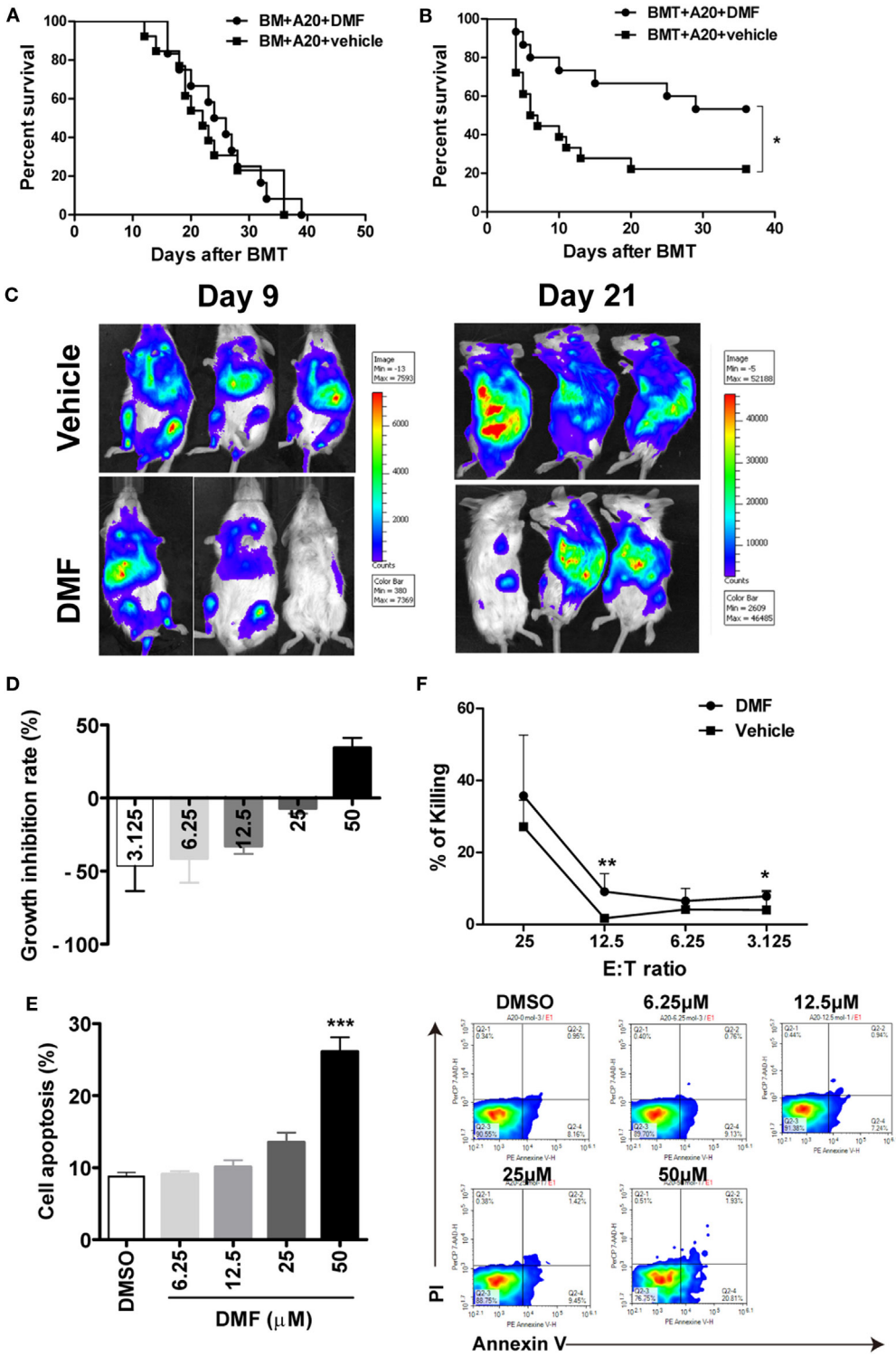

FIGURE 5 | Dimethyl fumarate (DMF) administration preserves GVL effect after bone marrow transplantation (BMT). Mice were transplated with BM or BM and spleen plus A20-luc to establish GVL model. Mice transplanted with allo-BM alone plus A20-luc leukemia cells all died from leukemia regardless of whether DMF was administered **(A)**. DMF administration to mice receiving allo-BMT plus A20-luc showed prolonged survival time and reduced tumor burden compared with mice receiving vehicle control **(B,C)**. The effects of DMF on A20 cell proliferation **(D)** and apoptosis **(E)** were examined by CCK-8 assay and Annexin V/PI staining. Splenocytes from transplanted recipients 14 days after BMT were used as killing cells, and their killing ability of A20 targets was measured using CytoTox 96 nonradioactive cytotoxicity assay kit **(F)**. Survival data were analyzed by log-rank test and Kaplan–Meier survival curves were generated using GraphPad Prism. Data shown are mean ± SD. $^{*}P < 0.05$; $^{**}P < 0.01$, compared with DMSO group (ANOVA with Dunnett's test) or vehicle group (Student's *t*-test).

significant immunosuppression. It is effective in treating immune-mediated diseases, including psoriasis, MS as well as colitis (28–30). aGVHD is an immune-mediated disease which resulting from the activation of donor T lymphocytes by host antigen-presenting cell (APC) (2). During aGVHD, donor T cells activated by APCs express multiple immune effector molecules, such as fas ligand, perforin, IL-1β, IFN-γ, and TNF-α, leading to tissue damage (31, 32). We therefore hypothesize that DMF may be a new promising drug for the treatment of aGVHD.

In the present study, we first evaluated the effect of DMF on alloreactive T cell responses in MLR assays. We found that DMF significantly inhibited the proliferation and proinflammatory cytokine production of alloreactive T cells in a dose-dependent manner. In addition, DMF could also induce cell apoptosis of activated alloreactive T cells *in vitro*. In agreement with our results, Joachim et al., showed that DMF could inhibit lymphocyte proliferation and inflammatory cytokine secretion in human peripheral blood mononuclear cells (PBMCs) stimulated with LPS or lectin phytohemagglutinin or in human MLR assays (11). In addition, DMF could block IFN-γ- and LPS-induced Th1 chemokine (CXCL9 and CXCL10) production in a dose-dependent manner in PBMCs (33). DMF has also been shown to decrease adhesion molecule expression, such as CD25, HLA-DR and cutaneous lymphocyte-associated antigens (34). In our study, we also observed that DMF treatment significantly inhibited T cell activation and downregulated CD69, CD44, as well as PD-1 expressions, and IFN-γ production by donor $CD4^+$ T and $CD8^+$ T cells in spleen.

The maximum tolerated dose of DMF in human patients is 240 mg taken two to three times daily by oral for treatment of psoriasis (35), and MS (36). In preclinical studies, the effective and safe dose of DMF was 30 mg/kg in experimental autoimmune encephalomyelitis (37), experimental colitis (30) and tumor studies (38) *in vivo*. Therefore, based on the previous animal studies, we chose 30 mg/kg DMF in this study. We found, for the first time, that administration of DMF significantly ameliorated aGVHD in an MHC-mismatched BMT model. Interestingly, the administration window of DMF for treatment of aGVHD was −3 to +3 days post-BMT in our study, while the protective effect of DMF on aGVHD was not as effective when DMF was given from day 0 to day 7 (Data not shown), suggesting that DMF could regulate the sensitivity of the GVHD target organ to radiation induced injury. Administration of DMF pre-transplant is necessary to exert its protective effect. However, this notion still need further investigation.

Dimethyl fumarate protects the host from aGVHD may be *via* multiple mechanisms due to its dual role in Nrf2 pathway and NF-κB signaling. DMF treatment of T cells has previously been shown to decrease Th1 cytokine production, including IL-12, IFN-γ, TNF-α, and IL-17, and promote the expression of Th2 cytokines, such as IL-4 and IL-10 (10, 16, 39). In addition, DMF could also inhibit DCs maturation and subsequent DC mediated T cell responses (17). However, DMF metabolite monomethyl fumarate (MMF) can enhance $CD56^+$ NK cells function by the upregulation of CD107a and granzyme B (40). In our murine aGVHD model, we found that DMF treatment reduced the proliferation and activation of donor T cells in spleen. Similarly, the IFN-γ expression by donor T cells, as well as the serum level of proinflammatory cytokines, was significantly decreased. Besides immune regulation, DMF also activates the Nrf2-dependent ARE pathway. We found that DMF could significantly inhibit ROS production in a dose-dependent manner in activated T cells. Moreover, the Nrf2 levels and antioxidant defense enzymes HO-1 and GST-α1 expressions were both unregulated in recipients given DMF. The ARE activation is involved in the induction of multiple downstream responses that protect cells from intracellular oxidative stress and injury, as well as modulate c cytokine and chemokine production (41). Therefore, our results suggest that DMF ameliorates aGVHD by modulating donor T cell activation and effector function, as well as upregulating antioxidant enzymes.

In our study, the activation makers on donor T cells were all downregulated upon DMF treatment except CD25. On the contrary, DMF significantly increased CD25 expression on activated T cells. Previous study showed that DMF promoted IL-2 secretion during human MLR (11). However, there is no evidence showing that DMF can regulate Treg cell development. We found that Treg cells were significantly increased in DMF-treated recipients compared with vehicle control in spleen on day 14 after allo-HSCT, accompanied by increased serum levels of TGF-β. *In vitro* MLR assay showed that DMF could promote Treg cell development in a dose-dependent manner. In addition, the depletion of Tregs in DMF recipients aggravated aGVHD mortality compared with IgG control recipients. Thus, promotion of Tregs cell development may be one of the mechanism that DMF inhibits aGVHD. Further studies are needed to explore the molecular mechanism of DMF in regulating Tregs development and function.

Alloreactive T-cells mediating aGVHD are also important for GVL activity, the ultimate goal of allo-HSCT is to separate GVHD from GVL effect. It has been suggested that GVL effect is primarily mediated by donor $CD8^+$ T cells and NK cells, whereas $CD4^+$ T cells mainly contribute to the development of aGVHD. In our study, we found that DMF administration did not weaken the GVL effect. Meanwhile, we did not observe inhibition of leukemia cell growth *in vitro* and *in vivo* by DMF treatment, suggesting that the antileukemia effect of DMF may be associated with its effect in maintaining cytolytic activity of donor $CD8^+$ T cells and NK cells. To support this notion, cytotoxicity assay showed that CTLs from DMF-treated recipients has comparable, or even increased killing activity against leukemia cells compared to vehicle controls. Previous study has shown that DMF metabolite MMF can augment the NK cell lysis of K562 and RAJI leukemia cells through CD107a and Granzyme B (40). In addition, our results found that $CD8^+$T cell numbers were not decreased upon DMF treatment, on the contrary, its proportions were significantly increased, which could be the reason for preserved GVL effects. Interestingly, it was reported that DMF treatment resulted in a preferential loss of $CD8^+$ T cells compared with $CD4^+$ T cells in patients with MS (42–46), while the proportions of Treg cells, circulating CD56(hi) NK cells, monocytes, and DCs were unaffected (43, 47). Although the underlying mechanisms remain largely

unknown, recent data suggest that it maybe due to the differential susceptibility of distinct cell subsets to DMF-induced apoptosis (39). However, the differential effects of DMF on various immune cell subsets in different disease models need further investigation.

In conclusion, we provide evidence for the first time that the Nrf2 activator DMF reduces aGVHD with retention of GVL effect. DMF treatment promoted donor Treg development and reduced alloreactive T cells response, as well as upregulated antioxidant enzyme expressions. Our findings demonstrated DMF as a promising agent for the prevention of aGVHD after allo-HSCT.

ETHICS STATEMENT

All animal experiments were carried out and approved according to the guidelines of the animal care and use committee at Soochow University.

AUTHOR CONTRIBUTIONS

HL and DW designed the study; SM, JH, and HG performed the experiments; SL, LL, BH, and YX contributed to the experiments; SM analyzed the data; and SM, HL, and DW wrote the manuscript. All authors have discussed and revised the manuscript.

FUNDING

This work has been supported by the grants from National Natural Science Foundation of China (81400145), Natural Science Foundation of Jiangsu Province (BK201500352), China Postdoctoral Science Foundation (7131702415). The Priority Academic Program Development of Jiangsu Higher Education Institutions (PAPD). The Innovation Capability Development Project of Jiangsu Province (no. BM2015004). The National Key Research And Development Program (2016YFC0902800).

SUPPLEMENTARY MATERIAL

The Supplementary Material for this article can be found online at http://www.frontiersin.org/article/10.3389/fimmu.2017.01605/full#supplementary-material.

FIGURE S1 | DMF inhibited T cells proliferation and DCs maturation *in vitro*. $CD3^+$T cells were isolated from spleen of C57BL/6 mice and activated by plate bound anti-CD3 (5 μg/ml) and anti-CD28 (1 μg/ml) in the presence of DMF or DMSO for 48 h. cell proliferation was measured by ^{3}H-TdR **(A)**, Data shown are mean ± SD. ***$P < 0.001$, compared with DMSO group (ANOVA with Dunnett's test). BM-derived DCs were generated and expanded from BALB/c mice with GM-CSF (10 ng/ml) and IL-4 (10 ng/ml). DCs were treated with DMF or DMSO for 24 h in the present or absence of LPS (1 μg/ml), CD80, CD86, and CD40 on the DCs were examined by FACS **(B–D)**. Cytokines IL-6, TNF-α, IFN-γ in the supernatants were collected and measured by ELISA **(E–G)**. Data shown are mean ± SD. ***$P < 0.001$ compared with LPS group (ANOVA with Dunnett's test).

REFERENCES

1. Mohty B, Mohty M. Long-term complications and side effects after allogeneic hematopoietic stem cell transplantation: an update. *Blood Cancer J* (2011) 1(4):e16. doi:10.1038/bcj.2011.14
2. Choi SW, Reddy P. Current and emerging strategies for the prevention of graft-versus-host disease. *Nat Rev Clin Oncol* (2014) 11(9):536–47. doi:10.1038/nrclinonc.2014.102
3. Coghill JM, Sarantopoulos S, Moran TP, Murphy WJ, Blazar BR, Serody JS. Effector CD4+ T cells, the cytokines they generate, and GVHD: something old and something new. *Blood* (2011) 117(12):3268–76. doi:10.1182/blood-2010-12-290403
4. Cetin T, Arpaci F, Yilmaz MI, Saglam K, Ozturk B, Komurcu S, et al. Oxidative stress in patients undergoing high-dose chemotherapy plus peripheral blood stem cell transplantation. *Biol Trace Elem Res* (2004) 97(3):237–47. doi:10.1385/BTER:97:3:237
5. Shen H, Yu H, Liang PH, Cheng H, XuFeng R, Yuan Y, et al. An acute negative bystander effect of gamma-irradiated recipients on transplanted hematopoietic stem cells. *Blood* (2012) 119(15):3629–37. doi:10.1182/blood-2011-08-373621
6. Tkachev V, Goodell S, Opipari AW, Hao LY, Franchi L, Glick GD, et al. Programmed death-1 controls T cell survival by regulating oxidative metabolism. *J Immunol* (2015) 194(12):5789–800. doi:10.4049/jimmunol.1402180
7. Li W, Kong AN. Molecular mechanisms of Nrf2-mediated antioxidant response. *Mol Carcinog* (2009) 48(2):91–104. doi:10.1002/mc.20465
8. Nieboer C, de Hoop D, van Loenen AC, Langendijk PN, van Dijk E. Systemic therapy with fumaric acid derivates: new possibilities in the treatment of psoriasis. *J Am Acad Dermatol* (1989) 20(4):601–8. doi:10.1016/S0190-9622(89)70071-2
9. US Food and Drug Administration. *FDA Approves New Multiple Sclerosis Treatment: Tecfidera*. Silver Spring, MD: FDA gov (2013).
10. Gill AJ, Kolson DL. Dimethyl fumarate modulation of immune and antioxidant responses: application to HIV therapy. *Crit Rev Immunol* (2013) 33(4):307–59. doi:10.1615/CritRevImmunol.2013007247
11. Lehmann JC, Listopad JJ, Rentzsch CU, Igney FH, von Bonin A, Hennekes HH, et al. Dimethylfumarate induces immunosuppression via glutathione depletion and subsequent induction of heme oxygenase 1. *J Invest Dermatol* (2007) 127(4):835–45. doi:10.1038/sj.jid.5700686
12. Scannevin RH, Chollate S, Jung MY, Shackett M, Patel H, Bista P, et al. Fumarates promote cytoprotection of central nervous system cells against oxidative stress via the nuclear factor (erythroid-derived 2)-like 2 pathway. *J Pharmacol Exp Ther* (2012) 341(1):274–84. doi:10.1124/jpet.111.190132
13. Gillard GO, Collette B, Anderson J, Chao J, Scannevin RH, Huss DJ, et al. DMF, but not other fumarates, inhibits NF-kappaB activity in vitro in an Nrf2-independent manner. *J Neuroimmunol* (2015) 283:74–85. doi:10.1016/j.jneuroim.2015.04.006
14. Liu X, Zhou W, Zhang X, Lu P, Du Q, Tao L, et al. Dimethyl fumarate ameliorates dextran sulfate sodium-induced murine experimental colitis by activating Nrf2 and suppressing NLRP3 inflammasome activation. *Biochem Pharmacol* (2016) 112:37–49. doi:10.1016/j.bcp.2016.05.002
15. Ockenfels HM, Schultewolter T, Ockenfels G, Funk R, Goos M. The antipsoriatic agent dimethylfumarate immunomodulates T-cell cytokine secretion and inhibits cytokines of the psoriatic cytokine network. *Br J Dermatol* (1998) 139(3):390–5. doi:10.1046/j.1365-2133.1998.02400.x
16. Ghoreschi K, Bruck J, Kellerer C, Deng C, Peng H, Rothfuss O, et al. Fumarates improve psoriasis and multiple sclerosis by inducing type II dendritic cells. *J Exp Med* (2011) 208(11):2291–303. doi:10.1084/jem.20100977
17. Peng H, Guerau-de-Arellano M, Mehta VB, Yang Y, Huss DJ, Papenfuss TL, et al. Dimethyl fumarate inhibits dendritic cell maturation via nuclear factor kappaB (NF-kappaB) and extracellular signal-regulated kinase 1 and 2 (ERK1/2) and mitogen stress-activated kinase 1 (MSK1) signaling. *J Biol Chem* (2012) 287(33):28017–26. doi:10.1074/jbc.M112.383380
18. Cross SA, Cook DR, Chi AW, Vance PJ, Kolson LL, Wong BJ, et al. Dimethyl fumarate, an immune modulator and inducer of the antioxidant response, suppresses HIV replication and macrophage-mediated neurotoxicity: a novel candidate for HIV neuroprotection. *J Immunol* (2011) 187(10):5015–25. doi:10.4049/jimmunol.1101868

19. McGuire VA, Ruiz-Zorrilla Diez T, Emmerich CH, Strickson S, Ritorto MS, Sutavani RV, et al. Dimethyl fumarate blocks pro-inflammatory cytokine production via inhibition of TLR induced M1 and K63 ubiquitin chain formation. *Sci Rep* (2016) 6:31159. doi:10.1038/srep31159
20. Liu Y, Wu Y, Wang Y, Cai Y, Hu B, Bao G, et al. IL-35 mitigates murine acute graft-versus-host disease with retention of graft-versus-leukemia effects. *Leukemia* (2015) 29(4):939–46. doi:10.1038/leu.2014.310
21. Cai Y, Ma S, Liu Y, Gong H, Cheng Q, Hu B, et al. Adoptively transferred donor IL-17-producing CD4+ T cells augment, but IL-17 alleviates, acute graft-versus-host disease. *Cell Mol Immunol* (2016). doi:10.1038/cmi.2016.37
22. Saha A, O'Connor RS, Thangavelu G, Lovitch SB, Dandamudi DB, Wilson CB, et al. Programmed death ligand-1 expression on donor T cells drives graft-versus-host disease lethality. *J Clin Invest* (2016) 126(7):2642–60. doi:10.1172/JCI85796
23. Long J, Chang L, Shen Y, Gao WH, Wu YN, Dou HB, et al. Valproic acid ameliorates graft-versus-host disease by downregulating Th1 and Th17 cells. *J Immunol* (2015) 195(4):1849–57. doi:10.4049/jimmunol.1500578
24. Hu B, Bao G, Zhang Y, Lin D, Wu Y, Wu D, et al. Donor NK cells and IL-15 promoted engraftment in nonmyeloablative allogeneic bone marrow transplantation. *J Immunol* (2012) 189(4):1661–70. doi:10.4049/jimmunol.1103199
25. Cooke KR, Hill GR, Crawford JM, Bungard D, Brinson YS, Delmonte J Jr, et al. Tumor necrosis factor-alpha production to lipopolysaccharide stimulation by donor cells predicts the severity of experimental acute graft-versus-host disease. *J Clin Invest* (1998) 102(10):1882–91. doi:10.1172/JCI4285
26. Anderson BE, McNiff JM, Jain D, Blazar BR, Shlomchik WD, Shlomchik MJ. Distinct roles for donor- and host-derived antigen-presenting cells and costimulatory molecules in murine chronic graft-versus-host disease: requirements depend on target organ. *Blood* (2005) 105(5):2227–34. doi:10.1182/blood-2004-08-3032
27. Liang Y, Ma S, Zhang Y, Wang Y, Cheng Q, Wu Y, et al. IL-1beta and TLR4 signaling are involved in the aggravated murine acute graft-versus-host disease caused by delayed bortezomib administration. *J Immunol* (2014) 192(3):1277–85. doi:10.4049/jimmunol.1203428
28. Sorensen PS, Sellebjerg F. Oral fumarate for relapsing-remitting multiple sclerosis. *Lancet* (2008) 372(9648):1447–8. doi:10.1016/S0140-6736(08)61605-0
29. Bovenschen HJ, Langewouters AM, van de Kerkhof PC. Dimethylfumarate for psoriasis: pronounced effects on lesional T-cell subsets, epidermal proliferation and differentiation, but not on natural killer T cells in immunohistochemical study. *Am J Clin Dermatol* (2010) 11(5):343–50. doi:10.2165/11533240-000000000-00000
30. Casili G, Cordaro M, Impellizzeri D, Bruschetta G, Paterniti I, Cuzzocrea S, et al. Dimethyl fumarate reduces inflammatory responses in experimental colitis. *J Crohns Colitis* (2016) 10(4):472–83. doi:10.1093/ecco-jcc/jjv231
31. Liang Y, Mao X, Liu H. Proteasome inhibitor clioquinol as a candidate drug in prophylaxis and treatment of acute graft-versus-host disease. *Med Hypotheses* (2011) 76(3):400–2. doi:10.1016/j.mehy.2010.11.002
32. Ferrara JL, Reddy P. Pathophysiology of graft-versus-host disease. *Semin Hematol* (2006) 43(1):3–10. doi:10.1053/j.seminhematol.2005.09.001
33. Stoof TJ, Flier J, Sampat S, Nieboer C, Tensen CP, Boorsma DM. The antipsoriatic drug dimethylfumarate strongly suppresses chemokine production in human keratinocytes and peripheral blood mononuclear cells. *Br J Dermatol* (2001) 144(6):1114–20. doi:10.1046/j.1365-2133.2001.04220.x
34. Rubant SA, Ludwig RJ, Diehl S, Hardt K, Kaufmann R, Pfeilschifter JM, et al. Dimethylfumarate reduces leukocyte rolling in vivo through modulation of adhesion molecule expression. *J Invest Dermatol* (2008) 128(2):326–31. doi:10.1038/sj.jid.5700996
35. Balak DM, Fallah Arani S, Hajdarbegovic E, Hagemans CA, Bramer WM, Thio HB, et al. Efficacy, effectiveness and safety of fumaric acid esters in the treatment of psoriasis: a systematic review of randomized and observational studies. *Br J Dermatol* (2016) 175(2):250–62. doi:10.1111/bjd.14500
36. Fox RJ, Miller DH, Phillips JT, Hutchinson M, Havrdova E, Kita M, et al. Placebo-controlled phase 3 study of oral BG-12 or glatiramer in multiple sclerosis. *N Engl J Med* (2012) 367(12):1087–97. doi:10.1056/NEJMoa1206328
37. Chen H, Assmann JC, Krenz A, Rahman M, Grimm M, Karsten CM, et al. Hydroxycarboxylic acid receptor 2 mediates dimethyl fumarate's protective effect in EAE. *J Clin Invest* (2014) 124(5):2188–92. doi:10.1172/JCI72151
38. Nicolay JP, Muller-Decker K, Schroeder A, Brechmann M, Mobs M, Geraud C, et al. Dimethyl fumarate restores apoptosis sensitivity and inhibits tumor growth and metastasis in CTCL by targeting NF-kappaB. *Blood* (2016) 128(6):805–15. doi:10.1182/blood-2016-01-694117
39. Wu Q, Wang Q, Mao G, Dowling CA, Lundy SK, Mao-Draayer Y. Dimethyl fumarate selectively reduces memory T cells and shifts the balance between Th1/Th17 and Th2 in multiple sclerosis patients. *J Immunol* (2017) 198(8):3069–80. doi:10.4049/jimmunol.1601532
40. Vego H, Sand KL, Hoglund RA, Fallang LE, Gundersen G, Holmoy T, et al. Monomethyl fumarate augments NK cell lysis of tumor cells through degranulation and the upregulation of NKp46 and CD107a. *Cell Mol Immunol* (2016) 13(1):57–64. doi:10.1038/cmi.2014.114
41. Singh S, Vrishni S, Singh BK, Rahman I, Kakkar P. Nrf2-ARE stress response mechanism: a control point in oxidative stress-mediated dysfunctions and chronic inflammatory diseases. *Free Radic Res* (2010) 44(11):1267–88. doi:10.3109/10715762.2010.507670
42. Fleischer V, Friedrich M, Rezk A, Buhler U, Witsch E, Uphaus T, et al. Treatment response to dimethyl fumarate is characterized by disproportionate CD8+ T cell reduction in MS. *Mult Scler* (2017). doi:10.1177/1352458517703799
43. Gross CC, Schulte-Mecklenbeck A, Klinsing S, Posevitz-Fejfar A, Wiendl H, Klotz L. Dimethyl fumarate treatment alters circulating T helper cell subsets in multiple sclerosis. *Neurol Neuroimmunol Neuroinflamm* (2016) 3(1):e183. doi:10.1212/NXI.0000000000000183
44. Berkovich R, Weiner LP. Effects of dimethyl fumarate on lymphocyte subsets. *Mult Scler Relat Disord* (2015) 4(4):339–41. doi:10.1016/j.msard.2015.06.002
45. Spencer CM, Crabtree-Hartman EC, Lehmann-Horn K, Cree BA, Zamvil SS. Reduction of CD8(+) T lymphocytes in multiple sclerosis patients treated with dimethyl fumarate. *Neurol Neuroimmunol Neuroinflamm* (2015) 2(3):e76. doi:10.1212/NXI.0000000000000076
46. Chaves C, Ganguly R, Ceresia C, Camac A. Lymphocyte subtypes in relapsing-remitting multiple sclerosis patients treated with dimethyl fumarate. *Mult Scler J Exp Transl Clin* (2017) 3(2):2055217317702933. doi:10.1177/2055217317702933
47. Longbrake EE, Ramsbottom MJ, Cantoni C, Ghezzi L, Cross AH, Piccio L. Dimethyl fumarate selectively reduces memory T cells in multiple sclerosis patients. *Mult Scler* (2016) 22(8):1061–70. doi:10.1177/1352458515608961

Conflict of Interest Statement: The authors declare that the research was conducted in the absence of any commercial or financial relationships that could be construed as a potential conflict of interest.

frontiers in Immunology

ORIGINAL RESEARCH
published: 06 July 2018
doi: 10.3389/fimmu.2018.01552

Nrf2 Is a Central Regulator of Metabolic Reprogramming of Myeloid-Derived Suppressor Cells in Steady State and Sepsis

Kim Ohl[1†], Athanassios Fragoulis[2,3†], Patricia Klemm[1], Julian Baumeister[1], Wiebke Klock[1], Eva Verjans[1,4], Svenja Böll[1,4], Julia Möllmann[5], Michael Lehrke[5], Ivan Costa[6], Bernd Denecke[6], Angela Schippers[1], Johannes Roth[7], Norbert Wagner[1], Christoph Wruck[2‡] and Klaus Tenbrock[1*‡]*

[1] Department of Pediatrics, Medical Faculty, RWTH Aachen, Aachen, Germany, [2] Department of Anatomy and Cell Biology, Medical Faculty, RWTH Aachen, Aachen, Germany, [3] Department of General Visceral and Transplantation Surgery, Molecular Tumor Biology, Medical Faculty, RWTH Aachen, Aachen, Germany, [4] Institute of Pharmacology and Toxicology, RWTH Aachen, Aachen, Germany, [5] Department of Medicine I, Medical Faculty, RWTH Aachen, Aachen, Germany, [6] Interdisciplinary Centre for Clinical Research (IZKF) Aachen, Medical Faculty, RWTH Aachen, Aachen, Germany, [7] Institute of Immunology, University of Münster, Münster, Germany

Arising in inflammatory conditions, myeloid-derived suppressor cells (MDSCs) are constantly confronted with intracellular and extracellular reactive oxygen species molecules and oxidative stress. Generating mice with a constitutive activation of Nuclear factor (erythroid-derived 2)-like 2 (Nrf2) we show a pivotal role of the antioxidant stress defense for development of these immune-modulatory cells. These mice are characterized by a massive increase of splenic CD11b$^+$Gr-1$^+$ cells, which exhibit typical suppressive characteristics of MDSCs. Whole transcriptome analysis revealed Nrf2-dependent activation of cell cycle and metabolic pathways, which resemble pathways in CD11b$^+$Gr-1$^+$ MDSCs expanded by *in vivo* LPS exposure. Constitutive Nrf2 activation thereby regulates activation and balance between glycolysis and mitochondrial metabolism and hence expansion of highly suppressive MDSCs, which mediate protection in LPS-induced sepsis. Our study establishes Nrf2 as key regulator of MDSCs and acquired tolerance against LPS-induced sepsis.

Keywords: Nrf2, myeloid-derived suppressor cell, LPS, sepsis, ROS

OPEN ACCESS

Edited by:
Rudolf Lucas,
Augusta University, United States

Reviewed by:
Shengjun Wang,
Jiangsu University, China
Suowen Xu,
University of Rochester, United States

***Correspondence:**
Kim Ohl
kohl@ukaachen.de;
Klaus Tenbrock
ktenbrock@ukaachen.de

†These authors have shared first authorship.

‡These authors have shared last authorship.

Specialty section:
This article was submitted to Inflammation, a section of the journal Frontiers in Immunology

Received: *03 March 2018*
Accepted: *22 June 2018*
Published: *06 July 2018*

Citation:
Ohl K, Fragoulis A, Klemm P, Baumeister J, Klock W, Verjans E, Böll S, Möllmann J, Lehrke M, Costa I, Denecke B, Schippers A, Roth J, Wagner N, Wruck C and Tenbrock K (2018) Nrf2 Is a Central Regulator of Metabolic Reprogramming of Myeloid-Derived Suppressor Cells in Steady State and Sepsis. Front. Immunol. 9:1552. doi: 10.3389/fimmu.2018.01552

INTRODUCTION

Myeloid-derived suppressor cells (MDSCs) are a heterogeneous population of immature myeloid cells (IMCs), induced under pathological conditions such as infection and sepsis, chronic inflammation, and cancer (1). The main feature of these cells is their potent immunosuppressive activity. It is therefore not surprising that MDSCs have emerged as major regulators of pathogenic and inflammatory

Abbreviations: ECAR, extracellular acidification rate; DMF, dimethyl fumarate; G6pd, glucose-6-phosphate dehydrogenase; Glut3, glucose transporter 3; Hk, hexokinase; IMCs, immature myeloid cells; Keap1, Kelch ECH associating protein 1; mLN, mesenterial lymph node; MDSC, myeloid-derived suppressor cell; Nrf2, nuclear factor (erythroid-derived 2)-like 2; OCR, oxygen consumption rate; Pgd, phosphogluconate dehydrogenase; Pkm2, pyruvate kinase isozyme M2; PPP, pentose phosphate pathway; ROS, reactive oxygen species; TJL, The Jackson Laboratory Score; Tkt, transketolase; T_{reg} cell, regulatory T cell.

immune responses (2). In addition to its important role in cancer, MDSCs expand during murine sepsis as well as in septic patients (3, 4). Although sepsis patients have high levels of inflammatory mediators, components of their immune system are suppressed as well. This modified steady state of innate immunity after infection is referred to as innate memory (5, 6). Innate memory is based on epigenetic reprogramming which is broadly defined as sustained change in transcription programs and cell physiology (5, 7). Induction of innate memory is thus accompanied by significant changes in cellular metabolism. When inappropriately activated, innate memory programs can become maladaptive as in post-sepsis immune paralysis, which is associated with severe energy metabolism defects of leukocytes (8). Molecular mechanism that mediate innate memory at the level of cell types and the immunological metabolic and epigenetic processes behind are therefore an important area of research. By suppressing innate as well as adaptive immune responses, MDSCs have protective roles in the initial hyper-inflammatory reaction, however, are also involved in sepsis-induced innate immunoparalysis (3, 4, 9–11). We would therefore specify MDSCs as central player in innate memory. However, there still remain open questions about, how expansion and functions of MDSCs are regulated in sepsis and how metabolic dysregulations of MDSCs affect innate immunity in sepsis.

Cellular metabolism and oxidative stress are intimately linked, immune cells are constantly confronted with intracellular and extracellular reactive oxygen species (ROS) molecules in steady state and moreover in inflammatory conditions. During sepsis, enhanced levels of ROS molecules, either produced by NADPH oxidases during oxidative bursts or by mitochondrial dysfunction, lead to oxidative stress conditions (12). Interestingly immune cell types vary with regard to their ROS susceptibility and although ROS are toxic to most cells, MDSC survive despite their elevated content and release of ROS (13). Moreover, high numbers of MDSCs arise in oxidative stress prone conditions such as inflammation, infection, and cancer.

This prompted us to analyze ROS-mediated signaling pathways in myeloid cells in steady state and sepsis. We hereby identified Nuclear factor (erythroid-derived 2)-like 2 (Nrf2), the transcriptional regulator of the antioxidant stress defense, as key regulator of metabolic reprogramming of MDSCs.

MATERIALS AND METHODS

Mice Strains

Experiments were performed with age-matched WT, $Keap^{fl/fl}$, $VAV^{cre}Keap^{fl/fl}$, and $Nrf2^{-/-}$ mice (all C57BL/6). $VAV^{cre}Keap^{fl/fl}$ mice were generated by crossing Keap1-flox mice (14) with VAVcre mice. $VAV^{cre-}Keap^{fl/fl}$ mice were used as controls (denoted as $Keap^{fl/fl}$). $Nrf2^{-/-}$ mice have been described previously (15) and were bred in our animal facility and kept under standardized conditions, as were the OT-II mice, CD45.1 congenic mice (C57BL/6), and $RAG^{-/-}$ mice used.

LPS Treatment

8- to 10-week-old mice with at least 25 g were used for this study. Treatments were conducted with either vehicle + lethal dose 5 mg/kg BW LPS (sepsis group) or low dose + lethal doses 30 mg/kg BW LPS (tolerance group) in 250 µl 0.9% NaCl i.p. All animals were monitored thrice per day in 6 h intervals to document weight and body temperature.

Rapamycin was first solved in ethanol and then diluted in 5.2% PEG/Tween in NaCl. Mice received either vehicle (5.2% PEG/Tween) or 2 mg/kg of body weight rapamycin by daily i.p. injections.

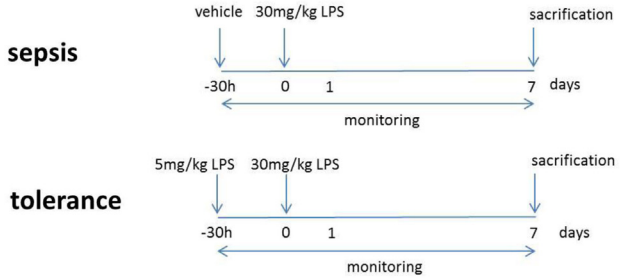

Transfer Colitis

To induce transfer colitis, $RAG2^{-/-}$ mice were adoptively transferred with either 2×10^6 $CD4^+CD25^-$ T cells alone, with 2×10^6 $CD11b^+Gr\text{-}1^+$ cells alone or with both 2×10^6 $CD4^+$ T cells and 2×10^6 $CD11b^+Gr1^+$ cells. After 6 weeks, the mice were sacrificed. Spleens and mesenterial lymph nodes (mLNs) were harvested for further analysis. One part of the colon was fixed in formalin for histological scoring and the other part was fixed in RNAlater (Qiagen, Germany) for subsequent mRNA analysis.

Histological Scoring

4 µm paraffin sections from the fixed colon were cut serially, mounted onto glass slides, and deparaffinized. The colon sections were stained with hematoxylin and eosin by the Core Facility (IZKF) of the RWTH Aachen University. Blinded histological scoring was performed using a standard microscope, based on The Jackson Laboratory Score method as described previously (16, 17). Each colon section was scored for the four general criteria: severity, degree of hyperplasia, degree of ulceration, if present, and percentage of area involved. A subjective range of 1–3 (1 = mild, 2 = moderate, 3 = severe) was used for the first three categories. Severity: focally small or widely separated multifocal areas of inflammation limited to the lamina propria were graded as mild lesions (1). Multifocal or locally extensive areas of inflammation extending to the submucosa were graded as moderate lesions (2). If the inflammation extended to all layers of the intestinal wall or the entire intestinal epithelium was destroyed, lesions were graded as severe (3). Hyperplasia: mild hyperplasia consisted of morphologically normal lining epithelium that was at least twice as thick (length of crypts) as adjacent or control mucosa. Moderate hyperplasia was characterized by the lining epithelium being two or three times normal thickness, cells were hyperchromatic, numbers of goblet cells were decreased, and scattered individual crypts developed an arborizing pattern. Severe hyperplastic regions exhibited markedly thickened epithelium (four or more times normal thickness), marked hyperchromasia of cells, few to no goblet cells, a high mitotic index of cells within the crypts, and numerous crypts with arborizing pattern.

Ulceration was graded as: 0 = no ulcer, 1 = 1–2 ulcers (involving up to a total of 20 crypts), 2 = 1–4 ulcers (involving a total of 20–40 crypts), and 3 = any ulcers exceeding the former in size. A 10% scale was used to estimate the area involved in the inflammatory process (0 = 0%, 1 = 10–30%, 2 = 40–70%, 3 = >70%).

BrdU Assay

Mice were fed orally with 0.8 mg/ml BrdU (BD) in drinking water. Drinking water was changed every 2 days. After 14 days mice were sacrificed, spleens and BMDCs were harvested, and BrdU incorporation was assessed by flow cytometry according to the manufacturer's instructions (BrdU Flow, Kit, BD).

Mixed Bone Marrow Chimeras

BM cells were isolated from femurs and tibias of age-matched donor animals (WT CD45.1 and $VAV^{cre}Keap^{fl/fl}$ CD45.2). $RAG2^{-/-}$ mice were lethally irradiated (2 Gy × 6.8 Gy) and co-injected with 5×10^6 cells of each genotype after irradiation, or injected with 10×10^6 cells of only one genotype (WT CD45.1 or $VAV^{cre}Keap^{fl/fl}$ CD45.2 cells). The mice received antibiotic treatment for 14 days [40 µl Borgal-solution (24%)/100 ml drinking water]. Eight weeks later, the mice were sacrificed and spleens analyzed by flow cytometry.

Cell Isolation

Mouse BM cells were flushed from femurs and tibias with Dulbecco medium. Erythrocytes were lysed with lysis buffer (eBioscience) for 3 min at room temperature, and the remaining cells were washed once with PBS. Single cell suspensions were isolated from spleens and erythrocytes were lysed with lysis buffer. MDSCs were isolated from splenocytes by magnetic cell separation (Miltenyi, Germany). Flow cytometric analysis revealed high purity (90%) of isolated $CD11b^+Gr\text{-}1^+$ cells. $CD4^+$ cells were isolated by magnetic cell separation using the $CD4^+$ T cell isolation kit (Miltenyi), while $CD4^+CD25^+$ Treg cell isolation kits (Miltenyi) were used to isolate $CD4^+CD25^-$ cells and perform adoptive transfer colitis.

Flow Cytometry

For surface staining, single cell suspensions were stained with anti-CD11b, anti-Gr-1, anti-CD4, anti-CD3, anti-CD8, anti-CD25, anti-CD19, anti-CD11c, anti-F4/80, anti-CD45.1, and anti-CD45.2 (all from eBioscience, Germany). To analyze Foxp3, pS6, p4EBP-1, Nos2, p-mTOR, and arginase expression, cells were fixed and permeabilized with a FOXP3 staining buffer set (eBioscience, Germany) following the manufacturer's instructions and stained with anti-Foxp3 antibodies (eBioscience, Germany), anti pS6, p4EBP-1 (BD Biosciences), anti-p-mTOR (ebioscience, Germany), anti-arginase and sheep-IgG (both R&D), or anti-NOS2 and mouse-IgG2a (both eBiosience) antibodies for 30 min. To analyze mitochondrial mass by flow cytometry, cells were incubated with 25 ng/ml nonyl acridine orange (Thermo Fischer Scientific) for 10 min at 37°C and maintained on ice until flow cytometric analysis. Glucose uptake was determined by means of a glucose uptake cell-based kit (Cayman Chemical). 2×10^6 cells/ml were incubated in glucose-free medium for 2 h. Afterwards 100 µg/ml 2-NBDG was added and incubation continued in a cell incubator at 37°C. Incubation was stopped by immediate transfer of cell culture plates to 4°C conditions. Cells were washed with a cell-based assay buffer according to the manufacturer's instructions and kept at 4°C until flow cytometric analysis. A total reactive oxygen species assay kit (eBioscience) was used to identify ROS, following the manufacturer's instructions. In detail, this involved incubation of the cells with ROS assay stain for 60 min at 37°C, washing once with PBS and analysis on the flow cytometer. To identify apoptotic cells, cells were first labeled with cell viability dye (eBioscience) and then incubated with fluorochrome conjugated Annexin-V (eBioscience) in Annexin-V binding buffer according to the manufacturer's instructions. BrdU staining was performed according to the manufacturer's protocol with BrdU Flow Kit (BD Pharmingen). 7-AAD staining was performed by adding 7-AAD (BD Pharmingen) directly to the cells before measurement.

Flow cytometry was carried out using FACSCanto II device (BD Biosciences, Germany). Data analysis was performed using FCS Express Software.

RNA Isolation and Real-Time PCR

Total RNA from isolated MDSCs and colon tissue was isolated using the RNeasy Mini Kit (Qiagen, Germany). cDNA was then generated from 200 ng total RNA using the RevertAid H Minus First Strand cDNA Synthesis Kit (Thermo Fisher Scientific, USA) according to the manufacturer's instructions. RT-PCR was performed using the SYBR Green PCR kit (Eurogentec, Germany) and data were acquired with the ABI prism 7300 RT-PCR system (Applied Biosystems/Life Technologies, Germany). Each measurement was set up in duplicate. After normalization to the endogenous reference control gene β-actin for mice, the relative expression was calculated. The sequences of primers used in this study are listed in Table S1 in Supplementary Material.

Seahorse Assay

2×10^5 cells were seeded on gelatin-coated plates and OCR/ECAR measured using the XF96 Extracellular Flux Analyzer (Seahorse Bioscience) following the manufacturer's instructions. OCR was measured in XF media containing 11 mmol/l glucose and 1 mmol/l sodium pyruvate under basal conditions and in response to 1 µmol/l oligomycin, 1 µmol/l carbonyl cyanide p-trifluoromethoxyphenylhydrazone (FCCP), and 0.1 µmol/l rotenone plus 0.1 µmol/l antimycin A. Extracellular acidification rate (ECAR) was measured in assay medium (XF Media supplemented with 4.5 g/l glucose and 2 mM glutamine) under basal conditions and in response to 10 mM glucose, 1 M oligomycin, and 100 mM 2-deoxyglucose.

In Vitro MDSC Generation

2×10^6 murine bone marrow cells per ml were cultured in RPMI with 2 g/l glucose supplemented with 10% heat-inactivated FCS (Life Technologies). In some experiments, glucose concentrations were adapted as indicated. To obtain BM-derived MDSCs, medium was supplemented with IL-6 (10 ng/ml) and GM-CSF (20 ng/ml) (both Peprotech). On day 3 of culture, the original medium was replaced with fresh medium containing cytokines and cultures were maintained at 37°C in 5% CO_2-humidified

atmosphere for an additional 3 days. To analyze effects of rapamycin, 1 μM rapamycin (Cayman Chemical) were added at day 0 and 3.

To analyze dimethyl fumarate (DMF) effects on human cells, 2×10^6 human PBMCs per ml were cultured in RPMI in the presence or absence of 2 μg/ml DMF.

Suppression Assays

DCs were generated by culturing BM cells in the presence of GM-CSF (50 ng/ml) and IL-4 (40 ng/ml) for 6 days. Cells were fed with OVA peptide (1 μM) for 2 h and extensively washed with PBS. $CD4^+$ OT-II cells were isolated by magnetic cell separation and labeled with cell proliferation dye (5 μM) (eBioscience) according to the manufacturer's instructions. DCs and $CD4^+$ T cells were co-cultured in a 1:10 ratio in U-bottom 96-well plates. MDSCs were isolated by magnetic cell isolation and were added to DC/T cell cultures in ratios of 1:1 or 1:0.5. After 3 days, proliferation of CD4 T cells was assessed by flow cytometry.

RNA Extraction and Microarray for Gene Expression Analysis

Genome wide transcriptome analyses for $VAV^{cre}Keap^{fl/fl}$ and WT ($VAV^{cre-}Keap^{fl/fl}$) MDSCs were performed in independent triplicates using Gene Chip® Mouse Gene 2.0 arrays (Affymetrix, Santa Clara, CA, USA). Total RNA extraction was carried out using the RNeasy Micro Kit (Qiagen, Germany) according to the manufacturer's protocol and then quantified (Nanodrop). RNA quality was assessed using the RNA 6000 Nano Assay with the 2100 Bioanalyzer (Agilent, Santa Clara, CA, USA). Samples for the Gene 2.0 arrays were prepared and hybridized to the arrays according to the Affymetrix WT Plus Kit manual. Briefly, for each sample, 100 ng of total RNA was reversed transcribed into cDNA using a random hexamer oligonucleotide tagged with a T7 promoter sequence. After second strand synthesis, double strand cDNA was used as a template for amplification with T7 RNA polymerase to obtain antisense cRNA. Random hexamers and dNTPs spiked out with dUTP were then used to reverse transcribe the cRNA into single stranded sense strand cDNA. The cDNA was then fragmented with uracil DNA glycosylase and apurinic/apyrimidic endonuclease 1. Fragment size was checked using the 2100 Bioanalyzer and ranged from 50 to 200 bp. Fragmented sense cDNA was biotin-endlabeled with TdT and probes were hybridized to the Gene 2.0 arrays at 45°C for 16 h with 60 rpm. Hybridized arrays were washed and stained on a Fluidics Station 450 (program: FS450 0002) and scanned on a GeneChip® Scanner 3000 7 G (both Affymetrix). Raw image data were analyzed with Affymetrix® Expression Console™ Software (Affymetrix, USA), and gene expression intensities were normalized and summarized with a robust multiarray average algorithm (18). Transcripts that were expressed differently more than 1.5-fold with a raw p-value lower than 0.05 between the sample groups were categorized as regulated. Enrichment analysis for Wiki pathways was performed using WebGestalt (19). For the enrichment analysis, only genes changed at least 1.5-fold with a p-value lower than 0.05 between $VAV^{cre}Keap^{fl/fl}$ and WT ($VAV^{cre-}Keap^{fl/fl}$) samples were taken into consideration.

Statistical Analysis

All data are presented as mean ± SEM or SD if indicated. Differences between two groups were evaluated using two-tailed, unpaired or paired (if indicated) Student's t-test. All statistical analysis and subsequent graphics generation were performed using GraphPad Prism version 7.0 (GraphPad Software, USA). A p-value <0.05 was considered to be statistically significant.

Study Approval

The study was approved by the regional government authorities and animal procedures were performed according to German legislation for animal protection. Permission for the projects was granted by the Regierungspräsident/LANUV Nordrhein-Westfalen.

RESULTS

$VAV^{cre}Keap^{fl/fl}$ Mice Develop Splenomegaly Due to an Accumulation of $CD11b^+Gr\text{-}1^+$ Cells

To analyze oxidative stress signaling in immune cells, we generated a mouse with constitutive Nrf2 activation in all hematopoietic cells by breeding Kelch ECH associating protein 1 (Keap1)-flox mice with VAV-CRE recombinase mice ($Vav^{cre}Keap^{fl/fl}$). Keap1 suppresses Nrf2 transcriptional activity under basal conditions, thus deletion of Keap1 results in constitutive nuclear accumulation and activation of Nrf2 (20). $Vav^{cre}Keap^{fl/fl}$ mice are born at expected Mendelian ratios, are healthy and cancer-free, and have a normal life span. However, on aging, $Vav^{cre}Keap^{fl/fl}$ mice develop splenomegaly (**Figures 1A,B**) due to an increase in cell size (Figure S1A in Supplementary Material). Flow cytometric analysis of immune cells in the spleens revealed a specific enrichment of two immunosuppressive cell subsets, namely regulatory T (T_{reg}) and $CD11b^+Gr\text{-}1^+$ cells (**Figures 1C,D**). While absolute numbers (Figure S1B in Supplementary Material) and frequencies (**Figure 1D**) of B cells ($CD19^+$), DCs ($CD11c^+$), macrophages ($CD11b^+F4/80^+$) and T cells ($CD3^+$), as well as cytotoxic T cells ($CD3^+CD8^+$) and T helper cells ($CD3^+CD4^+$) were not raised in $VAV^{cre}Keap^{fl/fl}$ mice compared to $Keap^{fl/fl}$ mice, frequencies and numbers of $CD3^+CD4^+CD25^+Foxp3^+$ as well as $CD11b^+Gr\text{-}1^+$ cells were altered significantly. $CD11b^+Gr\text{-}1^+$ cells are already expanded in spleens of younger mice but their numbers increased progressively with age (**Figure 1E**) in correlation with spleen weight (**Figure 1B**). The dominant cell type among $CD11b^+$ cells of $VAV^{cre}Keap^{fl/fl}$ mice were $Ly6G^+$ PMN-MDSCs, and levels of these were significantly enhanced (**Figure 1F**). It has been shown before that $Keap^{fl/fl}$ mice already reveal reduced expression of Keap1 protein in various tissues compared to WT mice (21), we therefore additionally compared numbers of $CD11b^+Gr\text{-}1^+$ cells in B6-WT and $Keap^{fl/fl}$ mice, however, numbers of MDSC were not altered in these groups (Figure S1C in Supplementary Material) and we concluded from this that $Keap^{fl/fl}$ and WT controls are comparably fitting controls in our experiments. NAD(P)H quinine oxidoreductase (Nqo-1), which is one of the most specific Nrf2 targets, was strongly enhanced in $VAV^{cre}Keap^{fl/fl}$ $CD11b^+Gr\text{-}1^+$ cells compared to $Keap^{fl/fl}$ cells, while

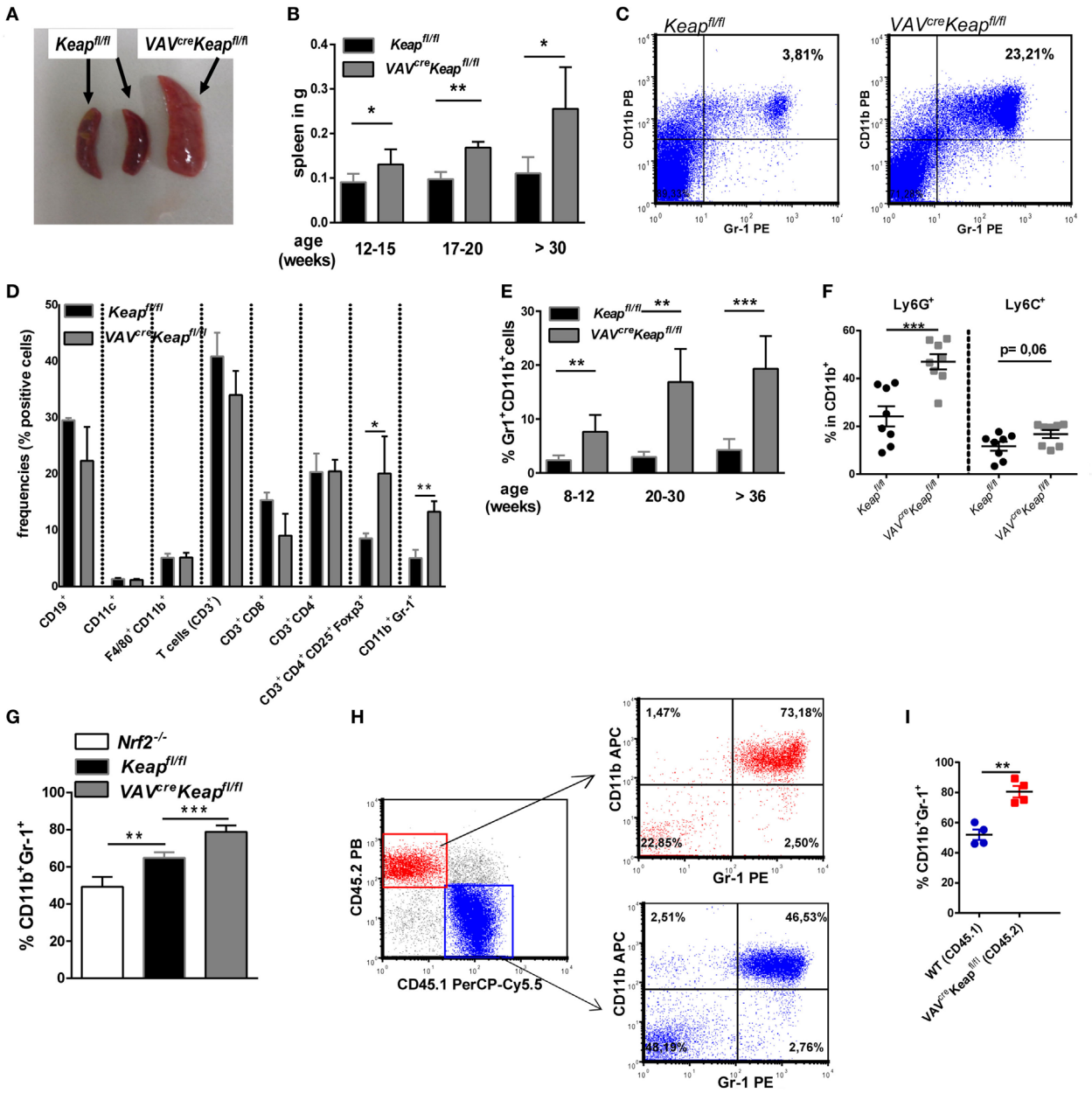

FIGURE 1 | Nrf2 activation enhances CD11b$^+$ Gr-1$^+$ cells. **(A)** Spleens from old (50–52 weeks) *Keap*$^{fl/fl}$ and *VAV*^{cre}*Keap*$^{fl/fl}$ mice. **(B)** Weight of spleens from *Keap*$^{fl/fl}$ and *VAV*^{cre}*Keap*$^{fl/fl}$ mice at different ages. Bars indicate mean ± SD of at least three mice per group. **(C)** Representative dot plot depicting frequencies of CD11b$^+$Gr-1$^+$ cells in spleens from old (50–52 weeks) *Keap*$^{fl/fl}$ and *VAV*^{cre}*Keap*$^{fl/fl}$ mice. **(D)** Frequencies of immune cell populations in spleens from 16-week-old *Keap*$^{fl/fl}$ and *VAV*^{cre}*Keap*$^{fl/fl}$ mice. Bars indicate mean ± SEM of three mice per group. **(E)** Frequencies of CD11b$^+$ Gr-1$^+$ cells in spleens from *Keap*$^{fl/fl}$ and *VAV*^{cre}*Keap*$^{fl/fl}$ mice at different ages. Bars indicate mean ± SD of at least six mice per group. **(F)** Frequencies of Ly6G$^+$ and Ly6C$^+$ cells within splenic CD11b$^+$ cells from *Keap*$^{fl/fl}$ and *VAV*^{cre}*Keap*$^{fl/fl}$ mice. **(G)** BM-derived cells were incubated with GM-CSF and IL-6 and frequencies of CD11b$^+$Gr-1$^+$ cells were assessed by flow cytometry. Bars indicate mean ± SD of at least three mice per group. **(H)** Mixed BM chimeric mice were analyzed 8 weeks after transfer of *CD45.1 WT* and *CD45.2 VAV*^{cre}*Keap*$^{fl/fl}$ BM cells into lethally irradiated RAG2$^{-/-}$ recipient mice. WT mice were used, since *Keap*$^{fl/fl}$ CD45.1 mice were not available. Representative dot plots of splenic CD45.2$^+$ Gr-1$^+$CD11b$^+$ and CD45.1$^+$ Gr-1$^+$CD11b$^+$ cells are shown. **(I)** Percentages of splenic CD11b$^+$Gr-1$^+$ cells of *CD45.1* and *CD45.2* origin in bone marrow chimeras. For **(F,I)**, each symbol indicates an individual mouse. Horizontal lines represent the mean; error bars represent SEM. Two-tailed unpaired *t*-tests were used to determine *p*-values for all statistical analysis.

CD11b$^+$Gr-1$^+$ cells from *Nrf2*$^{-/-}$ mice exhibited reduced Nqo-1 expression (Figure S1D in Supplementary Material), which shows that Nrf2 is hyperactivated in *VAV*^{cre}*Keap*$^{fl/fl}$ compared to *Keap*$^{fl/fl}$ cells. CD11b$^+$Gr-1$^+$ cells in BM are IMCs, which differentiate into mature granulocytes, macrophages, or DCs in healthy individuals. However, proliferation of IMCs and blockade of

their differentiation can result in the accumulation of MDSCs in lymphoid organs. In most cases, accumulation of MDSCs is caused by pathogenic conditions such as cancer, inflammation, and autoimmunity (1). We therefore wanted to find out whether the observed expansion of CD11b$^+$Gr-1$^+$ cells is a secondary effect or whether it is indeed regulated by cell autonomous Nrf2/Keap1 signaling in these cells. To answer this question, we performed *in vitro* MDSC generation assays with BM-derived cells from *Keap$^{fl/fl}$*, Nrf2$^{-/-}$, and *VAV^{cre}Keap$^{fl/fl}$* mice. Culturing of BM cells from naive mice with GM-CSF and IL-6 has previously been shown to lead to an enrichment of suppressive Gr-1$^+$CD11b$^+$ cells (22, 23). Interestingly, Nrf2-deficient BM-derived cells exhibited a quite low expression of Gr-1 and CD11b in comparison to *Keap$^{fl/fl}$* BM-derived cells, whereas *VAV^{cre}Keap$^{fl/fl}$* cells showed the highest capacity to acquire a CD11b$^+$Gr-1$^+$ phenotype (**Figure 1G**). To further confirm that Nrf2/Keap1 signaling directly induces CD11b$^+$Gr-1$^+$ cells, we generated mixed BM chimeras. To this end, we transferred equal numbers of CD45.1 WT and CD45.2 *VAV^{cre}Keap$^{fl/fl}$* BM cells into lethally irradiated *Rag$^{-/-}$* mice, which led to complete reconstitution of the hematopoietic system within 8 weeks. As expected, numbers of splenic CD11b$^+$Gr-1$^+$ CD45.1$^+$ (WT derived) cells were lower than numbers of splenic CD45.2$^+$ (*Keap$^{-/-}$* derived) cells in the recipient mice (**Figures 1H,I**).

Nrf2 Activation in Myeloid Cells Results in Cells Which Display MDSC Characteristics

Expression of Gr-1 and CD11b are known characteristics of MDSCs. However, these markers are expressed by a quite heterogeneous cell population and additional attributes are required to define cells as MDSCs. These include the expression of immune suppressive factors such as arginase (encoded by *ARG1*), inducible nitric oxide synthase (also known as Nos2) an increase in the production of ROS. Interestingly, *VAV^{cre}Keap$^{fl/fl}$* CD11b$^+$ Gr-1$^+$ cells showed all the characteristic hallmarks of MDSCs such as production of arginase (**Figure 2A**; Figure S2A in Supplementary Material) and Nos2 (**Figures 2B,C**). ROS production was lower in *VAV^{cre}Keap$^{fl/fl}$* CD11b$^+$ Gr-1$^+$ cells than in *Keap$^{fl/fl}$* cells (**Figures 2D,E**). This may be explained by a high activity of the anti-oxidative machinery in *VAV^{cre}Keap$^{fl/fl}$* cells, leading to a rapid scavenging of produced ROS molecules in these cells. Interestingly, most notably *VAV^{cre}Keap$^{fl/fl}$* Ly6G$^+$ CD11b$^+$ cells revealed a reduction of ROS molecules (Figure S2B in Supplementary Material). In addition, such as WT CD11b$^+$Gr-1$^+$ cells, *VAV^{cre}Keap$^{fl/fl}$* CD11b$^+$Gr-1$^+$ cells showed a lower expression of maturation and differentiation markers like CD11c, CD80, CD86, and MHC-II compared to CD11b$^+$Gr-1$^-$ cells (Figure S2C in Supplementary Material). With regard to inflammatory cytokines, IL-6 was not detectable and levels of *IL-1* and *IL-12* were markedly reduced in *VAV^{cre}Keap$^{fl/fl}$* compared to *Keapfl/fl* CD11b$^+$Gr-1$^+$ cells (**Figure 2F**). Furthermore, inhibition of T cells by means of T cell suppression assays is the "gold" standard for evaluation of MDSC function (2). Addition of *Keapfl/fl* and *VAV^{cre}Keap$^{fl/fl}$* CD11b$^+$Gr-1$^+$ cells to antigen-specific stimulated T cells reduced percentages of proliferated cells (**Figures 2G,H**), diminished absolute numbers of T cells (**Figure 2I**), and enhanced percentages of dead T cells (**Figure 2J**). Furthermore, *VAV^{cre}Keap$^{fl/fl}$* CD11b$^+$Gr-1$^+$ suppressed T cell mediated transfer colitis (**Figure 2K**). While RAG-deficient (RAG2$^{-/-}$) recipients of CD4$^+$ T cells suffered from severe colitis with weight loss and high-grade intestinal inflammation (**Figure 2K**; Figures S3A,B,C in Supplementary Material), co-transfer of Keap-deficient CD11b$^+$Gr-1$^+$ cells markedly reduced loss of weight and intestinal inflammation (**Figure 2K**; Figures S3B,C in Supplementary Material). Absolute numbers of CD3$^+$CD4$^+$ cells in spleens and mLNs were reduced as well (**Figure 2L**). Furthermore, T_{reg} cells numbers increased (Figure S3D in Supplementary Material) while levels of inflammatory cytokines in the gut were markedly reduced in RAG2$^{-/-}$ mice transferred with MDSCs in addition to CD4$^+$ T cells (Figure S3E in Supplementary Material).

We conclude from these experiments that CD11b$^+$Gr-1$^+$ *VAV^{cre}Keap$^{fl/fl}$* cells show all hallmarks and functional properties of MDSCs, such as production of arginase and Nos2 but low expression of maturation and differentiation markers and inflammatory cytokines and a high ability to suppress T cell proliferation *in vitro* and *in vivo*.

Metabolic Pathways and Cell Cycle Pathways Are Enriched in MDSC With Constitutive Nrf2 Activation

Next, to investigate how Nrf2/Keap1 signaling induces expansion of MDSCs, we performed whole transcriptome analysis in MDSCs isolated from *VAV^{cre}Keap$^{fl/fl}$* mice and *Keap$^{fl/fl}$* mice using Affymetrix arrays. Several genes, which belong to the *oxidative stress pathway*, *Nrf2/Keap1 signaling pathway*, and *glutathione metabolism*, were activated in *VAV^{cre}Keap$^{fl/fl}$* MDSCs and differed significantly from WT MDSCs, which confirm constitutive Nrf2 activation in these cells at a transcriptional level (**Figures 3A,B**). Most interestingly, in addition to this, we noticed altered expression of genes belonging to metabolic as well as cell cycle pathways (**Figures 3A,B**). In detail, genes of the *cell cycle,* the *pentose phosphate pathway* (*PPP*), and *nucleotide, metabolism* showed enhanced expression in *VAV^{cre}Keap$^{fl/fl}$* compared to WT MDSCs.

Nrf2 Enhances Proliferation of CD11b$^+$Gr-1$^+$ Cells

Based on our microarray data, we hypothesized that the accumulation of MDSCs in spleen is caused by a higher proliferation rate. Analysis of Ki-67 expression in the spleen and BM cells confirmed a larger growth fraction within *VAV^{cre}Keap$^{fl/fl}$* CD11b$^+$Gr-1$^+$ cells compared to *Keap$^{fl/fl}$* cells (**Figures 4A,B**). Furthermore, *in vitro* generated MDSCs from *VAV^{cre}Keap$^{fl/fl}$* mice displayed higher Ki-67 expression as well (**Figure 4C**). In addition, BM CD11b$^+$Gr-1$^+$ cells from *VAV^{cre}Keap$^{fl/fl}$* mice exhibited a higher BrdU incorporation than the respective CD11b$^+$Gr-1$^+$ cells from *Keap$^{fl/fl}$* (**Figures 4D,E**) while BrdU incorporation into CD11b$^+$Gr1$^+$ cells from *VAV^{cre}Keap$^{fl/fl}$* spleens was only tendentially increased (**Figure 4E**). However, the rates of apoptosis, as analyzed by the frequencies of early apoptotic (AnnexinV$^+$ cell viability dye$^-$) and late apoptotic (AnnexinV$^+$ cell viability dye$^+$) MDSCs were the same in *Keap$^{fl/fl}$* and *VAV^{cre}Keap$^{fl/fl}$* mice (Figure S4 in Supplementary Material). From that, we conclude that Nrf2 accelerates proliferation of MDSCs without affecting apoptosis.

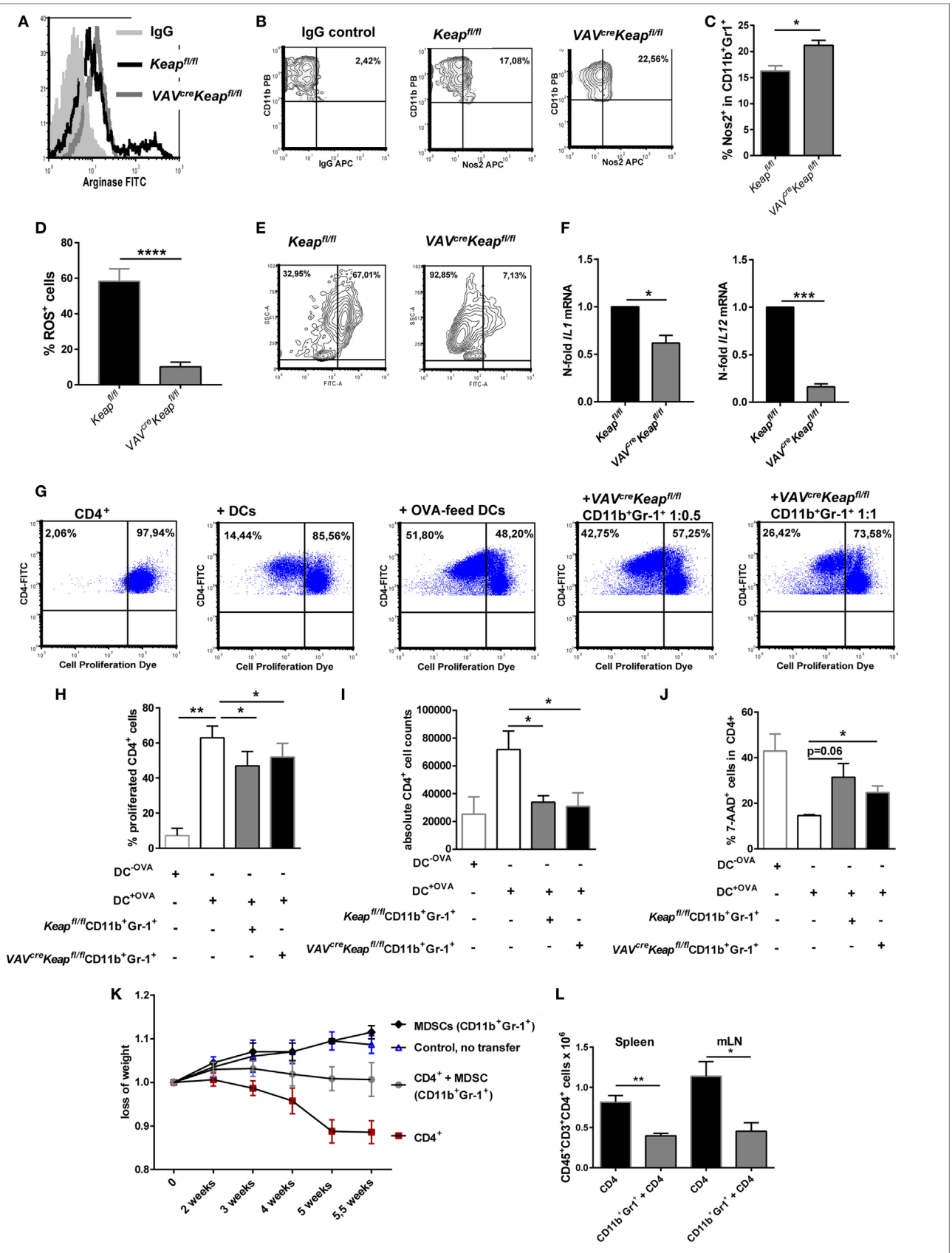

FIGURE 2 | Continued

FIGURE 2 | CD11b$^+$Gr-1$^+$ cells from *VAV^{cre}Keap$^{fl/fl}$* reveal characteristics of myeloid-derived suppressor cells (MDSCs). **(A)** Representative arginase-histogram showing overlays of pre-gated CD11b$^+$Gr-1$^+$ cells in spleens from *Keap$^{fl/fl}$* (black), *VAV^{cre}Keap$^{fl/fl}$* mice (gray), and an appropriate isotype control. **(B)** Flow cytometric analysis of Nos2 expression in pre-gated CD11b$^+$Gr-1$^+$ cells from spleens. Representative contour plots showing isotype control (left) and Nos2 expression from *Keap$^{fl/fl}$* (middle) and *VAV^{cre}Keap$^{fl/fl}$* mice (right). **(C)** Statistical analysis of Nos2-positive cells in pre-gated CD11b$^+$Gr-1$^+$ *Keap$^{fl/fl}$* ($n = 3$) and *VAV^{cre}Keap$^{fl/fl}$* ($n = 3$) mice, two-tailed unpaired *t*-test. Bars indicate mean and error bars SEM of three mice per group. **(D)** Statistical analysis of ROS$^+$ cells in pre-gated CD11b$^+$Gr-1$^+$ from *Keap$^{fl/fl}$* ($n = 6$) and *VAV^{cre}Keap$^{fl/fl}$* ($n = 8$) mice, two-tailed unpaired *t*-test. **(E)** Representative contour plots showing reactive oxygen species (ROS) positive cells pre-gated on CD11b$^+$Gr-1$^+$ cells cultured at 37°C for 1 h. **(F)** N-fold mRNA expression of cytokines in MACS isolated *Keap$^{fl/fl}$* and *VAV^{cre}Keap$^{fl/fl}$* CD11b$^+$Gr-1$^+$ ($n = 4$) cells analyzed by RT-qPCR. Bars indicate mean and error bars SEM, two-tailed one sample test. **(G–J)** OT-II CD4$^+$ T cells were labeled with the cell proliferation dye eFluor 660 and cultured alone, in the presence of DCs, or in the presence of OVA-fed DCs, or co-cultured with OVA-fed DCs or different ratios of Gr1$^+$CD11b$^+$ cells from *VAV^{cre}Keap$^{fl/fl}$* mice. **(G)** After 3 days of culture, T cell proliferation was measured by loss of eFluor fluorescence on flow cytometry. **(H)** Statistical analysis of cell proliferation, as assessed by percentages of proliferated cells. Bars indicate the mean of three independent experiments and error bars SEM (two-tailed, paired *t*-test). **(I)** Statistical analysis of absolute CD4$^+$ cells after 3 days of culture. **(J)** Statistical analysis of dead CD4$^+$ T cells, as determined by incorporation of 7-AAD, two-tailed unpaired *t*-test. Bars indicate the mean of three independently performed experiments and error bars SEM. **(K)** CD4$^+$CD25$^-$ transfer colitis: body weight as a percent of starting weight of control mice ($n = 4$, blue symbols), MDSC recipient control mice ($n = 2$, black), CD4$^+$CD25$^-$ recipient mice ($n = 8$, red), and CD4$^+$CD25$^-$ + MDSCs recipient mice (gray, $n = 7$) over the course of 5.5 weeks. **(L)** Statistical analysis of frequencies of CD4$^+$ T cells in spleen and mesenterial lymph nodes (mLNs).

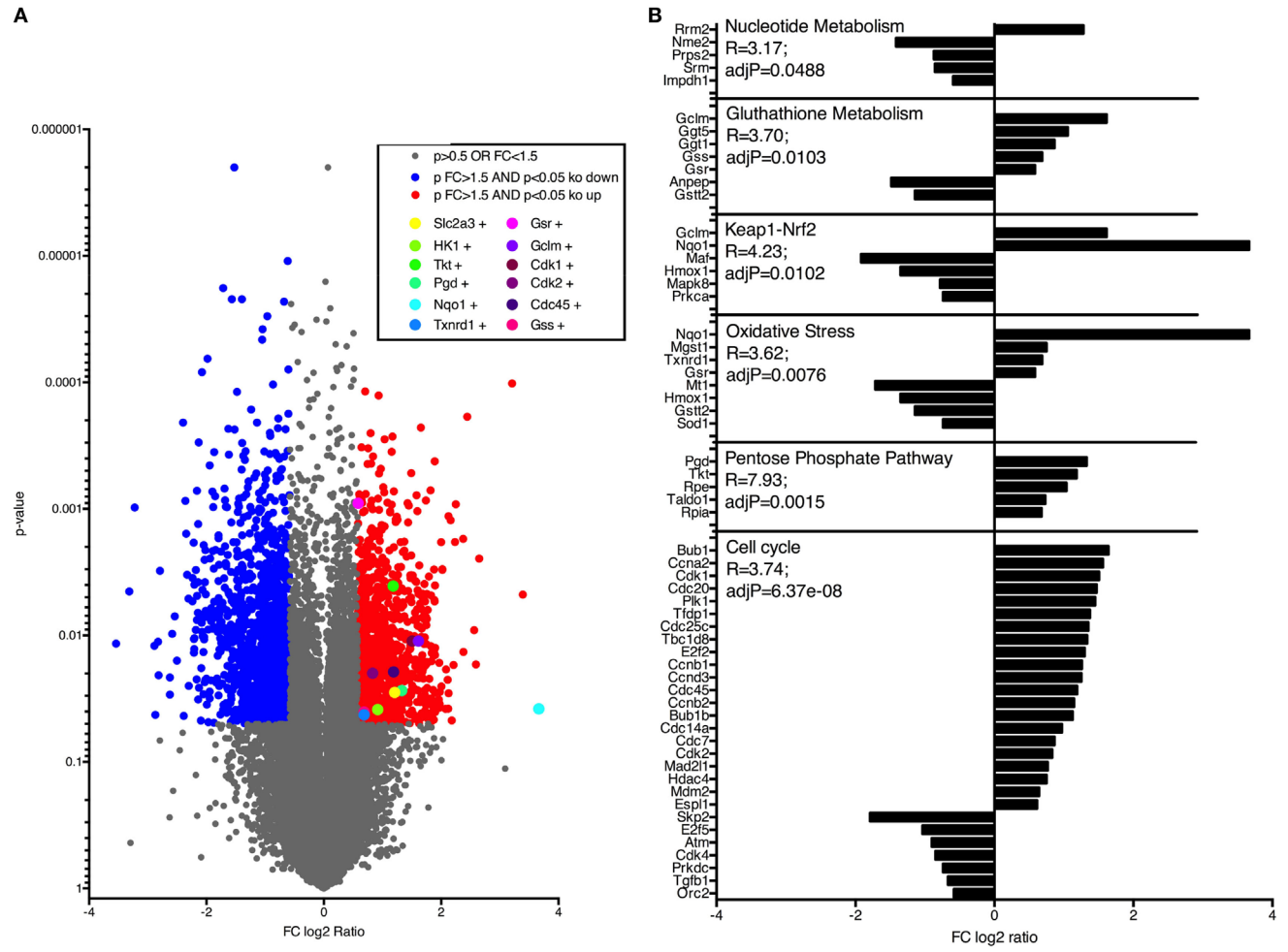

FIGURE 3 | Nrf2 activates genes regulating cell cycle and metabolic pathways in myeloid-derived suppressor cells (MDSCs). **(A)** Gene expression in CD11b$^+$Gr-1$^+$ cells from *Keap$^{fl/fl}$* and *VAV^{cre}Keap$^{fl/fl}$* mice. Colors indicate significant upregulation (of at least 1.5-fold; red) or downregulation (of at least 1.5-fold; blue). **(B)** Selection of pathways and associated genes which were significantly enriched.

Nrf2 Enhances Metabolic Activity of CD11b$^+$Gr-1$^+$Cells

The metabolic characteristics regulating MDSCs have not yet been fully elucidated and may also differ within this quite heterogeneous cell population. Tumor-infiltrating MDSCs increase fatty acid oxidation compared to splenic MDSCs (24). On the other hand, rapamycin, the specific inhibitor of mTOR, decreased M-MDSC in mice with allografts or tumors (25). A significant enrichment

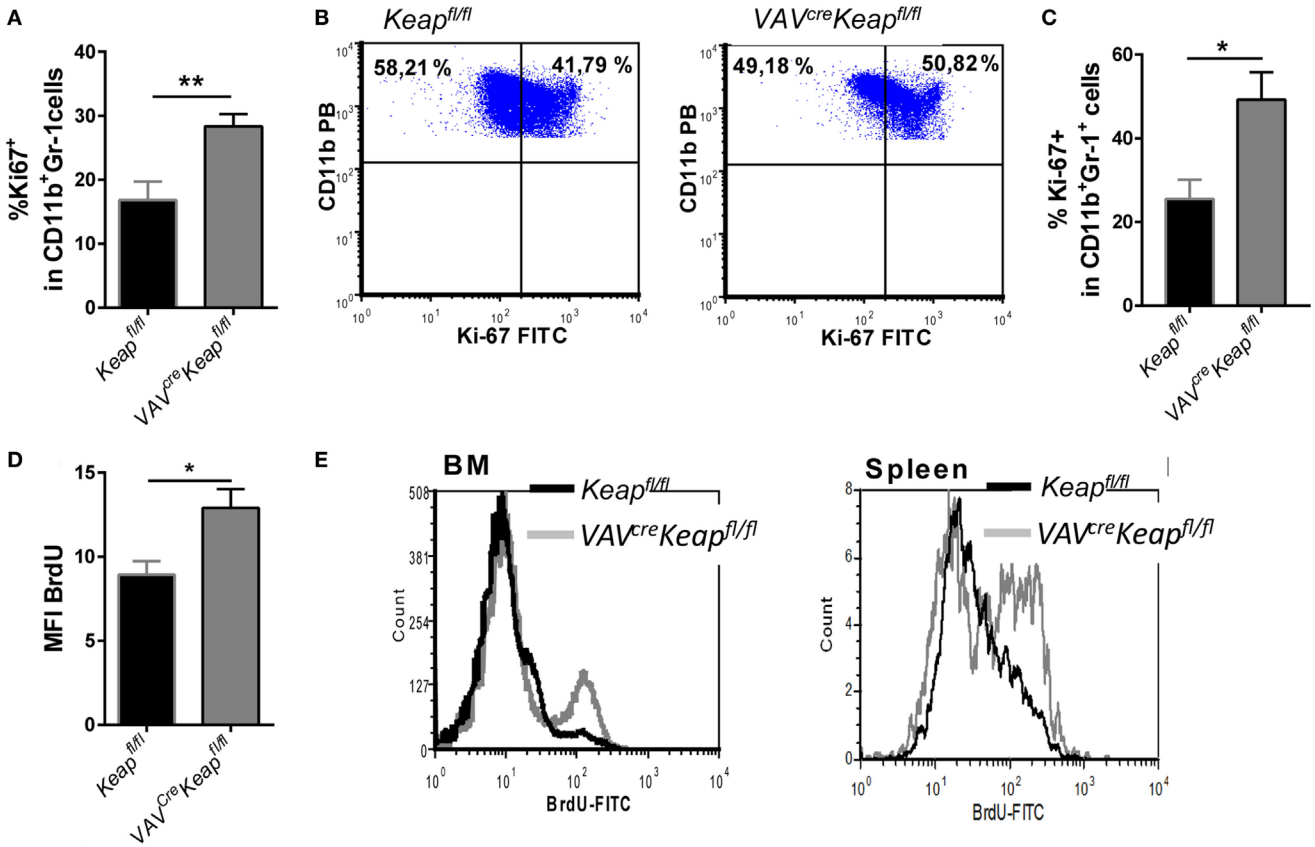

FIGURE 4 | Nrf2 induces proliferation of myeloid-derived suppressor cells (MDSCs). **(A)** Statistical analysis of Ki-67 expression in pre-gated splenic CD11b$^+$Gr-1$^+$ *Keap*$^{fl/fl}$ (n = 5) and *VAV*^{cre}*Keap*$^{fl/fl}$ (n = 5) cells. Bars indicate mean of mean fluorescence intensity and error bars SEM. **(B)** Representative dot plots showing Ki-67 expression in pre-gated CD11b$^+$Gr-1$^+$ BM-derived cells. **(C)** BM-derived cells were incubated with GM-CSF and IL-6 for 8 days and frequencies of Ki-67$^+$ cells within CD11b$^+$Gr-1$^+$ cells were assessed by flow cytometry. Bars indicate mean ± SEM of four independently performed experiments. **(D)** *Keap*$^{fl/fl}$ and *VAV*^{cre}*Keap*$^{fl/fl}$ mice were fed orally with BrdU for 14 days. Statistical analysis of BrdU incorporation among pre-gated CD11b$^+$Gr-1 cells of *Keap*$^{fl/fl}$ (n = 5) and *VAV*^{cre}*Keap*$^{fl/fl}$ (n = 6) mice. **(E)** Representative histogram shows overlays of BrdU incorporation in pre-gated CD11b$^+$Gr-1$^+$ cells of spleen and BM. Two-tailed unpaired t-tests were used to determine p-values for all statistical analysis.

of genes of the *PPP* was observed in our microarray data, together with an enhancement of genes involved in glycolysis. RT-qPCR was used to validate upregulation of the following genes: *glucose transporter 3* (*Glut3, SLC2A3*), the glucose receptor of white blood cells, *hexokinase (Hk)1* and *Hk2*, enzymes responsible for committing glucose to the glycolytic pathway, *6-phosphofructo-2-kinase/fructose-2,6-biphosphatase 3* (PFKFB3) which is known as vital regulator of glycolysis and furthermore promotes cell cycle progression, *glucose-6-phosphate dehydrogenase* (*G6pd*) the rate-limiting enzyme of the *PPP*, *phosphogluconate dehydrogenase* (*Pgd*), the second dehydrogenase in the *PPP*, *transketolase* (*Tkt*), which delivers excess sugar phosphates for glycolysis in the *PPP*, and *pyruvate kinase isozyme M2* (*Pkm2*), which catalyzes the last step within glycolysis (**Figures 5A,B**). In addition, glucose uptake, as measured by flow cytometry, was faster in *VAV*^{cre}*Keap*$^{fl/fl}$ MDSCs compared to *Keap*$^{fl/fl}$ MDSCs (**Figure 5C**) and glucose availability was a prerequisite for generation of MDSCs *in vitro* (**Figure 5D**). MDSC generation in WT cells was enhanced by glucose in a dose-dependent manner, while *VAV*^{cre}*Keap*$^{fl/fl}$ cells differentiated into MDSCs even with low amounts of glucose, which suggests a more efficient uptake and faster utilization of glucose. Nrf2-deficient cells benefit from higher glucose levels, but failed to reach the same frequencies as *Keap*$^{fl/fl}$ cells even at high glucose concentrations (**Figure 5D**). Moreover, rapamycin, a specific mTOR inhibitor which is known to decrease glucose uptake during MDSC differentiation *in vitro* and thereby inhibits MDSC differentiation *in vitro* (25) restores the enhanced MDSC differentiation of *VAV*^{cre}*Keap*$^{fl/fl}$ BM cells to WT levels (**Figures 5E,F**). P-mTOR expression was enhanced in splenic *VAV*^{cre}*Keap*$^{fl/fl}$ MDSCs as well (**Figure 5G**) and activation of mTOR signaling was reflected in the phosphorylation of S6 ribosomal protein (p-S6) (**Figure 5H**). In addition, mitochondrial mass was enhanced in *VAV*^{cre}*Keap*$^{fl/fl}$ MDSCs (**Figure 5I**). Seahorse assays revealed higher maximal respiration rates (OCR) (**Figures 5J,K**), while extracellular acidification rates (ECAR), a measurement of lactate production, were not enhanced (**Figure 5L**), which in addition to the higher mitochondrial mass rates might suggests that *VAV*^{cre}*Keap*$^{fl/fl}$ MDSCs use oxidative phosphorylation to generate ATP from glucose instead of glycolysis with subsequent lactate secretion. Overall, we conclude from these data that

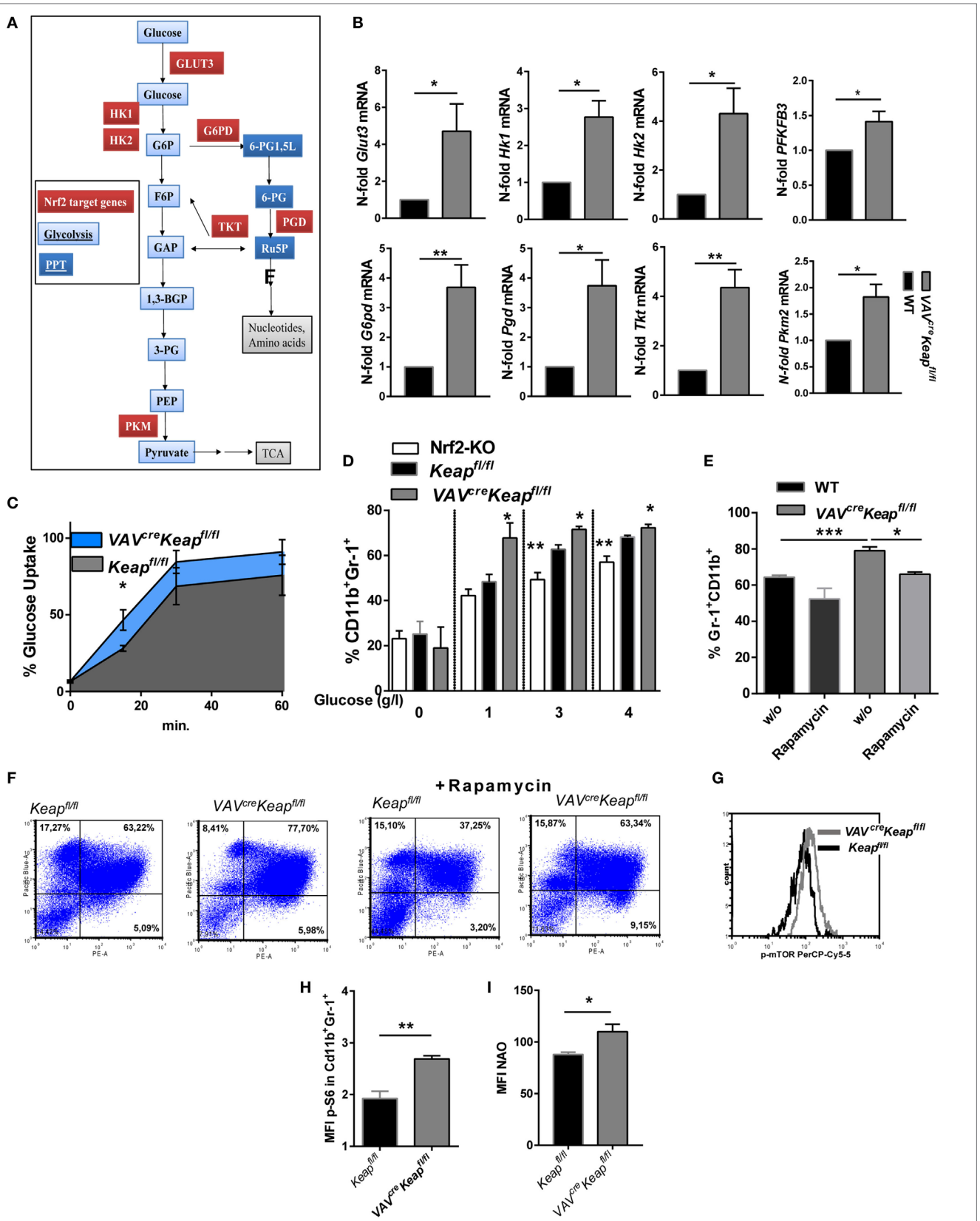

FIGURE 5 | Continued

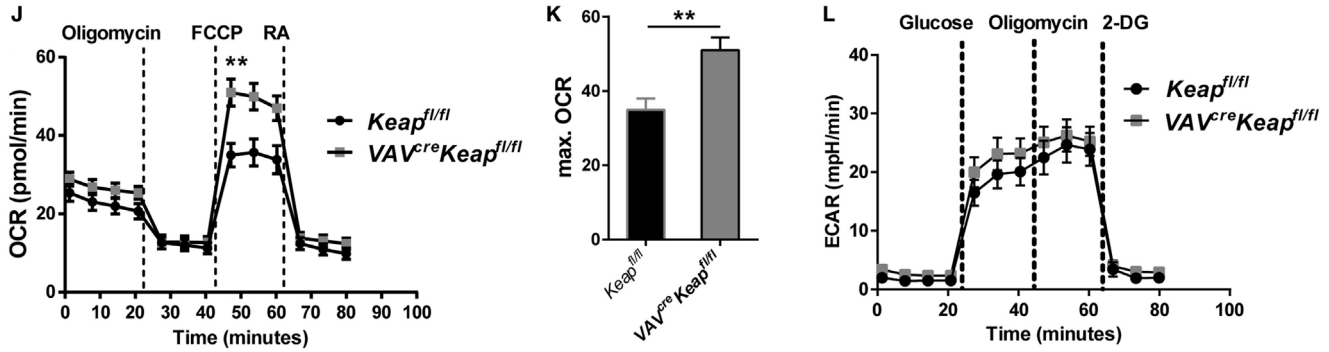

FIGURE 5 | Nrf2 induces metabolic activity in myeloid-derived suppressor cells (MDSCs). **(A)** Metabolic enzymes regulated by Nrf2 in glucose metabolism in MDSCs (own microarray and RT-qPCR data). **(B)** N-fold mRNA expression of metabolic enzymes in MACS isolated *Keap*$^{fl/fl}$ and *VAV*^{cre}*Keap*$^{fl/fl}$ CD11b$^+$Gr-1$^+$ (n = 7–8, PFKFB3 n = 5) cells analyzed by RT-qPCR. Bars indicate mean and error bars SEM, two-tailed one sample test. **(C)** 2NBD-glucose incorporation was analyzed in CD11b$^+$Gr1$^+$ splenocytes from *Keap*$^{fl/fl}$ (n = 3) and *VAV*^{cre}*Keap*$^{fl/fl}$ (n = 4) mice at different time-points, two-tailed unpaired t-test. **(D)** BM-derived cells were incubated with GM-CSF and IL-6 for 8 days with different glucose concentrations, and frequencies of CD11b$^+$Gr-1$^+$ cells were assessed by flow cytometry. Bars indicate mean ± SEM of three independent experiments per group, two-tailed unpaired t-test. **(E,F)** BM-derived cells were incubated with GM-CSF and IL-6 for 8 days in the absence or presence of 1 μM rapamycin, n = 4, two-tailed unpaired t-test. **(G)** Representative histogram of five experiments (p = 0.0155, two-tailed paired t-test) showing p-mTOR expression in splenic CD11b$^+$Gr-1$^+$ cells. **(H)** Mean fluorescent intensity of pS6 expression in CD11b$^+$Gr-1$^+$ cells. **(I)** Statistical analysis of mitochondrial mass of *Keap*$^{fl/fl}$ (n = 4) and *VAV*^{cre}*Keap*$^{fl/fl}$ (n = 4) CD11b$^+$Gr-1$^+$ cells evaluated by assessing NAO mean fluorescence intensity, n = 3, two-tailed unpaired t-test. **(J)** OCR measured under basal conditions and after addition of the indicated drugs. Points indicate mean from six *Keap*$^{fl/fl}$ (n = 6) and six *VAV*^{cre}*Keap*$^{fl/fl}$ (n = 6) CD11b$^+$Gr-1$^+$ cells, error bars SEM. **(K)** Statistical analysis of max. OCR. Bars indicate mean ± SEM. **(L)** ECAR measured under basal conditions and after addition of the indicated drugs. Points indicate mean from six *Keap*$^{fl/fl}$ (n = 6) and six *VAV*^{cre}*Keap*$^{fl/fl}$ (n = 6) CD11b$^+$Gr-1$^+$ cells, error bars SEM, two-tailed unpaired t-test.

Keap1-deficient MDSCs exhibit higher uptake of abundant nutrients and a higher overall metabolic activity, which leads to an increase in metabolic pathways and pushes them into proliferative states.

Nrf2 Activation Resembles LPS-Induced MDSC Expansion

Myeloid-derived suppressor cells strongly expand under septic conditions in mice and men (3, 4). We also observed higher levels of Nrf2 protein expression in CD11b$^+$Gr-1$^+$ cells after treating mice with sublethal doses LPS (**Figure 6A**). We therefore speculated whether LPS-induced MDSCs are regulated by Nrf2 signaling and would show similarities with MDSCs of *VAV*^{cre}*Keap*$^{fl/fl}$ mice. Mice were treated with sublethal doses of LPS (5 mg/kg/bw) which resulted in a significant enrichment of CD11b$^+$Gr-1$^+$ cells in spleens (**Figure 6B**). Systems biology analysis identified a high number of alike regulated genes in LPS-treated MDSCs and *VAV*^{cre}*Keap*$^{fl/fl}$ MDSCs (**Figure 6C**), which revealed strikingly more transcriptional similarities (e.g., less differentially expressed genes) between LPS-induced MDSCs and *Keap*$^{fl/fl}$ MDSCs than between MDSCs of *Keap*$^{fl/fl}$ mice vs. *Keap*$^{fl/fl}$ mice (**Figure 6C**). In detail, we identified 1,798 genes showing significant expression changes (>2-fold change, $p < 0.05$) in LPS-treated vs. *Keap*$^{fl/fl}$ mice. By contrast, only 214 genes were differentially expressed between LPS treated and *VAV*^{cre}*Keap*$^{fl/fl}$ MDSCs using the same significance criteria (**Figure 6C**). In addition, pathway gene set enrichment analysis revealed similar patterns in *VAV*^{cre}*Keap*$^{fl/fl}$ MDSC and LPS-induced MDSCs, which included metabolic pathways like the *PPP* pathway, as well as *nucleotide metabolism* and the *cell cycle* pathway. The same was true for the statin pathway, *complement activation* and *macrophage markers* (Figure S5 in Supplementary Material). Consequently, LPS-induced CD11b$^+$Gr-1$^+$ cells revealed higher Ki-67 expression (**Figure 6D**) and enhanced mRNA levels of genes, which belong to the glucose and PPP pathway (**Figure 6E**) as well as faster glucose uptake (**Figure 6F**). LPS-induced CD11b$^+$Gr-1$^+$ cells had increased ECAR on a basal level and after addition of glucose and furthermore after addition of Oligomycin, which blocks mitochondrial ATP production and promotes maximal rates of glycolysis (**Figure 6G**). In addition to this, OCR was enhanced as well under basal conditions but also after addition of Oligomycin and FCCP, which uncouples oxidative phosphorylation from electron transport and allows maximal respiration (**Figure 6H**). While OCR was enhanced in *VAV*^{cre}*Keap*$^{fl/fl}$ MDSCs as well, an enhanced ECAR seems to be more specific for LPS-induced MDSCs and might occur independently of Nrf2 signaling. To proof if inhibition of mTOR influences LPS-mediated induction of MDSC *in vivo*, we treated mice with sublethal doses of LPS together with rapamycin. *In vivo* administration of rapamycin (2 mg/kg/bw i.p. every day) significantly reduced numbers of CD11b$^+$Gr-1$^+$ cells in spleens of LPS-treated mice (**Figure 6I**). In conclusion, these data show that LPS-induced MDSCs show some similarities with Nrf2-activated MDSCs and are as well characterized by an activation of metabolic pathways and higher proliferation states.

Nrf2 Activation Contributes to TLR4-Mediated MDSCs Expansion

To finally analyze the functional significance of our findings *in vivo* we performed an acute lethal model and a tolerance sepsis model. Mice were treated with either lethal doses (acute,

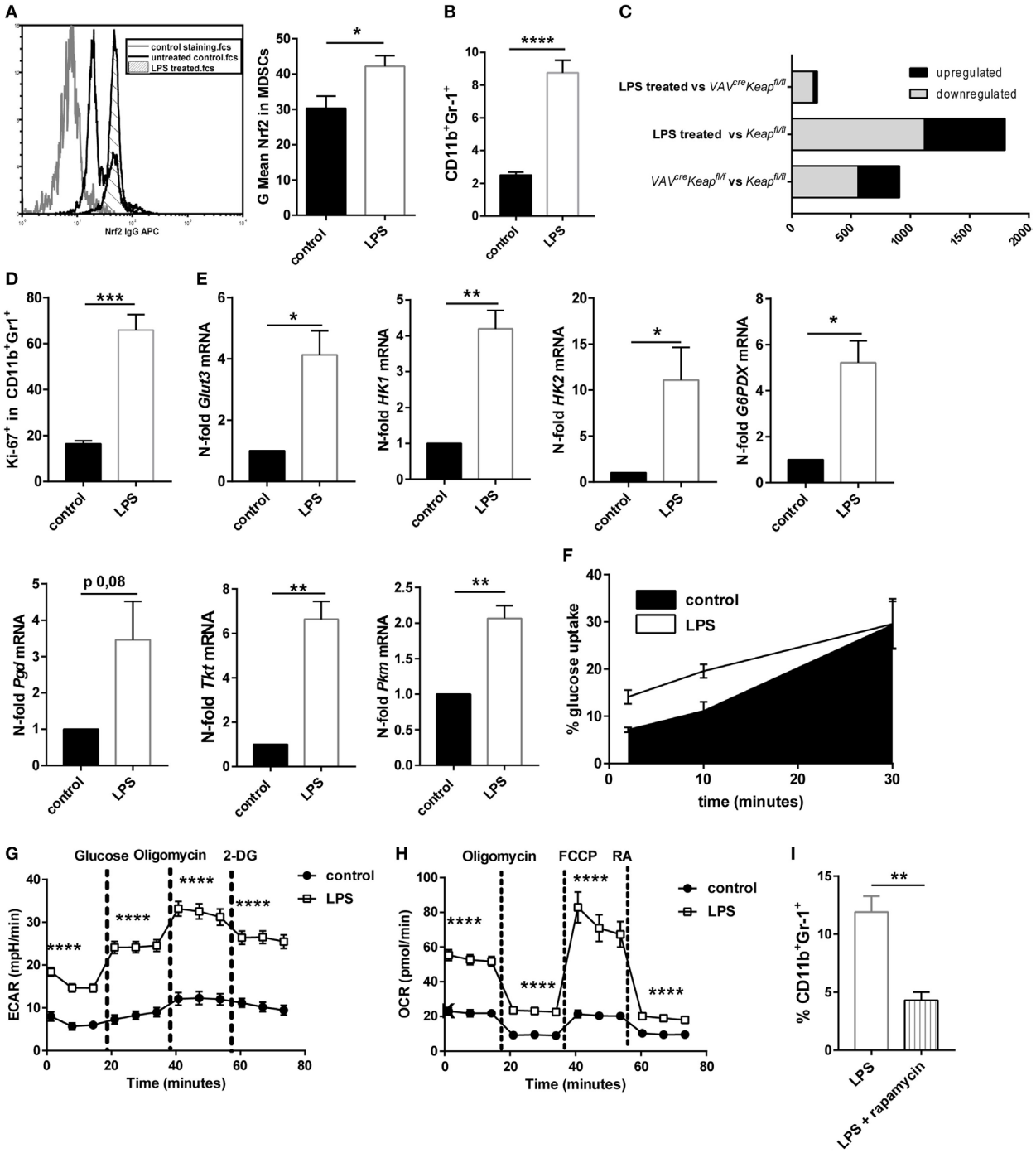

FIGURE 6 | Nrf2 activation resembles LPS-induced myeloid-derived suppressor cell (MDSC) expansion. **(A)** MFI of Nrf2 expression in CD11b$^+$Gr-1$^+$ cells of untreated mice and mice after low-dose LPS treatment, unpaired one-tailed *t*-test, $n = 3$. Bars indicate mean ± SEM. **(B)** Flow cytometric analysis of CD11b$^+$Gr-1$^+$ cells in spleens from untreated *Keap*$^{fl/fl}$ mice and mice after LPS treatment. Bars indicate mean and error bars SEM of three experiments with a total of nine mice per group. **(C)** Diagram of differentially expressed genes ($p < 0.05$, >2-fold) between LPS-induced MDSCs vs. *VAV*^{cre}*Keap*$^{fl/fl}$ (top), LPS-induced MDSCs vs. *Keap*$^{fl/fl}$ (middle), and of *VAV*^{cre}*Keap*$^{fl/fl}$ and WT (bottom). **(D)** Statistical analysis of Ki-67 expression in pre-gated splenic CD11b$^+$Gr-1$^+$ cells from untreated ($n = 4$) and LPS treated ($n = 4$) mice. Bars indicate mean of mean fluorescence intensity and error bars SEM, two-tailed, unpaired *t*-test. **(E)** N-fold mRNA expression of metabolic enzymes in MACS isolated CD11b$^+$Gr-1$^+$ cells analyzed by RT-qPCR. Bars indicate mean and error bars SEM, $n = 5$, two-tailed, one sample test. **(F)** 2NBD-glucose incorporation was analyzed in CD11b$^+$Gr1$^+$ splenocytes from control ($n = 6$) and LPS treated *Keap*$^{fl/fl}$ mice ($n = 6$) mice at different time-points. **(G)** ECAR measured under basal conditions and after addition of the indicated drugs. Points indicate mean from three control and three LPS treated *Keap*$^{fl/fl}$ mice ± SEM of quintuplicates. **(H)** OCR measured under basal conditions and after addition of the indicated drugs. Points indicate mean CD11b$^+$Gr-1$^+$ cells from three control and three LPS treated *Keap*$^{fl/fl}$ mice ± SEM of quintuplicates. **(I)** Flow cytometric analysis of CD11b$^+$Gr-1$^+$ cells in spleens from *Keap*$^{fl/fl}$ mice 4 days after LPS treatment and daily administration of vehicle or rapamycin. Bars indicate mean and error bars SEM of three experiments with a total of four mice per group.

lethal model) or either with sublethal (tolerizing) and subsequent lethal LPS doses (tolerance model). While treatment with low doses and subsequent lethal doses of LPS expectedly induced MDSC expression in wild-type mice and induced a protection against the lethal dose, *Nrf2*$^{-/-}$ mice had to be taken out of the experiment and sacrificed at day 2 or 3 without acquiring an enhanced MDSC population (**Figures 7A,B**). But it should be considered that the reduced numbers of MDSCs during the sepsis experiment in Nrf2$^{-/-}$ mice might be related to the early death of the mice. However, mice with deletion of Nrf2 were not protected by a tolerizing dose of LPS and died after the second lethal dose of LPS, while WT mice that underwent the same procedure were protected and displayed expanded numbers of MDSCs. In addition, mice with a constitutive expression of Nrf2 in hematopoietic cells (*VAV*^{cre}*Keap*$^{fl/fl}$) were resistant against lethal doses of LPS even without previous treatment with tolerizing LPS doses (**Figures 7A,B**). To further test if LPS mediates MDSC expansion and metabolic activation by promoting Nrf2 activation, we analyzed *VAV*^{cre}*Keap*$^{fl/fl}$ CD11b^{+}Gr-1^{+} cells after tolerizing LPS treatment. While LPS significantly enhanced ECAR also in *VAV*^{cre}*Keap*$^{fl/fl}$ CD11b^{+}Gr-1^{+} cells, which was comparable to the effect in wild-type MDSCs (**Figure 7C**), the OCR was only slightly enhanced compared to LPS-induced OCR activation of WT CD11b^{+}Gr-1^{+} cells (**Figures 7D,E**). This experiment shows clearly that LPS favors aerobic glycolysis and lactate production in CD11b^{+}Gr-1^{+} cells independently from Nrf2, but that Nrf2 translocation indeed contributes to enhanced ATP generation from oxidative phosphorylation in MDSCs, which might be protective in LPS-induced septic shock.

DISCUSSION

Nrf2 is a key transcriptional regulator, driving antioxidant gene expression and protection from oxidant injury, and is activated by ROS. Nrf2 regulated genes include a battery of antioxidant enzymes such as Nqo-1. Under quiescent conditions, Nrf2 is bound to Keap1 in the cytoplasm, resulting in proteasomal degradation. Cellular stimuli, such as oxidative stress, induce conformational changes in Keap1 resulting in the release of Nrf2 (26). Subsequently, Nrf2 translocates to the nucleus and transactivates expression of genes containing an antioxidant response element in their promoter regions (27). Nrf2 has been described before as a positive regulator of myeloid differentiation (28) and it skews the differentiation potential of HSCs toward the granulocyte-monocyte lineage (29). Nevertheless, the role for Nrf2 activation in MDSCs in different relevant diseases like cancer is contra dictionary (13, 30, 31). We therefore performed a comprehensive approach to study Nrf2/Keap1 signaling in MDSCs in steady state and sepsis and identified Nrf2 as a key metabolic regulator of these immunosuppressive cells.

In detail, we could show that Nrf2/Keap1 signaling enhances MDSCs in a cell intrinsic manner, Nrf2 activated MDSCs are suppressive *in vitro* and *in vivo* and reveal other characteristics of MDSCs such as expression of arginase and NOS2 and low expression of inflammatory cytokines. Furthermore, Nrf2 induces transcriptional reprogramming of MDSCs, which resembles the transcriptional profile of LPS-induced MDSCs and might thus critically contribute to LPS-mediated tolerance. While it was shown before that Nrf2 is protective in models of sepsis by suppressing LPS-induced inflammatory cytokine expression in macrophages (32–35), these studies did not address MDSCs and our observations in metabolic reprogramming of MDSCs might critically contribute to the protective role of Nrf2 in this context.

Nrf2 is involved in metabolic reprogramming of cancer cells and in regulation of mitochondrial respiration (36–38). Furthermore, a direct mTOR activation by Nrf2 has been shown in human cell lines (39). These earlier data from other cell types support our study, as we also detected an higher metabolic activity, higher glucose uptake and mitochondrial masses, and high mTOR phosphorylation in Nrf2-induced MDSCs cells and could even block Nrf2-induced MDSC generation with rapamycin.

Collectively our study suggests that Nrf2 is a key modulator of MDSCs which might contribute to innate memory in sepsis. Nrf2 activation induces expansion of MDSCs; Nrf2 is also necessary to expand MDSCs in the situation of LPS tolerance. Finally, these MDSCs are protective in acute LPS-induced sepsis. While Nrf2 activated MDSCs share several transcriptional similarities with LPS-tolerized WT MDSCs, we found one striking difference in energy consumption between *VAV*^{cre}*Keap*$^{fl/fl}$ MDSCs and LPS-tolerized WT MDSCs. The latter ones prefer aerobic glycolysis for ATP generation. Even the *VAV*^{cre}*Keap*$^{fl/fl}$ MDSCs can change their metabolic expenditures after LPS treatment to enhanced aerobic glycolysis, which suggests that glycolysis with subsequent lactate production is mainly regulated independently of Nrf2. One advantage of glycolysis in comparison to oxidative phosphorylation is a better maintenance of the redox balance. Most of cellular ROS is produced during oxidative phosphorylation in the mitochondria (40). *VAV*^{cre}*Keap*$^{fl/fl}$ MDSCs show low levels of intracellular ROS despite enhanced mitochondrial mass. This can be explained by constitutive activation and availability of antioxidant enzymes in these cells and might be an important mechanism which enables the cells to enhance mitochondrial ATP production by counteracting subsequent high ROS levels at the same time. With this regard, it is interesting that Nrf2 activation in particular enhances PMN-MDSCs, which are known to produce excessive amount of ROS (41) and that Nrf2 activation also mainly reduces this high ROS levels in PMN-MDSCs and not in M-MDSCs. Therefore, PM-MDSCs may benefit more from Nrf2 activation and subsequent reduction of oxidative stress.

Host defense against recurrent infections is mediated by innate immune memory. The phenomena of trained immunity and endotoxin tolerance are examples of such innate-type memory, with trained immunity describing an adaption that results in the long-lasting capacity to respond more strongly and tolerance describing a hypoinflammatory state. However, it is not clear if these are two fundamentally divergent programs or just represent different facets of innate memory (5). Whereas the priming with β-glucan from *Candida albicans* leads to a state of trained immunity with a potentiation of inflammatory cytokine production, TLR4 stimulation with LPS can induce a state of endotoxin tolerance and suppression of inflammatory cytokines. Recent studies showed that aerobic glycolysis is the metabolic basis for trained immunity (42). The metabolism of tolerant myeloid cells, especially of MDSCs, is less clear and was matter of our study.

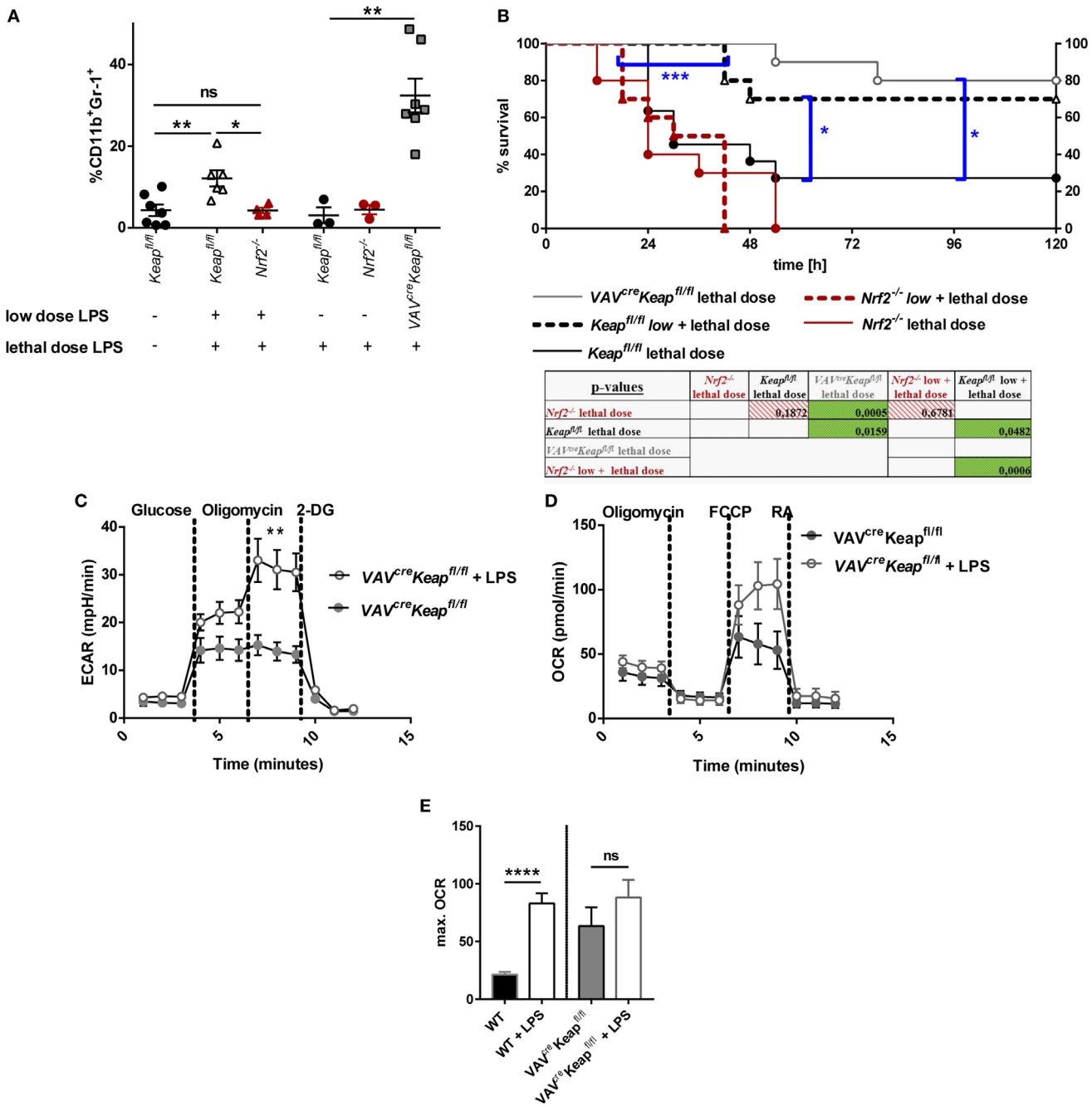

FIGURE 7 | Nrf2 activation in myeloid-derived suppressor cells (MDSCs) regulates LPS-mediated disease. **(A)** Mice were injected with either a low dose of LPS (5 mg/kg of body weight) and subsequently with a lethal dose of LPS (30 mg/kg of body weight) or solely with a lethal dose of LPS (30 mg/kg of body weight). Mice were euthanized depending on a scoring system (usually within the first 48 h after the single lethal dose) or 72 h after injection of the subsequent lethal dose and frequencies of $CD11b^{+}Gr\text{-}1^{+}$ cells were determined, unpaired, two-tailed *t*-test, ±SEM, *N* = 10 mice/group. **(B)** Kaplan–Meyer survival curves of mice, *p*-values were determined by Log-rank/Mantel-Cox Test of survival curves (single comparisons) and a subsequent FDR correction of single *p*-value for multiple comparison test. **(C)** ECAR measured under basal conditions and after addition of the indicated drugs. Points indicate mean from three control and three LPS treated $VAV^{cre}Keap^{fl/fl}$ splenic MDSCs ± SEM. **(D)** OCR measured under basal conditions and after addition of the indicated drugs. Points indicate $CD11b^{+}Gr\text{-}1^{+}$ cells from three control and three LPS treated mice ± SEM. **(E)** Statistical analysis of max. OCR. Bars indicate mean ± SEM.

It is generally accepted that, naïve or tolerant cells rely mainly on oxidative phosphorylation as energy sources while activated cells, e.g., after LPS stimulation, shift their metabolism toward aerobic glycolysis (43). By contrast, leukocytes from patients with severe sepsis and immunoparalysis display a generalized metabolic defect at the level of both glycolysis and oxidative metabolism in cellular

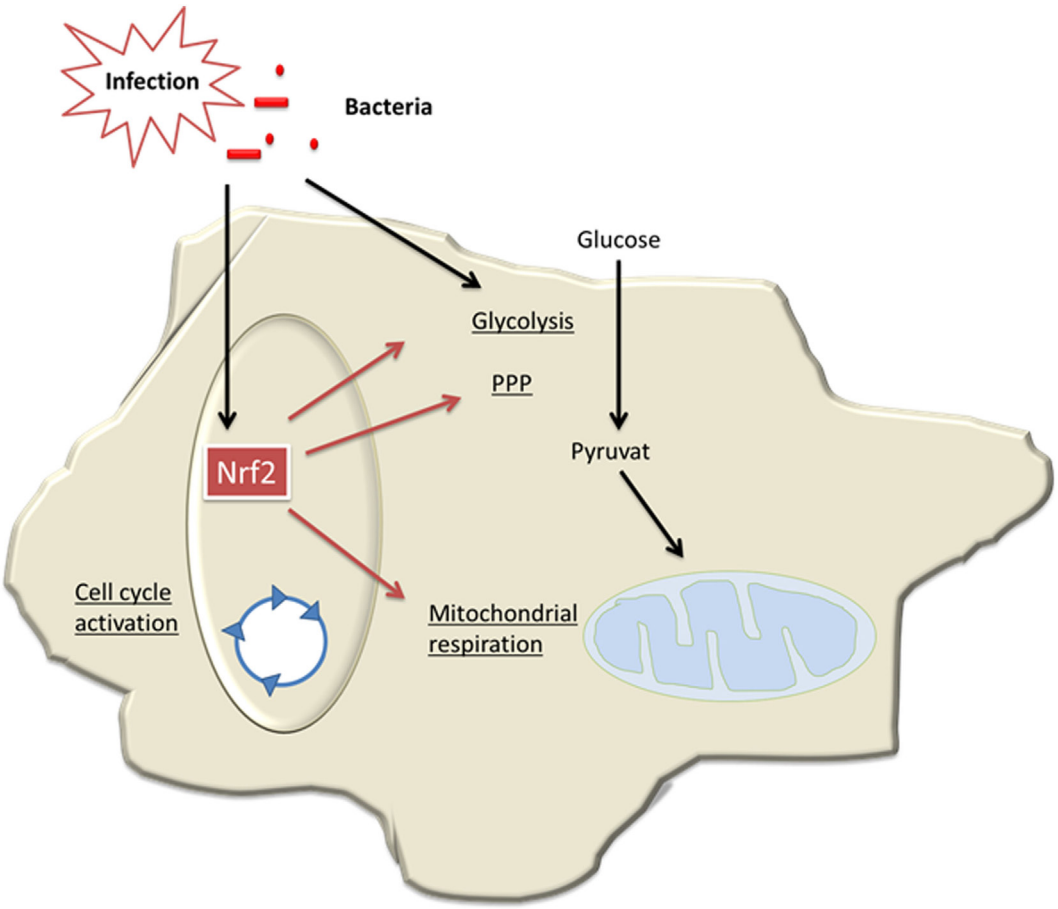

FIGURE 8 | Model of Nrf2-mediated roles in myeloid-derived suppressor cells (MDSCs) in sepsis. During infection and sepsis, Nrf2 is activated by reactive oxygen species (ROS) molecules or TLR pathways. Nrf2 induces cell cycle activation and enhances metabolic activity and thereby contributes to expansion of MDSCs in sepsis.

energy metabolism (5), which means that a complete metabolic reprogramming occurs between acute sepsis and immunoparalysis. We could show that tolerizing mice with a low-dose LPS induced an activation of both glycolysis and OXPHOS in MDSCs. Mice with a constitutive Nrf2 activation already revealed at least higher OCR level and were even protected without any tolerizing pretreatment. Interestingly, MDSCs generated during infection show a strong anti-inflammatory phenotype, compared to splenic $CD11b^{+}Gr1^{+}$ cells under steady-state conditions (11) and we also detected reduced level of inflammatory cytokines *in* $VAV^{cre}Keap^{fl/fl}$ mice compared to untreated MDSCs. This further suggests that MDSCs need to be primed to acquire an anti-inflammatory phenotype either by LPS and/or by Nrf2 activation.

One limitation of our study is that we so far only used LPS injections as a model for sepsis, therefore further studies will also include the cecal ligation and puncture model in order to test the effects of Nrf2 activation in different animal models of sepsis.

In conclusion, our data demonstrate for the first time that Nrf2/Keap signaling critically contributes to generation of tolerant MDSCs, which bear an intact cellular energy metabolism and are protective in sepsis (**Figure 8**). Thereby, our study provides new insights into the regulation of MDSCs, a myeloid cell population that might be relevant in trained immunity of the innate immune system (11, 44).

ETHICS STATEMENT

The study was approved by the regional government authorities and animal procedures were performed according to German legislation for animal protection. Permission for the projects was granted by the Regierungspräsident/LANUV Nordrhein-Westfalen.

AUTHOR CONTRIBUTIONS

KO developed the study, performed experiments, analyzed data, and wrote the paper. AF generated $VAV^{cre}Keap^{fl/fl}$ mice and performed *in vivo* sepsis experiments. PK, WK, and JB performed experiments. ML and JM performed seahorse assays. IC performed bioinfomatic analyses. BD performed and analyzed microarrays. EV and SB performed experiments. AS, JR, and NW contributed to the writing of the paper. CW and KT developed the study and wrote the paper.

ACKNOWLEDGMENTS

We would like to thank Lilia Kopp for assistance in this study. This research project was supported by the START-Program of the Faculty of Medicine (15/16), RWTH Aachen and by the DFG (OH 252/2-1).

SUPPLEMENTARY MATERIAL

The Supplementary Material for this article can be found online at https://www.frontiersin.org/articles/10.3389/fimmu.2018.01552/full#supplementary-material.

REFERENCES

1. Gabrilovich DI, Nagaraj S. Myeloid-derived suppressor cells as regulators of the immune system. *Nat Rev Immunol* (2009) 9:162–74. doi:10.1038/nri2506
2. Bronte V, Brandau S, Chen SH, Colombo MP, Frey AB, Greten TF, et al. Recommendations for myeloid-derived suppressor cell nomenclature and characterization standards. *Nat Commun* (2016) 7:12150. doi:10.1038/ncomms12150
3. Darcy CJ, Minigo G, Piera KA, Davis JS, McNeil YR, Chen Y, et al. Neutrophils with myeloid derived suppressor function deplete arginine and constrain T cell function in septic shock patients. *Crit Care* (2014) 18:R163. doi:10.1186/cc14003
4. Derive M, Bouazza Y, Alauzet C, Gibot S. Myeloid-derived suppressor cells control microbial sepsis. *Intensive Care Med* (2012) 38:1040–9. doi:10.1007/s00134-012-2574-4
5. Netea MG, Joosten LA, Latz E, Mills KH, Natoli G, Stunnenberg HG, et al. Trained immunity: a program of innate immune memory in health and disease. *Science* (2016) 352:aaf1098. doi:10.1126/science.aaf1098
6. Seeley JJ, Ghosh S. Molecular mechanisms of innate memory and tolerance to LPS. *J Leukoc Biol* (2017) 101:107–19. doi:10.1189/jlb.3MR0316-118RR
7. Saeed S, Quintin J, Kerstens HH, Rao NA, Aghajanirefah A, Matarese F, et al. Epigenetic programming of monocyte-to-macrophage differentiation and trained innate immunity. *Science* (2014) 345:1251086. doi:10.1126/science.1251086
8. Cheng SC, Scicluna BP, Arts RJ, Gresnigt MS, Lachmandas E, Giamarellos-Bourboulis EJ, et al. Broad defects in the energy metabolism of leukocytes underlie immunoparalysis in sepsis. *Nat Immunol* (2016) 17:406–13. doi:10.1038/ni.3398
9. Delano MJ, Scumpia PO, Weinstein JS, Coco D, Nagaraj S, Kelly-Scumpia KM, et al. MyD88-dependent expansion of an immature GR-1(+)CD11b(+) population induces T cell suppression and Th2 polarization in sepsis. *J Exp Med* (2007) 204:1463–74. doi:10.1084/jem.20062602
10. McPeak MB, Youssef D, Williams DA, Pritchett CL, Yao ZQ, McCall CE, et al. Frontline science: myeloid cell-specific deletion of Cebpb decreases sepsis-induced immunosuppression in mice. *J Leukoc Biol* (2017) 102(2):191–200. doi:10.1189/jlb.4HI1216-537R
11. Sander LE, Sackett SD, Dierssen U, Beraza N, Linke RP, Muller M, et al. Hepatic acute-phase proteins control innate immune responses during infection by promoting myeloid-derived suppressor cell function. *J Exp Med* (2010) 207:1453–64. doi:10.1084/jem.20091474
12. Mantzarlis K, Tsolaki V, Zakynthinos E. Role of oxidative stress and mitochondrial dysfunction in sepsis and potential therapies. *Oxid Med Cell Longev* (2017) 2017:5985209. doi:10.1155/2017/5985209
13. Beury DW, Carter KA, Nelson C, Sinha P, Hanson E, Nyandjo M, et al. Myeloid-derived suppressor cell survival and function are regulated by the transcription factor Nrf2. *J Immunol* (2016) 196:3470–8. doi:10.4049/jimmunol.1501785
14. Okawa H, Motohashi H, Kobayashi A, Aburatani H, Kensler TW, Yamamoto M. Hepatocyte-specific deletion of the keap1 gene activates Nrf2 and confers potent resistance against acute drug toxicity. *Biochem Biophys Res Commun* (2006) 339:79–88. doi:10.1016/j.bbrc.2005.10.185
15. Chan K, Lu R, Chang JC, Kan YW. NRF2, a member of the NFE2 family of transcription factors, is not essential for murine erythropoiesis, growth, and development. *Proc Natl Acad Sci U S A* (1996) 93:13943–8. doi:10.1073/pnas.93.24.13943
16. Bleich A, Mahler M, Most C, Leiter EH, Liebler-Tenorio E, Elson CO, et al. Refined histopathologic scoring system improves power to detect colitis QTL in mice. *Mamm Genome* (2004) 15:865–71. doi:10.1007/s00335-004-2392-2
17. Pils MC, Bleich A, Prinz I, Fasnacht N, Bollati-Fogolin M, Schippers A, et al. Commensal gut flora reduces susceptibility to experimentally induced colitis via T-cell-derived interleukin-10. *Inflamm Bowel Dis* (2011) 17:2038–46. doi:10.1002/ibd.21587
18. Irizarry RA, Hobbs B, Collin F, Beazer-Barclay YD, Antonellis KJ, Scherf U, et al. Exploration, normalization, and summaries of high density oligonucleotide array probe level data. *Biostatistics* (2003) 4:249–64. doi:10.1093/biostatistics/4.2.249
19. Wang J, Duncan D, Shi Z, Zhang B. WEB-based GEne SeT AnaLysis Toolkit (WebGestalt): update 2013. *Nucleic Acids Res* (2013) 41:W77–83. doi:10.1093/nar/gkt439
20. Wakabayashi N, Itoh K, Wakabayashi J, Motohashi H, Noda S, Takahashi S, et al. Keap1-null mutation leads to postnatal lethality due to constitutive Nrf2 activation. *Nat Genet* (2003) 35:238–45. doi:10.1038/ng1248
21. Taguchi K, Maher JM, Suzuki T, Kawatani Y, Motohashi H, Yamamoto M. Genetic analysis of cytoprotective functions supported by graded expression of Keap1. *Mol Cell Biol* (2010) 30:3016–26. doi:10.1128/MCB.01591-09
22. Drujont L, Carretero-Iglesia L, Bouchet-Delbos L, Beriou G, Merieau E, Hill M, et al. Evaluation of the therapeutic potential of bone marrow-derived myeloid suppressor cell (MDSC) adoptive transfer in mouse models of autoimmunity and allograft rejection. *PLoS One* (2014) 9:e100013. doi:10.1371/journal.pone.0100013
23. Marigo I, Bosio E, Solito S, Mesa C, Fernandez A, Dolcetti L, et al. Tumor-induced tolerance and immune suppression depend on the C/EBPbeta transcription factor. *Immunity* (2010) 32:790–802. doi:10.1016/j.immuni.2010.05.010
24. Hossain F, Al-Khami AA, Wyczechowska D, Hernandez C, Zheng L, Reiss K, et al. Inhibition of fatty acid oxidation modulates immunosuppressive functions of myeloid-derived suppressor cells and enhances cancer therapies. *Cancer Immunol Res* (2015) 3:1236–47. doi:10.1158/2326-6066.CIR-15-0036
25. Wu T, Zhao Y, Wang H, Li Y, Shao L, Wang R, et al. mTOR masters monocytic myeloid-derived suppressor cells in mice with allografts or tumors. *Sci Rep* (2016) 6:20250. doi:10.1038/srep20250
26. Huang Y, Li W, Su ZY, Kong AN. The complexity of the Nrf2 pathway: beyond the antioxidant response. *J Nutr Biochem* (2015) 26:1401–13. doi:10.1016/j.jnutbio.2015.08.001
27. Kensler TW, Wakabayashi N, Biswal S. Cell survival responses to environmental stresses via the Keap1-Nrf2-ARE pathway. *Annu Rev Pharmacol Toxicol* (2007) 47:89–116. doi:10.1146/annurev.pharmtox.46.120604.141046
28. Bobilev I, Novik V, Levi I, Shpilberg O, Levy J, Sharoni Y, et al. The Nrf2 transcription factor is a positive regulator of myeloid differentiation of acute myeloid leukemia cells. *Cancer Biol Ther* (2011) 11:317–29.
29. Murakami S, Shimizu R, Romeo PH, Yamamoto M, Motohashi H. Keap1-Nrf2 system regulates cell fate determination of hematopoietic stem cells. *Genes Cells* (2014) 19:239–53. doi:10.1111/gtc.12126
30. Hiramoto K, Satoh H, Suzuki T, Moriguchi T, Pi J, Shimosegawa T, et al. Myeloid lineage-specific deletion of antioxidant system enhances tumor metastasis. *Cancer Prev Res (Phila)* (2014) 7:835–44. doi:10.1158/1940-6207.CAPR-14-0094
31. Satoh H, Moriguchi T, Taguchi K, Takai J, Maher JM, Suzuki T, et al. Nrf2-deficiency creates a responsive microenvironment for metastasis to the lung. *Carcinogenesis* (2010) 31:1833–43. doi:10.1093/carcin/bgq105
32. Kim JH, Choi YK, Lee KS, Cho DH, Baek YY, Lee DK, et al. Functional dissection of Nrf2-dependent phase II genes in vascular inflammation and endotoxic injury using Keap1 siRNA. *Free Radic Biol Med* (2012) 53:629–40. doi:10.1016/j.freeradbiomed.2012.04.019
33. Kobayashi EH, Suzuki T, Funayama R, Nagashima T, Hayashi M, Sekine H, et al. Nrf2 suppresses macrophage inflammatory response by blocking proinflammatory cytokine transcription. *Nat Commun* (2016) 7:11624. doi:10.1038/ncomms11624

34. Kong X, Thimmulappa R, Craciun F, Harvey C, Singh A, Kombairaju P, et al. Enhancing Nrf2 pathway by disruption of Keap1 in myeloid leukocytes protects against sepsis. *Am J Respir Crit Care Med* (2011) 184:928–38. doi:10.1164/rccm.201102-0271OC
35. Thimmulappa RK, Scollick C, Traore K, Yates M, Trush MA, Liby KT, et al. Nrf2-dependent protection from LPS induced inflammatory response and mortality by CDDO-imidazolide. *Biochem Biophys Res Commun* (2006) 351:883–9. doi:10.1016/j.bbrc.2006.10.102
36. Dinkova-Kostova AT, Abramov AY. The emerging role of Nrf2 in mitochondrial function. *Free Radic Biol Med* (2015) 88:179–88. doi:10.1016/j.freeradbiomed.2015.04.036
37. Holmstrom KM, Baird L, Zhang Y, Hargreaves I, Chalasani A, Land JM, et al. Nrf2 impacts cellular bioenergetics by controlling substrate availability for mitochondrial respiration. *Biol Open* (2013) 2:761–70. doi:10.1242/bio.20134853
38. Mitsuishi Y, Taguchi K, Kawatani Y, Shibata T, Nukiwa T, Aburatani H, et al. Nrf2 redirects glucose and glutamine into anabolic pathways in metabolic reprogramming. *Cancer Cell* (2012) 22:66–79. doi:10.1016/j.ccr.2012.05.016
39. Bendavit G, Aboulkassim T, Hilmi K, Shah S, Batist G. Nrf2 transcription factor can directly regulate mTOR: linking cytoprotective gene expression to a major metabolic regulator that generates redox activity. *J Biol Chem* (2016) 291:25476–88. doi:10.1074/jbc.M116.760249
40. Holmstrom KM, Finkel T. Cellular mechanisms and physiological consequences of redox-dependent signalling. *Nat Rev Mol Cell Biol* (2014) 15:411–21. doi:10.1038/nrm3801
41. Parker KH, Beury DW, Ostrand-Rosenberg S. Myeloid-derived suppressor cells: critical cells driving immune suppression in the tumor microenvironment. *Adv Cancer Res* (2015) 128:95–139. doi:10.1016/bs.acr.2015.04.002
42. Cheng SC, Quintin J, Cramer RA, Shepardson KM, Saeed S, Kumar V, et al. mTOR- and HIF-1alpha-mediated aerobic glycolysis as metabolic basis for trained immunity. *Science* (2014) 345:1250684. doi:10.1126/science.1250684
43. O'Neill LA, Kishton RJ, Rathmell J. A guide to immunometabolism for immunologists. *Nat Rev Immunol* (2016) 16:553–65. doi:10.1038/nri.2016.70
44. Katoh H, Wang D, Daikoku T, Sun H, Dey SK, Dubois RN. CXCR2-expressing myeloid-derived suppressor cells are essential to promote colitis-associated tumorigenesis. *Cancer Cell* (2013) 24:631–44. doi:10.1016/j.ccr.2013.10.009

Conflict of Interest Statement: The authors declare that the research was conducted in the absence of any commercial or financial relationships that could be construed as a potential conflict of interest.

frontiers in Immunology

ORIGINAL RESEARCH
published: 26 March 2018
doi: 10.3389/fimmu.2018.00537

PKCδ-Mediated Nox2 Activation Promotes Fluid-Phase Pinocytosis of Antigens by Immature Dendritic Cells

*Bhupesh Singla[1], Pushpankur Ghoshal[1], Huiping Lin[1], Qingqing Wei[2], Zheng Dong[2] and Gábor Csányi[1,3]**

[1] Vascular Biology Center, Medical College of Georgia, Augusta University, Augusta, GA, United States, [2] Department of Cellular Biology and Anatomy, Medical College of Georgia, Augusta University, Augusta, GA, United States, [3] Department of Pharmacology and Toxicology, Medical College of Georgia, Augusta University, Augusta, GA, United States

Aims: Macropinocytosis is a major endocytic pathway by which dendritic cells (DCs) internalize antigens in the periphery. Despite the importance of DCs in the initiation and control of adaptive immune responses, the signaling mechanisms mediating DC macropinocytosis of antigens remain largely unknown. The goal of the present study was to investigate whether protein kinase C (PKC) is involved in stimulation of DC macropinocytosis and, if so, to identify the specific PKC isoform(s) and downstream signaling mechanisms involved.

Methods: Various cellular, molecular and immunological techniques, pharmacological approaches and genetic knockout mice were utilized to investigate the signaling mechanisms mediating DC macropinocytosis.

Results: Confocal laser scanning microscopy confirmed that DCs internalize fluorescent antigens (ovalbumin) using macropinocytosis. Pharmacological blockade of classical and novel PKC isoforms using calphostin C abolished both phorbol ester- and hepatocyte growth factor-induced antigen macropinocytosis in DCs. The qRT-PCR experiments identified PKCδ as the dominant PKC isoform in DCs. Genetic studies demonstrated the functional role of PKCδ in DC macropinocytosis of antigens, their subsequent maturation, and secretion of various T-cell stimulatory cytokines, including IL-1α, TNF-α and IFN-β. Additional mechanistic studies identified NADPH oxidase 2 (Nox2) and intracellular superoxide anion as important players in DC macropinocytosis of antigens downstream of PKCδ activation.

Conclusion: The findings of the present study demonstrate a novel mechanism by which PKCδ activation *via* stimulation of Nox2 activity and downstream redox signaling promotes DC macropinocytosis of antigens. PKCδ/Nox2-mediated antigen macropinocytosis stimulates maturation of DCs and secretion of T-cell stimulatory cytokines. These findings may contribute to a better understanding of the regulatory mechanisms in DC macropinocytosis and downstream regulation of T-cell-mediated responses.

Keywords: dendritic cells, macropinocytosis, protein kinase C, NADPH oxidase, reactive oxygen species

OPEN ACCESS

Edited by:
Manuela Mengozzi, University of Sussex, United Kingdom

Reviewed by:
Chinten James Lim, University of British Columbia, Canada
Hideki Nakano, National Institute of Environmental Health Sciences (NIH), United States

***Correspondence:**
Gábor Csányi
gcsanyi@augusta.edu

Specialty section:
This article was submitted to Inflammation, a section of the journal Frontiers in Immunology

Received: *15 December 2017*
Accepted: *02 March 2018*
Published: *26 March 2018*

Citation:
Singla B, Ghoshal P, Lin H, Wei Q, Dong Z and Csányi G (2018) PKCδ-Mediated Nox2 Activation Promotes Fluid-Phase Pinocytosis of Antigens by Immature Dendritic Cells. Front. Immunol. 9:537. doi: 10.3389/fimmu.2018.00537

INTRODUCTION

Dendritic cells (DCs) are professional antigen-presenting cells (APCs) that initiate and direct adaptive immune responses (1–3). Immature DCs (iDCs) in peripheral tissue constantly sample their surroundings for antigens. Following antigen internalization, iDCs exhibit dramatic functional and morphological changes, called *maturation*, which optimizes antigen processing and maximizes antigen presentation to naïve T cells. During maturation, iDCs acquire a phenotype of professional APCs, synthetize and secrete T-cell costimulatory cytokines, increase plasma membrane expression of CD86 and CD80, and translocate major histocompatibility complex class I and II (MHC I/II) molecules from the late endocytic compartments to the plasma membrane (4). Mature DCs migrate to draining lymph nodes and present the processed antigenic peptides on MHC I/II to T lymphocytes to initiate antigen-specific immune responses (2). The ability of mature DCs to internalize and process antigens is inhibited to restrict their ability to present additional antigens encountered after the initial immunogenic stimulus (5).

Immature DCs capture antigens by several distinct mechanisms, including "non-specific" internalization by macropinocytosis and "specific" uptake *via* receptor-mediated endocytosis and phagocytosis (4). Importantly, the endocytic process by which antigens are internalized not only determines the intracellular trafficking of the antigen but also influences the type of T-cell epitope being presented on MHC molecules (6). Previous studies showed that macropinocytosis is distinct in many ways from receptor-mediated endocytosis and phagocytosis (7). Indeed, phagocytosis and receptor-mediated endocytosis are strictly ligand-receptor-driven processes (4, 8), while macropinocytosis is characterized by receptor-independent internalization of extracellular fluid and pericellular solutes (4, 9). Phagocytosis is initiated by recognition and binding of the particle to the plasma membrane, followed by localized actin remodeling, formation of a phagocytic cup around the particle and its subsequent internalization into the phagosome (7). Unlike phagocytosis, receptor-mediated endocytosis is largely an actin-independent process in mammalian cells (10). In receptor-mediated endocytosis, specific cell surface receptors, such as C-type lectin receptors, Fcγ and Fcε receptors mediate antigen internalization by DCs (11). On the contrary, macropinocytosis involves particle-independent, global activation of the actin cytoskeleton resulting in extensive plasma membrane ruffling over the entire surface of the cell. Some of the membrane ruffles curve into O-shaped macropinocytotic cups and close or fuse with the non-extended plasma membrane, leading to macropinosome formation and non-specific internalization of extracellular fluid and associated solutes (4, 7, 9).

Previous studies demonstrated that membrane ruffling and macropinocytosis can be stimulated by various growth factors, including epidermal growth factor (12) and hepatocyte growth factor (HGF) (13), cytokines (14, 15), and phorbol esters (15, 16). Although the precise signaling mechanisms responsible for stimulation of macropinocytosis in DCs and other cell types are incompletely defined, phosphatidylinositol phosphates have been shown to play an important role (17). Plasma membrane phosphatidylinositol 4,5-bisphosphate [$PI(4,5)P_2$] regulates the activity of a number of actin-binding proteins and, thus, plays an important role in controlling submembranous actin polymerization and reorganization during macropinocytosis (10). $PI(4,5)P_2$ is phosphorylated to $PI(3,4,5)P_3$ by phosphatidylinositol-3-kinase (PI3K) followed by recruitment and activation of small GTPase Rac1 and Rab5 to mediate cup closure and initiate macropinosome formation (10, 18). Furthermore, $PI(4,5)P_2$ is a substrate for phospholipase C, which produces two important signaling molecules: diacylglycerol (DAG) and inositol trisphosphate (IP_3) (17). Recent studies by our lab and others have demonstrated that DAG-mediated protein kinase C (PKC) activation in macrophages plays an important role in macropinocytosis (15, 17). The PKC family has been categorized into three groups, namely the DAG/Ca^{2+}-dependent classical (α, β, and γ), DAG-dependent novel (δ, ε, η, and θ), and DAG/Ca^{2+}-independent atypical (λ, ι, μ, and ζ) PKC isoforms. Importantly, the PKC isoforms differ in their mechanism of activation, substrates, and signaling in the cell (19–21). The specific PKC isoform(s) mediating DC macropinocytosis of antigens and the signaling mechanisms downstream of PKC leading to macropinocytosis are currently unknown.

The NADPH oxidases (Noxs) are transmembrane proteins that transfer electrons across biological membranes to reduce oxygen to superoxide anion ($O_2^{\bullet-}$) or its dismuted form, hydrogen peroxide (H_2O_2) (22). The Nox family consists of seven members, namely Nox1–Nox5, dual oxidase (DUOX) 1, and DUOX2. Nox2, the prototype isoform of the Nox family, consists of flavocytochrome b558, an integral membrane heterodimer comprising $gp91^{phox}$ and $p22^{phox}$, and four cytoplasmic protein subunits: $p47^{phox}$, $p67^{phox}$, $p40^{phox}$, and Rac1 (23). Nox2 is dormant in resting cells and becomes rapidly activated on stimulation by growth factors, cytokines, and phorbol esters (15, 24–26). During activation, PKC mediates phosphorylation of $p47^{phox}$, leading to its translocation to the catalytic core of Nox2 along with the cytosolic subunits, followed by NADPH-mediated electron transfer and $O_2^{\bullet-}$ generation (26). Although signal transduction mediators upstream of Nox2 activation, such as PKC and Rac1, play an important role in macropinocytosis (10) and Nox2 activators also stimulate macropinocytosis (13, 15, 26, 27), the role of Nox2 in DC macropinocytosis has not been previously investigated.

The goal of the present study was to identify the specific PKC isoform(s) involved in DC macropinocytosis. We also tested the hypothesis that Nox2 activation downstream of PKC contributes to DC macropinocytosis of antigens, leading to their maturation and secretion of T- cell stimulatory cytokines. The data shown herein demonstrate the involvement of a previously unidentified mechanism by which DAG-inducible PKCδ *via* stimulation of Nox2 activity promotes DC macropinocytosis of antigens. PKCδ–Nox2-mediated antigen macropinocytosis induced MHC II translocation to the membrane, increased expression of CD86, and secretion of various T-cell stimulatory cytokines. These findings may be relevant for various immune disorders involving elevated uptake of antigens by DC, and ultimately leading to enhanced T-cell-mediated inflammatory responses.

MATERIALS AND METHODS

Reagents and Antibodies

Mouse recombinant granulocyte-macrophage colony-stimulating factor (GM-CSF), interleukin-4 (IL-4), recombinant murine FLT3-Ligand (FLT3L) and HGF were obtained from Peprotech (Rocky Hill, NJ, USA). FM™ 4-64 Dye and Alexa Fluor 488-conjugated ovalbumin (OVA) was procured from Molecular Probes (Eugene, OR, USA). Calphostin C, superoxide dismutase (SOD), diphenyleneiodonium chloride (DPI), LY294002, 5-(N-ethyl-N-isopropyl) amiloride (EIPA), phorbol 12-myristate 13-acetate (PMA), cytochalasin D, lipopolysaccharide (LPS), and OVA were purchased from Sigma-Aldrich (St. Louis, MO, USA). Protease and phosphatase inhibitor cocktail tablets were purchased from Roche Diagnostics GmbH (Mannheim, Germany). FITC-OVA and dihydroethidium (DHE) were obtained from Thermofisher Scientific (Grand Island, New York, NY, USA). EUK-134 was purchased from Cayman Chemical (Ann Arbor, MI, USA). L-012 was obtained from Wako Chemicals (Richmond, VA, USA). PE/Cy7-CD11c (clone N418), APC-CD11c (clone N418), FITC-MHCII (clone M5/114.15.2), APC-CD86 (clone GL1) monoclonal antibodies, and respective isotype controls were purchased from Thermofisher Scientific.

Animals

All experimental protocols were approved by the Institutional Animal Care and Use Committee of Augusta University and conducted in accordance with the National Institutes of Health Guide for the Care and Use of Laboratory Animals. Eight- to ten-week-old male, C57BL/6 (wild type) and Nox2$^{y/-}$ mice were purchased from The Jackson Laboratory (Bar Harbor, ME, USA). Breeding pairs of PKCδ$^{+/-}$ mice (kindly provided by Dr. Zheng Dong, Augusta University, USA), were used to generate PKCδ$^{+/-}$, PKCδ$^{-/-}$, and PKCδ$^{+/+}$ mice. Mice were housed at constant temperature (21–23°C) with *ad libitum* access to standard rodent chow and water, and were maintained in 12 h light-dark cycles. Mice were anesthetized (isoflurane inhalation, 3%) and sacrificed by cervical dislocation and exsanguination.

Generation of Mouse Bone Marrow-Derived Immature Dendritic Cells (BMiDCs) and Isolation of Splenic DCs

Bone Marrow-Derived Immature Dendritic Cells

The femur and tibia of sacrificed mice were cleaned of adherent muscle and connective tissue. Bone marrow was flushed from bone marrow cavities using a 27-gauge needle syringe containing Harvest Buffer [phosphate-buffered saline (PBS) and 2% heat-inactivated FBS] (28). Cells were plated in RPMI-1640 medium containing 10% FBS and differentiated into DCs with GM-CSF (20 ng/mL) and IL-4 (2 ng/mL) for 7 days. After 7 days, non-adherent and loosely attached cells were collected by gentle washing and used for experiments. For FLT3L-iDCs, mouse bone marrow cells were differentiated in complete RPMI-1640 medium containing 200 ng/mL mouse recombinant FLT3L for 9 days without disturbing (29). iDCs were identified by CD11c positivity, low- to intermediate expression of MHC II, and low expression of CD86. LPS (500 ng/mL, 24 h), a known inducer of DC maturation, was used to validate the immature phenotype of differentiated DCs.

Splenic DCs

Isolated mouse spleens were minced and digested with collagenase/dispase solution (collagenase: 0.1 U/mL, dispase: 0.8 U/mL) (Roche Diagnostics Corporation, Indianapolis, IN, USA) for 45 min at 37°C. After digestion, the cell suspension was filtered through a 70-μm cell strainer and CD11c$^+$ cells were isolated using mouse CD11c MicroBeads (Miltenyi Biotec Inc. Auburn, CA, USA) according to the manufacturer's instructions.

Flow Cytometry

Splenic DCs and BMiDCs were incubated with FITC-OVA (50 μg/mL; 45,000 MW) in the presence and absence of PMA (1 μM) for 1 and 5 h, respectively. In separate experiments, BMiDCs were incubated with vehicle or HGF (100 ng/mL) and FITC-OVA internalization was investigated. After the incubation time, cells were washed twice with ice-cold PBS, stained with PE/Cy7- or APC-labeled CD11c (or respective isotype controls) monoclonal antibodies, fixed in 2% paraformaldehyde (PFA), resuspended in fluorescence-activated cell sorting (FACS) buffer (2% BSA and 0.01% sodium azide in PBS) and analyzed using a Becton Dickinson FACSCalibur flow cytometer. CD11c$^+$ cells were gated and analyzed for FITC-OVA uptake.

Confocal Microscopy

Bone marrow-derived immature dendritic cells were plated on poly-d lysine-coated glass bottom dishes and allowed to adhere for 90 min. Cells were incubated with FM™ 4-64 (5 μg/mL, 10 min) to label the plasma membrane and treated with Alexa Fluor 488-OVA (50 μg/mL; 45,000 MW). Macropinocytosis was stimulated by incubation with PMA (1 μM, 30 min). Accumulation of Alexa Fluor 488-OVA in membrane-derived macropinosomes was visualized using a Zeiss 780 inverted confocal microscope in live cells.

In separate experiments, BMiDCs were treated with FITC-OVA, incubated with vehicle or PMA for 5 h, and centrifuged at 300 × *g* for 10 min to sediment on gelatin-coated coverslips. Cells were fixed in 2% PFA, permeabilized with 0.1% Triton X-100, and stained with TRITC-phalloidin (Sigma-Aldrich, St. Louis, MO, USA) and Hoechst 33342 (Life Technologies, Grand Island, NY). Images were captured using a Zeiss 780 inverted confocal microscope. Image fluorescence analysis was performed with the NIH Image J software.

Real-Time PCR

Total RNA was isolated using the RNA purification kit from IBI Scientific (Peosta, IA, USA). The TaqMan® Reverse Transcriptase kit (Applied Biosystems, Carlsbad, CA, USA) was used to generate complementary DNA from 500 ng of RNA template as per the manufacturer's instructions. Real-time PCR was performed using SYBR Green Supermix (Applied Biosystems). All amplification reactions were performed in triplicate, and GAPDH was used as internal control. The primer sequences used for real-time PCR are shown in Table S1 in Supplementary Material.

Western Blot

Western blotting was performed as previously described using the Odyssey CLx Infrared Imaging System (Li-Cor Biosciences) (30). The membranes were probed with the following primary antibodies: phospho-PKCδ (tyr^{311}), total PKCδ, and GAPDH. Phospho-PKCδ (tyr^{311}) was obtained from Cell Signaling Technology (Danvers, MA, USA). Total PKCδ and anti-GAPDH antibodies were procured from Santa Cruz Biotechnology (Dallas, TX, USA). The IRDye-conjugated secondary antibodies (Li-Cor Biosciences) were used to detect the primary antibodies.

Reactive Oxygen Species (ROS) Measurement

L-012 Chemiluminescence

L-012 (400 μM, Wako Chemicals), a luminol-based chemiluminescent probe, was used to determine $O_2^{\bullet-}$ generation as described previously (15). Fifty thousand CD11c$^+$ BMiDCs were plated in white flat bottom 96-well microplates in sterile PBS and superoxide production by stimulated by PMA (1 μM). The chemiluminescence signal was measured every 2 min for 2 h at 37°C using a Clariostar Monochromator Microplate Reader (BMG Labtech, Cary, NC, USA). The specificity of L-012 for $O_2^{\bullet-}$ was confirmed by the addition of SOD (150 U/mL).

Dihydroethidium

CD11c$^+$ BMiDCs were plated in 24-well plates and preincubated with 5 μM DHE for 30 min at 37°C. Cells were treated with vehicle or PMA (1 μM) for 30 min. The reaction was stopped by placing the culture plate on ice. The cells were washed twice with ice-cold PBS, fixed in 2% PFA, and fluorescence (excitation/emission: 518 nm/605 nm) was measured using flow cytometry.

Maturation of DCs

Dendritic cells were treated with vehicle + unlabeled OVA (50 μg/mL), PMA (1 μM) + OVA, or PMA alone for 24 h. DCs were then washed twice with ice-cold PBS and stained with PE/Cy7-CD11c, FITC-MHC II, and APC-CD86 monoclonal antibodies or respective isotype controls for 30 min at 4°C. FACS analysis was performed to determine CD86 and MHCII expression in CD11c$^+$ iDCs.

Proinflammatory Cytokine Gene Expression and Cytokine Secretion

CD11c$^+$ BMiDCs/splenic iDCs were incubated with vehicle or treated with PMA in the presence or absence of OVA for 24 h. Cells were harvested and used to determine mRNA levels of various cytokines using real-time PCR. Cytokine secretion into the media was quantified using the LEGENDplex™ (mouse inflammation panel) bead-based immunoassay (BioLegend, San Diego, CA, USA) according to the manufacturer's instructions. Data were acquired using four-color BD FACSCalibur (BD Biosciences, San Jose, CA, USA) and analyzed using the LEGENDplex Data Analysis software (BioLegend).

Statistical Analysis

The data are expressed as mean ± SD. Statistical analysis was performed using GraphPad Prism (La Jolla, CA, USA). Student's *t*-test and one- or two-way ANOVA, followed by a Bonferroni *post hoc* test, were used as appropriate for the particular experiment and treatment groups. A *p*-value less than 0.05 was considered statistically significant.

RESULTS

PKC Promotes Macropinocytosis of Antigens in Stimulated iDCs

Although previous studies demonstrated that DCs use macropinocytosis to internalize antigens (5, 31), the signaling mechanisms involved remain poorly understood. iDCs were characterized by high-level expression of CD11c (CD11c$^+$), low- to intermediate-level expression of MHC II, and low-level expression of CD86 (Figures S1 and S2 in Supplementary Material). LPS from *Escherichia coli*, a known DC maturation agent, was used as a positive control to determine the maturation status of DCs. FACS analysis demonstrated that PMA treatment stimulated internalization of fluorescent OVA in wild-type (WT) BMiDCs compared to vehicle-treated controls (**Figure 1A**). Gating strategy for FACS analysis is shown in Figure S1 in Supplementary Material. PMA-induced internalization of OVA was confirmed by confocal laser scanning microscopy (**Figure 1B**). Membrane ruffle formation and internalized Alexa Fluor 488-OVA in membrane-derived macropinosomes (~2–3 μm in diameter) following PMA treatment indicate macropinocytosis as the endocytic mechanism responsible for antigen uptake (**Figure 1C**). Macropinocytosis is pharmacologically characterized by its sensitivity to inhibitors of actin polymerization (32, 33), PI3K (30, 34), and sodium–hydrogen (Na^+/H^+) exchangers (15, 35). As shown in **Figures 1D,E** and Figure S3 in Supplementary Material, preincubation of BMiDCs with the actin perturbant, cytochalasin D (1 μM, 30 min), PI3K inhibitor, LY294002 (10 μM, 30 min), and Na^+/H^+ blocker, EIPA (25 μM, 30 min) completely blocked PMA-induced antigen internalization. Taken together, these data demonstrate that PMA stimulates internalization of antigens in DCs *via* macropinocytosis. Next, we investigated the role of PKC in DC macropinocytosis. BMiDCs were preincubated with vehicle or calphostin C (100 nM, 30 min), an inhibitor of classical and novel PKC isoforms (36), and macropinocytosis was stimulated using PMA. As shown in **Figures 1F,G**, calphostin C pretreatment inhibited PMA-stimulated macropinocytosis. To confirm the physiological importance of PKC in macropinocytosis, BMiDCs were incubated with HGF (100 ng/mL, 5 h), a physiologically relevant stimulator of macropinocytosis (13) and OVA uptake was analyzed by FACS analysis. HGF-stimulated OVA internalization in BMiDCs was inhibited by calphostin C pretreatment (100 nM, 30 min) (**Figure 1H**). These data demonstrate that activation of PKC in iDCs is required for stimulated macropinocytosis of OVA.

PKCδ Activation Plays a Critical Role in Macropinocytosis of Antigens by iDCs

To identify the potential PKC isoform(s) involved in DC macropinocytosis, we first examined mRNA expression of classical and novel PKC isoforms in WT CD11c$^+$ BMiDCs using real-time PCR. As shown in **Figure 2A**, the DAG-dependent

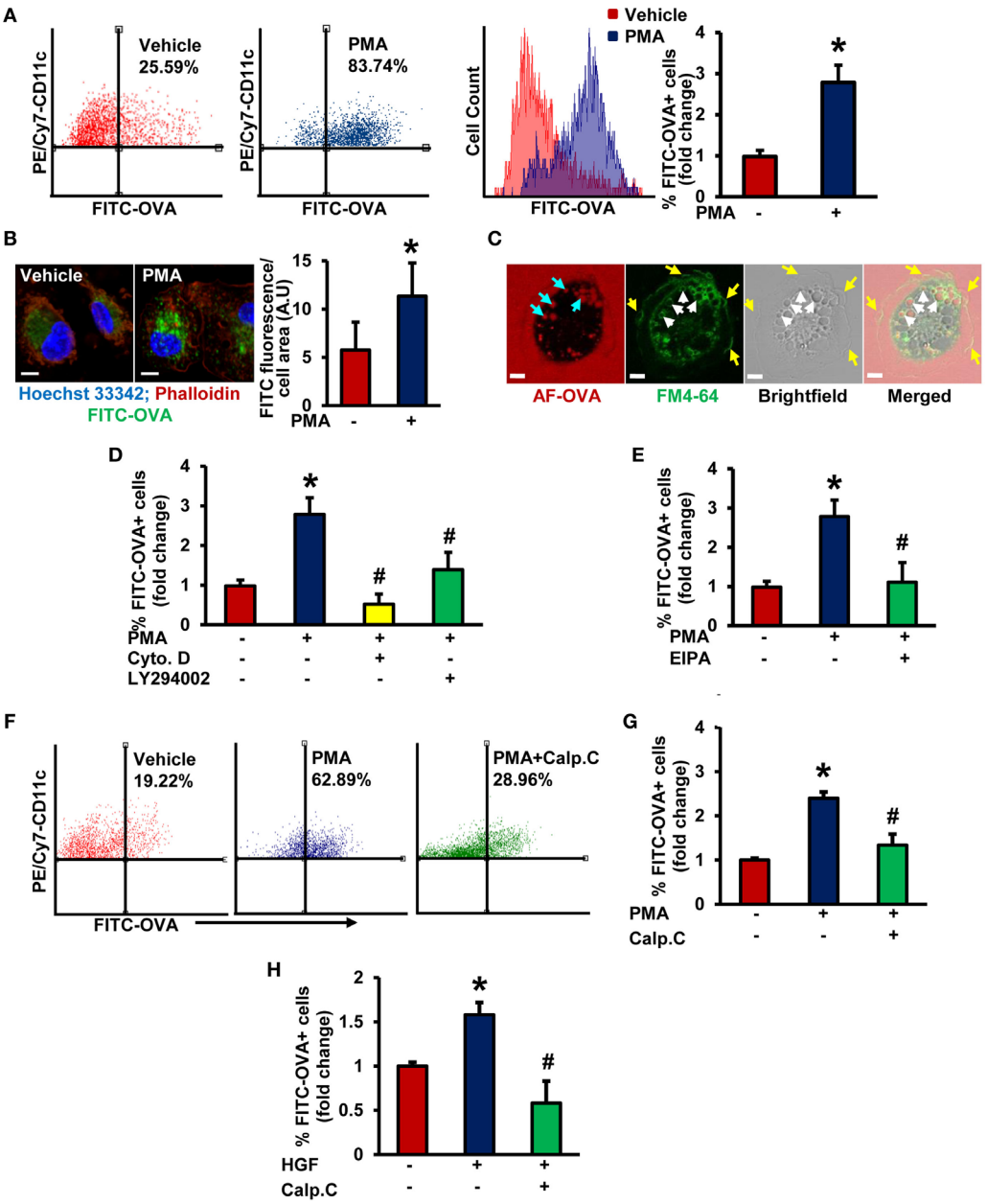

FIGURE 1 | Protein kinase C activation promotes macropinocytosis of antigens in stimulated immature DCs (iDCs). **(A)** Wild-type (WT) bone marrow-derived immature dendritic cells (BMiDCs) were incubated with FITC-OVA (50 μg/mL; 45,000 MW) and treated with or without phorbol 12-myristate 13-acetate (PMA, 1 μM) for 5 h. Cells were stained with PE/Cy7-conjugated CD11c (or respective isotype control) monoclonal antibodies, fixed in 2% paraformaldehyde, and FITC fluorescence analyzed in PE/Cy7-gated CD11c$^+$ cells using a Becton Dickinson FACSCalibur flow cytometer. Gating strategy for flow cytometry analysis is shown in Figure S1 in Supplementary Material. Bar diagram shows the mean fold change in percentage of FITC fluorescence$^+$ cells among CD11c$^+$ population ($n = 7$). **(B)** WT CD11c$^+$ BMiDC were incubated with FITC-OVA (50 μg/mL, green) and stimulated with vehicle or PMA (1 μM) for 5 h. Cells were fixed in 2% PFA, and stained with TRITC-phalloidin (red) and Hoechst 33342 (blue). Images were taken using a Zeiss 780 inverted confocal microscope (63×). Similar findings have been observed in three independent experiments. Scale bar: 5 μm. Bar diagram represents quantified mean FITC fluorescence normalized to cell area in vehicle- and PMA-treated cells. **(C)** WT CD11c$^+$ BMiDCs were treated with PMA (1 μM) for 30 min and incubated with the plasma membrane dye FM™ 4-64 (green) and Alexa Fluor 488-OVA (AF-OVA, 50 μg/mL, red) for 10 min. Live cell imaging was performed using a Zeiss 780 inverted confocal microscope. Yellow arrows indicate membrane ruffles, white arrows indicate membrane-derived macropinosomes, and blue arrows point to internalized extracellular solutes in macropinosomes. Images are representative of three independent experiments. Scale bar: 5 μm. **(D)** WT BMiDC were preincubated with vehicle, cytochalasin D (Cyto. D, 1 μM, 30 min) or LY294002 (10 μM, 30 min), treated with PMA (1 μM), and incubated with FITC-OVA for 5 h. FITC-OVA uptake was analyzed by fluorescence-activated cell sorting (FACS) ($n = 3$). **(E)** WT BMiDC were preincubated with vehicle or EIPA (25 μM) for 30 min, and challenged with PMA (1 μM, 5 h) in the presence of FITC-OVA. FITC-OVA internalization was analyzed by FACS ($n = 5$). **(F,G)** WT BMiDC were preincubated with vehicle or calphostin C (Calp. C, 100 nM, 30 min), treated with PMA, and FACS was performed as described above ($n = 3$). **(H)** WT BMiDC were preincubated with vehicle or calphostin C (Calp. C, 100 nM, 30 min), treated with HGF (100 ng/mL) in the presence of FITC-OVA for 5 h and FACS was performed to analyze FITC-OVA internalization. Bar diagram represents the mean fold change in FITC fluorescence$^+$ cells ($n = 3$). Data represent the mean ± SD. $^*p < 0.05$ vs. vehicle, $^\#p < 0.05$ vs. PMA/HGF.

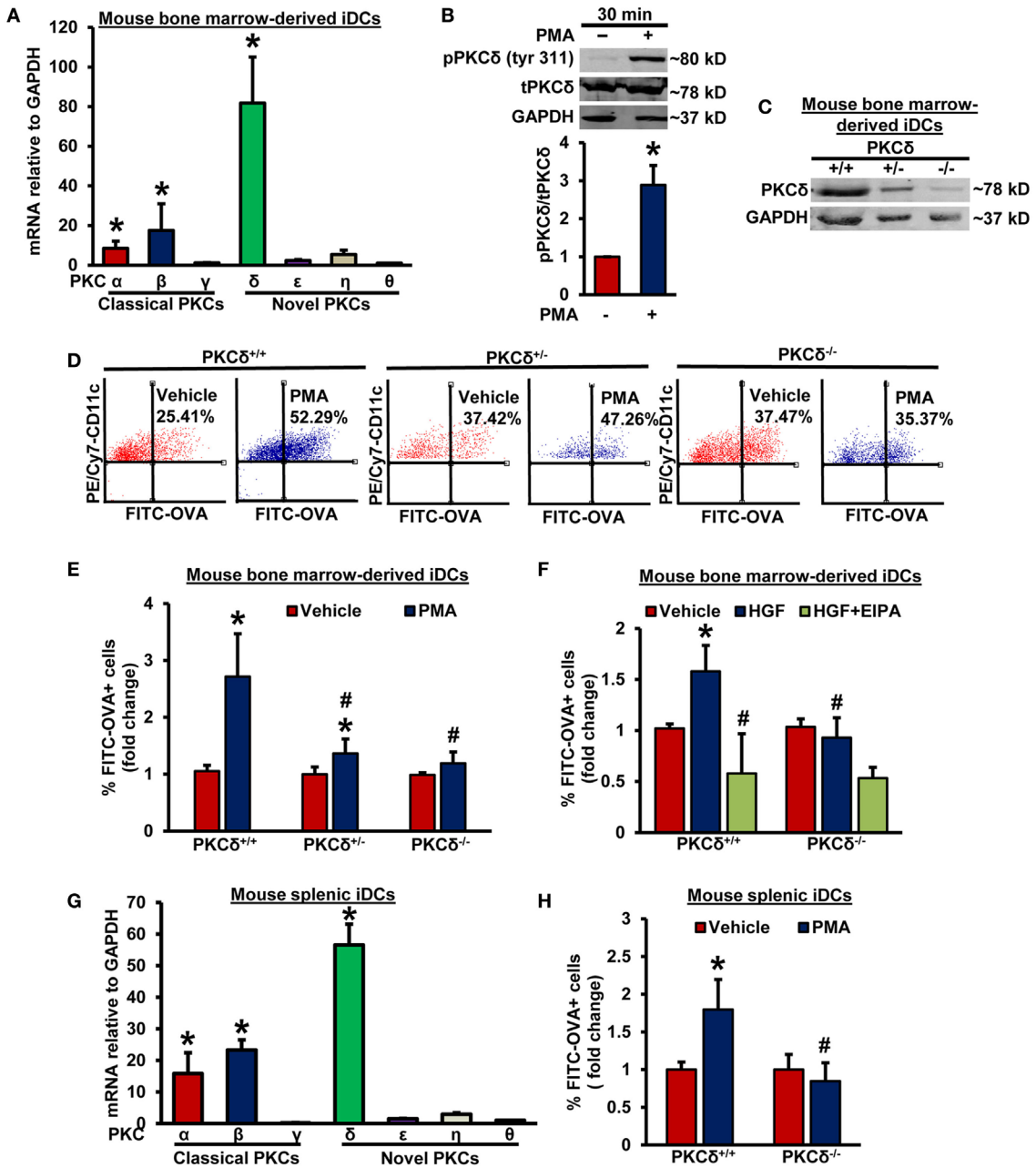

FIGURE 2 | PKCδ activation mediates macropinocytosis of antigens by iDCs. **(A)** WT CD11c$^+$ BMiDCs were subjected to qRT-PCR to determine mRNA expression of classical and novel protein kinase C (PKC) isoforms. GAPDH was used as an internal control. The transcript levels were calculated using delta–delta-CT method. Bar graph represents mRNA levels of classical and novel PKC isoforms in comparison to PKCθ (gene with lowest expression). Data represent the mean ± SEM. *$p < 0.05$ vs. PKCθ. **(B)** WT BMiDCs were treated with vehicle or PMA (1 μM) for 30 min. Cell lysates were used for Western blot analysis of phospho- PKCδ (tyr311), total PKCδ, and GAPDH protein expression. Representative Western blot images are shown. Bar graph represents averaged protein levels determined using densitometric analysis and expressed as a ratio of phospho- to total PKCδ ($n = 6$). **(C)** CD11c$^+$ BMiDCs from three PKCδ$^{+/+}$, PKCδ$^{+/-}$, and PKCδ$^{-/-}$ mice were pooled and Western blot was performed with cell lysates to validate deletion of PKCδ in DCs. **(D)** PKCδ$^{+/+}$, PKCδ$^{+/-}$, and PKCδ$^{-/-}$ BMiDC were incubated with FITC-OVA (50 μg/mL) with or without PMA (1 μM) for 5 h. FITC fluorescence was analyzed using a Becton Dickinson FACSCalibur flow cytometer. **(E)** Bar diagram shows the fold change in mean FITC fluorescence$^+$ cells among CD11c$^+$ PKCδ$^{+/+}$, PKCδ$^{+/-}$, and PKCδ$^{-/-}$ DCs ($n = 6$). **(F)** PKCδ$^{+/+}$ and PKCδ$^{-/-}$ BMiDC were preincubated for 30 min with EIPA (25 μM), and treated with hepatocyte growth factor (HGF, 100 ng/mL) for 5 h in the presence of FITC-OVA. FITC-OVA internalization was analyzed by fluorescence-activated cell sorting (FACS) ($n = 4$). **(G)** WT CD11c$^+$ splenic iDCs were subjected to qRT-PCR for determination of various PKC isoforms. GAPDH was used as an internal control. Bar graph represents mRNA levels of PKC isoforms in comparison to PKCθ (gene with lowest expression). Data represent the mean ± SEM. *$p < 0.05$ vs. PKCθ. **(H)** Splenic iDCs from PKCδ$^{+/+}$ and PKCδ$^{-/-}$ mice were treated as described in Figure 2D for 1 h, and FITC fluorescence analyzed using FACS ($n = 3$). Data represent the mean ± SD. *$p < 0.05$ vs. vehicle, and $^{\#}p < 0.05$ vs. PKCδ$^{+/+}$ PMA/HGF.

novel PKC isozyme, PKCδ, is the dominant PKC isoform in BMiDCs. Western blot results show that incubation of BMiDCs with PMA (1 μM, 30 min) activates PKCδ as demonstrated by its increased Tyr^{311} phosphorylation (**Figure 2B**) (37). To determine the functional role of PKCδ in DC macropinocytosis, we evaluated the ability of BMiDCs derived from WT $PKC\delta^{+/+}$ controls, heterozygous $PKC\delta^{+/-}$, and homozygous $PKC\delta^{-/-}$ mice to internalize antigens following PMA stimulation. The genotype of mice was confirmed by PCR analysis of genomic DNA (Figure S4 in Supplementary Material). PKCδ deletion in BMiDCs was confirmed by Western blotting (**Figure 2C**). FACS data demonstrated that PMA-induced antigen internalization is significantly attenuated in both $PKC\delta^{+/-}$ and $PKC\delta^{-/-}$ BMiDCs compared to $PKC\delta^{+/+}$ controls (**Figures 2D,E**). To test the physiological relevance of PKCδ in antigen macropinocytosis in iDCs, $PKC\delta^{+/+}$ and $PKC\delta^{-/-}$ BMiDCs were incubated with HGF (100 ng/mL, 5 h) and FITC-OVA internalization was investigated. HGF-stimulated internalization of FITC-OVA in $PKC\delta^{+/+}$ iDCs, however, we observed no stimulation in $PKC\delta^{-/-}$ iDCs (**Figure 2F**). The macropinocytosis inhibitor EIPA (25 μM, 30 min) abolished HGF-induced FITC-OVA uptake in $PKC\delta^{+/+}$ iDCs confirming the uptake mechanism as macropinocytosis. Consistent with our results in BMiDCs, RT-PCR experiments demonstrate that PKCδ is the dominant PKC isoform expressed in wild-type $CD11c^+$ splenic and FLT3L-differentiated BM-derived DCs (**Figure 2G**; Figure S5A in Supplementary Material). Similar to BMiDCs, PMA stimulated FITC-OVA internalization in $CD11c^+$ $PKC\delta^{+/+}$ splenic iDCs, but not in $PKC\delta^{-/-}$ splenic iDCs (**Figure 2H**). Taken together, these results suggest for the first time that stimulated iDC macropinocytosis involves PKCδ activation.

Stimulation of Nox2 Activity Facilitates Macropinocytosis of Antigens in iDCs

As stimulation of PKC with phorbol esters and growth factors phosphorylates the Nox organizer subunit $p47^{phox}$, leading to Nox2 activation and subsequent $O_2^{\bullet-}$ generation (26, 27, 38, 39), we postulated that (a) $O_2^{\bullet-}$ is involved as a signaling molecule in iDC macropinocytosis and (b) Nox2 activation contributes to antigen macropinocytosis by iDCs. Interestingly, a recent study by our laboratory has demonstrated the role of Nox2 in macrophage macropinocytosis of native LDL, leading to lipid accumulation and foam cell formation (15). To our knowledge, no prior studies have investigated the role of Nox enzymes and $O_2^{\bullet-}$ generation in DC macropinocytosis. Pretreatment of BMiDCs with diphenyleneiodonium (DPI; 10 μM, 30 min), a flavoenzyme inhibitor of Nox enzymes and other oxidases, and EUK-134 (10 μM, 30 min), a cell-permeable $O_2^{\bullet-}$ scavenger, inhibited PMA-induced antigen macropinocytosis (**Figure 3A**). As shown in **Figure 3B**, Figures S5B,C in Supplementary Material, Nox2 is the most highly expressed Nox isoform in GM-CSF/IL-4- and FLT3L-differentiated murine BMiDCs and splenic iDCs [Nox5 is not expressed in rodents (40)]. No significant difference was observed in Nox2 expression between $PKC\delta^{+/+}$ and $PKC\delta^{-/-}$ BMiDCs (Figure S5D in Supplementary Material). Control experiments also demonstrated that PKCδ expression in $Nox2^{y/+}$ and $Nox2^{y/-}$ BMiDCs is not different (Figure S5E in Supplementary Material). L-012 chemiluminescence and DHE fluorescence assays demonstrate that treatment of WT ($Nox2^{y/+}$) iDCs with PMA stimulates $O_2^{\bullet-}$ generation, but there was no induction in $Nox2^{y/-}$ iDCs (**Figures 3C,D**; Figure S6 in Supplementary Material). Furthermore, time-course L-012 chemiluminescence experiments demonstrate that Nox2-derived $O_2^{\bullet-}$ generation precedes or occurs concomitantly with PMA-induced PKCδ Tyr^{311} phosphorylation in iDCs (Figures S7A,B in Supplementary Material). The specificity of L-012 for $O_2^{\bullet-}$ was confirmed by the addition of SOD (150 U/ml) (not shown). The functional role of PKCδ in PMA-induced $O_2^{\bullet-}$ generation is demonstrated in Figure S7C in Supplementary Material.

To investigate the role of Nox2 in DC macropinocytosis of antigens, we treated splenic iDCs and BMiDCs isolated from WT and Nox2 knockout mice with fluorescently labeled OVA, stimulated cells with PMA and analyzed fluorescence using FACS. As shown in **Figure 3E** and Figure S8 in Supplementary Material, PMA-induced antigen accumulation was significantly attenuated in both $Nox2^{y/-}$ splenic and BM-derived iDCs compared to WT controls. Finally, loss of Nox2 in BMiDCs inhibited HGF-induced macropinocytosis of antigens (**Figure 3F**). Taken together, these observations suggest that the PKCδ/Nox2/$O_2^{\bullet-}$ signaling pathway plays an important role in antigen macropinocytosis by iDCs.

PKCδ- and Nox2-Mediated Antigen Macropinocytosis Facilitates Maturation of iDCs

Immature DCs internalize antigens and present the processed antigenic peptides loaded on MHC II molecules to naïve T-cells in lymphoid organs to initiate adaptive immune responses (41, 42). During this process, iDCs acquire a phenotype of mature DCs, which includes translocation of MHC II from intracellular endocytic compartments to the plasma membrane and increased surface expression of costimulatory molecules, such as CD86 (43). Next, we sought to investigate whether PKCδ–Nox2-mediated macropinocytosis of antigens by iDCs stimulates their maturation into mature and antigen-presenting DCs. PMA treatment in the presence of OVA stimulated plasma membrane expression of MHC II and CD86 in WT DCs, demonstrating that antigen macropinocytosis induces DC maturation (**Figures 4A,D**). Importantly, the results of our FACS analysis also indicate that PMA in the presence of OVA did not stimulate MHC II and CD86 plasma membrane expression in $PKC\delta^{-/-}$ and $Nox2^{y/-}$ DCs (**Figures 4B,C,E,F**). Altogether, these data suggest that iDCs derived from $PKC\delta^{-/-}$ and $Nox2^{y/-}$ mice have reduced maturation and antigen-presenting capacity due to their attenuated ability to internalize antigens *via* macropinocytosis.

PKCδ- and Nox2-Mediated Antigen Macropinocytosis Plays an Important Role in DC Secretion of T-Cell-Regulatory Cytokines

The antigen-specific T-cell receptor-mediated signaling, the co-stimulatory signals-mediated by DC CD80/CD86, and soluble cytokines secreted by DCs determine T-helper cell polarization and the functional consequences of antigen internalization (44).

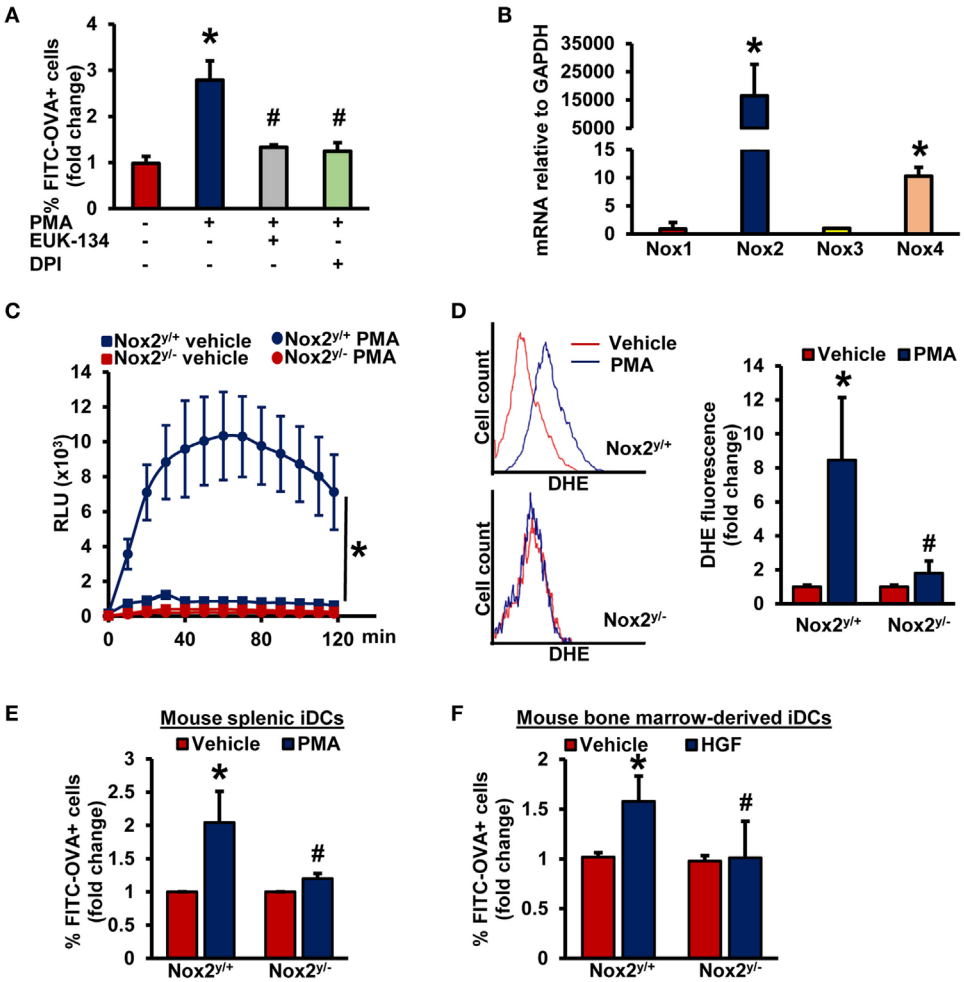

FIGURE 3 | Nox2 activation induces macropinocytosis of antigens in iDCs. **(A)** WT BMiDCs were preincubated with EUK-134 (10 μM) or DPI (10 μM) for 30 min, and treated with PMA (1 μM) in the presence of FITC-OVA for 5 h. Percentage of $CD11c^+$ FITC-OVA^+ cells was analyzed by fluorescence-activated cell sorting (FACS) ($n = 3$). **(B)** qRT-PCR was used to determine mRNA expression of Nox1, Nox2, Nox3, and Nox4 in iDCs. GAPDH was used as an internal control. Data are representative of three independent experiments done in triplicate. **(C)** $Nox2^{y/+}$ and $Nox2^{y/-}$ BMiDCs were treated with vehicle or PMA (1 μM) and $O_2^{\cdot-}$ production was monitored using L-012 chemiluminescence ($n = 3$). **(D)** Intracellular $O_2^{\cdot-}$ production in vehicle and PMA-treated $Nox2^{y/+}$ and $Nox2^{y/-}$ BMiDCs was measured using dihydroethidium (DHE, 5 μM, 30 min.). Dihydroethidium (DHE) fluorescence was determined using fluorescence-activated cell sorting (FACS) analysis. Representative FACS histograms and bar graph are shown ($n = 3$). **(E,F)** $Nox2^{y/+}$ and $Nox2^{y/-}$ splenic **(E)** and BMiDCs **(F)** were incubated with vehicle, PMA, or HGF in the presence of FITC-OVA. FITC fluorescence was analyzed using FACS ($n = 4$). Data represent the mean ± SD. $^*p < 0.05$ vs. vehicle and $^\#p < 0.05$ vs. $Nox2^{y/+}$ PMA/HGF.

DCs secrete T_H1-cell-polarizing factors, such as interleukin (IL)-12, interferons (IFNs) (44), TNF-α (45), and IL-27 (46). T_H2 cell polarizing factors include monocytic chemotactic protein 1 (MCP1, also known as CCL2) and OX40 ligand (44); and IL-6, TGF-β, IL-1 (47), and IL-23 (48, 49) are known as T_H17-cell-inducing cytokines. Hence, we next investigated the ability of DCs to produce various T-cell polarizing cytokines following PKCδ/Nox2-mediated antigen macropinocytosis. As shown in **Figures 5A–C**, OVA macropinocytosis stimulated secretion of IL-1α, TNF-α, and IFN-β proteins in WT iDCs. IL-1α, TNF-α, and IFN-β secretion by $PKC\delta^{-/-}$ and $Nox2^{y/-}$ iDCs was significantly decreased compared to WT controls (**Figures 5A–C**). Similarly, IL-6 mRNA levels were stimulated by OVA macropinocytosis in WT, but not in $PKC\delta^{-/-}$ and $Nox2^{y/-}$, iDCs (**Figure 5D**). Levels of IL-1β, IL-10, IL-12p70, IL-23, IL-27, IL-17A, and IFN-γ cytokines were also examined in cell culture supernatant, but we found either no stimulation of these cytokines following OVA macropinocytosis or were undetectable (data not shown). These changes in cytokines were also confirmed employing $CD11c^+$ splenic DCs from WT, $PKC\delta^{-/-}$, and $Nox2^{y/-}$ mice. As shown in **Figures 5E–G** PMA-stimulated OVA macropinocytosis induced mRNA expression of IL-6, TNF-α, and IL-1α in WT splenic DCs; however, there was no increase in cytokine levels in $PKC\delta^{-/-}$ and $Nox2^{y/-}$ splenic DCs. Overall, these data demonstrate that PKCδ- and Nox2-mediated macropinocytosis of antigens plays an important role in DC secretion of T_H1- and T_H17-cell polarizing cytokines and may influence downstream T-cell function and signaling.

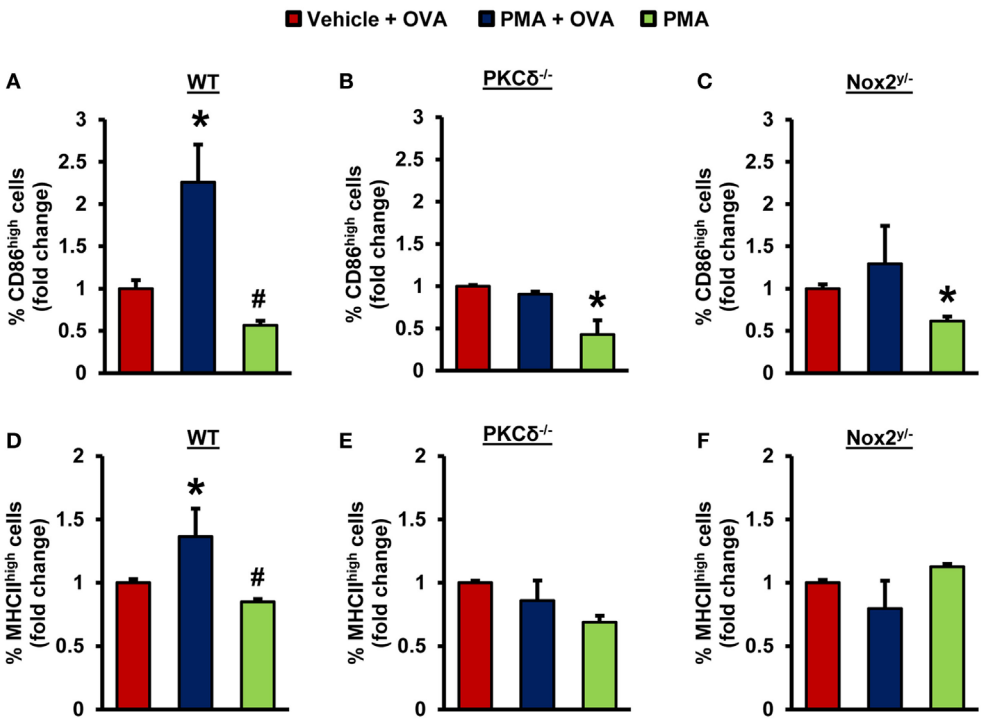

FIGURE 4 | PKCδ- and Nox2-mediated antigen macropinocytosis stimulates maturation of iDCs. WT (C57BL/6J), PKCδ$^{-/-}$, and Nox2$^{y/-}$ BMiDCs were treated with vehicle + unlabeled OVA (50 μg/mL), PMA (1 μM) + OVA, or PMA alone for 24 h. FACS analysis was performed to determine CD86 **(A–C)** and MHCII **(D–F)** expression in CD11c^{+} iDCs. Bar graphs show fold changes in the percentage of CD86^{high}/MHCII^{high} cells compared to "vehicle + OVA" treatment ($n = 3$). Data represent the mean ± SD. $^{*}p < 0.05$ vs. vehicle + OVA, $^{\#}p < 0.05$ vs. PMA + OVA.

DISCUSSION

Dendritic cell macropinocytosis is a major mechanism of receptor-independent and indiscriminate sampling of extracellular proteins for antigen presentation (4, 5). Although our knowledge of the regulatory mechanisms in macropinocytosis has greatly increased in recent years (10, 31, 50), the precise signaling pathways responsible for the initiation and completion of DC macropinocytosis remain unknown. The present study demonstrates for the first time that PKCδ-mediated Nox2 activation stimulates DC macropinocytosis of antigens, leading to their maturation and secretion of specific inflammatory cytokines that may influence T-helper cell polarization and adaptive immunity. As such, these results may contribute to a better understanding of antigen macropinocytosis in DCs and downstream regulation of adaptive immune responses.

Recent studies by our lab and others have demonstrated that DAG-induced activation of PKC in macrophages stimulates macropinocytosis (15, 17). However, the role of PKC in DC macropinocytosis is currently unknown. The goal of the present study was to examine whether PKC activation stimulates DC macropinocytosis and, if so, to investigate the particular PKC isoform(s) involved and downstream signaling mechanisms leading to macropinocytosis. The members of PKC family are classified into three groups on the basis of their structure and cofactor requirements. *Classical PKCs* (α, β, and γ) are activated by DAG and Ca^{2+}, *novel PKCs* (δ, ε, η, and θ) require only DAG for activation, while *atypical PKC isoforms* (λ, ι, μ, and ζ) are DAG-/Ca^{2+}-independent enzymes (51, 52). Classical PKC isoforms contain tandem C1A/C1B motifs that bind DAG and a C2 domain that binds anionic phospholipids in a calcium-dependent manner. Novel PKCs also contain twin C1A/C1B domains and a C2 domain; however, the positions of the C1A/C1B and C2 domains are switched and novel PKC C2 domains do not bind calcium (53). Previous studies reported that growth factors and phorbol esters stimulate activation of DAG-dependent PKCs and peripheral actin reorganization (54, 55), suggesting a potential role for classical and/or novel PKC isoforms in DC macropinocytosis. To investigate the role of PKCs in DC macropinocytosis, we first pretreated iDCs with calphostin C, a known inhibitor of classical and novel PKCs, incubated cells with fluorescently labeled OVA and stimulated macropinocytosis. FACS data indicated that calphostin C inhibited both growth factor (HGF)- and phorbol ester-induced antigen internalization, suggesting a role of classical or novel PKC isoforms in DC macropinocytosis. The qRT-PCR experiments identified PKCδ as the dominant PKC isoform in FLT3L- and GM-CSF/IL-4-induced BMiDCs and splenic iDCs. Next, we investigated the role of PKCδ in DC macropinocytosis of OVA. Our results demonstrated that loss of PKCδ in iDCs completely inhibited OVA macropinocytosis in response to HGF- and PMA-treatments. These data indicate the role of novel PKC isoform, PKCδ as a signaling molecule in stimulated DC macropinocytosis. Consistent with

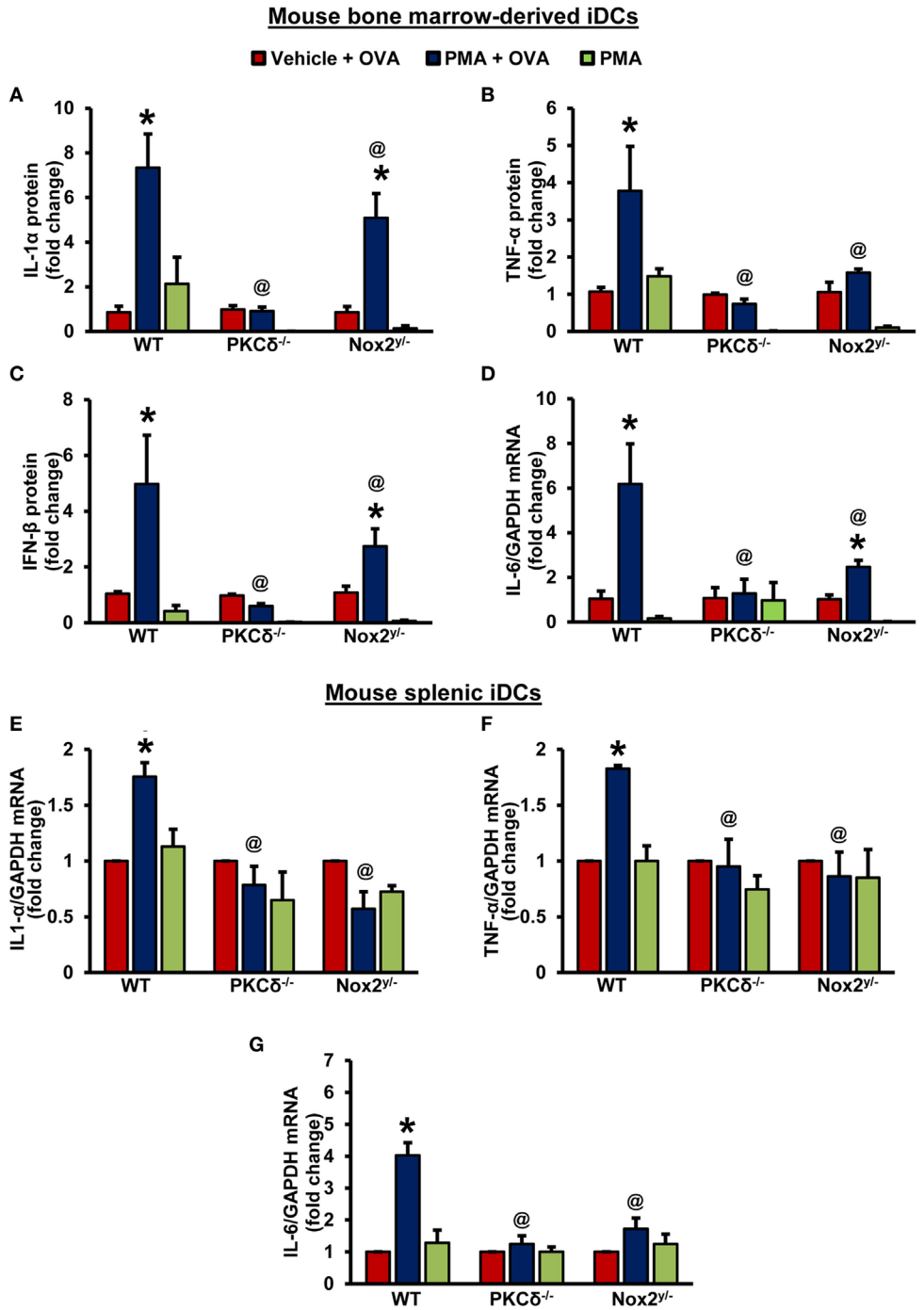

FIGURE 5 | PKCδ- and Nox2-mediated antigen macropinocytosis regulates DC secretion of T-cell regulatory cytokines. **(A–C)** Wild-type (WT) (C57BL/6J), PKCδ$^{-/-}$ and Nox2$^{y/-}$ BMiDCs were treated with vehicle or PMA in the presence of unlabeled OVA (50 μg/mL) or PMA alone for 24 h. Cell culture supernatants were collected and levels of secreted cytokines determined using LEGENDplex™ bead-based immunoassay assay. Bar graphs show fold changes in cytokine secretion compared to "vehicle + OVA" treatment. Data are representative of three independent experiments and values are expressed as mean ± SD. **(D)** BMiDCs were treated as described above. The mRNA levels of IL-6 were determined by qRT-PCR. Bar graphs show fold change in the expression of IL-6 compared to "vehicle + OVA" treatment ($n = 3$) and data represent the mean ± SD. **(E–G)** WT, PKCδ$^{-/-}$, and Nox2$^{y/-}$ CD11c^{+} splenic iDCs were treated with vehicle + OVA, PMA + OVA, or PMA alone for 24 h. The mRNA levels of cytokines were determined by qRT-PCR. Data are representative of three independent experiments performed in triplicate and represent the mean ± SEM. Bar graphs show fold change in the expression compared to "vehicle + OVA" treatment. *$p < 0.05$ vs. vehicle + OVA, and $^{@}p < 0.05$ vs. WT PMA + ova.

our observations, previous studies demonstrated that rottlerin, which has been used as a PKCδ inhibitor, inhibit virus-induced macropinocytosis in endothelial cells (56) and attenuate parasite macropinocytosis by macrophages (57). It is important to add, however, that a number of studies questioned the selectivity of rottlerin as a PKCδ inhibitor and reported that it inhibits other kinases and non-kinase proteins and not PKCδ (58–60). Interestingly, previous findings also suggest a potential role of classical PKCs in macrophage and cancer cell macropinocytosis. Welliver and Swanson showed that PKCα levels are increased in macropinocytotic cups in macrophages following M-CSF stimulation (61). A more recent study by Yamamoto et al. reported that phorbol ester-induced macropinocytosis is inhibited in cancer cells expressing a mutant PKCγ isoform (62). We speculate that differences between these studies and our present work are related to the cell types used to study macropinocytosis, different PKC isoform expression, and differences in the mechanisms of macropinocytosis stimulation.

Phorbol esters mimic endogenously produced DAG and stimulate PKC activation, leading to a robust and long-lasting activation of Nox2 in phagocytes (24). Similarly, growth factors and M-CSF are known to stimulate Nox2-derived $O_2^{\bullet-}$ generation *via* PKC activation (15, 27, 39). Although these Nox2 activators are considered as the prototype stimulators of macropinocytosis, information regarding the role of Nox enzymes in DC macropinocytosis and downstream redox regulation of the multistep signaling process leading to macropinosome formation remains scant. To address this gap in knowledge, we investigated whether Nox-derived ROS in DCs contribute to stimulation of macropinocytosis in response to phorbol ester and growth factor treatments. The qRT-PCR data demonstrated that Nox2 is the major Nox isoform expressed in both BMiDCs (FLT3L- or GM-CSF/IL-4-induced) and *bonafide* splenic iDCs. Consistent with the role of Nox2 as the major source of ROS in DCs, two independent $O_2^{\bullet-}$ detection techniques (L-012 chemiluminescence and DHE fluorescence) demonstrated that PMA-induced $O_2^{\bullet-}$ production is significantly inhibited in Nox2 knockout iDCs compared to WT controls. It is important to note that increased DHE fluorescence in PMA-treated WT, but not in PKCδ$^{-/-}$ or Nox2$^{y/-}$ iDCs indicate that PKCδ-mediated Nox2 activation stimulates intracellular $O_2^{\bullet-}$ generation. Next, we demonstrated that DPI, a promiscuous inhibitor of flavin-containing oxidases, and EUK-134, a membrane-permeant $O_2^{\bullet-}$ scavenger, inhibited antigen uptake in iDCs, suggesting a potential role for Nox and intracellular $O_2^{\bullet-}$ signaling in macropinocytosis. To further extend these findings and to use a more specific approach, we incubated WT and Nox2 knockout splenic and bone marrow-derived iDCs with OVA and stimulated macropinocytosis with PMA and HGF. Our data demonstrated that both HGF- and PMA-induced macropinocytosis of fluorescently labeled OVA was significantly attenuated in Nox2$^{y/-}$ iDCs compared with WT cells. To our knowledge, these results are the first to demonstrate the role of Nox2 in DC macropinocytosis. Nox2 enzymes expressed in internal membrane structures produce ROS intracellularly and play an important role as initiators and modulators of redox sensitive signaling pathways (63). Relevant to this point, we have recently demonstrated that Nox2 activation in macrophages stimulates intracellular ROS, leading to dephosphorylation of the actin-binding protein cofilin, membrane ruffling, and macropinocytosis (15). Interestingly, previous studies showed that endogenous ROS derived from Nox enzymes release slingshot phosphatase-1L (SSH-1L) from the inhibitory interaction with regulatory 14-3-3 proteins, leading to cofilin dephosphorylation and actin cytoskeleton reorganization (64). Based on these studies, we speculate that SSH-1L-mediated cofilin activation downstream of PKCδ/Nox2 signaling contributes to macropinocytosis stimulation. In addition to this potential mechanism, a number of other proteins involved in cytoskeletal reorganization are potential targets for oxidative modification and glutathiolation, including Src, Csk, actin, and protein tyrosine phosphatases that could be also playing a role in macropinocytosis (65).

Immature DCs after internalization of antigens undergo maturation and become professional APCs. During maturation, DCs lose their ability to endocytose antigens, increase surface expression of co-stimulatory molecules, such as CD86 and CD80, translocate MHCII to the plasma membrane, and change their morphology (66). We next investigated whether PKCδ/Nox2-mediated antigen macropinocytosis stimulates maturation of iDCs. Our results demonstrated that incubation of WT iDCs with PMA in the presence of OVA increased plasma membrane expression of CD86 and MHCII compared to PMA and OVA treatment alone, suggesting that macropinocytosis of antigens stimulates DC maturation. By contrast, PMA + OVA treatment did not stimulate plasma membrane expression of CD86 and MHCII in PKCδ and Nox2 knockout DCs. These findings indicate that iDCs derived from PKCδ$^{-/-}$ and Nox2$^{y/-}$ mice have decreased maturation capacity due to their reduced macropinocytic potential. Previous studies showed that pharmacological stimulation of PKC activity, and increased intracellular ROS production in the absence of antigens induce DC maturation and production of T-cell stimulatory cytokines (67–69). Consistent with these results, we found that PMA treatment alone (no OVA) stimulates IL-1α and TNF-α secretion in WT DCs (Figure S9 in Supplementary Material). New findings provided by the present study demonstrate that administration of PMA and OVA together significantly stimulates IL-1α and TNF-α secretion in WT DCs compared to PMA treatment alone. Based on these results, we propose that PKC–Nox2 signaling contributes to DC maturation through multiple mechanisms, including direct $O_2^{\bullet-}$-mediated signaling and stimulation of antigen macropinocytosis. It should also be noted that contrary to our observation a previous study found no stimulation of OVA internalization in DCs following PMA treatment (70). In this study, OVA was added 3 h after PMA treatment at which time point no stimulation of macropinocytosis is observed (15).

$CD4^+$ T-cells play a major role in immune response and aid B cells to make antibodies, activate phagocytes, and recruit other immune cells to the site of infection/inflammation. Naïve $CD4^+$ T-cells can differentiate into T_H1, T_H2, or T_H17 cells, depending on pro-/anti-inflammatory cytokines present in the microenvironment (71). Mature DCs produce various cytokines and chemokines to orchestrate an efficient T_H-cell response against infection (72). A variety of cytokines are produced by mature DCs, including IL-1, 6, 12 (73, 74), 23 (75), 27 (76, 77), TNF-α

(73, 74), TGF-β (78), and IFNs (74), which play an important role in T_H-cell polarization (44, 47). Macropinocytosis of OVA in WT BMiDCs stimulated secretion of IL-1α, TNF-α, and IFN-β and increased mRNA expression of IL-6. The observed increase in production of proinflammatory cytokines in WT cells were completely inhibited (IL-1α, TNF-α, IFN-β, and IL-6) or attenuated (IL-1α, IFN-β, and IL-6) in BMiDCs lacking PKCδ and Nox2, respectively. These findings suggest that IL-1α, IFN-β, and IL-6 secretion are mediated by Nox2-dependent and Nox2-independent pathways downstream of PKC. DC-derived TNF-α and IFNs have been shown to stimulate T_H1 cell polarization and induce cytotoxic T lymphocyte-mediated immune responses (44, 79). Similarly, upregulation of transcript levels of IL-1α, TNF-α, and IL-6 were observed in WT splenic DCs and PKCδ/Nox2 deletion from these cells abrogated elevation of these cytokines. IL-1 and IL-6 promote differentiation and function of T_H17 cells (80, 81). T_H17 cells secrete IL-17 (IL-17A and IL-17F) cytokines, which are crucial for clearance of *Candida albicans* infection (82). Secretion of IL-17, IL-21, and IL-22 by T_H17 cells correlates with the pathogenesis of several autoimmune (rheumatoid arthritis, systemic lupus erythematosus, multiple sclerosis, and psoriasis) and inflammatory diseases (inflammatory bowel disease and allergy and asthma) (83–89). The observed changes in the pattern of cytokine release and production suggest that PKCδ/Nox2-mediated antigen macropinocytosis may play a regulatory role in the development of specific T_H1 and T_H17 cells. In that respect, we expect future studies to investigate the role of DC antigen macropinocytosis in T-cell polarization, which is outside the scope of the present study.

In summary, our findings identified a previously unknown mechanism by which the novel PKC isoform, PKCδ *via* stimulation of Nox2 activity promotes macropinocytosis of antigens in DCs. The work presented herein shows that genetic blockade of PKCδ and Nox2 in DCs inhibit phorbol ester-stimulated macropinocytosis of antigens. Importantly, the role of PKCδ and Nox2 in DC macropinocytosis of antigens was also demonstrated in response to treatment with HGF, a physiologically relevant stimulator of macropinocytosis. PKCδ/Nox2-mediated antigen macropinocytosis stimulated DC maturation and induced secretion of various T_H cell regulatory cytokines. To our knowledge, these results are the first to describe redox regulation of macropinocytosis in DCs. As such, the present study may contribute to a better understanding of the regulatory mechanisms in DC macropinocytosis and downstream T-cell-mediated processes.

ETHICS STATEMENT

All experimental procedures were approved by the Institutional Animal Care and Use Committee of Augusta University and conducted in accordance with the National Institutes of Health Guide for the Care and Use of Laboratory Animals.

AUTHOR CONTRIBUTIONS

Conception or design of the work: GC, BS, and PG; acquisition, data collection, and analysis: BS, PG, HL, and GC; writing and reviewing of manuscript: BS and GC. ZD provided PKCδ$^{+/-}$ mice and QW helped with breeding and genotyping of animals. All authors approved the final version of the manuscript and agreed to be accountable for all aspects of the work in ensuring that questions related to the accuracy or integrity of any part of the work are appropriately investigated and resolved.

ACKNOWLEDGMENTS

The authors are grateful to Dr. Santhakumar Manicassamy (Augusta University) for his valuable suggestions on DC culture and maturation experiments. The authors wish to thank Immune Monitoring Shared Resources Laboratory, Augusta University for help with the LEGENDplex™ immunoassay experiments. Authors are also thankful to Jeanene Pihkala (Campus Flow Cytometry Core Facility, Augusta University) for her help with cell sorting and FACS experiments.

FUNDING

This work was supported by National Institutes of Health grants (K99HL114648 and R00HL114648) awarded to GC and AHA Postdoctoral Fellowship (17POST33661254) given to BS.

SUPPLEMENTARY MATERIAL

The Supplementary Material for this article can be found online at https://www.frontiersin.org/articles/10.3389/fimmu.2018.00537/full#supplementary-material.

FIGURE S1 | Gating strategy used for multicolor flow cytometry analysis. WT bone marrow-derived cells were incubated with FITC-OVA for 5 h, stained either with PE/Cy7-labeled CD11c **(B)** or respective IgG control **(A)** monoclonal antibodies, fixed in 2% paraformaldehyde, and processed for flow cytometry analysis. The cells were first gated on size and then doublets excluded using forward scatter area and forward scatter height. Cells were gated on CD11c$^+$ population to identify dendritic cells (R1; green). Ovalbumin internalization was determined by measuring FITC fluorescence in R1 population (green) **(C)**.

FIGURE S2 | Confirmation of immature phenotype of BMDCs. CD11c$^+$ cells were incubated with vehicle or lipopolysaccharide (LPS) (500 ng/mL) for 24 h, fixed, and incubated with FITC-MHCII (clone M5/114.15.2), APC-CD86 (clone GL1) or respective IgG control monoclonal antibodies. CD86 **(A)** and MHC II **(B)** expression in CD11c$^+$ dendritic cells were determined using flow cytometry. $^*p < 0.05$ vs. vehicle.

FIGURE S3 | EIPA inhibits FITC-OVA uptake in bone marrow-derived immature dendritic cells (BMiDCs). **(A)** Wild-type (WT) CD11c$^+$ BMiDCs were treated with vehicle or phorbol 12-myristate 13-acetate (PMA, 1 μM, 5 h), or pretreated with EIPA (25 μM, 30 min.) followed by PMA treatment in the presence of FITC-OVA. FITC-OVA internalization (green) was analyzed by confocal microscopy. Scale bar: 5 μm. **(B)** Bar diagram shows quantified FITC fluorescence intensity normalized to cell area ($n = 3$). At least five images per treatment were analyzed for each independent experiment using Image J. $^*p < 0.05$ vs. vehicle, $^\#p < 0.05$ vs. PMA.

FIGURE S4 | Representative Agarose gel electrophoresis image showing mice genotyping for PKCδ expression.

FIGURE S5 | PKCδ and Nox2 is the dominant PKC and Nox isoform in FLT3L-induced immature DCs (iDCs). **(A)** WT FLT3L-differentiated CD11c$^+$ iDCs were subjected to qRT-PCR for determination of various PKCs levels. GAPDH was used as an internal control. Data are representative of three independent

experiments performed in triplicate. Bar graph represents mRNA levels in comparison to PKCθ. *$p < 0.05$ vs. PKCθ. **(B)** Transcript levels of Nox1, Nox2, Nox3, and Nox4 in WT FLT3L-differentiated CD11c$^+$ iDCs. Bar graph represents mRNA levels in comparison to Nox1 (gene with lowest expression). *$p < 0.05$ vs. Nox1. **(C)** Nox1, Nox2, Nox3, and Nox4 mRNA expression in WT CD11c$^+$ splenic iDCs. *$p < 0.05$ vs. Nox1. **(D)** PKCδ expression in Nox2$^{y/+}$ and Nox2$^{y/-}$ BMiDCs ($n = 3$). **(E)** Nox2 expression in PKCδ$^{+/+}$ and PKCδ$^{-/-}$ BMiDCs ($n = 3$). Data represent the mean ± SEM **(A–E)**.

FIGURE S6 | Nox2 activation stimulates reactive oxygen species production in iDCs. Nox2$^{y/+}$ (wild type) and Nox2$^{y/-}$ BMiDCs were treated with vehicle or PMA (1 μM) and $O_2^{\bullet-}$ production was monitored using L-012 chemiluminescence. The diagram represents the mean fold change of L-012 chemiluminescence area under the curve obtained in three independent experiments. *$p < 0.05$ vs. vehicle, $^{\#}p < 0.05$ vs. Nox2$^{y/+}$ PMA.

FIGURE S7 | Stimulation of Nox2-derived $O_2^{\bullet-}$ generation in PMA-treated immature DCs precedes or occurs simultaneously with PKCδ activation. **(A)** $O_2^{\bullet-}$ generation was measured in vehicle- and PMA-treated Nox2$^{y/+}$ (wild type) and Nox2$^{y/-}$ BMiDCs using L-012 chemiluminescence ($n = 3$). **(B)** WT BMiDCs were treated with vehicle (30 min) or incubated with PMA (1 μM) for 5, 15, and 30 min. Cells were lysed and subjected to Western blot analysis for phospho-PKCδ (tyr^{311}), total PKCδ, and GAPDH protein expression. Representative Western blot images are shown. The bar graph represents the ratio of phospho- to total PKCδ from three to six independent experiments. **(C)** Dihydroethidium (DHE) fluorescence was quantified in vehicle- and PMA (1 μM, 30 min.)-treated PKCδ$^{+/+}$ and PKCδ$^{-/-}$ BMiDCs using fluorescence-activated cell sorting analysis. Representative histograms showing DHE fluorescence are presented (left and middle panels). Bar diagram indicates fold change in mean fluorescence intensity ($n = 3$). *$p < 0.05$ vs. vehicle, $^{\#}p < 0.05$ vs. PKCδ$^{+/+}$ PMA.

FIGURE S8 | Loss of Nox2 in BMiDCS attenuates PMA-stimulated macropinocytosis of ovalbumin (OVA). Nox2$^{y/+}$ and Nox2$^{y/-}$ BMiDCs were incubated with vehicle or stimulated with PMA (1 μM, 5 h) in the presence of FITC-OVA. FITC fluorescence was analyzed in CD11c$^+$ cells using fluorescence-activated cell sorting (FACS) ($n = 3$). *$p < 0.05$ vs. vehicle, $^{\#}p < 0.05$ vs. Nox2$^{y/+}$ PMA.

FIGURE S9 | "PMA + OVA" treatment induces a more pronounced secretion of DC-derived T-cell regulatory cytokines compared to PMA treatment alone. **(A–B)** WT BMiDCs left untreated or treated with PMA or PMA + OVA for 24 h. Cell culture supernatants were collected and levels of secreted cytokines determined using the LEGENDplex™ bead-based immunoassay. *$p < 0.05$ vs. vehicle, and $^{@}p < 0.05$ vs. PMA. **(C–D)** WT, PKCδ$^{-/-}$, and Nox2$^{y/-}$ BMiDCs were left untreated or treated with PMA for 24 h. Cell culture supernatants used for cytokine estimation as described in **(A–B)**. Data are representative of three independent experiments and values are expressed as mean ± SD. *$p < 0.05$ vs. vehicle and $^{@}p < 0.05$ vs. WT PMA.

TABLE S1 | List of primers used for mRNA quantitation using real-time-PCR.

REFERENCES

1. Mellman I, Steinman RM. Dendritic cells: specialized and regulated antigen processing machines. *Cell* (2001) 106(3):255–8. doi:10.1016/S0092-8674(01)00449-4
2. Trombetta ES, Mellman I. Cell biology of antigen processing in vitro and in vivo. *Annu Rev Immunol* (2005) 23:975–1028. doi:10.1146/annurev.immunol.22.012703.104538
3. Villadangos JA, Schnorrer P. Intrinsic and cooperative antigen-presenting functions of dendritic-cell subsets in vivo. *Nat Rev Immunol* (2007) 7(7):543–55. doi:10.1038/nri2103
4. Liu Z, Roche PA. Macropinocytosis in phagocytes: regulation of MHC class-II-restricted antigen presentation in dendritic cells. *Front Physiol* (2015) 6:1. doi:10.3389/fphys.2015.00001
5. Norbury CC. Drinking a lot is good for dendritic cells. *Immunology* (2006) 117(4):443–51. doi:10.1111/j.1365-2567.2006.02335.x
6. Humeniuk P, Dubiela P, Hoffmann-Sommergruber K. Dendritic cells and their role in allergy: uptake, proteolytic processing and presentation of allergens. *Int J Mol Sci* (2017) 18(7):E1491. doi:10.3390/ijms18071491
7. Mercer J, Helenius A. Virus entry by macropinocytosis. *Nat Cell Biol* (2009) 11(5):510–20. doi:10.1038/ncb0509-510
8. Stuart LM, Ezekowitz RA. Phagocytosis: elegant complexity. *Immunity* (2005) 22(5):539–50. doi:10.1016/j.immuni.2005.05.002
9. Lim JP, Gleeson PA. Macropinocytosis: an endocytic pathway for internalising large gulps. *Immunol Cell Biol* (2011) 89(8):836–43. doi:10.1038/icb.2011.20
10. Bohdanowicz M, Grinstein S. Role of phospholipids in endocytosis, phagocytosis, and macropinocytosis. *Physiol Rev* (2013) 93(1):69–106. doi:10.1152/physrev.00002.2012
11. Roche PA, Furuta K. The ins and outs of MHC class II-mediated antigen processing and presentation. *Nat Rev Immunol* (2015) 15(4):203–16. doi:10.1038/nri3818
12. Bryant DM, Kerr MC, Hammond LA, Joseph SR, Mostov KE, Teasdale RD, et al. EGF induces macropinocytosis and SNX1-modulated recycling of E-cadherin. *J Cell Sci* (2007) 120(Pt 10):1818–28. doi:10.1242/jcs.000653
13. Dowrick P, Kenworthy P, McCann B, Warn R. Circular ruffle formation and closure lead to macropinocytosis in hepatocyte growth factor/scatter factor-treated cells. *Eur J Cell Biol* (1993) 61(1):44–53.
14. BoseDasgupta S, Moes S, Jenoe P, Pieters J. Cytokine-induced macropinocytosis in macrophages is regulated by 14-3-3zeta through its interaction with serine-phosphorylated coronin 1. *FEBS J* (2015) 282(7):1167–81. doi:10.1111/febs.13214
15. Ghoshal P, Singla B, Lin H, Feck DM, Cantu-Medellin N, Kelley EE, et al. Nox2-mediated PI3K and cofilin activation confers alternate redox control of macrophage pinocytosis. *Antioxid Redox Signal* (2017) 26(16):902–16. doi:10.1089/ars.2016.6639
16. Swanson JA. Phorbol esters stimulate macropinocytosis and solute flow through macrophages. *J Cell Sci* (1989) 94(Pt 1):135–42.
17. Yoshida S, Gaeta I, Pacitto R, Krienke L, Alge O, Gregorka B, et al. Differential signaling during macropinocytosis in response to M-CSF and PMA in macrophages. *Front Physiol* (2015) 6:8. doi:10.3389/fphys.2015.00008
18. Swanson JA. Shaping cups into phagosomes and macropinosomes. *Nat Rev Mol Cell Biol* (2008) 9(8):639–49. doi:10.1038/nrm2447
19. Nishikawa K, Toker A, Johannes FJ, Songyang Z, Cantley LC. Determination of the specific substrate sequence motifs of protein kinase C isozymes. *J Biol Chem* (1997) 272(2):952–60. doi:10.1074/jbc.272.2.952
20. Sudan R, Srivastava N, Pandey SP, Majumdar S, Saha B. Reciprocal regulation of protein kinase C isoforms results in differential cellular responsiveness. *J Immunol* (2012) 188(5):2328–37. doi:10.4049/jimmunol.1101678
21. Gong R, Hong AW, Plouffe SW, Zhao B, Liu G, Yu FX, et al. Opposing roles of conventional and novel PKC isoforms in Hippo-YAP pathway regulation. *Cell Res* (2015) 25(8):985–8. doi:10.1038/cr.2015.88
22. Segal AW. The function of the NADPH oxidase of phagocytes and its relationship to other NOXs in plants, invertebrates, and mammals. *Int J Biochem Cell Biol* (2008) 40(4):604–18. doi:10.1016/j.biocel.2007.10.003
23. Bedard K, Krause KH. The NOX family of ROS-generating NADPH oxidases: physiology and pathophysiology. *Physiol Rev* (2007) 87(1):245–313. doi:10.1152/physrev.00044.2005
24. Inanami O, Johnson JL, McAdara JK, Benna JE, Faust LR, Newburger PE, et al. Activation of the leukocyte NADPH oxidase by phorbol ester requires the phosphorylation of p47PHOX on serine 303 or 304. *J Biol Chem* (1998) 273(16):9539–43. doi:10.1074/jbc.273.16.9539
25. Lavigne MC, Malech HL, Holland SM, Leto TL. Genetic demonstration of p47phox-dependent superoxide anion production in murine vascular smooth muscle cells. *Circulation* (2001) 104(1):79–84. doi:10.1161/01.CIR.104.1.79
26. Meijles DN, Fan LM, Howlin BJ, Li JM. Molecular insights of p47phox phosphorylation dynamics in the regulation of NADPH oxidase activation and superoxide production. *J Biol Chem* (2014) 289(33):22759–70. doi:10.1074/jbc.M114.561159

27. Schroder K, Schutz S, Schloffel I, Batz S, Takac I, Weissmann N, et al. Hepatocyte growth factor induces a proangiogenic phenotype and mobilizes endothelial progenitor cells by activating Nox2. *Antioxid Redox Signal* (2011) 15(4):915–23. doi:10.1089/ars.2010.3533
28. Pierre P, Turley SJ, Gatti E, Hull M, Meltzer J, Mirza A, et al. Developmental regulation of MHC class II transport in mouse dendritic cells. *Nature* (1997) 388(6644):787–92. doi:10.1038/42039
29. Xu Y, Zhan Y, Lew AM, Naik SH, Kershaw MH. Differential development of murine dendritic cells by GM-CSF versus Flt3 ligand has implications for inflammation and trafficking. *J Immunol* (2007) 179(11):7577–84. doi:10.4049/jimmunol.179.11.7577
30. Csanyi G, Feck DM, Ghoshal P, Singla B, Lin H, Nagarajan S, et al. CD47 and Nox1 mediate dynamic fluid-phase macropinocytosis of native LDL. *Antioxid Redox Signal* (2017) 26(16):886–901. doi:10.1089/ars.2016.6834
31. Sandgren KJ, Wilkinson J, Miranda-Saksena M, McInerney GM, Byth-Wilson K, Robinson PJ, et al. A differential role for macropinocytosis in mediating entry of the two forms of vaccinia virus into dendritic cells. *PLoS Pathog* (2010) 6(4):e1000866. doi:10.1371/journal.ppat.1000866
32. Oliveira CA, Kashman Y, Mantovani B. Effects of latrunculin A on immunological phagoctosis and macrophage spreading-associated changes in the F-actin/G-actin content of the cells. *Chem Biol Interact* (1996) 100(2):141–53. doi:10.1016/0009-2797(96)03695-2
33. Aleksandrowicz P, Marzi A, Biedenkopf N, Beimforde N, Becker S, Hoenen T, et al. Ebola virus enters host cells by macropinocytosis and clathrin-mediated endocytosis. *J Infect Dis* (2011) 204(Suppl 3):S957–67. doi:10.1093/infdis/jir326
34. Kruth HS, Jones NL, Huang W, Zhao B, Ishii I, Chang J, et al. Macropinocytosis is the endocytic pathway that mediates macrophage foam cell formation with native low density lipoprotein. *J Biol Chem* (2005) 280(3):2352–60. doi:10.1074/jbc.M407167200
35. Koivusalo M, Welch C, Hayashi H, Scott CC, Kim M, Alexander T, et al. Amiloride inhibits macropinocytosis by lowering submembranous pH and preventing Rac1 and Cdc42 signaling. *J Cell Biol* (2010) 188(4):547–63. doi:10.1083/jcb.200908086
36. Larsen EC, DiGennaro JA, Saito N, Mehta S, Loegering DJ, Mazurkiewicz JE, et al. Differential requirement for classic and novel PKC isoforms in respiratory burst and phagocytosis in RAW 264.7 cells. *J Immunol* (2000) 165(5):2809–17. doi:10.4049/jimmunol.165.5.2809
37. Nakashima H, Frank GD, Shirai H, Hinoki A, Higuchi S, Ohtsu H, et al. Novel role of protein kinase C-delta Tyr 311 phosphorylation in vascular smooth muscle cell hypertrophy by angiotensin II. *Hypertension* (2008) 51(2):232–8. doi:10.1161/HYPERTENSIONAHA.107.101253
38. Belambri SA, Hurtado-Nedelec M, Senator A, Makni-Maalej K, Fay M, Gougerot-Pocidalo MA, et al. Phosphorylation of p47phox is required for receptor-mediated NADPH oxidase/NOX2 activation in Epstein-Barr virus-transformed human B lymphocytes. *Am J Blood Res* (2012) 2(3):187–93.
39. Heppner DE, van der Vliet A. Redox-dependent regulation of epidermal growth factor receptor signaling. *Redox Biol* (2016) 8:24–7. doi:10.1016/j.redox.2015.12.002
40. Fulton DJ. Nox5 and the regulation of cellular function. *Antioxid Redox Signal* (2009) 11(10):2443–52. doi:10.1089/ARS.2009.2587
41. Winzler C, Rovere P, Rescigno M, Granucci F, Penna G, Adorini L, et al. Maturation stages of mouse dendritic cells in growth factor-dependent long-term cultures. *J Exp Med* (1997) 185(2):317–28. doi:10.1084/jem.185.2.317
42. Steinman RM, Pack M, Inaba K. Dendritic cells in the T-cell areas of lymphoid organs. *Immunol Rev* (1997) 156:25–37. doi:10.1111/j.1600-065X.1997.tb00956.x
43. Reis e Sousa C. Dendritic cells in a mature age. *Nat Rev Immunol* (2006) 6(6):476–83. doi:10.1038/nri1845
44. Kapsenberg ML. Dendritic-cell control of pathogen-driven T-cell polarization. *Nat Rev Immunol* (2003) 3(12):984–93. doi:10.1038/nri1246
45. Lutz MB, Schuler G. Immature, semi-mature and fully mature dendritic cells: which signals induce tolerance or immunity? *Trends Immunol* (2002) 23(9):445–9. doi:10.1016/S1471-4906(02)02281-0
46. Pflanz S, Timans JC, Cheung J, Rosales R, Kanzler H, Gilbert J, et al. IL-27, a heterodimeric cytokine composed of EBI3 and p28 protein, induces proliferation of naive CD4+ T cells. *Immunity* (2002) 16(6):779–90. doi:10.1016/S1074-7613(02)00324-2
47. DuPage M, Bluestone JA. Harnessing the plasticity of CD4(+) T cells to treat immune-mediated disease. *Nat Rev Immunol* (2016) 16(3):149–63. doi:10.1038/nri.2015.18
48. Aggarwal S, Ghilardi N, Xie MH, de Sauvage FJ, Gurney AL. Interleukin-23 promotes a distinct CD4 T cell activation state characterized by the production of interleukin-17. *J Biol Chem* (2003) 278(3):1910–4. doi:10.1074/jbc.M207577200
49. Gee K, Guzzo C, Che Mat NF, Ma W, Kumar A. The IL-12 family of cytokines in infection, inflammation and autoimmune disorders. *Inflamm Allergy Drug Targets* (2009) 8(1):40–52. doi:10.2174/187152809787582507
50. Sarkar K, Kruhlak MJ, Erlandsen SL, Shaw S. Selective inhibition by rottlerin of macropinocytosis in monocyte-derived dendritic cells. *Immunology* (2005) 116(4):513–24. doi:10.1111/j.1365-2567.2005.02253.x
51. Parker PJ, Murray-Rust J. PKC at a glance. *J Cell Sci* (2004) 117(Pt 2):131–2. doi:10.1242/jcs.00982
52. Newton AC. Protein kinase C: poised to signal. *Am J Physiol Endocrinol Metab* (2010) 298(3):E395–402. doi:10.1152/ajpendo.00477.2009
53. Steinberg SF. Cardiac actions of protein kinase C isoforms. *Physiology (Bethesda)* (2012) 27(3):130–9. doi:10.1152/physiol.00009.2012
54. Arber S, Barbayannis FA, Hanser H, Schneider C, Stanyon CA, Bernard O, et al. Regulation of actin dynamics through phosphorylation of cofilin by LIM-kinase. *Nature* (1998) 393(6687):805–9. doi:10.1038/31729
55. Reyhani V, Tsioumpekou M, van Wieringen T, Rask L, Lennartsson J, Rubin K. PDGF-BB enhances collagen gel contraction through a PI3K-PLCgamma-PKC-cofilin pathway. *Sci Rep* (2017) 7(1):8924. doi:10.1038/s41598-017-08411-1
56. Raghu H, Sharma-Walia N, Veettil MV, Sadagopan S, Chandran B. Kaposi's sarcoma-associated herpesvirus utilizes an actin polymerization-dependent macropinocytic pathway to enter human dermal microvascular endothelial and human umbilical vein endothelial cells. *J Virol* (2009) 83(10):4895–911. doi:10.1128/JVI.02498-08
57. Barrias ES, Reignault LC, De Souza W, Carvalho TM. Trypanosoma cruzi uses macropinocytosis as an additional entry pathway into mammalian host cell. *Microbes Infect* (2012) 14(14):1340–51. doi:10.1016/j.micinf.2012.08.003
58. Soltoff SP. Rottlerin: an inappropriate and ineffective inhibitor of PKCdelta. *Trends Pharmacol Sci* (2007) 28(9):453–8. doi:10.1016/j.tips.2007.07.003
59. Davies SP, Reddy H, Caivano M, Cohen P. Specificity and mechanism of action of some commonly used protein kinase inhibitors. *Biochem J* (2000) 351(Pt 1):95–105. doi:10.1042/0264-6021:3510095
60. Gschwendt M, Muller HJ, Kielbassa K, Zang R, Kittstein W, Rincke G, et al. Rottlerin, a novel protein kinase inhibitor. *Biochem Biophys Res Commun* (1994) 199(1):93–8. doi:10.1006/bbrc.1994.1199
61. Welliver TP, Swanson JA. A growth factor signaling cascade confined to circular ruffles in macrophages. *Biol Open* (2012) 1(8):754–60. doi:10.1242/bio.20121784
62. Yamamoto K, Seki T, Yamamoto H, Adachi N, Tanaka S, Hide I, et al. Deregulation of the actin cytoskeleton and macropinocytosis in response to phorbol ester by the mutant protein kinase C gamma that causes spinocerebellar ataxia type 14. *Front Physiol* (2014) 5:126. doi:10.3389/fphys.2014.00126
63. Brown DI, Griendling KK. Nox proteins in signal transduction. *Free Radic Biol Med* (2009) 47(9):1239–53. doi:10.1016/j.freeradbiomed.2009.07.023
64. Zhou Y, Yan H, Guo M, Zhu J, Xiao Q, Zhang L. Reactive oxygen species in vascular formation and development. *Oxid Med Cell Longev* (2013) 2013:374963. doi:10.1155/2013/374963
65. Valdivia A, Duran C, San Martin A. The role of Nox-mediated oxidation in the regulation of cytoskeletal dynamics. *Curr Pharm Des* (2015) 21(41):6009–22. doi:10.2174/1381612821666151029112624
66. Platt CD, Ma JK, Chalouni C, Ebersold M, Bou-Reslan H, Carano RA, et al. Mature dendritic cells use endocytic receptors to capture and present antigens. *Proc Natl Acad Sci U S A* (2010) 107(9):4287–92. doi:10.1073/pnas.0910609107
67. Do Y, Hegde VL, Nagarkatti PS, Nagarkatti M. Bryostatin-1 enhances the maturation and antigen-presenting ability of murine and human dendritic cells. *Cancer Res* (2004) 64(18):6756–65. doi:10.1158/0008-5472.CAN-03-4002
68. Romero MM, Basile JI, Corra Feo L, Lopez B, Ritacco V, Aleman M. Reactive oxygen species production by human dendritic cells involves TLR2 and dectin-1 and is essential for efficient immune response against Mycobacteria. *Cell Microbiol* (2016) 18(6):875–86. doi:10.1111/cmi.12562

69. Matsue H, Edelbaum D, Shalhevet D, Mizumoto N, Yang C, Mummert ME, et al. Generation and function of reactive oxygen species in dendritic cells during antigen presentation. *J Immunol* (2003) 171(6):3010–8. doi:10.4049/jimmunol.171.6.3010
70. Majewski M, Bose TO, Sille FC, Pollington AM, Fiebiger E, Boes M. Protein kinase C delta stimulates antigen presentation by Class II MHC in murine dendritic cells. *Int Immunol* (2007) 19(6):719–32. doi:10.1093/intimm/dxm034
71. Kaiko GE, Horvat JC, Beagley KW, Hansbro PM. Immunological decision-making: how does the immune system decide to mount a helper T-cell response? *Immunology* (2008) 123(3):326–38. doi:10.1111/j.1365-2567.2007.02719.x
72. Piemonti L, Monti P, Allavena P, Sironi M, Soldini L, Leone BE, et al. Glucocorticoids affect human dendritic cell differentiation and maturation. *J Immunol* (1999) 162(11):6473–81.
73. Dixon GL, Newton PJ, Chain BM, Katz D, Andersen SR, Wong S, et al. Dendritic cell activation and cytokine production induced by group B *Neisseria meningitidis*: interleukin-12 production depends on lipopolysaccharide expression in intact bacteria. *Infect Immun* (2001) 69(7):4351–7. doi:10.1128/IAI.69.7.4351-4357.2001
74. Morelli AE, Zahorchak AF, Larregina AT, Colvin BL, Logar AJ, Takayama T, et al. Cytokine production by mouse myeloid dendritic cells in relation to differentiation and terminal maturation induced by lipopolysaccharide or CD40 ligation. *Blood* (2001) 98(5):1512–23. doi:10.1182/blood.V98.5.1512
75. Roses RE, Xu S, Xu M, Koldovsky U, Koski G, Czerniecki BJ. Differential production of IL-23 and IL-12 by myeloid-derived dendritic cells in response to TLR agonists. *J Immunol* (2008) 181(7):5120–7. doi:10.4049/jimmunol.181.7.5120
76. Ziblat A, Domaica CI, Spallanzani RG, Iraolagoitia XL, Rossi LE, Avila DE, et al. IL-27 stimulates human NK-cell effector functions and primes NK cells for IL-18 responsiveness. *Eur J Immunol* (2015) 45(1):192–202. doi:10.1002/eji.201444699
77. Zhang X, Tao Y, Wang J, Garcia-Mata R, Markovic-Plese S. Simvastatin inhibits secretion of Th17-polarizing cytokines and antigen presentation by DCs in patients with relapsing remitting multiple sclerosis. *Eur J Immunol* (2013) 43(1):281–9. doi:10.1002/eji.201242566
78. Jin Y, Wi HJ, Choi MH, Hong ST, Bae YM. Regulation of anti-inflammatory cytokines IL-10 and TGF-beta in mouse dendritic cells through treatment with *Clonorchis sinensis* crude antigen. *Exp Mol Med* (2014) 46:e74. doi:10.1038/emm.2013.144
79. Jordan SJ, Gupta K, Ogendi BM, Bakshi RK, Kapil R, Press CG, et al. The predominant CD4(+) Th1 Cytokine Elicited to *Chlamydia trachomatis* infection in women is tumor necrosis factor alpha and not interferon gamma. *Clin Vaccine Immunol* (2017) 24(4):e10–7. doi:10.1128/CVI.00010-17
80. Sutton C, Brereton C, Keogh B, Mills KH, Lavelle EC. A crucial role for interleukin (IL)-1 in the induction of IL-17-producing T cells that mediate autoimmune encephalomyelitis. *J Exp Med* (2006) 203(7):1685–91. doi:10.1084/jem.20060285
81. Bettelli E, Carrier Y, Gao W, Korn T, Strom TB, Oukka M, et al. Reciprocal developmental pathways for the generation of pathogenic effector TH17 and regulatory T cells. *Nature* (2006) 441(7090):235–8. doi:10.1038/nature04753
82. Conti HR, Shen F, Nayyar N, Stocum E, Sun JN, Lindemann MJ, et al. Th17 cells and IL-17 receptor signaling are essential for mucosal host defense against oral candidiasis. *J Exp Med* (2009) 206(2):299–311. doi:10.1084/jem.20081463
83. Zenewicz LA, Antov A, Flavell RA. CD4 T-cell differentiation and inflammatory bowel disease. *Trends Mol Med* (2009) 15(5):199–207. doi:10.1016/j.molmed.2009.03.002
84. Maddur MS, Miossec P, Kaveri SV, Bayry J. Th17 cells: biology, pathogenesis of autoimmune and inflammatory diseases, and therapeutic strategies. *Am J Pathol* (2012) 181(1):8–18. doi:10.1016/j.ajpath.2012.03.044
85. Lubberts E, Koenders MI, van den Berg WB. The role of T-cell interleukin-17 in conducting destructive arthritis: lessons from animal models. *Arthritis Res Ther* (2005) 7(1):29–37. doi:10.1186/ar1478
86. Doreau A, Belot A, Bastid J, Riche B, Trescol-Biemont MC, Ranchin B, et al. Interleukin 17 acts in synergy with B cell-activating factor to influence B cell biology and the pathophysiology of systemic lupus erythematosus. *Nat Immunol* (2009) 10(7):778–85. doi:10.1038/ni.1741
87. Komiyama Y, Nakae S, Matsuki T, Nambu A, Ishigame H, Kakuta S, et al. IL-17 plays an important role in the development of experimental autoimmune encephalomyelitis. *J Immunol* (2006) 177(1):566–73. doi:10.4049/jimmunol.177.1.566
88. Ma HL, Liang S, Li J, Napierata L, Brown T, Benoit S, et al. IL-22 is required for Th17 cell-mediated pathology in a mouse model of psoriasis-like skin inflammation. *J Clin Invest* (2008) 118(2):597–607. doi:10.1172/JCI33263
89. Cosmi L, Maggi L, Santarlasci V, Capone M, Cardilicchia E, Frosali F, et al. Identification of a novel subset of human circulating memory CD4(+) T cells that produce both IL-17A and IL-4. *J Allergy Clin Immunol* (2010) 125(1):e1–4. doi:10.1016/j.jaci.2009.10.012

Conflict of Interest Statement: The authors declare that the research was conducted in the absence of any commercial or financial relationships that could be taken as a potential conflict of interest.

frontiers in Immunology

ORIGINAL RESEARCH
published: 11 July 2018
doi: 10.3389/fimmu.2018.01555

Altered Humoral Immune Responses and IgG Subtypes in NOX2-Deficient Mice and Patients: A Key Role for NOX2 in Antigen-Presenting Cells

*Julien Cachat[1], Christine Deffert[2], Marco Alessandrini[1], Pascale Roux-Lombard[2], Audrey Le Gouellec[3,4], Marie-José Stasia[3,4], Stéphanie Hugues[1] and Karl-Heinz Krause[1]**

[1] Department of Pathology and Immunology, Geneva University Hospitals (HUG) and Faculty of Medicine, University of Geneva, Geneva, Switzerland, [2] Division of Laboratory Medicine, Department of Genetic and Laboratory Medicine and Department of Medical Specialities, Geneva University Hospitals (HUG) and Faculty of Medicine, University of Geneva, Geneva, Switzerland, [3] TheREx (Thérapeutique Recombinante Expérimentale), Laboratoire TIMC-IMAG, University Grenoble Alpes, CNRS, Grenoble, France, [4] Laboratoire BEP, Pôle Biologie, CHU Grenoble Alpes, Grenoble, France

OPEN ACCESS

Edited by:
Rudolf Lucas,
Augusta University,
United States

Reviewed by:
Selinda Jane Orr,
Cardiff University,
United Kingdom
David Dombrowicz,
Institut National de la Santé et de la Recherche Médicale (INSERM), France

***Correspondence:**
Karl-Heinz Krause
karl-heinz.krause@unige.ch

Specialty section:
This article was submitted to Inflammation, a section of the journal Frontiers in Immunology

Received: 31 January 2018
Accepted: 25 June 2018
Published: 11 July 2018

Citation:
Cachat J, Deffert C, Alessandrini M, Roux-Lombard P, Le Gouellec A, Stasia M-J, Hugues S and Krause K-H (2018) Altered Humoral Immune Responses and IgG Subtypes in NOX2-Deficient Mice and Patients: A Key Role for NOX2 in Antigen-Presenting Cells. Front. Immunol. 9:1555. doi: 10.3389/fimmu.2018.01555

Chronic granulomatous disease (CGD) is a primary immunodeficiency resulting from loss of function mutations in the reactive oxygen species generating phagocyte NADPH oxidase (NOX2). CGD patients are prone to infection, but also have an increased susceptibility to autoimmune diseases. The aim of this study was to investigate the role of NOX2 in the regulation of specific immunity. In both CGD patients and NOX2-deficient mice, we observed an alteration in the basal proportions of IgG subtypes. Upon immunization with curdlan—a dectin 1 agonist—NOX2-deficient mice showed increased production of IgG2c compared to controls, and restimulation of lymph node-derived cells led to increased production of IFNγ, but not IL-5, indicative hallmark of an enhanced Th1 response. T cell activation was increased in NOX2-deficient mice and a similar trend was observed *in vitro* when T cells were co-cultured with NOX2-deficient bone marrow-derived cells. In contrast, no difference in T cell activation was observed when NOX2-deficient T cells were co-cultured with wild-type BMDC. Following stimulation of NOX2-deficient dendritic cells (DCs), no difference in costimulatory molecules was observed, while there was an increase in the release of Th1-driving cytokines. In summary, both CGD patients and CGD mice have an altered IgG subtype distribution, which is associated with an increased IFNγ production. Thus, NOX2 within DCs appears to be an important regulator at the interface of innate and specific immunity, especially after activation of the dectin 1 pathway, limiting immune activation and the development of autoimmunity.

Keywords: NOX2, B cells, T cells, immunoglobulin, antigen-presenting cells, curdlan, IgG subtype

INTRODUCTION

Chronic granulomatous disease (CGD) is a primary immunodeficiency disorder leading to life-threatening bacterial and fungal infections. The genetic cause of CGD is the loss of function mutations in genes coding for the phagocyte NADPH oxidase NOX2. NOX2 is a multi-subunit enzyme generating reactive oxygen species (ROS) and is an essential component of the neutrophil oxidative burst leading to microbial killing (1). While the role of NOX2-derived ROS in innate neutrophil activity is well established, NOX2 has other important functions in immune system regulation. Early reports of CGD had described an increase in immunoglobulin levels (2), but this feat has since

received little attention. B cells express a functional NOX2 (3). NOX2 may have a role in antibody production, but only a few studies reported an impact of NOX2 deficiency on B cell biology and immunoglobulin production. CGD mice show increased immunoglobulin responses to injection of collagen (4) and to UV-inactivated bacteria (5). One study in NOX2-deficient mice observed an enhanced antibody production in response to T cell-independent antigens (6). To date, no study has carefully analyzed the effect of NOX2 on IgG subclass production.

In addition, recent observations argue in favor of an excessive inflammatory response and autoimmunity in CGD (7). CGD patient show increased prevalence of autoimmune diseases, including systemic lupus erythematosus, juvenile rheumatoid arthritis, and idiopathic thrombocytopenic purpura (8–11). Autoantibodies play a role in the pathogenesis of these immune diseases (12). The sera of patients with CGD also show high levels of anti-*Saccharomyces cerevisiae*, anti-OmpC, or anti-CBir1 antibodies, which are associated with Crohn disease (13). In rodents, a seminal paper by the team of Rikard Holmdahl demonstrated that a loss of function polymorphism in the *Ncf1* gene—which codes for the $p47^{phox}$ subunit of NOX2—is a main driver of experimental rheumatoid arthritis (14, 15). Since then, observation converges toward a role of NOX2-derived ROS in T cell activation. Indeed adoptive T cell transfer from arthritic NOX2-deficient mice is sufficient to induce the disease in healthy wild-type (WT) mice (14). Thus, NOX2-derived ROS limit T cell activation, although the underlying mechanisms are still incompletely understood. NOX2-derived ROS, generated either by T cells themselves or antigen-presenting cells (APCs), might directly inhibit T cells, possibly through surface oxidation (16), ROS inhibition of lymphocyte ion channels (17), or other redox-sensitive signaling elements (18). Alternatively, NOX2-derived ROS might play a role in APCs and indirectly affect T cell function. For example, a recent study reported altered antigen processing, resulting in a different epitope repertoire in NOX2-deficient dendritic cells (DCs) (19), while another study has shown that oxidative modification of presented autoantigens enhances T cell response (20). NOX2-derived ROS appear to fundamentally control specific immune responses as mice deficient in *Ncf1* also exhibit an increased sensitivity to autoimmune encephalitis (EAE) (21) and NOX2-deficient mice an increased sensitivity to lupus erythematous (22). Interestingly, a recent human genetic study also found that a missense variant in *NCF1* is associated with susceptibility to multiple autoimmune diseases (23). Altogether, these studies suggest that the link between NOX2 and autoimmune disease is not limited to CGD patients, but also exists for less severe polymorphisms of the NOX2 system. Nevertheless, although patients with NOX2 deficiency present with increased risk to infection due to the impaired neutrophil oxidative burst, autoimmune features are not always visible and probably require specific additional stimuli. We have previously shown that dectin-1 activation strongly induces a CGD-associated hyperinflammation. Injection of curdlan, a β-glucan, which is a potent activator of dectin-1, results in a massive subcutaneous swelling and high levels of IL-6 and IFNγ in NOX2-deficient mice, while lipopolysaccharide was inactive (24). Altogether, the current literature indicates clinical and experimental links between NOX2-dependent ROS generation, production of immunoglobulins, specific hyperinflammatory states, and the development of autoimmune diseases.

In the present study, we measured IgG subclasses in the sera of NOX2-deficient mice and in CGD patients and detected altered IgG subtype production in NOX2 deficiency. We also addressed experimentally the activation of T cells following immunization with an ovalbumin-derived peptide ($OVA_{323–339}$) and the impact of specific adjuvants *in vivo* and in BMDC and T cell co-culture experiments. Our results point toward a key role of dectin-1-dependent NOX2 in DCs in limiting T cell activation, IFNγ release, and the production of Th1-driving cytokines. This suggests that NOX2-deficient DCs release increased amount of Th1-driving cytokines, leading to the release of an increased amount of IFNγ, which in turn may drive a higher IgG2c generation by B cells.

MATERIALS AND METHODS

Mice

C57Bl/6j (WT), B6.129S-Cybbtm1Din/J (NOX2KO), and B6.Cg-Tg(TcraTcrb)425Cbn/J (OTII) were purchased from The Jackson Laboratory and bred at the Animal Production facilities of the University of Geneva. Double OTII/NOX2KO-mutant mice were obtained by breeding B6.129S-Cybbtm1Din/J mice with B6.Cg-Tg(TcraTcrb)425Cbn/J mice. For the experiments, mice of age 8–12 months were used. The protocol was approved by the office cantonal vétérinaire du Canton de Genève, Switzerland (authorization no. 23624).

Patients

Patients were diagnosed as having CGD on the basis of their clinical symptoms and the inability of their phagocytes to generate ROS detectable by the dihydrorhodamine (DHR) flow cytometric test and the nitroblue tetrazolium dye reduction slide test. Blood samples were obtained from the CGD patients with appropriate institutional informed consent. Peripheral blood samples taken from healthy donors were obtained from the "Etablissement Français du sang" at the Grenoble University Hospital, France after their informed consent.

Flow Cytometry

Cells were suspended at 10^6/ml in FACS buffer (PBS with 0.5% bovine serum albumin (BSA) and 5 mM ethylenediaminetetraacetate (EDTA)). Fc receptors were blocked by a 10 min incubation at 4°C with the mouse BD Fc block (BD Biosciences, USA) at a dilution of 1:100. The cells were then washed with FACS buffer and centrifuged at 5,000 rpm for 5 min. Cells were then resuspended in FACS buffer with the antibody of interest and incubated for 15 min at 4°C. After incubation, the cells were washed with FACS buffer, centrifuged at 5,000 rpm for 5 min and resuspended in FACS buffer for flow cytometry analysis.

Immunization

Wild-type and NOX2KO mice were immunized by subcutaneous injection into the outer ear, using 50 µl of 1 µg ovalbumin protein and curdlan (Sigma-Aldrich, USA) (100 µg/ml) or Alum (ThermoFisher Scientific, USA) (50%) as adjuvant, which

was diluted in PBS. After 10 and 14 days, blood was collected from the caudal vein. Serum was obtained by coagulation and centrifugation for 2 min at 2,500 rpm, and stocked at −20°C until ELISA was performed. Serum from non-immunized mice was also collected to determine basal levels of the IgG subgroup.

Hyperinflammation Measurements

Ear thickness was measured using a caliper before immunization (basal ear thickness), at day 10 and 14 after immunization. The change in ear thickness (Δ ear thickness) was obtained by subtracting the basal ear thickness to the values obtained on days 10 and 14.

ELISA

High binding ELISA 96-well microplate (Corning®, Sigma-Aldrich, USA) were coated overnight at 4°C with either 10 µg/ml of ovalbumin (Sigma-Aldrich, USA) diluted in PBS to measure ovalbumin-specific antibody, or with purified goat anti-mouse total IgG (Biolegend, USA, dilution 1:100,000) to measure basal level of IgG subgroup. Plates were washed three times with PBS containing 0.05% tween-20 to remove unbound ovalbumin. A volume of 100 µl of PBS-BSA 1% was used for blocking for 1 h at room temperature. Fifty microliters per well of diluted serum sample were added to corresponding wells in duplicate. A pool of serum was used to obtain a standard curve by serial dilution. Sample dilutions were chosen to obtain a signal within the linear phase of the standard curve. The plates were incubated at room temperature for 1 h and washed three times. To measure ovalbumin-specific antibody, anti-mouse IgG2c, anti-mouse IgG2b, and anti-mouse IgG3 (Biolegend, USA) or anti-mouse IgG1 (ThermoFisher Scientific, USA) coupled to peroxidase was added to wells at the dilution of 1:1,000 for anti-mouse IgG2c and IgG1 and 1:500 for anti-mouse IgG2b and IgG3. Those secondary antibodies were incubated for 1 h at room temperature. For the measure of basal level of IgG subgroups, anti-mouse IgG2c (Biolegend, USA) or anti-mouse IgG1 (ThermoFisher Scientific, USA) or anti-mouse IgG3 (ThermoFisher Scientific, USA) or anti-mouse IgG2b (ThermoFisher Scientific, USA) coupled to peroxidase was added to wells at a dilution of 1:1,000 and incubated for 1 h at room temperature. Plates were washed three times and 50 µl of streptavidin coupled with horse-peroxidase was added to the plates, and incubated at room temperature for 20 min. After three washes, the signal was revealed by adding 50 µl of tetramethylbenzidine (TMB) and the plates were incubated at room temperature for 15 min in the dark. The reaction was stopped by adding 25 µl of H_2SO_4 2N. Optical density at 492 nm was measured using the fluoSTAR OPTIMA (BMG Labtech, Germany) plate reader.

Measurements of Serum Immunoglobulin G and A and IgG Subclass Levels

Sera from normal ($n = 6$) and CGD patients ($n = 16$) were collected and stored at −80°C before testing. Levels of serum immunoglobulin G and A were measured on a Dimension VISTA® system (Siemens, Germany) with IGG Flex® and IGA Flex® reagent cartridges according to the dimension VISTA® Operator's Guide. Serum IgG subclasses were measured by nephelometric assay with human IgG subclass liquid reagent kits (Siemens, Germany, including N Latex IgG1, N Latex IgG2, N Latex IgG3, and N Latex IgG4) on the automatic protein analyzer BN Prospect-II (Siemens, Germany) according to the manufacturer's instructions.

Anti-Nuclear Antibody (ANA) and Anti-Neutrophil Cytoplasmic Antibodies (ANCA) Determination

Anti-nuclear antibody was determined by indirect immunofluorescence (IFI) on Hep2 slides and ANCA by IFI on ethanol- and formalin-fixed neutrophils (Inova Diagnostics, USA). Briefly, for both types of autoantibodies, the corresponding slides were incubated with serial dilutions of serum in phosphate buffered saline with 10% Tween for 30 min, washed with PBS-Tween, and incubated with fluorescein-isothiocyanate (FITC)-conjugated goat polyclonal anti-human IgG containing Evans blue (Inova Diagnostics, USA). After washing steps, slides were mounted with glycerine mounting medium and cover slips and read using a fluorescence microscope Axioscope 2plus (Carl Zeiss Microscopy GmBh, Germany). Sera were considered positive for autoantibodies when a staining was observed for a dilution equal to or greater than 1/80 for ANA and 1/40 for ANCA.

Lymph Node Cellularity

Immunized mice were sacrificed 14 days after immunization and draining lymph nodes (cervical lymph node) and non-draining lymph nodes (inguinal lymph node) were dissected. Lymph nodes were digested with 1 mg/ml collagenase D (ThermoFisher Scientific, USA) and 10 µg/ml DNAse I (ThermoFisher Scientific, USA) in 2 ml HBSS at 37°C for 40 min. Digestion was stopped by adding 15 ml of a PBS-BSA 1% plus 5 mM EDTA solution and digested lymph nodes were passed through a 70 µm cell strainer. The total number of cells obtained after lymph node digestion and cell subgroup were analyzed by flow cytometry with the following antibodies: anti-CD4 Percp (1:200), anti-CD8 PE (1:100), and anti-IgD fitc (1:100) (ThermoFisher Scientific, USA).

Lymph Node Cell Restimulation

Lymph node cells were plated in a 96-well plate at a concentration of 2×10^6 cells per well and restimulated with 100 µg/ml of ovalbumin. 3 days after restimulation, supernatants were analyzed for the presence of IFNγ and IL5 using commercially available ELISA kits (ThermoFisher Scientific, USA), according to the manufacturer's instructions.

Bone Marrow-Derived DCs (BMDCs)

Hind leg bones of WT and NOX2KO mice were dissected and the bone marrow flushed with RPMI medium, complemented with 1% streptomycin–penicillin and 10% fetal bovine serum, and plated in a petri dish. Bone marrow cells were centrifuged at 5,000 rpm for 5 min and the pellet resuspended in a solution of 155 mM NH_4Cl and 12 mM $NaHCO_3$ for 1 min to lyse red blood cells. 20 ng/ml of GM-CSF (Peprotech) was added to the medium to drive differentiation to DCs. Medium and GM-CSF were renewed at day 3 and 6. At day 10, purity of BMDCs was verified by flow cytometry using anti-CD11c APC (1:100) antibody.

Isolation of OTII and OTII/NOX2 T Cells

Lymph node of OTII or OTII/NOX2 mice were dissected and passed through a 15 µm cell strainer to obtain a single cell suspension of lymph node cells. T cells were isolated using a microbead-based T cell isolation kit (Miltenyi Biotec, Germany), according to the manufacturer's instruction. Purity of the isolated T cells was verified by flow cytometry using anti-CD4 PE antibody (1:200).

In Vitro Co-Culture Experiments

Wild-type and NOX2KO BMDCs were plated in RPMI (completed with 10% fetal bovine serum, 1% streptomycin–penicillin, 50 µM β-mercaptoethanol, and 1 mM sodium pyruvate) in a 96-well plate at a concentration of 10^4 cells per well. Curdlan at 5 µg/ml was added to the wells for BMDC activation. Finally, increasing concentrations (5–500 nM) of $OVA_{323–339}$ peptide were added to the culture. After 1 day, BMDCs were harvested and washed twice with the prepared RPMI medium to remove the curdlan and peptide. Then, freshly isolated OTII or OTII/NOX2 T cells were added to the wells with the same medium preparation at a concentration of 10^5 T cells per well. For the experiment on T cell proliferation, freshly isolated T cells were first labeled with 5 µM carboxyfluorescein succinimidyl ester (CFSE) for 10 min at 37°C and washed three times. T cell activation was assessed by flow cytometry after 16 h of co-culture and after staining with anti-CD4 PercP (1:200) and anti-CD69 PE (1:200) antibody. T cell proliferation was assessed by flow cytometry after 4 days of co-culture and after staining with anti-CD4 PercP. The proliferation index and percent of dividing cells were calculated with FlowJo Software.

In Vivo T Cell Activation

Wild-type and NOX2KO mice were immunized with 0.5 µg of $OVA_{(323–339)}$ and 100 µg/ml of curdlan in PBS subcutaneously in the outer ear (50 µl of the solution was injected by ear). 1 day after immunization, freshly isolated OTII or OTII/NOX2KO T cells were labeled with 5 µM CFSE and injected intravenously in immunized mice. For T cell activation, draining lymph nodes were dissected 16 h after T cell adoptive transfer. Lymph nodes were then scratched and lymph node cells were stained with anti-CD4 PercP (1:200) and anti-CD69 PE antibody (1:200) for flow cytometry analysis. For T cell proliferation, lymph node dissection was performed 3 days after immunization and was stained with anti-CD4 PercP antibody. For comparison of T cell activation and proliferation between OTII and OTII/NOX2KO T cells, the experiment were performed similarly except that OTII T cells were labeled with CFSE as described above and OTII/NOX2KO T cells were labeled with 1 µM CellTracker™ Orange Cmtmr ((5-(and-6)-(((4-chloromethyl)benzoyl)amino) tetramethyl-rhodamine)) (ThermoFisher scientific, USA) at 37°C for 15 min, and then washed three times.

T Cell Activation and Survival in Presence of H_2O_2

Freshly isolated T cells were plated in a 96-well plate at a concentration of 10^5 T cell per well in the same culture medium as for co-culture experiments. Anti-CD3 (0.5 µg/ml) and anti-CD28 (2 µg/ml) antibody were then added to the culture to activate T cells. At the same time, increasing concentrations of H_2O_2 from 16 to 150 µM were added. After 16 h of treatment, T cells were stained with anti-CD4 PercP (1:200) antibody and anti-CD69 (1:200) PE antibody, and analyzed *via* flow cytometry. For T cell survival, activated T cell was stained with propidium iodide.

BMDC Activation

Bone marrow-derived dendritic cells were plated in a 96-well plate in same medium than for co-culture experiments at a concentration of 10^5 cells per well. Curdlan at concentration of 50, 25, and 5 µg/ml was added to the culture for BMDCs activation. After 24 h, BMDCs were harvested and supernatants were kept for further analysis at −20°C. BMDCs were stained with anti-CD11c Percp (1:200) or anti-CD11c APC (1:100), anti-DC-Sign APC (1:100), anti-ICOSL PE (1:100), anti-PD-L1 PE (1:100), anti-CD80 PE (1:400), anti-CD86 fitc (1:200), and anti-MHCII PE (1:1000). IL1β, IL10, and IL6 were measured by ELISA kit (eBioscience) in the supernatant, according to the manufacturer's instructions.

Statistical Analysis

All data were analyzed using GraphPad Prism software. For sample sizes of $n \geq 7$, data were first tested for normality using the Shapiro–Wilk test. If normally distributed, the Student's *t*-test was used for statistical comparison. For datasets not normally distributed and where sample sizes $n \leq 7$, the Mann–Whitney *U* test was used.

RESULTS

We first analyzed immunoglobulin levels in serum samples from healthy donor and CGD patients. As expected, higher levels of immunoglobulin where found in patients with CGD (Table S1 in Supplementary Material). Six CGD patients had increased IgA serum levels of which four were adults. In contrast, of the six CGD patients that had higher levels of serum IgM, four were below the age of two. For serum IgG, five CGD patients had levels above the normal range, of which three were adults and two children. When investigating the presence of autoantibodies, 6 out of 16 CGD samples (37%) were positive for ANCA, while 3 out of 16 samples (19%) were positive for ANA (Table S1 in Supplementary Material). Thus, we confirmed previous observations that CGD patients are prone to hypergammaglobulinemia and a higher frequency of autoantibodies.

We further characterized different IgG subtypes and compared the relative amounts of IgG1 and IgG2. Since no reference values for the ratios of IgG1/IgG and IgG2/IgG exist, we compared these values for CGD patients relative to a control group of comparable ages. In the control group, IgG1 represented ~70% of total IgG. In CGD patients, these levels were statistically significantly decreased ($p = 0.026$; **Figure 1A**). In contrast, IgG2 represented ~30% of total IgG in controls, and were significantly increased to ~40% in CGD patients ($p = 0.01$; **Figure 1B**).

To determine whether the differences in IgG subtypes were also present in NOX2-deficient mice, we measured the basal levels of each IgG subtype (IgG1, IgG2b, IgG2c, and IgG3) in

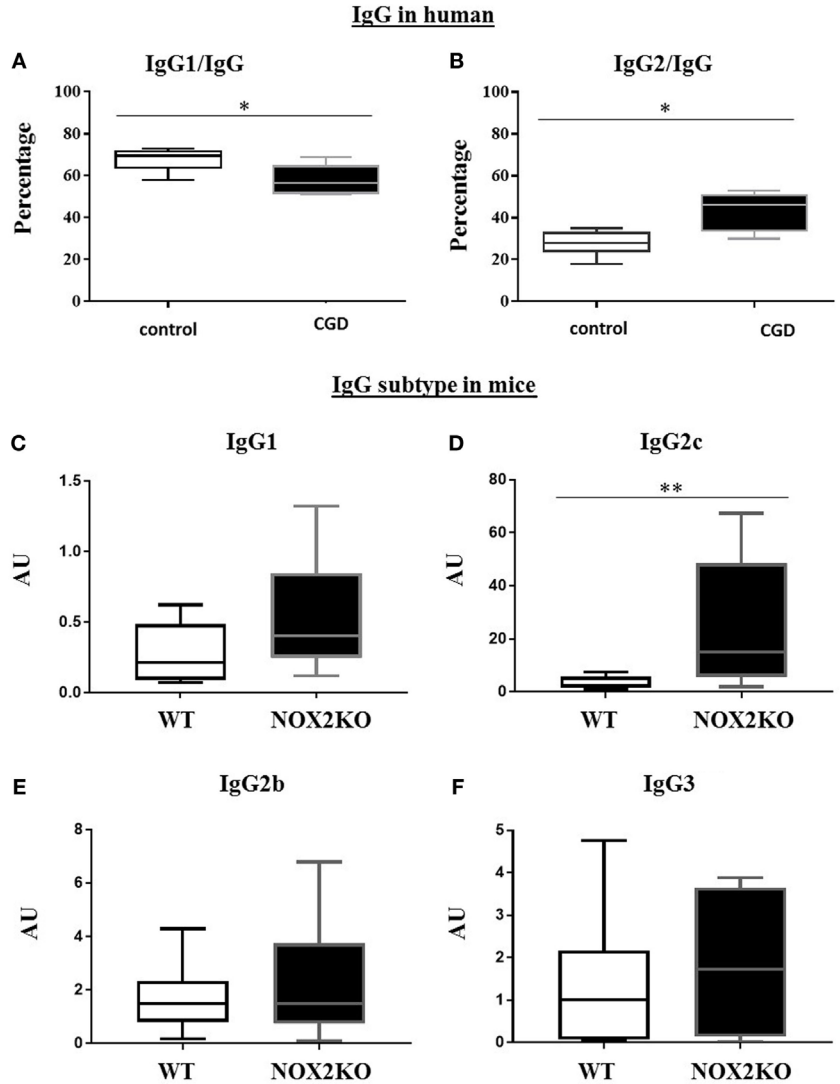

FIGURE 1 | Relative levels of IgG1 and IgG2 in CGD patients and healthy donors and basal levels of immunoglobulin subtypes in wild-type (WT) and NOX2-deficient mice. **(A,B)** Proportion of serum IgG1 and IgG2 subtypes relative to total IgG. Basal level of IgG1 **(C)**, IgG2c **(D)**, IgG2b **(E)** and IgG3 **(F)** in WT and NOX2 deficient mice (NOX2KO). *$p < 0.05$ and **$p < 0.01$.

NOX2-deficient and WT mice (**Figures 1C–F**). Similar to our human data, levels of some, but not all, IgG subtypes were impacted by the presence of NOX2. We did not find significant differences in IgG1, IgG2b, and IgG3 levels between WT and NOX2-deficient mice (**Figures 1C,E,F**). However, levels of IgG2c were significantly increased in NOX2-deficient mice ($p < 0.008$; **Figure 1D**). Thus, an alteration of IgG subtypes was observed in human CGD samples and in NOX2-deficient mice.

In order to examine how NOX2 deficiency affects the production of antibodies, we compared the levels of antigen-specific IgG in response to immunization of control and NOX2-deficient mice. As a model antigen, we used ovalbumin, and either alum or curdlan as adjuvants. The two different adjuvants were chosen for the following reasons. Alum is a standard adjuvant used in most routine experiments, and it mostly induces IgG1 response. In contrast, curdlan is an adjuvant that privileges IgG2c responses. Immunization was performed by injection in the ear skin. Different investigations were performed 10 and/or 14 days after immunization, including ear thickness, serum IgG levels, and lymph node analysis (cellularity and cytokines). Anti-ovalbumin IgG subtypes were examined. Prior to immunization, no anti-ovalbumin IgG was detected (data not shown). After immunization, the level of anti-ovalbumin IgG3 was still below detection level (data not shown). In control mice, immunization with either alum or curdlan as adjuvant led to the generation of modest, but clearly detectable, amounts of anti-ovalbumin IgG1. In immunized NOX2-deficient mice, the IgG1 levels were broadly increased in comparison to control mice (**Figures 2A,D**). The situation of anti-ovalbumin IgG2b was slightly more complex. With alum as adjuvant, the level of anti-ovalbumin IgG2b remained

low for all samples (**Figure 2B**). With curdlan as adjuvant, even though most of the samples had a low level of IgG2b, one sample in WT mice and two samples in NOX2KO mice exerted levels at least 10 times higher (**Figure 2E**). In contrast, there was a notable impact of NOX2 deficiency on the pattern of IgG2c production, which was primarily influenced by the choice of adjuvant. With alum as adjuvant, IgG2c responses were completely absent in both WT and NOX2-deficient mice (**Figure 2C**). However, with curdlan as adjuvant, while only minor elevated IgG2c levels were observed in WT mice, considerable and statistically significant IgG2c elevations were detected in the sera of NOX2-deficient mice (**Figure 2F**).

The mechanisms leading to antibody production are complex and involve different cell types to reach a full humoral response. In order to address the mechanisms behind the marked increased IgG2c production in NOX2-deficient mice, we investigated inflammation resulting from the immunization, both locally and in draining lymph nodes. Measurement of ear thickness was performed as a read-out for the local inflammatory reaction. Ear thickness, prior to immunization, did not differ between WT and NOX2-deficient mice (data not shown). After intra-auricular immunization, a moderate increase in ear thickness was measured in WT mice (0.1–0.2 mm), which was similar when both alum and curdlan adjuvants were used. In NOX2-deficient mice, the ear thickness was strongly increased with curdlan as adjuvant, but not with alum (**Figure 3A**), indicating that curdlan induces an increased inflammatory reaction upon immunization.

To characterize the inflammatory response, we investigated the total cell numbers of draining (cervical) and non-draining (inguinal) lymph nodes after immunization with ovalbumin and curdlan. In draining lymph nodes, there was a threefold median increase in cellularity ($p < 0.0001$) in NOX2-deficient mice when compared to WT mice (**Figure 3B**). In non-draining lymph nodes, the total number of cells was relatively low and there was no difference between WT and NOX2-deficient mice. We next analyzed the different subpopulations of lymph node cells. The proportion of CD4 positive T cells in draining lymph nodes of NOX2-deficient mice was significantly lower ($p = 0.001$) when compared to control WT mice (**Figure 3D**), whereas the proportion of IgD-positive B cell population was significantly higher (**Figure 3C**). Eventhough the proportion of CD4-positive T cells is decreased in NOX2-deficient immunized mice, it is important to notice that the absolute numbers of both CD4-positive T cells and IgD-positive B cells are increased in NOX2-deficient mice compared to WT (Figure S1 in Supplementary Material). Taken together, our data demonstrate that immunization of NOX2-deficient mice with curdlan as adjuvant leads to an increase of the total cell number in the draining lymph nodes, which is predominantly accounted for by an increase in IgD-positive B cells.

We next investigated the levels of cytokine release by cells isolated from draining lymph nodes, as an indirect measure of T cell differentiation and/or proliferation in response to immunization. For these experiments, mice were immunized with ovalbumin and curdlan, as described above. 10 days post immunization,

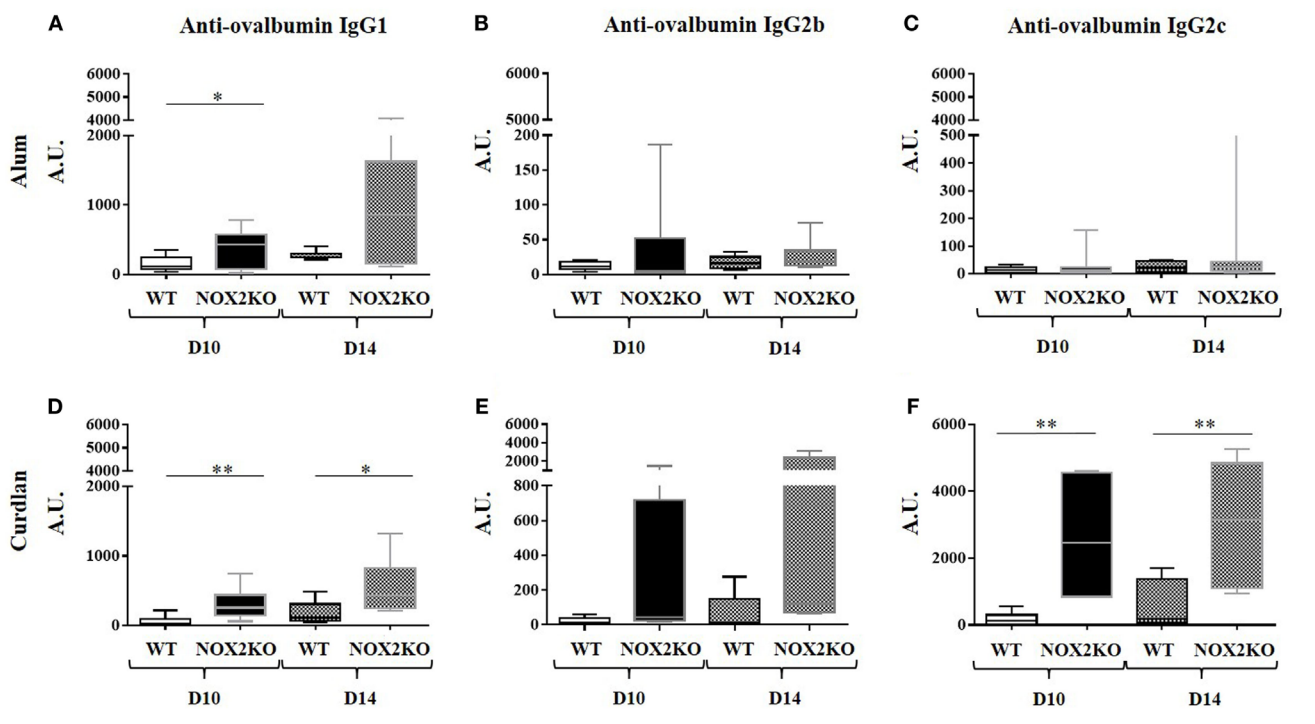

FIGURE 2 | Enhanced immunoglobulin generation in CGD mice: IgG subtype and adjuvant dependence. Mice were immunized by subcutaneous injection into the outer ear of ovalbumin with either alum **(A–C)** or curdlan **(D–F)** as adjuvant. Levels of Anti-ovalbumin IgG1 **(A,D)**, IgG2b **(B,E)** and IgG2c **(C,F)** were measured 10 and 14 days following immunization ($n = 12$). *$p < 0.05$; **$p < 0.01$; and ***$p < 0.001$.

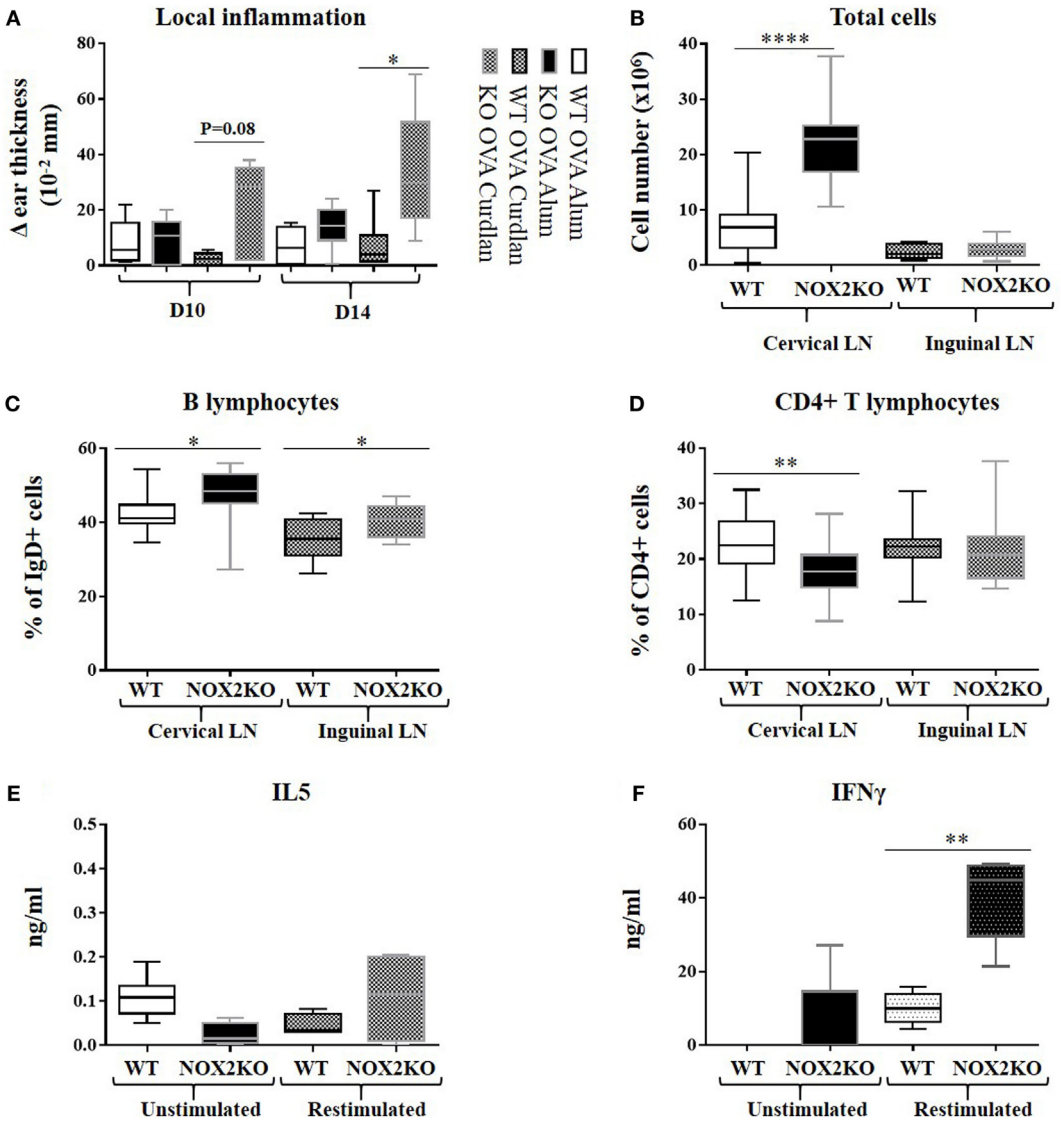

FIGURE 3 | Enhanced inflammation and release of inflammatory mediators upon immunization of CGD mice. Mice were immunized by subcutaneous injection into the outer ear of ovalbumin with either alum or curdlan as adjuvant. **(A)** Ear thickness, reflecting the inflammatory response, was measured 10 and 14 days following immunization. **(B–D)** Draining cervical and non-draining inguinal lymph nodes were removed 14 days post immunization, dissociated, and analyzed by flow cytometry: **(B)** total cell number; **(C)** percentage of IgD-positive B cells; **(D)** percentage of CD4-positive T cells ($n = 10$). **(E,F)** Draining lymph nodes were isolated 10 days post immunization with ovalbumin and curdlan, and release of IL5 **(E)** and IFNγ **(F)** was measured 24 h after restimulation of lymph node homogenates with ovalbumin ($n = 10$). *$p < 0.05$; **$p < 0.01$; and ****$p < 0.0001$. The legend next to panel **(A)** refers only to this panel.

draining lymph nodes were mechanically dissociated and cultured for 72 h in the presence or absence of ovalbumin. Low-level IL-5 production persisted for all conditions (**Figure 3E**), suggesting limited Th2 response. However, significant differences were observed with respect to the IFNγ levels (Th1): restimulation with ovalbumin led to a moderate increase in IFNγ levels from WT lymph node cells, while the production of IFNγ was strongly increased in NOX2-deficient lymph node cells (**Figure 3F**). These results suggest that immunization of NOX2-deficient mice with curdlan as adjuvant preferentially leads to an antigen-specific Th1 response.

To perform a more in-depth analysis of T cell responses, we used an *in vitro* co-culture system with $OVA_{(323–339)}$-specific T cells (OTII T cells) and WT or NOX2-deficient (NOX2KO) BMDCs. T cell activation was assessed by the upregulation of CD69 at the surface of CD4 T cells after 16 h of co-culture. CD69 is an early T cell activation marker. In absence of $OVA_{(323–339)}$ peptide, barely no $CD69^{hi}$ $CD4^+$ T cells were detectable (Figure S2 in Supplementary Material). Addition of different $OVA_{(323–339)}$ concentrations led to low to moderate T cell activation (identified as $CD69^{hi}$ $CD4^+$ T cells) in a dose-dependent manner (Figure S2 in Supplementary Material). For each $OVA_{(323–339)}$

peptide concentration tested, there was a trend toward a higher percentage of CD69^{hi} T cells when T cells were co-cultured with NOX2KO BMDCs compared to WT BMDCs. This difference was highest at 500 nM of OVA$_{(323–339)}$ peptide, where a 2.5-fold higher T cell activation was observed for NOX2KO BMDCs compared to WT DCs (**Figure 4A**).

To further characterize the effect of NOX2 in BMDCs on T cell responses, we measured T cell proliferation. For that purpose, we

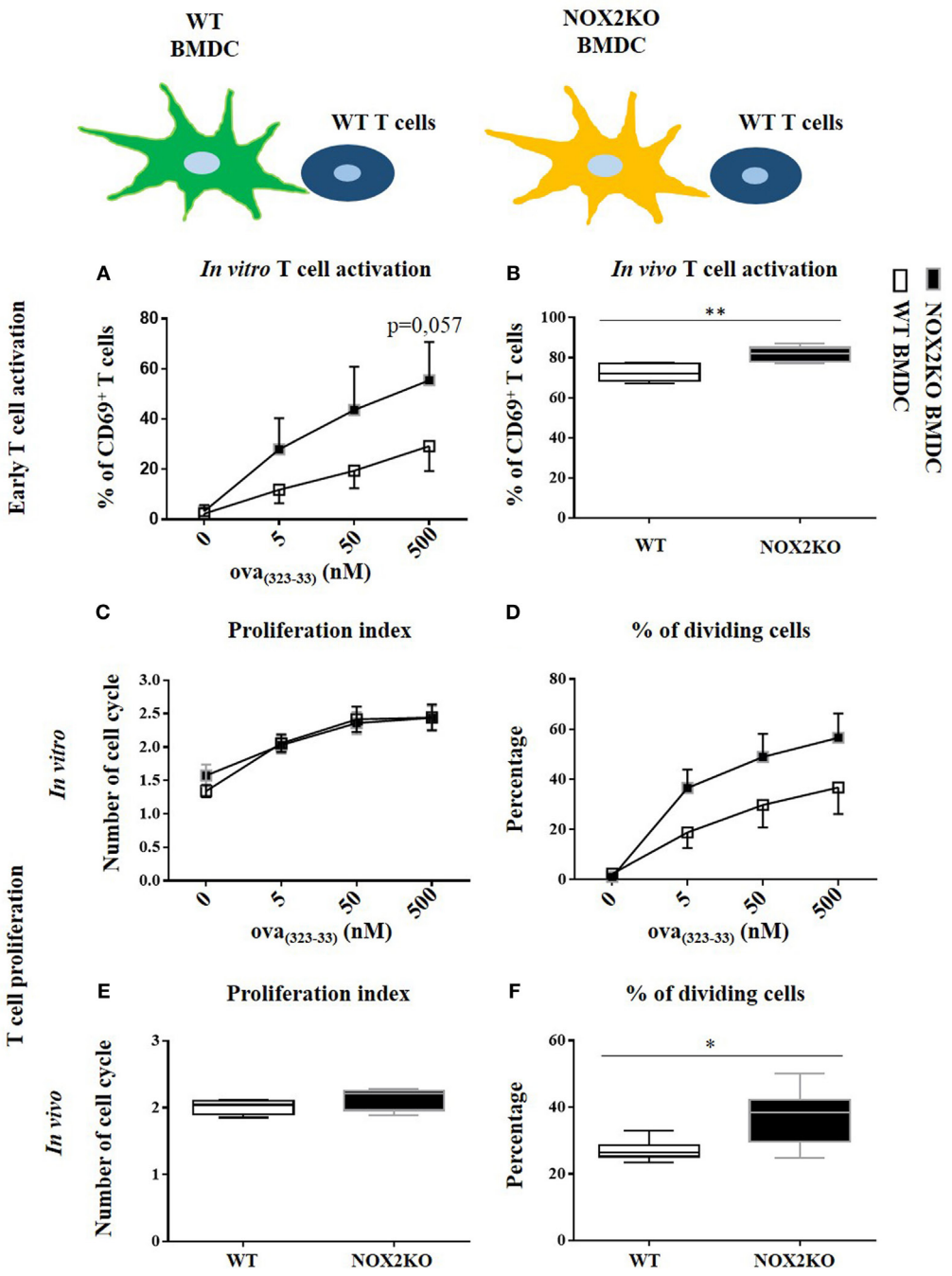

FIGURE 4 | Effect of NOX2 in dendritic cells on T cell activation and proliferation *in vitro* and *in vivo*. OTII T cells were co-cultured with wild-type (WT) or NOX2KO bone marrow-derived dendritic cells (BMDCs) in the presence of different concentrations of OVA$_{(323–339)}$ peptide (5, 50, and 500 nM) for *in vitro* experiments **(A,C,D)**, or were labeled with carboxyfluorescein succinimidyl ester (CFSE) and injected in OVA$_{(323–339)}$ pre-immunized WT or NOX2KO mice for *in vivo* experiments **(B,E,F)**. T cell activation was determined 16 h after co-culture or 16 h after T cell injection by measuring the upregulation of CD69 by flow cytometry. **(A)** Percentage of CD69^{hi}CD4^{hi} T cells *in vitro*. **(B)** Percentage of CD69^{hi}CD4^{hi}CFSE^{hi} T cells *in vivo*. For T cell proliferation, T cells were labeled with CFSE for the *in vivo* and *in vitro* experiments. The proliferation index and the percent of dividing cells were determined by the dilution of the CFSE signal in the OTII T cell population: **(C,E)** proliferation index and **(D,F)** percent of dividing cells *in vitro* **(C,D)** (n = 7) and *in vivo* **(E,F)**. *p < 0.05 and **p < 0.01.

used the property of the CFSE vital dye, for which fluorescence is equally divided by two in daughter cells after each cell division, allowing to study cell division. In the absence of antigen, T cells were not activated and did not enter into cell division. There was, therefore, only one peak of CFSE fluorescence (Figure S3 in Supplementary Material). With the addition of $OVA_{(323–339)}$ peptide to the co-culture, T cells started to divide and different peaks of CFSE fluorescence were detected. The percentage of cells that entered into division increased as a function of $OVA_{(323–339)}$ peptide concentration (Figure S3 in Supplementary Material). Co-culture of T cells with either WT or NOX2KO BMDCs did not change their proliferation index (**Figure 4C**). In contrast, there was also a trend toward a higher percentage of T cells that entered into cell cycle when T cells were incubated with NOX2KO BMDCs compared to WT BMDCs (**Figure 4D**). Therefore, the absence of NOX2 in BMDCs might facilitate the entry of T cells into cell division but once T cells went into cell division, they behaved similarly when incubated with either WT or NOX2KO DCs. These results confirm the above observations, and suggest an increase in early T cell activation with NOX2KO DCs compared to WT DCs.

Given the observed trends in our *in vitro* data, we wanted to independently confirm our results and further address the question *in vivo*. WT or NOX2KO mice were immunized subcutaneously in the outer ear with curdlan and $OVA_{(323–339)}$ peptide. 1 day later, CFSE-labeled OTII T cells were injected intravenously. The T cell response was analyzed in the draining and the non-draining lymph nodes at day 1 for early T cell activation (CD69 expression) and at day 3 for T cell proliferation (CFSE dilution). The upregulation of CD69 on $CFSE^{hi}$ $CD4^+$ T cells in the draining lymph nodes demonstrated an activation of T cells 1 day after immunization, which was not the case in non-draining lymph nodes (data not shown). Recapitulating our *in vitro* co-culture assays, the percent of $CD69^{hi}$ $CD4^+$ $CFSE^{hi}$ T cell was higher 1 day after immunization of NOX2KO mice compared to WT controls (**Figure 4B**). At day 3, the percentage of CFSE-labeled OTII T cells that had initiated proliferation was markedly higher in CGD mice, as compared to WT (**Figure 4F**), whereas there was no difference in the proliferation index (**Figure 4E**). Thus, both *in vitro* and *in vivo*, the number of $CD4^+$ T cells upregulating the early activation marker and entering into cell division is increased when the APCs do not express NOX2.

To determine whether NOX2 expression in T cells contribute to the above observations, we assessed whether NOX2-deficient and WT T cells behave differently *in vitro* and *in vivo*. For that purpose, we crossed OTII mice with NOX2KO mice, as a source of T cells that were OVA-specific (OTII) and NOX2-deficient. For *in vitro* experiments, OTII WT and OTII NOX2KO T cells were co-cultured with curdlan-activated $OVA_{(323–339)}$ peptide loaded WT BMDCs. For *in vivo* experiments, OTII WT and OTII NOX2KO T cells were labeled with two different fluorescent vital dyes: a mixture of OTII WT and OTII NOX2KO T cells (ratio 1:1) was injected intravenously in WT mice that had been previously immunized with the $OVA_{(323–339)}$ peptide and curldan. Using this system, we were able to analyze and compare the activation of both WT and NOX2KO T cells in the same recipient mice. Both *in vitro* and *in vivo* experiments showed neither difference in T cell activation nor T cell proliferation between WT and NOX2KO $CD4^+$ T cells. Percentages of $CD69^{hi}$ $CD4^+$ T cells were identical when OTII WT and OTII NOX2KO where used, *in vivo* and *in vitro* (**Figures 5A,B**), and both the proliferation index and the percent of dividing cells were identical *in vitro* (**Figures 5C,D**). Thus, T cells from control and NOX2-deficient mice responded similarly to activation by DCs, refuting claims of a cell autonomous effect of NOX2 in T cells.

Finally, several NOX2-dependent mechanisms limiting T cell activation by BMDCs were tested: (i) a paracrine effect of BMDC-derived H_2O_2 on T cells, (ii) a NOX2-dependent modulation of costimulatory molecules in BMDCs, which are known to influence the strength of T cell activation, and (iii) an impact of NOX2 on the release of T cell modulatory cytokines by BMDCs. For the first mechanism, the possible effect of BMDC-derived H_2O_2 on T cells was assessed by activating T cells from WT mice with anti-CD3/anti-CD28 antibodies and exposing them to increasing concentrations of exogenous H_2O_2. The percentage of $CD69^{hi}$ $CD4^+$ T cells was not affected by H_2O_2, even at cytotoxic concentrations of H_2O_2 (**Figures 6A,B**). This excludes a direct role of BMDC-derived H_2O_2 on T cells. To test the second possibility, co-stimulatory molecule expression at the BMDC surface was analyzed by measuring the level of expression of MHCII, CD80, CD86, ICOSL, PDL1, and DC-SIGN after exposure of BMDCs to different concentrations of curdlan. All these molecules were similarly expressed by NOX2KO and WT BMDCs (**Figures 6C,E,G**; Figures S4A–C in Supplementary Material), ruling out an effect of NOX2 on the phenotype of BMDCs. To test the third mechanism, the production of T cell modulatory cytokines by NOX2 and WT BMDCs was measured after stimulation with curdlan. Whereas no effect of NOX2 deficiency was observed for the production of Th1 unrelated cytokines (IL-6 and IL-10) (**Figure 6H**; Figure S4D in Supplementary Material), NOX2-deficient BMDCs produced increased amounts of the pro-Th1 cytokines IL-12 and IL-1β compared to WT BMDCs (**Figures 6D,F**). In conclusion, our data neither favor a direct impact of NOX2-derived H_2O_2 on lymphocytes, nor a signaling through costimulatory receptors. In contrast, our data indicate an important role of NOX2 in BMDCs for limiting the release of pro-Th1 cytokines.

DISCUSSION

Our study represents, to the best of our knowledge, the first analysis of the impact of the phagocyte NADPH oxidase (NOX2) on the pattern of IgG subtype repartition. The results show that NOX2 not only limits the amount of circulating antibodies, but also contributes to the determination of the composition of IgG subtypes. Indeed, upon immunization, NOX2-deficient mice show increased IgG2c levels. As underlying mechanisms, we propose that the increased release of Th1-driving cytokines from NOX2-deficient APCs leads to enhanced IFNγ production by activated T cells, which may in turn promote IgG2c production by B cells.

First reports describing CGD in the late 1950s had already described increased immunoglobulin levels (2), even before the lack of microbicidal activity of phagocytes in CGD was discovered (25). Subsequently, however, the increased immunoglobulin

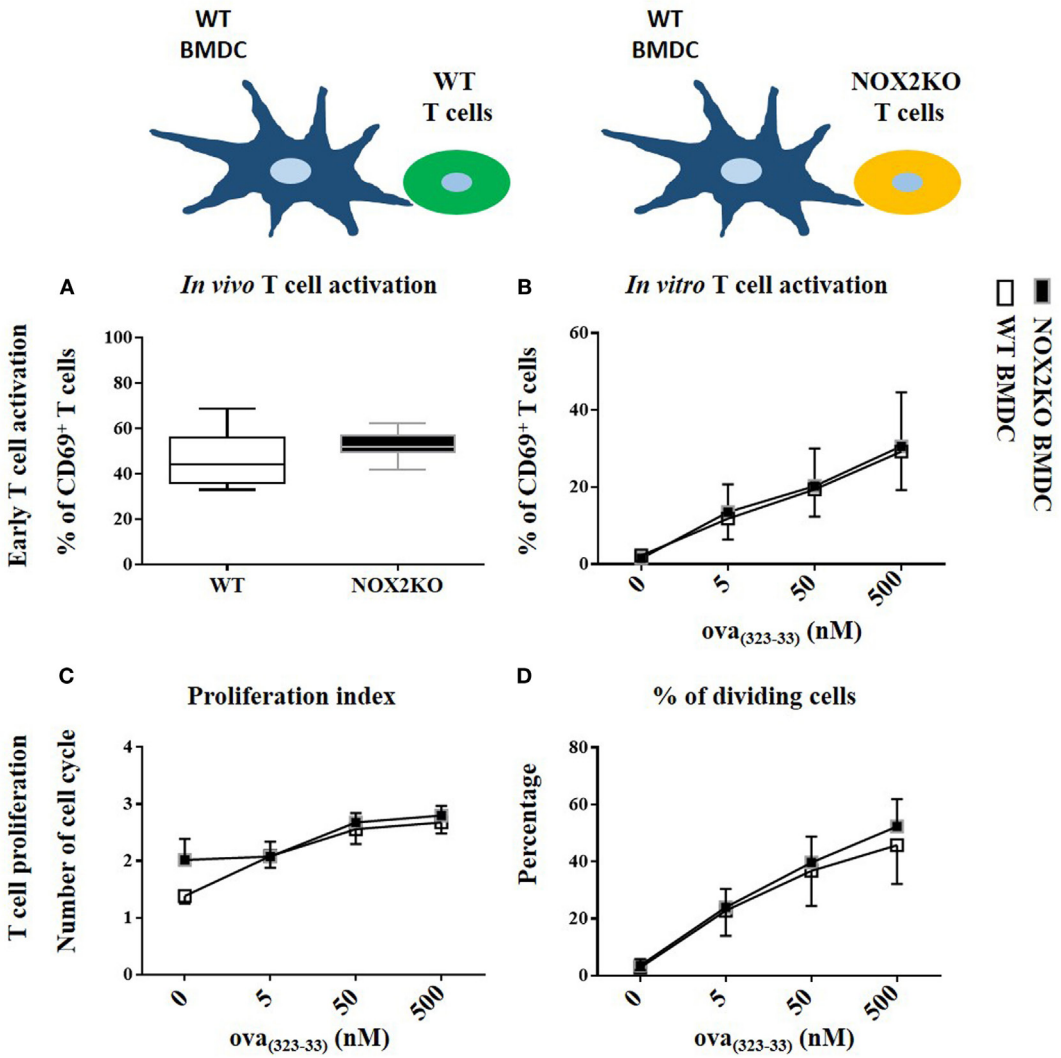

FIGURE 5 | NOX2 in T cells does not impact T cell activation and proliferation *in vitro* and *in vivo*. Percent of $CD69^{hi}$ in NOX2 and wild-type $CD4^+$ T cells *in vitro* **(A)** and *in vivo* **(B)**. Proliferation index **(C)** and percent of dividing cells **(D)** at the different concentration of $OVA_{323-339}$ peptide *in vitro* ($n = 7$).

levels in CGD patients received little attention and were mostly attributed to repeated infections. Our study confirms that even in the absence of an experimental immunization, CGD mice have altered immunoglobulins levels. We found that serum levels of IgG2c were increased in a statistically significant manner. Note that these mice never developed a clinical apparent infection. Thus, we assume that the daily host–pathogen interaction, even in the absence of infection or controlled immunization is sufficient to reveal the tendency of CGD mice to produce a different subset of IgG. However, the controlled immunization performed in this study allowed us to further characterize the immune phenotype. Interestingly, the impact of NOX2 deficiency on IgG subtype production depends on the nature of the adjuvant. Alum (known to drive a Th2 response) promotes a modest IgG1 production in both WT and NOX2-deficient mice. Neither WT nor NOX2-deficient mice produced IgG2c with alum as adjuvant. Curdlan has been described to induce both Th1 and Th17 responses, with the Th1 response being predominant (26). However, in a previous study, our laboratory showed that IFNγ but not IL-17 is increased in NOX2-deficient mice after injection of curdlan in the outer ear of mice (27). Accordingly, we found a low level of the Th2-driven anti-ovalbumin IgG1 subtype in both WT and NOX2-deficient mice. In contrast, curdlan induces a marked increase in the production of IgG2c in WT mice, which was strikingly enhanced in NOX2-deficient mice. Thus, NOX2 deficiency by itself does not alter the type of the immune response elicited by a given adjuvant, but rather amplifies its response. Our results suggest the following scenario: in WT mice, curdlan activation of the dectin-1 pathway in DCs leads to production of Th1-driving cytokines, such as IL-12 and IL-1β, the magnitude of these cytokines being limited by NOX2-dependent ROS generation. In the absence of NOX2, the Th1 response is not kept under control, resulting in an enhancement of this pathway, and a subsequent deviation toward IgG2c responses. It will be of major interest to identify the

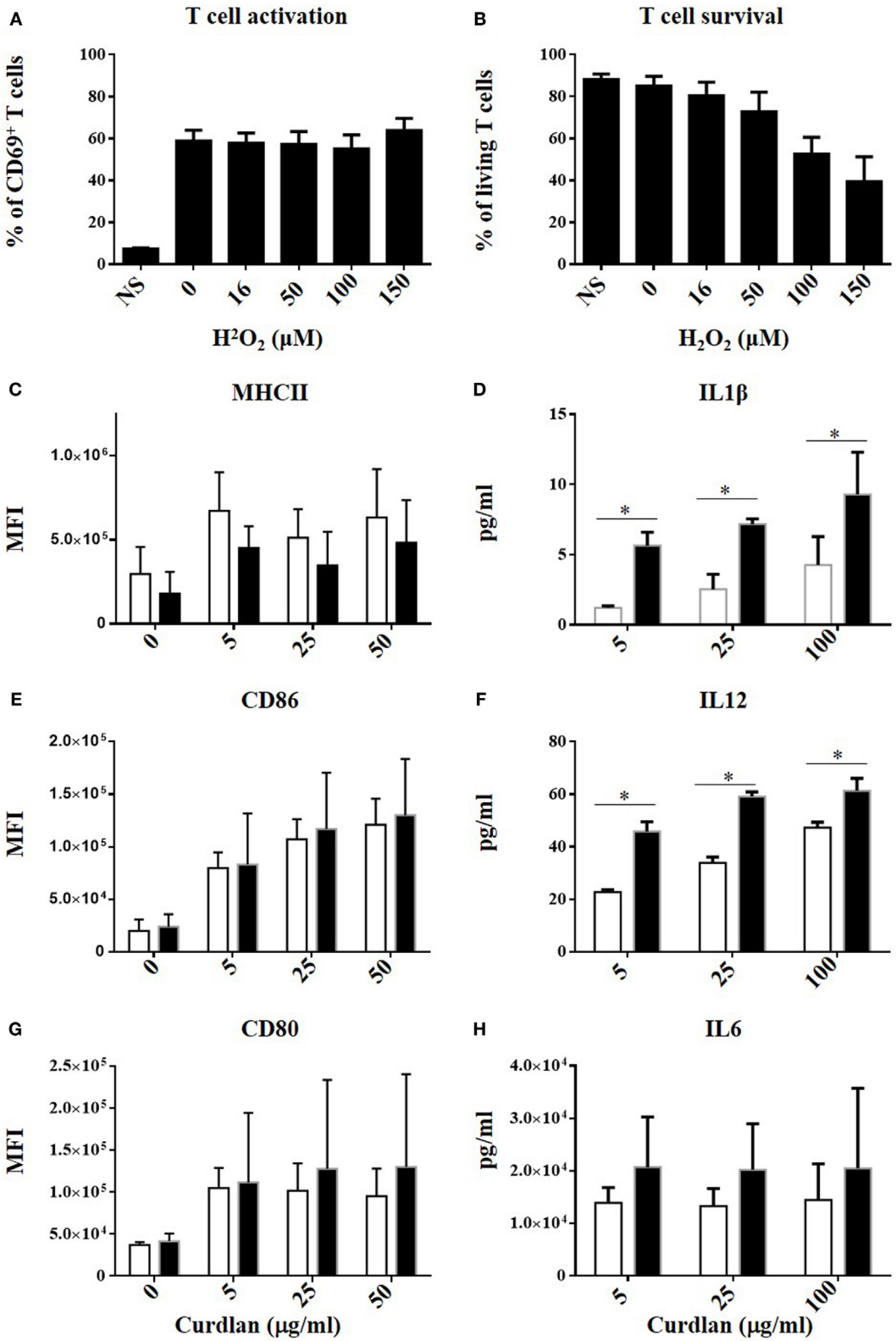

FIGURE 6 | No direct effect of H_2O_2 on T cell activation but increased IL12 and IL1β production by NOX2KO bone marrow-derived dendritic cells (BMDCs) after activation by curdlan. Effect of increasing concentration of H_2O_2 on CD69 upregulation **(A)** and survival **(B)** in anti-CD3/anti-CD28 activated $CD4^+$ T cell ($n = 4$). Expression level of MHCII **(C)**, CD86 **(E)**, and CD80 **(G)** in curdlan-activated wild-type (WT) and NOX2 BMDC was analyzed by flow cytometry ($n = 4$; MFI, mean fluorescent intensity). Level of IL-1β **(D)**, IL-12 **(F)**, and IL-6 **(H)** present in the supernatant of curdlan-activated WT and NOX2KO BMDC ($n = 3$).

ROS target in DCs. Typically, ROS signaling may occur through oxidation of redox-sensitive cysteines, for example, within the catalytic site of protein phosphatases (28). The identification of the ROS target would potentially pave the way toward innovative immunomodulatory treatments. Interestingly, a study showed an enhanced IL12 production after stimulation of NOX2-deficient BMDCs with IFNγ/LPS of NOX2 and this effect was correlated with a decreased p38-MAPK (29). Therefore, it would be interesting to investigate this pathway in order to elucidate the mechanism by which NOX2 controls IL12 production.

Understanding which NOX2 expressing cells influence the antibody responses is essential, the more relevant candidates being APCs, T cells, and B cells. Our results argue against a role for NOX2 in T cells. This is supported by previous publications suggesting that NOX2 is virtually not expressed in T cells (30). Our results rather support a role for APCs: when studying *in vitro* and *in vivo* T cell priming by DCs, we observed a trend toward an enhanced T cell activation by NOX2-deficient DCs *in vitro*, which was confirmed by an enhanced T cell activation *in vivo* in NOX2-deficient mice. However, we cannot exclude that NOX2 in other cell types might contribute to increase the T cell activation and altered IgG production. Indeed, fully functional NOX2 is expressed in B cells.

There is now increasing consensus that specific immunity, including humoral immune responses are enhanced in CGD patients. For most parts, these findings have also been documented in CGD mice. However, there are certain differences between the results reported in different studies that should be noted. Indeed, studies using the TLR4 ligand LPS as adjuvant, did not find increased T cell activation by phagocyte NADPH oxidase-deficient DCs (4, 31). Note that in our study, we have also observed differences between adjuvants, namely the use of alum vs. the dectin-1 ligand curdlan. Thus, different ways of DC activation yields distinct T and B cell responses, adding to the complexity of the specific immunity in CGD patients. At least two observations argue in favor of the *in vivo* relevance of our observations: (i) dectin-1 is increasingly recognized as a relevant activator of DCs (32) and (ii) altered IgG subtypes in CGD patients were identified in our study.

The enhanced T cell activation by NOX2-deficient DCs might be explained through at least four different mechanisms:

(i) Direct impact of ROS on T cells. Our study did not find direct impact of hydrogen peroxide on T cell activation (**Figure 6A**). Interestingly, other studies using adaptive transfer of athritogenic T cells derived from Ncf1-deficient rodents report that hydrogen peroxide attenuates the athritogenic properties of such T cells (30, 33). Thus, depending on the experimental set-up there might be a direct effect of hydrogen peroxide. Also, the primary product of NOX2 activation is the superoxide radical anion $O_2^{\bullet -}$ and these experiments do not address the impact of NOX2-derived oxidants, other than H_2O_2.

(ii) Antigen processing in NOX2KO DCs. Some studies have described an altered antigen processing in NOX2KO DCs, resulting in an altered cross-presentation or in a different epitopic repertoire (19, 34–37). However, we have used the $OVA_{(323–339)}$ peptide for our experiment on T cell activation, which does not require further peptidic cleavage to be presented through MHC class II molecules. Although, we cannot exclude that mechanism such as peptide transport and post-proteolytic modifications might be impacted by NOX2 deficiency, our results cannot be explained by a difference in proteases activity.

(iii) Alteration of surface proteins (in particular costimulatory molecules). We have investigated expression of costimulatory molecules by WT and NOX2-deficient DCs and did not observe any differences.

(iv) Altered release of soluble mediators (in particular cytokines): this mechanism is strongly supported by our data, as we find important differences in the release of two important T cell modulatory cytokines, namely IL1-β and IL-12, which polarize T cell toward a Th1 effector phenotype. Thus, in our hands, the release of soluble mediators from DCs is important for the understanding of the enhanced immune response in the CGD situation.

Another novel and unexpected result of both our *in vitro* and *in vivo* studies is the observation that the enhanced immune activation in NOX2-deficient mice concurred with an increased entry of T cells into the cell cycle, rather than an increased T cell proliferation rate. This observation is in line with our results suggesting that there is no cell autonomous effect of NOX2 in T cells, but rather that the initiation of T cell activation is controlled by NOX2 in DCs.

The human situation is more complex, due to first, the limitation of our knowledge on the IgG isotype switch, and second, the difficulty to perform clinical studies in CGD patients investigating the response to a specific antigen after immunization. Although the nomenclature is close between human and mice IgG subclass, their function differ in many aspects and direct comparison between high mouse IgG2c in mice and altered IgG1/IgG and IgG2/IgG ratio in human should be interpreted with caution. Nevertheless, our study has identified a remarkable, hitherto not described, pattern of IgG subtype distribution. The proportion of IgG2 was increased in adult CGD patients, while there was a relative decrease in IgG1. The increased levels of IgG2 were not observed at birth, but rather developed over the first 12 years of life. This suggests that there might be similarities between our experimental results obtained in NOX2-deficient mice and the condition of CGD children exposed to antigens. The age-dependent increase in IgG2 in human CGD patients might possibly reflect exposure to encapsulated bacteria (38). The increased IgG, and in particular IgG2, levels might provide compensatory mechanisms for the host defense against infections in CGD patients. However, such an increased propensity toward antibody generation is likely to come at a price. Indeed, as discussed in the Section "Introduction," CGD patients are prone to autoimmune diseases. In our serum samples from CGD patients, we found an increased proportion of positivity for the ANCA autoantibody (31%). In adult controls, only 6% (58 out of 924) serum samples were found positive using a similar IFI method (39). However, the results are largely variable among laboratories and methods. In addition, a further confounding factor is that ANCA formation

is triggered by infection, and since CGD patients often encounter repeated infection, it would not be possible to exclude this as a cause of increased ANCA prevalence in these patients (40). ANA antibodies were positive in 3 out of 16 CGD patients (19%) while the percentage is 13.3% in control adults (41). The percentage of ANCA and ANA positivity is unknown in children, but autoantibody frequency usually increases with age and positivity is, therefore, likely to be decreased in children compared to adults. Altogether, our results confirm the increased prevalence of autoantibodies in CGD patients.

In summary, our results provide novel insights into the mechanisms underlying increased specific immune responses in CGD patients. Augmented cytokine production by NOX2-deficient DCs appears to be a crucial mechanism implicated in enhanced T cell activation and autoantibody production. Thus, targeting the overshooting release of T cell modulatory cytokines might be a promising approach for the treatment of hyperimmune disorders in CGD patients. It would, however, be beneficial to better understand how ROS dampen the release of cytokines in DCs. The identification of NOX2-derived ROS targets would open the path to novel immunomodulatory strategies at the interface of innate and specific immunity.

ETHICS STATEMENT

Blood samples were obtained from the CGD patients with appropriate institutional informed consent. This study also includes peripheral blood samples taken from healthy donors obtained from the "Etablissement Français du sang" at the Grenoble University Hospital, France after their informed consent. For animal subject, the protocol was approved by the office cantonal vétérinaire du Canton de Genève, Switzerland (authorization no. 23624).

AUTHOR CONRIBUTIONS

JC conceived the study, designed and performed experiments, analyzed the data, and wrote the manuscript. CD helped in the design of the study and the analysis of data. MA edited the manuscript. PR-L performed the autoantibody titer in human. AG performed the measurement of serum immunoglobulin in human. MJS diagnosed and characterized the mutation of CGD patients. SH helped in the design of T cell experiment *in vivo* and *in vitro*. K-HK conceived the study, wrote and edited the manuscript. All authors read and approved the final manuscript.

ACKNOWLEDGMENTS

This study was supported by the Swiss National Science Foundation ProDoc Research Module, PDFMP3-127302. The authors would like to thank the collaborators at the animal core facility, Cécile Gameiro at the flow cytometry core facility, and Yves Alexandre Cambet at READS units at the CMU of the University of Geneva. The authors would also like to thank Lesly Guery for discussions and help for the co-culture experiments. We are grateful to Olivier Plastre, for technical help and Vincent Jaquet for extensive editing of the manuscript.

SUPPLEMENTARY MATERIAL

The Supplementary Material for this article can be found online at https://www.frontiersin.org/articles/10.3389/fimmu.2018.01555/full#supplementary-material.

TABLE S1 | Demographic and blood biochemistry values for CGD patients and healthy controls. CGD patient samples are listed from 1–16, while healthy controls are assigned A–F. Values exceeding laboratory reference values are indicated in red shading. Reference values: IgG = 7–10 g/l; IgA = 0.9–2.3 g/l; IgM = 0.4–0.9 g/l; anti-MPO < 6 U; anti-PR3 < 5 U; and ANA < 80. Abbreviations: F, female; M, male; NA, not available; ND, not detected (below detection level); CGD, chronic granulomatous disease; $A47^0$, $p47^{phox}$-deficient autosomal recessive CGD; $A67^0$, $p67^{phox}$-deficient autosomal recessive CGD; $A22^0$, $p22^{phox}$-deficient autosomal recessive CGD; ANCA, anti-neutrophil cytoplasmic antibodies; ANA, anti-nuclear antibody.

FIGURE S1 | Enhanced inflammation of draining lymph node: draining cervical and non-draining inguinal lymph nodes were removed 14 days post immunization, dissociated, and analyzed by flow cytometry: **(A)** absolute number of IgD^+ B cells and **(B)** absolute number of $CD4^+$ T cells.

FIGURE S2 | Representative dot plot graphs showing CD69 expression in CD4-positive T cells after co-culture with different concentration of $OVA_{(323–339)}$ peptide.

FIGURE S3 | Representative histogram of carboxyfluorescein succinimidyl ester dilution at different concentration of $OVA_{323–339}$ peptide after 3 days of co-culture with wild-type or NOX2KO BMDC.

FIGURE S4 | NOX2 deficiency has no impact on the expression level of ICOSL **(A)**, PDL1 **(B)** and DC-SIGN **(C)** or the level of IL10 **(D)** present in the supernatant, after activation of BMDCs by increasing concentration of curdlan.

REFERENCES

1. Bedard K, Krause KH. The NOX family of ROS-generating NADPH oxidases: physiology and pathophysiology. *Physiol Rev* (2007) 87:245–313. doi:10.1152/physrev.00044.2005
2. Janeway CA, Craig J, Davidson M, Downey W, Gitlin D. Hypergammaglobulinemia associated with severe recurrent and chronic nonspecific infection. *Am J Dis Child* (1954) 88:388–92.
3. Maly FE, Nakamura M, Gauchat JF, Urwyler A, Walker C, Dahinden CA, et al. Superoxide-dependent nitroblue tetrazolium reduction and expression of cytochrome b-245 components by human tonsillar B lymphocytes and B cell lines. *J Immunol* (1989) 142:1260–7.
4. Gelderman KA, Hultqvist M, Pizzolla A, Zhao M, Nandakumar KS, Mattsson R, et al. Macrophages suppress T cell responses and arthritis development in mice by producing reactive oxygen species. *J Clin Invest* (2007) 117:3020–8. doi:10.1172/JCI31935
5. Vasilevsky S, Liu Q, Koontz SM, Kastenmayer R, Shea K, Jackson SH. Role of p47phox in antigen-presenting cell-mediated regulation of humoral immunity in mice. *Am J Pathol* (2011) 178:2774–82. doi:10.1016/j.ajpath.2011.02.038
6. Richards SM, Clark EA. BCR-induced superoxide negatively regulates B-cell proliferation and T-cell-independent type 2 Ab responses. *Eur J Immunol* (2009) 39:3395–403. doi:10.1002/eji.200939587
7. Cachat J, Deffert C, Hugues S, Krause KH. Phagocyte NADPH oxidase and specific immunity. *Clin Sci (Lond)* (2015) 128:635–48. doi:10.1042/CS20140635
8. Winkelstein JA, Marino MC, Johnston RB Jr, Boyle J, Curnutte J, Gallin JI, et al. Chronic granulomatous disease – report on a national registry of 368 patients. *Medicine* (2000) 79:155–69. doi:10.1097/00005792-200005000-00003
9. Foster CB, Lehrnbecher T, Mol F, Steinberg SM, Venzon DJ, Walsh TJ, et al. Host defense molecule polymorphisms influence the risk for immune-mediated complications in chronic granulomatous disease. *J Clin Invest* (1998) 102:2146–55. doi:10.1172/JCI5084
10. De Ravin SS, Naumann N, Cowen EW, Friend J, Hilligoss D, Marquesen M, et al. Chronic granulomatous disease as a risk factor for autoimmune disease. *J Allergy Clin Immunol* (2008) 122:1097–103. doi:10.1016/j.jaci.2008.07.050

11. Van den Berg JM, van Koppen E, Ahlin A, Belohradsky BH, Bernatowska E, Corbeel L, et al. Chronic granulomatous disease: the European experience. *PLoS One* (2009) 4(4):e5234. doi:10.1371/journal.pone.0005234
12. Jacob N, Stohl W. Autoantibody-dependent and autoantibody-independent roles for B cells in systemic lupus erythematosus: past, present, and future. *Autoimmunity* (2010) 43:84–97. doi:10.3109/08916930903374600
13. Yu JE, De Ravin SS, Uzel G, Landers C, Targan S, Malech HL, et al. High levels of Crohn's disease-associated anti-microbial antibodies are present and independent of colitis in chronic granulomatous disease. *Clin Immunol* (2011) 138:14–22. doi:10.1016/j.clim.2010.08.003
14. Olofsson P, Holmberg J, Tordsson J, Lu S, Akerström B, Holmdahl R. Positional identification of Ncf1 as a gene that regulates arthritis severity in rats. *Nat Genet* (2003) 33:25–32. doi:10.1038/ng1058
15. Hultqvist M, Holmdahl R. Ncf1 (p47phox) polymorphism determines oxidative burst and the severity of arthritis in rats and mice. *Cell Immunol* (2005) 233:97–101. doi:10.1016/j.cellimm.2005.04.008
16. Gelderman KA, Hultqvist M, Holmberg J, Olofsson P, Holmdahl R. T cell surface redox levels determine T cell reactivity and arthritis susceptibility. *Proc Natl Acad Sci U S A* (2006) 103:12831–6. doi:10.1073/pnas.0604571103
17. Bogeski I, Kummerow C, Al-Ansary D, Schwarz EC, Koehler R, Kozai D, et al. Differential redox regulation of ORAI ion channels: a mechanism to tune cellular calcium signaling. *Sci Signal* (2010) 3. doi:10.1126/scisignal.2000672
18. Kwon J, Devadas S, Williams M. T cell receptor-stimulated generation of hydrogen peroxide inhibits MEK-ERK activation and lck serine phosphorylation. *Free Radic Biol Med* (2003) 35:406–17. doi:10.1016/S0891-5849(03)00318-6
19. Allan ER, Tailor P, Balce DR, Pirzadeh P, McKenna NT, Renaux B, et al. NADPH oxidase modifies patterns of MHC class II-restricted epitopic repertoires through redox control of antigen processing. *J Immunol* (2014) 192:4989–5001. doi:10.4049/jimmunol.1302896
20. Yang M, Haase C, Viljanen J, Xu B, Ge C, Kihlberg J, et al. Cutting edge: processing of oxidized peptides in macrophages regulates T cell activation and development of autoimmune arthritis. *J Immunol* (2017) 199:3937–42. doi:10.4049/jimmunol.1700774
21. Hultqvist M, Olofsson P, Holmberg J, Bäckström BT, Tordsson J, Holmdahl R. Enhanced autoimmunity, arthritis, and encephalomyelitis in mice with a reduced oxidative burst due to a mutation in the Ncf1 gene. *Proc Natl Acad Sci U S A* (2004) 101:12646–51. doi:10.1073/pnas.0403831101
22. Campbell AM, Kashgarian M, Shlomchik MJ. NADPH oxidase inhibits the pathogenesis of systemic lupus erythematosus. *Sci Transl Med* (2012) 4(157):157ra141. doi:10.1126/scitranslmed.3004801
23. Zhao J, Ma J, Deng Y, Kelly JA, Kim K, Bang SY, et al. A missense variant in NCF1 is associated with susceptibility to multiple autoimmune diseases. *Nat Genet* (2017) 49:433–7. doi:10.1038/ng.3782
24. Schäppi M, Deffert C, Fiette L, Gavazzi G, Herrmann F, Belli D, et al. Branched fungal beta-glucan causes hyperinflammation and necrosis in phagocyte NADPH oxidase-deficient mice. *J Pathol* (2008) 214:434–44. doi:10.1002/path.2298
25. Baehner RL, Nathan DG. Leukocyte oxidase: defective activity in chronic granulomatous disease. *Science* (1967) 155:835–6. doi:10.1126/science.155.3764.835
26. LeibundGut-Landmann S, Gross O, Robinson MJ, Osorio F, Slack EC, Tsoni SV, et al. Syk- and CARD9-dependent coupling of innate immunity to the induction of T helper cells that produce interleukin 17. *Nat Immunol* (2007) 8:630–8. doi:10.1038/ni1460
27. Deffert C, Carnesecchi S, Yuan H, Rougemont AL, Kelkka T, Holmdahl R, et al. Hyperinflammation of chronic granulomatous disease is abolished by NOX2 reconstitution in macrophages and dendritic cells. *J Pathol* (2012) 228:341–50. doi:10.1002/path.4061
28. Meng TC, Fukada T, Tonks NK. Reversible oxidation and inactivation of protein tyrosine phosphatases in vivo. *Mol Cell* (2002) 9:387–99. doi:10.1016/S1097-2765(02)00445-8
29. Jendrysik MA, Vasilevsky S, Yi L, Wood A, Zhu N, Zhao Y, et al. NADPH oxidase-2 derived ROS dictates murine DC cytokine-mediated cell fate decisions during CD4 T helper-cell commitment. *PLoS One* (2011) 6:e28198. doi:10.1371/journal.pone.0028198
30. Hultqvist M, Olofsson P, Gelderman KA, Holmberg J, Holmdahl R. A new arthritis therapy with oxidative burst inducers. *PLoS Med* (2006) 3:e348. doi:10.1371/journal.pmed.0030348
31. Padgett LE, Tse HM. NADPH oxidase-derived superoxide provides a third signal for CD4 T cell effector responses. *J Immunol* (2016) 197:1733–42. doi:10.4049/jimmunol.1502581
32. Agrawal S, Gupta S, Agrawal A. Human dendritic cells activated via dectin-1 are efficient at priming Th17, cytotoxic CD8 T and B cell responses. *PLoS One* (2010) 5:e13418. doi:10.1371/journal.pone.0013418
33. Yang Z, Shen Y, Oishi H, Matteson EL, Tian L, Goronzy JJ, et al. Restoring oxidant signaling suppresses proarthritogenic T cell effector functions in rheumatoid arthritis. *Sci Transl Med* (2016) 8:331ra338. doi:10.1126/scitranslmed.aad7151
34. Savina A, Jancic C, Hugues S, Guermonprez P, Vargas P, Moura IC, et al. NOX2 controls phagosomal pH to regulate antigen processing during crosspresentation by dendritic cells. *Cell* (2006) 126:205–18. doi:10.1016/j.cell.2006.05.035
35. Rybicka JM, Balce DR, Chaudhuri S, Allan ER, Yates RM. Phagosomal proteolysis in dendritic cells is modulated by NADPH oxidase in a pH-independent manner. *EMBO J* (2012) 31:932–44. doi:10.1038/emboj.2011.440
36. Crotzer VL, Matute JD, Arias AA, Zhao H, Quilliam LA, Dinauer MC, et al. Cutting edge: NADPH oxidase modulates MHC class II antigen presentation by B cells. *J Immunol* (2012) 189:3800–4. doi:10.4049/jimmunol.1103080
37. Balce DR, Li B, Allan ER, Rybicka JM, Krohn RM, Yates RM. Alternative activation of macrophages by IL-4 enhances the proteolytic capacity of their phagosomes through synergistic mechanisms. *Blood* (2011) 118:4199–208. doi:10.1182/blood-2011-01-328906
38. Kuijpers TW, Weening RS, Out TA. IgG subclass deficiencies and recurrent pyogenic infections, unresponsiveness against bacterial polysaccharide antigens. *Allergol Immunopathol (Madr)* (1992) 20:28–34.
39. Damoiseaux J, Csernok E, Rasmussen N, Moosig F, van Paassen P, Baslund B, et al. Detection of antineutrophil cytoplasmic antibodies (ANCAs): a multicentre European Vasculitis Study Group (EUVAS) evaluation of the value of indirect immunofluorescence (IIF) versus antigen-specific immunoassays. *Ann Rheum Dis* (2016) 76(4):647–53. doi:10.1136/annrheumdis-2016-209507
40. Konstantinov KN, Ulff-Moller CJ, Tzamaloukas AH. Infections and antineutrophil cytoplasmic antibodies: triggering mechanisms. *Autoimmun Rev* (2015) 14:201–3. doi:10.1016/j.autrev.2014.10.020
41. Tan EM, Feltkamp TE, Smolen JS, Butcher B, Dawkins R, Fritzler MJ, et al. Range of antinuclear antibodies in "healthy" individuals. *Arthritis Rheum* (1997) 40(9):1601–11. doi:10.1002/art.1780400909

Conflict of Interest Statement: K-HK holds shares of Genkyotex SA, a company aiming at developing NOX inhibitors. The remaining authors declare that the research was conducted in the absence of any commercial or financial relationships that could be construed as a potential conflict of interest.

frontiers in Immunology

ORIGINAL RESEARCH
published: 08 May 2018
doi: 10.3389/fimmu.2018.00973

NoxO1 Controls Proliferation of Colon Epithelial Cells

*Franziska Moll[1], Maria Walter[1], Flávia Rezende[1], Valeska Helfinger[1], Estefania Vasconez[1], Tiago De Oliveira[2], Florian R. Greten[2], Catherine Olesch[3], Andreas Weigert[3], Heinfried H. Radeke[4] and Katrin Schröder[1]**

[1] Institute for Cardiovascular Physiology, Goethe-University, Frankfurt, Germany, [2] Institute for Tumor Biology and Experimental Therapy, Georg-Speyer-Haus, Frankfurt, Germany, [3] Institute of Biochemistry I, Faculty of Medicine, Goethe-University, Frankfurt, Germany, [4] Pharmazentrum Frankfurt, Goethe-University, Frankfurt, Germany

Aim: Reactive oxygen species (ROS) produced by enzymes of the NADPH oxidase family serve as second messengers for cellular signaling. Processes such as differentiation and proliferation are regulated by NADPH oxidases. In the intestine, due to the exceedingly fast and constant renewal of the epithelium both processes have to be highly controlled and balanced. Nox1 is the major NADPH oxidase expressed in the gut, and its function is regulated by cytosolic subunits such as NoxO1. We hypothesize that the NoxO1-controlled activity of Nox1 contributes to a proper epithelial homeostasis and renewal in the gut.

Results: NoxO1 is highly expressed in the colon. Knockout of NoxO1 reduces the production of superoxide in colon crypts and is not subsidized by an elevated expression of its homolog p47phox. Knockout of NoxO1 increases the proliferative capacity and prevents apoptosis of colon epithelial cells. In mouse models of dextran sulfate sodium (DSS)-induced colitis and azoxymethane/DSS induced colon cancer, NoxO1 has a protective role and may influence the population of natural killer cells.

Conclusion: NoxO1 affects colon epithelium homeostasis and prevents inflammation.

Keywords: reactive oxygen species, colon, Nox1, NoxO1, proliferation, inflammation

OPEN ACCESS

Edited by:
Rudolf Lucas, Augusta University, United States

Reviewed by:
Gabor Csanyi, Augusta University, United States
Robert Jaster, Universitätsmedizin Rostock, Germany

****Correspondence:***
Katrin Schröder
schroeder@vrc.uni-frankfurt.de

Specialty section:
This article was submitted to Inflammation, a section of the journal Frontiers in Immunology

Received: *31 January 2018*
Accepted: *18 April 2018*
Published: *08 May 2018*

Citation:
Moll F, Walter M, Rezende F, Helfinger V, Vasconez E, De Oliveira T, Greten FR, Olesch C, Weigert A, Radeke HH and Schröder K (2018) NoxO1 Controls Proliferation of Colon Epithelial Cells. Front. Immunol. 9:973. doi: 10.3389/fimmu.2018.00973

INTRODUCTION

Colon is an organ with an enormous tissue turnover, i.e., a relatively high level of cell renewal. This can be even further elevated by the presence of pathogens, non-specific injury, or dietary factors such as high levels of bile acids (1). Interestingly, hyperproliferation may also serve as a host defense mechanism against invading pathogens, including gastrointestinal-dwelling nematodes. At least in the large intestine, the hyperproliferation and increased movement act as an "epithelial escalator" to expel the pathogens (2).

Reactive oxygen species (ROS) affect proliferation and differentiation of multiple cells, such as adipocytes, osteoclasts, and smooth muscle cells (3–5). A major source of controlled ROS formation is the family of NADPH oxidases. The seven members of the NADPH oxidase family, namely Nox1–5 and Duox1 and 2, differ in their cellular localization as well as in their mode of activation. While Nox1–2 need to be activated by cytosolic subunits, Nox4 appears to be constitutively active, Nox5 is activated by Ca^{2+}, and the Duoxes are activated by membrane-bound subunits (6). The predominant isoforms found in the intestinal system are Nox1 and Duox2, with Nox1 being mainly expressed in the ileum, cecum, and colon, while Duox2 can be found in all compartments of the intestinal tract (7). Both Nox1 and Duox2 have been shown to play a role in the development, progression,

and healing of ulcerative colitis (8–11). Nox1 contributes to ROS formation and mediates symbiosis between the gut microbiota and the intestine (12). Nox1 further regulates processes involved in homeostasis and injury repair of the colon (13, 14). Duox2 and Nox1 both build multicomponent complexes. Duox2 is associated with DuoxA2 and produces hydrogen peroxide (H_2O_2) in a Ca^{2+}-dependent manner (15). The Nox1 complex consists of the scaffolding protein p22phox, an activating subunit NoxA1, and an organizing subunit NoxO1 (16). NoxO1 is considered to contribute to a constitutive production of $O_2^{\cdot-}$ by Nox1 and thereby contributes to a shift in cellular behavior and differentiation as shown for endothelial cells, where it mediates the maintenance of a stalk cell phenotype and limits angiogenesis (17). A role for NoxO1 in intestinal tissues has not been identified so far. In human colon cancer cells, proteasomal degradation of NoxO1 reduces the Nox1-dependent ROS formation, and expression and stability of NoxO1 were significantly increased in human colon cancer tissues compared to normal colon (18). This finding suggests a role of NoxO1 in cancer. However, whether or not NoxO1 upregulation is the cause or the consequence of colon cancer remains elusive. The same holds true for the physiological role of NoxO1 in the colon. Within the present study, we characterize the function of NoxO1 in colon homeostasis and pathology. This includes NoxO1s localization and its role in the production of ROS in the colon.

MATERIALS AND METHODS

Animals and Animal Procedures

All animal experiments were approved by the local governmental authorities (approval number: FU1074, F28/46) and were performed in accordance with the animal protection guidelines. Knockout mice for NoxO1 ($NoxO1^{-/-}$) were generated as previously described and bred heterozygous, to obtain wild-type (WT) and knockout littermates (17). Mice deficient of p47phox ($p47phox^{-/-}$) were kindly provided by Ajay M Shah, Kings College London. $Nox1y/^{-}$ mice were kindly provided by Karl-Heinz Krause (19). Mice were housed in a specified pathogen-free facility with 12/12 hours day and night cycle and free access to water and chow every time.

Colitis was induced by with 2% dextran sulfate sodium (DSS) (#16011080; MP Biomedicals) in drinking water for 5 days, with a recovery phase of 3 days and were sacrificed on day 8. Body weight and physical condition were controlled daily. For the induction of colon carcinomas, a combination of the pro-inflammatory DSS together with a single intraperitoneal injection of 10 mg/kg body weight azoxymethane (AOM, Sigma-Aldrich) was used. One week after AOM injection, three cycles of 5 days with 1.5% DSS-enriched drinking water followed by 2 weeks with usual drinking water were applied. Then, mice were sacrificed, and the colon was used for further analysis. To generate colon swiss rolls, colon was isolated, flushed, and cut longitudinally. It was then rolled from proximal to distal, fixed overnight in 4% PFA, dehydrated, and embedded in paraffin.

Flow Cytometry

Characterization of immune cell subsets was performed essentially as described previously (20). Samples were acquired with a LSRII/Fortessa flow cytometer (BD Biosciences) and analyzed using FlowJo software Vx (Treestar). All antibodies and secondary reagents were titrated to determine optimal concentrations. CompBeads (BD) were used for single-color compensation to create multi-color compensation matrices. For gating, fluorescence minus one controls were used. The instrument calibration was controlled daily using Cytometer Setup and Tracking beads (BD). For characterization of immune cell subsets, the following antibodies were used: anti-CD3-PE-CF594, anti-CD4-BV711, anti-CD11c-AlexaFluor700, anti-CD19-APC-H7, anti-CD326-BV711, anti-Ly-6C-PerCP-Cy5.5, anti-NK1.1-BV510 (all from BD Biosciences), anti-CD8-BV650, anti-CD11b-BV605, anti-F4/80-PE-Cy7, anti-GITR-FITC, anti-Ly-6G-APC-Cy7 (from BioLegend), anti-CD31-PE-Cy7, anti-CD117-APC-eFluor780 (from eBioscience), anti-CD45-VioBlue, and anti-HLA-DR-APC (from Miltenyi).

Histological Colitis Scoring

Sections were stained with hematoxylin and eosin according to standard protocols, and severity of colitis was assessed in a blinded way as described before (21). The colonic epithelial damage score was assigned as follows: 0, normal; 1, hyperproliferation; 2, mild-to-moderate loss of crypts, 10–50%; 3, severe loss of crypts, 50–90%; 4, complete loss of crypts, intact epithelium; and 5, ulcerated epithelium. The infiltration with inflammatory cells score was assigned separately for: mucosa (0 = normal, 1 = mild, 2 = modest, and 3 = severe), submucosa, and muscle/serosa (0 = normal, 1 = mild to modest, and 2 = severe). The scores for epithelial damage and inflammatory cell infiltration were added, resulting in a total score ranging from 0 to 12.

RNAscope® *In Situ* Hybridization

In situ hybridization by RNAscope® technique was performed according to the manufacturer's instructions [Advanced Cell Diagnostics (ACD), Newark, CA, USA]. Briefly, 4 µm thick sections were deparaffinized and treated with H_2O_2 followed by antigen retrieval and protease treatment. For murine tissue, probes for NoxO1 ACD #466541, Nox1 ACD # 464651, p47phox ACD # 481991, Nox2 ACD # 403381, Lgr5 ACD # 312171, Adgre1 ACD #460651, and positive/negative controls (peptidylprolyl isomerase B ACD #313911/*Bacillus subtilis* dihydrodipicolinate reductase ACD #310043) were used. For human samples, POLR2A-positive control ACD # 310451 and NoxO1 ACD # 482071 probes were used. Probes were hybridized for 2 h followed by six amplification steps. The signal was detected with RNAscope® 2.5 HD detection kit Brown (ACD #322310) and specimens counterstained with Gill's hematoxylin No1. For the duplex staining, probes were hybridized for 2 h followed by 10 amplification steps. The signal was detected by RNAscope® 2.5 HD Duplex Reagent Kit ACD # 322430 and visualized with a light microscope.

Immunohistochemistry

Paraffin blocks were cut, and slides were deparaffinized for further staining in descending ethanol series from 100 to 70%. For antigen retrieval, the slides were boiled 10 min in 1× antigen retrieval buffer (Dako). After blocking with 3% hydrogen peroxide for 10 min and BSA for 1 h, primary antibodies were applied

over night at 4°C. For NoxO1 (non-commercial) and phospho-Histone3 (Millipore), the slides were incubated with goat-anti-rabbit HRP (Jackson immune research) secondary antibody for 2 h at room temperature. After incubation with F4/80 (AbD Serotech) primary antibody, the slides were incubated with anti-rat Histofine® Simple Stain mouse MaxPO (Nichirei Biosciences) for 30 min at room temperature. Staining was developed with DAB (Vector Laboratories), and nuclei were counterstained with Gill's No1 hematoxylin. Human samples were purchased from OriGene.

Multiplex Immunohistochemistry and Immunofluorescence Analysis

Colon swiss rolls were stained and analyzed using the Phen-Optics system with Opal™ 6-Color Fluorescent IHC Kits according to the manufacturer's instructions (Perkin-Elmer, Rodgau, Germany). The following antibodies were used for the staining: pan-cytokeratin (Pan-CK) (Abcam; ab27988), cleaved Caspase 3 (cCasp3) (Cell Signaling, #9661), Ki67 (clone: SP6) (Abcam, ab16667), and alpha-smooth muscle actin (Sigma, F3777). Nuclei were counterstained with DAPI, and the slides were mounted with Fluoromount-G (SouthernBiotech, Birmingham, AL, USA). For image acquisition at 4× and 20×, the Vectra® 3 automated quantitative pathology imaging system (Perkin-Elmer) was used, and the images were analyzed using inForm2.0 Software (Perkin-Elmer).

Crypt Isolation and Intestinal Organoids

Crypt isolation and organoid cultures from murine intestine were performed based on the methods of Mahe and colleagues (22) and using the Intesticult™ system from StemCell Technologies according to manufacturer's instructions. Additionally, 100 ng/mL murine Wnt3a (Peprotech) was added to the medium. Colons were isolated from mice and crypts isolated as described. 700 crypts were seeded in 50 µL mixture of Matrigel and Intesticult™ medium in 24-well plates. 400 µL medium per well was used. On day 7 after isolation, the organoids were analyzed by light microscopy and qRT-PCR.

ROS Measurements

HEK293 or CaCo2 cells were transiently transfected with plasmids (final concentration of 1.5 µg/3.5 cm dish) coding for the human sequence of Nox1, NoxO1, NoxA1, p47phox, p67phox, or GFP using lipofectamine 2000 (Thermo Fisher Scientific) according to the manufacturer's instructions.

Reactive oxygen species production was assessed in intact cells and crypts. Measurement more specific for $O_2^{\cdot-}$ was carried out with L-012 (Wako Chemicals) (200 µmol/L) in a Berthold TriStar2 microplate reader (LB942, Berthold, Wildbad, Germany). All measurements were performed in HEPES-Tyrode buffer containing 137 mmol/L NaCl, 2.7 mmol/L KCl, 0.5 mmol/L $MgCl_2$, 1.8 mmol/L $CaCl_2$, 5 mmol/L glucose, 0.36 mmol/L NaH_2PO_4, 10 mmol/L HEPES. Activation of p47phox was triggered by phorbol myristate acetate (PMA, Sigma-Aldrich, 100 nmol/L). Superoxide dismutase (SOD, Sigma-Aldrich, 300 U/mL) was used to determine the specificity of the signal for $O_2^{\cdot-}$. H_2O_2 formation was measured with the Amplex Red assay (50 µM; Invitrogen, HRP, 2 U/mL, Sigma) as previously described (23). PEG-catalase (50 U/mL) served as a negative control.

For dihydroethidium (DHE)-based ROS detection, isolated crypts were incubated with DHE and DHE + 300 U/mL PEG-SOD for 30 min at 37°C in Hanks buffer containing 100 µmol/L diethylenetriaminepentaacetic acid pentasodium salt. For fluorescence detection, DHE and its oxidation products were separated by HPLC (Hitachi, Elite Lachrom system L3130 pump) using a C18 column (EC, Nucleosil, 100-5, 250/4.6 Macherey Nagel) and a mobile phase A of H_2O:acetonitrile:TFA (9:1:0.1) and phase B of acetonitrile + 0.1% TFA. A gradient from 0 to 40% of B was achieved within 10 min and to 100% B in 20 min with a 0.5 mL/min flow. The oxidation products of DHE (40 µmol/L), 2-dihydroxyethidium (2EOH), and ethidium (E), were separated by HPLC and analyzed either by fluorescence 510 nm/595 nm excitation/emission for 2EOH in intact cells of crypts isolated from small intestine from different mouse strains.

Analysis of mRNA Expression

Total mRNA from frozen homogenized tissue, isolated crypts, or cultured organoids were isolated with a RNA-Mini-kit (Bio&Sell, Feucht, Germany) according to the manufacturer's protocol. Random hexamer primers (Promega, Madison, WI, USA) and Superscript III Reverse Transcriptase (Invitrogen, Darmstadt, Germany) were used for cDNA synthesis. Semi-quantitative real-time PCR was performed with AriaMx qPCR cycler (Agilent Technologie, Santa Clara, CA, USA) using iQ™ SYBR® Green Supermix (BioRad, Hercules, CA, USA) with appropriate primers as listed below. Relative expression of target genes were normalized to eukaryotic translation elongation factor 2 or β-actin, analyzed by delta-delta-Ct method and represented as percentage of control samples.

	Forward 3′–5′	Reverse 3′–5′
h,m,r EEF2	GACATCACCAAGGGTGTGCAG	GCGGTCAGCACACTGGCATA
m β-actin	TGACAGGATGCAGAAGGAGA	GCTGGAAGGTGGACAGTGAG
m Duox2	TCTTCACCATGATGCGGTCC	GGAGTCCGGTTGATGAACGA
m Lgr5	CCTACTCGAAGACTTACCCAGT	GCATTGGGGTGAATGATAGCA
m Nox1	CCTCCTGACTGTGCCAAAGG	ATTTGAACAACAGCACTCACCAA
m NoxA1	AGATACGGGACTGGCACCG	CATCCTAGCCAGCGGCTCTC
m NoxO1	ACTTAAACGCCTGTGCCATC	CCCCAACACTGCCCTAAGTA
m p22phox	TGTGGTGAAGCTTTTCGGGC	GGATGGCTGCCAGCAGATAGAT
m p47phox	TCCCAACTACGCAGGTGAAC	CCTGGGTTATCTCCTCCCCA
m p67phox	CTATCTGGGCAAGCCTACGGTT	CACAAAGCCAAACAATACGCG

Protein and Western Blot Analysis

Samples were lysed using the following lysis buffer (pH 7.4, concentrations in mmol/L): Tris-HCl (50), NaCl (150), sodium pyrophosphate (10), sodium fluoride (20), nonidet P40 (1%), sodium deoxycholate (0.5%), proteinase inhibitor mix, phenylmethylsulfonyl fluoride (1), orthovanadate (2), and okadaic acid (0.00001). Then, they were cooked in Lämmli buffer and separated by SDS-PAGE followed by Western blotting. NoxO1 primary antibodies were made in our laboratory; LC3 antibody was obtained from MBL (#PM036); p62 antibody was obtained from Enzo (BML-PW9860-0100); and infrared-fluorescent-dye-conjugated secondary antibodies were obtained from Licor (Bad Homburg). Western blot analyses were performed with an infrared-based detection system (Odyssey, Licor, Bad Homburg, Germany).

Statistics

Unless otherwise indicated, data are given as mean ± standard error of mean. Calculations were performed with Prism 5.0. Individual statistics of unpaired samples was performed by *t*-test and if not normal distributed by the Mann–Whitney test. A *p*-value of <0.05 was considered significant. Unless otherwise indicated, *n* indicates the number of individual experiments or animals.

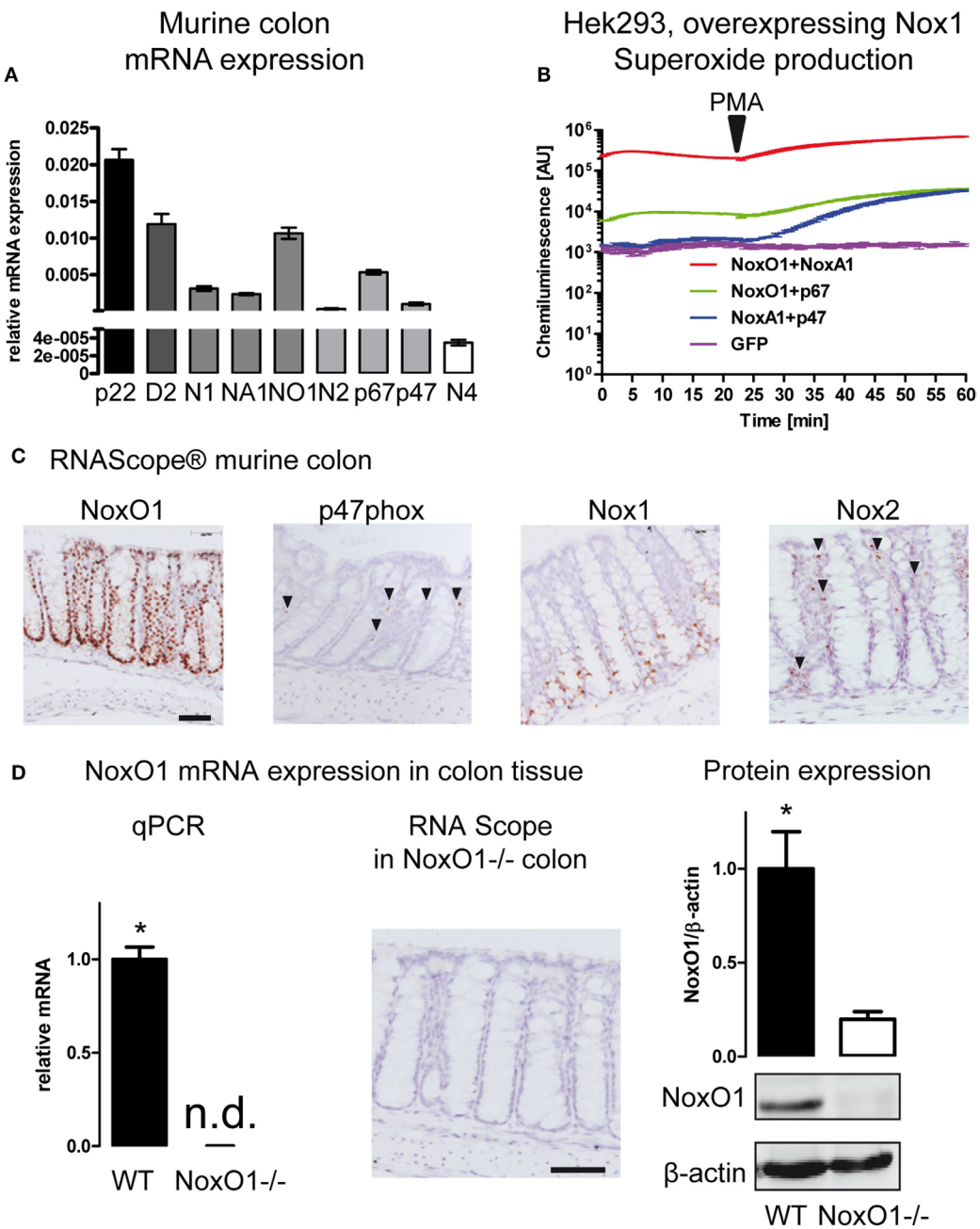

FIGURE 1 | NADPH oxidase expression in the colon. **(A)** Analysis of mRNA expression in murine colon tissue. Relative expression to housekeeping gene EF. Genes indicated are p22phox (p22), Duox2 (D2), Nox1 (N1), NoxA1 (NA1), NoxO1 (N01), Nox2 (N2) p67phox (p67), p47phox (p47), and Nox4 (N4). $n = 7–8$. **(B)** HEK293 cells overexpressing Nox1 were transfected with cytosolic subunits of the NADPH oxidase complex as indicated. Reactive oxygen species were measured with L012 (200 μmol/L). Activation of p47phox was triggered by phorbol myristate acetate (100 nmol/L). **(C)** *In situ* hybridization (RNAScope® DAB staining) showing the expression of NADPH oxidase subunits NoxO1, p47phox, Nox1, and Nox2 in murine colon tissue. Nuclei were counterstained with hematoxylin. Scale bars indicate 100 μm. **(D)** Quantitative RT-PCR, RNAScpoe®, and immunoblotting analysis of Nox1 protein expression and in colon tissue of wild-type (WT) and NoxO1 knockout (NoxO1$^{-/-}$), $n = 6$, $^*p < 0.05$ WT vs. NoxO1$^{-/-}$.

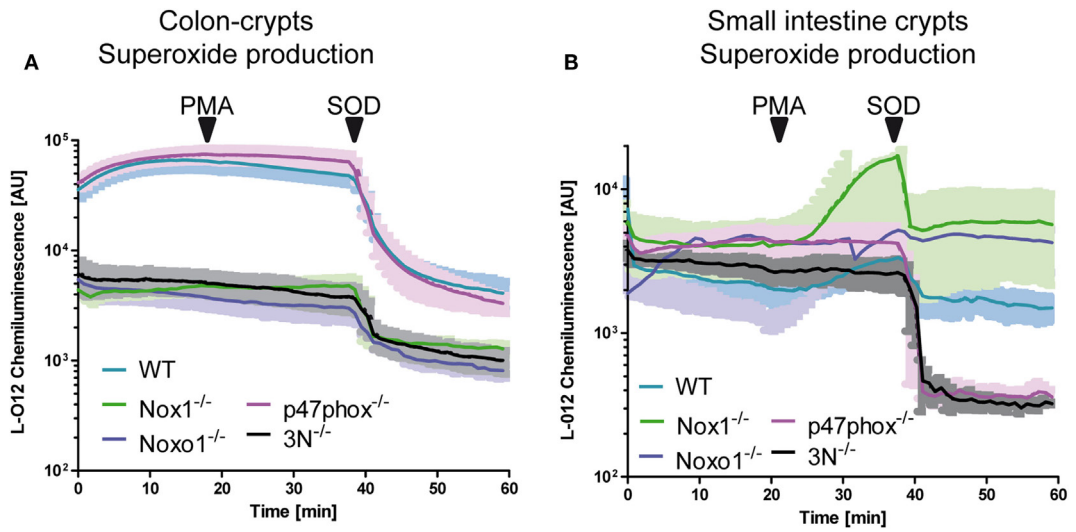

FIGURE 2 | NoxO1-dependent reactive oxygen species (ROS) formation in colon crypts. A + B Crypts from colon **(A)** or small intestine **(B)** were isolated. ROS were measured by chemiluminescence with L-012 (200 µmol/L). Activation of p47phox was triggered by phorbol myristate acetate (PMA, 100 nmol/L). Superoxide anions were decomposed with superoxide dismutase (SOD, 300 U/mL); $n = 4$.

RESULTS

NoxO1 Is Highly Expressed in the Colon Epithelium

The expression of members of the NADPH oxidase family in the colon was analyzed by qRT-PCR (**Figure 1A**; Figures S1 and S2 in Supplementary Material). The scaffolding component of the NADPH oxidase complex p22phox showed the highest expression level, followed by Duox2 and NoxO1, Nox1, and the activating subunit NoxA1. Furthermore, the activating subunits of Nox2, p47phox, and p67phox, which serve as organizer and activator of the Nox2 enzyme complex are expressed at relatively high levels in the colon. In an overexpression system, p47phox and p67phox can substitute NoxO1 and NoxA1 in the Nox1 complex and *vice versa*. In such a system, Nox1 together with NoxA1 and NoxO1 produced a large amount of $O_2^{\cdot-}$ in a constitutive manner, while the complex of Nox1 with NoxO1/p67phox produces constitutively lower levels of $O_2^{\cdot-}$. The combination of p47phox/NoxA1 under basal conditions does not change the level of $O_2^{\cdot-}$. Upon stimulation with PMA, p47phox is activated, and ROS formation increases to the level of the Nox1/p67phox/NoxO1 complex (**Figure 1B**). Overexpression of Nox1 or NoxO1 alone in CaCo cells revealed much lower $O_2^{\cdot-}$ formation than overexpression of all three components of the complex (Figure S2C in Supplementary Material). Importantly, when measuring mainly H_2O_2 with the aid of Amplex Red, overexpression of neither the single nor the combination of the plasmids revealed any difference in the formation of H_2O_2 (Figure S2D in Supplementary Material). Those results indicate that indeed, NoxO1, together with Nox1 and NoxA1, contributes to a constant $O_2^{\cdot-}$ formation in colon crypts. To explore a potential substitution of NoxO1 by p47phox in the colon, we analyzed the localization of the NADPH oxidase components in the colon (**Figure 1C**). For that purpose, *in situ* hybridization by RNAScope® was performed in colon Swiss rolls from WT animals. As shown for the vascular system (24), also in the colon p47phox does not occur in the same cells as NoxO1 and therefore may have totally distinct roles than NoxO1 in the colon. Rather than in epithelial cells, p47phox was located in capillaries, while the expression of NoxO1 was strongly restricted to epithelial cells. We confirmed that Nox1 mRNA expression is present in the lower two thirds of the colon crypts (25). Expression of NoxO1 in WT and NoxO1$^{-/-}$ colons was analyzed by qRT-PCR and RNAScope, while protein expression of NoxO1 was analyzed by Western blot (**Figure 1D**).

Knockout of NoxO1 Leads to Loss of Superoxide Production

Whether or not Nox1 and NoxO1 form a functional complex in colon crypts was analyzed *via* the measurement of ROS in isolated colon crypts (**Figure 2A**). To simultaneously analyze, if there is a functional substitution for the lack of NoxO1 by p47phox, we also used isolated crypts from p47phox$^{-/-}$ mice. ROS were analyzed using L-012 chemiluminescence and DHE, to concentrate more on the formation of $O_2^{\cdot-}$ than of H_2O_2, and crypts from mice with a knock out for Nox1, Nox2, and Nox4 (3N$^{-/-}$) were analyzed to learn what would be the basal level of NADPH oxidase-independent production of $O_2^{\cdot-}$. Knockout of Nox1 and NoxO1 drastically reduced the formation of $O_2^{\cdot-}$, while the deletion of p47phox had no effect on the formation of ROS in colon crypts. Importantly, triple knockout of Nox1, Nox2, and Nox4 reduced the $O_2^{\cdot-}$ formation to the level of Nox1 or NoxO1 knockout. Stimulation of the ROS formation with the p47phox activator PMA had no effect on ROS formation in colon crypts, but in crypts from the duodenum (**Figure 2B**). ROS formation in the duodenum crypts is 10× lower than in colon. Obviously, the basal duodenal ROS formation is Nox independent but SOD sensitive, as analyzed by a DHE-based measurement of $O_2^{\cdot-}$ (Figure S2B in Supplementary Material). This

is a reflection of the fact that NoxO1 expression is high in the colon and masks the low PMA-activated ROS formation by p47phox. In fact, the difference in ROS formation corresponds to the expression of NoxO1 (1 ± 0.1 in the duodenum vs. 9.1 ± 0.6 in the colon).

NoxO1 Affects Proliferation and Differentiation *In Vivo*

As pointed out already, ROS affect proliferation. So far, no protocol has been successfully established for a primary culture of colon epithelial cells. Therefore, to analyze the role of NoxO1 in proliferation and differentiation independent from pathogens or gut flora and food intake, 3D organoid cultures from colon crypts were established (**Figure 3A**). The number of organoids indicates the potential of the crypts to form organoids, while organoid diameters correspond to the proliferative capacity of the cells. Unexpectedly, no difference in both parameters was observed when comparing WT and NoxO1$^{-/-}$ organoids (**Figure 3B**). These puzzling data were clarified when comparing freshly isolated colon crypts and established colon organoids, which revealed a reduction of NoxO1 expression by 80%. In contrast, the stem cell marker Lgr5 was increased more than twofold (**Figure 3C**). This indicates, although stemness is maintained in the organoids, that NoxO1 expression is drastically reduced and therefore does not impact proliferation.

Having found that analysis of the influence of NoxO1 on proliferation *in vitro* was not possible, we went on to the analyses of *in vivo* samples by immunohistochemistry. Staining for the stem cell marker Lgr5 by *in situ* hybridization (**Figure 4A**) and analysis of its mRNA expression (**Figure 4B**) indicated no difference between the stem cell potential in crypts from WT and NoxO1 knockout mice. Staining for pH3, an indicator of active mitosis, indicated a higher proliferative activity in the absence of NoxO1 (**Figure 4C**). Importantly, no effect of NoxO1 knock out was found when we analyzed for autophagy (Figure S3 in Supplementary Material). Subsequently, the cells in the mucosa were phenotyped according to their marker expression (**Figure 4D**). Alpha-SMA-positive cells represent smooth muscle cells and were found below and between the crypts. Pan-cytokeratin is a marker for epithelial cells and was used for the definition of differentiated cells. The expected gradient of pan-cytokeratin was observed along the crypt axis, with an increase at the top of the crypt. While not significant, a trend indicated a reduced differentiation of the crypt cells in the absence of NoxO1. Ki67 is an established marker for proliferating cells. Although about 50% of all cells in the mucosa were pan-cytokeratin (Pan-CK) positive, these cells still may proliferate and therefore are Ki67/Pan-CK double positive. Both pan-CK/Ki67 double positive cells and total Ki67 staining were increased in colons from mice deficient in NoxO1 (**Figures 4C,D**). Interestingly, cells undergoing apoptosis and positive for cleaved caspase 3 were reduced in NoxO1-deficient colons. Together, the results suggest that the absence of NoxO1 results in a diminished differentiation, more proliferation, and less apoptosis in epithelial cells of colon crypts.

NoxO1 Has a Protective Role in DSS-Induced Colitis

The combination of less differentiation, less apoptosis, and more proliferation results in more S-phase cells, which are sensitive to DNA damage. This may increase the risk of neoplastic transformation and enhanced tumor incidence (2).

To analyze this possibility, mice were subjected to the DSS-induced colitis and DSS/AOM colon cancer model. RNAScope® analysis in colon samples upon DSS treatment verified that Nox1 and NoxO1 expression remains only in the epithelium, whereas Nox2 and p47phox were expressed in infiltrating immune cells (**Figure 5A**). To analyze disease severity, the inflammatory damage score was analyzed. Crypt damage, immune cell infiltration, and development of ulcers were more severe in NoxO1$^{-/-}$ mice

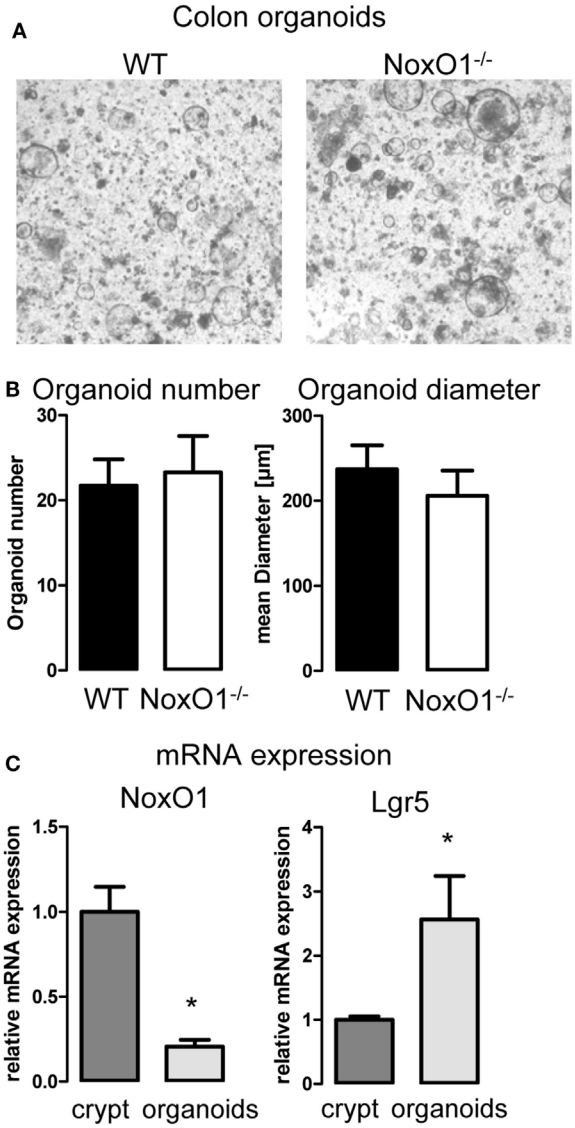

FIGURE 3 | Colon organoid growth. **(A)** 3D culture of organoids generated from colon crypts isolated from wild-type (WT) and NoxO1 knockout (NoxO1$^{-/-}$) animals. Representative pictures of organoids after 7 days in culture. **(B)** Analysis of organoid number and mean diameter of organoids cultured for 7 days. Organoids were counted per field of vision. Per animal two wells were analyzed. $n = 5$. **(C)** mRNA expression relative to housekeeping gene EF of NoxO1 and stem cell marker Lgr5 in freshly isolated crypts and organoids cultured for 7 days. $n = 3$, $^*p < 0.05$.

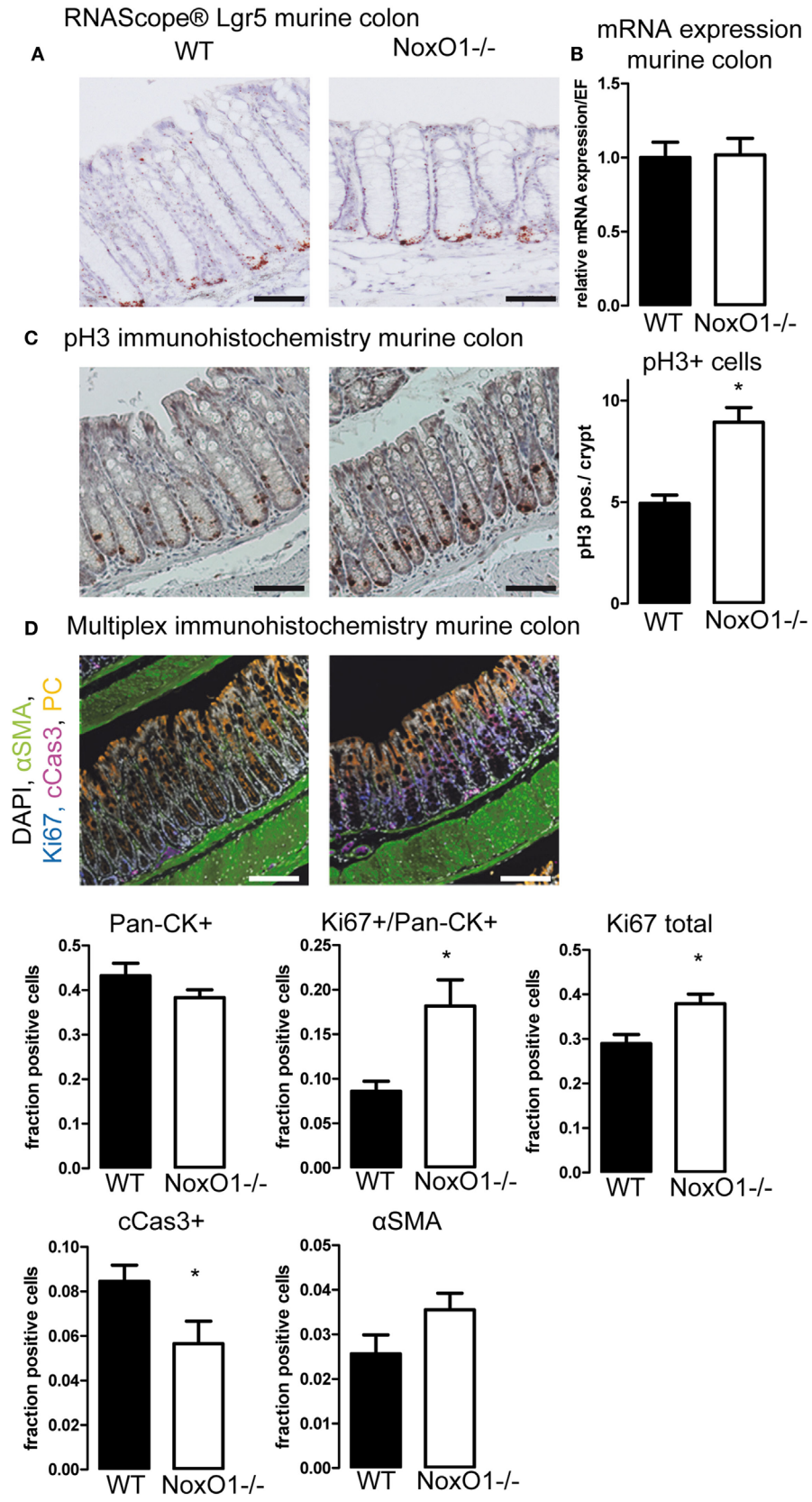

FIGURE 4 | Continued

FIGURE 4 | Immunohistochemistry of colons. **(A)** *In situ* hybridization (RNAScope®) of Lgr5 in murine colon. Nuclei were counterstained with hematoxylin, scale bars indicate 100 μm **(B)** Lgr5 mRNA expression relative to housekeeping gene EF in colon tissue from wild-type (WT) and NoxO1 knockout (NoxO1$^{-/-}$) mice. $n = 7$. **(C)** Immunohistochemistry staining of mitosis marker phospho-Histone 3 (pH3). Representative pictures and analysis of pH3-positive cells per crypt. $n = 3$, $^*p < 0.05$. Scale bars indicate 200 μm. **(D)** Multiplex immunohistochemistry of murine colon. Tissue was stained for DAPI (white), alpha-smooth muscle actin (aSMA, green), Ki67 (blue), cleaved Caspase 3 (cCas3, magenta), and pan-cytokeratin (Pan-CK, orange); scale bars indicate 100 μm. Positive cell fractions for indicated phenotypes in the mucosa were analyzed using the in Form 2.0 software. $n = 5$, $^*p < 0.05$.

(**Figure 5B**). This was also confirmed by immunohistochemical staining of macrophages by F4/80 (**Figure 5C**). Analysis of immune cell populations did further unmask a difference in the content of natural killer cells in DSS-treated mice (NK cells as percentage of all immune cells: 5.6 ± 1.2 WT ctl; 6.6 ± 0.6 NoxO1$^{-/-}$ ctl; 8.0 ± 0.7 WT DSS; 4.8 ± 0.8* NoxO1$^{-/-}$ DSS; $^*p < 0.05$ WT DSS vs. NoxO1$^{-/-}$ DSS). In contrast, in the tumor AOM/DSS model, less macrophages were found in NoxO1$^{-/-}$-deficient tumors, as analyzed by conventional immunohistochemistry (Figure S4A in Supplementary Material) and a costaining of F4/80 (Adgre1) and the Noxes on mRNA level (Figure S4B in Supplementary Material). Interestingly, macrophage infiltration into colon tumors after an initial increase appears to decrease after a while (26). This effect of a reduced content of F4/80-positive cells at day 70 can be seen in NoxO1$^{-/-}$ mice as well (Figure S4 in Supplementary Material). DSS/AOM treatment induced a loss of body weight, indicating the severity of the inflammation due to DSS. Weight loss was more severe in NoxO1$^{-/-}$ mice (**Figure 5D**). Eventually, although not significant, there was a trend for a higher tumor burden and mortality, in NoxO1-deficient animals when compared to their WT littermates (**Figure 5E**; Figures S4C,D in Supplementary Material).

DISCUSSION

The colon epithelium is constantly renewed and arises from only a few intestinal stem cells residing at the crypt base. From these amplifying cells, the epithelial cell layer derives that progressively differentiates until the top of the villi. This process is redox sensitive. Especially, Nox1-derived ROS may influence the balance of proliferation and differentiation in the gut epithelium. Nox1 upregulation enhances Wnt/β-catenin and Notch pathways and disrupts tumor progression by pro-apoptotic mechanisms. An excellent review on redox signaling in the gastrointestinal tract has been published by Pérez et al. (27).

While Nox1 indeed is the central molecule of the NADPH oxidase in the colon, the cytosolic subunits determine the signaling mediated by Nox1-derived ROS. Those cytosolic subunits are the activators p67phox or NoxA1 and the organizers p47phox and NoxO1. In an overexpressing system, the combination of NoxO1/p67phox and NoxO1/NoxA1 together with Nox1 enables a constitutive formation of superoxide, while the combination of Nox1 with NoxA1 and p47phox enables an acutely inducible ROS formation. This is due to the fact that NoxO1 is missing the autoinhibitory loop, which prevents the activity of p47phox. Upon serine phosphorylation, p47phox is activated and organizes the Nox1 complex. Therefore, p47phox-mediated ROS formation can be switched on and off (16). Consequently, p47phox may contribute to acute ROS-sensitive signaling, while NoxO1 serves as a mediator of constant redox-dependent signaling, such as differentiation, proliferation, or survival of a cell. In fact, NoxO1 and p47phox appear to have totally distinct functions and do not substitute for each other *in vivo* (24, 28). The current study indicates that the distinct expression site and the behavior of not subsidizing for each other are also true for the intestinal system. However, the role of NoxO1 in the gut was uncertain. In endothelial cells, NoxO1 is needed to maintain the activity of the Notch signaling pathway by enabling the activity of a disintegrin and metalloproteinases (ADAM) as measured in an ADAM10/17 activity assay. In contrast, this task was not fulfilled by p47phox (17). Notch also plays an extraordinary important role in the renewal of the colon epithelium, and ADAM10 is abundantly expressed throughout the gastrointestinal tract. During intestinal renewal homeostasis, ADAM10 regulates cellular processes such as cell fate specification and maintenance of intestinal stem cell/progenitor populations, controlling intestinal injury/regenerative responses and may drive intestinal inflammation and colon cancer initiation and progression (29). Therefore, a role of NoxO1 in all these processes is possible. In fact, proliferation was enhanced, while apoptosis was reduced in the absence of NoxO1 in murine colons. Those data perfectly fit an earlier study showing that Nox1 is required for reconstitution of the epithelium after colitis induction (10), indicating that NoxO1 together with Nox1 mediates ROS formation and facilitates proliferation of colon epithelial cells. Colitis as such, however, appears to be more severe in the absence of NoxO1. This could be a consequence of a reduced number of natural killer cells. Importantly, the activity of natural killer cells has been found to be significantly below normal levels in both remissive and active stages of inflammatory bowel disease patients (30). In fact, natural killer cells protect mice from DSS-induced colitis by regulating neutrophil function *via* the NKG2A receptor (31). Why less natural killer cells are present in DSS-treated NoxO1$^{-/-}$ mice is beyond the scope of this manuscript. One possibility is that NoxO1 is essential for the differentiation of those cells from their progenitors (24). Nevertheless, inflammatory bowel disease patients have a higher incidence of cancer (32). A similar effect was found in this study. The absence of NoxO1 increased the likelihood for tumor development and the number of tumors in the AOM/DSS colon cancer model. This is potentially a consequence of the increased DSS-induced inflammation in the absence of NoxO1, together with an enormous proliferation and reduction in apoptosis of epithelial cells. This combination is prone to support malignant transformation and the development of tumors (33).

In conclusion, NoxO1 contributes to a constitutive ROS formation in colon epithelial cells. NoxO1 cannot be substituted by p47phox. NoxO1 limits proliferation and increases the ability of epithelial cells to undergo apoptosis. Colitis, as induced by DSS, is more severe in the absence of NoxO1 in mice. Eventually, while

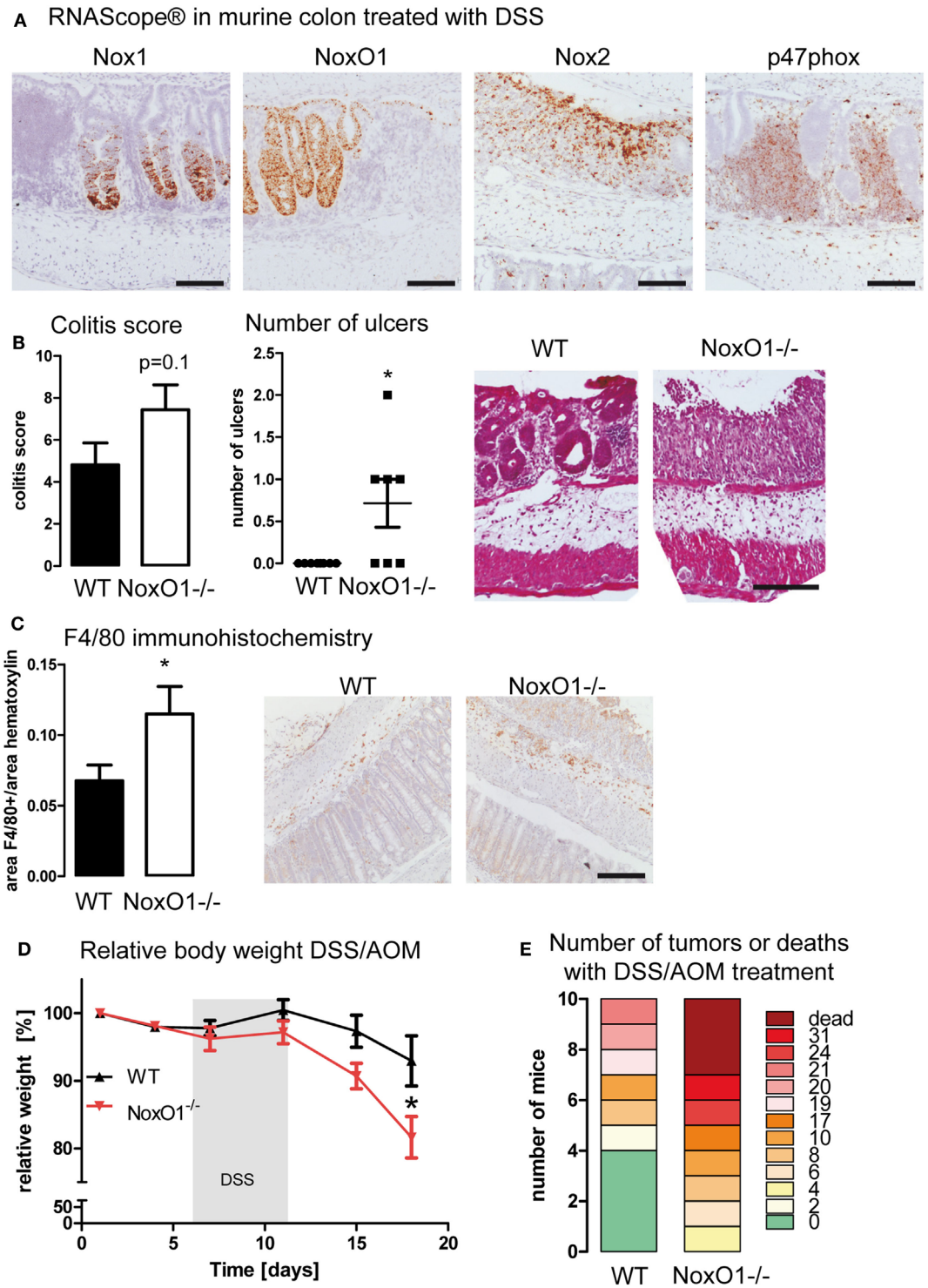

FIGURE 5 | NoxO1 has a protective role in dextran sulfate sodium (DSS)-induced colitis and DSS/azoxymethane (AOM) colon carcinoma. **(A)** *In situ* hybridization (RNAScope®) showing the expression of Nox1, NoxO1, Nox2, and p47phox in murine colon tissue upon treatment with DSS. Nuclei were counterstained with hematoxylin, scale bars indicate 100 μm. **(B)** Quantification of histological damage and number of ulcers on day 8 of the colitis model. $n = 7–8$, $^*p < 0,05$, Mann–Whitney exact test. Representative pictures of hematoxylin and eosin (H&E) staining for wild-type (WT) and NoxO1$^{-/-}$ are shown. Scale bar indicates 200 μm. **(C)** Immunohistochemistry staining of macrophage marker F4/80. Representative pictures and analysis of F4/80-positive staining per nuclei. $n = 7–8$, $^*p < 0.05$. Scale bars indicate 500 μm. **(D)** Body weight relative to day 0 of WT and NoxO1$^{-/-}$ mice treated with AOM at day 0 and 3 cycles of DSS in drinking water. $n = 9$, $^*p < 0.05$. **(E)** Tumor burden at day 70 of DSS/AOM-treated animals. $n = 8–10$.

deserving further studies, in an AOM/DSS murine colon cancer model NoxO1 appeared to be protective.

ETHICS STATEMENT

All animal experiments were approved by the local governmental authorities (approval number: FU1074, F28/46) and were performed in accordance with the animal protection guidelines.

AUTHOR CONTRIBUTIONS

All the authors performed experiments, collected or analyzed data, and helped with techniques. FM and KS wrote the manuscript.

FUNDING

This research was supported by the Else Kröner-Fresenius Foundation (EKFS), Research Training Group Translational Research Innovation – Pharma (TRIP) and by grants from the Deutsche Forschungsgemeinschaft (DFG) (to KS SCHR1241/1-1, SFB815/TP1, SFB834/TPA2).

SUPPLEMENTARY MATERIAL

The Supplementary Material for this article can be found online at https://www.frontiersin.org/articles/10.3389/fimmu.2018.00973/full#supplementary-material.

REFERENCES

1. Deschner EE. Cell turnover and colon tumor development. *Prev Med* (1987) 16(4):580–5. doi:10.1016/0091-7435(87)90075-2
2. Cliffe LJ, Humphreys NE, Lane TE, Potten CS, Booth C, Grencis RK. Accelerated intestinal epithelial cell turnover: a new mechanism of parasite expulsion. *Science* (2005) 308(5727):1463–5. doi:10.1126/science.1108661
3. Di Marco E, Gray SP, Kennedy K, Szyndralewiez C, Lyle AN, Lassègue B, et al. NOX4-derived reactive oxygen species limit fibrosis and inhibit proliferation of vascular smooth muscle cells in diabetic atherosclerosis. *Free Radic Biol Med* (2016) 97:556–67. doi:10.1016/j.freeradbiomed.2016.07.013
4. Goettsch C, Babelova A, Trummer O, Erben RG, Rauner M, Rammelt S, et al. NADPH oxidase 4 limits bone mass by promoting osteoclastogenesis. *J Clin Invest* (2013) 123(11):4731–8. doi:10.1172/JCI67603
5. Schröder K, Wandzioch K, Helmcke I, Brandes RP. Nox4 acts as a switch between differentiation and proliferation in preadipocytes. *Arterioscler Thromb Vasc Biol* (2009) 29(2):239–45. doi:10.1161/ATVBAHA.108.174219
6. Brandes RP, Weissmann N, Schröder K. Nox family NADPH oxidases: molecular mechanisms of activation. *Free Radic Biol Med* (2014) 76:208–26. doi:10.1016/j.freeradbiomed.2014.07.046
7. Rada B, Leto TL. Oxidative innate immune defenses by Nox/Duox family NADPH oxidases. *Contrib Microbiol* (2008) 15:164–87. doi:10.1159/000136357
8. Tréton X, Pedruzzi E, Guichard C, Ladeiro Y, Sedghi S, Vallée M, et al. Combined NADPH oxidase 1 and interleukin 10 deficiency induces chronic endoplasmic reticulum stress and causes ulcerative colitis-like disease in mice. *PLoS One* (2014) 9(7):e101669. doi:10.1371/journal.pone.0101669
9. Schwerd T, Bryant RV, Pandey S, Capitani M, Meran L, Cazier J-B, et al. NOX1 loss-of-function genetic variants in patients with inflammatory bowel disease. *Mucosal Immunol* (2017). doi:10.1038/mi.2017.74
10. Kato M, Marumo M, Nakayama J, Matsumoto M, Yabe-Nishimura C, Kamata T. The ROS-generating oxidase Nox1 is required for epithelial restitution following colitis. *Exp Anim* (2016) 65(3):197–205. doi:10.1538/expanim.15-0127
11. Hayes P, Dhillon S, O'Neill K, Thoeni C, Hui KY, Elkadri A, et al. Defects in NADPH oxidase genes NOX1 and DUOX2 in very early onset inflammatory bowel disease. *Cell Mol Gastroenterol Hepatol* (2015) 1(5):489–502. doi:10.1016/j.jcmgh.2015.06.005
12. Neish AS, Jones RM. Redox signaling mediates symbiosis between the gut microbiota and the intestine. *Gut Microbes* (2014) 5(2):250–3. doi:10.4161/gmic.27917
13. Kajla S, Mondol AS, Nagasawa A, Zhang Y, Kato M, Matsuno K, et al. A crucial role for Nox 1 in redox-dependent regulation of Wnt-β-catenin signaling. *FASEB J* (2012) 26(5):2049–59. doi:10.1096/fj.11-196360
14. Coant N, Ben Mkaddem S, Pedruzzi E, Guichard C, Tréton X, Ducroc R, et al. NADPH oxidase 1 modulates WNT and NOTCH1 signaling to control the fate of proliferative progenitor cells in the colon. *Mol Cell Biol* (2010) 30(11):2636–50. doi:10.1128/MCB.01194-09
15. El Hassani RA, Benfares N, Caillou B, Talbot M, Sabourin J-C, Belotte V, et al. Dual oxidase2 is expressed all along the digestive tract. *Am J Physiol Gastrointest Liver Physiol* (2005) 288(5):G933–42. doi:10.1152/ajpgi.00198.2004
16. Schröder K, Weissmann N, Brandes RP. Organizers and activators: cytosolic Nox proteins impacting on vascular function. *Free Radic Biol Med* (2017) 109:22–32. doi:10.1016/j.freeradbiomed.2017.03.017
17. Brandes RP, Harenkamp S, Schürmann C, Josipovic I, Rashid B, Rezende F, et al. The cytosolic NADPH oxidase subunit NoxO1 promotes an endothelial stalk cell phenotype. *Arterioscler Thromb Vasc Biol* (2016) 36(8):1558–65. doi:10.1161/ATVBAHA.116.307132
18. Joo JH, Oh H, Kim M, An EJ, Kim R-K, Lee S-Y, et al. NADPH oxidase 1 activity and ROS generation are regulated by Grb2/Cbl-mediated proteasomal degradation of NoxO1 in colon cancer cells. *Cancer Res* (2016) 76(4):855–65. doi:10.1158/0008-5472.CAN-15-1512
19. Gavazzi G, Deffert C, Trocme C, Schappi M, Herrmann FR, Krause K-H. NOX1 deficiency protects from aortic dissection in response to angiotensin II. *Hypertension* (2007) 50(1):189–96. doi:10.1161/HYPERTENSIONAHA.107.089706
20. Weichand B, Popp R, Dziumbla S, Mora J, Strack E, Elwakeel E, et al. S1PR1 on tumor-associated macrophages promotes lymphangiogenesis and metastasis via NLRP3/IL-1β. *J Exp Med* (2017) 214(9):2695–713. doi:10.1084/jem.20160392
21. Diamanti MA, Gupta J, Bennecke M, Oliveira T, de, Ramakrishnan M, Braczynski AK, et al. IKKα controls ATG16L1 degradation to prevent ER stress during inflammation. *J Exp Med* (2017) 214(2):423–37. doi:10.1084/jem.20161867
22. Mahe MM, Aihara E, Schumacher MA, Zavros Y, Montrose MH, Helmrath MA, et al. Establishment of gastrointestinal epithelial organoids. *Curr Protoc Mouse Biol* (2013) 3(4):217–40. doi:10.1002/9780470942390.mo130179
23. Rezende F, Löwe O, Helfinger V, Prior K-K, Walter M, Zukunft S, et al. Unchanged NADPH oxidase activity in Nox1-Nox2-Nox4 triple knockout mice: what do NADPH-stimulated chemiluminescence assays really detect? *Antioxid Redox Signal* (2016) 24(7):392–9. doi:10.1089/ars.2015.6314
24. Rezende F, Moll F, Walter M, Helfinger V, Hahner F, Janetzko P, et al. The NADPH organizers NoxO1 and p47phox are both mediators of diabetes-induced vascular dysfunction in mice. *Redox Biol* (2017) 15:12–21. doi:10.1016/j.redox.2017.11.014
25. Geiszt M, Lekstrom K, Brenner S, Hewitt SM, Dana R, Malech HL, et al. NAD(P)H Oxidase 1, a product of differentiated colon epithelial cells, can partially replace glycoprotein 91phox in the regulated production of superoxide by phagocytes. *J Immunol* (2003) 171(1):299–306. doi:10.4049/jimmunol.171.1.299
26. Shang K, Bai Y-P, Wang C, Wang Z, Gu H-Y, Du X, et al. Crucial involvement of tumor-associated neutrophils in the regulation of chronic colitis-associated carcinogenesis in mice. *PLoS One* (2012) 7(12):e51848. doi:10.1371/journal.pone.0051848
27. Pérez S, Taléns-Visconti R, Rius-Pérez S, Finamor I, Sastre J. Redox signaling in the gastrointestinal tract. *Free Radic Biol Med* (2017) 104:75–103. doi:10.1016/j.freeradbiomed.2016.12.048
28. Kiss PJ, Knisz J, Zhang Y, Baltrusaitis J, Sigmund CD, Thalmann R, et al. Inactivation of NADPH oxidase organizer 1 results in severe imbalance. *Curr Biol* (2006) 16(2):208–13. doi:10.1016/j.cub.2005.12.025
29. Dempsey PJ. Role of ADAM10 in intestinal crypt homeostasis and tumorigenesis. *Biochim Biophys Acta* (2017) 1864(11 Pt B):2228–39. doi:10.1016/j.bbamcr.2017.07.011

30. Yadav PK, Chen C, Liu Z. Potential role of NK cells in the pathogenesis of inflammatory bowel disease. *J Biomed Biotechnol* (2011) 2011:348530. doi:10.1155/2011/348530
31. Hall LJ, Murphy CT, Quinlan A, Hurley G, Shanahan F, Nally K, et al. Natural killer cells protect mice from DSS-induced colitis by regulating neutrophil function via the NKG2A receptor. *Mucosal Immunol* (2013) 6(5):1016–26. doi:10.1038/mi.2012.140
32. Jung YS, Han M, Park S, Kim WH, Cheon JH. Cancer risk in the early stages of inflammatory bowel disease in Korean patients: a nationwide population-based study. *J Crohns Colitis* (2017) 11(8):954–62. doi:10.1093/ecco-jcc/jjx040
33. Helfinger V, Gall FF, Henke N, Kunze MM, Schmid T, Heidler J, et al. Hydrogen peroxide formation by Nox4 limits malignant transformation. *bioRxiv* (2017) 177055. doi:10.1101/177055

Conflict of Interest Statement: The authors declare that the research was conducted in the absence of any commercial or financial relationships that could be construed as a potential conflict of interest.

The reviewer GC and handling Editor declared their shared affiliation.

frontiers in Immunology

ORIGINAL RESEARCH
published: 14 May 2018
doi: 10.3389/fimmu.2018.00701

Reactive Oxygen Species Deficiency Due to Ncf1-Mutation Leads to Development of Adenocarcinoma and Metabolomic and Lipidomic Remodeling in a New Mouse Model of Dextran Sulfate Sodium-Induced Colitis

Lina Carvalho[1], Joana R. M. Gomes[2†], Ludgero C. Tavares[2†], Ana R. Xavier[2†], Karel D. Klika[3], Rikard Holmdahl[4], Rui A. Carvalho[5,6‡] and M. Margarida Souto-Carneiro[2,6‡]*

[1]Faculty of Medicine, Institute of Anatomic Pathology, University of Coimbra, Coimbra, Portugal, [2]Center for Neuroscience and Cell Biology, University of Coimbra, Coimbra, Portugal, [3]Molecular Structure Analysis Department, Deutsches Krebsforschungszentrum (DKFZ), Heidelberg, Germany, [4]Department of Medical Biochemistry and Biophysics, Karolinska Instituite (KI), Stockholm, Sweden, [5]Department of Life Sciences, Faculty of Science and Technology, Center for Functional Ecology, University of Coimbra, Coimbra, Portugal, [6]Department of Rhematology, Medical Clinic 5, Universitätsklinikum Heidelberg, Heidelberg, Germany

Inflammatory bowel disease is characterized by chronic relapsing idiopathic inflammation of the gastrointestinal tract and persistent inflammation. Studies focusing on the immune-regulatory function of reactive oxygen species (ROS) are still largely missing. In this study, we analyzed an ROS-deficient mouse model leading to colon adenocarcinoma. Colitis was induced with dextran sulfate sodium (DSS) supplied *via* the drinking water in wild-type (WT) and Ncf1-mutant (Ncf1) B10.Q mice using two different protocols, one mimicking recovery after acute colitis and another simulating chronic colitis. Disease progression was monitored by evaluation of clinical parameters, histopathological analysis, and the blood serum metabolome using ^{1}H nuclear magnetic resonance spectroscopy. At each experimental time point, colons and spleens from some mice were removed for histopathological analysis and internal clinical parameters. Clinical scores for weight variation, stool consistency, colorectal bleeding, colon length, and spleen weight were significantly worse for Ncf1 than for WT mice. Ncf1 mice with only a 7-day exposure to DSS followed by a 14-day resting period developed colonic distal high-grade dysplasia in contrast to the low-grade dysplasia found in the colon of WT mice. After a 21-day resting period, there was still β-catenin-rich inflammatory infiltration in the Ncf1 mice together with high-grade dysplasia and invasive well-differentiated adenocarcinoma, while in the WT mice, high-grade dysplasia was prominent without malignant invasion and only low inflammation. Although exposure to DSS generated less severe histopathological changes in the WT group, the blood serum metabolome revealed an increased fatty acid content with moderate-to-strong correlations to inflammation score, weight variation, colon length, and spleen weight. Ncf1 mice also

OPEN ACCESS

Edited by:
Giovanna Schiavoni, Istituto Superiore di Sanità, Italy

Reviewed by:
Ildiko Szanto, Geneva University Hospitals (HUG), Switzerland
Eduardo Villablanca, Karolinska Institute (KI), Sweden

***Correspondence:**
M. Margarida Souto-Carneiro margarida.souto-carneiro@med.uni-heidelberg.de

†These authors have contributed equally to this work as second authors.

‡These authors have contributed equally to this work as senior authors.

Specialty section:
This article was submitted to Cancer Immunity and Immunotherapy, a section of the journal Frontiers in Immunology

Received: *01 November 2017*
Accepted: *21 March 2018*
Published: *14 May 2018*

Citation:
Carvalho L, Gomes JRM, Tavares LC, Xavier AR, Klika KD, Holmdahl R, Carvalho RA and Souto-Carneiro MM (2018) Reactive Oxygen Species Deficiency Due to Ncf1-Mutation Leads to Development of Adenocarcinoma and Metabolomic and Lipidomic Remodeling in a New Mouse Model of Dextran Sulfate Sodium-Induced Colitis. Front. Immunol. 9:701. doi: 10.3389/fimmu.2018.00701

displayed a similar pattern but with lower coefficients and showed consistently lower glucose and/or higher lactate levels which correlated with inflammation score, weight variation, and spleen weight. In our novel, DSS-induced colitis animal model, the lack of an oxidative burst ROS was sufficient to develop adenocarcinoma, and display altered blood plasma metabolic and lipid profiles. Thus, oxidative burst seems to be necessary to prevent evolution toward cancer and may confer a protective role in a ROS-mediated self-control mechanism.

Keywords: reactive oxygen species, dextran sulfate sodium, adenocarcinoma, colitis, metabolism, nicotinamide adenine dinucleotide phosphate oxidase, nuclear magnetic resonance, lipids

INTRODUCTION

Inflammatory bowel disease (IBD) is characterized by chronic relapsing idiopathic inflammation of the gastrointestinal tract. The two major known forms of IBD are Crohn's disease and ulcerative colitis (UC). Discontinuous transmural lesions may appear in any segment of the gastrointestinal tract in Crohn's disease whereas UC is restricted to lesions in the colon and rectum mucosae. These two separate conditions have distinct clinical, endoscopic, and histological profiles though they share some overlapping clinical features (1–7). In both cases, there are no definitive treatments and the active and remission cycles are managed with anti-inflammatory or immunomodulatory drugs and eventually surgery, compromising the patients quality of life (8). Perhaps one of the most pressing factors for routine monitoring is the heightened risk of cancer development in chronic inflammatory lesions, namely colorectal carcinoma and small bowel adenocarcinoma (9–11). Regarding colorectal carcinoma, two major forms are pathophysiologically distinguishable, sporadic colorectal cancer, and colitis-associated colorectal cancer. Although they share common pathogenic elements, their progression follows different molecular mechanisms (12, 13). Tumor-promoting inflammation and genomic predisposition and instability provide favorable ground for cancer onset while the deregulation of cellular bioenergetics and immune-evasion have recently been identified as emerging hallmarks (14). Even though the complexity of the thematic does not allow the pinpoint of a single root cause of the problem, evidence from research suggests a pivotal role for oxygen and reactive oxygen species (ROS) in carcinogenesis, particularly in promoting inflammation, causing oxidative DNA damage, altering signaling pathways and modulating metabolism and immune response (14, 15). Regular cellular function will generate ROS but the balance between pro- and antioxidants is a delicate one. This homeostatic regulation may be achieved through several scavenging processes, namely superoxide dismutase, glutathione and catalase, among others. Excessive oxidative stress may cause extensive damage and signal cell death either by necrosis or apoptosis, but on the other hand, homeostatic levels regulate many signal transduction pathways and promote cell proliferation and survival (16, 17). Additionally, ROS generation is of seminal importance for immune responses to pathogens, in particular, bacteria and fungi. In granulocytes and macrophages, phagocytic activity generates an oxidative burst from superoxide anion production by NADPH oxidase complex 2 (NOX2), which is then dismutated into peroxide and other reactive species toxic to bacteria (18). ROS function equally as immunological regulators, preventing chronic inflammation and autoimmunity (19).

Reactive oxygen species imbalances also contribute indirectly to the aerobic glycolysis that generally characterizes cancerous cells—the Warburg effect. Hypoxia and increased ROS levels inhibit prolyl hydroxylases, which lead to hypoxia-inducible transcription factor (HIF-1α) stabilization and subsequent gene expression thus triggering upregulation of glucose transporters and glycolytic enzymes essential to aerobic glycolysis (20). Other signaling pathways may play a role in modulating metabolism in cancer cells, such as activation of the c-Myc transcription factor or the oncogene *KRAS*, or the loss of function of the tumor suppressor gene *P53* (17). Cancerous cells may also exhibit adaptation to the heightened oxidative stress by upregulating ROS-scavenging enzymes, controlling excessive protein/DNA damage, and lipid peroxidation, thereby avoiding cell death (17).

A set of contributing factors are required to develop IBD, namely genetic predisposition, detrimental gut microbiota, defective mucosal barrier function, exacerbated immune response, and environmental triggers (6). Unresolved inflammation may develop dysplasia and eventually favor cancer onset (21). Interestingly, a rare inheritable disease, chronic granulomatous disease (CGD) characterized by defective NOX2, renders phagocytes unable to produce superoxide anion (22). In fact, CGD patients frequently have an associated IBD and exhibit Crohn-like symptoms (22, 23). Research on the link between IBD and cancer has been using several genetically engineered mice models prone to colorectal cancer whereby colitis is chemically induced by dextran sodium sulfate (DSS) supplied *via* the drinking water (24).

Abbreviations: DSS, dextran sulfate sodium; HE, hematoxylin/eosin; HIF, hypoxia-inducible factor; IBD, inflammatory bowel disease; Ncf1, Ncf1-mutant; NADPH, nicotinamide adenine dinucleotide phosphate; NOX, nicotinamide adenine dinucleotide phosphate oxidase; PCA, principal component analysis; PLS–DA, partial least squares–discriminant analysis; PPP, pentose phosphate pathway; NMR, nuclear magnetic resonance; ROS, reactive oxygen species; TIGAR, *TP53*-inducible glycolysis and apoptosis regulator; UC, ulcerative colitis; VIP, variable importance in projection; WT, wild-type; WHO, World Health Organization.

Studies focused on the immune-regulatory function of ROS and how their deficiency impacts metabolism and inflammation-mediated tumorigenesis, surprisingly, are still largely missing. B10.Q mice with a point mutation in the p47 NOX subunit [Ncf1-mutant (Ncf1)/p47^{phox}] lack ROS production leading to deficient T-cell tolerance induction, triggering autoimmunity with a type I interferon signature [reviewed in Ref. (19)]. The absence of ROS in these mice led to poor recovery from two cycles of acute DSS-induced colitis and was characterized by extensive nitric oxide-dependent mucosal inflammation and dysplasia (25). The oral administration of DSS to rodents induced colonic inflammation that was clinically and histologically similar to human UC (25). Like the human disease, DSS-induced chronic UC is complicated by the development of colorectal dysplasia and adenocarcinoma (26, 27). Therefore, in the present study, B10.Q/Ncf1 mice were used to develop a new model of inflammation-driven colon carcinoma by induction of colitis with DSS and address the putative role of ROS in tumor formation and systemic metabolic alterations.

MATERIALS AND METHODS

Animals

Male and female homozygous Ncf1 (BQ.*Ncf1$^{m1J/m1J}$*, abbreviated to Ncf1, $n = 30$) and wild-type (WT, $n = 30$) B10.Q mice between 6 and 8 weeks old were obtained from breeding heterozygous mice followed by genotyping as previously described (28). Animals were bred and maintained under standard conditions at the specific pathogen-free animal facility of the Faculty of Pharmacy, University of Coimbra with food and water supplied *ad libitum* within a controlled temperature environment, and alternating 12-h light/dark cycles. All animal studies were approved by the internal FFUC Animal Facility Ethics Committee and were in accordance with EU legislation for experimental animal welfare.

Induction of Colitis

Colitis was induced by oral administration of 3% w/v DSS (average mol. wt. 40,000 g/mol, AppliChem, Darmstadt, Germany) in the first induction period and 2.5% w/v DSS in the second induction period *via* drinking water supplied *ad libitum*. The DSS concentration was reduced for the second cycle to prevent premature death so that animals survived till the end of the experiment. DSS reduction also minimized weight loss and rectal bleeding, thus limiting excessive suffering.

Two different colitis-induction protocols were used: in protocol remission (r), mice were subjected to a 7-day DSS induction followed by 21 days of resting on normal water; in protocol induction (i), mice were subjected to 7 days of DSS induction, followed by 14 days of resting on normal water and then a second 7-day DSS-induction period.

Clinical Evaluation

Animals were monitored every third day for alterations in colitis-related clinical scores: weight variation, stool consistency, and colorectal bleeding. Pain was monitored on a daily basis through observation of animal activity for 5 min during the resting (light cycle) and active (dark cycle) periods. Blood and stool scorings were performed as previously described (25). In brief, blood scoring: 0- no blood; 1- visible blood; 2- rectal bleeding; stool consistency scoring: 0- normal; 1- soft but formed; 2- very soft; 3- diarrhea. Five mice from each group were sacrificed by cervical dislocation under anesthesia at three experimental time points: days 0 (baseline controls), 22 and 30. Tissues were collected for histopathological analysis (*vide infra*) and assessment of colon length and spleen weight.

Histopathological Evaluation of Colitis

Swiss rolls of the whole colon, rolled from the rectum to cecum, were formalin fixed and paraffin embedded. Sections were hematoxylin/eosin (HE) stained according to standard protocols.

Immunohistochemistry was performed on distal colon sections. In brief, endogenous peroxidase activity was quenched by 15 min incubation with 3% diluted hydrogen peroxide. Non-specific binding was blocked with Ultra V Block (Ultra Vision Kit; TP-125-UB; Lab Vision Corporation, Fremont, CA, USA). Incubation with the primary rabbit monoclonal antibody against β-catenin (clone D10A8, Cell Signaling Technology Europe, Frankfurt am Main, Germany) was followed by incubation with biotin-labeled secondary antibody (Ultra Vision Kit; TP-125-BN; Lab Vision Corporation, Fremont, CA, USA). Primary antibody binding was localized in tissues using peroxidase-conjugated streptavidin (Ultra Vision Kit; TP-125-HR; Lab Vision Corporation, Fremont, CA, USA) and 3,3-diaminobenzidine tetrahydrochloride (RE7190-K; Novocastra Laboratories Ltd., Newcastle, UK) was used as chromogen, according to manufacturer's instructions. Hematoxylin was used to counterstain the slides.

Inflammation was scored in proximal and distal segments halves regarding the number of inflammatory foci: 0- no inflammatory focus; 1- one inflammatory focus; 2- two inflammatory foci; 3- three or more inflammatory foci. Lymphocytes, plasma cells, and neutrophils infiltration were scored based on cell morphology, with approximate percentage validation of each subset within the total observed inflammatory cells in inflammatory foci, as previously described (25).

Epithelial morphology was scored based on the presence of tubular and villous patterns: tubular-glandular hyperplasia above the *muscularis mucosae* and villous formation of superficial villous projections. Dysplasia was scored in the same segments using a semi-quantitative scale according to the World Health Organization (WHO) 2010 guidelines for colon adenocarcinoma classification (26): 0- no dysplasia; 1- hyperchromatic nuclear pluristratification and *lamina propria* separated glands; 2- epithelial low-grade dysplasia (complex ramified glands with cell hyperplasia and pluristratified hyperchromatic nuclei); 3- epithelial high-grade dysplasia (beyond low-grade dysplasia, nuclear atypia, mitosis and reduced *lamina propria* area).

Nuclear Magnetic Resonance (NMR) Spectroscopic Analysis

Blood serum from mice was collected for metabolic profiling using ^{1}H NMR spectroscopy. Samples consisted of 70 µL of sera plus 70 µL of D_2O (99.9%) together with 35 µL of sodium fumarate (10 mM) and phosphate buffer dissolved in D_2O (99.9%)

for use as an internal reference. Samples (total volume 175 μL) were placed into 2.5 mm NMR tubes and spectra acquired using a 600 MHz Bruker NMR spectrometer equipped with an inverse configuration probe. For all samples, regular ^{1}H acquisition with presaturation (sw = 10 kHz, ns = 32, td = 60 k, aq = 3 s) and Carr–Purcell–Meiboom–Gill (CPMG) (28) (sw = 10 kHz, ns = 350, spin-echo time = 200 168 ms, td = 60 k, aq = 3 s) spectra were acquired. Spectra were processed with TopSpin using 0.2 Hz of line broadening and manual phasing while AMIX was used for metabolite assignment and multivariate statistics. For metabolomics integration, spectra were subjected to bucketing by AMIX from 0.5–9 ppm (excluding the solvent region) with the spectral area normalized to the sum of all points. All metabolomics data have been deposited to the EMBL-EBI MetaboLights database (DOI: 10.1093/nar/gks1004. PubMed PMID: 23109552) with the identifier MTBLS593.

Statistical Analysis

All data were tested for normal distribution with Levene's test. Since data did not follow a normal distribution, the non-parametric Kruskal–Wallis test followed by a non-parametric Mann–Whitney *U* test were used to compare values between groups and time points using GraphPrism 6.01 (GraphPad Software Inc., CA, USA).

Statistical differences between curves were determined using a two-sided hypothesis permutation test with 10,000 permutations (http://bioinf.wehi.edu.au/software/compareCurves/index.html) (29). Bivariate correlation studies (Spearman, two-sided) were performed using SPSS 17. Differences were considered significant for $p < 0.05$. For NMR metabolomics analysis, data were analyzed using MetaboAnalyst software performing interquartile range filtering, log transformation, and pareto scaling prior to principal component analysis (PCA) or partial least squares–discriminant analysis (PLS–DA) modeling (30).

RESULTS

Clinical Signs of DSS-Induced Colitis

Colitis induction with DSS led to a reduction in the colon length in both the WT and the Ncf1 mice resulting in a

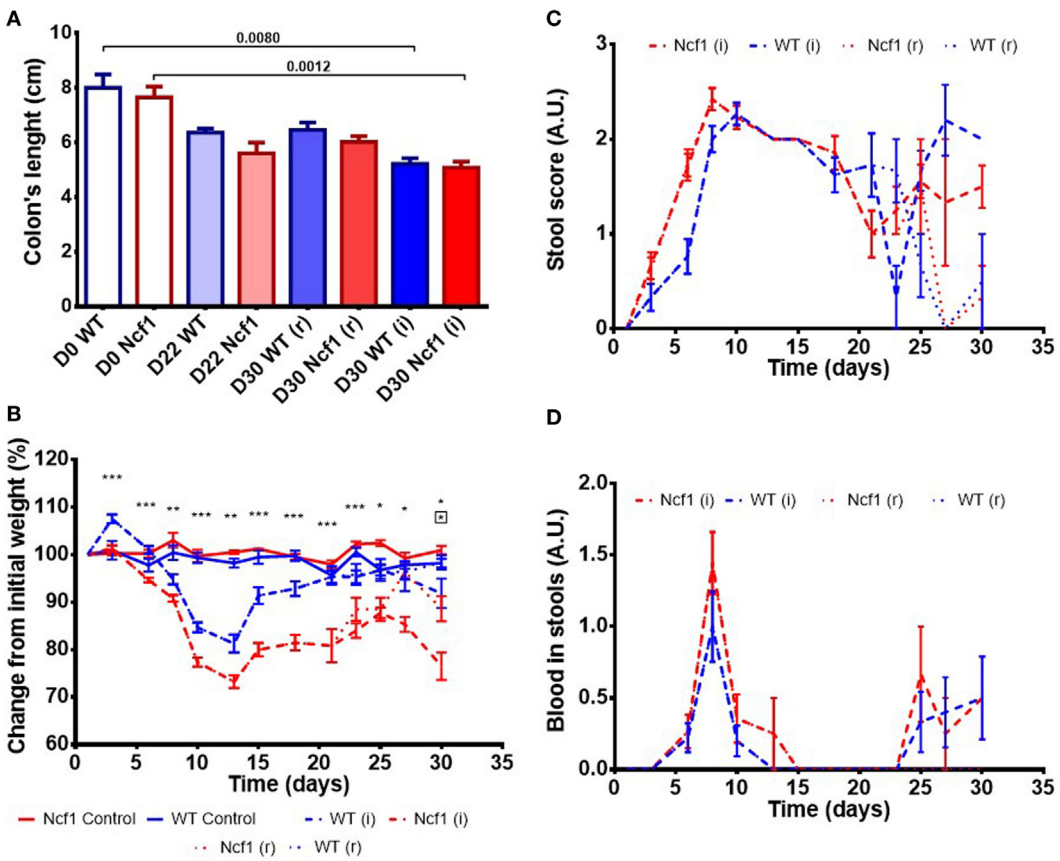

FIGURE 1 | Ncf1-mutant (Ncf1) mice presented more severe clinical scores than their wild-type (WT) counterparts. **(A)** Colon lengths in centimeters for days 0, 22, and 30 of control, recovery (r), and twice colitis-induced (i) WT and Ncf1 groups. **(B)** Change in body weights from the initial average baseline weight over the experimental period, average weight ± SE (baseline weights: WT = 29.8 ± 3.90 g, Ncf1 = 31.3 ± 3.9 g). Differences between groups and time points were calculated by two-way ANOVA. **(C)** Mice stool consistency score after colitis induction with dextran sulfate sodium (DSS). **(D)** Colorectal bleeding score after colitis induction. Weight, stool consistency, and colorectal bleeding scorings are detailed in Section "Materials and Methods.". Asterisks indicate significant differences: $^*p < 0.05$, $^{**}p < 0.001$, $^{***}p < 0.0001$ between WT and Ncf1 mice receiving DSS; boxed asterisks indicate significant differences: $^*p < 0.05$ between Ncf1 recovery (r) and induction (i) groups.

significant shortening of the colon after a second induction period (**Figure 1A**).

Body weight was monitored throughout the study (**Figure 1B**). At baseline, the weights of Ncf1 and WT mice were comparable (WT = 29.8 ± 3.90 g, Ncf1 = 31.3 ± 3.9 g). Weight loss began on day 3 after DSS colitis induction with all DSS-treated animals reaching the minimum weight on day 13 (i.e., during the recovery period) and with Ncf1 mice presenting a greater weight loss than WT mice. In protocol (r), the WT mice recovered their baseline weight while Ncf1 only recovered, at most, up to 90% of their original weight. The mice which were subjected to a second cycle of DSS-induced colitis [protocol (i)], partially recovered their weight until day 25 when a new phase of weight loss set in. Ncf1 mice suffered greater weight loss (reduction to 75% of baseline weight) than the WT mice (reduction to only 90% of baseline weight). While WT mice on both protocols had comparable weights until the end of the experimental period, Ncf1 mice under the (i) protocol had a greater weight loss than those under the (r) protocol.

The presence of colorectal blood and the consistency of the feces are two further clinical signs of DSS-induced colitis. During the first induction period, both Ncf1 and WT groups had decreased stool consistency and increased anal bleeding. During the resting period, both groups started to recover with respect to these two clinical parameters. WT and Ncf1 mice submitted to protocol (i) both presented a new surge in anal bleeding together with softer stools, these clinical symptoms were significantly different to those animals undergoing protocol (r) (**Figures 1C,D**).

Histopathologic Assessment of DSS-Induced Colitis

To evaluate epithelial morphology, inflammation, and dysplasia, the defined colon histopathology scores were applied using untreated WT and Ncf1 animals as controls and registered after colitis induction at day 22 for both experiments and day 30 for protocol r and protocol i.

At baseline, WT mice had well defined glands above *muscularis mucosae*, whereas Ncf1 mice presented a reduced number of glandular tubules (**Figure 2** D0), both with the absence of dysplasia and inflammation.

On day 22, WT mice maintained preserved epithelial morphology and superficial villous projections with low-grade distal dysplasia (1.4 ± 0.2) and low-distal inflammation (1.8 ± 0.4). The Ncf1 group also presented villous projections, but these were formed by compacted glands with less interstitial vascularization in addition to glandular higher grade dysplasia (2.0 ± 0.3, $p = 0.5$) and foci of well-differentiated adenocarcinoma accompanied by higher distal inflammation (3.0 ± 0.0, $p = 0.039$) (**Figure 2** D22; **Figure 3**). Even though Ncf1 inflammatory score was higher than the WT, the cellular composition of the inflammatory infiltrates

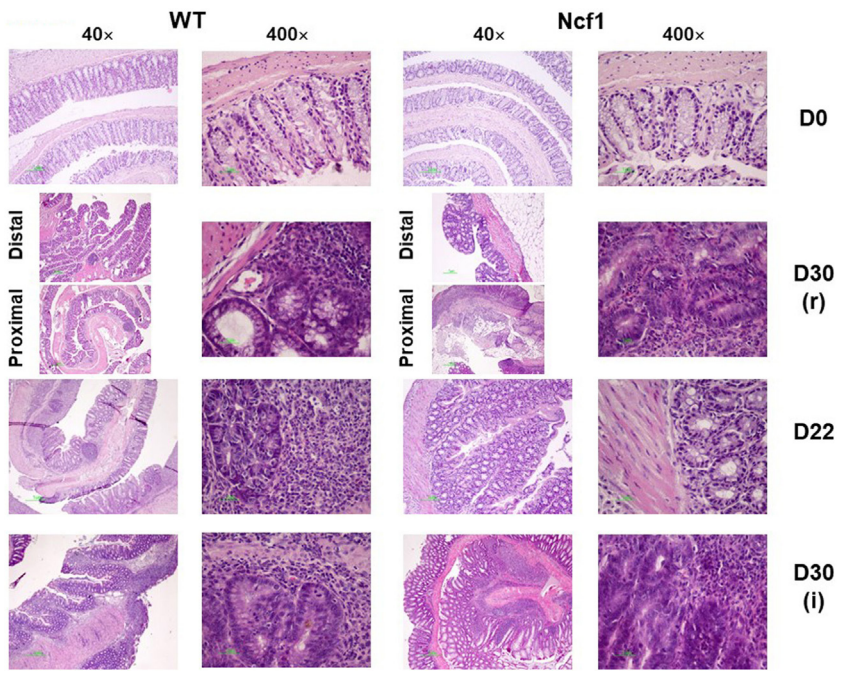

FIGURE 2 | Colonic mucosa of control, recovery (r), and twice colitis-induced (i) wild-type (WT) and Ncf1-mutant (Ncf1) groups. *Day 0*: glands are smaller, fewer, and with small epithelial cell nuclei in Ncf1 mice colon compared with WT mice. *Day 30 of recovery*: WT mouse colon with basal small gland hyperplasia and villous epithelial adaptation; Ncf1 mouse colon with superficial villous adaptation, high-grade dysplasia, and intramucosal adenocarcinoma. *Day 22 for both experiments*: both WT and Ncf1 mice colons with superficial villous glandular hyperplasia, and inflammation-reactive atypia in WT mouse colon; low-grade dysplasia; and mucinous cells hyperplasia in tubular glands of WT mouse colon contrasting to basal high-grade dysplasia in Ncf1 mouse colon. *Day 30 of the second colitis induction*: Superficial villous mucosae and basal cell glandular persistence with high-grade dysplasia in WT mouse colon compared with the superficial villous atrophy and well-differentiated adenocarcinoma in Ncf1 mouse colon. hematoxylin/eosin staining with 40× and 400× magnifications.

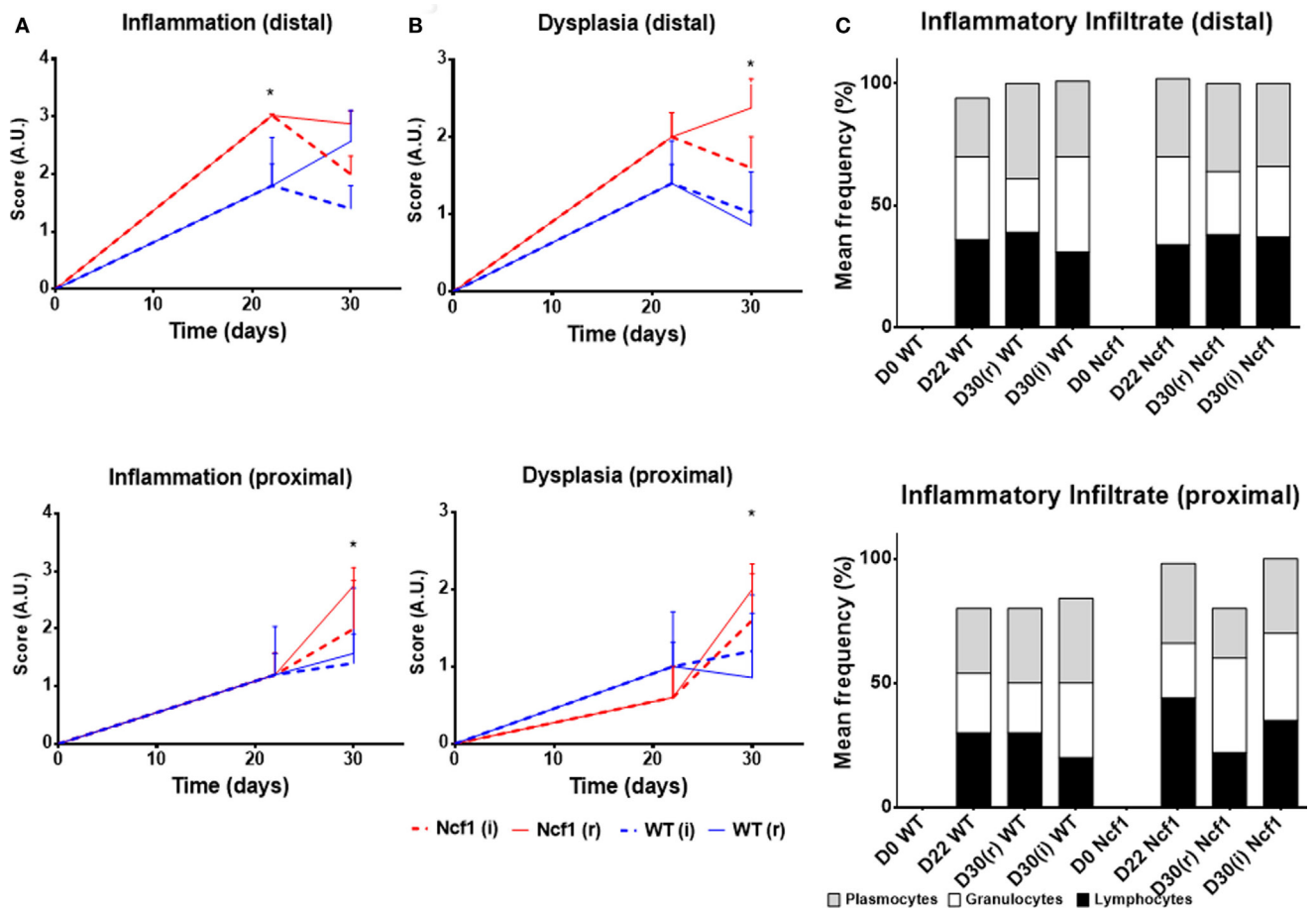

FIGURE 3 | Histological evaluation of inflammation **(A)**, dysplasia **(B)**, and cellular composition of the inflammatory infiltrate **(C)** at distal and proximal segments of the colon for Ncf1-mutant (Ncf1)* mice, and WT mice. Asterisks indicate $p < 0.05$, Mann–Whitney *U* test between Ncf1(r) and WT (r) and Ncf1(i) and WT(i). Inflammation and dysplasia scoring systems are detailed in Section "Materials and Methods."

had similar frequencies of grnaulocytes, lymphocytes, and plasmacytes in both groups. Proximal inflammation and dysplasia were low in both groups.

On day 30 for protocol r [**Figure 2** D30(r); **Figures 3** and **4** D30(r)], WT mice maintained villous projections corresponding to half of the *mucosae* length, supported by tubular-glandular hyperplasia above the *muscularis mucosae*, with different sizes and segments of very small glands with low-grade dysplasia foci. Scattered lymphocytes in small inflammatory infiltrates expressed β-catenin. In Ncf1 mice colons, there were a reduced number of glands under villous projections in the colon, although the morphology was similar to day 22. In general, Ncf1 mice had more high-grade dysplasia (with anisocariosis with persistent nucleoli and visible mitosis) and foci of well-differentiated adenocarcinoma with large inflammatory infiltrates rich in β-catenin-expressing lymphocytes (total mean scores for dysplasia WT = 2.20 ± 0.49, Ncf1 = 3.20 ± 0.74, $p = 0.42$; total mean scores for inflammation WT = 2.80 ± 0.66, Ncf1 = 4.00 ± 0.95, $p = 0.31$).

On day 30 for protocol i [**Figure 2**, Day 30(i); **Figures 3** and **4** D30(i)], a persistent adaptation of the colonic sections was observed. WT colon presented superficial epithelial villous projections without extensive inflammation. In distal segments, high-grade dysplasia persisted in both groups. Ncf1 proximal and distal colonic segments maintained a glandular morphology with hyperchromatic nuclei and mucosa-associated lymphoid tissue hyperplasia. Additionally, Ncf1 colon developed invasive well-differentiated adenocarcinoma in segments where narrower, reserve microglands were visible above the *mucularis mucosae*, invading till the *muscularis propria*, accompanied by extensive inflammatory infiltrates harboring lymphocytes expressing high levels of β-catenin (mean scores for total dysplasia WT = 1.71 ± 0.52, Ncf1 = 4.38 ± 0.26, $p = 0.001$; mean scores for total inflammation WT = 4.14 ± 0.51, Ncf1 = 5.25 ± 0.31, $p = 0.03$).

Considering the dysplasia score in WT vs Ncf1 mice, we found a very strong positive correlation between dysplasia score and inflammation score ($r_s = 0.835$) in Ncf1 mice, while this correlation was only moderate for the WT mice ($r_s = 0.591$) (**Table 1**). Moderate-to-strong positive correlations could be observed for the infiltrating leukocytes in both groups (**Table 1**). The dysplasia score is also negatively correlated with the colon length in both groups, consistent with the previous results in **Figure 1A**.

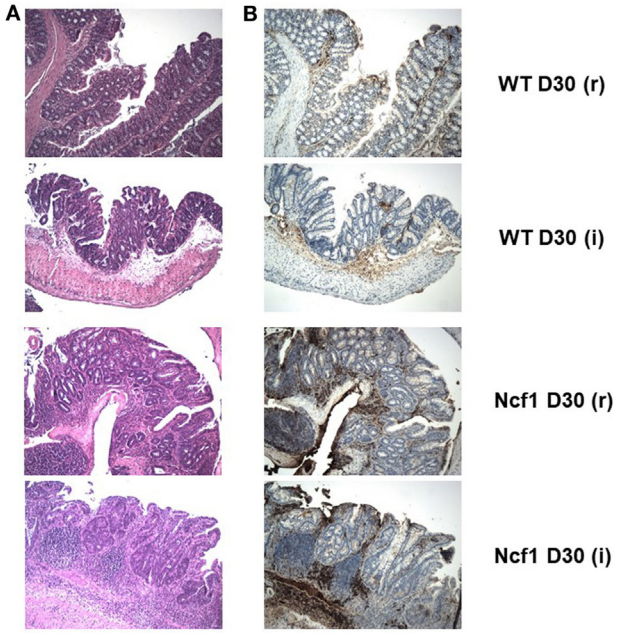

FIGURE 4 | The extensive inflammatory infiltrates present in the recovery (r) and twice colitis-induced (i) Ncf1-mutant (Ncf1) mouse colons harbor lymphocytes expressing high levels of β-catenin. In wild-type (WT) mice, some inflammatory foci contain scattered β-catenin-expressing lymphocytes. **(A)** Hematoxylin/eosin staining of representative colon sections of each protocol at D30 with 100× magnification; and the corresponding **(B)** β-catenin staining (brown) with 100× magnification. The colon sections are from the same samples as **Figure 2**, thus corresponding to the description of the histological features in that legend.

TABLE 1 | Spearman correlations and *p*-values for dysplasia score vs inflammation score, frequency of leukocytes infiltrating the colon mucosa and colon length.

Spearman correlations		Dysplasia score		
		All groups (*n* = 45)	**Ncf1 (*n* = 22)**	**WT (*n* = 23)**
Inflammation score	Correlation coefficient	0.838**	0.835**	0.591**
	Sig. (two-tailed)	0.000	0.000	0.003
Lymphocytes (%)	Correlation coefficient	0.527**	0.489*	0.556**
	Sig. (two-tailed)	0.000	0.021	0.006
Granulocytes (%)	Correlation coefficient	0.676**	0.745**	0.595**
	Sig. (two-tailed)	0.000	0.000	0.003
Plasmocytes (%)	Correlation coefficient	0.446**	0.460*	0.473*
	Sig. (two-tailed)	0.002	0.031	0.023
Colon length	Correlation coefficient	−0.574**	−0.507*	−0.452*
	Sig. (two-tailed)	0.000	0.016	0.035

*The table summarizes the significant correlations considering all groups together and Ncf1-mutant (Ncf1) vs wild-type (WT) groups. Significant correlations are indicated by asterisks: *p < 0.05; **p < 0.01.*

Metabolic Profile of Blood Serum of DSS-Induced Colitis Mice

Blood serum samples were analyzed using two types of ^{1}H NMR experiments, the basic ^{1}H spectrum (single pulse-acquire), and the CPMG pulse sequence. The basic ^{1}H spectrum exhibits all of the signals from both small metabolites and macromolecules resulting in an uneven baseline and the overlap of various signals from different compounds. The CPMG pulse sequence, on the other hand, suppresses the broad signals from macromolecules, namely lipids and proteins, resulting in clear peaks and a very well-defined baseline, thereby allowing better characterization and assignment of the signals arising from the small metabolites (**Figure 5**). A number of metabolites were able to be identified and quantified: (1) isoleucine, (2) leucine, (3) valine, (4) β-hydroxybutyrate, (5) lactate, (6) threonine, (7) alanine, (8) acetate, (9) proline, (10) glutamate, (11) glutamine, (12) methionine, (13) malate, (14) creatine, (15) choline, (16) phosphorylcholine/glycerophosphocholine, (17) taurine, (18) glycine, (19) serine, (20) water, (21) α-glucose, and (22) fumarate. Due to the breadth of the lipid signals, lipid signals were assessed and designated by moieties only: (L1) lipid methyls, (L2) lipid aliphatic chain, (L3) lipid β-methylenes, (L4) lipid allylic methylenes, (L5) lipid α-methylenes, (L6) lipid polyunsaturated allylic methylenes, and (L7) lipid alkenes (31). **Figure 6A** depicts the scores plot for the comparison of the CPMG spectra between control groups. Each sample is plotted according to the scores for PC1 and PC2, values that are calculated through the loadings plot (**Figure 6B**) where each dot represents a data point (a spectral bucket). Although the CPMG and the basic ^{1}H (**Figures 6C,D**) provide slightly different information, the score plots are similar and WT and Ncf1 groups still overlap. However, considering the WT and Ncf1 separately, on the basis of the PCA for the Ncf1 mice, the control group is separable from the DSS-induced groups with the recovery group brought closer to the control group (**Figures 7B,D**). This contrasts with WT mice which present overlapping metabolomics profiles between control, recovery, and second colitis-induced groups (**Figures 7A,C**). Given these differences, a plot of all DSS-induced groups was prepared to see if the metabolic profile is different between WT and Ncf1 mice. The unsupervised PCA (**Figures 8A,B**) still shows some group overlap, but for this data set we were able to calculate a valid PLS–DA model ($r^2 = 0.70$, $q^2 = 0.43$) (**Figures 8C,D**). While the recovery groups drifted toward a common metabolic profile, the Ncf1 and WT groups after the second DSS-induction colitis are distinct from each other with lower blood glucose [variable importance in projection (VIPs) at 3.23, 3.37, 3.41, 3.52, and 5.22] and higher lactate levels (VIPs at 1.31, 4.10, and 4.15) on the Ncf1 group.

Correlation Between Blood Serum Metabolites and Clinical Parameters

The metabolites assigned by NMR were quantified from both ^{1}H and CPMG spectra and were correlated with clinical parameters. Due to the broad signals of the lipids in the ^{1}H spectra, lipid signals were assessed and designated by moieties relative to the lipid methyl group (L1). Regarding the dysplasia score and the metabolome, we could only find weak-to-moderate correlations in pooled samples (**Table 2**). Analyzing in more detail, these correlations are only statistically significant for isoleucine, lactate, and proline in the Ncf1 group.

As regards the inflammation score, the pooled data set only presents weak-to-moderate correlations (**Table 3**). However, the

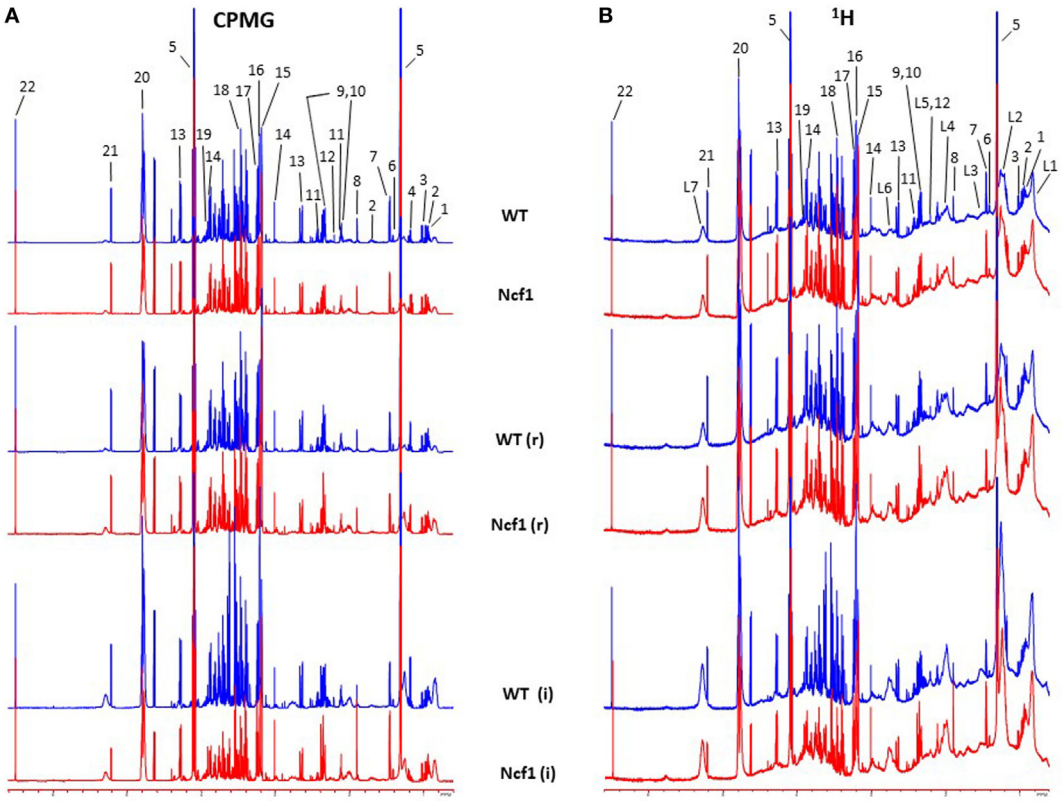

FIGURE 5 | Representative Carr–Purcell–Meiboom–Gill (CPMG) **(A)** and ^{1}H **(B)** nuclear magnetic resonance spectra of blood sera from wild-type (WT) and Ncf1-mutant (Ncf1) mice at baseline, after recovery of the first period of dextran sulfate sodium (DSS)-induced colitis (r) and after the second period of DSS-induced colitis (i). The CPMG pulse sequence suppresses the broad signals from macromolecules allowing a better characterization of the signals arising from the small metabolites. Signal assignments: (1) isoleucine, (2) leucine, (3) valine, (4) β-hydroxybutyrate, (5) lactate, (6) threonine, (7) alanine, (8) acetate, (9) proline, (10) glutamate, (11) glutamine, (12) methionine, (13) malate, (14) creatine, (15) choline, (16) phosphorylcholine/glycerophosphocholine, (17) taurine, (18) glycine, (19) serine, (20) water, (21) α-glucose, (22) fumarate, (L1) lipid methyls, (L2) lipid aliphatic chain, (L3) lipid β-methylenes, (L4) lipid allylic methylenes, (L5) lipid α-methylenes, (L6) lipid polyunsaturated allylic methylenes, and (L7) lipid alkenes.

inflammation score seems to have a more profound effect on the WT mice blood serum metabolome, with seven moderate-to-strong statistically significant correlations: positive for L2/L1, L6/L1, and L7/L1 and negative for L3/L1, valine, acetate, and choline while the Ncf1 mice blood serum metabolome only depicts a moderate negative correlation with glucose.

Weight variation [defined as the percentage of weight loss (negative) or gain (positive) over the course of the experiment relative to the baseline] was only weakly to moderately correlated in the pooled group but when separated into WT and Ncf1 groups, significant correlations arise, mostly for the Ncf1 group (**Table 4**). With the exception of glucose which is positively correlated with weight gain, all other significant correlations are negative, namely L4/L1, L6/L1, L7/L1, leucine, lactate, creatine, and proline.

Colon length was diminished in the treated groups (**Figure 1A**) and this marker shows stronger correlations with blood serum metabolites for the WT group (positive for L3/L1, valine, and acetate and negative for L2/L1, L6/L1, L7/L1, and GPC/Cho) than for the Ncf1 group (negative for leucine and isoleucine) (**Table 5**).

For spleen weight, several weak-to-moderate correlations are present in the pooled data set (**Table 6**). When analyzing groups by genotype, the WT group shows strong positive correlations for the lipid moieties L2/L1, L3/L1, L6/L1, and L7/L1 and negative moderate correlations for valine, acetate, and choline. Conversely, spleen weight for the Ncf1 group only achieves moderate correlations, positive for L2/L1 and L7/L1 and negative for glucose, glutamine, phosphocholine, and glycine.

DISCUSSION

Models based on DSS-induced colitis are commonly used to experimentally address inflammation-associated carcinogenesis in different mouse strains (27, 32). Several studies report either a carcinogenic path dependent on longer periods or multiple cycles of DSS induction or use carcinogenic compounds to reduce the exposure periods (33–36). This contrasts with our model which develops adenocarcinoma with only two induction cycles, thereby allowing us to understand the peculiarities of epithelial morphology alterations and how they depend on ROS production. Furthermore, our model challenges the paradigm that ROS are promoters of inflammation-dependent carcinogenesis, thus allowing the possibility of studying how ROS deficiency impacts on systemic metabolomic and lipid remodeling. We show that Ncf1 mice lacking ROS production developed colonic distal

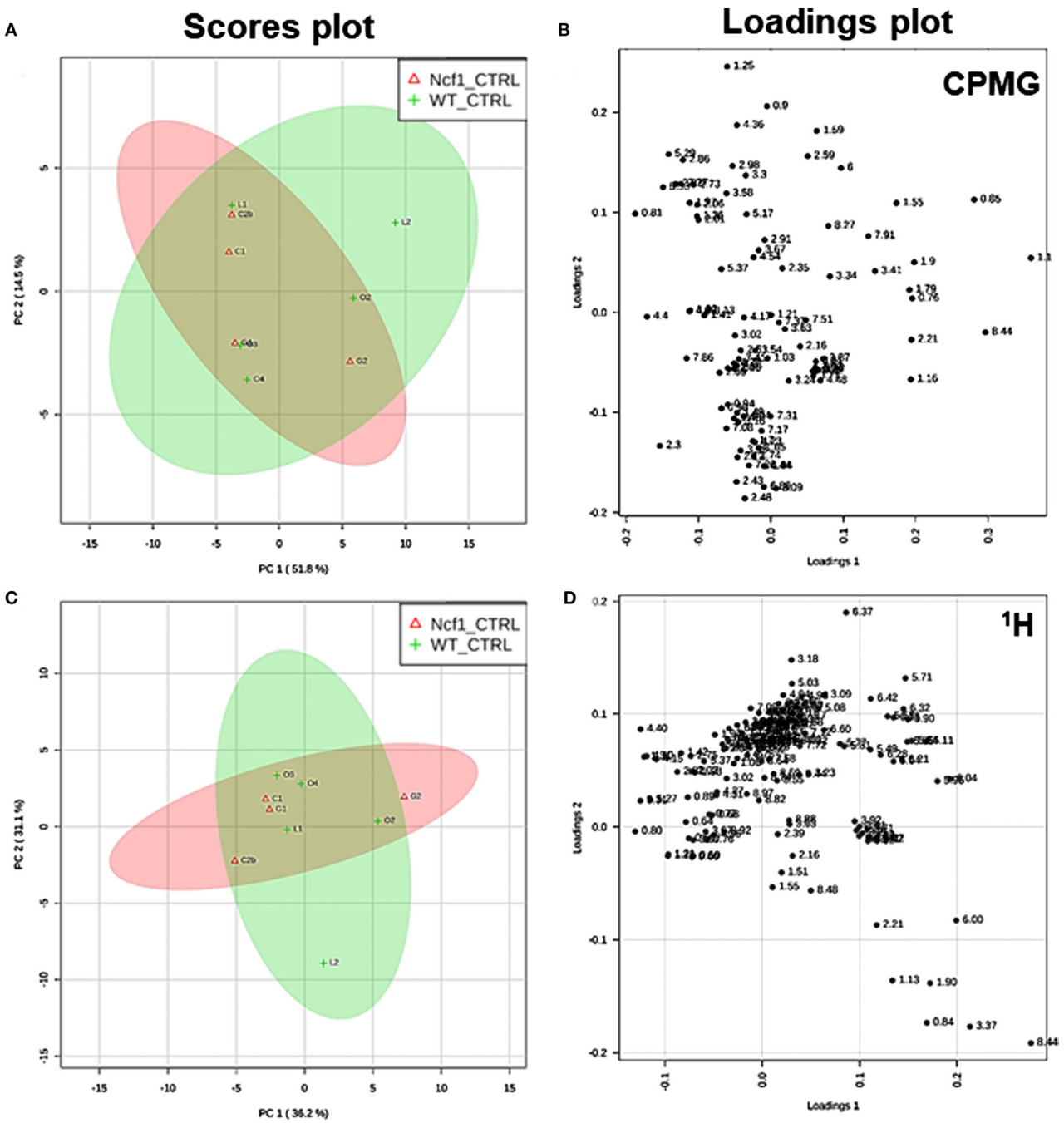

FIGURE 6 | Control wild-type (WT) and Ncf1-mutant (Ncf1) mice display similar metabolomic profiles showing no difference in small molecule metabolites and lipid and macromolecular fractions. The scores plot **(A)** accounts for 66.3% of the total variance (PC1 = 51.8%, PC2 = 14.5%) and the loadings plot **(B)** shows the δ of each variable (bucket) for the principal component analysis (PCA) analysis of Carr–Purcell–Meiboom–Gill (CPMG) spectra of Ncf1 and WT control groups. The CPMG pulse sequence suppresses the broad signals from macromolecules allowing analyze small molecule metabolites. The scores plot **(C)** summarizes 67.3% of the total variance (PC1 = 36.2%, PC2 = 31.1%) and the loadings plot **(D)** shows the δ of each variable (bucket) of the PCA analysis of ^{1}H spectra of Ncf1 vs WT control groups. The ^{1}H spectra allow analysis of the aqueous lipid fraction and other macromolecules.

high-grade dysplasia after a single 7-day exposure to 3% DSS in drinking water followed by a 14-day resting period, in contrast to the low-grade dysplasia in the colon of ROS-competent WT mice. Furthermore, after a 21-day resting period we observed lower inflammatory reparation and high-grade dysplasia and invasive well-differentiated adenocarcinoma in the Ncf1 mice while in the WT mice, dysplasia was also prominent without malignant invasion. The presence of adenocarcinoma has severely compromised.

In human colon cancer, the inactivation of the adenomatous polyposis coli (APC) gene is present in the large majority of patients, with concomitant stabilization and accumulation of β-catenin especially in the epithelium [reviewed in Ref. (37)].

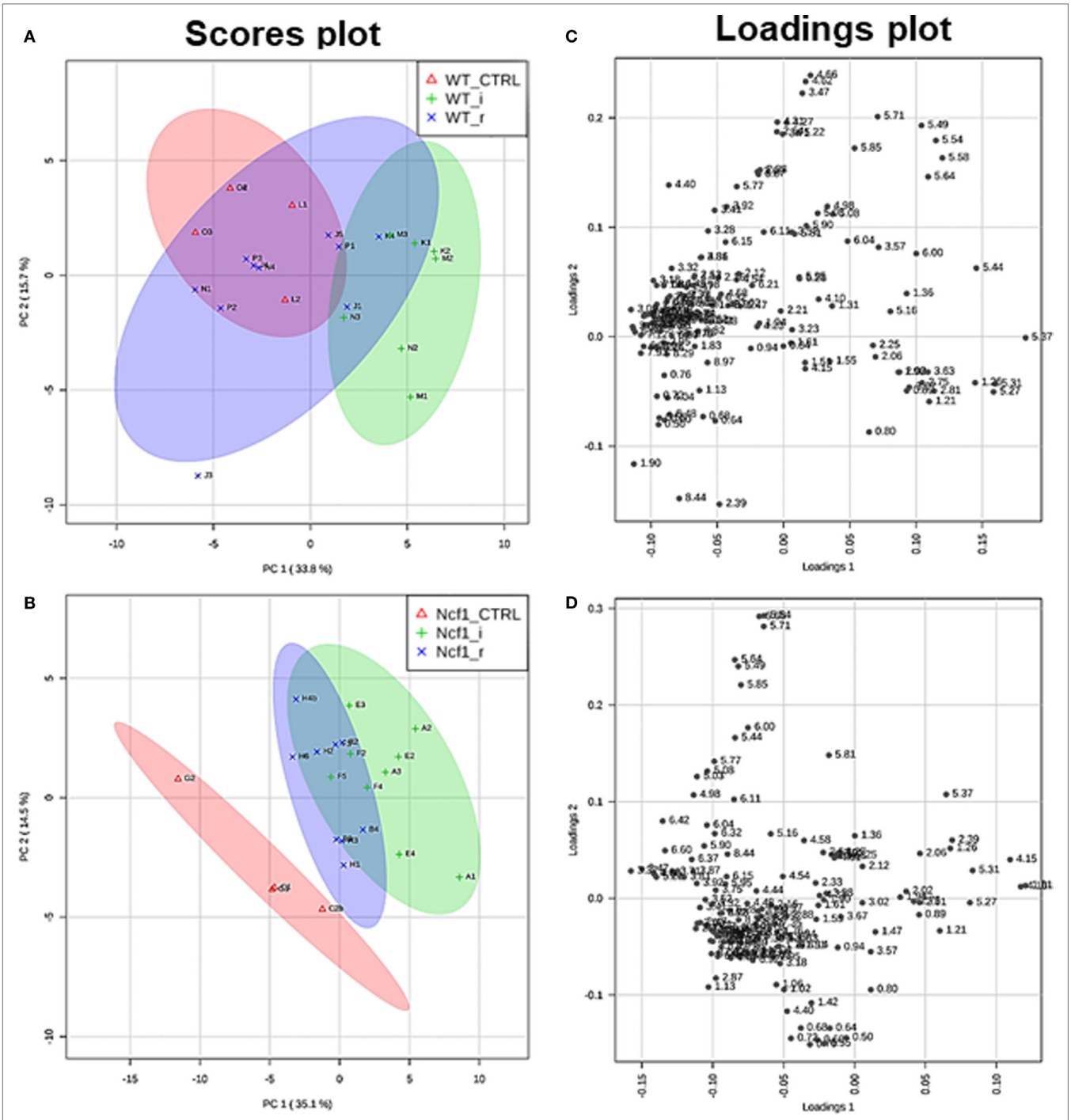

FIGURE 7 | The presence of the Ncf1-mutant (Ncf1) mutation leads to distinct metabolomic profiles in mice either recovering from (r) or after a second period of DSS-induced colitis (i). This contrasts with wild-type (WT) mice which present overlapping metabolomic profiles between control, recovery, and second colitis-induced groups. Principal component analysis of ^{1}H spectra of WT and Ncf1mice. The scores plot for the WT reaches 49.4% of the total variance (PC1 = 33.8%, PC2 = 15.6%) **(A)**; for the Ncf1 achieves 49.6% of the total variance (PC1 = 35.1%, PC2 = 14.5%) **(B)**. The loadings plot shows the δ of each variable (bucket) for the WT **(C)** and the Ncf1 **(D)** groups.

Recently, it has been demonstrated that in colon carcinoma patients the T cells present in the inflammatory foci in the colon express elevated levels of β-catenin, and mice with over-activation of β-catenin develop chronic colonic inflammation and subsequent carcinogenesis (38). In a previous study, we could not detect any alteration on the expression levels of the *Apc* gene in Ncf1 mice bread either in SPF or germ-free conditions (39). However, we observe an accumulation of β-catenin expressing lymphocytes in the inflammatory foci of the Ncf1 colon near well-differentiated adenocarcinoma. In our previous study on

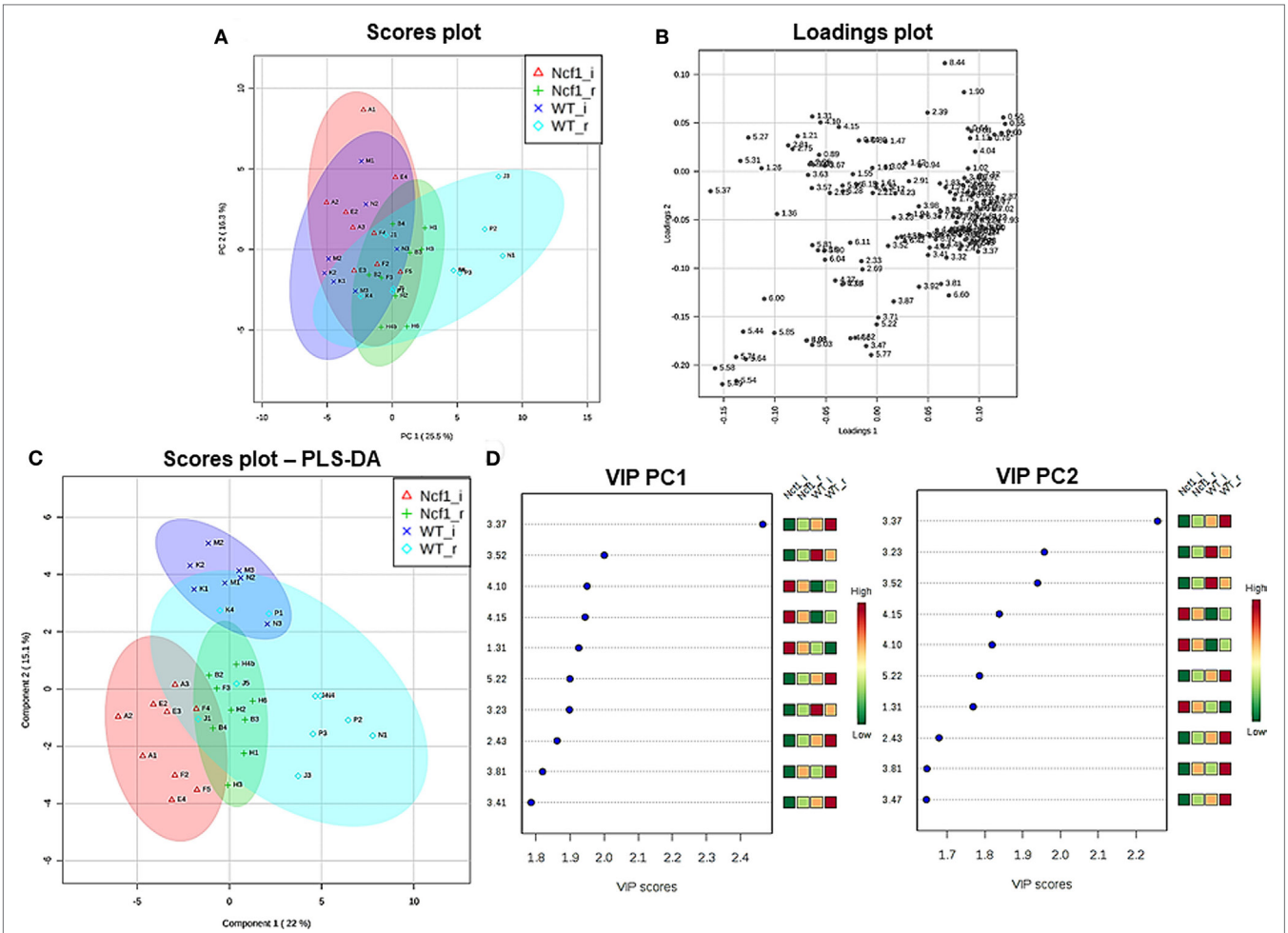

FIGURE 8 | The systemic metabolic profile after a second period of dextran sulfate sodium-induced colitis is markedly distinct between mice bearing the Ncf1-mutation (Ncf1) and the wild-type (WT) group. However, the two recovery groups tend to diverge from the induced groupings and edge toward a common metabolic profile. Principal component analysis (PCA) and partial least squares–discriminant analysis (PLS–DA) analysis of ^{1}H spectra of Ncf1 vs WT after the second colitis induction (i) and recovery (r) groups. The PCA scores plot explains 41.8% of the total variance (PC1 = 25.5%, PC2 = 16.3%) **(A)** and the loadings plot shows the δ of each variable (bucket) **(B)**. The PLS–DA model **(C)** and variable importance in projection (VIP) variables **(D)** for the four groups ($r^2 = 0.70$, $q^2 = 0.43$).

acute colitis, we have seen a massive infiltration of T cells into those inflammatory foci (25). Hence, it is worth exploring further the possible link between ROS-dependent failure in tolerance induction in Ncf1 T cells and dysregulation of β-catenin expression, which may contribute to promote chronic inflammation and ultimately carcinogenesis.

Even though both unchallenged WT and Ncf1 mice exhibit a similar blood serum metabolic fingerprint, their response to DSS exposure led to distinct metabolomic rearrangements. The metabolomics approach highlighted lower blood glucose and higher lactate levels in the Ncf1 mice, which may reflect compromised intestinal nutrient absorption (40). This is supported by the observation of bloody feces, reduced colon length, and reduced body weight, all distinct signs of colitis onset. Regarding clinical parameters and blood serum metabolites in Ncf1 mice, we consistently found lower glucose and/or higher lactate levels correlating with dysplasia and inflammation score and weight variation.

Another interesting correlation concerns the blood plasma lipid remodeling upon the development of colitis. Although WT DSS-induced colitis mice exhibited less severe histopathological changes, the blood serum metabolome displayed an increase in the fatty acids as evidenced by gains in L2, L6, and L7 and exhibited moderate-to-strong correlations with inflammation score, weight variation, colon length, and spleen weight. The Ncf1 mice exhibited a similar response, though with lower correlation coefficients. Considering that DSS-induced colitis may alter hepatic metabolism (41), these lipid rearrangements can modulate the immune response, and the inflammatory process itself (42, 43). Moreover, a broader systemic metabolic remodeling might be in play, with recent studies relating dietary patterns and hormonal regulation (43–45). Strong localized inflammation may release cytokines, such as IL-6 and C-reactive protein, into the circulatory system and activate a systemic response by the sympathetic nervous system and hypothalamic–pituitary–adrenal axis (44, 46). This response may generate a hormonally induced

TABLE 2 | Summary of all statistically significant Spearman correlations for dysplasia score vs metabolite concentrations considering either all mice pooled together or Ncf1-mutant (Ncf1) vs wild-type (WT) groups.

Spearman correlations		Dysplasia score		
		All groups ($n = 44$)	Ncf1 ($n = 22$)	WT ($n = 22$)
Glucose	Correlation coefficient	−0.342*	−0.344	−0.199
	Sig. (two-tailed)	0.023	0.117	0.376
L3/L1	Correlation coefficient	−0.353*	−0.321	−0.379
	Sig. (two-tailed)	0.019	0.145	0.082
L4/L1	Correlation coefficient	0.408**	0.228	0.131
	Sig. (two-tailed)	0.006	0.308	0.561
Leucine	Correlation coefficient	0.471**	0.446*	0.417
	Sig. (two-tailed)	0.001	0.037	0.053
Isoleucine	Correlation coefficient	0.511**	0.513*	0.175
	Sig. (two-tailed)	0.000	0.015	0.437
Lactate	Correlation coefficient	0.409**	0.517*	0.136
	Sig. (two-tailed)	0.006	0.014	0.545
Proline	Correlation coefficient	0.457**	0.520*	0.213
	Sig. (two-tailed)	0.002	0.013	0.341

*Significant correlations are indicated by asterisks: *p < 0.05; **p < 0.01.*

TABLE 3 | Summary of all statistically significant Spearman correlations for inflammation score vs metabolites concentrations considering either all mice pooled together or Ncf1-mutant (Ncf1) vs wild-type (WT) groups.

Spearman correlations		Inflammation score		
		All groups ($n = 44$)	Ncf1 ($n = 22$)	WT ($n = 22$)
Glucose	Correlation coefficient	−0.394**	−0.550**	−0.168
	Sig. (two-tailed)	0.008	0.008	0.456
L2/L1	Correlation coefficient	0.457**	0.164	0.659**
	Sig. (two-tailed)	0.002	0.465	0.001
L3/L1	Correlation coefficient	−0.470**	−0.242	−0.777**
	Sig. (two-tailed)	0.001	0.278	0.000
L4/L1	Correlation coefficient	0.364*	0.313	−0.032
	Sig. (two-tailed)	0.015	0.157	0.887
L6/L1	Correlation coefficient	0.470**	0.384	0.527*
	Sig. (wo-tailed)	0.001	0.078	0.012
L7/L1	Correlation coefficient	0.530**	0.359	0.645**
	Sig. (two-tailed)	0.000	0.101	0.001
Leucine	Correlation coefficient	0.346*	0.323	0.157
	Sig. (two-tailed)	0.021	0.142	0.487
Isoleucine	Correlation coefficient	0.428**	0.419	0.016
	Sig. (two-tailed)	0.004	0.052	0.943
Valine	Correlation coefficient	−0.241	−0.088	−0.578**
	Sig. (two-tailed)	0.116	0.696	0.005
Acetate	Correlation coefficient	−0.208	0.012	−0.561**
	Sig. (two-tailed)	0.175	0.957	0.007
Glutamine	Correlation coefficient	−0.298*	−0.098	−0.302
	Sig. (two-tailed)	0.049	0.665	0.173
Choline	Correlation coefficient	−0.197	−0.065	−0.477*
	Sig. (two-tailed)	0.200	0.773	0.025
PhosphoCholine	Correlation coefficient	−0.322*	−0.336	−0.109
	Sig. (two-tailed)	0.033	0.126	0.630
Proline	Correlation coefficient	0.321*	0.388	−0.056
	Sig. (two-tailed)	0.034	0.074	0.804

*Significant correlations are indicated by asterisks: *p < 0.05; **p < 0.01.*

TABLE 4 | Summary of all statistically significant Spearman correlations for weight variation vs metabolites concentrations considering either all mice pooled together or Ncf1-mutant (Ncf1) vs wild-type (WT) groups.

Spearman correlations		Weight variation		
		All groups ($n = 44$)	Ncf1 ($n = 22$)	WT ($n = 22$)
Glucose	Correlation coefficient	0.359*	0.424*	0.149
	Sig. (two-tailed)	0.017	0.049	0.509
L2/L1	Correlation coefficient	−0.301*	−0.248	−0.383
	Sig. (two-tailed)	0.047	0.267	0.079
L3/L1	Correlation coefficient	0.340*	0.415	0.207
	Sig. (two-tailed)	0.024	0.055	0.355
L4/L1	Correlation coefficient	−0.527**	−0.427*	0.010
	Sig. (two-tailed)	0.000	0.048	0.966
L6/L1	Correlation coefficient	−0.518**	−0.519*	−0.444*
	Sig. (two-tailed)	0.000	0.013	0.038
L7/L1	Correlation coefficient	−0.418**	−0.514*	−0.449*
	Sig. (two-tailed)	0.005	0.014	0.036
Leucine	Correlation coefficient	−0.353*	−0.490*	−0.156
	Sig. (two-tailed)	0.019	0.021	0.488
Isoleucine	Correlation coefficient	−0.565**	−0.632**	−0.193
	Sig. (two-tailed)	0.000	0.002	0.389
Lactate	Correlation coefficient	−0.477**	−0.443*	−0.384
	Sig. (two-tailed)	0.001	0.039	0.078
Creatine	Correlation coefficient	−0.266	−0.433*	−0.208
	Sig. (two-tailed)	0.081	0.044	0.353
Proline	Correlation coefficient	−0.511**	−0.600**	−0.293
	Sig. (two-tailed)	0.000	0.003	0.186

*Significant correlations are indicated by asterisks: *p < 0.05; **p < 0.01.*

TABLE 5 | Summary of all statistically significant Spearman correlations for colon length vs metabolites concentrations considering either all mice pooled together or Ncf1 (Ncf1) vs wild-type (WT) groups.

Spearman correlations		Colon length		
		All groups ($n = 43$)	Ncf1 ($n = 22$)	WT ($n = 21$)
L2/L1	Correlation coefficient	−0.513**	−0.212	−0.748**
	Sig. (two-tailed)	0.000	0.343	0.000
L3/L1	Correlation coefficient	0.574**	0.418	0.735**
	Sig. (two-tailed)	0.000	0.053	0.000
L6/L1	Correlation coefficient	−0.666**	−0.510*	−0.738**
	Sig. (two-tailed)	0.000	0.015	0.000
L7/L1	Correlation coefficient	−0.669**	−0.471*	−0.830**
	Sig. (two-tailed)	0.000	0.027	0.000
GPC/Cho	Correlation coefficient	−0.258	−0.133	−0.531*
	Sig. (two-tailed)	0.095	0.556	0.013
Leucine	Correlation coefficient	−0.420**	−0.443*	−0.283
	Sig. (two-tailed)	0.005	0.039	0.213
Isoleucine	Correlation coefficient	−0.338*	−0.512*	0.011
	Sig. (two-tailed)	0.026	0.015	0.962
Valine	Correlation coefficient	0.245	−0.053	0.541*
	Sig. (two-tailed)	0.113	0.814	0.011
Acetate	Correlation coefficient	0.295	0.045	0.555**
	Sig. (two-tailed)	0.055	0.842	0.009

*Significant correlations are indicated by asterisks: *p < 0.05; **p < 0.01.*

metabolic shift, including possible peripheral insulin resistance and inhibiting the storage of energy-rich substrates in the liver, muscle, and adipocytes. The increased levels of circulatory

TABLE 6 | Summary of all statistically significant Spearman correlations for spleen weight vs metabolites concentrations considering either all mice pooled together or Ncf1-mutant (Ncf1) vs wild-type (WT) groups.

Spearman correlations		Spleen weight		
		All groups ($n = 42$)	Ncf1 ($n = 22$)	WT ($n = 20$)
Glucose	Correlation coefficient	−0.291	−0.463*	−0.059
	Sig. (two-tailed)	0.062	0.030	0.806
L2/L1	Correlation coefficient	0.550**	0.479*	0.660**
	Sig. (two-tailed)	0.000	0.024	0.002
L3/L1	Correlation coefficient	−0.468**	−0.292	−0.654**
	Sig. (two-tailed)	0.002	0.188	0.002
L6/L1	Correlation coefficient	0.475**	0.330	0.578**
	Sig. (two-tailed)	0.001	0.134	0.008
L7/L1	Correlation coefficient	0.591**	0.523*	0.693**
	Sig. (two-tailed)	0.000	0.013	0.001
Valine	Correlation coefficient	−0.283	−0.243	−0.472*
	Sig. (two-tailed)	0.070	0.277	0.036
Acetate	Correlation coefficient	−0.370*	−0.361	−0.504*
	Sig. (two-tailed)	0.016	0.099	0.024
Glutamine	Correlation coefficient	−0.428**	−0.489*	−0.323
	Sig. (two-tailed)	0.005	0.021	0.164
Choline	Correlation coefficient	−0.395**	−0.510*	−0.456*
	Sig. (two-tailed)	0.010	0.015	0.043
PhosphoCholine	Correlation coefficient	−0.402**	−0.491*	−0.247
	Sig. (two-tailed)	0.008	0.020	0.295
Glycine	Correlation coefficient	−0.332*	−0.489*	−0.119
	Sig. (two-tailed)	0.032	0.021	0.618

*Significant correlations are indicated by asterisks: *$p < 0.05$; **$p < 0.01$.*

energy-rich substrates may fuel activated immune cells, which can be crucial in the context of IBD, where nutrient absorption is directly impaired. Furthermore, the increase of circulatory unsaturated fatty acids may also exert a pro-inflammatory positive feedback loop (43, 44). However, this is still a fairly controversial notion given the plethora of lipids classes where microbiota-derived short-chain fatty acids and unsaturated lipids of dietary origin seem to promote anti-inflammatory effects (47, 48) while an altered polyunsaturated lipid profile in colonic mucosa correlates with the severity of inflammation (49).

Besides lipid rearrangements, DSS-induced Ncf1 mice also displayed an increase in a few blood serum amino acids, e.g., leucine, isoleucine, and proline. This was probably related to protein breakdown for energetic purposes, a conjecture supported by the observed low-blood glucose levels and weight loss (40). These highlighted metabolic responses are consonant with those previously described in DSS-induced colitis protocols (50, 51).

Despite a few studies on animal models and CGD patients showing that ROS have a crucial role in immune regulation (19, 52, 53), oxidative burst and the concomitant production of ROS are still regarded mainly as pro-inflammatory events. However, in this study we stress their protective role against chronic inflammation and tumor development. The lack of capacity of NOX2 to generate oxidative burst in the Ncf1 model enhanced the DSS-induced colitis symptoms as far as cancer onset.

Another feature of NOX2 activity is the consumption of reducing equivalents, either as cofactor for the reaction itself or by ROS-scavenging enzymes. Taken together with the transient O_2 depletion and HIF signaling, we might expect metabolic rearrangements in several pathways, namely for mitochondrial and lipogenic activities. Unfortunately, only a very few studies focused on the metabolic changes in colitis mucosa. The pentose phosphate pathway (PPP) is a major NADPH generator, especially in O_2 deficient environments. *TP53*-inducible glycolysis and apoptosis regulator (TIGAR) may redirect glycolytic metabolism toward PPP, but also present divergent regenerative or tumorigenic outcomes, while in DSS-induced colitis, TIGAR dampens mild oxidative stress, promoting cellular regeneration; however, in cancer with deregulated p53 responses, it enhances proliferation by limiting excessive ROS generation and providing nucleotides (54). Thus, it will be interesting to understand whether this mechanism is impaired in Ncf1 mice, and if intact NOX2 activity may promote TIGAR activity to maintain NADPH levels through PPP thereby adding another protective layer.

Furthermore, lipogenesis may be impaired given the requirement of NADPH by fatty acid synthase, resulting in disturbed mucosal lipid metabolism. Again, the scarce literature only mentions a fatty acid synthase increased expression in both DSS-induced colitis mucosa and colorectal cancer (55, 56) and our work only focused on the systemic blood serum metabolome.

In our study, the lack of inflammatory-derived ROS on Ncf1 DSS-induced colitis model was sufficient to develop adenocarcinoma and exhibit a different blood plasma lipid profile. Even though oxidative burst is responsible for several pro-inflammatory signaling events, it is also required for initiating resolution of inflammatory processes in an ROS-mediated self-control mechanism. Although mainstream lines of research focus on ROS generation, the answer for this paradoxical mechanism may lie in the substrates, the transiently variable O_2 concentrations in the microenvironment, and the cofactor NADPH. Further research on the metabolic pathways involved, especially for the regeneration of NADPH through PPP and *de novo* lipogenesis, may provide new targets which until now have been disregarded.

The present study also reveals some, as yet unaddressed, peculiarities of the development of colon adenocarcinoma. In the histological analysis of the colon from our model, we followed the 2010 WHO classification of tumors of the digestive system (26) applying the human nomenclature for low-grade dysplasia and high-grade dysplasia/intraepithelial neoplasia. The present study shows that villous/superficial papillary adaptation of the flat mucosa was not relevant to adenocarcinoma morphology and that the inflammation process in Ncf1 colon form a spectrum from acute to the adaptive presence of inflammatory cells. We show that basal glands, the hallmark of the WT response, were mostly insignificant in Ncf1 mice, which displayed installed dysplasia, quickly evolving to invasive well-differentiated adenocarcinoma. The WHO nomenclature and other studies recognize several patterns for colonic tumors: adenocarcinoma, mucinous adenocarcinoma, signet-ring cell carcinoma, and undifferentiated carcinoma (26, 57). Our model was only capable of inducing well-differentiated tubular/glandular adenocarcinoma, with sporadic mucinous cells hyperplasia in the foci of high-grade dysplasia. These important findings suggest that hyperplastic villous

patterns, either in the mucosa or in villous and tubulo-villous adenomas, may correspond to an epithelial adaptive modification also observed in gastric peptic ulcer re-epithelization (64). ROS influence in the studied carcinogenesis was underlined by the morphological alterations that were more prominent in Ncf1 mice, whereas the presence of ROS may allow mucosal adaptation in WT mice.

This work brings new data on the relevance of an intact ROS production for an effective resolution of chronic colon inflammation thus helping prevent degeneration into a carcinogenic process with systemic metabolomic and lipidomic shifts.

ETHICS STATEMENT

This study was carried out in accordance with the recommendations of EU legislation for experimental animal welfare. The protocol was approved by the internal FFUC Animal Facility Ethics Committee.

AUTHOR CONTRIBUTIONS

LT, AX, JG, and KK performed experimental work and participated in the study design. AX, JG, and LT performed data analysis. LT, KK, RH, LC, RC, and MS-C contributed with experimental design, data acquisition/analysis, and writing.

ACKNOWLEDGMENTS

We would like to thank I Vitória, H Carvalheiro, and T Rodrigues-Sousa for technical support in mouse breeding and maintenance, and the technical personnel from the Animal Facility of the Faculty of Pharmacy, University of Coimbra.

FUNDING

This work was funded by a Marie Curie grant PERG-GA-2008-239422 to MS-C; by the European Regional Development Fund (ERDF), through Centro 2020 Regional Operational Programme: project CENTRO-01-0145-FEDER-000012-HealthyAging2020 to LT; by the COMPETE 2020-Operational Programme for Competitiveness and Internationalisation and Portuguese national funds *via* FCT – Fundação para a Ciência e a Tecnologia, I.P, project POCI-01-0145-FEDER-007440; by the FEDER/COMPETE/Fundação para a Ciência e Tecnologia project Pest/C-SAU/LA0001/2013-2014; by the Swedish Research Council grant 2015-02662 and the Knut and Alice Wallenberg grant KAW 2015.0063 foundation to RH.

REFERENCES

1. Abraham C, Cho JH. Inflammatory bowel disease. *N Engl J Med* (2009) 361(21):2066–78. doi:10.1056/NEJMra0804647
2. Blumberg RS, Strober W. Prospects for research in inflammatory bowel disease. *JAMA* (2001) 285(5):643–7. doi:10.1001/jama.285.5.643
3. Bouma G, Strober W. The immunological and genetic basis of inflammatory bowel disease. *Nat Rev Immunol* (2003) 3(7):521–33. doi:10.1038/nri1132
4. Hanauer SB. Inflammatory bowel disease: epidemiology, pathogenesis, and therapeutic opportunities. *Inflamm Bowel Dis* (2006) 12(Suppl 1):S3–9. doi:10.1097/01.MIB.0000195385.19268.68
5. Rubin DC, Shaker A, Levin MS. Chronic intestinal inflammation: inflammatory bowel disease and colitis-associated colon cancer. *Front Immunol* (2012) 3:107. doi:10.3389/fimmu.2012.00107
6. Sartor RB. Mechanisms of disease: pathogenesis of Crohn's disease and ulcerative colitis. *Nat Clin Pract Gastroenterol Hepatol* (2006) 3(7):390–407. doi:10.1038/ncpgasthep0528
7. Xavier RJ, Podolsky DK. Unravelling the pathogenesis of inflammatory bowel disease. *Nature* (2007) 448(7152):427–34. doi:10.1038/nature06005
8. Kim YS, Jung SA, Lee KM, Park SJ, Kim TO, Choi CH, et al. Impact of inflammatory bowel disease on daily life: an online survey by the Korean association for the study of intestinal diseases. *Intest Res* (2017) 15(3):338–44. doi:10.5217/ir.2017.15.3.338
9. Axelrad JE, Lichtiger S, Yajnik V. Inflammatory bowel disease and cancer: the role of inflammation, immunosuppression, and cancer treatment. *World J Gastroenterol* (2016) 22(20):4794–801. doi:10.3748/wjg.v22.i20.4794
10. Eaden JA, Abrams KR, Mayberry JF. The risk of colorectal cancer in ulcerative colitis: a meta-analysis. *Gut* (2001) 48(4):526–35. doi:10.1136/gut.48.4.526
11. Fornaro R, Caratto M, Caratto E, Caristo G, Fornaro F, Giovinazzo D, et al. Colorectal cancer in patients with inflammatory bowel disease: the need for a real surveillance program. *Clin Colorectal Cancer* (2016) 15(3):204–12. doi:10.1016/j.clcc.2016.02.002
12. Feagins LA, Souza RF, Spechler SJ. Carcinogenesis in IBD: potential targets for the prevention of colorectal cancer. *Nat Rev Gastroenterol Hepatol* (2009) 6(5):297–305. doi:10.1038/nrgastro.2009.44
13. Rogler G. Chronic ulcerative colitis and colorectal cancer. *Cancer Lett* (2014) 345(2):235–41. doi:10.1016/j.canlet.2013.07.032
14. Hanahan D, Weinberg RA. Hallmarks of cancer: the next generation. *Cell* (2011) 144(5):646–74. doi:10.1016/j.cell.2011.02.013
15. Saha SK, Lee SB, Won J, Choi HY, Kim K, Yang GM, et al. Correlation between oxidative stress, nutrition, and cancer initiation. *Int J Mol Sci* (2017) 18(7). doi:10.3390/ijms18071544
16. Blaser H, Dostert C, Mak TW, Brenner D. TNF and ROS crosstalk in inflammation. *Trends Cell Biol* (2016) 26(4):249–61. doi:10.1016/j.tcb.2015.12.002
17. Trachootham D, Alexandre J, Huang P. Targeting cancer cells by ROS-mediated mechanisms: a radical therapeutic approach? *Nat Rev Drug Discov* (2009) 8(7):579–91. doi:10.1038/nrd2803
18. Winterbourn CC, Kettle AJ. Redox reactions and microbial killing in the neutrophil phagosome. *Antioxid Redox Signal* (2013) 18(6):642–60. doi:10.1089/ars.2012.4827
19. Holmdahl R, Sareila O, Olsson LM, Bäckdahl L, Wing K. Ncf1 polymorphism reveals oxidative regulation of autoimmune chronic inflammation. *Immunol Rev* (2016) 269(1):228–47. doi:10.1111/imr.12378
20. Unwith S, Zhao H, Hennah L, Ma D. The potential role of HIF on tumour progression and dissemination. *Int J Cancer* (2015) 136(11):2491–503. doi:10.1002/ijc.28889
21. Tang A, Li N, Li X, Yang H, Wang W, Zhang L, et al. Dynamic activation of the key pathways: linking colitis to colorectal cancer in a mouse model. *Carcinogenesis* (2012) 33(7):1375–83. doi:10.1093/carcin/bgs183
22. Rosenzweig SD. Inflammatory manifestations in chronic granulomatous disease (CGD). *J Clin Immunol* (2008) 28(Suppl 1):S67–72. doi:10.1007/s10875-007-9160-5
23. Freudenberg F, Wintergerst U, Roesen-Wolff A, Albert MH, Prell C, Strahm B, et al. Therapeutic strategy in p47-phox deficient chronic granulomatous disease presenting as inflammatory bowel disease. *J Allergy Clin Immunol* (2010) 125(4):943–6.e1. doi:10.1016/j.jaci.2010.01.035
24. Kanneganti M, Mino-Kenudson M, Mizoguchi E. Animal models of colitis-associated carcinogenesis. *J Biomed Biotechnol* (2011) 2011:342637. doi:10.1155/2011/342637
25. Rodrigues-Sousa T, Ladeirinha AF, Santiago AR, Carvalheiro H, Raposo B, Alarcão A, et al. Deficient production of reactive oxygen species leads to severe chronic DSS-induced colitis in Ncf1/p47phox-mutant mice. *PLoS One* (2014) 9(5):e97532. doi:10.1371/journal.pone.0097532
26. Bosman FT, World Health Organization, International Agency for Research on Cancer. *WHO Classification of Tumours of the Digestive System. World Health Organization Classification of Tumours*. 4th ed. Lyon: IARC Press (2010). 417 p.

27. Tanaka T, Suzuki R, Kohno H, Sugie S, Takahashi M, Wakabayashi K. Colonic adenocarcinomas rapidly induced by the combined treatment with 2-amino-1-methyl-6-phenylimidazo[4,5-b]pyridine and dextran sodium sulfate in male ICR mice possess beta-catenin gene mutations and increases immunoreactivity for beta-catenin, cyclooxygenase-2 and inducible nitric oxide synthase. *Carcinogenesis* (2005) 26(1):229–38. doi:10.1093/carcin/bgh292
28. Meiboom S, Gill D. Modified spin-echo method for measuring nuclear relaxation times. *Rev Sci Instrum* (1958) 29(8):688–91. doi:10.1063/1.1716296
29. Baldwin T, Sakthianandeswaren A, Curtis JM, Kumar B, Smyth GK, Foote SJ, et al. Wound healing response is a major contributor to the severity of cutaneous leishmaniasis in the ear model of infection. *Parasite Immunol* (2007) 29(10):501–13. doi:10.1111/j.1365-3024.2007.00969.x
30. Xia J, Wishart DS. Web-based inference of biological patterns, functions and pathways from metabolomic data using metaboanalyst. *Nat Protoc* (2011) 6(6):743–60. doi:10.1038/nprot.2011.319
31. Aursand M, Mabon F, Martin GJ. High-resolution 1H and 2H NMR spectroscopy of pure essential fatty acids for plants and animals. *Magn Reson Chem* (1997) 35(13):S91–100. doi:10.1002/(SICI)1097-458X(199712)35:13<S91::AID-OMR201>3.0.CO;2-G
32. De Robertis M, Massi E, Poeta ML, Carotti S, Morini S, Cecchetelli L, et al. The AOM/DSS murine model for the study of colon carcinogenesis: from pathways to diagnosis and therapy studies. *J Carcinog* (2011) 10:9. doi:10.4103/1477-3163.78279
33. Barrett CW, Fingleton B, Williams A, Ning W, Fischer MA, Washington MK, et al. MTGR1 is required for tumorigenesis in the murine AOM/DSS colitis-associated carcinoma model. *Cancer Res* (2011) 71(4):1302–12. doi:10.1158/0008-5472.CAN-10-3317
34. Cooper HS, Murthy S, Kido K, Yoshitake H, Flanigan A. Dysplasia and cancer in the dextran sulfate sodium mouse colitis model. Relevance to colitis-associated neoplasia in the human: a study of histopathology, B-catenin and p53 expression and the role of inflammation. *Carcinogenesis* (2000) 21(4):757–68. doi:10.1093/carcin/21.4.757
35. Nojiri A, Toyoda T, Tanaka T, Yoshida T, Tatematsu M, Tsukamoto T. Inflammation enhanced X-irradiation-induced colonic tumorigenesis in the min mouse. *Asian Pac J Cancer Prev* (2013) 14(7):4135–9. doi:10.7314/APJCP.2013.14.7.4135
36. Wang W, Li X, Zheng D, Zhang D, Peng X, Zhang X, et al. Dynamic changes and functions of macrophages and M1/M2 subpopulations during ulcerative colitis-associated carcinogenesis in an AOM/DSS mouse model. *Mol Med Rep* (2015) 11(4):2397–406. doi:10.3892/mmr.2014.3018
37. Kwong LN, Dove WF. APC and its modifiers in colon cancer. *Adv Exp Med Biol* (2009) 656:85–106. doi:10.1007/978-1-4419-1145-2_8
38. Keerthivasan S, Aghajani K, Dose M, Molinero L, Khan MW, Venkateswaran V, et al. beta-Catenin promotes colitis and colon cancer through imprinting of proinflammatory properties in T cells. *Sci Transl Med* (2014) 6(225):225ra28. doi:10.1126/scitranslmed.3007607
39. Kelkka T, Kienhöfer D, Hoffmann M, Linja M, Wing K, Sareila O, et al. Reactive oxygen species deficiency induces autoimmunity with type 1 interferon signature. *Antioxid Redox Signal* (2014) 21(16):2231–45. doi:10.1089/ars.2013.5828
40. Martin FP, Rezzi S, Philippe D, Tornier L, Messlik A, Hölzlwimmer G, et al. Metabolic assessment of gradual development of moderate experimental colitis in IL-10 deficient mice. *J Proteome Res* (2009) 8(5):2376–87. doi:10.1021/pr801006e
41. Chen C, Shah YM, Morimura K, Krausz KW, Miyazaki M, Richardson TA, et al. Metabolomics reveals that hepatic stearoyl-CoA desaturase 1 downregulation exacerbates inflammation and acute colitis. *Cell Metab* (2008) 7(2):135–47. doi:10.1016/j.cmet.2007.12.003
42. Huang CH, Hou YC, Pai MH, Yeh CL, Yeh SL. Dietary omega-6/omega-3 polyunsaturated fatty acid ratios affect the homeostasis of Th/Treg cells in mice with dextran sulfate sodium-induced colitis. *JPEN J Parenter Enteral Nutr* (2017) 41(4):647–56. doi:10.1177/0148607116638493
43. Okada Y, Tsuzuki Y, Sato H, Narimatsu K, Hokari R, Kurihara C, et al. Trans fatty acids exacerbate dextran sodium sulphate-induced colitis by promoting the up-regulation of macrophage-derived proinflammatory cytokines involved in T helper 17 cell polarization. *Clin Exp Immunol* (2013) 174(3):459–71. doi:10.1111/cei.12200
44. Karrasch T, Obermeier F, Straub RH. Systemic metabolic signaling in acute and chronic gastrointestinal inflammation of inflammatory bowel diseases. *Horm Metab Res* (2014) 46(6):445–51. doi:10.1055/s-0034-1374587
45. Rossin D, Calfapietra S, Sottero B, Poli G, Biasi F. HNE and cholesterol oxidation products in colorectal inflammation and carcinogenesis. *Free Radic Biol Med* (2017) 111:186–95. doi:10.1016/j.freeradbiomed.2017.01.017
46. Haghikia A, Jörg S, Duscha A, Berg J, Manzel A, Waschbisch A, et al. Dietary fatty acids directly impact central nervous system autoimmunity via the small intestine. *Immunity* (2015) 43(4):817–29. doi:10.1016/j.immuni.2015.09.007
47. Camuesco D, Gálvez J, Nieto A, Comalada M, Rodríguez-Cabezas ME, Concha A, et al. Dietary olive oil supplemented with fish oil, rich in EPA and DHA (n-3) polyunsaturated fatty acids, attenuates colonic inflammation in rats with DSS-induced colitis. *J Nutr* (2005) 135(4):687–94. doi:10.1093/jn/135.4.687
48. Smith PM, Howitt MR, Panikov N, Michaud M, Gallini CA, Bohlooly-Y M, et al. The microbial metabolites, short-chain fatty acids, regulate colonic Treg cell homeostasis. *Science* (2013) 341(6145):569–73. doi:10.1126/science.1241165
49. Pearl DS, Masoodi M, Eiden M, Brümmer J, Gullick D, McKeever TM, et al. Altered colonic mucosal availability of n-3 and n-6 polyunsaturated fatty acids in ulcerative colitis and the relationship to disease activity. *J Crohns Colitis* (2014) 8(1):70–9. doi:10.1016/j.crohns.2013.03.013
50. Dong F, Zhang L, Hao F, Tang H, Wang Y. Systemic responses of mice to dextran sulfate sodium-induced acute ulcerative colitis using 1H NMR spectroscopy. *J Proteome Res* (2013) 12(6):2958–66. doi:10.1021/pr4002383
51. Schicho R, Nazyrova A, Shaykhutdinov R, Duggan G, Vogel HJ, Storr M. Quantitative metabolomic profiling of serum and urine in DSS-induced ulcerative colitis of mice by (1)H NMR spectroscopy. *J Proteome Res* (2010) 9(12):6265–73. doi:10.1021/pr100547y
52. Biermann MH, Podolska MJ, Knopf J, Reinwald C, Weidner D, Maueröder C, et al. Oxidative burst-dependent NETosis is implicated in the resolution of necrosis-associated sterile inflammation. *Front Immunol* (2016) 7:557. doi:10.3389/fimmu.2016.00557
53. Holland SM. Chronic granulomatous disease. *Hematol Oncol Clin North Am* (2013) 27(1):89–99, viii. doi:10.1016/j.hoc.2012.11.002
54. Cheung EC, Athineos D, Lee P, Ridgway RA, Lambie W, Nixon C, et al. TIGAR is required for efficient intestinal regeneration and tumorigenesis. *Dev Cell* (2013) 25(5):463–77. doi:10.1016/j.devcel.2013.05.001
55. Matsuo S, Yang WL, Aziz M, Kameoka S, Wang P. Fatty acid synthase inhibitor C75 ameliorates experimental colitis. *Mol Med* (2014) 20:1–9. doi:10.2119/molmed.2013.00113
56. Rashid A, Pizer ES, Moga M, Milgraum LZ, Zahurak M, Pasternack GR, et al. Elevated expression of fatty acid synthase and fatty acid synthetic activity in colorectal neoplasia. *Am J Pathol* (1997) 150(1):201–8.
57. Rau TT, Agaimy A, Gehoff A, Geppert C, Jung K, Knobloch K, et al. Defined morphological criteria allow reliable diagnosis of colorectal serrated polyps and predict polyp genetics. *Virchows Arch* (2014) 464(6):663–72. doi:10.1007/s00428-014-1569-7

Conflict of Interest Statement: The authors declare that the research was conducted in the absence of any commercial or financial relationships that could be construed as a potential conflict of interest.

The reviewer EV declared a shared affiliation, though no other collaboration, with one of the authors RH to the handling Editor.

frontiers in Immunology

ORIGINAL RESEARCH
published: 07 May 2018
doi: 10.3389/fimmu.2018.00938

Immuno-Spin Trapping-Based Detection of Oxidative Modifications in Cardiomyocytes and Coronary Endothelium in the Progression of Heart Failure in Tgαq*44 Mice

*Bartosz Proniewski[1], Joanna Czarny[1], Tamara I. Khomich[2†], Kamil Kus[1], Agnieszka Zakrzewska[1] and Stefan Chlopicki[1,3]**

[1] Jagiellonian Centre for Experimental Therapeutics (JCET), Jagiellonian University, Krakow, Poland, [2] Institute of Pharmacology and Biochemistry, NAS of Belarus, Grodno, Belarus, [3] Chair of Pharmacology, Jagiellonian University Medical College, Krakow, Poland

Recent studies suggest both beneficial and detrimental role of increased reactive oxygen species and oxidative stress in heart failure (HF). However, it is not clear at which stage oxidative stress and oxidative modifications occur in the endothelium in relation to cardiomyocytes in non-ischemic HF. Furthermore, most methods used to date to study oxidative stress are either non-specific or require tissue homogenization. In this study, we used immuno-spin trapping (IST) technique with fluorescent microscopy-based detection of DMPO nitrone adducts to localize and quantify oxidative modifications of the hearts from Tgαq*44 mice; a murine model of HF driven by cardiomyocyte-specific overexpression of Gαq* protein. Tgαq*44 mice and age-matched FVB controls at early, transition, and late stages of HF progression were injected with DMPO *in vivo* and analyzed *ex vivo* for DMPO nitrone adducts signals. Progressive oxidative modifications in cardiomyocytes, as evidenced by the elevation of DMPO nitrone adducts, were detected in hearts from 10- to 16-month-old, but not in 8-month-old Tgαq*44 mice, as compared with age-matched FVB mice. The DMPO nitrone adducts were detected in left and right ventricle, septum, and papillary muscle. Surprisingly, significant elevation of DMPO nitrone adducts was also present in the coronary endothelium both in large arteries and in microcirculation simultaneously, as in cardiomyocytes, starting from 10-month-old Tgαq*44 mice. On the other hand, superoxide production in heart homogenates was elevated already in 6-month-old Tgαq*44 mice and progressively increased to high levels in 14-month-old Tgαq*44 mice, while the enzymatic activity of catalase, glutathione reductase, and glutathione peroxidase was all elevated as early as in 4-month-old Tgαq*44 mice and stayed at a similar level in 14-month-old Tgαq*44. In summary, this study demonstrates that IST represents a unique method that allows to quantify oxidative modifications in cardiomyocytes and coronary endothelium in the heart. In Tgαq*44 mice with slowly developing HF, driven by cardiomyocyte-specific overexpression of Gαq* protein, an increase in superoxide production, despite compensatory activation of antioxidative mechanisms, results in the development of oxidative modifications not only in cardiomyocytes but also in coronary endothelium, at the transition phase of HF, before the end-stage disease.

Keywords: immuno-spin trapping, oxidative stress, oxidative modifications, heart failure, cardiomyocytes, coronary endothelium, Tgαq*44 murine model, DMPO

OPEN ACCESS

Edited by:
Rudolf Lucas, Augusta University, United States

Reviewed by:
Suowen Xu, University of Rochester, United States
Eric E. Kelley, West Virginia University, United States

***Correspondence:**
Stefan Chlopicki
stefan.chlopicki@jcet.eu

[†]*Deceased.*

Specialty section:
This article was submitted to Inflammation, a section of the journal Frontiers in Immunology

Received: *31 January 2018*
Accepted: *16 April 2018*
Published: *07 May 2018*

Citation:
*Proniewski B, Czarny J, Khomich TI, Kus K, Zakrzewska A and Chlopicki S (2018) Immuno-Spin Trapping-Based Detection of Oxidative Modifications in Cardiomyocytes and Coronary Endothelium in the Progression of Heart Failure in Tgαq*44 Mice. Front. Immunol. 9:938. doi: 10.3389/fimmu.2018.00938*

INTRODUCTION

Cardiovascular diseases remain one of the most frequent causes of death globally, with an estimated 17.3 million deaths in 2013 and oxidative stress-related mechanisms play a dominant role in their pathogenesis including heart failure (HF) (1, 2). The heart is one of the most oxygen-consuming organs, and therefore changes in redox signaling play a crucial role in the pathophysiology of both acute and chronic diseases affecting the myocardium (3). In the cardiomyocytes, numerous sources of reactive oxygen species are identified, such as the mitochondria (4), NADPH oxidases (Noxs), uncoupled NO synthase, xanthine oxidase, and monoamine oxidase-A (5). Among seven Nox isoforms known to date, Nox2 and Nox4 are found in the cardiomyocytes (6). While Nox2 activation is responsible for increased superoxide production in the myocardium and promotes disease progression (7), the Nox4 isoform is reported to have either a beneficial (8), or detrimental role (9), depending on the studied model (10). Oxidative stress is linked with inflammation and fibrosis that play also an important role in HF progression (11–13). Progression of oxidative stress is prevented by various antioxidant mechanisms including endogenous antioxidant enzymes. Recently reductive stress has also been identified as an important factor in pathophysiology of oxidative stress in HF (14, 15).

Methods used to date to study oxidative stress rely on the detection of either steady-state intermediates or end products of oxidation or measurements of oxidative modifications of an exogenous probing molecule, such as lucigenin, [(3-boronophenyl) methyl]triphenyl-phosphonium, monobromide (mitoB) (16, 17), dihydroethidium (DHE), mitochondria-targeted hydroethidine (MitoSOX®), 10-acetyl-3,7-dihydroxyphenoxazine (*N*-acetyl-3,7-dihydroxyphenoxazine) (AmplexRed) or various EPR spin traps and probes (18–21). Depending on the choice of methodology, the aforementioned techniques have significant limitations, as they can either be specific to a predetermined oxidant [e.g., high performance liquid chromatography (HPLC) detection of DHE oxidation by superoxide (22)], eluding the information about the specific sites of oxidative stress due to required tissue homogenization, or allow localization of the oxidant generation at the expense of specificity [e.g., fluorescent detection of DHE oxidation (23)]. Some of these methodologies are also burdened with probe redox cycling (e.g., lucigenin), leading to possible over-estimation of oxidant abundance, or with high unspecific reactivity leading to high background and low sensitivity toward subtle changes. Moreover, these techniques leave an important question unanswered—what are the long-term repercussions in terms of tissue damage of a particular level of oxidative stress detected. Protein carbonylation, based on detection of dinitrophenyl hydrazine (24) or 3-nitrotyrosine levels using HPLC (25) are common methods to assess protein modifications. Other techniques allow for quantification of lipid peroxidation end products, such as 4-hydroxynonenal or malondialdehyde, which are commonly detected as their covalent protein adducts using Western Blot or immunohistochemistry with specific antibodies. Being a distinct marker of lipid peroxidation and an indication of increased oxidative stress, these assays are, however, more qualitative then quantitative as these are prone to variable levels of modifications, baseline variations, antibody specificity issues, and cross-reactivity (26). Oxidative modifications to DNA are most frequently studied with the assays for 8-hydroxy-2′-deoxyguanosine (27) to analyze oxidatively modified guanine (28). A number of other oxidative stress biomarkers/assays exist, e.g., thiobarbituric acid reactive substances (29, 30), oxidized low density lipoprotein or measurement of reduced glutathione (GSH)/oxidized glutathione (GSSG) ratio, reduced cysteine (Cys)/oxidized cysteine (CySS) ratio, or the non-enzymatic total antioxidant capacity assay (31). Their relevance to assess oxidant stress in HF has been extensively reviewed in literature (32–35).

A relatively new approach to study oxidative stress that can provide an additive insight is called immuno-spin trapping (IST) and was originally developed by Mason (36). It capitalizes on the specific, high reactivity of 5,5-dimethyl-1-pyrroline *N*-oxide (DMPO), an intracellular EPR spin trap, exhibiting low toxicity in cells (37) and animals (38) with damaged DNA in the nuclei and mitochondria as well as with protein, and lipid radicals (39–41). The covalent bond forms stable nitrone adducts upon DMPO injection *in vivo*, which can be then detected with DMPO-specific antibodies *ex vivo* (42) using immunohistochemistry or Western Blots (40, 43, 44), or alternatively it can be also used as a contrast agent in molecular MRI (45–49).

In this work, we have used IST with fluorescent detection of DMPO nitrone adducts to proteins and/or lipids to characterize and quantify the progression of oxidative modifications in the cardiomyocytes and coronary endothelium in hearts of Tgαq*44 mice with cardiomyocyte-specific overexpression of the Gαq* protein (50) mimicking constant neurohormonal overstimulation of cardiomyocytes by renin–angiotensin–aldosterone, sympathetic, and ET-1-dependent systems, mediated *via* angiotensin AT1, adrenergic α1, endothelin ET-A receptor stimulation, respectively. Tgαq*44 mice represent a unique and relevant model of human HF pathophysiology, on a molecular, morphological and functional level. Importantly, Tgαq*44 mice model is characterized by a prolonged course of HF progression with early activation of hypertrophic genes [atrial natriuretic peptide (ANP), brain natriuretic peptide (BNP), and myosin heavy chain beta (MHC-β)], cardiomyocyte hypertrophy, fibrosis (50, 51), and relatively long-term survival (52). The involvement of renin–angiotensin system (53), changes in ACE/ACE2 balance (54), metabolic remodeling (55), mitochondrial alterations (4), or coronary endothelial dysfunction (56) has been previously described in this model. Taking advantage of the protracted time course of progression to overt HF in Tgαq*44 mice, we have recently comprehensively analyzed the deterioration of cardiac function by MRI *in vivo*, identifying three distinct phases of HF progression reflecting early, transition and end-stage phases of HF in this model: initial alterations in cardiac performance including changes in LV strains and rotation, suggestive of diastolic dysfunction that coincides with impairment in atrial function (6 months of age); the transition phase, encompassing progressive impairment in basal systolic and diastolic cardiac performance, with preserved response to dobutamine (8–10 months of age); end-stage phase of HF with fully impaired systolic and diastolic cardiac performance, impaired response to dobutamine (54), and profoundly impaired physical activity (starting at the age of

12 months) (57). Overexpression of the Gαq* protein is limited to cardiomyocytes and results in increased superoxide generation in hearts of Tgαq*44 mice as well as coronary endothelial dysfunction in the end stage of HF (56). However, it is not known at which stage of HF development oxidative modifications occur in cardiomyocytes and coronary endothelium, and what is the temporal relationship for oxidative modifications in the cardiomyocytes as compared with coronary endothelium.

Accordingly, in this work, we used IST method to quantify oxidative modifications in the cardiomyocytes and coronary endothelium in the hearts of Tgαq*44 mice, HPLC-based DHE detection to quantify superoxide production in the heart and classical methods for the assessment of activities of cardiac antioxidant enzymes: superoxide dismutase (SOD), catalase (CAT), glutathione reductase (GR), and glutathione peroxidase (GPx). Tgαq*44 mice have been studied at age groups representative for three stages of HF progression: early, transition, and end-stage (3–6, 8–10, and 12–16 months of age, respectively) and compared with age-matched FVB mice. Our approach allowed for the investigation of onset and development of oxidative modifications in the cardiomyocytes as well as coronary endothelium of large and small vessels along the progression of HF, in relationship with increased superoxide production and activity of antioxidative mechanisms in the heart.

MATERIALS AND METHODS

Animals

Transgenic, homozygous Tgαq*44 mice, characterized by cardiac-specific expression of activated Gαq protein, developed previously (50), as well as wild-type control mice (FVB) were bred at the Animal House of the Institute of Experimental and Clinical Medicine of the Polish Academy of Sciences in Warsaw. Successful transgene incorporation in hearts of Tgαq*44 mice was confirmed by PCR with transgene-specific primers. Increased mRNA level and protein expression of activated Gαq subunit in Tgαq*44 hearts were verified by RT-PCR and Western Blotting methods, respectively (50). Before the experiments, the animals were transported to the animal house at the Faculty of Pharmacy, Medical College, Jagiellonian University in Krakow (Poland). Mice were housed four to six per cage and maintained at 22–24°C under a 12-h light/day cycle with *ad libitum* access to water and rodent chow. Female Tgαq*44 mice of various ages were used: 3-month-old mice, $N = 5$ (for DHE analysis); 4-month-old mice, $N = 6$ (for antioxidant activity); 6-month-old mice, $N = 13$ (6 for DHE analysis and 7 for LC/MS–MS); 8-month-old mice, $N = 5$ (for IST); 9-month-old mice; $N = 4$ (for DHE analysis); 10-month-old mice, $N = 5$ (for IST); 12-month-old mice, $N = 21$ (5 for IST, 6 for antioxidant activity, and 10 for LC/MS–MS); 14-month-old mice, $N = 20$ (6 for IST, 8 for DHE analysis, and 6 for antioxidant activity), and 16-month-old mice, $N = 4$ (for IST). Age-matched FVB wild-type mice were used for comparison: 3-month-old mice, $N = 5$ (for DHE analysis); 4-month-old mice, $N = 6$ (for antioxidant activity); 6-month-old mice, $N = 14$ (6 for DHE analysis and 8 for LC/MS–MS); 8-month-old mice, $N = 5$ (for IST); 9-months-old mice; $N = 4$ (for DHE analysis); 10-month-old mice, $N = 5$ (for IST); 12-month-old mice, $N = 16$ (5 for IST, 4 for antioxidant activity, and 7 for LC/MS–MS); 14-month-old mice, $N = 23$ (6 for IST, 11 for DHE analysis, and 6 for antioxidant activity), and 16-month-old mice, $N = 4$ (for IST). All experimental procedures were compliant with the Guide for the Care and Use of Laboratory Animals published by the U.S. National Institutes of Health (NIH Publication No. 85-23, revised 1996) and were approved by the Second Local Ethical Committee on Animal Testing at the Institute of Pharmacology PAN in Krakow, Poland (permit no. 15/2016).

Quantification of Oxidative Modifications by IST

DMPO Injection Protocol

A total dose of 1.5 g/kg DMPO was used, delivered in 3 equal intra peritoneal (i.p.) injections at approximately 24, 12, and 6 h before sacrifice (43). Body weight of all animals was measured just before the initial DMPO injection. Mice were sacrificed at the age of 8–16 months (ketamine and xylazine, 100 and 10 mg kg^{-1}, respectively). The mouse chest was surgically opened and perfused *via* left (systemic circulation) and right (pulmonary circulation) ventricles with ice-cold PBS for total of 10 min. Hearts were isolated and immediately placed in ice-cold 30 mM KCl (dissolved in PBS) to ensure cardiac arrest in diastole. From each heart, the apex was cutoff and retained for Western Blot analysis. The remainder of the hearts was fixed in formalin and paraffin embedded.

Immunohistochemical Analysis of DMPO Nitrone Adducts in Cardiomyocytes

Formalin-fixed and paraffin-embedded hearts were cut into 5 μm slices on Accu-Cut SRM 200 (Sakura) rotational microtome. Antigen retrieval was performed according to the standard protocol using Leica Autostainer XL (Leica Biosystems). To visualize the extent of DMPO nitrone adducts, the slices were incubated with the primary anti-DMPO nitrone adduct antibody (1 h, dilution 1:300; Abcam, ab23702), secondary goat anti-rabbit IgG Cy3 (30 min, dilution 1:1,000; Jackson ImmunoResearch, cat no. 111-165-003) and Hoechst 33258 to visualize the nucleus (10 min, dilution 1:2,000; Sigma, cat no. 861405-100MG). Some slides were co-stained with biotinylated lectin to stain the endothelium (1 h, dilution 1:200; Vector Laboratories, cat no. B-1105) and visualized with Alexa Fluor® 488 streptavidin (1 h, dilution 1:375; Jackson ImmunoResearch, cat no. 016-540-084). Slides were kept in the dark at 4°C until imaged. Slices without the primary anti-DMPO antibody served as blank control. For every animal $n = 2$ heart slices were analyzed. Randomly chosen homogenous, non-obstructed images covering the papillary muscle ($n = 1$/slice), right and left ventricle ($n = 3$/slice each), and the septum ($n = 3$/slice) were acquired with Axio Observer D1 (Zeiss) inverted microscope equipped with AxioCamHR3 camera and LD Plan-Neofluar 40×/0.6 Korr M27 objective in three channels: Hoechst (nucleus; excitation at 358 nm, emission at 461 nm), FITC (autoflourescence/endothelium; excitation at 494 nm, emission at 519 nm), and Cy3 (DMPO nitrone adducts; excitation at 552 nm, emission at 570 nm). Since blood vessels cover only few percent

of imaged area (FVB mice: median = 2.8%, Q1 = 1.9% and Q3 = 4.6%; Tgαq*44: median = 3.1% Q1 = 1.9% and Q3 = 5.1%) the DMPO-specific fluorescent signal measured and analyzed in the whole cross-sections of the heart was considered to originate mainly from cardiomyocytes, thus is described thereafter to evaluate oxidative modifications in cardiac myocytes. Due to the broad age range of mice in this study, Tgαq*44 mice were analyzed with regards to their aged-matched FVB controls, as mice at the specific age were sacrificed on a single day. Images were analyzed in Columbus (PerkinElmer Inc.), and the DMPO nitrone adducts were expressed as the mean Cy3 fluorescence intensity, normalized to tissue autoflourescence (FITC channel), to overcome the bleaching effect. Furthermore, the heart specimens have been submerged in formalin for a different amount of time up to 4 months (for the oldest group), before the entire staining procedure for all groups has been done within a short period of time. For this reason, results from Tgαq*44 mice were first normalized to appropriate aged-matched controls, to become independent of any effects of various length of tissue pre-processing.

Immunohistochemical Analysis of DMPO Nitrone Adducts in Coronary Endothelium

Some slides were co-stained with biotinylated lectin to stain the endothelium (1 h, dilution 1:200; Vector Laboratories, cat no. B-1105) and visualized with Alexa Fluor® 488 Streptavidin (1 h, dilution 1:375; Jackson ImmunoResearch, cat no. 016-540-084). Images were used to segment and quantify DMPO nitrone adducts within the coronary endothelium of large- and microvessels in ImageJ (58). For large coronaries, at least $n = 6$ vessels per mouse within the left ventricle were captured and segmented according to the following scheme: selection of the entire vessel and discerption of the remainder of the image, segmentation of the endothelial layer, based on Otsu threshold in the FITC channel, copy this selection onto the Cy3 channel, and measurement of the mean fluorescent signal. Results of endothelium-specific DMPO nitrone adducts are expressed as the mean Cy3 signal, normalized to the tissue autoflourescence and endothelial area. Detection of DMPO nitrone adducts in the coronary microvasculature of the left ventricle and septum ($n = 47–72$ images per age group) followed a similar analysis, and are expressed as the mean Cy3 signal within the lectin-positive area, normalized to tissue autoflourescence and to the number of microvessels per square millimeter, quantified using automated morphological manipulations in ImageJ software (i.e., conversion to binary, dilation, hole filling, erosion, and particle analysis) of images on the thresholded ("Otsu dark" Auto Threshold) FITC channel.

Western Blot Detection of DMPO Nitrone Adducts in Heart Apex Homogenates

Heart apex were weighed and homogenized in the Tissue Protein Extraction buffer (T-PER®, Thermo Fisher Scientific cat no. 78510) for protein extraction with protease and phosphatase inhibitors (Roche, cat no. 04693132001 and 04906837001). Protein concentration was measured with BCA assay. After addition of loading buffer, samples were heated at 95°C for 5 min and then frozen at −80°C. Samples were reduced and denatured by tris(2-carboxyethyl) phosphine (50 mM) instead of β-mercaptoethanol, as described previously by Khoo et al. (43). Each time, 30 µg of protein was loaded and run on the gel (Bio-Rad, cat no. 161-0185), then transferred to nitrocellulose membrane, blocked with 5% dry milk in TBST, and incubated overnight at 4°C with the primary DMPO nitrone adduct antibody (Abcam, ab23702). The appropriate HRP-conjugated secondary antibodies were from Santa Cruz Biotechnology (cat no. sc-2004), incubated for 1 h at room temperature. Equal protein loading was controlled after electrophoresis and transfer for gels and membranes, respectively, using stain-free technique provided by Bio-Rad (59). Blots were developed using enhanced chemiluminescence substrate (Bio-Rad, cat no. 1705061). Band intensity was assessed using Image Lab software.

DHE-Based Analysis of Superoxide Production in the Heart

Mice aged at 3, 6, 9, and 14 months were used to assess superoxide production in the myocardium using HPLC detection of 2-hydroxyethiudium (2-OH-E+). Subsequent to anesthesia (100 mg kg^{-1} ketamine + 10 mg kg^{-1} xylazine, i.p.), the mouse chest was surgically opened and perfused *via* left (systemic circulation) and right (pulmonary circulation) ventricles with ice-cold PBS for a total of 10 min. Hearts were isolated, sectioned into appropriate fragments when necessary and incubated at 37°C for 45 min in freshly prepared 500 µl of 10 µM DHE in PBS under low light conditions. The tissues were dried on a piece of Kimwipe paper, snap frozen in liquid nitrogen, and stored at −80°C. On the day of HPLC analysis, the samples were thawed on ice, homogenized in 500 µl in 0.1% Triton X–100 (dissolved in PBS) and centrifuged (at 1,000 *g* for 5 min at 4°C). 100 µl of the supernatant was collected, mixed 1:1 (v/v) with 0.2 M $HClO_4$ in MeOH, vortexed for 10 s and, kept on ice for 90 min. Next, the samples were centrifuged at 16,600 *g* for 30 min at 4°C, 120 µl of the resulting supernatant was collected and mixed 1:1 (v/v) with 1 M KPi pH 2.6 and centrifuged once more at 16,600 *g* for 15 min at 4°C. 200 µl of this homogenate was used for HPLC analysis of the DHE oxidation products, as described previously (60) with minor modifications (61). Results were normalized to the protein content of each sample, assessed in the initial supernatant.

Assessment of Endogenous Antioxidant Systems and Redox State in the Heart

Heart tissue homogenate supernatant was used to estimate the levels of endogenous antioxidants in 4-, 12-, and 14-month-old mice by measuring activities of SOD, CAT, GPx, GR, as well as reduced GSH. After sacrifice, the hearts were quickly removed, washed out in cold 0.9% NaCl, dried on the filter, and placed into liquid nitrogen for freezing. The tissues were kept in −80°C. The homogenates from frozen tissues were prepared in glass homogenizer using ice-cold (4°C) 0.01 M PBS buffer, pH 7.2, containing 0.15 M KCl in dilution (w/v) 1:9. Homogenates were centrifuged at 13,000 rpm for 15 min (4°C), and supernatant was taken for analysis.

Assay of SOD Activity

The total superoxide dismutase (SOD) activity was determined according to the method of Misra and Fridovich (62) at 30°C. Supernatant (10 µl) was added to 960 µl of carbonate buffer (0.05 M, pH 10.2, 0.1 mM EDTA). Then epinephrine 30 mM (30 µl) (in 0.05% acetic acid) was added, and absorbance was measured at 480 nm for 4 min on a PerkinElmer Lambda 950 spectrophotometer. SOD activity was expressed in unit per milligram protein. Amount of enzyme that inhibits the oxidation of epinephrine by 50% was defined as 1 U.

Assay of Catalase Activity

The method of Aebi (63) was used to measure the catalase activity. In brief, to a quartz cuvette, 50 µl of supernatant was

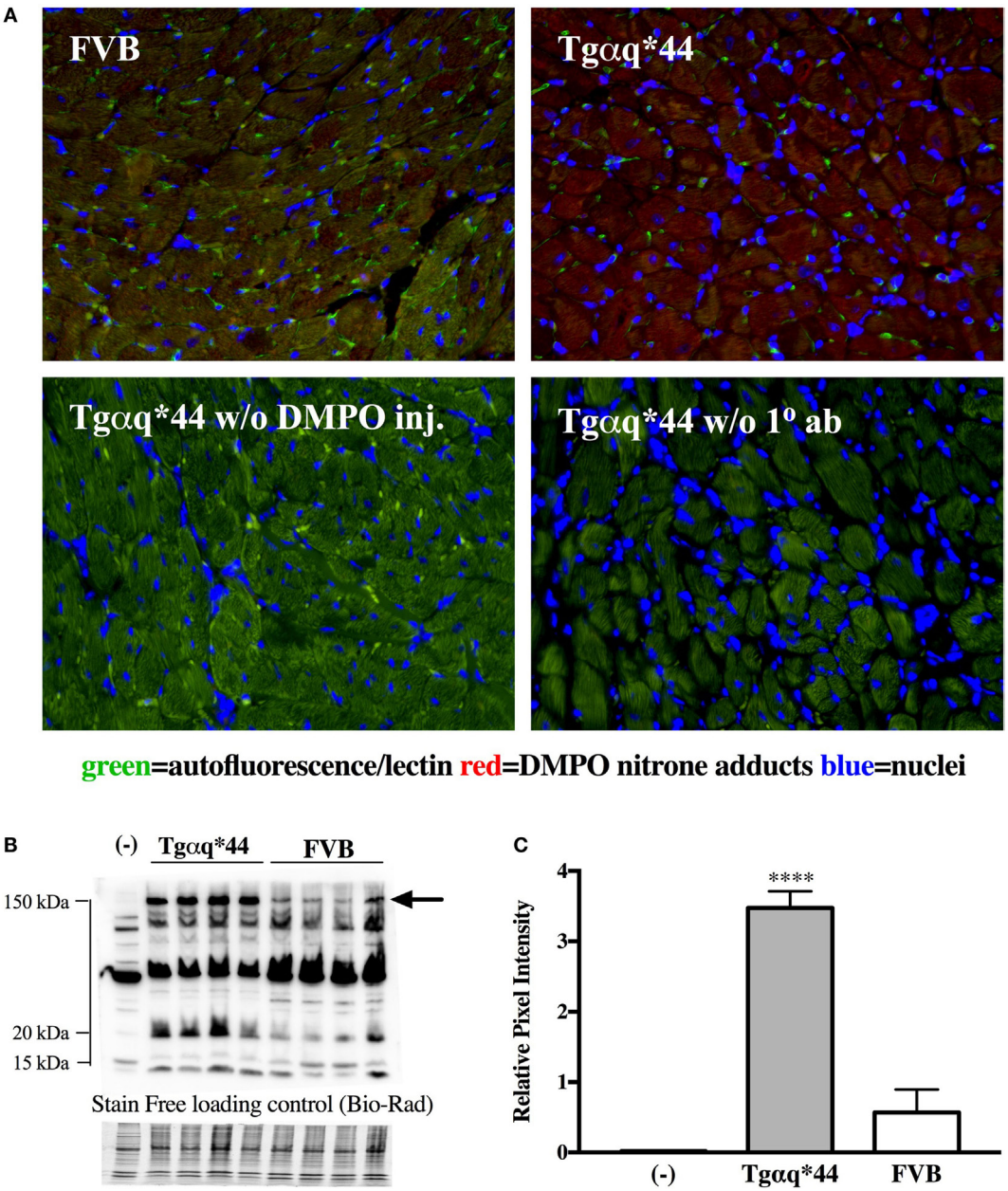

FIGURE 1 | DMPO immuno-spin trapping in the myocardium of Tgαq*44 vs FVB mice. **(A)** Immunohistochemical images of hearts from FVB and Tgαq*44 mice, along with methodological negative controls without DMPO injection (w/o DMPO inj.) or without anti-DMPO primary Ab (w/o 1° ab) (see Materials and Methods for details). **(B)** Representative DMPO nitrone adduct Western Blots of heart apex from 16-month-old mice. Equal protein loading was controlled after electrophoresis and transfer for gels and membranes, respectively, using a stain-free technique provided by Bio-Rad and is shown below the Western Blot image (see Section "Materials and Methods" for details). **(C)** Densitometric analysis of the 150 kDa DMPO nitrone adduct-specific lane, for Western Blots marked in panel **(B)** with an arrow, presented as median ± IQR. For panels **(B,C)**, (-) indicates tissue from age-matched FVB mice injected with 0.9% NaCl. Statistical significance was assessed using an unpaired two-tailed *t*-test, ****$P < 0.001$.

added to 650 µl of 50 mM potassium phosphate buffer, and the reaction was started by addition of 300 µl of 30 mM hydrogen peroxide (H_2O_2). The decomposition of H_2O_2 was monitored at 240 nm, 30°C for 3 min. The catalase activity was expressed as micromoles of H_2O_2 consumed per minute per milligrams of sample protein.

Assay of GR Activity

Glutathione reductase (GR) activity was determined according to method of Carlberg and Mannervik (64). NADPH (50 µl; 2 mM) in 10 mM Tris buffer (pH 7.0) was added in a cuvette containing 50 µl of GSSG (20 mM) in phosphate buffer (0.5 M, pH 7.0, 0.1 mM EDTA) and 850 µl of phosphate buffer. Supernatant (50 µl) was added to the NADPH–GSSG-buffered solution, and absorbance was measured at 340 nm for 3 min at 37°C. The molar extinction coefficient of 6.22×10^3 M cm^{-1} was used to determine GR activity. One unit of activity was equal to the millimolars of NADPH oxidized per minute per milligrams of protein.

Assay of GPx Activity

The modified method of V. Moin was used to determine activity of Glutathione Peroxidase (GPx) (65). The optimal conditions for assays of enzyme activity were as follows: the incubation medium consisted of 0.1 M Tris–HCl buffer, pH 8.5 containing 5 mM EDTA; 10 mM sodium azide; 4.0 mM reduced glutathione; and 1.4 mM tert-butyl hydroperoxide. Supernatant (10–50 µl) was added to the mixture and after 5 min of incubation at 37°C Ellman's reagent was added. The concentration of reduced glutathione before and after incubation was determined colorimetrically using standard Ellman's reaction (see below) in control and tested samples.

Reduced Glutathione

Reduced glutathione was estimated by the method of Ellman (66). The reaction mixture consisted of 10% trichloroacetic acid, 0.1 mM 5,5′-dithio-bis (2-nitrobenzoic acid) in 0.1 M phosphate buffer (pH 8.0) and requisite amount of tissue supernatant. Absorbance was measured at 412 nm.

Protein contents in samples were determined by the method of Bradford (67) with BSA as the standard.

Measurement of GSH/GSSG and NADPH/NADP Ratio

To quantify the GSH/GSSG and the NADPH/NADP ratios in whole-heart homogenates from 6- and 12-month-old Tgαq*44 and FVB mice, LC/MS–MS-based method was used as described previously (68). Briefly, the heart tissue samples were homogenized in PBS containing BHT (1:6 w/v). An aliquot of 10 µl of plasma or tissue homogenate was used to extract the metabolites by addition of 0.5 ml of dry-ice-cold (−70°C) extraction mixture (acetonitrile:methanol:water 5:2:3, v/v/v). The extraction mixture was prepared at least 4–5 h before the experiment and placed in freezer. The samples were vortexed for 5 min and placed on dry ice for 30 min for protein precipitation. After that time, samples were centrifuged at 15,000 *g*, 4°C for 15 min. Supernatant was lyophilized, and dry extract were kept at −80°C until analysis. The metabolite extracts were reconstituted in 50 µl of LC/MS–MS grade water and was injected onto LC/MS–MS column. Chromatographic studies were performed on a UFLC Nexera (Shimadzu, Kyoto, Japan). The analytical column employed was an Acquity UPLC BEH C18, 1.7 µm 2.1 mm × 100 mm (Waters, Milford, MA, USA). The samples were measured twice, injecting onto analytical column 5 µl of sample acetonitrile:100 mM ammonium formate (pH 5.0) 95:5 v/v and 5 mM ammonium formate (pH 5.0) were used as a mobile phase in gradient elution in a run time of 8 min for positive and 5.5 min for negative ionization. Detection was performed with a QTRAP 5500 mass spectrometer (Sciex, Framingham, MA, USA) employed with an electrospray interface operated in positive and negative ionization MRM modes. The ion source operation conditions were as follows: curtain gas: 25 psi, collision gas: medium, temperature: 500°C, ion source gas 1: 40 arb., ion source gas 2: 50 arb., and ion spray voltage: 5,500 V and −4,500 V for positive and negative ionization modes, respectively.

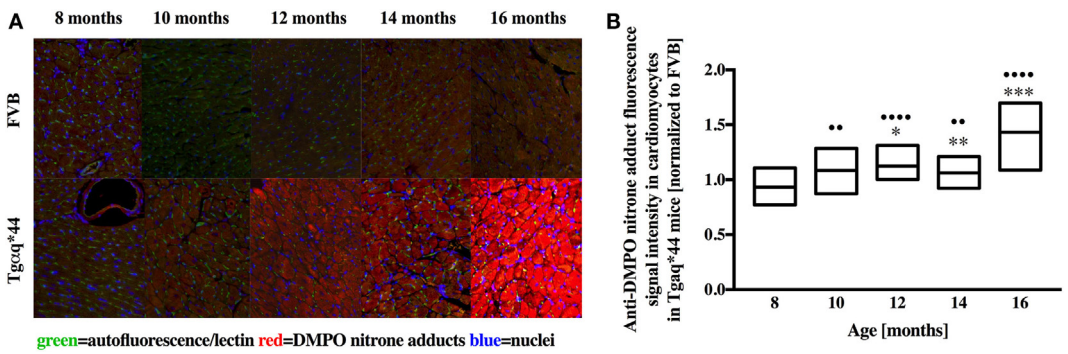

FIGURE 2 | Immunohistochemical detection of DMPO nitrone adducts in the hearts of Tgαq*44 normalized to aged-matched FVB mice. **(A)** Representative images of the left ventricle from 8- to 16-month-old mice. **(B)** Quantification of oxidative modifications, based on the DMPO fluorescent signal, normalized to aged-matched FVB mice (see Section "Materials and Methods" for details). Results presented as median ± IQR. Statistical significance was assessed using the Kruskal–Wallis ANOVA, with *post hoc* Dunn's test to compare oxidative modifications to 8-month-old group, with $^{\bullet\bullet}P < 0.01$ and $^{\bullet\bullet\bullet\bullet}P < 0.001$. Statistical significance between Tgαq*44 and FVB mice in aged-matched groups was assessed using non-parametric, two-sided Mann–Whitney *U* test, $^{*}P < 0.05$, $^{**}P < 0.01$, and $^{***}P < 0.005$. $N = 4$–6 mice per group, $n = 10$ slices per mice.

Statistical Analysis

Data are expressed as median and interquartile ranges (Q1–Q3, IQR). Normality of the data distribution was tested with Shapiro–Wilk's test and variance homogeneity using Bartlett's or *F* test. The significance of differences between age-matched groups was analyzed with two-sided Student's *t*-test or the non-parametric Mann–Whitney *U* test. Differences along the progression of HF were analyzed using one-way ANOVA followed by *post hoc* multiple comparisons LSD Fisher's test or Kruskal–Wallis non-parametric test, followed by *post hoc* multiple comparisons Dunn's test, depending on the variable distribution. Detailed descriptions can be found in the caption under each figure. Statistical tests were done using GraphPad Prism 7 (GraphPad Software, Inc., CA, USA) software. P values < 0.05 were considered statistically significant.

RESULTS

Oxidative Modifications in Cardiomyocytes

Representative microphotograph of a specific, robust immunofluorescent staining of DMPO nitrone adducts in whole-heart cross-sections from 16-month-old Tgαq*44 mice with the use of anti-DMPO antibody is shown in **Figure 1A**. The signal was absent or very weak in age-matched FVB mice. High level of DMPO nitrone adducts in the heart apex from 16-month-old Tgαq*44 as compared with age-matched FVB was confirmed by Western Blot analysis (**Figures 1B,C**). Using immunofluorescent staining of DMPO nitrone adducts, progression of oxidative stress was quantified in 8- to 16-month-old Tgαq*44 mice as compared with age-matched FVB mice (**Figure 2A**). For 8-month-old mice, the fluorescent signal of DMPO nitrone adducts quantified collectively for the various areas of the hearts of Tgαq*44 and FVB was similar, but increased gradually with age (**Figure 2B**), attaining the significant difference between Tgαq*44 groups at the age of 10 months (••) and compared with FVB at the age of 12 months (*), with a profound amplification in 16-month-old Tgαq*44 mice. When the left and right ventricles, septum, and papillary muscles were analyzed independently, a moderate, yet statistically significant increase of DMPO-specific fluorescence, was also appreciated in 10-month-old Tgαq*44 mice in the left and right ventricles (**Figures 3A,B**), and in 12-month-old Tgαq*44 mice in the septum (**Figure 3C**); however, the papillary muscles (**Figure 3D**) became affected at the very late stage of HF (16-month-old Tgαq*44 mice).

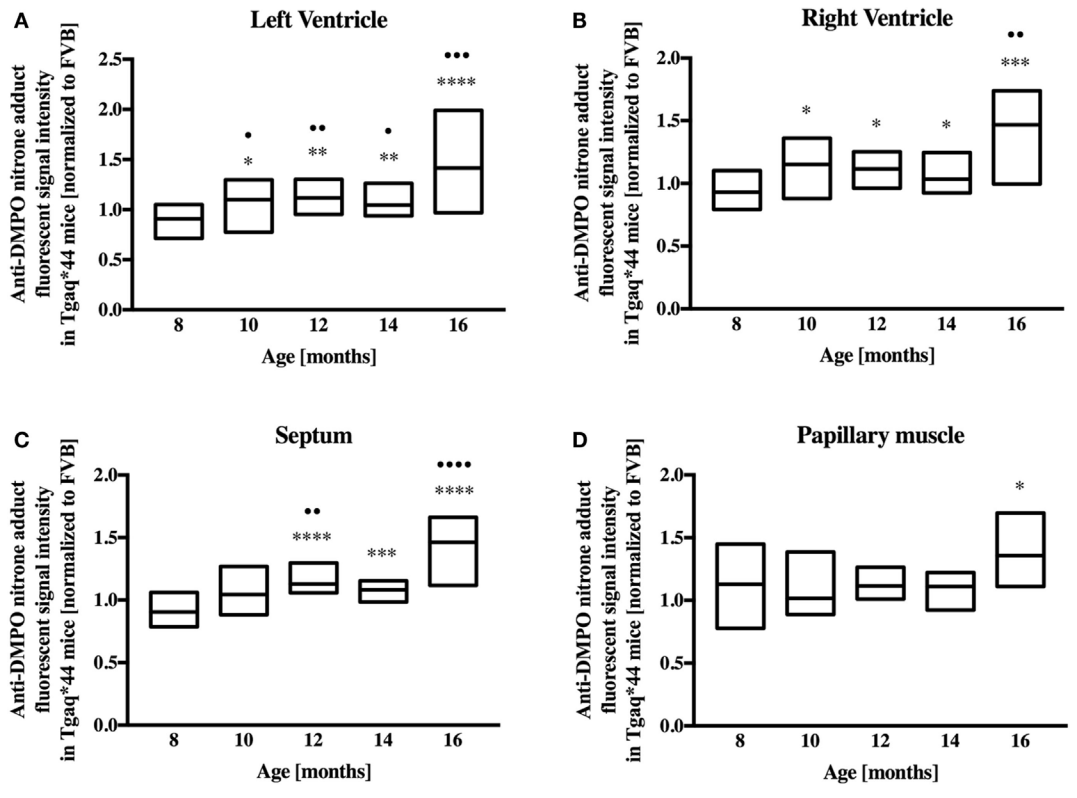

FIGURE 3 | Regional oxidative modifications analyzed using immunohistochemical detection of DMPO nitrone adducts in hearts of Tgαq*44 normalized to aged-matched FVB mice. Quantification of oxidative modifications in the **(A)** left and **(B)** right ventricles, **(C)** septum, and **(D)** papillary muscle of the myocardium showed inhomogeneous distribution of oxidative modifications in the analyzed regions. Results presented as median ± IQR. Statistical significance of changes compared with the 8-month-old group for the left ventricle, right ventricle, and septum were assessed using Kruskal–Wallis ANOVA with *post hoc* Dunn's test (n = 24–30 fields per group), while data for the papillary muscle were analyzed by one-way ANOVA with *post hoc* LSD test (n = 8–12 images per group); •$P < 0.05$, ••$P < 0.01$, •••$P < 0.005$, and ••••$P < 0.001$. Significant differences between aged-matched Tgαq*44 and FVB mice were tested using two-sided Student's *t*-test; *$P < 0.05$, **$P < 0.01$, ***$P < 0.005$, and ****$P < 0.001$.

Oxidative Modifications in the Endothelium of Large- and Microcoronary Vessels

Fluorescent detection of DMPO nitrone adducts, coupled with lectin co-staining, allowed for determination of oxidative modifications localized in the endothelium within the heart sections analyzed. Following a manual selection of large vessels from the left ventricle [vessel radius, expresses as median (Q1–Q3) was 42.9 (27.5–58.4) μm] for each mice, a lectin-positive area was automatically segmented and DMPO-specific fluorescence analyzed (**Figure 4A**). The general tendency was similar to that seen within the cardiomyocytes, with significant elevation of DMPO-specific fluorescence in 10-month-old Tgαq*44 mice, with the sharpest further increase seen between 12- and 14-month-old Tgαq*44 mice (**Figure 4B**).

Lectin-positive staining was also used to quantify the changes in the left ventricle microvasculature. There was a progressive deterioration of microvessel density in the Tgαq*44 mice, which begun at the age of 10 months and led to the loss of roughly 50% of lectin-positive microvessels in 16-month-old Tgαq*44 mice (**Figure 5**). Gradual loss of microvessels was also detected in the 16-month-old FVB mice strain, albeit these changes were not significant. Using lectin-positive staining, the DMPO nitrone adduct fluorescence within the microvessel endothelium was segmented (**Figure 6A**) and was clearly increased in Tgαq*44 mice as compared with FVB mice, starting at the age of 10 months, with a sharp increase for 16-month-old Tgαq*44 mice (**Figure 6B**).

Superoxide Anion Production in the Heart

Heart homogenates were used to assess superoxide *ex vivo* using the HPLC-based detection of 2-hydroxyethidium (**Figures 7A–C**). When the entire heart was homogenized (**Figure 7A**), increased 2-hydroxyethidium levels in the heart was seen in Tgαq*44 mice at the age of 6–9 months, with a dramatic increase for 14-month-old Tgαq*44 mice. As shown in **Figures 7B,C**, in the left ventricle (isolated along with the septum) from 6- to 9-month-old Tgαq*44 mice 2-hydroxyethidium level increased significantly (**Figure 7B**), whereas in the right ventricle, despite apparently higher superoxide levels, there was only a modest increase in 6-month-old, but not in 9-month-old Tgαq*44 mice (**Figure 7C**).

Activity of Antioxidant Enzymes and Redox State in the Heart

Superoxide dismutase activity in Tgαq*44 mice was lower than in FVB controls, at a very early stage of HF development (at the age of 4 months) and further decreased in 12-month-old Tgαq*44 mice (**Figure 8A**). Interestingly, SOD activity also declined with age for the FVB controls and was comparable in 14-month-old Tgαq*44 and FVB mice. Other antioxidant enzymes studied (**Figures 8B–D**) exhibited an elevated activity in the Tgαq*44, when compared with aged-matched controls. This was evident and significant for catalase (**Figure 8B**), GR (**Figure 8C**) and GPx (**Figure 8D**). There were no significant differences in reduced glutathione levels in Tgαq*44 vs FVB mice [in μmol/g tissue for 4-month-old: 0.92 (0.86–0.97) vs 0.86 (0.82–0.89); 12-month-old: 0.99 (0.88–1.09) vs 0.9 (0.86–0.98) and 14-month-old: 0.95 (0.86–1.06) vs 0.92 (0.81–1.01)]. Furthermore, the ratio of GSH/GSSG remained unchanged at the early (6-month-old) and late (12-month-old) stages of HF development in these mice (**Figure 8E**); however, the NADPH/NADP ratio was decreased in Tgαq*44 vs FVB mice, significantly for 12-month-old mice (**Figure 8F**), due to significantly lower NADPH content in the

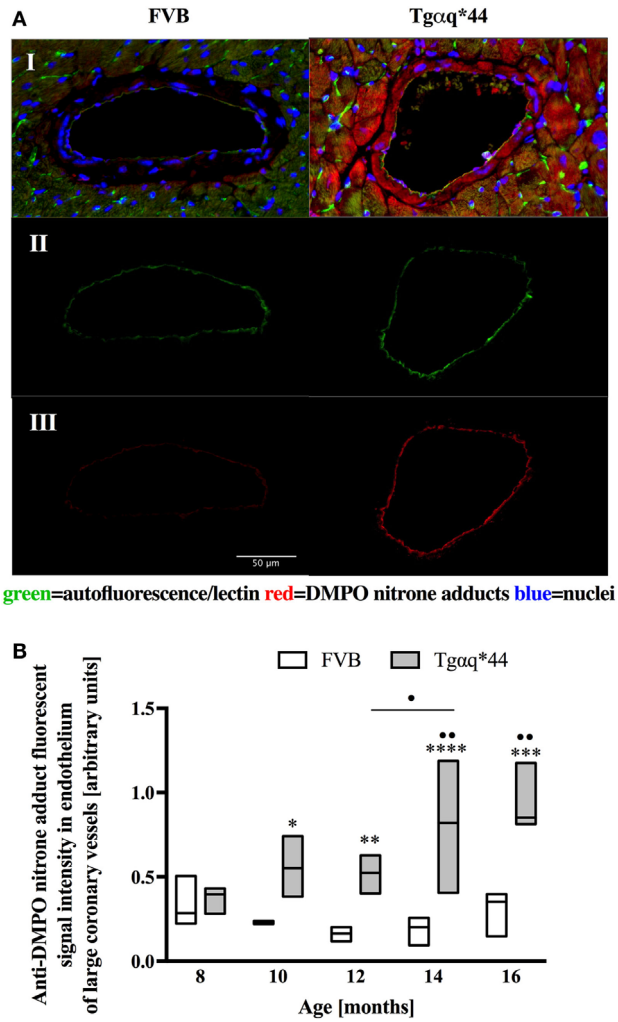

FIGURE 4 | Oxidative modifications analyzed using immunohistochemical detection of DMPO nitrone adducts in the endothelium of large coronary vessels. **(A)** Segmentation steps for representative images of vessels in the left ventricle of 14-month-old mice (image size 250 μm × 150 μm); I: initial, triple-strained fluorescent images; II: endothelium segmentation based on lectin-positive staining of the vessel wall; III: DMPO nitrone adduct fluorescent signal specific to the endothelium area. **(B)** Quantification of the endothelium-specific oxidative modification (see Section "Materials and Methods" for details). Data presented as median ± IQR. Statistical significance was assessed using the two-way ANOVA, with *post hoc* LSD's test between groups. $^{*}P < 0.05$, $^{**}P < 0.01$, $^{***}P < 0.005$, and $^{****}P < 0.001$ denote significant differences in aged-matched groups, while $^{\bullet}P < 0.05$ and $^{\bullet\bullet}P < 0.01$ between Tgαq*44 groups compared with 8-month-old Tgαq*44 group and 12- to 14-month-old groups. $N = 3–6$ mice/group, $n = 5–6$ vessels/mice.

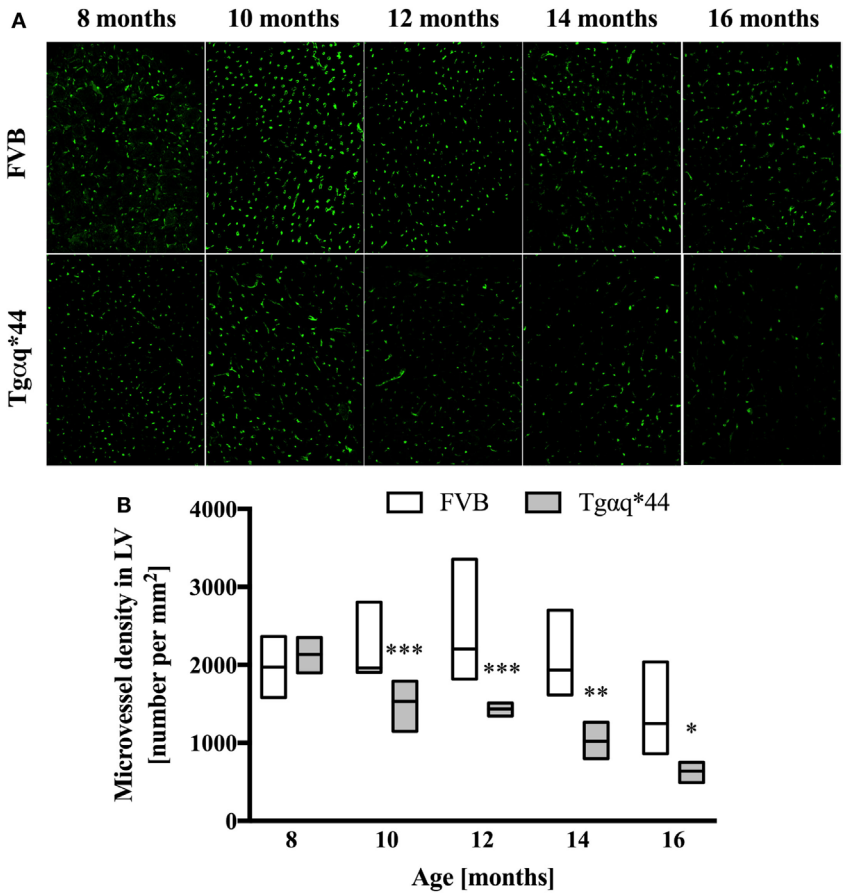

FIGURE 5 | Microvessel density in the heart of Tgαq*44 and FVB mice. **(A)** Representative images of microvessels in the left ventricle stained using lectin from 8- to 16-month-old Tgαq*44 and FVB mice. **(B)** The number of microvessels per square millimeters, quantified using automated morphological manipulations of images on the thresholded FITC channel, as described in Section "Materials and Methods." Data shown as median ± IQR. Statistical significance was assessed using two-way ANOVA, with *post hoc* LSD's test between groups. $^{*}P < 0.05$, $^{**}P < 0.01$, and $^{***}P < 0.005$ denote significant differences in aged-matched groups. Furthermore, one-way ANOVA within Tgαq*44 mice showed a strong linear trend ($P < 0.001$) for decrease in microvessel density. $n = 4$–9 slices per group.

hearts of Tgαq*44 vs FVB [in nmol/mg tissue for 6-month old: 13.7 (11.7–17.2) vs 21.3 (17.2–26.4) and 12-month old: 17.6 (14.3–18.8) vs 30.9 (21.9–35.6)].

DISCUSSION

In this study, we applied, to the best of our knowledge for the first time, DMPO IST-based method to detect *in vivo* oxidative modifications in cardiomyocytes and coronary endothelium of large- and microvessels in a mouse HF model. We provided evidence that in Tgαq*44 mice with slowly developing HF, resembling the progression of HF in humans on a molecular, morphological, and functional levels (4, 50, 54–57, 69), increased production of superoxide resulted in the development of oxidative modifications that occurred not only in cardiomyocytes, but simultaneously in the coronary endothelium at the transition phase of HF, before the end-stage disease. Altogether, these results underscore the important role of coronary endothelial dysfunction in the progression of HF, in a model driven by a cardiomyocyte-specific overexpression of Gαq* protein, whereby coronary endothelial function is initially preserved (56).

Previous work identified three distinct phases of HF progression in Tgαq*44 mice; early (subtle diastolic perturbations at 6 months of age), transition (decreased basal cardiac function, with preserved cardiac reserve beginning at 8 months of age), and end-stage (impaired global cardiac performance and cardiac reserve starting at 12 months of age) (54). As summarized in **Figure 9**, in this work, we demonstrated that superoxide production in the heart was significantly increased in 6-month-old Tgαq*44 mice, which was accompanied by a compensatory activation of antioxidative mechanisms in the myocardium of Tgαq*44 mice, namely upregulation of catalase (CAT), glutathione reductase (GR), and glutathione peroxidase (GPx), opposed to superoxide dismutase (SOD) which was downregulated. Prior studies of oxidative stress in this animal model showed increased NADPH-oxidase dependent superoxide production using lucigenin assay in 2- to 4-month-old Tgαq*44 mice, which further progressed (56); however, changes in antioxidant systems were not as yet

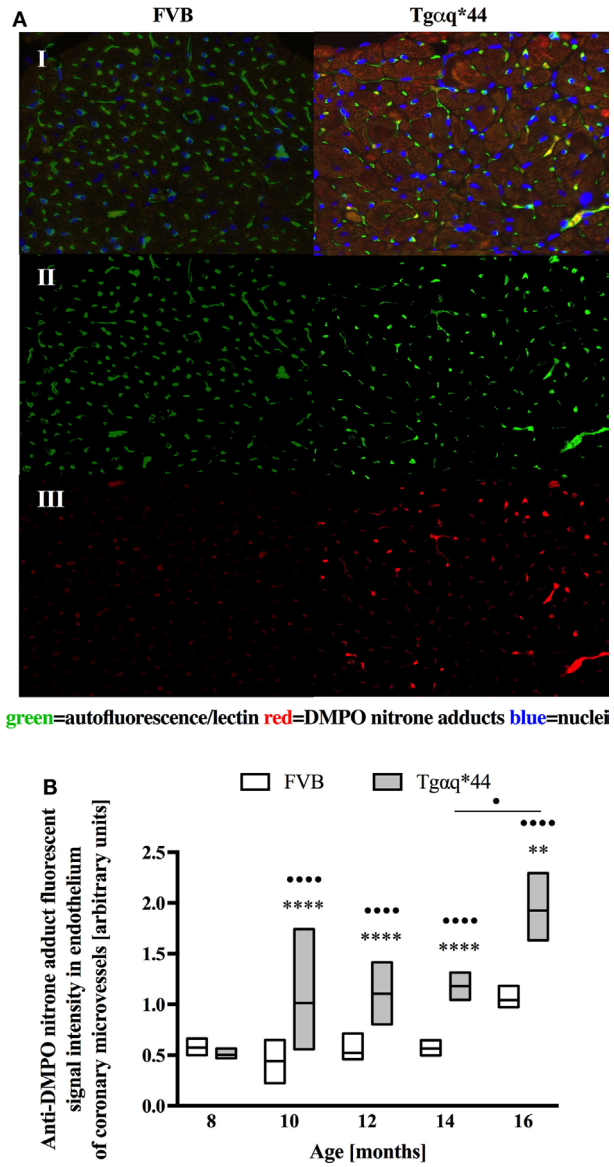

FIGURE 6 | Oxidative modifications analyzed using immunohistochemical detection of DMPO nitrone adducts within the coronary microvessels in Tgαq*44 and FVB mice. **(A)** Microvessel-specific DMPO signal pre-processing steps for a representative pair of Tgαq*44 and FVB left ventricle free wall images of 12-month-old mice; I: initial, triple-strained fluorescent images; II: microvessel segmentation based on lectin-positive staining; III: DMPO nitrone adduct fluorescent signal specific to the microvessels, **(B)** quantification of the microvessel-specific fluorescence. Results presented as median ± IQR. Statistical significance was assessed using the ANOVA Kruskal–Wallis test, with *post hoc* Dunn's test between groups. $^{**}P < 0.01$ and $^{****}P < 0.001$ denote significant differences in aged-matched groups, while $^{\bullet}P < 0.05$ and $^{\bullet\bullet\bullet\bullet}P < 0.001$ between Tgαq*44 groups compared with 8-month-old Tgαq*44 group and between 14- and 16-month-old Tgαq*44 mice. $N = 4$–6 mice/group, $n \geq 5$ fields/mice.

characterized. In this work, cardiac superoxide production was unaltered in 3-month-old Tgαq*44 mice, whereas the 14-month-old group showed a substantial increase (**Figure 7A**), with assay differences possibly explaining for the discrepancy in results for young mice between current and previous studies (56). Our results are compatible with the regulatory role of increased reactive oxygen species production in cardiomyocyte hypertrophy response and activation of fetal phenotype, which occurred quite early in Tgαq*44 mice, as evidenced by the activation of hypertrophic genes (ANP, BNP, and MHC-β), cardiomyocyte hypertrophy, fibrosis in 4-month-old Tgαq*44 mice (50, 51). On the other hand, mitochondrial dysfunction in cardiomyocytes using EPR detection of semiquinones content and Fe-S clusters (4), was identified in 10-month-old Tgαq*44 mice.

Here, we demonstrated that in Tgαq*44 hearts antioxidant systems are upregulated. Elevated activity of catalase (**Figure 8B**) is especially interesting, since cardiac-specific overexpression of catalase has been shown to abolish oxidative stress and prevent the progression to overt HF in an alternative Gαq-overexpressing transgenic mouse model (70). On the other hand, Nox4-derived hydrogen peroxide both in cardiomyocytes and endothelial cells was shown to mediate protection against pressure overload cardiac remodeling (71). Our analysis showed that increased activity of CAT was associated with elevated activity of GPx, which overexpression in mice was previously shown to prevent left ventricular failure after myocardial infarction (72). Since both enzymes are involved in hydrogen peroxide metabolism, it might well be that their upregulation protect the failing heart synergistically. GR activity was also enhanced in Tgαq*44 mice, which might have contributed to NADPH depletion and a decreased NADPH/NADP ratio for 12-month-old Tgαq*44 mice. On the other hand, increased GR activity could at least partially explain the preservation of GSH cardiac pool and GSH/GSSG ratio, despite increased ROS production.

In contrast to early increase in ROS production and early activation of antioxidant systems in Tgαq*44 mice, fluorescent detection of DMPO nitrone adducts in the whole heart showed a statistically significant increase in Tgαq*44 mice compared with aged-matched FVB mice starting at the age of 12 months, with an age-dependent progression (**Figure 2**) and a sharp increase in signal for the 16-month-old Tgαq*44 mice. Comparable trends were appreciated when the left or right ventricle and septum regions of the heart were analyzed independently, with only exception being the papillary muscle, where oxidative modifications developed only for the 16-month-old Tgαq*44 mice (**Figure 3**). The specificity of fluorescent IST analysis was confirmed using Western Blot detection of DMPO nitrone adducts in heart apex homogenates, with a nearly sixfold intensity increase in DMPO nitrone adducts in the myocardium of Tgαq*44 mice, with a semi-quantitative analysis (**Figure 1C**) of the protein band at roughly 150 kDa. This particular band might be related to oxidatively modified oxygen-regulated protein 150, a chaperonin known to be expressed in tissues undergoing hypoxic or endoplasmic reticulum stress (73), involved in VEGF transport (74). However, here we did not analyze the origin of the 150 kDa band seen in DMPO-specific Western Blot that might be determined by mass spectrometry (75). We used this band as a representative for the analysis and quantification of the oxidative modification process. Obviously there are a number of protein modifications reported to form DMPO nitrone adducts that can be identified, for example tyrosine nitration of carboxypeptidase B1 (76), Cys and tyrosine

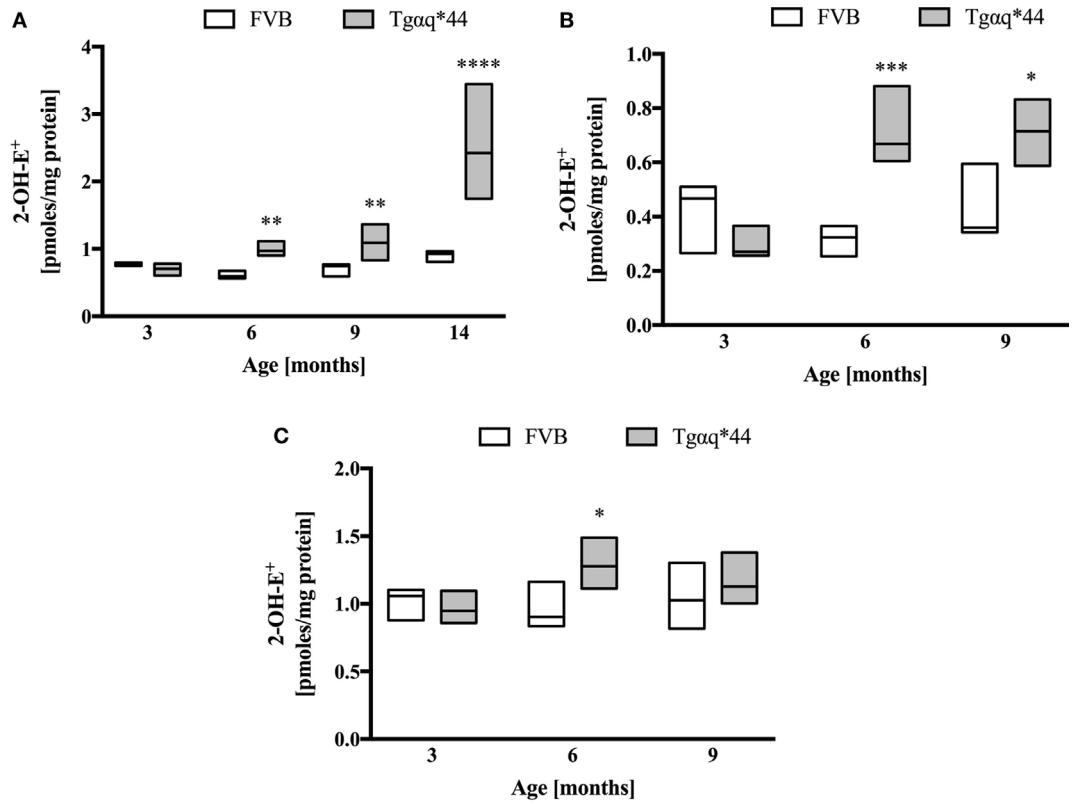

FIGURE 7 | Superoxide production in heart homogenates of Tgαq*44 vs FVB mice. **(A)** Whole heart, **(B)** left ventricle and septum, and **(C)** right ventricle. Tissue samples were incubated with dihydroethidium, followed by superoxide-specific 2-hydroxyethiudium (2-OH-E+) detection using high performance liquid chromatography, as described in Section "Materials and Methods." Data represent median ± IQR. Results presented as median ± IQR. Statistical significance in panel **(A)** for aged-matched groups was assessed using the non-parametric Mann–Whitney *U* test, $N = 5$–6 hearts (3- to 9-month-old groups) and $N = 8$–11 (14-month-old group). In panels **(B,C)**, statistical significance in aged-matched groups was assessed using the non-parametric Mann–Whitney test (for 3-month-old mice) or unpaired two-tailed *t*-test (all other), $N = 5$ hearts per group; $^{*}P < 0.05$, $^{**}P < 0.01$, and $^{***}P < 0.005$.

superoxide-specific modifications of NADH dehydrogenase (77) or superoxide-dependent succinate ubiquinone reductase (SQR)-derived protein radical (78). It is worth adding that the extent of protein radicals reacting with DMPO is counterbalanced in part by intrinsic reactions with GSH (79, 80) (and ascorbate, molecular oxygen lipid, or other radicals), being a potential source of underestimation of oxidative modifications detected by IST (41).

In this work, we analyzed and quantified oxidative modifications not only in cardiomyocytes but also in coronary endothelium in Tgαq*44 hearts based on co-staining of the left ventricle with anti-DMPO and lectin antibodies that enabled the segmentation and quantification of DMPO nitrone adducts specific to the endothelium of large coronaries and microvessels. Literature describes the use of CD31 (81) or various lectins (82–84) for imaging of the capillary bed. In our experience, the lectin antibody (see Materials and Methods) was better suited to stain the capillary vessels within the left ventricle specimens, as reported previously (85). Compared with FVB controls, Tgαq*44 mice had more oxidative modifications found in the endothelium from the age of 10 months onward, regardless of whether large vessels (**Figure 4**) or capillaries (**Figure 6**) were analyzed. The most pronounced increase in oxidative modifications to the endothelium of large coronaries and microvessels was found in the end-stage of HF, at 12–16 months of age. Using the lectin-positive staining, we were also able to quantify the capillary density in the left ventricle (**Figure 5**). For the youngest mice group, both Tgαq*44 and control mice exhibit start with around 2,000 capillaries/mm^2. Already at 10 months of age, Tgαq*44 mice display a significant decrease in capillary density, which progressed to below 1,000 capillaries/mm^2 for 16-month-old Tgαq*44 mice. The loss of capillaries in this HF model was not due to cardiomyocyte hypertrophy, as normalization of number of capillaries to cardiomyocyte length, width or their volume, did also confirm capillary loss (data not shown). Interestingly, as shown by Tyrankiewicz et al. (54), a prominent ACE/Ang II pathway activation was present at the phase of decompensated HF suggesting that ACE/Ang II pathway could be involved in development of coronary endothelial damage (86). Obviously, number of other mechanisms could be involved in coronary capillary loss and their dysfunction in HF in Tgαq*44 mice, and they were not studied here.

Various *in vivo* studies using DMPO-based IST are described in literature; however, this work is the first to implement and extend the IST methodology in an *in vivo* protracted HF model, with an additional emphasis on cellular localization and recognition

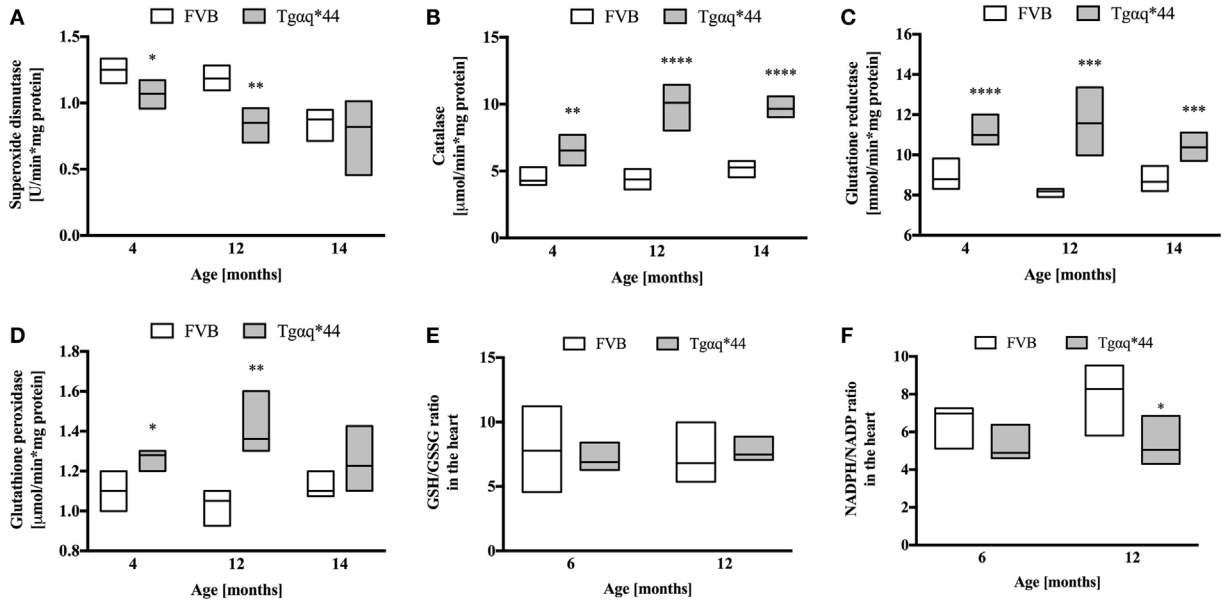

FIGURE 8 | Levels of endogenous antioxidant enzymes activity and redox state in the hearts of Tgαq*44 vs FVB mice. **(A)** Superoxide dismutase, **(B)** catalase, **(C)** glutathione reductase, **(D)** glutathione peroxidase (GPx), **(E)** GSH/GSSG ratio, and **(F)** NADPH/NADP ratio. Data represent median ± IQR, $N = 4–8$ mice/group. Statistical significance between aged-matched groups was assessed using an unpaired two-tailed *t*-test, except data for GPx and 4-month data for catalase, where the non-parametric Mann–Whitney *U* test was used; $^{*}P < 0.05$, $^{**}P < 0.01$, $^{***}P < 0.005$, and $^{****}P < 0.001$.

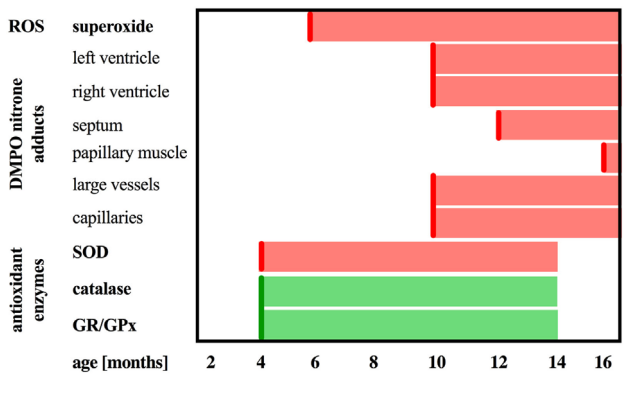

FIGURE 9 | Summary of DMPO immuno-spin trapping results in relation to reactive oxygen species generation and antioxidant activity in Tgαq*44 mice. Scheme representing the sequence of events in terms of upregulation of catalase and glutathione reductase and peroxidase (GR/GPx), downregulation of superoxide dismutase (SOD) activity, increased superoxide production in the heart, followed by oxidative modifications in the heart in the relation to the age of Tgαq*44 mice.

of the progression of oxidative modifications in the cardiomyocytes and coronary endothelium in relationship with functional deteriorations of the cardiac function in this model as reported previously (54). Indeed, most previous work studied the effects of acute and lethal oxidative interventions, such as acetone-induced ketosis (87), lipopolysaccharide-induced systemic inflammation (76), or rat liver ischemia/reperfusion injury model (88). A more recent report described free radical formation in high fat diet in mice and in monocrotaline-induced pulmonary hypertension, and right HF rat model (43), demonstrated considerably more DMPO nitrone adducts in both diseases; however, the authors did analyze only the late stage of the disease progression. In contrast, in this work, we provided evidence that IST can reveal progressive nature of oxidative modifications along the extended time period of the progression of HF in Tgαq*44 mice (52).

CONCLUSION

In this work, we characterized oxidative modifications in HF in Tgαq*44 mice. The increased abundance of DMPO nitrone adducts identified in the myocardium of Tgαq*44 mice occurred at the stage of impairment of basal systolic and diastolic cardiac performance, and diminished capillarization of Tgαq*44 hearts, suggesting that the presence of DMPO nitrone adducts in cardiomyocytes, and in coronary endothelium may reflect a stage of a significant cardiac and cardiac capillaries damage of a failing heart. Given the fact that HF in Tgαq*44 mice is initiated by a cardiomyocyte-specific alteration, development of oxidative modifications in parallel in cardiomyocytes and in the endothelium of large coronaries and capillaries suggests that a cardiomyocyte-derived mechanism is responsible for coronary capillaries damage and might contribute to the progression of HF in Tgαq*44 mice. The nature of this mechanism remains to be established.

ETHICS STATEMENT

All experimental procedures were compliant with the Guide for the Care and Use of Laboratory Animals published by the U.S. National Institutes of Health (NIH Publication No. 85-23, revised

1996) and were approved by the Second Local Ethical Committee on Animal Testing at the Institute of Pharmacology PAN in Krakow, Poland (permit no. 15/2016).

AUTHOR CONTRIBUTIONS

Conceived and designed the study: BP and SC. Performed the study: BP, JC, TK, KK, and AZ. Analyzed the data: BP and JC. Drafted the manuscript: BP, JC, and SC. All the authors have corrected or have approved the final version of the manuscript.

FUNDING

This study was supported by the National Science Centre, Miniatura I grant no. DEC-2017/01/X/NZ5/01104 and Symfonia grant no. DEC-2015/16/W/NZ4/00070.

REFERENCES

1. Benjamin EJ, Blaha MJ, Chiuve SE, Cushman M, Das SR, Deo R, et al. Heart disease and stroke statistics-2017 update: a report from the American Heart Association. *Circulation* (2017) 135(10):e146–603. doi:10.1161/CIR.0000000000000485
2. Moris D, Spartalis M, Tzatzaki E, Spartalis E, Karachaliou GS, Triantafyllis AS, et al. The role of reactive oxygen species in myocardial redox signaling and regulation. *Ann Transl Med* (2017) 5(16):324–324. doi:10.21037/atm.2017.06.17
3. Shah AM, Mann DL. In search of new therapeutic targets and strategies for heart failure: recent advances in basic science. *Lancet* (2011) 378(9792):704–12. doi:10.1016/S0140-6736(11)60894-5
4. Elas M, Bielanska J, Pustelny K, Plonka PM, Drelicharz L, Skorka T, et al. Detection of mitochondrial dysfunction by EPR technique in mouse model of dilated cardiomyopathy. *Free Radic Biol Med* (2008) 45(3):321–8. doi:10.1016/j.freeradbiomed.2008.04.016
5. Santos CX, Raza S, Shah AM. Redox signaling in the cardiomyocyte: from physiology to failure. *Int J Biochem Cell Biol* (2016) 74:145–51. doi:10.1016/j.biocel.2016.03.002
6. Heymes C, Bendall JK, Ratajczak P, Cave AC, Samuel JL, Hasenfuss G, et al. Increased myocardial NADPH oxidase activity in human heart failure. *J Am Coll Cardiol* (2003) 41(12):2164–71. doi:10.1016/S0735-1097(03)00471-6
7. Sirokmány G, Donkó Á, Geiszt M. Nox/duox family of NADPH oxidases: lessons from knockout mouse models. *Trends Pharmacol Sci* (2016) 37(4):318–27. doi:10.1016/j.tips.2016.01.006
8. Zhang M, Brewer AC, Schröder K, Santos CX, Grieve DJ, Wang M, et al. NADPH oxidase-4 mediates protection against chronic load-induced stress in mouse hearts by enhancing angiogenesis. *Proc Natl Acad Sci U S A* (2010) 107(42):18121–6. doi:10.1073/pnas.1009700107
9. Kuroda J, Ago T, Matsushima S, Zhai P, Schneider MD, Sadoshima J. NADPH oxidase 4 (Nox4) is a major source of oxidative stress in the failing heart. *Proc Natl Acad Sci U S A* (2010) 107(35):15565–70. doi:10.1073/pnas.1002178107
10. Burgoyne JR, Mongue-Din H, Eaton P, Shah AM. Redox signaling in cardiac physiology and pathology. *Circ Res* (2012) 111(8):1091–106. doi:10.1161/CIRCRESAHA.111.255216
11. Katare PB, Bagul PK, Dinda AK, Banerjee SK. Toll-like receptor 4 inhibition improves oxidative stress and mitochondrial health in isoproterenol-induced cardiac hypertrophy in rats. *Front Immunol* (2017) 8:341. doi:10.3389/fimmu.2017.00719
12. Sun X-Q, Abbate A, Bogaard H-J. Role of cardiac inflammation in right ventricular failure. *Cardiovasc Res* (2017) 113(12):1441–52. doi:10.1093/cvr/cvx159
13. Toprak G, Yüksel H, Demirpençe Ö, Islamoglu Y, Evliyaoglu O, Mete N. Fibrosis in heart failure subtypes. *Eur Rev Med Pharmacol Sci* (2013) 17(17):2302–9.
14. Münzel T, Camici GG, Maack C, Bonetti NR, Fuster V, Kovacic JC. Impact of oxidative stress on the heart and vasculature: part 2 of a 3-part series. *J Am Coll Cardiol* (2017) 70(2):212–29. doi:10.1016/j.jacc.2017.05.035
15. Handy DE, Loscalzo J. Responses to reductive stress in the cardiovascular system. *Free Radic Biol Med* (2017) 109:114–24. doi:10.1016/j.freeradbiomed.2016.12.006
16. Chouchani ET, Pell VR, Gaude E, Aksentijević D, Sundier SY, Robb EL, et al. Ischaemic accumulation of succinate controls reperfusion injury through mitochondrial ROS. *Nature* (2014) 515(7527):431–5. doi:10.1038/nature13909
17. Logan A, Shabalina IG, Prime TA, Rogatti S, Kalinovich AV, Hartley RC, et al. In vivo levels of mitochondrial hydrogen peroxide increase with age in mtDNA mutator mice. *Aging Cell* (2014) 13(4):765–8. doi:10.1111/acel.12212
18. Dikalov S, Griendling KK, Harrison DG. Measurement of reactive oxygen species in cardiovascular studies. *Hypertension* (2007) 49(4):717–27. doi:10.1161/01.HYP.0000258594.87211.6b
19. Villamena FA, Zweier JL. Detection of reactive oxygen and nitrogen species by EPR spin trapping. *Antioxid Redox Signal* (2004) 6(3):619–29. doi:10.1089/152308604773934387
20. Lee R, Margaritis M, Channon KM, Antoniades C. Evaluating oxidative stress in human cardiovascular disease: methodological aspects and considerations. *Curr Med Chem* (2012) 19(16):2504–20. doi:10.2174/092986712800493057
21. Zielonka J, Kalyanaraman B. Hydroethidine- and MitoSOX-derived red fluorescence is not a reliable indicator of intracellular superoxide formation: another inconvenient truth. *Free Radic Biol Med* (2010) 48(8):983–1001. doi:10.1016/j.freeradbiomed.2010.01.028
22. Zielonka J, Hardy M, Kalyanaraman B. HPLC study of oxidation products of hydroethidine in chemical and biological systems: ramifications in superoxide measurements. *Free Radic Biol Med* (2009) 46(3):329–38. doi:10.1016/j.freeradbiomed.2008.10.031
23. Daiber A, Oelze M, Steven S, Kröller-Schön S, Münzel T. Taking up the cudgels for the traditional reactive oxygen and nitrogen species detection assays and their use in the cardiovascular system. *Redox Biol* (2017) 12:35–49. doi:10.1016/j.redox.2017.02.001
24. Levine RL, Garland D, Oliver CN, Amici A, Climent I, Lenz AG, et al. Determination of carbonyl content in oxidatively modified proteins. *Methods Enzymol* (1990) 186:464–78. doi:10.1016/0076-6879(90)86141-H
25. Nuriel T, Deeb RS, Hajjar DP, Gross SS. Protein 3-nitrotyrosine in complex biological samples: quantification by high-pressure liquid chromatography/electrochemical detection and emergence of proteomic approaches for unbiased identification of modification sites. *Methods Enzymol* (2008) 441:1–17. doi:10.1016/S0076-6879(08)01201-9
26. Milne GL, Dai Q, Roberts LJ. The isoprostanes – 25 years later. *Biochim Biophys Acta* (2015) 1851(4):433–45. doi:10.1016/j.bbalip.2014.10.007
27. Di Minno A, Turnu L, Porro B, Squellerio I, Cavalca V, Tremoli E, et al. 8-hydroxy-2-deoxyguanosine levels and heart failure: a systematic review and meta-analysis of the literature. *Nutr Metab Cardiovasc Dis* (2017) 27(3):201–8. doi:10.1016/j.numecd.2016.10.009
28. Cooke MS, Olinski R, Evans MD. Does measurement of oxidative damage to DNA have clinical significance? *Clin Chim Acta* (2006) 365(1–2):30–49. doi:10.1016/j.cca.2005.09.009
29. Yücel D, Aydoğdu S, Cehreli S, Saydam G, Canatan H, Seneş M, et al. Increased oxidative stress in dilated cardiomyopathic heart failure. *Clin Chem* (1998) 44(1):148–54.
30. Yücel D, Aydoğdu S, Seneş M, Topkaya BC, Nebioğlu S. Evidence of increased oxidative stress by simple measurements in patients with dilated cardiomyopathy. *Scand J Clin Lab Invest* (2002) 62(6):463–8. doi:10.1080/00365510260390019
31. Griendling KK, Touyz RM, Zweier JL, Dikalov S, Chilian W, Chen YR, et al. Measurement of reactive oxygen species, reactive nitrogen species, and redox-dependent signaling in the cardiovascular system: a scientific statement from the American Heart Association. *Circ Res* (2016) 119(5):e39–75. doi:10.1161/RES.0000000000000110
32. Trachtenberg BH, Hare JM. Biomarkers of oxidative stress in heart failure. *Heart Fail Clin* (2009) 5(4):561–77. doi:10.1016/j.hfc.2009.04.003
33. Frijhoff J, Winyard PG, Zarkovic N, Davies SS, Stocker R, Cheng D, et al. Clinical relevance of biomarkers of oxidative stress. *Antioxid Redox Signal* (2015) 23(14):1144–70. doi:10.1089/ars.2015.6317

34. Ho E, Karimi Galougahi K, Liu CC, Bhindi R, Figtree GA. Biological markers of oxidative stress: applications to cardiovascular research and practice. *Redox Biol* (2013) 1(1):483–91. doi:10.1016/j.redox.2013.07.006
35. Marrocco I, Altieri F, Peluso I. Measurement and clinical significance of biomarkers of oxidative stress in humans. *Oxid Med Cell Longev* (2017) 2017:6501046. doi:10.1155/2017/6501046
36. Mason RP. Using anti-5,5-dimethyl-1-pyrroline N-oxide (anti-DMPO) to detect protein radicals in time and space with immuno-spin trapping. *Free Radic Biol Med* (2004) 36(10):1214–23. doi:10.1016/j.freeradbiomed.2004.02.077
37. Khan N, Wilmot CM, Rosen GM, Demidenko E, Sun J, Joseph J, et al. Spin traps: in vitro toxicity and stability of radical adducts. *Free Radic Biol Med* (2003) 34(11):1473–81. doi:10.1016/S0891-5849(03)00182-5
38. Schaefer CF, Janzen EG, West MS, Poyer JL, Kosanke SD. Blood chemistry changes in the rat induced by high doses of nitronyl free radical spin traps. *Free Radic Biol Med* (1996) 21(4):427–36. doi:10.1016/0891-5849(96)00039-1
39. Ramirez DC, Mason RP. Immuno-spin trapping: detection of protein-centered radicals. *Curr Protoc Toxicol* (2005) Chapter 17:Unit 17.7. doi:10.1002/0471140856.tx1707s24
40. Ramirez DC, Gomez-Mejiba SE, Mason RP. Immuno-spin trapping analyses of DNA radicals. *Nat Protoc* (2007) 2(3):512–22. doi:10.1038/nprot.2007.5
41. Gomez-Mejiba SE, Zhai Z, Della-Vedova MC, Muñoz MD, Chatterjee S, Towner RA, et al. Immuno-spin trapping from biochemistry to medicine: advances, challenges, and pitfalls. Focus on protein-centered radicals. *Biochim Biophys Acta* (2014) 1840(2):722–9. doi:10.1016/j.bbagen.2013.04.039
42. Detweiler CD, Deterding LJ, Tomer KB, Chignell CF, Germolec D, Mason RP. Immunological identification of the heart myoglobin radical formed by hydrogen peroxide. *Free Radic Biol Med* (2002) 33(3):364–9. doi:10.1016/S0891-5849(02)00895-X
43. Khoo NK, Cantu-Medellin N, Devlin JE, St Croix CM, Watkins SC, Fleming AM, et al. Obesity-induced tissue free radical generation: an in vivo immuno-spin trapping study. *Free Radic Biol Med* (2012) 52(11–12):2312–9. doi:10.1016/j.freeradbiomed.2012.04.011
44. Mason RP. Imaging free radicals in organelles, cells, tissue, and in vivo with immuno-spin trapping. *Redox Biol* (2016) 8:422–9. doi:10.1016/j.redox.2016.04.003
45. Towner RA, Smith N, Doblas S, Tesiram Y, Garteiser P, Saunders D, et al. In vivo detection of C-met expression in a rat C6 glioma model. *J Cell Mol Med* (2008) 12(1):174–86. doi:10.1111/j.1582-4934.2008.00220.x
46. Towner RA, Smith N, Saunders D, De Souza PC, Henry L, Lupu F, et al. Combined molecular MRI and immuno-spin-trapping for in vivo detection of free radicals in orthotopic mouse GL261 gliomas. *Biochim Biophys Acta* (2013) 1832(12):2153–61. doi:10.1016/j.bbadis.2013.08.004
47. Towner RA, Garteiser P, Bozza F, Smith N, Saunders D, d' Avila JC, et al. In vivo detection of free radicals in mouse septic encephalopathy using molecular MRI and immuno-spin trapping. *Free Radic Biol Med* (2013) 65(December):828–37. doi:10.1016/j.freeradbiomed.2013.08.172
48. Towner RA, Smith N, Saunders D, Lupu F, Silasi-Mansat R, West M, et al. In vivo detection of free radicals using molecular MRI and immuno-spin trapping in a mouse model for amyotrophic lateral sclerosis. *Free Radic Biol Med* (2013) 63:351–60. doi:10.1016/j.freeradbiomed.2013.05.026
49. Towner RA, Smith N, Saunders D, Carrizales J, Lupu F, Silasi-Mansat R, et al. In vivo targeted molecular magnetic resonance imaging of free radicals in diabetic cardiomyopathy within mice. *Free Radic Res* (2015) 49(9):1140–6. doi:10.3109/10715762.2015.1050587
50. Mende U, Semsarian C, Martins DC, Kagen A, Duffy C, Schoen FJ, et al. Dilated cardiomyopathy in two transgenic mouse lines expressing activated G protein alpha(Q): lack of correlation between phospholipase C activation and the phenotype. *J Mol Cell Cardiol* (2001) 33(8):1477–91. doi:10.1006/jmcc.2001.1411
51. Mackiewicz U, Czarnowska E, Brudek M, Pajak B, Duda M, Emanuel K, et al. Preserved cardiomyocyte function and altered desmin pattern in transgenic mouse model of dilated cardiomyopathy. *J Mol Cell Cardiol* (2012) 52(5):1–10. doi:10.1016/j.yjmcc.2012.01.008
52. Edes IF, Tóth A, Csányi G, Lomnicka M, Chłopicki S, Edes I, et al. Late-stage alterations in myofibrillar contractile function in a transgenic mouse model of dilated cardiomyopathy (Tgalphaq*44). *J Mol Cell Cardiol* (2008) 45(3):363–72. doi:10.1016/j.yjmcc.2008.07.001
53. Woźniak M, Tyrankiewicz U, Drelicharz Ł, Skórka T, Jabłońska M, Heinze-Paluchowska S, et al. Wpływ Zahamowania Układu Renina–Angiotensyna–Aldosteron Na Czynność Mięśnia Sercowego We Wczesnym I Późnym Etapie Rozwoju Kardiomiopatii Rozstrzeniowej U Myszy Tgaq*44. *Kardiol Pol* (2013) 71(7):730–7. doi:10.5603/KP.2013.0161
54. Tyrankiewicz U, Olkowicz M, Skórka T, Jablonska M, Orzyłowska A, Bar A, et al. Activation pattern of ACE2/Ang-(1-7) and ACE/Ang II pathway in course of heart failure assessed by multiparametric MRI in vivo in Tgαq*44 mice. *J Appl Physiol* (2017) 124(1):52–65. doi:10.1152/japplphysiol.00571.2017
55. Czarnowska E, Bierła JB, Toczek M, Tyrankiewicz U, Pajak B, Domal-Kwiatkowska D, et al. Narrow time window of metabolic changes associated with transition to overt heart failure in Tgaq*44 mice. *Pharmacol Rep* (2016) 68(4):707–14. doi:10.1016/j.pharep.2016.03.013
56. Drelicharz L, Kozlovski V, Skorka T, Heinze-Paluchowska S, Jasinski A, Gebska A, et al. NO and PGI2 in coronary endothelial dysfunction in transgenic mice with dilated cardiomyopathy. *Basic Res Cardiol* (2008) 103(5):417–30. doi:10.1007/s00395-008-0723-2
57. Grassi B, Majerczak J, Bardi E, Buso A, Comelli M, Chlopicki S, et al. Exercise training in Tgαq*44 mice during the progression of chronic heart failure: cardiac vs. peripheral (soleus muscle) impairments to oxidative metabolism. *J Appl Physiol* (2017) 123(2):326–36. doi:10.1152/japplphysiol.00342.2017
58. Schneider CA, Rasband WS, Eliceiri KW. NIH Image to ImageJ: 25 years of image analysis. *Nat Methods* (2012) 9(7):671–5. doi:10.1038/nmeth.2089
59. Rivero-Gutiérrez B, Anzola A, Martínez-Augustin O, Sánchez de Medina F. Stain-free detection as loading control alternative to ponceau and house-keeping protein immunodetection in western blotting. *Anal Biochem* (2014) 467:1–3. doi:10.1016/j.ab.2014.08.027
60. Zielonka J, Vasquez-Vivar J, Kalyanaraman B. Detection of 2-hydroxyethidium in cellular systems: a unique marker product of superoxide and hydroethidine. *Nat Protoc* (2008) 3(1):8–21. doi:10.1038/nprot.2007.473
61. Kaczara P, Motterlini R, Kus K, Zakrzewska A, Abramov AY, Chlopicki S. Carbon monoxide shifts energetic metabolism from glycolysis to oxidative phosphorylation in endothelial cells. *FEBS Lett* (2016) 590(20):3469–80. doi:10.1002/1873-3468.12434
62. Misra HP, Fridovich I. The role of superoxide anion in the autoxidation of epinephrine and a simple assay for superoxide dismutase. *J Biol Chem* (1972) 247(10):3170–5.
63. Aebi H. Catalase in vitro. *Methods Enzymol* (1984) 105:121–6. doi:10.1016/S0076-6879(84)05016-3
64. Carlberg I, Mannervik B. Glutathione reductase. *Methods Enzymol* (1985) 113:484–90. doi:10.1016/S0076-6879(85)13062-4
65. Moin VM. [A simple and specific method for determining glutathione peroxidase activity in erythrocytes]. *Lab Delo* (1986) 12:724–7.
66. Ellman GL. Tissue sulfhydryl groups. *Arch Biochem Biophys* (1959) 82(1):70–7. doi:10.1016/0003-9861(59)90090-6
67. Bradford MM. A rapid and sensitive method for the quantitation of microgram quantities of protein utilizing the principle of protein-dye binding. *Anal Biochem* (1976) 72:248–54. doi:10.1016/0003-2697(76)90527-3
68. Kaczara P, Proniewski B, Lovejoy C, Kus K, Motterlini R, Abramov AY, et al. CORM-401 induces calcium signalling, NO increase and activation of pentose phosphate pathway in endothelial cells. *FEBS J* (2018) 285:1346–58. doi:10.1111/febs.14411
69. Tyrankiewicz U, Skórka T, Jablonska M, Petkow-Dimitrow P, Chlopicki S. Characterization of the cardiac response to a low and high dose of dobutamine in the mouse model of dilated cardiomyopathy by MRI in vivo. *J Magn Reson Imaging* (2013) 37(3):669–77. doi:10.1002/jmri.23854
70. Qin F, Lennon-Edwards S, Lancel S, Biolo A, Siwik DA, Pimentel DR, et al. Cardiac-specific overexpression of catalase identifies hydrogen peroxide-dependent and -independent phases of myocardial remodeling and prevents the progression to overt heart failure in G(alpha)Q-overexpressing transgenic mice. *Circ Heart Fail* (2010) 3(2):306–13. doi:10.1161/CIRCHEARTFAILURE.109.864785
71. Zhang M, Mongue-Din H, Martin D, Catibog N, Smyrnias I, Zhang X, et al. Both cardiomyocyte and endothelial cell Nox4 mediate protection against hemodynamic overload-induced remodeling. *Cardiovasc Res* (2017) 110:1364. doi:10.1093/cvr/cvx204
72. Shiomi T, Tsutsui H, Matsusaka H, Murakami K, Hayashidani S, Ikeuchi M, et al. Overexpression of glutathione peroxidase prevents left ventricular remodeling and failure after myocardial infarction in mice. *Circulation* (2004) 109(4):544–9. doi:10.1161/01.CIR.0000109701.77059.E9

73. Ng LL, O'Brien RJ, Quinn PA, Squire IB, Davies JE. Oxygen-regulated protein 150 and prognosis following myocardial infarction. *Clin Sci* (2007) 112(9):477–84. doi:10.1042/CS20060304
74. Ozawa K, Kondo T, Hori O, Kitao Y, Stern DM, Eisenmenger W, et al. Expression of the oxygen-regulated protein ORP150 accelerates wound healing by modulating intracellular VEGF transport. *J Clin Invest* (2001) 108(1): 41–50. doi:10.1172/JCI200111772
75. Gomez-Mejiba SE, Zhai Z, Akram H, Deterding LJ, Hensley K, Smith N, et al. Immuno-spin trapping of protein and DNA radicals: 'tagging' free radicals to locate and understand the redox process. *Free Radic Biol Med* (2009) 46(7):853–65. doi:10.1016/j.freeradbiomed.2008.12.020
76. Chatterjee S, Ehrenshaft M, Bhattacharjee S, Deterding LJ, Bonini MG, Corbett J, et al. Immuno-spin trapping of a post-translational carboxypeptidase B1 radical formed by a dual role of xanthine oxidase and endothelial nitric oxide synthase in acute septic mice. *Free Radic Biol Med* (2009) 46(4):454–61. doi:10.1016/j.freeradbiomed.2008.10.046
77. Chen Y-R, Chen C-L, Zhang L, Green-Church KB, Zweier JL. Superoxide generation from mitochondrial NADH dehydrogenase induces self-inactivation with specific protein radical formation. *J Biol Chem* (2005) 280(45):37339–48. doi:10.1074/jbc.M503936200
78. Chen Y-R, Chen C-L, Pfeiffer DR, Zweier JL. Mitochondrial complex II in the post-ischemic heart: oxidative injury and the role of protein S-glutathionylation. *J Biol Chem* (2007) 282(45):32640–54. doi:10.1074/jbc.M702294200
79. Gebicki JM, Nauser T, Domazou A, Steinmann D, Bounds PL, Koppenol WH. Reduction of protein radicals by GSH and ascorbate: potential biological significance. *Amino Acids* (2010) 39(5):1131–7. doi:10.1007/s00726-010-0610-7
80. Nauser T, Gebicki JM. Reaction rates of glutathione and ascorbate with Alkyl radicals are too slow for protection against protein peroxidation in vivo. *Arch Biochem Biophys* (2017) 633:118–23. doi:10.1016/j.abb.2017.09.011
81. Ismail JA, Poppa V, Kemper LE, Scatena M, Giachelli CM, Coffin JD, et al. Immunohistologic labeling of murine endothelium. *Cardiovasc Pathol* (2003) 12(2):82–90. doi:10.1016/S1054-8807(02)00166-7
82. Laitinen L. *Griffonia simplicifolia* lectins bind specifically to endothelial cells and some epithelial cells in mouse tissues. *Histochem J* (1987) 19(4):225–34. doi:10.1007/BF01680633
83. Alroy J, Goyal V, Skutelsky E. Lectin histochemistry of mammalian endothelium. *Histochemistry* (1987) 86(6):603–7. doi:10.1007/BF00489554
84. Porter GA, Palade GE, Milici AJ. Differential binding of the lectins *Griffonia simplicifolia* I and *Lycopersicon esculentum* to microvascular endothelium: organ-specific localization and partial glycoprotein characterization. *Eur J Cell Biol* (1990) 51(1):85–95.
85. Ren G, Michael LH, Entman ML, Frangogiannis NG. Morphological characteristics of the microvasculature in healing myocardial infarcts. *J Histochem Cytochem* (2002) 50(1):71–9. doi:10.1177/002215540205000108
86. Olkowicz M, Chlopicki S, Smoleński RT. Perspectives for angiotensin profiling with liquid chromatography/mass spectrometry to evaluate ACE/ACE2 balance in endothelial dysfunction and vascular pathologies. *Pharmacol Rep* (2015) 67(4):778–85. doi:10.1016/j.pharep.2015.03.017
87. Stadler K, Bonini MG, Dallas S, Duma D, Mason RP, Kadiiska MB. Direct evidence of iNOS-mediated in vivo free radical production and protein oxidation in acetone-induced ketosis. *Am J Physiol Endocrinol Metab* (2008) 295(2):E456–62. doi:10.1152/ajpendo.00015.2008
88. Dogan S, Ozlem Elpek G, Kirimlioglu Konuk E, Demir N, Aslan M. Measurement of intracellular biomolecular oxidation in liver ischemia-reperfusion injury via immuno-spin trapping. *Free Radic Biol Med* (2012) 53(3):406–14. doi:10.1016/j.freeradbiomed.2012.05.028

Conflict of Interest Statement: The authors declare that the research was conducted in the absence of any commercial or financial relationships that could be construed as a potential conflict of interest.

frontiers in Immunology

ORIGINAL RESEARCH
published: 12 June 2018
doi: 10.3389/fimmu.2018.01309

Hsp70 Suppresses Mitochondrial Reactive Oxygen Species and Preserves Pulmonary Microvascular Barrier Integrity Following Exposure to Bacterial Toxins

Xueyi Li[1], Yanfang Yu[1,2], Boris Gorshkov[1], Stephen Haigh[1], Zsuzsanna Bordan[1], Daniel Weintraub[1], Radu Daniel Rudic[3], Trinad Chakraborty[4], Scott A. Barman[3], Alexander D. Verin[1], Yunchao Su[3], Rudolf Lucas[1,3], David W. Stepp[3], Feng Chen[1,2] and David J. R. Fulton[1,3]**

[1] Vascular Biology Center, Medical College of Georgia at Augusta University, Augusta, Georgia, [2] Department of Forensic Medicine, Nanjing Medical University, Nanjing, Jiangsu, China, [3] Department of Pharmacology and Toxicology, Medical College of Georgia at Augusta University, Augusta, GA, United States, [4] Institute for Medical Microbiology, Justus-Liebig University Giessen, Giessen, Germany

OPEN ACCESS

Edited by:
Christoph Thiemermann,
Queen Mary University of London,
United Kingdom

Reviewed by:
Andrey V. Kozlov,
Institute for Experimental and Clinical Traumatology (LBG), Austria
Andrew C. B. Cato,
Karlsruher Institut für Technologie,
Germany

***Correspondence:**
Feng Chen
fchen@njmu.edu.cn;
David J. R. Fulton
dfulton@augusta.edu

Specialty section:
This article was submitted to Inflammation, a section of the journal Frontiers in Immunology

Received: 02 March 2018
Accepted: 25 May 2018
Published: 12 June 2018

Citation:
Li X, Yu Y, Gorshkov B, Haigh S, Bordan Z, Weintraub D, Rudic RD, Chakraborty T, Barman SA, Verin AD, Su Y, Lucas R, Stepp DW, Chen F and Fulton DJR (2018) Hsp70 Suppresses Mitochondrial Reactive Oxygen Species and Preserves Pulmonary Microvascular Barrier Integrity Following Exposure to Bacterial Toxins. Front. Immunol. 9:1309. doi: 10.3389/fimmu.2018.01309

Pneumonia is a leading cause of death in children and the elderly worldwide, accounting for 15% of all deaths of children under 5 years old. *Streptococcus pneumoniae* is a common and aggressive cause of pneumonia and can also contribute to meningitis and sepsis. Despite the widespread use of antibiotics, mortality rates for pneumonia remain unacceptably high in part due to the release of bacterial toxins. Pneumolysin (PLY) is a cholesterol-dependent toxin that is produced by *Streptococcus*, and it is both necessary and sufficient for the development of the extensive pulmonary permeability edema that underlies acute lung injury. The mechanisms by which PLY disrupts the pulmonary endothelial barrier are not fully understood. Previously, we found that reactive oxygen species (ROS) contribute to the barrier destructive effects of PLY and identified an unexpected but potent role of Hsp70 in suppressing ROS production. The ability of Hsp70 to influence PLY-induced barrier dysfunction is not yet described, and the goal of the current study was to identify whether Hsp70 upregulation is an effective strategy to protect the lung microvascular endothelial barrier from G^+ bacterial toxins. Overexpression of Hsp70 *via* adenovirus-mediated gene transfer attenuated PLY-induced increases in permeability in human lung microvascular endothelial cells (HLMVEC) with no evidence of cytotoxicity. To adopt a more translational approach, we employed a pharmacological approach using geranylgeranylacetone (GGA) to acutely upregulate endogenous Hsp70 expression. Following acute treatment (6 h) with GGA, HLMVECs exposed to PLY displayed improved cell viability and enhanced endothelial barrier function as measured by both Electric Cell-substrate Impedance Sensing (ECIS) and transwell permeability assays compared to control treated cells. PLY promoted increased mitochondrial ROS, decreased mitochondrial oxygen consumption, and increased caspase 3 cleavage and cell death, which were collectively improved in cells pretreated with GGA. In mice, IP

pretreatment with GGA 24 h prior to IT administration of PLY resulted in significantly less Evans Blue Dye extravasation compared to vehicle, indicating preserved endothelial barrier integrity and suggesting that the acute upregulation of Hsp70 may be an effective therapeutic approach in the treatment of lung injury associated with pneumonia.

Keywords: pneumolysin, endothelial barrier, reactive oxygen species, mitochondria, Hsp70

INTRODUCTION

Pneumonia is a pulmonary infection that can affect people of all ages, but is most severe in the elderly, children, and the immunocompromised. Infection and subsequent inflammation compromise the function of lung endothelial and epithelial barriers resulting in alveolar flooding, impaired gas exchange, and eventually lung consolidation, which collectively underlie the development of acute lung injury (ALI) and its more severe form, acute respiratory distress syndrome (ARDS) (1). Multiple pathogens can promote pneumonia, including bacteria, fungi, and viruses. Bacteria, in particular Gram positive (G^+) bacteria, are the most common cause (2, 3). Currently there are no effective pharmacological approaches for ALI/ARDS and patients treated with anti-inflammatory steroids treatment remain at significant risk of mortality (4).

A hallmark feature of ALI/ARDS is dysfunction of the pulmonary microvascular endothelial barrier resulting in an imbalance of Starling's forces and the passage of excess fluid into the alveoli (1). The mechanisms underlying the loss of the microvascular barrier function are complicated and involve diverse mechanisms in multiple cell types which can vary depending on the causative agent. A major cause of ALI is G^+ bacteria including *Streptococcus pneumoniae* which accounts for up to half of all community-acquired pneumonia (CAP) cases in the US and CAP is the most frequent cause of ARDS (3). Greater than 500,000 yearly cases of pneumonia and 25,000 pneumococcal-related deaths are reported in the US alone, resulting in a health-care burden that exceeds $5 billion dollars (5). The first-line treatment for *Streptococcus* pneumonia is antibiotic therapy. However, the onset of ARDS is resistant to antibiotics and paradoxically, bacteriolytic antibiotics can exacerbate lung injury (6). One likely reason for this is the G^+ toxin, pneumolysin (PLY), which is produced in *Streptococcus* and released by autolysis and in greater amounts in the presence of antibiotics that compromise the bacterial cell wall (7). PLY is a 53-kDa intracellular protein which belongs to the cholesterol-dependent cytolysin family (8). Upon binding to cholesterol molecules on the cell membrane of target cells, PLY induces the macromolecular assembly of ring shaped pores that promote calcium influx and alter intracellular signaling (9, 10). Subsequent to these changes, G^+-toxins robustly increase the intracellular production of reactive oxygen species (ROS) (6, 7, 11–13). Elevated ROS have been shown to have important roles in regulating a number of physiological and pathophysiological events, including cell apoptosis, survival, proliferation and migration, cell metabolism, DNA damage, inflammation, and disruption of the endothelial barrier (14). The major sources of ROS in endothelial cells are the NADPH oxidases (NOX enzymes), uncoupled eNOS, and the mitochondria. G^+-toxins have been reported to activate PKC and alter eNOS fidelity to disrupt the balance of nitric oxide and superoxide (13), activate NADPH oxidase (7), and increase mitochondria-derived ROS (mtROS) (15). There are also significant interactions between these ROS generating systems, where mitochondrial ROS can activate NOX enzymes and *vice versa* and increased ROS can lead to eNOS uncoupling and ROS production. Mitochondrial DNA (mtDNA) is highly sensitive to ROS and loss of mtDNA integrity can result in mitochondrial dysfunction, ATP deprivation, and cell apoptosis (16–19). NADPH-derived ROS have been shown to promote oxidative damage of mitochondrial proteins in particularly, complex I and complex II, which results in increased mitoROS production (20). Increased mitoROS can activate NADPH oxidase promoting a feed-forward relationship (20, 21). NOX2 has been identified as a potential target for mitochondrial superoxide production in endothelial cells (21, 22) and increased mtROS, secondary to a partial deficiency of mitochondrial superoxide dismutase, can trigger a cytosolic oxidative burst (21). On the other hand, inhibitors that reduce mtROS can also attenuate cytosolic ROS (21–23). ROS can deplete BH4 and alter the S-glutathionylation of eNOS, compromising NO formation and increasing ROS production (24, 25).

Mitochondria are increasingly recognized for their contributions to inflammation, and mtROS is a key factor mediating this process in endothelial cells in response to both physiological and pathophysiological stressors (16, 19). Along with the activation of NOX enzymes, mtROS also promote the activation of endothelial cells and increase proinflammatory cytokines (26) in a manner synergistic with cytosolic ROS. Antioxidants targeted to the mitochondria can reduce endothelial inflammation in hypertension animal models (27). The inflammatory process during pneumonia is complex, and different in the young versus elderly patients. In aged patients, inflammation may initiate at slowly in the early phase compared to young patients, but is more robust and enduring in the later stages (28). This deregulated inflammatory response is a risk factor for death in elderly patients, and broad anti-inflammatory strategies can result in compromised elimination of pathogens.

Heat-shock proteins (Hsp) are intracellular "chaperones" that guide the behavior (folding, function, and fate) of newly synthesized proteins and also associate stably with many signaling molecules (29). They are critical to the maintenance of cellular homeostasis under both physiological and stressed conditions (30). The major chaperones are Hsp90 and Hsp70 which together with co-chaperones mediate protein folding, complex assembly, intracellular transport, and also degradation (31, 32). Previously, we and others have shown that Hsp90 binds specifically to Nox proteins to regulate enzyme stability and ROS production (33, 34).

We also found that Hsp90 inhibitors can robustly upregulate Hsp70 expression and that Hsp70 alone can potently suppress NOX-derived ROS production in human pulmonary arterial endothelial cells (35).

Hsp70 has also been shown to be important for cell survival (36) and regulating mitoROS and mtDNA integrity (37), but whether it can provide protection from PLY-induced endothelial injury and loss of endothelial barrier function by suppressing ROS is not yet known. Therefore, the goals of this study were to assess the importance of Hsp70 in protecting the pulmonary microvascular endothelium from PLY, to identify the underlying mechanisms, and to advance the possibility of targeting Hsp70 as a promising therapy for *Streptococcus*-induced pneumonia.

MATERIALS AND METHODS

Cells and Reagents

Human lung microvascular endothelial cells (HLMVECs) were obtained from Lonza. Cells were cultured with 5% CO_2 at 37°C using EBM-2 MV medium supplemented with EGM-2 MV that was purchased from Lonza. All of the *in vitro* experiments were performed using passage 3 to passage 5 HLMVECs. PLY was a gift from Dr. Trinad Chakraborty (Institute for Medical Microbiology, Justus-Liebig University, Giessen, Germany) PLY was purified from a recombinant *Listeria innocua* 6a strain expressing LPS-free PLY. Geranylgeranylacetone (GGA, Sigma) was prepared in DMSO. Tempol, LPS, Glucose, pyruvate, and L-glutamine were obtained from Millipore Sigma. Oligomycin, FCCP, and antimycin were provided in the Seahorse XF Cell Mito Stress Test Kit from Agilent. FITC dextran (Fluorescein isothiocyanate–dextran 4000 and Fluorescein isothiocyanate–dextran 70000) were obtained from Sigma. Antibodies for western blotting included Hsp70 from BD Bioscience, cleaved caspase 3, NF-κB, and GAPDH were from Cell Signaling and Hsp90 from BD Bioscience. Nox_1 antibody from Sigma. GFP and Hsp70 adenoviruses were generated in house using established methodologies (38, 39).

Animals

8- to 10-weeks-old male C57BL6 mice, weighing 19–21 g were obtained from Harlan and were kept at the animal facilities at Augusta University. All animal studies conformed to National Institutes of Health guidelines. The experimental procedure was approved by the Augusta University Institutional Animal Care and Use Committee.

Assessment of Pulmonary Vascular Barrier Function *In Vivo*

Mice were pretreated with 500 mg/kg GGA (in ethanol) administered IP 24 h prior to toxin instillation. Mice were anesthetized with IP ketamine (150 mg/kg) and acetylpromazine (15 mg/kg), the trachea was exposed and PLY (60 ng) instilled IT for 6 h *via* a 20-gauge catheter. Evans blue dye (EBD)/albumin mixture (30 mg/kg in saline; 0.5% EBD conjugated to 4% BSA, Fraction V; Sigma-Aldrich, St. Louis, MO, USA) was injected into the tail vein, 2 h prior the conclusion of the experiment, in order to assess vascular leak. The lungs were homogenized, incubated with formamide (18 h at + 60°C), and centrifuged at 5,000 × *g* for 30 min. The optical density of the supernatant was determined spectrophotometrically at 620–750 nm. The concentration of extravasated EBD in the lungs was calculated by using a standard curve (micrograms of EBD per gram of wet lung tissue), as described previously (40).

Western Blotting

Cells were washed three times with HBSS before lysing with Laemmli sample buffer. Lysed cells were briefly sonicated to ensure protein extraction, proteins size fractionated by SDS PAGE and transferred to nitrocellulose membranes. Membranes were incubated overnight at 4°C with antibodies diluted to the manufacturer's specifications. Secondary IgG antibodies (Invitrogen) conjugated with horseradish peroxidase were used to detect antigen–antibody complexes.

Cell Viability Assay

Cell viability was assessed using the Muse Cell Analyzer (Millipore Sigma). HLMVECs were seeded at a density of 6×10^5 in 6-well plates with complete EBM-2 MV culture medium with or without 30 μM GGA or DMSO for 6 h. PLY was added to dishes 4 h before the viability test. The percentage of live HLMVECs was determined using the Muse cell count and viability kit (Millipore Sigma). In brief, 50 μl of suspended HLMVECs was mixed with 450 μl of count and viability reagent, gently mixed, and injected into the Muse Cell Analyzer. Statistical analysis was performed based on three independent experiments. *p* Value was compared to the cell treated with GGA plus PLY group.

Endothelial Cell Permeability Assays

Transwell Cell Permeability Assay

Sub confluent HLMVECs were split into 24 transwell inserts with a 0.4-μm pore sized filter. Following seeding, cells were maintained in complete EBM-2 MV medium and then treated for overnight with or without 30 μM GGA. Prior to exposure to PLY, complete medium was removed, and HLMVECs were washed carefully with HBSS three times before transitioning to FITC-dextran containing serum-free medium. Fresh FITC-conjugated dextran was prepared using serum-free medium and 50 ng/ml PLY was added to the endothelial cells. The lower compartment was filled with 1.5 ml of serum-free medium without FITC-dextran. At each time point, 50 μl of lower chamber medium was transferred to a 96-well plate for quantitation. The amount of FITC-dextran permeating through the HLMVEC monolayer into the lower chamber was measured using plate reader with excitation wave length 488 nm and emission wave length 520 nm. Three independent experiments were performed and the data are shown as mean ± SEM.

Transendothelial Electrical Resistance Measurements

Transendothelial electrical resistance was measured in HLMVEC using electric cell-substrate impedance sensing equipment (ECIS). HLMVECs were split into ECIS array chambers (8W10E)

at a density of 1,000 cells per well according to the manufacturer's instructions. On the following day, complete medium was removed, and cells were washed with HBSS for three times. The cells were then cultured in serum-free medium and exposed to PLY to initiate changes in barrier function. Normalized resistance (Ohms) representing HLMVEC barrier integrity was recorded for up to 3 h. Data were aggregated as the mean normalized resistance of eight individual wells.

MitoSOX Assay

Human lung microvascular endothelial cells were transferred into glass-bottomed dishes and cultured in complete EBM-2 MV medium and pretreated with or without 30 μM GGA. On the following day, cells were washed in HBSS, the culture medium changed to serum-free EBM-2. MitoSOX Red and MitoTracker Green were diluted with pre-warmed appropriate medium to a final concentration of 5 μM and 250 nM, respectively. Medium containing MitoSOX Red and MitoTracker Green was applied to the HLMVECs, stimulated with PLY and cells were incubated in 37°C for 15 min prior to observation using a Zeiss 780 inverted confocal microscope. MitoSOX Red mitochondrial superoxide indicator signal was measured at excitation/emission wavelength of 510/580 nm, and MitoTracker Green was detected using an excitation/emission wavelength of 488/516 nm. Wells without dyes were tested for MitoSOX Red and MitoTracker Green signals, respectively, as background signals. Nuclear blue was used to stain the nucleus. Equivalent experiments were performed using a fluorescent plate reader (POLARstar OMEGA) for quantification. After subtracting the background from the signal recorded in the presence of each dye, the ratio of MitoSOX Red signal over MitoTracker Green was used to determine the amount of mitochondrial ROS. The data are presented as fold change over control HLMVEC cells.

Mitochondrial Stress Assay

Mitochondrial stress in HLMVEC was assessed using the Seahorse XF96 analyzer. Low passage number HLMVECs were cultured in the XF96 well plate at a density of 7.0×10^3 cell per well in complete EBM-2 MV medium with or without GGA (30 μM) overnight. The sensor cartridge of a XF96 seahorse plate was hydrated overnight at 37°C in a non CO_2 incubator. The following day, fresh seahorse assay medium was prepared with the addition of glucose (10 mM), pyruvate (1.0 mM), and L-glutamine (2 mM). The pH of the medium was adjusted to 7.4 using NaOH. Cell confluency was assessed under light microscopy, and the plate was incubated in a non CO_2 incubator for 1 h. After calibration of the sensor cartridge, the XF96 plate was placed into the seahorse instrument and OCR measured as pmole per minute per cell. Analysis of mitochondrial function was made using changes in OCR in the presence of oligomycin (inhibits mitochondrial ATP synthase), and phenylhydrazone (FCCP, mitochondrial membrane potential) which were injected at final concentrations of 1.0 μM each. Lastly, antimycin A was injected at a final concentration of 0.5 μM to inhibit both complex I and III. After each injection, the Seahorse instrument measured OCR for three times at five time points. The average of three measurements was used for data analysis.

Statistical Analysis

Data are presented as means ± SEM. Single comparisons were made using a Student's *t*-test and multiple comparisons were made using one way ANOVA with an appropriate *post hoc* test (Tukey). $p < 0.05$ was considered a statistically significant difference.

RESULTS

Hsp70 Protects HLMVECs From PLY-Induced Barrier Destruction

Pneumolysin has been well documented to disrupt barrier function in HLMVEC and increase endothelial permeability (12, 13, 41, 42). To determine the effect of Hsp70 on barrier function, HLMVECs were transduced with adenoviruses encoding Hsp70 (pAd Hsp70-GFP, 60MOI) or GFP (Control, 60MOI) overnight and then transferred to an ECIS plate. HLMVECs transduced with the Hsp70 adenovirus were significantly protected from PLY-induced barrier dysfunction as compared to control cells (**Figure 1A**). The protective effect of Hsp70 on barrier function was then confirmed using a distinct approach, the transwell permeability assay. HLMVECs transduced with pAd Hsp70-GFP or pAd-GFP were seeded into the upper compartments of transwell plates. FITC-dextran (70 kDa) was added to the medium in the upper compartments of test wells, the background wells remained without dextran and all were treated with PLY. FITC-dextran flow through was measured in the lower compartments using a fluorescence capable plate reader (BMG POLARstar Omega). Consistent with the ECIS assay, HLMVEC expressing Hsp70 were protected from PLY-induced barrier destruction (**Figure 1B**, left panel). Expression of transgenes was confirmed using fluorescent microscopy and western blot (**Figure 1B**, right panel).

The Pharmacological Inducer of Hsp70 Expression, GGA Protects HLMVECs From PLY-Induced Increases in Permeability

Geranylgeranylacetone (GGA) pharmacologically induces the upregulation of Hsp70 *via* actions on HSF1 to increase *HSP70* gene transcription (43). GGA exhibits low cellular toxicity and has been widely used in Japan for antiulcer therapy (44). HLMVECs treated with GGA overnight exhibited a dose-dependent increase in baseline microvascular barrier electrical resistance (**Figure 2A**). In contrast, PLY induced an acute and pronounced decrease in HLMVEC resistance, reflecting severe barrier disruption. However, in cells cultured with GGA, there was a dose-dependent protective effect from PLY-induced hyperpermeability (**Figure 2B**). Gram negative (G^-) bacterial toxins can also be a significant cause of pneumonia and compromised endothelial barrier function. To assess whether Hsp70 protects against the G^- bacterial toxin, LPS, HLMVEC were cultured in ECIS arrays and treated overnight with GGA (30 μM) or vehicle (DMSO). In control cells, exposure to LPS (1 μg/ml) resulted in a more gradual loss of barrier function that peaked at approximately 15 h. In HLMVEC pretreated with GGA, there was a significantly reduced ability of LPS to disrupt endothelial barrier function (**Figure 2C**).

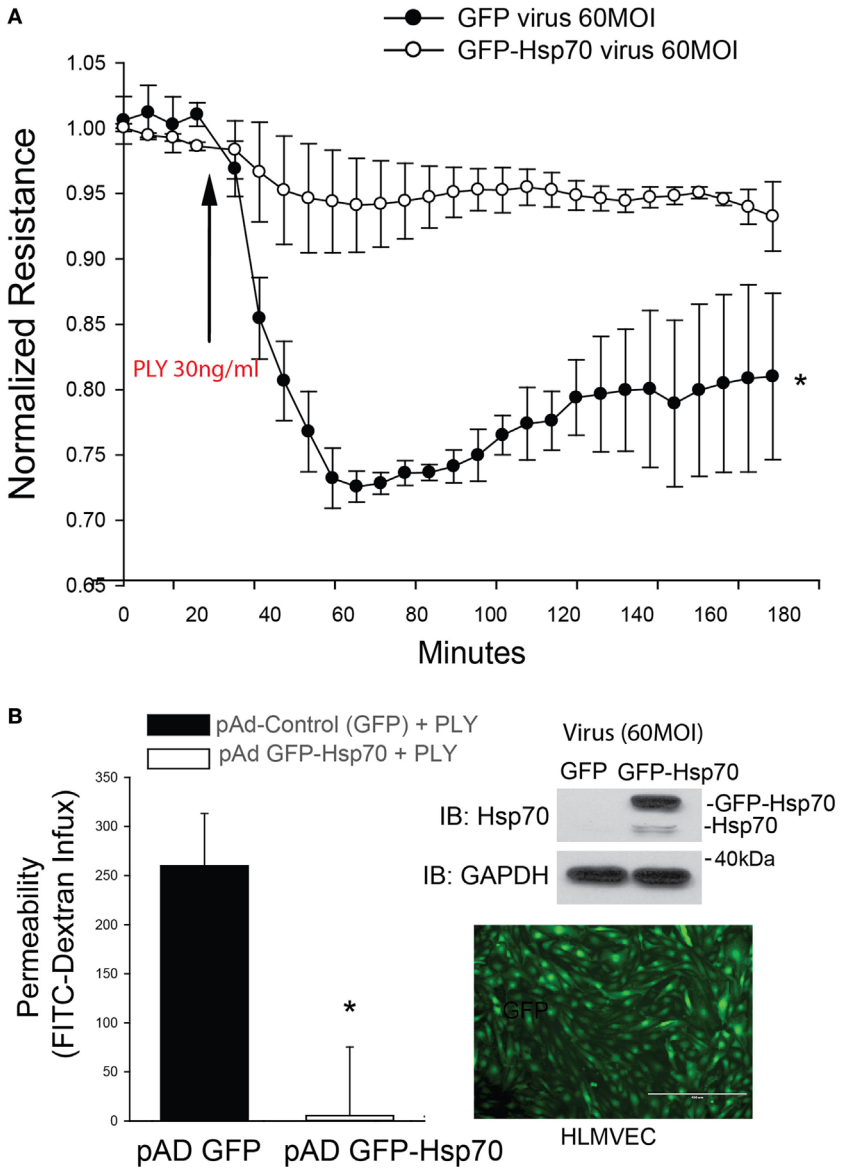

FIGURE 1 | Hsp70 provides robust protection against pneumolysin (PLY)-induced EC barrier disruption. In panel **(A)** human lung microvascular endothelial cells were transduced with pAD-GFP (Control) or pAD-GFP-Hsp70 at 60MOI and 48 h later, cells were assessed for barrier function using transendothelial resistance as monitored by electric cell-substrate impedance sensing (ECIS) in the presence and absence of PLY (30 ng/ml). In panel **(B)** (left) HLMEC were grown in transwells and similarly transduced with GFP or GFP-Hsp70 and the flux of FITC-dextran (70 kDa) into the bottom chamber determined using a fluorescent plate reader. On the right (top panel) relative expression of the GFP-Hsp70 transgene relative to endogenous and (bottom panel) image showing the expression pattern of GFP in transduced cells. Data are shown as mean ± SEM ($n = 3$ wells for each treatment). *$p < 0.05$ versus control.

PLY-induced EC dysfunction has been associated with its ability to upregulate ROS production (13). To determine the importance of ROS in mediating the loss of barrier function, we employed the superoxide inhibitor, tempol (TEM) in transwell assays. Consistent with previous findings, HLMVECs that were pretreated with GGA for overnight showed a robust decrease in dextran permeability in response to PLY (**Figures 3A–B**). Although transcellular dextran flux cannot be completely excluded, the decreased passage of both the 4- and 70-kDa FITC-dextran into the lower compartment reflects impaired endothelial monolayer integrity. Inhibition of superoxide with tempol also provided acute protection against PLY-induced barrier disruption (**Figures 3A–B**). GGA induced upregulation of Hsp70 provided more protection than that afforded by TEM.

GGA Protects HLMVECs From PLY Caused Mitochondrial Damage

Mitochondria are a major source of ROS production in endothelia cells. Given that Hsp70 and superoxide scavengers can protect

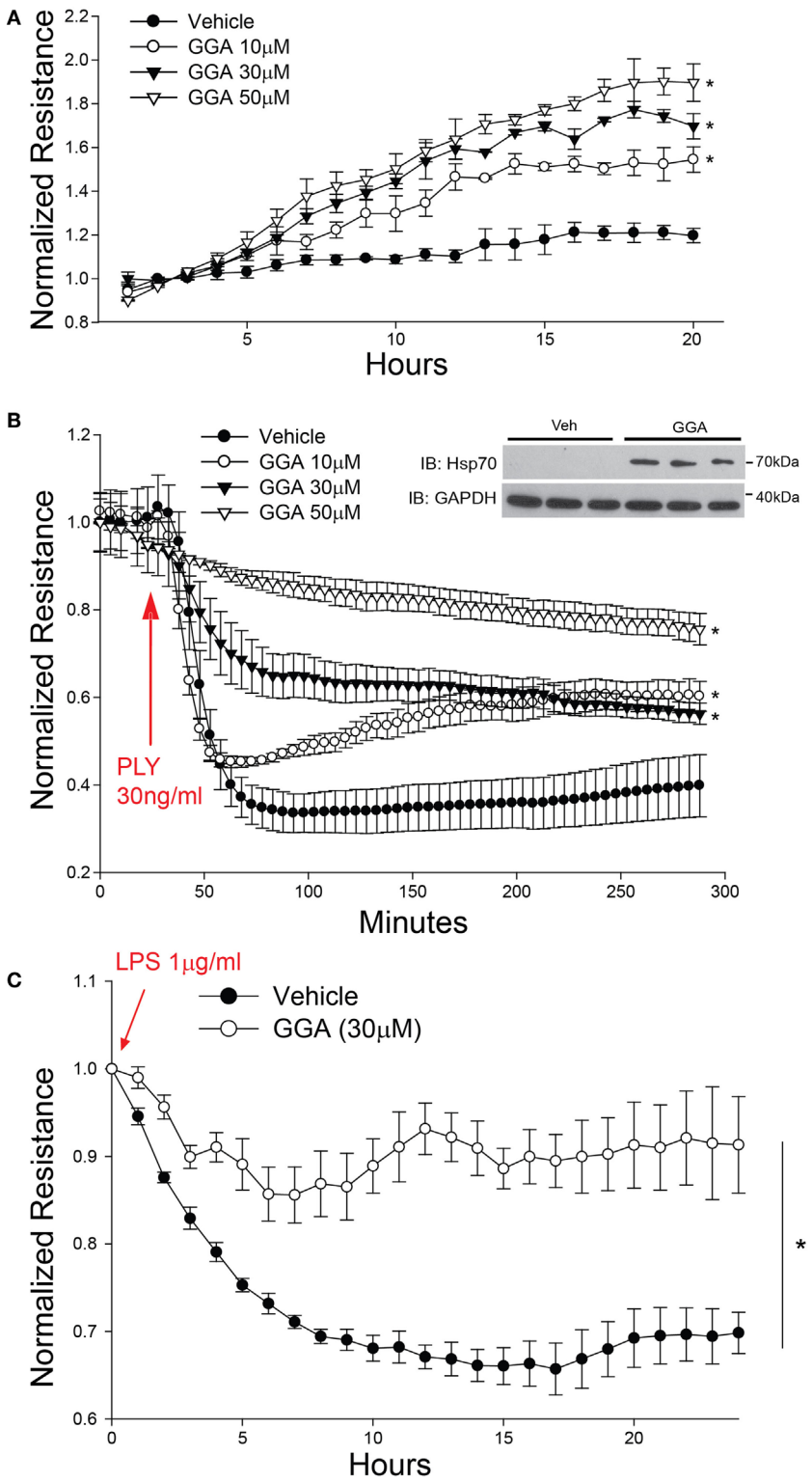

FIGURE 2 | Acute pharmacological upregulation of Hsp70 protects against pneumolysin (PLY) and LPS-induced EC barrier disruption *in vitro*. In panel **(A)** human lung microvascular endothelial cells (HLMVEC) were plated in electric cell-substrate impedance sensing (ECIS) arrays, treated with the indicated concentrations of geranylgeranylacetone (GGA) and changes in barrier strength determined by ECIS over time. Data shown as mean ± SED ($n = 4$ wells for each treatment), *$p < 0.05$. In panel **(B)** HLMVEC were treated with the indicated concentrations of GGA overnight and then were treated with or without PLY (30 ng/ml) and barrier function determined by ECIS. Data are shown as mean ± SEM ($n = 4$ wells for each treatment). *$p < 0.05$ versus vehicle. In panel **(C)** HLMVEC were pretreated overnight with GGA (30 μM) and then exposed to LPS (1 μg/ml). Data shown as mean ± SEM ($n = 4$ wells for each treatment). *$p < 0.05$ versus vehicle (DMSO).

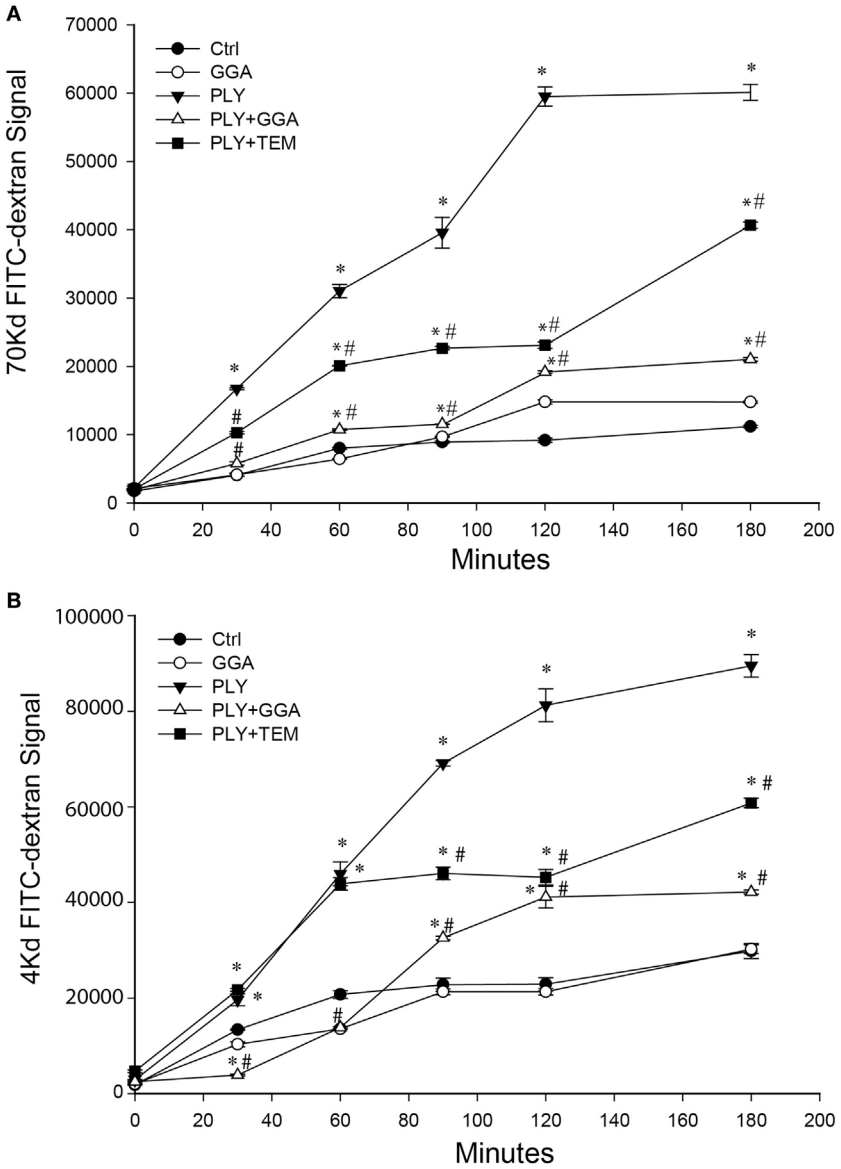

FIGURE 3 | Geranylgeranylacetone (GGA) and TEMPOL protect Human lung microvascular endothelial cell (HLMVEC) from pneumolysin (PLY)-induced barrier disruption. In panel **(A)** 70-kDa FITC-dextran permeability of HLMVEC pretreated with vehicle, GGA (30 μM) or tempol (TEM, 100 μM) then stimulated with PLY (50 ng/ml). *$p < 0.05$ versus control, #$p < 0.05$ versus PLY. Data shown as mean ± SEM ($n = 3$ wells for each treatment). **(B)** 4-kDa FITC-dextran permeability of HLMVEC pretreated with GGA (30 μM) or tempol (100 μM) then stimulated with PLY (50 ng/ml). *$p < 0.05$ versus control, #$p < 0.05$ versus PLY. Data shown as mean ± SEM ($n = 3$ wells for each treatment).

HLMVECs from PLY-induced increases in permeability, we next investigated whether the barrier protection afforded by Hsp70 might be mediated through changes in mitochondrial ROS production. HLMVECs were plated on glass bottom dishes, pretreated with 30 μM GGA for 24 h and then loaded with MitoSOX Red and MitoTracker Green. Serum-free medium containing 50 ng/ml PLY or vehicle was added prior to measurement of ROS. Using MitoTracker Green to label mitochondria, we were able to identify that mitochondrial numbers were similar among groups, while red florescence, which represented the ROS produced in the mitochondrial compartment, was significantly increased in HLMVEC stimulated with PLY (**Figures 4A,B**). In cells that were pretreated with GGA, PLY-failed to stimulate mitochondrial ROS production and cells pretreated with Tempol also demonstrated an attenuation of PLY-stimulated mitochondrial ROS production.

We next assessed whether PLY alters mitochondrial function using the Seahorse extracellular flux analyzer. HLMVECs were pretreated with or without GGA to induce Hsp70 expression and then challenged with or without PLY. Basal rates of mitochondrial respiration were similar among groups (**Figures 5A,B**). The addition of oligomycin which inhibits ATP synthase (complex V) reduced oxygen consumption in all groups, but

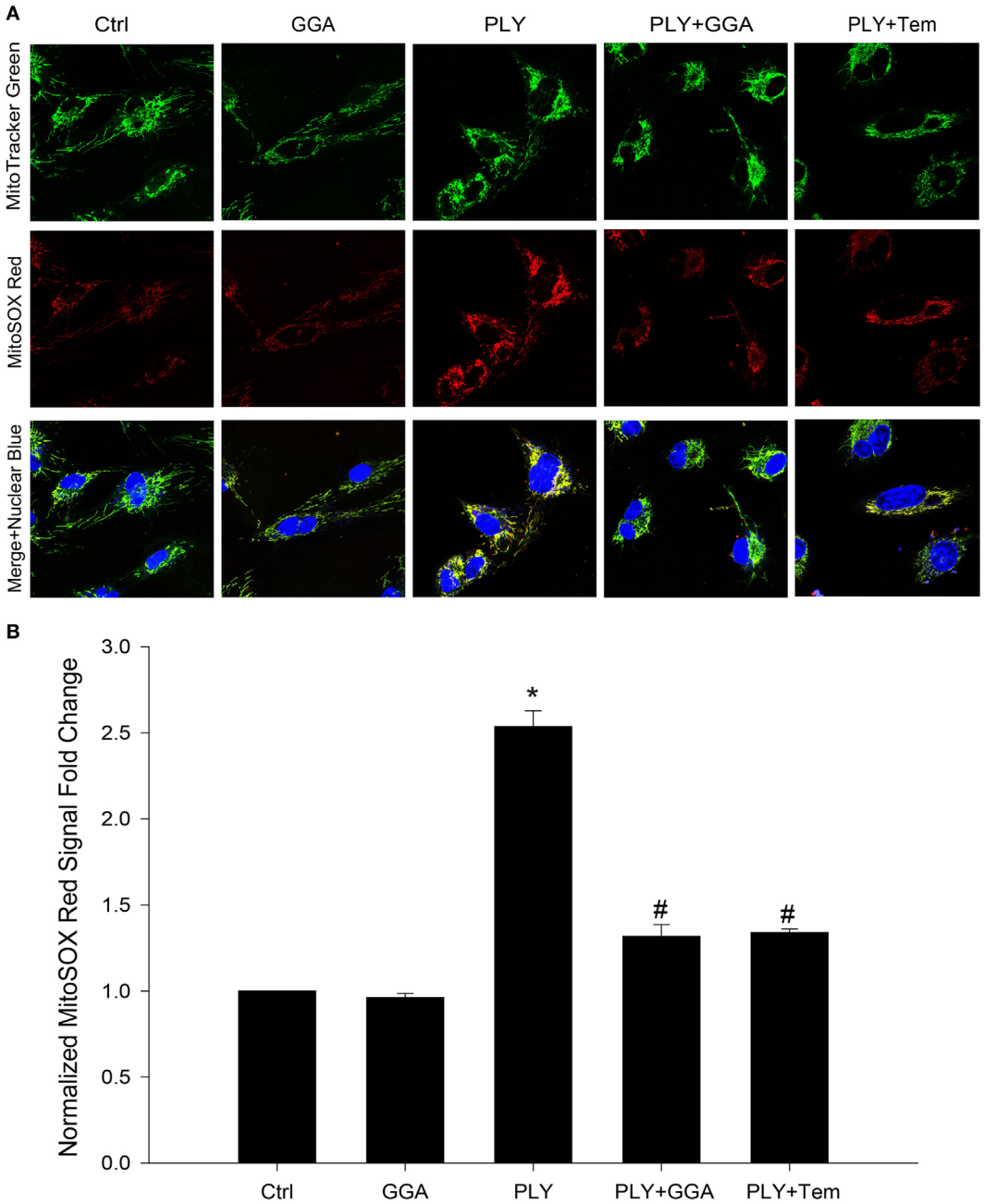

FIGURE 4 | Geranylgeranylacetone (GGA) protects against pneumolysin (PLY)-induced mitochondrial reactive oxygen species (ROS) production. In panel **(A)** representative confocal images of MitoSox red and MitoTracker green stained human lung microvascular endothelial cell reporting the degree of mitochondria localized ROS. In panel **(B)** analysis of fluorescent signal from MitoSox red normalized to MitoTracker green ($n = 4$ wells for each treatment). Data shown as mean ± SEM $^{*}p < 0.05$ versus control, $^{\#}p < 0.05$ versus PLY.

less so in cells that were treated with PLY (**Figures 5A,B** bottom left). This reflects a diminished ability of cells to use oxidative phosphorylation to generate ATP and the preservation of this ability in cells pretreated with GGA. The addition of the protonophore, FCCP [Carbonyl cyanide 4-(trifluoromethoxy) phenylhydrazone] collapses the proton gradient, disrupting the mitochondrial membrane potential, and drives maximal oxygen consumption (complex IV). Maximal respiration rates were decreased in HLMVEC exposed to PLY compared to control and significantly preserved in cells pretreated with GGA (**Figure 5B**, bottom right). Collectively, these data indicate that PLY compromises mitochondrial respiration and that upregulation of Hsp70 protects against the PLY-induced loss of function.

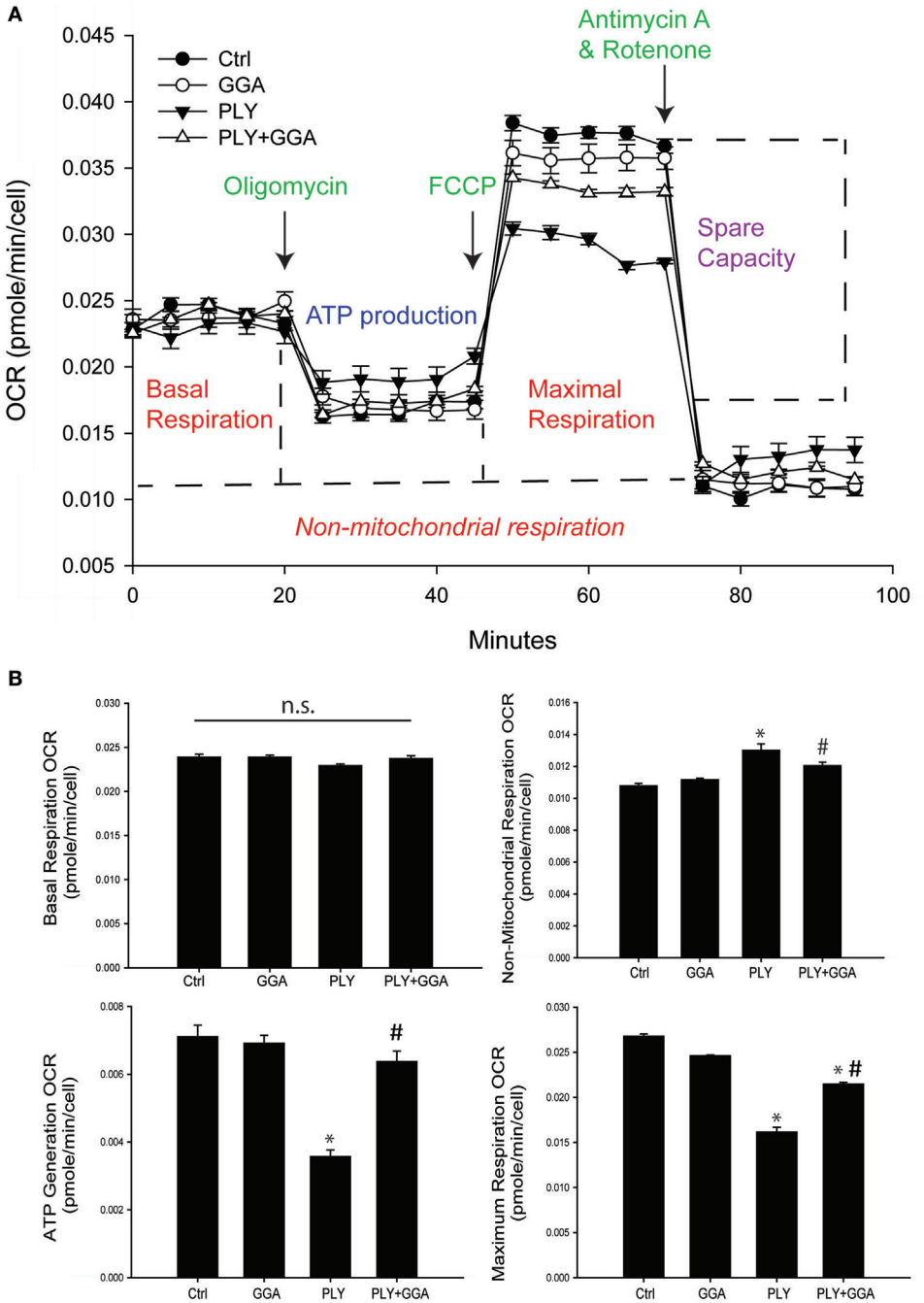

FIGURE 5 | Geranylgeranylacetone (GGA) protects human lung microvascular endothelial cells from pneumolysin (PLY)-induced mitochondrial dysfunction. **(A)** XF96 seahorse Mito stress assay profile with arrows showing the time of injections of oligomycin, carbonyl cyanide *p*-trifluoromethoxy-phenylhydrazone (FCCP), and antimycin A. Data are represented as mean ± SEM ($n = 5$ for each treatment). **(B)** Mitochondria function data were generated using the XF96 seahorse Mito stress assay. Basal respiration OCR (OCR before adding oligomycin-OCR and after adding antimycin A). Non-mitochondrial respiration OCR (stressed OCR after adding antimycin A). ATP generation OCR (basal respiration OCR after adding oligomycin). Maximum respiration OCR (stressed OCR after adding FCCP-stressed OCR after adding antimycin A). Data are shown as mean ± SEM. $^{*}p < 0.05$ versus control, $^{\#}p < 0.05$ versus PLY.

GGA Protects HLMVECs From PLY-Induced Cell Death

Hsp70 is an established cytoprotective factor that can reduce cell death (45, 46). We next assessed whether Hsp70 upregulation decreases cell death in response to PLY. HLMVECs were challenged with PLY and cell viability assessed by Muse flow cytometer. PLY (50 ng/ml) resulted in a significant decrease in cell viability (**Figure 6A**), which was significantly higher in cells pretreated with GGA (30 μM). To assess whether GGA impacts

PLY-induced apoptosis, we evaluated the expression levels of cleaved caspase 3, a commonly used marker of apoptosis in HLMVEC. PLY increased the expression of cleaved caspase 3, an effect that was decreased in cells pretreated with GGA. Neither PLY nor GGA treatment altered the expression levels of total caspase 3 or the loading control, Hsp90 (**Figure 6B**). Apoptosis can be triggered by both cytosolic ROS and mtROS. MitoSOX assays revealed less mtROS and decreased NOX1 protein expression in HLMVEC treated with GGA (**Figure 6C**). Given that mitochondrial, and mtROS can both increase inflammatory signaling, we assessed phosphorylated-NF-κB p65 (Ser536) levels in HLMVEC treated with 50 ng/ml PLY with or without GGA. NF-κB p65 phosphorylation was decreased with GGA treatment (**Figure 6D**).

GGA Protects Mice From PLY-Induced ALI

To assess the translational relevance of Hsp70 upregulation in a model of ALI, mice were administered GGA (500 mg/kg IP) or vehicle overnight and then challenged with IT PLY (60 ng). Endothelial barrier integrity was assessed by EBD extravasation. A single dose of GGA significantly increased Hsp70 protein expression in lung tissues relative to the loading control, GADPH (**Figure 7A**). Neither vehicle nor GGA alone influenced baseline levels of EBD in lung tissue, however, in vehicle treated mice, PLY administration evoked a significant increase in pulmonary vascular permeability and extravascular leak of EBD. Pretreatment with GGA significantly blunted the ability of PLY to induce EBD extravasation into the lungs consistent with greater preservation of the pulmonary endothelial barrier (**Figure 7B**).

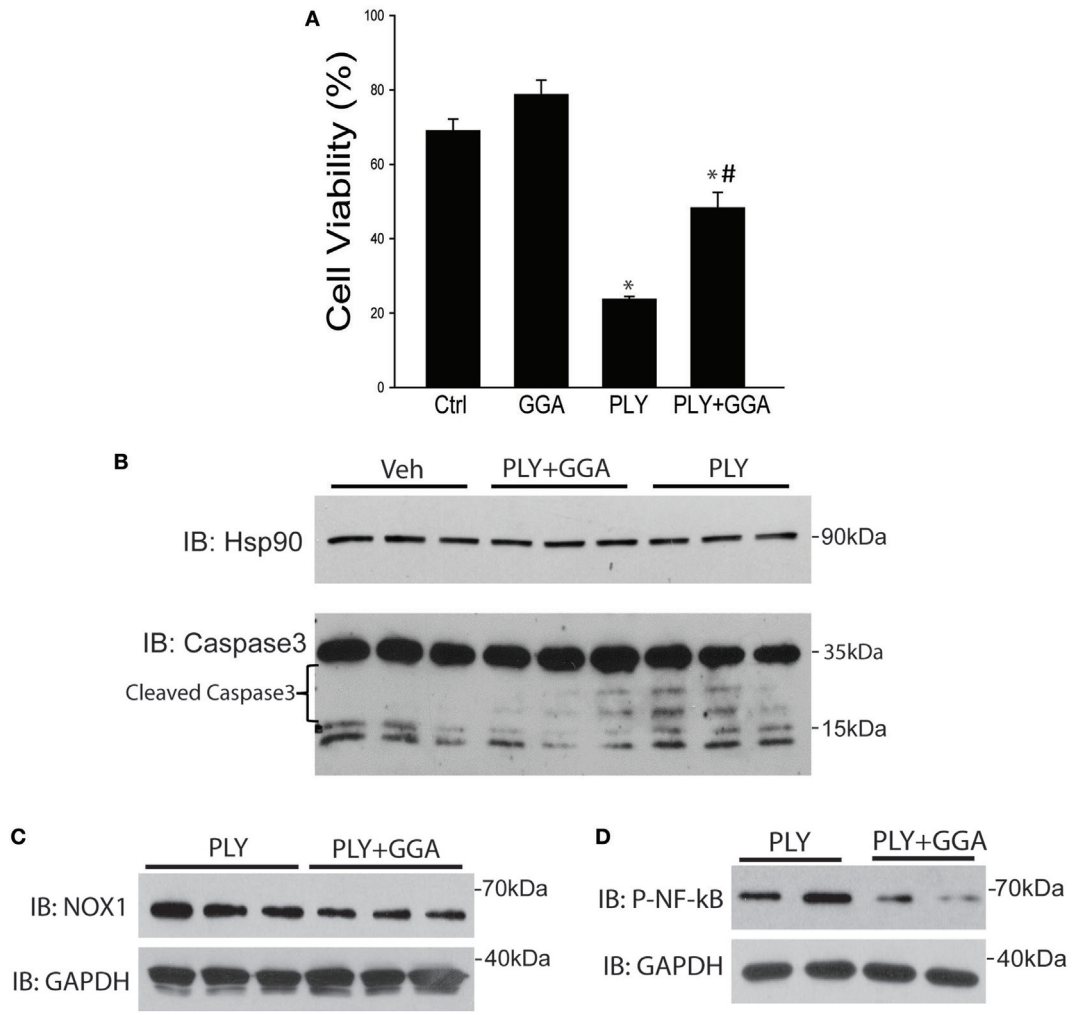

FIGURE 6 | Geranylgeranylacetone (GGA) protects against pneumolysin (PLY)-induced Human lung microvascular endothelial cells (HLMVEC) apoptosis. In panel **(A)** HLMVEC were pretreated 6 h with GGA (30 μM) and then challenged with PLY (50 ng/ml) for 4 h and cell viability determined (MUSE flow cytometry). Data are shown as mean ± SEM, $^{*}p < 0.05$ versus control, $^{\#}p < 0.05$ versus PLY. In panel **(B)** HLMVEC were challenged pretreated with vehicle or GGA (30 μM, 6 h) and then challenged with PLY (50 ng/ml) for 4 h. Cells were lysed and the level of cleaved caspase 3 was determined by western blot ($n = 3$). **(C)** HLMVECs were pretreated with vehicle or GGA overnight and then challenged with PLY (50 ng/ml) for 4 h. Cells were lysed and NOX1 levels determined by western blot. **(D)** HLMVECs were pretreated with vehicle or GGA (30 μM, 6 h) and then challenged with PLY (50 ng/ml) for 4 h. Cells were lysed and levels of phosphorylated (P-) NF-κB p65 were determined by western blot.

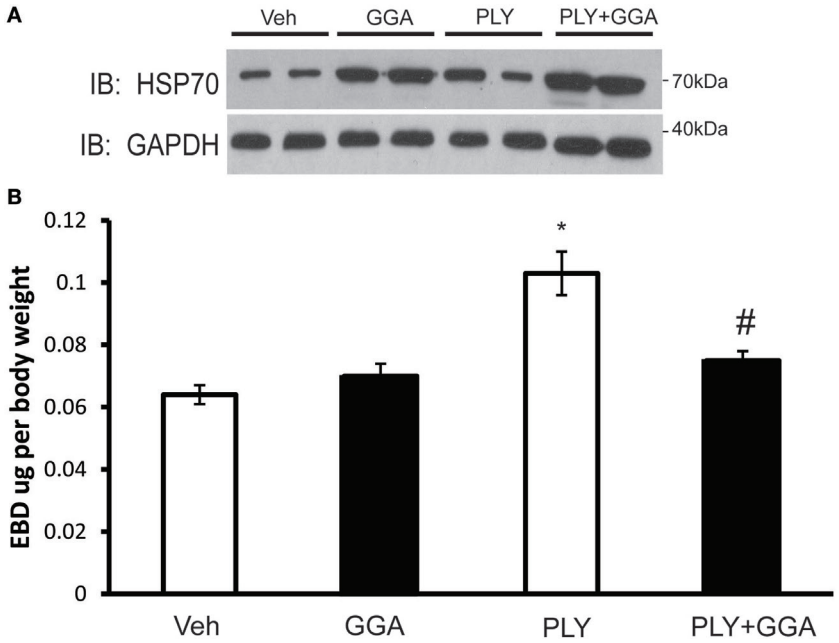

FIGURE 7 | Geranylgeranylacetone (GGA) provides protection against pneumolysin (PLY)-induced vascular leak *in vivo*. Mice were administered vehicle (10% ethanol, IP) or GGA (500 ng/kg, IP) and, 24 h later, were challenged with IT PLY 60 ng/mouse. Evans blue dye-albumin (EBD, 30 mg/kg-2 h) was injected IV *via* the tail vein 2 h before the administration of PLY to assess pulmonary vascular leak (n = 5–6). After the mice were sacrificed, lung tissue was lysed and the levels of Hsp70 and GAPDH were determined by Western blot **(A)**, and then the levels of EBD in lung tissue were determined spectrophotometrically at 620–750 nm **(B)**. Data are shown as mean ± SEM, $^{*}p < 0.05$ versus control, $^{\#}p < 0.05$ versus PLY.

DISCUSSION

Herein, we show that genetic and pharmacological upregulation of Hsp70 provides robust protection from bacterial toxin-induced destruction of the endothelial barrier both *in vitro* and *in vivo*. Increased Hsp70 expression, achieved through adenovirus-mediated gene transfer or activation of HSF with GGA, protected the integrity of the pulmonary microvascular endothelial barrier following challenge with both G^+ and G^- bacterial toxins. The G^+-toxin PLY promoted increased mitochondrial ROS, decreased mitochondrial function, increased caspase C cleavage, and increased cell death, effects that were mitigated by GGA treatment. In mice, GGA upregulated pulmonary Hsp70 expression and provided significant protection from PLY-induced pulmonary microvascular permeability. Collectively, these results suggest that Hsp70 can protect against bacterial toxin-induced increases in mitochondrial ROS which contribute to the loss of pulmonary endothelial barrier integrity.

Pneumolysin and other cholesterol-dependent pore-forming cytolysins from G^+-bacteria such as listeriolysin O have been shown to form plasma membrane pores that stimulate calcium entry and promote disruption of the endothelial barrier (12, 13, 41, 42, 47). Multiple mechanisms have been proposed, including activation of PKC, disruption of NO signaling, arginase induction, and inhibition of ENaC. A connecting theme between these mechanisms is the ability of G^+ toxins to increase ROS, but the sources of superoxide appear to be multifactorial and are incompletely defined (13). PLY has been shown to induce cell death and inflammation in the lung (48) and, in conjunction with elevated ROS it has been shown to promote cell death and apoptosis in multiple cell types including cardiomyocytes (49) epithelial cells (49–51), neurons (15, 52) and cerebral endothelial cells (53), and human umbilical vein endothelial cells (49). The ability of PLY to induce cell death in lung microvascular endothelial cells has not previously been described. Using MitoSOX red, we observed that PLY-stimulated ROS in the mitochondria of HLMVEC. An increase in ROS occurred alongside compromised mitochondrial function and increased cell death. Whether the increase in mitochondrial ROS contributes to PLY-induced cell death is not yet established.

Hsp70 belongs to large family (>13 members) of related 70 kDa Hsp that are both ubiquitous and highly conserved (54). Hsp70 family members share a similar structural organization composed of three basic domains: an N-terminal domain that encodes a highly conserved ATP-binding site, the M or middle domain binds which binds to numerous substrates, and the C-terminal domain facilitates protein folding and the binding of co-chaperones. Some of the Hsp70 genes are constitutively expressed and others are inducible in response to various stressors including increased heat (55), ROS (56), osmolarity (57), and toxins (58) to name a select few. The most abundant Hsp70s are HspA1A (Hsp70-1) and HspA1B (Hsp70-2). To simplify, we will use Hsp70 when referring to HspA1A. Hsp70 is found in the cytoplasm, nucleus, mitochondria, cell membranes, and in the extracellular space (59). Hsp70 influences many aspects of cellular function including binding to nascent proteins, preventing protein aggregation, facilitating protein folding and stability, and regulating protein activity. The upregulation of Hsp70 in response to cell stress provides a survival advantage (46, 60). Hsp70 has been shown to influence cell

survival *via* multiple mechanisms (45, 60, 61), which may differ based on the cell type and stimulus. We found that upregulation of Hsp70 provided protection against PLY-induced ROS, mitochondrial dysfunction and ultimately caspase 3 cleavage and cell death. Cell death is an important mechanism underlying ALI (62) and the ability of Hsp70 to provide cell survival may underlie is ability to preserve barrier integrity. While our studies focused primarily on the role of G^+ toxins, we also showed that Hsp70 upregulation can protect against the loss of barrier function induced by LPS. These data are consistent with other studies in which upregulation of a distinct Hsp70 family member, HspA12B, protects against the loss of barrier function in HUVECs (63). Hsp70 has also been shown to protect against hyperoxia-stimulated loss of endothelial barrier function (39).

Another important finding of our study was the ability of Hsp70 to suppress the production of ROS. Previously, we have shown that upregulation of Hsp70 inhibits the activity of the NADPH oxidases which are the major sources of cellular ROS (35, 64). In this study, we show that Hsp70 suppressed NOX1 expression which is consistent with our previous findings and protects against PLY-stimulated mitochondria ROS. How Hsp70 reduces mitochondrial ROS production in HLMVEC is not yet fully understood and evidence in the literature in other cell types suggest that multiple mechanisms are involved. PLY opens pores in the plasma membrane leading to a pronounced calcium influx that can impair mitochondrial coupling and promote superoxide formation. Within the inner membrane of mitochondria is an ATP sensitive potassium channel (mitoKATP) that can be activated by ATP deprivation and calcium overload. Studies have shown that GGA and Hsp70 reduce mitoROS in cardiomyocytes and protect from ischemia reperfusion injury. The protective effect of increased Hsp70 expression is abolished with the mitoKATP inhibitor, 5-hydroxydecanoate, which does not alter Hsp70 expression. These data suggest that Hsp70 reduces mitoROS accumulation by facilitating the opening of the mitoKATP channel. NADPH derived ROS have been shown to promote oxidative damage of mitochondrial proteins in particularly, complex I and complex II, which results in increased mitoROS production (20). Increased mitoROS can activate NADPH oxidase locking both enzymes into a feed forward relationship (20–22). The upregulation of Hsp70 in HLMVEC would be expected to break this vicious cycle between mtROS and NADPH oxidase through actions on both pathways. Hsp70 has also been shown to attenuate oxidative phosphorylation (65) which may reduce mitoROS generation. Hsp70 can also impair mitochondrial proteostasis (66) which may compromise local antioxidant (SOD2) pathways or improve the function of enzymes in the electron transport chain. Hsp70 has also been shown to inhibit NADPH oxidase activity (35) which can secondarily impact mitoROS. Finally, increased expression of Hsp70 has been shown to upregulate Akt-eNOS activity and the resulting increase in NO could indirectly suppress mitochondrial ROS by quenching superoxide (67).

Others have shown that Hsp70 can protect against cell death by mechanisms upstream of the mitochondria and by suppressing the ability of ROS (H_2O_2) to induce mitochondrial dysfunction (68, 69). There is little Hsp70 (1A1) in the mitochondria of normal cells; however, tumor cells have significantly increased amounts which provide a survival advantage. Depletion of Hsp70 in tumor cells disrupts mitochondria function and increases cell death (70). There is also a constitutive mitochondrial isoform of Hsp70 (HspA9 or motalin) which has important roles in protein translocation and although it is not induced by stress, it has also been shown to be important for cell survival (71). In our study, we upregulated Hsp70 using GGA and using adenoviral mediated gene transfer of a specific Hsp70 (HspA1A). How Hsp70 traffics to the mitochondria is not completely understood. Hsp70 can interact with lipids and in particular cardiolipin which is localized to the mitochondria (72). In addition to actions on Nox enzymes and the mitochondria, Hsp70 upregulation is also associated with reduced inflammation and the upregulation of antioxidant pathways (73). Inhibition of mitochondrial complexes I, II, and III has been shown to protect cardiomyocytes from hypoxia induced injury by reducing p38 phosphorylation as well as inflammatory signaling (74). Interestingly, blockade of ROS diffusion in the mitochondria using anion inhibitors also protects cardiomyocytes (74), which suggests an important role of mtROS in the initiation of inflammation during conditions of cellular stress. As the pulmonary inflammatory response can be very different in young versus elderly patients (28), future studies may want to compare the protective effects of Hsp70 in both young and aged animal models of PLY-induced ALI. Previously, we and others have shown that increased intracellular calcium is important in mediating the loss of endothelial barrier function in response to PLY (13, 75). Whether Hsp70 upregulation alters calcium-dynamics in HLMVEC is not yet known. Recent studies have revealed that PLY can activate TLR4 (76, 77) which is also the primary target of LPS. However, the kinetics of the loss of barrier function induced by PLY and LPS are quite different suggesting different mechanisms and furthermore, Hsp70 has been shown to both support and stimulate TLR4 signaling (78).

Hsp90 inhibitors have been shown to protect the endothelial barrier from G^- bacterial toxins and are potent anti-inflammatory agents (79, 80). However, Hsp90 inhibitors also upregulate Hsp70 and the prosurvival actions of Hsp70 limit the effectiveness of these agents in anticancer strategies (81). In acute settings, whether the effectiveness of Hsp90 inhibitors relates to their ability to upregulate Hsp70 remains to be determined. Hsp70 has been shown to be released into the extracellular space through a yet to be identified mechanism. Increased circulating Hsp70 levels reflect heightened inflammation and poor outcome and autoantibodies against Hsp70 have been observed in a number of diseases (59). Although, upregulation of Hsp70 may promote cell survival and potentially increase extracellular Hsp70, the negative effects of long-term upregulation appear to be minor. GGA is approved for use as an antiulcer medication in Japan and appears to have low toxicity. Any potential risks are expected to be lower in the short-term treatment of ALI.

In conclusion, our study reveals that Hsp70 upregulation is a rapid and potent modality to protect the pulmonary endothelial barrier from the G^+ bacterial toxin, PLY. Attractive features of this approach include the ability to rapidly upregulate Hsp70 with pharmacological agents and a broad spectrum of protection against both G^+ toxins, G^- toxins and hyperoxia. Hsp70 also targets multiple pathways including mitochondrial function, ROS production, and cell death which are key mechanisms that

underlie the loss of endothelial barrier integrity. Upregulation of Hsp70 may be of high clinical significance in the management of ARDS/ALI-related pulmonary barrier dysfunction.

ETHICS STATEMENT

All animal studies conformed to National Institutes of Health guidelines. The experimental procedure was approved by the Augusta University Institutional Animal Care and Use Committee.

AUTHOR CONTRIBUTIONS

XL: conceptual ideas, performed experiments, and wrote paper. YY and BG: performed experiments. SH and ZB: critical reading and performed experiments. DW, RR, SB, AV, and YS: critical reading. TC: provided reagents. RL: conceptual ideas, reagents, and critical reading. DS and DF: conceptual ideas and critical reading. FC: conceptual ideas, experiments, and critical reading.

FUNDING

This work was supported by NIH grants P01 HL101902-01A1 (AV and DF), R01HL124773 (SB and DF), R01HL125926 (DS and DF), extramural Success Award from the Vice President for Research at Augusta University (to RL), ADA grant #1-16-IBS-196 (to AV, RL, and DF), as well as by SFB grant TR-84 "Innate Immunity of the Lung" from the German Research Foundation (DFG) (to TC). RL is a Mercator Fellow of the DFG.

REFERENCES

1. Matthay MA, Ware LB, Zimmerman GA. The acute respiratory distress syndrome. *J Clin Invest* (2012) 122:2731–40. doi:10.1172/JCI60331
2. O'Brien KL, Wolfson LJ, Watt JP, Henkle E, Deloria-Knoll M, McCall N, et al. Burden of disease caused by *Streptococcus pneumoniae* in children younger than 5 years: global estimates. *Lancet* (2009) 374:893–902. doi:10.1016/S0140-6736(09)61204-6
3. Dreyfuss D, Ricard JD. Acute lung injury and bacterial infection. *Clin Chest Med* (2005) 26:105–12. doi:10.1016/j.ccm.2004.10.014
4. Matthay MA, McAuley DF, Ware LB. Clinical trials in acute respiratory distress syndrome: challenges and opportunities. *Lancet Respir Med* (2017) 5:524–34. doi:10.1016/S2213-2600(17)30188-1
5. Weycker D, Strutton D, Edelsberg J, Sato R, Jackson LA. Clinical and economic burden of pneumococcal disease in older US adults. *Vaccine* (2010) 28:4955–60. doi:10.1016/j.vaccine.2010.05.030
6. Lucas R, Czikora I, Sridhar S, Zemskov E, Gorshkov B, Siddaramappa U, et al. Mini-review: novel therapeutic strategies to blunt actions of pneumolysin in the lungs. *Toxins (Basel)* (2013) 5:1244–60. doi:10.3390/toxins5071244
7. Martner A, Dahlgren C, Paton JC, Wold AE. Pneumolysin released during *Streptococcus pneumoniae* autolysis is a potent activator of intracellular oxygen radical production in neutrophils. *Infect Immun* (2008) 76:4079–87. doi:10.1128/IAI.01747-07
8. Gilbert RJ. Cholesterol-dependent cytolysins. *Adv Exp Med Biol* (2010) 677:56–66. doi:10.1007/978-1-4419-6327-7_5
9. Tilley SJ, Orlova EV, Gilbert RJ, Andrew PW, Saibil HR. Structural basis of pore formation by the bacterial toxin pneumolysin. *Cell* (2005) 121:247–56. doi:10.1016/j.cell.2005.02.033
10. Gilbert RJ, Jimenez JL, Chen S, Andrew PW, Saibil HR. Structural basis of pore formation by cholesterol-binding toxins. *Int J Med Microbiol* (2000) 290:389–94. doi:10.1016/S1438-4221(00)80049-1
11. Kwon IS, Kim J, Rhee DK, Kim BO, Pyo S. Pneumolysin induces cellular senescence by increasing ROS production and activation of MAPK/NF-kappaB signal pathway in glial cells. *Toxicon* (2017) 129:100–12. doi:10.1016/j.toxicon.2017.02.017
12. Chen F, Wang Y, Rafikov R, Haigh S, Zhi WB, Kumar S, et al. RhoA S-nitrosylation as a regulatory mechanism influencing endothelial barrier function in response to G(+)-bacterial toxins. *Biochem Pharmacol* (2017) 127:34–45. doi:10.1016/j.bcp.2016.12.014
13. Chen F, Kumar S, Yu Y, Aggarwal S, Gross C, Wang Y, et al. PKC-dependent phosphorylation of eNOS at T495 regulates eNOS coupling and endothelial barrier function in response to G+ -toxins. *PLoS One* (2014) 9:e99823. doi:10.1371/journal.pone.0099823
14. Di A, Mehta D, Malik AB. ROS-activated calcium signaling mechanisms regulating endothelial barrier function. *Cell Calcium* (2016) 60:163–71. doi:10.1016/j.ceca.2016.02.002
15. Braun JS, Hoffmann O, Schickhaus M, Freyer D, Dagand E, Bermpohl D, et al. Pneumolysin causes neuronal cell death through mitochondrial damage. *Infect Immun* (2007) 75:4245–54. doi:10.1128/IAI.00031-07
16. Mikhed Y, Daiber A, Steven S. Mitochondrial oxidative stress, mitochondrial DNA damage and their role in age-related vascular dysfunction. *Int J Mol Sci* (2015) 16:15918–53. doi:10.3390/ijms160715918
17. Shokolenko I, Venediktova N, Bochkareva A, Wilson GL, Alexeyev MF. Oxidative stress induces degradation of mitochondrial DNA. *Nucleic Acids Res* (2009) 37:2539–48. doi:10.1093/nar/gkp100
18. Lemasters JJ, Theruvath TP, Zhong Z, Nieminen AL. Mitochondrial calcium and the permeability transition in cell death. *Biochim Biophys Acta* (2009) 1787:1395–401. doi:10.1016/j.bbabio.2009.06.009
19. Caja S, Enriquez JA. Mitochondria in endothelial cells: sensors and integrators of environmental cues. *Redox Biol* (2017) 12:821–7. doi:10.1016/j.redox.2017.04.021
20. Dikalov S. Cross talk between mitochondria and NADPH oxidases. *Free Radic Biol Med* (2011) 51:1289–301. doi:10.1016/j.freeradbiomed.2011.06.033
21. Kroller-Schon S, Steven S, Kossmann S, Scholz A, Daub S, Oelze M, et al. Molecular mechanisms of the crosstalk between mitochondria and NADPH oxidase through reactive oxygen species-studies in white blood cells and in animal models. *Antioxid Redox Signal* (2014) 20:247–66. doi:10.1089/ars.2012.4953
22. Nazarewicz RR, Dikalova AE, Bikineyeva A, Dikalov SI. Nox2 as a potential target of mitochondrial superoxide and its role in endothelial oxidative stress. *Am J Physiol Heart Circ Physiol* (2013) 305:H1131–40. doi:10.1152/ajpheart.00063.2013
23. Doughan AK, Harrison DG, Dikalov SI. Molecular mechanisms of angiotensin II-mediated mitochondrial dysfunction: linking mitochondrial oxidative damage and vascular endothelial dysfunction. *Circ Res* (2008) 102:488–96. doi:10.1161/CIRCRESAHA.107.162800
24. Chen CA, Wang TY, Varadharaj S, Reyes LA, Hemann C, Talukder MA, et al. S-glutathionylation uncouples eNOS and regulates its cellular and vascular function. *Nature* (2010) 468:1115–8. doi:10.1038/nature09599
25. Vasquez-Vivar J, Kalyanaraman B, Martasek P, Hogg N, Masters BS, Karoui H, et al. Superoxide generation by endothelial nitric oxide synthase: the influence of cofactors. *Proc Natl Acad Sci U S A* (1998) 95:9220–5. doi:10.1073/pnas.95.16.9220
26. Li X, Fang P, Yang WY, Chan K, Lavallee M, Xu K, et al. Mitochondrial ROS, uncoupled from ATP synthesis, determine endothelial activation for both physiological recruitment of patrolling cells and pathological recruitment of inflammatory cells. *Can J Physiol Pharmacol* (2017) 95:247–52. doi:10.1139/cjpp-2016-0515
27. Dikalov SI, Ungvari Z. Role of mitochondrial oxidative stress in hypertension. *Am J Physiol Heart Circ Physiol* (2013) 305:H1417–27. doi:10.1152/ajpheart.00089.2013
28. Boyd AR, Orihuela CJ. Dysregulated inflammation as a risk factor for pneumonia in the elderly. *Aging Dis* (2011) 2:487–500.
29. Nollen EA, Morimoto RI. Chaperoning signaling pathways: molecular chaperones as stress-sensing 'heat shock' proteins. *J Cell Sci* (2002) 115:2809–16.
30. Zou J, Guo Y, Guettouche T, Smith DF, Voellmy R. Repression of heat shock transcription factor HSF1 activation by HSP90 (HSP90 complex) that forms

a stress-sensitive complex with HSF1. *Cell* (1998) 94:471–80. doi:10.1016/S0092-8674(00)81588-3
31. Pratt WB, Toft DO. Regulation of signaling protein function and trafficking by the hsp90/hsp70-based chaperone machinery. *Exp Biol Med (Maywood)* (2003) 228:111–33. doi:10.1177/153537020322800201
32. Sharma K, Vabulas RM, Macek B, Pinkert S, Cox J, Mann M, et al. Quantitative proteomics reveals that Hsp90 inhibition preferentially targets kinases and the DNA damage response. *Mol Cell Proteomics* (2012) 11:M111.014654. doi:10.1074/mcp.M111.014654
33. Chen F, Pandey D, Chadli A, Catravas JD, Chen T, Fulton DJ. Hsp90 regulates NADPH oxidase activity and is necessary for superoxide but not hydrogen peroxide production. *Antioxid Redox Signal* (2011) 14:2107–19. doi:10.1089/ars.2010.3669
34. Madrigal-Matute J, Fernandez-Garcia CE, Gomez-Guerrero C, Lopez-Franco O, Munoz-Garcia B, Egido J, et al. HSP90 inhibition by 17-DMAG attenuates oxidative stress in experimental atherosclerosis. *Cardiovasc Res* (2012) 95:116–23. doi:10.1093/cvr/cvs158
35. Chen F, Yu Y, Qian J, Wang Y, Cheng B, Dimitropoulou C, et al. Opposing actions of heat shock protein 90 and 70 regulate nicotinamide adenine dinucleotide phosphate oxidase stability and reactive oxygen species production. *Arterioscler Thromb Vasc Biol* (2012) 32:2989–99. doi:10.1161/ATVBAHA.112.300361
36. Jolly C, Morimoto RI. Role of the heat shock response and molecular chaperones in oncogenesis and cell death. *J Natl Cancer Inst* (2000) 92:1564–72. doi:10.1093/jnci/92.19.1564
37. Tyc J, Klingbeil MM, Lukes J. Mitochondrial heat shock protein machinery hsp70/hsp40 is indispensable for proper mitochondrial DNA maintenance and replication. *MBio* (2015) 6(1):e02425-14. doi:10.1128/mBio.02425-14
38. Fulton D, Gratton JP, McCabe TJ, Fontana J, Fujio Y, Walsh K, et al. Regulation of endothelium-derived nitric oxide production by the protein kinase Akt. *Nature* (1999) 399:597–601. doi:10.1038/21218
39. Kondrikov D, Fulton D, Dong Z, Su Y. Heat shock protein 70 prevents hyperoxia-induced disruption of lung endothelial barrier via caspase-dependent and AIF-dependent pathways. *PLoS One* (2015) 10:e0129343. doi:10.1371/journal.pone.0129343
40. Gonzales JN, Gorshkov B, Varn MN, Zemskova MA, Zemskov EA, Sridhar S, et al. Protective effect of adenosine receptors against lipopolysaccharide-induced acute lung injury. *Am J Physiol Lung Cell Mol Physiol* (2014) 306:L497–507. doi:10.1152/ajplung.00086.2013
41. Lucas R, Yang G, Gorshkov BA, Zemskov EA, Sridhar S, Umapathy NS, et al. Protein kinase C-alpha and arginase I mediate pneumolysin-induced pulmonary endothelial hyperpermeability. *Am J Respir Cell Mol Biol* (2012) 47:445–53. doi:10.1165/rcmb.2011-0332OC
42. Xiong C, Yang G, Kumar S, Aggarwal S, Leustik M, Snead C, et al. The lectin-like domain of TNF protects from listeriolysin-induced hyperpermeability in human pulmonary microvascular endothelial cells – a crucial role for protein kinase C-alpha inhibition. *Vascul Pharmacol* (2010) 52:207–13. doi:10.1016/j.vph.2009.12.010
43. Otaka M, Yamamoto S, Ogasawara K, Takaoka Y, Noguchi S, Miyazaki T, et al. The induction mechanism of the molecular chaperone HSP70 in the gastric mucosa by geranylgeranylacetone (HSP-inducer). *Biochem Biophys Res Commun* (2007) 353:399–404. doi:10.1016/j.bbrc.2006.12.031
44. Hirakawa T, Rokutan K, Nikawa T, Kishi K. Geranylgeranylacetone induces heat shock proteins in cultured Guinea pig gastric mucosal cells and rat gastric mucosa. *Gastroenterology* (1996) 111:345–57. doi:10.1053/gast.1996.v111.pm8690199
45. Li CY, Lee JS, Ko YG, Kim JI, Seo JS. Heat shock protein 70 inhibits apoptosis downstream of cytochrome c release and upstream of caspase-3 activation. *J Biol Chem* (2000) 275:25665–71. doi:10.1074/jbc.M906383199
46. Riabowol KT, Mizzen LA, Welch WJ. Heat shock is lethal to fibroblasts microinjected with antibodies against hsp70. *Science* (1988) 242:433–6. doi:10.1126/science.3175665
47. Witzenrath M, Gutbier B, Hocke AC, Schmeck B, Hippenstiel S, Berger K, et al. Role of pneumolysin for the development of acute lung injury in pneumococcal pneumonia. *Crit Care Med* (2006) 34:1947–54. doi:10.1097/01.CCM.0000220496.48295.A9
48. Garcia-Suarez Mdel M, Florez N, Astudillo A, Vazquez F, Villaverde R, Fabrizio K, et al. The role of pneumolysin in mediating lung damage in a lethal pneumococcal pneumonia murine model. *Respir Res* (2007) 8:3. doi:10.1186/1465-9921-8-3
49. Zhou A, Wang H, Lan K, Zhang X, Xu W, Yin Y, et al. Apoptosis induced by pneumolysin in human endothelial cells involves mitogen-activated protein kinase phosphorylation. *Int J Mol Med* (2012) 29:1025–30. doi:10.3892/ijmm.2012.946
50. Feldman C, Anderson R, Cockeran R, Mitchell T, Cole P, Wilson R. The effects of pneumolysin and hydrogen peroxide, alone and in combination, on human ciliated epithelium in vitro. *Respir Med* (2002) 96:580–5. doi:10.1053/rmed.2002.1316
51. Li P, Shi J, He Q, Hu Q, Wang YY, Zhang LJ, et al. *Streptococcus pneumoniae* induces autophagy through the inhibition of the PI3K-I/Akt/mTOR pathway and ROS hypergeneration in A549 cells. *PLoS One* (2015) 10:e0122753. doi:10.1371/journal.pone.0122753
52. Braun JS, Sublett JE, Freyer D, Mitchell TJ, Cleveland JL, Tuomanen EI, et al. Pneumococcal pneumolysin and H(2)O(2) mediate brain cell apoptosis during meningitis. *J Clin Invest* (2002) 109:19–27. doi:10.1172/JCI12035
53. Bermpohl D, Halle A, Freyer D, Dagand E, Braun JS, Bechmann I, et al. Bacterial programmed cell death of cerebral endothelial cells involves dual death pathways. *J Clin Invest* (2005) 115:1607–15. doi:10.1172/JCI23223
54. Brocchieri L, Conway de Macario E, Macario AJ. hsp70 genes in the human genome: conservation and differentiation patterns predict a wide array of overlapping and specialized functions. *BMC Evol Biol* (2008) 8:19. doi:10.1186/1471-2148-8-19
55. Tissieres A, Mitchell HK, Tracy UM. Protein synthesis in salivary glands of *Drosophila melanogaster*: relation to chromosome puffs. *J Mol Biol* (1974) 84:389–98. doi:10.1016/0022-2836(74)90447-1
56. Madamanchi NR, Li S, Patterson C, Runge MS. Reactive oxygen species regulate heat-shock protein 70 via the JAK/STAT pathway. *Arterioscler Thromb Vasc Biol* (2001) 21:321–6. doi:10.1161/01.ATV.21.3.321
57. Shim EH, Kim JI, Bang ES, Heo JS, Lee JS, Kim EY, et al. Targeted disruption of hsp70.1 sensitizes to osmotic stress. *EMBO Rep* (2002) 3:857–61. doi:10.1093/embo-reports/kvf175
58. Koller M, Hensler T, Konig B, Prevost G, Alouf J, Konig W. Induction of heat-shock proteins by bacterial toxins, lipid mediators and cytokines in human leukocytes. *Zentralbl Bakteriol* (1993) 278:365–76. doi:10.1016/S0934-8840(11)80853-4
59. Radons J. The human HSP70 family of chaperones: where do we stand? *Cell Stress Chaperones* (2016) 21:379–404. doi:10.1007/s12192-016-0676-6
60. Jaattela M, Wissing D, Kokholm K, Kallunki T, Egeblad M. Hsp70 exerts its anti-apoptotic function downstream of caspase-3-like proteases. *EMBO J* (1998) 17:6124–34. doi:10.1093/emboj/17.21.6124
61. Nylandsted J, Gyrd-Hansen M, Danielewicz A, Fehrenbacher N, Lademann U, Hoyer-Hansen M, et al. Heat shock protein 70 promotes cell survival by inhibiting lysosomal membrane permeabilization. *J Exp Med* (2004) 200:425–35. doi:10.1084/jem.20040531
62. Cheng KT, Xiong S, Ye Z, Hong Z, Di A, Tsang KM, et al. Caspase-11-mediated endothelial pyroptosis underlies endotoxemia-induced lung injury. *J Clin Invest* (2017) 127:4124–35. doi:10.1172/JCI94495
63. Kang Q, Chen Y, Zhang X, Yu G, Wan X, Wang J, et al. Heat shock protein A12B protects against sepsis-induced impairment in vascular endothelial permeability. *J Surg Res* (2016) 202:87–94. doi:10.1016/j.jss.2015.12.034
64. Chen F, Haigh S, Yu Y, Benson T, Wang Y, Li X, et al. Nox5 stability and superoxide production is regulated by C-terminal binding of Hsp90 and CO-chaperones. *Free Radic Biol Med* (2015) 89:793–805. doi:10.1016/j.freeradbiomed.2015.09.019
65. Wang L, Schumann U, Liu Y, Prokopchuk O, Steinacker JM. Heat shock protein 70 (Hsp70) inhibits oxidative phosphorylation and compensates ATP balance through enhanced glycolytic activity. *J Appl Physiol* (2012) 113:1669–76. doi:10.1152/japplphysiol.00658.2012
66. Leu JI, Barnoud T, Zhang G, Tian T, Wei Z, Herlyn M, et al. Inhibition of stress-inducible HSP70 impairs mitochondrial proteostasis and function. *Oncotarget* (2017) 8:45656–69. doi:10.18632/oncotarget.17321
67. Zhou C, Bai J, Jiang C, Ye L, Pan Y, Zhang H. Geranylgeranylacetone attenuates myocardium ischemic/reperfusion injury through HSP70 and Akt/GSK-3beta/eNOS pathway. *Am J Transl Res* (2017) 9:386–95.
68. Chong KY, Lai CC, Lille S, Chang C, Su CY. Stable overexpression of the constitutive form of heat shock protein 70 confers oxidative protection. *J Mol Cell Cardiol* (1998) 30:599–608. doi:10.1006/jmcc.1997.0623
69. Polla BS, Kantengwa S, Francois D, Salvioli S, Franceschi C, Marsac C, et al. Mitochondria are selective targets for the protective effects of heat

shock against oxidative injury. *Proc Natl Acad Sci U S A* (1996) 93:6458–63. doi:10.1073/pnas.93.13.6458

70. Daugaard M, Rohde M, Jaattela M. The heat shock protein 70 family: highly homologous proteins with overlapping and distinct functions. *FEBS Lett* (2007) 581:3702–10. doi:10.1016/j.febslet.2007.05.039
71. Deocaris CC, Kaul SC, Wadhwa R. On the brotherhood of the mitochondrial chaperones mortalin and heat shock protein 60. *Cell Stress Chaperones* (2006) 11:116–28. doi:10.1379/CSC-144R.1
72. McCallister C, Kdeiss B, Nikolaidis N. HspA1A, a 70-kDa heat shock protein, differentially interacts with anionic lipids. *Biochem Biophys Res Commun* (2015) 467:835–40. doi:10.1016/j.bbrc.2015.10.057
73. Hirota K, Nakamura H, Arai T, Ishii H, Bai J, Itoh T, et al. Geranylgeranylacetone enhances expression of thioredoxin and suppresses ethanol-induced cytotoxicity in cultured hepatocytes. *Biochem Biophys Res Commun* (2000) 275:825–30. doi:10.1006/bbrc.2000.3392
74. Kulisz A, Chen N, Chandel NS, Shao Z, Schumacker PT. Mitochondrial ROS initiate phosphorylation of p38 MAP kinase during hypoxia in cardiomyocytes. *Am J Physiol Lung Cell Mol Physiol* (2002) 282:L1324–9. doi:10.1152/ajplung.00326.2001
75. Wippel C, Fortsch C, Hupp S, Maier E, Benz R, Ma J, et al. Extracellular calcium reduction strongly increases the lytic capacity of pneumolysin from *Streptococcus pneumoniae* in brain tissue. *J Infect Dis* (2011) 204:930–6. doi:10.1093/infdis/jir434
76. Malley R, Henneke P, Morse SC, Cieslewicz MJ, Lipsitch M, Thompson CM, et al. Recognition of pneumolysin by toll-like receptor 4 confers resistance to pneumococcal infection. *Proc Natl Acad Sci U S A* (2003) 100:1966–71. doi:10.1073/pnas.0435928100
77. Dessing MC, Hirst RA, de Vos AF, van der Poll T. Role of toll-like receptors 2 and 4 in pulmonary inflammation and injury induced by pneumolysin in mice. *PLoS One* (2009) 4:e7993. doi:10.1371/journal.pone.0007993
78. Asea A, Rehli M, Kabingu E, Boch JA, Bare O, Auron PE, et al. Novel signal transduction pathway utilized by extracellular HSP70: role of toll-like receptor (TLR) 2 and TLR4. *J Biol Chem* (2002) 277:15028–34. doi:10.1074/jbc.M200497200
79. Joshi AD, Dimitropoulou C, Thangjam G, Snead C, Feldman S, Barabutis N, et al. Heat shock protein 90 inhibitors prevent LPS-induced endothelial barrier dysfunction by disrupting RhoA signaling. *Am J Respir Cell Mol Biol* (2014) 50:170–9. doi:10.1165/rcmb.2012-0496OC
80. Chatterjee A, Snead C, Yetik-Anacak G, Antonova G, Zeng J, Catravas JD. Heat shock protein 90 inhibitors attenuate LPS-induced endothelial hyperpermeability. *Am J Physiol Lung Cell Mol Physiol* (2008) 294:L755–63. doi:10.1152/ajplung.00350.2007
81. Neckers L, Workman P. Hsp90 molecular chaperone inhibitors: are we there yet? *Clin Cancer Res* (2012) 18:64–76. doi:10.1158/1078-0432.CCR-11-1000

Conflict of Interest Statement: The authors declare that the research was conducted in the absence of any commercial or financial relationships that could be construed as a potential conflict of interest.

frontiers in Immunology

ORIGINAL RESEARCH
published: 27 September 2018
doi: 10.3389/fimmu.2018.02217

Exposure of Monocytic Cells to Lipopolysaccharide Induces Coordinated Endotoxin Tolerance, Mitochondrial Biogenesis, Mitophagy, and Antioxidant Defenses

John D. Widdrington[1,2†], Aurora Gomez-Duran[2,3,4†], Angela Pyle[2], Marie-Helene Ruchaud-Sparagano[1], Jonathan Scott[1], Simon V. Baudouin[5], Anthony J. Rostron[1], Penny E. Lovat[1], Patrick F. Chinnery[2,3,4] and A. John Simpson[1]*

[1] Institute of Cellular Medicine, Newcastle University, Newcastle upon Tyne, United Kingdom, [2] Institute of Genetic Medicine, Newcastle University, Newcastle upon Tyne, United Kingdom, [3] MRC Mitochondrial Biology Unit, Cambridge Biomedical Campus, Cambridge, United Kingdom, [4] Department of Clinical Neurosciences, University of Cambridge, Cambridge, United Kingdom, [5] Department of Anaesthesia, Royal Victoria Infirmary, Newcastle upon Tyne, United Kingdom

OPEN ACCESS

Edited by:
Gabor Csanyi,
Augusta University, United States

Reviewed by:
Krzysztof Guzik,
Jagiellonian University, Poland
Arnaud Millet,
INSERM U1209 Institut pour l'Avancée des Biosciences (IAB), France

***Correspondence:**
A. John Simpson
j.simpson@ncl.ac.uk

[†]Co-first authors

Specialty section:
This article was submitted to Inflammation, a section of the journal Frontiers in Immunology

Received: 19 June 2018
Accepted: 06 September 2018
Published: 27 September 2018

Citation:
Widdrington JD, Gomez-Duran A, Pyle A, Ruchaud-Sparagano M-H, Scott J, Baudouin SV, Rostron AJ, Lovat PE, Chinnery PF and Simpson AJ (2018) Exposure of Monocytic Cells to Lipopolysaccharide Induces Coordinated Endotoxin Tolerance, Mitochondrial Biogenesis, Mitophagy, and Antioxidant Defenses. Front. Immunol. 9:2217. doi: 10.3389/fimmu.2018.02217

In order to limit the adverse effects of excessive inflammation, anti-inflammatory responses are stimulated at an early stage of an infection, but during sepsis these can lead to deactivation of immune cells including monocytes. In addition, there is emerging evidence that the up-regulation of mitochondrial quality control mechanisms, including mitochondrial biogenesis and mitophagy, is important during the recovery from sepsis and inflammation. We aimed to describe the relationship between the compensatory immune and mitochondrial responses that are triggered following exposure to an inflammatory stimulus in human monocytic cells. Incubation with lipopolysaccharide resulted in a change in the immune phenotype of THP-1 cells consistent with the induction of endotoxin tolerance, similar to that seen in deactivated septic monocytes. After exposure to LPS there was also early evidence of oxidative stress, which resolved in association with the induction of antioxidant defenses and the stimulation of mitochondrial degradation through mitophagy. This was compensated by a parallel up-regulation of mitochondrial biogenesis that resulted in an overall increase in mitochondrial respiratory activity. These observations improve our understanding of the normal homeostatic responses that limit the adverse cellular effects of unregulated inflammation, and which may become ineffective when an infection causes sepsis.

Keywords: inflammation, endotoxin tolerance, mitochondria, mtDNA, mitophagy, mitochondrial biogenesis, antioxidants

INTRODUCTION

During sepsis an infection triggers a systemic inflammatory response, leading to organ dysfunction, shock and a significant risk of mortality (1). The clinical outcome of sepsis appears to be determined by the initial host inflammatory response to the infection and the subsequent compensatory mechanisms leading to the resolution of this inflammation (2). The dysregulation of any of

these processes may result in complications. In particular, an excessive or prolonged immune deactivation phase later in the sepsis illness leads to a vulnerability to nosocomial infections and increased mortality (3). Deactivation of blood monocytes, key innate immune cells, appears to be particularly important during this sepsis-induced immune deactivation but the mechanisms underlying this process are not well understood (4–6).

There is increasing evidence that impaired cellular respiration due to mitochondrial dysfunction during sepsis is associated with adverse clinical outcomes and may lead to impaired monocyte functions (7–9). Mitochondria are organelles with several critical cellular functions, particularly the generation of cellular energy at five enzyme complexes on the inner mitochondrial membrane during oxidative phosphorylation (OXPHOS) (10). The majority of mitochondrial constituents are encoded on the nuclear genome but mitochondria also contain circular mitochondrial DNA (mtDNA) with genes encoding 13 essential OXPHOS complex subunits (11). During sepsis mitochondria may become damaged or dysfunctional, leading to mtDNA depletion, impaired cellular respiration, and cell death (12, 13). The persistent presence of dysfunctional mitochondria can also lead to oxidative stress, as mitochondria are the main source of reactive oxygen species through the leakage of electrons during OXPHOS, and act as a potent stimulus for ongoing inflammation (14, 15).

The adverse effects of inflammation on mitochondria can be abrogated by several mechanisms. These include the induction of anti-inflammatory responses and antioxidant defenses, maintenance of mitochondrial integrity through the selective removal of dysfunctional mitochondria (mitophagy), and the generation of new organelles to replace them (mitochondrial biogenesis) (16, 17). However, the integration of these compensatory responses, and the interaction between mitochondria and immunity in monocytic cells following an inflammatory insult, are not well understood. In order to study these processes we assessed mitochondrial functions, biogenesis, and mitophagy in a time course model of endotoxin tolerance, a process whereby repeated exposure to lipopolysaccharide (LPS) from Gram negative bacteria leads to a change in immune phenotype similar to that seen in deactivated blood monocytes (18).

Here we show that there is a reversible induction of antioxidant defenses, mitophagy, and mitochondrial biogenesis in THP-1 cells rendered endotoxin tolerant following exposure to LPS, leading to a maintenance of cellular viability and respiration. These findings suggest that these processes are vital to cellular recovery following an inflammatory insult and that dysregulation of these compensatory mechanisms may contribute to adverse outcomes when an infection causes sepsis.

MATERIAL AND METHODS

THP-1 Cell Culture and Reagents

All reagents were obtained from ThermoFisher Scientific (Waltham, MA, USA) unless otherwise stated. THP-1 cells (ATCC®TIB-202TM) were kindly provided by Dr John Taylor's laboratory, Newcastle University. The cells were maintained at a concentration of $< 1 \times 10^6$ cells/ml in RPMI 1640 medium supplemented with 10% fetal calf serum (FCS) and contamination with Mycoplasma was periodically excluded. In all experiments 1×10^6 THP-1 cells were incubated in 25 cm^3 tissue flasks containing 5 ml growth medium to which LPS (100 ng/ml) from *Escherichia coli* O26/B6 (Sigma-Aldrich, St Louis, MO, USA) was added either 72 ($t = 0$ h), 48 ($t = 24$ h), 24 ($t = 48$ h), 6 ($t = 66$ h), or 2 ($t = 70$ h) h prior to the end of a 72 h pre-incubation period. After this pre-incubation the THP-1 cells were then pelleted, washed with PBS and re-suspended in fresh medium before comparing immune and mitochondrial functions to those in control cells pre-incubated for the previous 72 h in growth medium without LPS. The dose of LPS used in this model was selected on the basis of dose-finding experiments assessing the optimal induction of endotoxin tolerance (**Figure 1A**). *E. coli* O26/B6 LPS was chosen as we and others have shown inhalation to produce reproducible inflammation in human volunteers (19, 20).

Monocyte Isolation and Culture

Whole blood was obtained from 5 healthy volunteers (ethical approval was obtained from the relevant Research Ethics Committee and all volunteers provided informed, written consent). Human peripheral blood mononuclear cells (PBMCs) were extracted from the whole blood using dextran (Pharmacosmos, Holbaek, Denmark) sedimentation and Percoll (GE Healthcare Biosciences, Little Charlfort, UK) density-gradient centrifugation (21). Using the MACS Monocyte Isolation Kit II, MS columns and the Mini-MACS Separator (all Miltenyi Biotec, Auburn, CA, USA) monocytes were isolated from the PBMC fraction by negative selection. The purity of isolated monocytes was confirmed at >95% using morphological assessment following cytospin with Giemsa staining. The monocytes were re-suspended in IMDM medium supplemented with 10% autologous human serum and cultured with or without 10 ng/ml LPS for 24 h before measuring immune and mitochondrial functions.

Detection of Cytokine Production

2.5×10^5 THP-1 cells or 1×10^5 monocytes in 500 µl growth medium per well were seeded onto a 24 well plate (Grenier Bio-one, Stonehouse, UK) and incubated for 4 h at 37°C ± LPS (100 ng/ml for THP-1 cells and 10 ng/ml for monocytes). Subsequently, the release of TNFα and IL-8 in supernatant samples was measured by enzyme-linked immunosorbent assay (ELISA) using Novex® Human Antibody Pair kits and following the manufacturer's protocol.

THP-1 Cell Viability

Cell viability was assessed by measuring the proportion of THP-1 cells able to exclude propidium iodide (0.5 µg/ml) using the FACSCanto II flow cytometer (Becton Dickinson Biosciences, Franklin Lakes, NJ, USA).

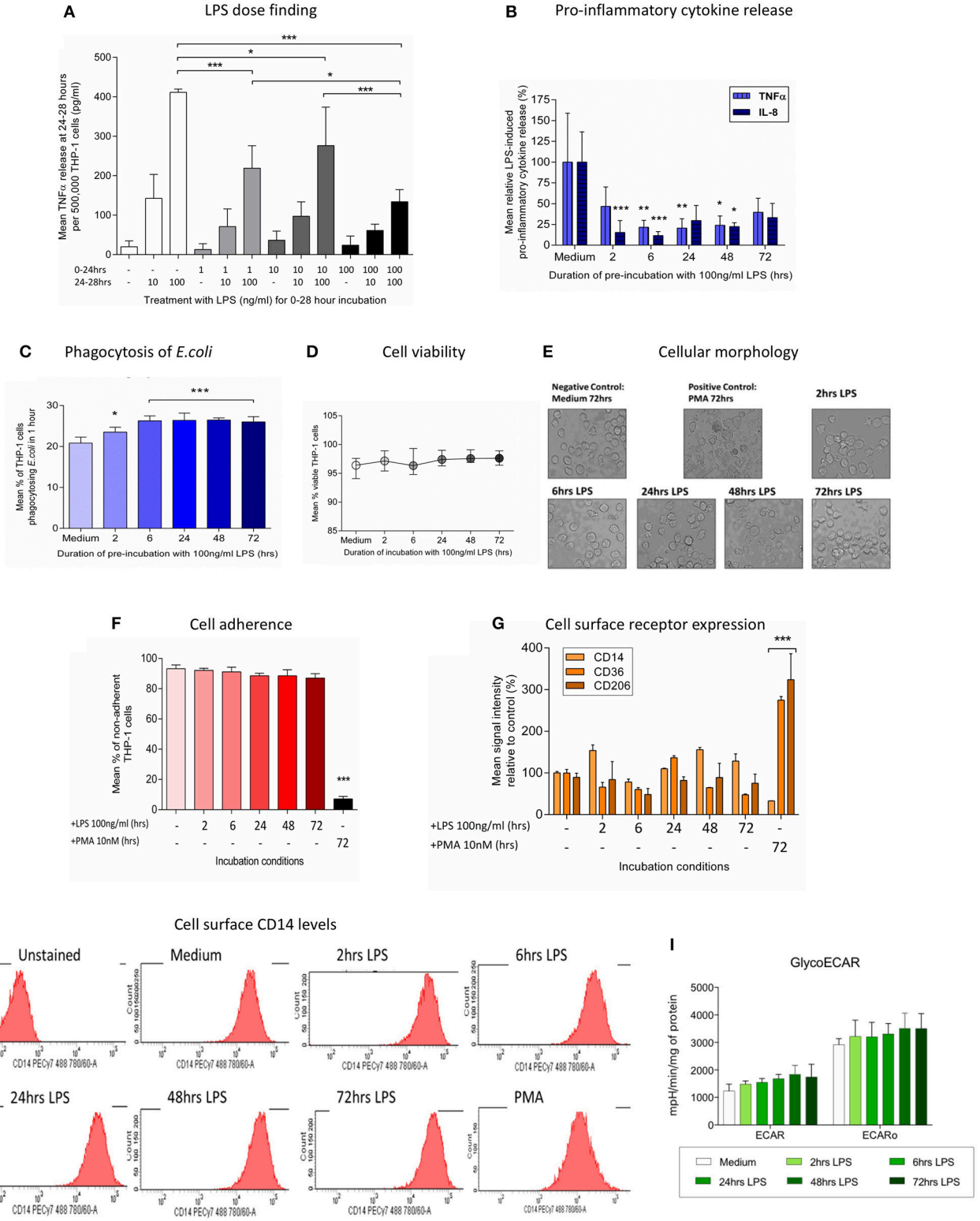

FIGURE 1 | Pre-incubation of THP-1 cells with LPS results in a change in immune phenotype consistent with endotoxin tolerance. THP-1 cells were pre-incubated with LPS (100 ng/ml) for 0–72 h and the ability to respond to a second inflammatory stimulus was then determined. **(A)** THP-1 cells were pre-incubated with 1, 10, or 100 ng/ml LPS for 24 h before measuring release of TNFα during a further 4-h exposure to a second stimulus of 10 or 100 ng/ml LPS by ELISA. **(B)**The release of pro-inflammatory TNFα and IL-8 in response to a second exposure to LPS (100 ng/ml) was measured by ELISA ($n = 6$). **(C)** Phagocytosis of fluorescein-labeled

(Continued)

FIGURE 1 | *Escherichia coli* (*E.coli*) in 1 h was measured by flow cytometry ($n = 4$). **(D)** Cell viability was determined by measuring the proportion of cells excluding propidium iodide following incubation with LPS (100 ng/ml) for 0–72 h ($n = 4$). **(E)** THP-1 cells were incubated with LPS (100 ng/ml) for 0–72 h before measuring macrophage differentiation in comparison to a positive control of cells treated with 10 nM PMA for 72 h. Representative images of THP-1 cell morphology on inversion light microscope at 40x magnifications. **(F)** THP-1 cell adherence to a 6 well plate was determined by cell counts before and after removal of adherent cells using a cell scraper ($n = 3$). **(G)** Flow cytometry was used to determine the relative signal intensity for the expression of the markers of macrophage differentiation CD14, CD36, and CD206 compared to the mean in the medium control ($n = 3$) **(H)** Representative histograms indicating the level of cell surface CD14 expression measured by flow cytometry. **(I)** Extracellular acidification rate with and without oligomycin following exposure to LPS (100 ng/ml) for 0–72 h as determined using the Seahorse XF96^e extracellular flux analyser ($n = 5$). All data are presented as mean ± standard deviation with the values in panel a expressed as relative cytokine release compared to the mean in the medium control; $^*p < 0.05$, $^{**}p < 0.01$, $^{***}p < 0.001$.

Assessment of Differentiation of THP-1 Cells to Macrophage-Like Cells

A qualitative assessment of THP-1 cell morphology was carried out by imaging a minimum of 100 cells in three separate wells on a 6 well plate using a DMI3000 B inversion microscope (Leica, Heidelberg, Germany). The adherence of THP-1 cells to a 6 well plate after 72 h incubation was assessed by cell counts before and after detaching any adherent cells using a cell scraper. Furthermore, the expression of macrophage differentiation markers CD14 (CD14-PECy7, 561385, Becton Dickinson Biosciences), CD36 (CD36-PE, 336206, BioLegend, San Diego, CA, USA), and CD206 (CD206-PE, 321106, BioLegend) on the surface of THP-1 cells was measured using the BD FACSCanto-II flow cytometer (Becton Dickinson Biosciences). As a positive control THP-1 cells were differentiated into macrophage-like cells by incubation with 10 nM phorbol-12-myristate 13-acetate (PMA) for 72 h (22).

MtDNA Sequencing and Bioinformatic Analysis

This process was carried out as previously described by our group (23). Firstly, mtDNA was enriched using long-range polymerase chain reaction. In order to prevent contamination with nuclear-mitochondrial sequences, amplicons were polymerised using PrimeSTAR GXL DNA polymerase (error rate = 0.00108%, Takara Bio, Saint-Germain-en-Laye, France) in two overlapping fragments, using primer set-1: CCC TCT CTC CTA CTC CTG-F (m.6222–6239) and CAG GTG GTC AAG TAT TTA TGG–R (m.16133–16153), and set-2: CAT CTT GCC CTT CAT TAT TGC–F (m.15295–15315) and GGC AGG ATA GTT CAG ACG-R (7773–7791). Primer efficiency and specificity was assessed as successful after no amplification of DNA from ρ0 cell lines lacking mtDNA. Amplified products and DNA positive/negative controls were assessed by gel electrophoresis, and quantified using a Qubit 2.0 fluorimeter. Each amplicon was individually purified using Agencourt AMPure XP beads (Beckman-Coulter, USA), pooled in equimolar concentrations and re-quantified. For the mtDNA sequencing pooled amplicons were "tagmented," amplified, cleaned, normalized, and pooled into 48 sample multiplexes using the Illumina Nextera XT DNA sample preparation kit (Illumina, CA, USA). The multiplex pools were sequenced using MiSeq Reagent Kit v3.0 (Illumina, CA, USA) in paired-end, 250 bp reads. Post run data, limited to reads with QV ≥ 30, were exported for analysis. Post-run FASTQ files were analyzed using an in-house developed bioinformatic pipeline. Reads were aligned to the revised Cambridge reference sequence (NC_012920) using BWA v0.7.10, invoking–mem (24). Aligned reads were sorted and indexed using Samtools v0.1.18 (25), duplicate reads were removed using Picard v1.85 (http://broadinstitute.github.io/picard/). Variant calling (including somatic calling) was performed in tandem using VarScan v2.3.8 (26, 27) (minimum depth = 1,500, supporting reads = 10, base-quality (BQ) ≥ 30, mapping quality (MQ) ≥ 20 and variant threshold = 1.0%), and LoFreq v0.6.1 (28). Concordance calling between VarScan and LoFreq was >99.5%. Concordant variants were annotated using ANNOVAR v529 (29) In-house Perl scripts were used to extract base/read quality data and coverage data.

Assessment of Mitochondrial Mass and Respiratory Chain Enzyme Activity

The uptake of 2.5 μM nonyl acridine orange (NAO, a dye that localizes to cardiolipin on the mitochondrial inner membrane) by THP-1 cells over 30 min was determined by measuring fluorescence (excitation wavelength 488 nm, bandpass filter 530/30 nm) using the FACSCanto-II flow cytometer (30). As a positive control mitochondrial mass was increased in THP-1 cells by pre-incubation for 72 h in DMEM supplemented with 5 mM galactose and lacking glucose (31).

Citrate synthase is a nuclear DNA-encoded enzyme that catalyzes the initial reaction in the citric acid cycle in the mitochondrial matrix and provides a quantitative marker of cellular mitochondrial content (32). A spectrophotometric assessment of the activity of citrate synthase on THP-1 cell homogenate was carried out as previously described using the MultiSkan Ascent plate reader (33). Complex IV activity was determined by the rate of oxidation of reduced cytochrome C using the Complex IV Human Specific Microplate Assay Kit (Abcam Danvers, MA, USA).

Phagocytosis of Fluorescein-Labeled *Escherichia coli*

Serum-opsonised fluorescein-labeled *Escherichia coli* K-12 strain were incubated with THP-1 cells at a multiplicity of infection of 10:1 for 1 h at 37°C. After washing and quenching extracellular fluorescence through the addition of 0.1% trypan blue (Sigma-Aldrich), the proportion of cells internalizing bacteria was then measured using the FACSCanto II flow cytometer (Becton Dickinson Biosciences, Franklin Lakes, NJ, USA).

Mitochondrial Bioenergetics Assessment

Mitochondrial membrane potential was measured following incubation with 5 μM JC-1 (T3168) for 30 min the red (excitation wavelength 561 nm, bandpass filter 186/15 nm) and green (488 nm, 530/30 nm) fluorescence using the LSRFortessa X20 flow cytometer (Becton Dickinson Biosciences). As a positive control cells were pre-treated for 10 min with 100 nM valinomycin, a potassium-selective ionophore that dissipates the mitochondrial membrane potential (34). The production of ROS was determined by measuring the oxidation of 1 μM DCF-DA (D399). After 30 min the fluorescence (absorption wavelength 488 nm, band pass filter 530/30 nm) was measured on the BD FACSCanto-II flow cytometer (35). As a positive control cells were treated with 100 μM hydrogen peroxide.

Mitochondrial respiration and Extracellular acidification rate (ECAR) was determined using the Seahorse XF96^e Extracellular Flux analyser (both Seahorse Biosciences, Chickopee, MA, USA) as previously described (36). 0.8×10^5 THP-1 cells were seeded in 175 μl of an assay medium per well, consisting of MEM supplemented with 11.1 mM D-Glucose and 2 mM L-Glutamine and adjusted to pH 7.0. Oxygen consumption rate (OCR) was measured at baseline and following the sequential addition of 1 μM oligomycin (a complex V inhibitor), 0.5 μM then 1 μM carbonyl cyanide 4-(trifluoromethoxy) phenylhydrazone (fCCP, an electron transport chain uncoupler) and finally 1 μM rotenone (a complex III inhibitor) plus 1 μM antimycin A (a complex I inhibitor). During each of the four stages of the assessment the OCR was measured in 16 wells per condition at 3 different time points. All OCR data were normalized to the total protein per well, which was determined using the Bradford assay.

Nucleic Acids Extraction and Quantification by Real Time PCR

For the determination of mtDNA copy number total DNA was extracted from cell pellets using the DNeasy blood and tissue kit (Qiagen, Valencia, CA, USA). The relative mtDNA copy number was determined by comparing the level of the mtDNA-encoded MT-ND1 gene (primers: F - ACGCCATAAAACTCTTCACC AAAG, R - GGGTTCATAGTAGAAGAGCGATGG) to that of the nuclear reference gene B2M (primers: F - CACTGAAAAAG ATGAGTATGCC, R - AACATTCCCTGACAATCCC) by real-time quantitative polymerase chain reaction (qPCR) using the SYBR® Green technique and the MyiQTM PCR machine (both BioRad, Hercules, CA, USA) (37).

In the quantification of mRNA levels, RNA was extracted from pellets of 4×10^6 THP-1 cells using the RNeasy mini kit (Qiagen) and single-stranded complementary DNA (cDNA) was synthesized using the High Capacity cDNA Reverse Transcription Kit. Following this the relative transcription of specific genes was determined by RTqPCR using the Taqman® Gene Expression Assay (β-ACTIN-Hs01060665_g1, GAPDH–Hs02758991_g1, HMOX1–Hs01110250_m1, SOD2–Hs00167309_m1) and the 7500 Fast Real Time PCR System. The relative amount of cDNA for each specific target was determined by comparison with the control housekeeping genes ACTB and GAPDH using the ΔCt method.

Western Blot

THP-1 cells were lysed using a lysis buffer containing 1% Triton X and the protease inhibitor phenylmethanesulfonyl fluoride (1 mM) (both Sigma-Aldrich) and the protein concentration in the lysates determined by Bradford assay. Equal amounts of protein were separated on the basis of size by sodium dodecyl sulfate polyacrylamide gel electrophoresis (SDS-PAGE), transferred onto polyvinylidene fluoride membranes and blotted with different antibodies, assessing the signal intensity after addition of an enhanced chemiluminescent substrate using the MultiSpectral Imaging System (UVP, Upland, CA, USA). The following antibodies were used; anti-mouse Ig-HRP (0260) and anti-rabbit-HRP (0448) from Dako (Cambridge, UK), β-actin (mouse, ab8226) and SOD2 (rabbit, ab13533) from Abcam (Danvers, MA, USA), LC3-I/II (rabbit, CS54995) from Cell Signalling (Beverley, MA, USA), Mitoprofile® Total OXPHOS antibody cocktail (mouse, MS604) from MitoSciences (Eugene, OR, USA) and TFAM (mouse, NBP1-71648) from Novus Biological (Cambridge, UK).

Measurement of Autophagy by Detection of LC3-II by Western Blot–

Following a 2 h incubation in the presence or absence of 10 μM chloroquine (an inhibitor of autophagosome degradation) protein was extracted from THP-1 cells and the amount of LC3-II relative to the housekeeping protein β-actin was determined by Western blot.

Confocal Microscopy to Assess Mitophagy

Serum-starved THP-1 cells incubated in RPMI 1640 medium without FCS for 2 h were used as a positive control for the induction of mitophagy and treatment with 5 nM bafilomycin A1 for 2 h was used to prevent autophagosome turnover. The THP-1 cells were adhered to slides by cytospin, fixed using 4% paraformaldehyde, permeabilised using 0.1% Triton X, and blocked to prevent non-specific antibody binding using 2% bovine serum albumin. The slides were then incubated with the primary antibodies (OXPHOS complex II–mouse, 459200, ThermoFisher Scientific; LC3-II–rabbit, CS54995, Cell signaling) for 16 h at 4°C, washed and incubated with fluorochrome-conjugated secondary antibodies (anti-mouse IgG-Oregon Green–O6380, anti-rabbit IgG-Alexa Fluor 568–A11011) and the nuclear dye DAPI (D3571) for a further 2 h at room temperature. Co-localisation of LC3-II and mitochondrial complex II was determined using the SB2 UV confocal microscope and the X63 HCX PL APO lens (both Leica, Heidelberg, Germany). Each experimental condition was assessed in triplicate with images taken for a minimum of 100 cells over 3 separate fields of view for each slide. The images were analyzed using Volocity software (PerkinElmer, Waltham, MA, USA). Co-localisation of mitochondrial complex II and LC3-II was assessed using the Mander's M1 co-localisation co-efficient (38).

STATISTICAL ANALYSIS

All experiments were carried out on a minimum of three biological replicates. The Shapiro-Wilk test was used to determine the normality of the data. Normally distributed data are presented as mean ± standard deviation, and were analyzed using one-way analysis of variance (ANOVA) with Dunnett's *post-hoc* analysis or independent *t*-tests. Non-normal data are presented as median and interquartile range and were analyzed using the Kruskal-Wallis analysis of variance with Dunn's *post-hoc* analysis. A p-value of <0.05 was defined as the threshold for statistical significance.

RESULTS

Pre-incubation With LPS Produces an Endotoxin Tolerance Phenotype in THP-1 Cells

After an initial exposure to LPS (100 ng/ml) for 0–72 h the ability of THP-1 cells to respond to a second inflammatory stimulus was assessed. THP-1 cells pre-incubated with LPS for 2–48 h had a significantly reduced ability to release the pro-inflammatory cytokines tumor necrosis factor alpha (TNFα) and interleukin (IL)-8 in response to a second stimulation with LPS (100 ng/ml) (**Figure 1B**). Conversely, following pre-incubation with LPS the ability of THP-1 cells to phagocytose *Escherichia coli* was significantly enhanced (**Figure 1C**). There was no evidence that exposure to LPS adversely affected THP-1 cell viability (**Figure 1D**). Study of the morphology (**Figure 1E**), adherence capacity (**Figure 1F**) and cell surface markers (**Figures 1G,H**) confirmed the absence of differentiation into macrophage-like cells as compared with the positive control treated with PMA for 72 h. Macrophage polarization correlates with changes in metabolism (39). Similarly to the surface markers, measurement of the Extracellular acidification rate of the media, which is widely used as glycolysis surrogate (40) did not show any changes after LPS treatment (**Figure 1I**). These findings are consistent with a change in immune phenotype of THP-1 cells following treatment with LPS that is characteristic of the induction of endotoxin tolerance (41).

Resolution of Early Oxidative Stress Following Exposure of THP-1 Cells to LPS

Next, we studied the effects of LPS treatment on mitochondrial dysfunction markers. We did not find any difference in the mitochondrial membrane potential on LPS-treated THP-1 cells (**Figure 2A**), confirming an absence of mitochondrial membrane depolarization, a process that reflects the leakage of proton across the inner mitochondrial membrane due to a loss of mitochondrial integrity (20). However, there was an early increase in reactive oxygen species production as measurement of hydrogen peroxide (**Figure 2B**), accompanied with higher mRNA levels of *heme oxygenase-1*, a gene that is up-regulated during oxidative stress (**Figure 2C**) (42). The resolution of this LPS-induced oxidative stress occurred in association with the stimulation of antioxidant defenses, as evidenced by increased levels of the mitochondrial antioxidant superoxide dismutase-2 (SOD2) (**Figure 2D**). Despite being particularly vulnerable to oxidative damage, we did not find any evidence of mtDNA deletions or mutations in LPS-exposed THP-1 cells (**Supplementary Table 1**). Thus, treatment of THP-1 cells with LPS leads to early oxidative stress, a process that is reversed by the induction of mitochondrial antioxidant defenses.

An Early Induction of Mitophagy Following Exposure of THP-1 Cells to LPS

Increased reactive oxygen species production is a feature of mitochondrial dysfunction, which has been found to activate mitophagy and target mitochondria for degradation (43). Consistent with this, treatment with LPS was found to stimulate both autophagy and mitophagy contemporaneously with the generation of oxidative stress, during the first hours of exposure. There was an early LPS-induced activation of autophagy, as indicated by significantly increased accumulation of the LC3-II protein, a constituent of the autophagosome, in THP-1 cells after treatment with LPS for 2–6 h (**Figure 3A**). The induction of mitophagy in LPS-treated THP-1 cells was then confirmed through the measurement of co-localization of mitochondria to autophagosomes using confocal microscopy (**Figures 3B,C**).

Induction of Mitochondrial Biogenesis and Increased Mitochondrial Respiration in LPS-Exposed THP-1 Cells

We next studied whether the induction of mitophagy after treatment with LPS was associated with changes in the overall mitochondrial mass. We did not observe changes in the level of the internal membrane marker cardiolipin (**Figure 4A**) or the matrix marker citrate synthase activity (**Figure 4B**), suggesting that there must be a parallel replacement of any degraded mitochondria. This was confirmed by assessments indicating that there was an early and sustained activation of mitochondrial biogenesis in THP-1 cells after LPS treatment. We observed a significant increase in THP-1 cell mtDNA copy number in THP-1 cells treated with LPS for 2–48 h (**Figure 4C**), that significantly correlated with the level of mitochondrial transcription factor A (TFAM), a key regulator of mitochondrial biogenesis that is bound to mtDNA (**Figures 4D,E**). Furthermore, LPS-treated THP-1 cells had a significant increase in protein levels for constituents of the inner mitochondrial membrane OXPHOS complexes I and IV, the two complexes containing the greatest number of mtDNA-encoded proteins (**Figure 4F**) (44). These results suggest that there is a coordinated up-regulation of mitochondrial biogenesis and mitophagy, leading to the maintenance of mitochondrial mass in THP-1 cells following an inflammatory insult in the form of LPS treatment.

The overall functional consequences of the increases in mitochondrial biogenesis and mitophagy were assessed by measurement of mitochondrial oxygen consumption. It was shown that exposure to LPS resulted in increased basal mitochondrial respiration and mitochondrial ATP production with no effect on non-mitochondrial oxygen consumption (**Figures 4G,H**), findings consistent with the increased levels of

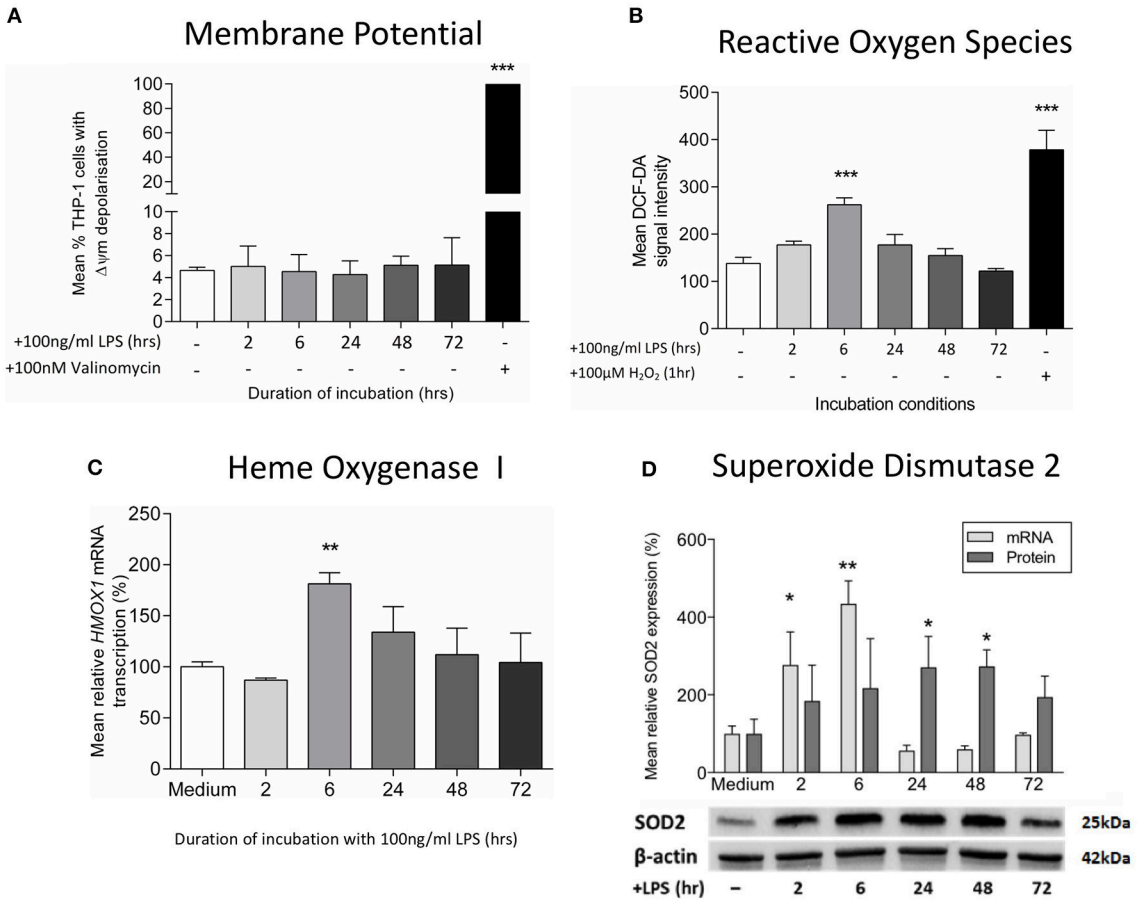

FIGURE 2 | Exposure to LPS leads to early oxidative stress but no increase in mitochondrial membrane potential. Mitochondrial membrane potential ($\Delta\psi m$) and oxidative stress were assessed following incubation of THP-1 cells with LPS (100 ng/ml) for 0–72 h. **(A)** The proportion of THP-1 cells with $\Delta\psi m$ was determined by measuring the JC1 fluorescence by flow cytometry (positive control—100 nM valinomycin) ($n = 3$). **(B)** Reactive oxygen species production was measured by oxidation of DCF-DA using flow cytometry (positive control—100 μM hydrogen peroxide, H_2O_2) ($n = 3$). **(C)** The mRNA transcription of *HMOX1* relative to *ACTB* and *GADPH* was determined by RTqPCR ($n = 3$). **(D)** The mRNA transcription (relative to *ACTB* and *GADPH*) and protein expression (relative to β-actin) of *SOD2* was measured using RTqPCR and Western blot ($n = 3$). Data are presented as mean ± standard deviation (mRNA and protein data are relative to the mean of the medium control); $^*p < 0.05$, $^{**}p < 0.01$, $^{***}p < 0.001$.

OXPHOS complexes I and IV (**Figure 4F**) and the increased activity of isolated complex IV (**Figure 4I**). Thus, in association with a shift to an endotoxin tolerance phenotype, THP-1 cells exposed to LPS have early evidence of oxidative stress which resolves in association with the induction of mitophagy and mitochondrial biogenesis, resulting in maintained cell viability and increased mitochondrial respiration.

Induction of Endotoxin Tolerance and Mitochondrial Biogenesis in Human Monocytes Treated With LPS

To confirm the relevance of the findings in THP-1 cells, human monocytes were pre-incubated with medium or 10 ng/ml LPS for 24 h before measuring cytokine release and mtDNA copy number. The induction of endotoxin tolerance was indicated by the finding that monocytes pre-incubated with LPS for 24 h had a significantly reduced ability to release TNFα release in response to a second exposure to LPS (**Figure 5A**). There was also a significant increase in mtDNA copy number in those monocytes treated with LPS, suggesting a similar induction of mitochondrial biogenesis to that seen in THP-1 cells (**Figure 5B**).

DISCUSSION

The regulation of the compensatory pro-survival cellular mechanisms that are triggered following an inflammatory insult and the mechanisms by which they become deranged during sepsis are not well understood. We have used an endotoxin tolerance model to induce a temporary state of immune deactivation in human monocytic cells resembling that seen in septic monocytes (18). This shift to an anti-inflammatory phenotype after exposure to LPS was found to occur in parallel with the activation of responses aimed at maintaining mitochondrial homeostasis; namely antioxidant

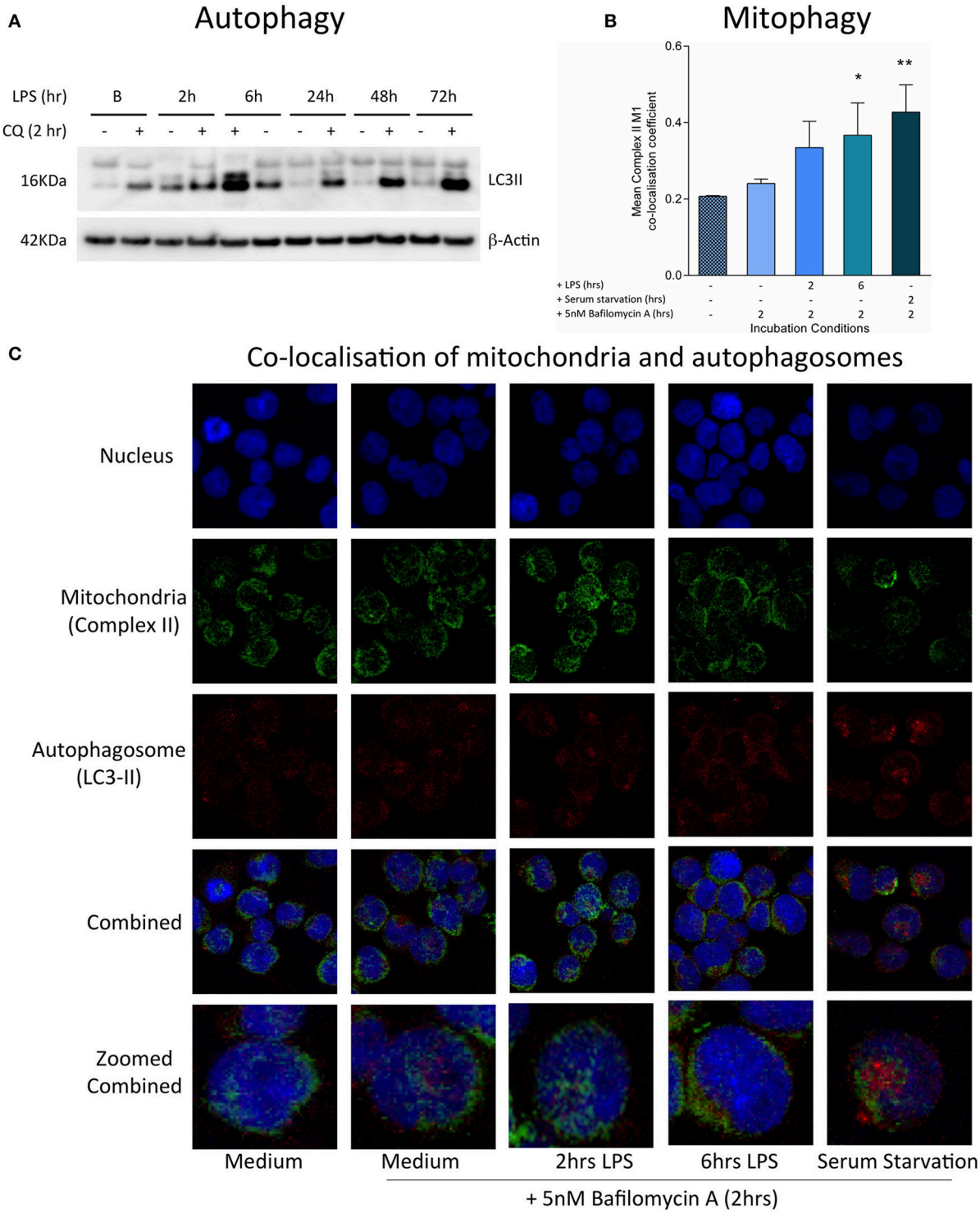

FIGURE 3 | Induction of mitophagy in THP-1 cells following exposure to LPS. THP-1 cells were incubated with LPS (100 ng/ml) before measuring the levels of autophagy and mitophagy. **(A)** Autophagic flux was assessed by measuring the accumulation of LC3-II relative to β-actin using Western blot ($n = 3$). **(B)** Confocal microscopy provided a measure of mitophagy by measuring the co-localisation of mitochondrial complex II with the autophagosome marker LC3-II using the Mander's M1 co-localisation co-efficient ($n = 4$). **(C)** Representative confocal microscopy images with staining for the nucleus (blue), mitochondrial complex II (green), and LC3-II (red) after incubation of THP-1 cells with LPS (100 ng/ml) for 0–6 h. In all experiments serum starvation was used a positive control and accumulation of autophagosomes was facilitated by treatment with 10 μM chloroquine (CQ) or 5 nM bafilomycin A1 for the final 2 h. Data are presented as mean ± standard deviation; $^{*}p < 0.05$, $^{**}p < 0.01$.

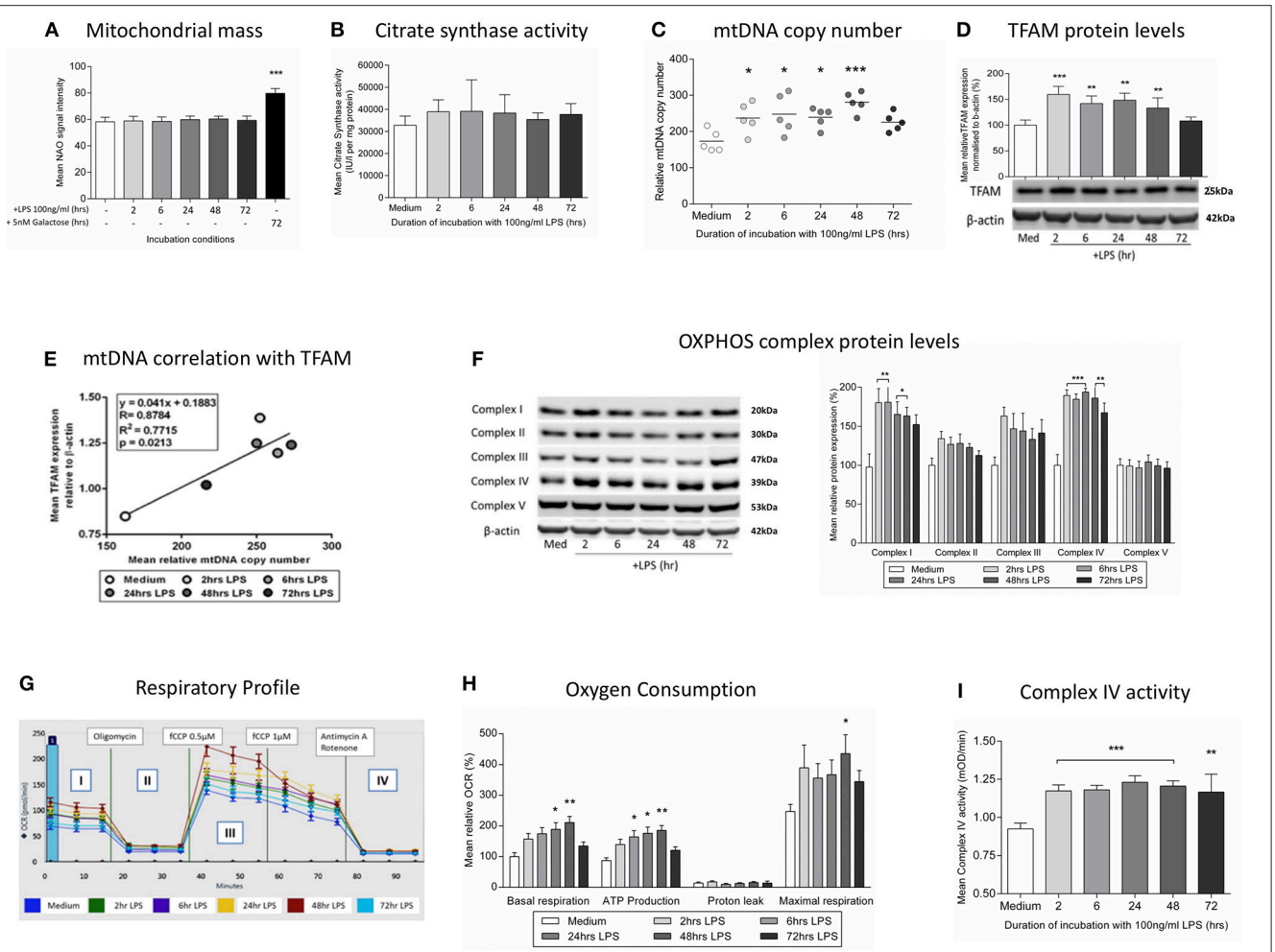

FIGURE 4 | Induction of mitochondrial biogenesis following exposure of THP-1 cells to LPS. THP-1 cells were incubated with LPS (100 ng/ml) for 0–72 h before assessing mitochondrial biogenesis and respiration. **(A)** Mitochondrial mass was assessed by measuring the uptake of NAO using flow cytometry, (positive control - glucose-free medium supplemented with 5 mM galactose) ($n = 4$). **(B)** A colorimetric assay was used to assess the activity of the mitochondrial matrix enzyme citrate synthase ($n = 3$). **(C)** mtDNA copy number was determined by measuring *MT-ND1* relative to *B2M* using qPCR ($n = 5$). **(D)** The level of TFAM protein relative to β-actin was determined by Western blot ($n = 4$). **(E)** Scatter plot, linear regression and Pearson's correlation of the relationship between mtDNA copy number and TFAM protein levels. $^*p < 0.05$, $^{**}p < 0.01$, $^{***}p < 0.001$. **(F)** Representative images of protein bands for subunits of the five mitochondrial OXPHOS complexes on PVDF membrane following Western blot and quantification of the subunits of the five mitochondrial OXPHOS complexes relative to β-actin ($n = 4$). **(G)** Representative example of the respiratory profile and **(H)** oxygen consumption rate for different aspects of mitochondrial respiration following exposure to LPS (100 ng/ml) for 0–72 h as determined using the Seahorse XF96^e extracellular flux analyser ($n = 5$). **(I)** A colorimetric assay was used to measure the activity of OXPHOS complex IV($n = 3$). The data are represented as **(A)** individual values with a line indicating the mean or **(B,C,F,H,I)** mean ± standard deviation relative to the mean in the medium control; $^*p < 0.05$, $^{**}p < 0.01$, $^{***}p < 0.001$.

defenses, mitophagy, and mitochondrial biogenesis. In this model the resultant selective replacement of dysfunctional mitochondria leads to an increase in overall mitochondrial efficiency, as evidenced by increased mitochondrial respiration despite unchanged mitochondrial mass, in association with the resolution of oxidative stress and the recovery of pro-inflammatory cytokine release by 72 h.

Mitophagy involves the lysosomal degradation of mitochondria following encapsulation in an autophagosome (45). This process is key for the maintenance of quality control because damaged mitochondria are specifically targeted for destruction (46). Although data from human studies are very limited, it appears that mitophagy may be insufficient during severe sepsis resulting in persistence of dysfunctional mitochondria that can lead to deficient respiration (47, 48). Moreover, animal sepsis models suggest that mitophagy is an important component of the recovery mechanisms, with inadequate mitochondrial degradation associated with increased organ damage, persistence of oxidative stress, and exacerbation of inflammation through increased inflammasome formation (49–51). In keeping with this, reports in cell culture and murine models indicate that autophagy and mitophagy are stimulated following ligand binding to pattern recognition receptors in a process which is implicated in suppressing pro-inflammatory

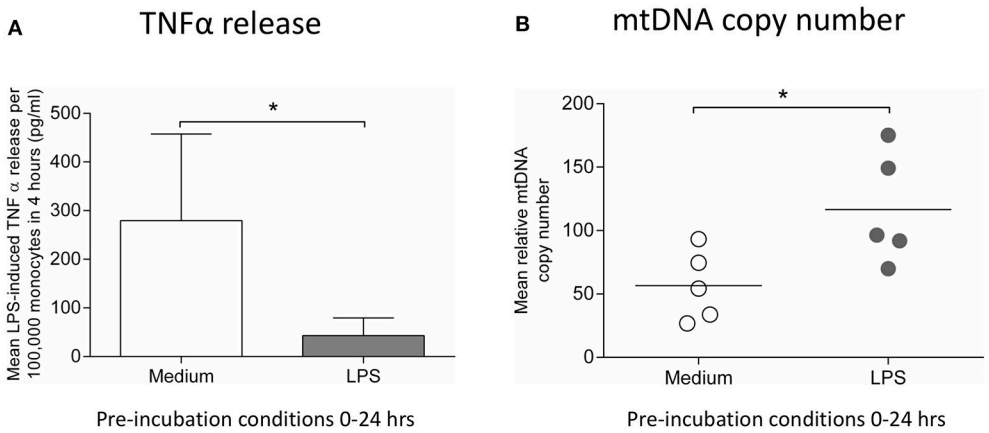

FIGURE 5 | Incubation of monocytes with LPS for 24 h results in reduced ability to release TNFα in response to a second LPS stimulus and increased mtDNA copy number. Blood monocytes were incubated with LPS (10 ng/ml) before measuring cytokine release and mtDNA copy number. **(A)** The release of TNFα in response to a second 4 h exposure to LPS (10 ng/ml) was measured by ELISA ($n = 5$). **(B)** mtDNA copy number was determined by measuring *MT-ND1* relative to *B2M* using qPCR ($n = 5$). Data are represented as **(A)** mean ± standard deviation or **(B)** individual values with a line representing the mean. *$p < 0.05$ on independent *t*-test.

cytokine release and oxidative stress through inhibition of the nucleotide-binding domain, leucine-rich-containing family, pyrin domain containing-3 (NLRP3) inflammasome (52, 53).

Mitochondrial biogenesis is a dynamic process during which pre-existing mitochondria grow and divide in response to physiological conditions or cellular energy requirements (54). It is controlled by a complex network of hormones and signaling pathways which regulate the expression of mitochondrial transcription factors that in turn co-ordinate the expression of mitochondrial genes in the nuclear and mitochondrial genomes (55). Mitochondrial biogenesis appears to be an essential response that is required to compensate for the adverse effects of inflammation on mitochondrial structure and function (56). In a wide variety of animal models and a few small observational human studies there is increasing evidence that expanding the mitochondrial population promotes the recovery from sepsis (57–59). The effects of this inflammation-induced mitochondrial biogenesis may actually extend beyond maintaining homeostasis and facilitate an increase in overall cellular respiration, as seen in our model, potentially leading to an increased resistance to the negative effects of excessive inflammation (36, 60).

Although human data have been lacking, animal models suggest that there is an integrated up-regulation of mitophagy and mitochondrial biogenesis following an inflammatory insult (43). Both processes appear to be directly triggered following the recognition of inflammatory stimuli; inhibition of Toll-like receptor-4 (TLR-4, the main pattern recognition receptor for LPS-induced signaling) after caecal ligation and puncture or LPS treatment prevents the activation of both mitophagy and mitochondrial biogenesis (48, 61). Mitochondrial turnover may be integrated with antioxidant defenses and anti-inflammatory responses through the activation of redox-sensitive signaling pathways (62). Murine models suggest that during sepsis the inducible antioxidant enzyme heme oxygenase-1 stimulates the expression of nuclear factor (erythroid-derived-2)-like 2 (Nrf2), a transcription factor that binds to anti-oxidant response elements on gene promoters for transcription factors regulating mitochondrial biogenesis, mitophagy, and anti-inflammatory responses (63, 64). $Nrf2^{-/-}$ knockout mice have impaired ability to upregulate these processes, leading to more severe sepsis (43, 65). Alternatively, a group of deacetylases termed silent information regulators (sirtuins), with activity dependent on the presence of the oxidized form of the respiratory chain enzyme nicotinamide adenine dinucleotide (NAD+), facilitate responses to alterations in cellular energy levels and may thus link metabolism with immunity (66). In the nucleus SIRT1 activates both mitochondrial biogenesis and autophagy, but is also involved in resolution of inflammation through the negative regulation of pro-inflammatory pathways (67, 68). In the mitochondria SIRT3 is essential for effective mitochondrial biogenesis and can increase OXPHOS activity and activate antioxidant responses (69). In one study, following exposure to LPS, the sequential activation of SIRT1 and SIRT3 was found to integrate the induction of mitochondrial biogenesis with the down-regulation of pro-inflammatory responses (36). Another potential link between immunity and mitochondrial homeostasis is suggested by findings that the intracellular chaperone heat shock protein-90 (HSP90) is both essential for effective clearance of defective mitochondria by mitophagy and implicated, through accumulation at the cell surface, in the suppression of TNFα production in response to LPS (70, 71).

To our knowledge we have shown for the first time that mitochondrial biogenesis and mitophagy are important in the responses of immunologically relevant human cells to an inflammatory insult, providing important insights into the compensatory mechanisms that may go wrong during sepsis. However, it should be noted that this study has some limitations. Firstly, our model predominantly used THP-1 cells because human monocytes have considerable inter-individual variability, a limited life span, a propensity to rapidly differentiate *in vitro*,

and are difficult to isolate in large numbers (72, 73). THP-1 cells have similar morphology, surface antigens and secretory products to blood monocytes and have been used extensively to study monocyte and macrophage functions (74, 75). However, they represent a simplified model and have important differences to human monocytes that are particularly relevant when assessing the response to LPS, including significantly reduced expression of the LPS receptor CD14 and altered cytokine production (76, 77). In view of this, while we have detected similar effects of LPS exposure on TNFα release and mtDNA copy number in monocytes, our results are only suggestive of responses that may occur in human monocytes and an *in vivo* validation, for example in a human LPS challenge model, is ultimately required (78).

It should also be noted that, while we have observed an immune phenotype consistent with endotoxin tolerance, there are other potential explanations for the decrease in pro-inflammatory cytokine release following prior exposure to LPS that have not been fully explored. These include the presence of LPS-binding protein, a down-regulation in TLR-4 expression or a failure of internalization of TLR-4-LPS complexes (79, 80). Similarly, although we have found no evidence that LPS exposure leads to THP-1 cell macrophage-like differentiation, M2 polarization remains a potential mechanism for the change in immune phenotype and mitochondrial respiration seen in this study (81, 82). In addition, endotoxin tolerance is not an ideal model of sepsis as a single, sterile stimulus does not mimic the overwhelming, multiple, and persistent inflammatory triggers seen in sepsis. Rather, by using endotoxin tolerance, we are likely to mimic the processes occurring when an infection is successfully cleared instead of a situation in which sepsis is triggered. Furthermore, the dose of LPS required to induce endotoxin tolerance in this study (100 ng/ml) is significantly higher than the concentration of LPS that has been measured in the serum of patients with septic shock (83). Finally, we have not elucidated the mechanisms underlying our observations, which means that causality and the precise relationships between the changes observed remain to be determined.

In clinical studies and animal models survival and recovery of cellular functions in sepsis appear to be dependent on the induction of compensatory responses, including those aimed at preventing excessive inflammation and those that maintain mitochondrial homeostasis through the activation of mitochondrial biogenesis, mitophagy and antioxidant defenses. Here we show for the first time in human monocyte-like cells that there is a contemporaneous, co-ordinated upregulation of mitochondrial biogenesis, mitophagy and antioxidant defenses during endotoxin tolerance, which results in the resolution of oxidative stress and increased mitochondrial respiratory activity. This provides important insights into the relationship between mitochondria and the innate immune response, as well as the coordination of compensatory responses that are required to maintain cell viability and function following an inflammatory insult. We speculate that these processes may go awry when the insult leads to sepsis.

AUTHOR CONTRIBUTIONS

JW, AG-D, SB, AR, PL PC, and AS formulated the research hypothesis and designed the experiments. JW, AG-D, AP, M-HR-S, and JS carried out the experimental procedures and data analysis, assisted with data collection, and interpretation. The manuscript was prepared by JW, AG-D, AS, and PC.

FUNDING

JW was funded by a Wellcome Trust Translational Medicine and Therapeutics Fellowship. PC is a Wellcome Trust Senior Fellow in Clinical Science (101876/Z/13/Z), and a UK NIHR Senior Investigator, who receives support from the Medical Research Council Mitochondrial Biology Unit (MC_UP_1501/2), the Wellcome Trust Centre for Mitochondrial Research (096919Z/11/Z), the Medical Research Council (UK) Centre for Translational Muscle Disease (G0601943), EU FP7 TIRCON, and the National Institute for Health Research (NIHR) Biomedical Research Centre based at Cambridge University Hospitals NHS Foundation Trust and the University of Cambridge. The views expressed are those of the author(s) and not necessarily those of the NHS, the NIHR or the Department of Health.

SUPPLEMENTARY MATERIAL

The Supplementary Material for this article can be found online at: https://www.frontiersin.org/articles/10.3389/fimmu.2018.02217/full#supplementary-material

REFERENCES

1. Singer M, Deutschman CS, Seymour C, Shankar-Hari M, Annane D, Bauer M, et al. The third international consensus definitions for sepsis and septic shock (sepsis-3). *JAMA* (2016) 315:801–10. doi: 10.1001/jama.2016.0287
2. Kox WJ, Volk T, Kox SN, Volk HD. Immunomodulatory therapies in sepsis. *Intensive Care Med.* (2000) 26(Suppl. 1):S124–8. doi: 10.1007/s001340051129
3. Hotchkiss RS, Monneret G, Payen D. Immunosuppression in sepsis: a novel understanding of the disorder and a new therapeutic approach. *Lancet Infect Dis.* (2013) 13:260–8. doi: 10.1016/S1473-3099(13)70001-X
4. Hall MW, Knatz NL, Vetterly C, Tomarello S, Wewers MD, Volk HD, et al. Immunoparalysis and nosocomial infection in children with multiple organ dysfunction syndrome. *Intens Care Med.* (2011) 37:525–32. doi: 10.1007/s00134-010-2088-x
5. Landelle C, Lepape A, Voirin N, Tognet E, Venet F, Bohé J, et al. Low monocyte human leukocyte antigen-DR is independently associated with nosocomial infections after septic shock. *Intens Care Med.* (2010) 36:1859–66. doi: 10.1007/s00134-010-1962-x
6. Monneret G, Lepape A, Voirin N, Bohé J, Venet F, Debard AL, et al. Persisting low monocyte human leukocyte antigen-DR expression predicts mortality in septic shock. *Intens Care Med.* (2006) 32:1175–83. doi: 10.1007/s00134-006-0204-8
7. Belikova I, Lukaszewicz AC, Faivre V, Damoisel C, Singer M, Payen D. Oxygen consumption of human peripheral blood mononuclear cells in severe human sepsis. *Critic Care Med.* (2007) 35:2702–8. doi: 10.1097/00003246-200712000-00004
8. Brealey D, Brand M, Hargreaves I, Heales S, Land J, Smolenski R, et al. Association between mitochondrial dysfunction and severity and outcome

of septic shock. *Lancet* (2002) 360:219–23. doi: 10.1016/S0140-6736(02)09459-X
9. Pyle A, Burn DJ, Gordon C, Swan C, Chinnery PF, Baudouin SV. Fall in circulating mononuclear cell mitochondrial DNA content in human sepsis. *Intens Care Med.* (2010) 36:956–62. doi: 10.1007/s00134-010-1823-7
10. Greaves LC, Reeve AK, Taylor RW, Turnbull DM. Mitochondrial DNA and disease. *J Pathol.* (2012) 226:274–86. doi: 10.1002/path.3028
11. Chinnery PF, Hudson G. Mitochondrial genetics. *Br Med Bull.* (2013) 106:135–59. doi: 10.1093/bmb/ldt017
12. Brealey D, Singer M. Mitochondrial dysfunction in sepsis. *Curr Infect Dis Rep.* (2003) 5:365–71. doi: 10.1007/s11908-003-0015-9
13. Singer M. Mitochondrial function in sepsis: acute phase versus multiple organ failure. *Critic Care Med.* (2007) 35:S441–8. doi: 10.1097/01.CCM.0000278049.48333.78
14. Galley HF. Oxidative stress and mitochondrial dysfunction in sepsis. *Br J Anaest.* (2011) 107:57–64. doi: 10.1093/bja/aer093
15. Zhang Q, Raoof M, Chen Y, Sumi Y, Sursal T, Junger W, et al. Circulating mitochondrial DAMPs cause inflammatory responses to injury. *Nature* (2010) 464:104–7. doi: 10.1038/nature08780
16. López-Armada MJ, Riveiro-Naveira RR, Vaamonde-García C, Valcárcel-Ares MN. Mitochondrial dysfunction and the inflammatory response. *Mitochondrion* (2013) 13:106–18. doi: 10.1016/j.mito.2013.01.003
17. Piantadosi CA, Suliman HB. Redox regulation of mitochondrial biogenesis. *Free Radic Biol Med.* (2012) 53:2043–53. doi: 10.1016/j.freeradbiomed.2012.09.014
18. Cavaillon JM, Adib-Conquy M. Bench-to-bedside review: endotoxin tolerance as a model of leukocyte reprogramming in sepsis. *Critical Care* (2006) 10:233. doi: 10.1186/cc5055
19. Barr LC, Brittan M, Morris AC, McAuley DF, McCormack C, Fletcher AM, et al. A randomized controlled trial of peripheral blood mononuclear cell depletion in experimental human lung inflammation. *Am J Resp Critic Care Med.* (2013) 188:449–55. doi: 10.1164/rccm.201212-2334OC
20. Shyamsundar M, S.McKeown TW, O'Kane CM, Craig TR, Brown V, Thickett DR, et al. Simvastatin decreases lipopolysaccharide-induced pulmonary inflammation in healthy volunteers. *Am J Resp Critic Care Med.* (2009) 179:1107–14. doi: 10.1164/rccm.200810-1584OC
21. Haslett C, Guthrie LA, Kopaniak MM. Modulation of multiple neutrophil functions by preparative methods or trace concentrations of bacterial lipopolysaccharide. *Am J Pathol.* (1985) 119:101–10.
22. Daigneault M, Preston JA, Marriott HM, Whyte MK, Dockrell DH. The identification of markers of macrophage differentiation in PMA-stimulated THP-1 cells and monocyte-derived macrophages. *PLoS ONE* (2010) 5:8668 doi: 10.1371/journal.pone.0008668
23. Coxhead J, Kurzawa-Akanbi M, Hussain R, Pyle A, Chinnery P, Hudson G. Somatic mtDNA variation is an important component of Parkinson's disease. *Neurobiol Aging* (2016) 38:217.e1-217.e6. doi: 10.1016/j.neurobiolaging.2015.10.036
24. Li H, Durbin R. Fast and accurate short read alignment with Burrows-Wheeler transform. *Bioinformatics* (2009) 25:1754–60. doi: 10.1093/bioinformatics/btp324
25. Li H, Handsaker B, Wysoker A, Fennell T, Ruan J, Homer N, et al. The sequence alignment/map format and SAMtools. *Bioinformatics* (2009) 25:2078–9. doi: 10.1093/bioinformatics/btp352
26. Koboldt DC, Chen K, Wylie T, Larson DE, McLellan MD, Mardis ER, et al. VarScan: variant detection in massively parallel sequencing of individual and pooled samples. *Bioinformatics* (2009) 25:2283–5. doi: 10.1093/bioinformatics/btp373
27. Koboldt DC, Zhang Q, Larson DE, Shen D, McLellan MD, Lin L, et al. VarScan 2: somatic mutation and copy number alteration discovery in cancer by exome sequencing. *Genome Res.* (2012) 22:568–76. doi: 10.1101/gr.129684.111
28. Wilm A, Aw PP, Bertrand D, Yeo GH, Ong SH, Wong CH, et al. LoFreq: a sequence-quality aware, ultra-sensitive variant caller for uncovering cell-population heterogeneity from high-throughput sequencing datasets. *Nucleic Acids Res.* (2012) 40:11189–201. doi: 10.1093/nar/gks918
29. Wang K, Li M, Hakonarson H. ANNOVAR: functional annotation of genetic variants from high-throughput sequencing data. *Nucleic Acids Res.* (2010) 38:e164. doi: 10.1093/nar/gkq603
30. Cottet-Rousselle C, Ronot X, Leverve X, Mayol JF. Cytometric assessment of mitochondria using fluorescent probes. *Cytometry Part A* (2011) 79 A:405-425. doi: 10.1002/cyto.a.21061
31. Morán M, Rivera H, Sánchez-Aragó M, Blázquez A, Merinero B, Ugalde C, et al. Mitochondrial bioenergetics and dynamics interplay in complex I-deficient fibroblasts. *Biochim Biophys Acta Mol Basis Dis.* (2010) 1802:443–53. doi: 10.1016/j.bbadis.2010.02.001
32. R.Rodenburg JT, Schoonderwoerd GC, Tiranti V, Taylor RW, Rötig A, Valente L, et al. A multi-center comparison of diagnostic methods for the biochemical evaluation of suspected mitochondrial disorders. *Mitochondrion* (2012) 13:36–43. doi: 10.1016/j.mito.2012.11.004
33. Kirby DM, Thorburn DR, Turnbull DM, Taylor RW. Biochemical assays of respiratory chain complex activity. *Methods Cell Biol.* (2007) 80:93–119. doi: 10.1016/S0091-679X(06)80004-X
34. Salvioli S, Ardizzoni A, Franceschi C, Cossarizza A. JC-1, but not DiOC6(3) or rhodamine 123, is a reliable fluorescent probe to assess $\Delta\Psi$ changes in intact cells: Implications for studies on mitochondrial functionality during apoptosis. *FEBS Lett.* (1997) 411:77–82. doi: 10.1016/S0014-5793(97)00669-8
35. Winterbourn CC. The challenges of using fluorescent probes to detect and quantify specific reactive oxygen species in living cells. *Biochim Biophys Acta General Sub.* (2013) 1840:730–8. doi: 10.1016/j.bbagen.2013.05.004
36. Liu TF, Vachharajani V, Millet P, Bharadwaj MS, Molina AJ, McCall CE. Sequential actions of SIRT1-RELB-SIRT3 coordinate nuclear-mitochondrial communication during immunometabolic adaptation to acute inflammation and sepsis. *J Biol Chem.* (2015) 290:396–408. doi: 10.1074/jbc.M114.566349
37. Payne BA, Wilson IJ, Hateley CA, Horvath R, Santibanez-Koref M, Samuels DC, et al. Mitochondrial aging is accelerated by anti-retroviral therapy through the clonal expansion of mtDNA mutations. *Nat Genet.* (2011) 43:806–10. doi: 10.1038/ng.863
38. Zinchuk V, Zinchuk O, Okada T. Quantitative colocalization analysis of multicolor confocal immunofluorescence microscopy images: pushing pixels to explore biological phenomena. *Acta Histochem Cytochem.* (2007) 40:101–11. doi: 10.1267/ahc.07002
39. O'Neill LA. A Metabolic roadblock in inflammatory macrophages. *Cell Rep.* (2016) 17:625–6. doi: 10.1016/j.celrep.2016.09.085
40. TeSlaa T, Teitell MA. Techniques to monitor glycolysis. *Methods Enzymol.* (2014) 542:91–114. doi: 10.1016/B978-0-12-416618-9.00005-4
41. Biswas SK, Lopez-Collazo E. Endotoxin tolerance: new mechanisms, molecules and clinical significance. *Trends Immunol.* (2009) 30:475–87. doi: 10.1016/j.it.2009.07.009
42. Alam J, Cook JL. Transcriptional regulation of the heme oxygenase-1 gene via the stress response element pathway. *Curr Pharm Des.* (2003) 9:2499–511. doi: 10.2174/1381612033453730
43. Chang AL, Ulrich A, Suliman HB, Piantadosi CA. Redox regulation of mitophagy in the lung during murine Staphylococcus aureus sepsis. *Free Radic Biol Med.* (2015) 78:179–89. doi: 10.1016/j.freeradbiomed.2014.10.582
44. Schon EA, DiMauro S, Hirano M. Human mitochondrial DNA: roles of inherited and somatic mutations. *Nat Rev Genet.* (2012) 13:878–90. doi: 10.1038/nrg3275
45. Lee J, Giordano S, Zhang J. Autophagy, mitochondria and oxidative stress: cross-talk and redox signalling. *Biochem J.* (2012) 441:523–40. doi: 10.1042/BJ20111451
46. Youle RJ, Narendra DP. Mechanisms of mitophagy. *Nat Rev Mol Cell Biol.* (2011) 12:9–14. doi: 10.1038/nrm3028
47. J.M.Gunst DP, Derese IB, Aertgeerts AB, Ververs JB, Wauters AB, Van den Berghe GMDP, et al. Insufficient autophagy contributes to mitochondrial dysfunction, organ failure, and adverse outcome in an animal model of critical illness*. *Critic Care Med.* (2013) 41:182–94. doi: 10.1097/CCM.0b013e3182676657
48. Mannam P, Shinn AS, Srivastava A, Neamu RF, Walker WE, Bohanon M, et al. MKK3 regulates mitochondrial biogenesis and mitophagy in sepsis-induced lung injury. *Am J Physiol Lung Cell Mol Physiol.* (2014) 306:L604–19. doi: 10.1152/ajplung.00272.2013
49. Motori E, Puyal J, Toni N, Ghanem A, Angeloni C, Malaguti M, et al. Inflammation-induced alteration of astrocyte mitochondrial dynamics requires autophagy for mitochondrial network maintenance. *Cell Metabol.* (2013) 18:844–59. doi: 10.1016/j.cmet.2013.11.005

50. Nakahira K, Haspel JA, Rathinam AK, Lee SJ, Dolinay T, Lam HC, et al. Autophagy proteins regulate innate immune responses by inhibiting the release of mitochondrial DNA mediated by the NALP3 inflammasome. *Nature Immunol.* (2011) 12:222–30. doi: 10.1038/ni.1980
51. Zhou R, Yazdi AS, Menu P, Tschopp J. A role for mitochondria in NLRP3 inflammasome activation. *Nature* (2011) 469:221–5. doi: 10.1038/nature09663
52. Chuang SY, Yang CH, Chou CC, Chiang YP, Chuang TH, Hsu LC. TLR-induced PAI-2 expression suppresses IL-1β processing èia increasing autophagy and NLRP3 degradation. *Proc Natl Acad Sci USA.* (2013) 110:16079–84. doi: 10.1073/pnas.1306556110
53. Kim MJ, Bae SH, Ryu JC, Kwon Y, Oh JH, Kwon J, et al. SESN2/sestrin2 suppresses sepsis by inducing mitophagy and inhibiting NLRP3 activation in macrophages. *Autophagy* (2016) 12:1272–91. doi: 10.1080/15548627.2016.1183081
54. Lee HC, Wei YH. Mitochondrial biogenesis and mitochondrial DNA maintenance of mammalian cells under oxidative stress. *Int J Biochem Cell Biol.* (2005) 37:822–34. doi: 10.1016/j.biocel.2004.09.010
55. Weitzel JM, Alexander Iwen K. Coordination of mitochondrial biogenesis by thyroid hormone. *Mol Cell Endocrinol.* (2011) 342:1–7. doi: 10.1016/j.mce.2011.05.009
56. Kozlov A, Bahrami S, Calzia E, Dungel P, Gille L, Kuznetsov A, et al. Mitochondrial dysfunction and biogenesis: do ICU patients die from mitochondrial failure? *Ann Intens Care* (2011) 1:41. doi: 10.1186/2110-5820-1-41
57. Carré JE, Orban JC, Re L, Felsmann K, Iffert W, Bauer M, et al. Survival in critical illness is associated with early activation of mitochondrial biogenesis. *Am J Resp Critic Care Med.* (2010) 182:745–51. doi: 10.1164/rccm.201003-0326OC
58. Islam MN, Das SR, Emin MT, Wei M, Sun L, Westphalen K, et al. Mitochondrial transfer from bone-marrow-derived stromal cells to pulmonary alveoli protects against acute lung injury. *Nat Med.* (2012) 18:759–65. doi: 10.1038/nm.2736
59. Sweeney TE, Suliman HB, Hollingsworth JW, Piantadosi CA. Differential regulation of the PGC family of genes in a mouse model of staphylococcus aureus sepsis. *PLoS ONE* (2010) 5:e11606. doi: 10.1371/journal.pone.0011606
60. Stetler RA, Leak RK, Yin W, Zhang L, Wang S, Gao Y, et al. Mitochondrial biogenesis contributes to ischemic neuroprotection afforded by LPS pre-conditioning. *J Neurochem.* (2012) 123:125–37. doi: 10.1111/j.1471-4159.2012.07951.x
61. Carchman EH, Whelan S, Loughran P, Mollen K, Stratamirovic S, Shiva S, et al. Experimental sepsis-induced mitochondrial biogenesis is dependent on autophagy, TLR4, and TLR9 signaling in liver. *FASEB J.* (2013) 27:4703–11. doi: 10.1096/fj.13-229476
62. Piantadosi CA, Suliman HB. Transcriptional control of mitochondrial biogenesis and its interface with inflammatory processes. *Biochim Biophys Acta General Sub.* (2012) 1820:532–41. doi: 10.1016/j.bbagen.2012.01.003
63. MacGarvey NC, Suliman HB, Bartz RR, Fu P, Withers CM, Welty-Wolf KE, et al. Activation of mitochondrial biogenesis by heme oxygenase-1–mediated NF-E2–related factor-2 induction rescues mice from lethal *Staphylococcus aureus* sepsis. *Am J Resp Critic Care Med.* (2012) 185:851–61. doi: 10.1164/rccm.201106-1152OC
64. Piantadosi CA, Withers CM, Bartz RR, MacGarvey NC, Fu P, Sweeney TE, et al. Heme oxygenase-1 couples activation of mitochondrial biogenesis to anti-inflammatory cytokine expression. *J Biol Chem.* (2011) 286:16374–85. doi: 10.1074/jbc.M110.207738
65. Athale J, Ulrich A, Chou MacGarvey N, Bartz RR, Welty-Wolf KE, Suliman HB, et al. Nrf2 promotes alveolar mitochondrial biogenesis and resolution of lung injury in *Staphylococcus aureus* pneumonia in mice. *Free Radic Biol Med.* (2012) 53:1584–94. doi: 10.1016/j.freeradbiomed.2012.08.009
66. Preyat N, Leo O. Sirtuin deacylases: a molecular link between metabolism and immunity. *J Leukocyte Biol.* (2013) 93:669–80. doi: 10.1189/jlb.1112557
67. Liu TF, Yoza BK, El Gazzar M, Vachharajani VT, McCall CE. NAD+-dependent SIRT1 deacetylase participates in epigenetic reprogramming during endotoxin tolerance. *J Biol Chem.* (2011) 286:9856–64. doi: 10.1074/jbc.M110.196790
68. Takeda-Watanabe A, Kitada M, Kanasaki K, Koya D. SIRT1 inactivation induces inflammation through the dysregulation of autophagy in human THP-1 cells. *Biochem Biophys Res Commun.* (2012) 427:191–6. doi: 10.1016/j.bbrc.2012.09.042
69. Brenmoehl J, Hoeflich A. Dual control of mitochondrial biogenesis by sirtuin 1 and sirtuin 3. *Mitochondrion* (2013) 13:755–61. doi: 10.1016/j.mito.2013.04.002
70. Bzowska M, Nogiec A, Bania K, Zygmunt M, Zarebski M, Dobrucki J, Guzik K. Involvement of cell surface 90 kDa heat shock protein (HSP90) in pattern recognition by human monocyte-derived macrophages. *J Leukocyte Biol.* (2017) 102:763–74. doi: 10.1189/jlb.2MA0117-019R
71. Joo JH, Dorsey FC, Joshi A, Hennessy-Walters KM, Rose KL, McCastlain K, et al. Hsp90-Cdc37 chaperone complex regulates Ulk1- and Atg13-mediated mitophagy. *Mol Cell* (2011) 43:572–85. doi: 10.1016/j.molcel.2011.06.018
72. Patel AA, Zhang Y, Fullerton JN, Boelen L, Rongvaux A, Maini AA, et al. The fate and lifespan of human monocyte subsets in steady state and systemic inflammation. *J Exp Med.* (2017). 214:1913–23. doi: 10.1084/jem.20170355
73. Safi W, Kuehnl A, Nüssler A, Eckstein H-H, Pelisek J. Differentiation of human CD14+ monocytes: an experimental investigation of the optimal culture medium and evidence of a lack of differentiation along the endothelial line. *Exp Mol Med.* (2016) 48:e227. doi: 10.1038/emm.2016.11
74. Auwerx J. The human leukemia cell line, THP-1: a multifacetted model for the study of monocyte-macrophage differentiation. *Experientia* (1991) 47:22–31. doi: 10.1007/BF02041244
75. Chanput W, Mes JJ, Wichers HJ. THP-1 cell line: an *in vitro* cell model for immune modulation approach. *Int Immunopharmacol.* (2014) 23:37–45. doi: 10.1016/j.intimp.2014.08.002
76. Bosshart H, Heinzelmann M. THP-1 cells as a model for human monocytes. *Ann Trans Med.* (2016) 4:438. doi: 10.21037/atm.2016.08.53
77. Schildberger A, Rossmanith E, Eichhorn T, Strassl K, Weber V. Monocytes, peripheral blood mononuclear cells, and THP-1 cells exhibit different cytokine expression patterns following stimulation with lipopolysaccharide. *Med Inflamm.* (2013) 2013:697972. doi: 10.1155/2013/697972
78. Kox M, De Kleijn S, Pompe JC, Ramakers BP, Netea MG, Van Der Hoeven JG, et al. Differential *ex vivo* and *in vivo* endotoxin tolerance kinetics following human endotoxemia. *Critic Care Med.* (2011) 39:1866–70. doi: 10.1097/CCM.0b013e3182190d5d
79. Husebye H, Halaas O, Stenmark H, Tunheim G, Sandanger O, Bogen B, et al. Endocytic pathways regulate Toll-like receptor 4 signaling and link innate and adaptive immunity. *EMBO J.* (2006) 25:683–92. doi: 10.1038/sj.emboj.7600991
80. Zweigner J, Gramm HJ, Singer OC, Wegscheider K, Schumann RR. High concentrations of lipopolysaccharide-binding protein in serum of patients with severe sepsis or septic shock inhibit the lipopolysaccharide response in human monocytes. *Blood* (2001) 98:3800–8. doi: 10.1182/blood.V98.13.3800
81. Gkikas I, Palikaras K, Tavernarakis N. The role of mitophagy in innate immunity. *Front Immunol.* (2018) 9:1283. doi: 10.3389/fimmu.2018.01283
82. Quero L, Hanser E, Manigold T, Tiaden AN, Kyburz D. TLR2 stimulation impairs anti-inflammatory activity of M2-like macrophages, generating a chimeric M1/M2 phenotype. *Arthritis Res Ther.* (2017) 19:245. doi: 10.1186/s13075-017-1447-1
83. Opal SM, Scannon PJ, Vincent JL, White M, Carroll SF, Palardy JE, et al. Relationship between plasma levels of lipopolysaccharide (LPS) and LPS-binding protein in patients with severe sepsis and septic shock. *J Infect Dis.* (1999) 180:1584–9. doi: 10.1086/315093

Conflict of Interest Statement: The authors declare that the research was conducted in the absence of any commercial or financial relationships that could be construed as a potential conflict of interest.

frontiers in Immunology

MINI REVIEW
published: 05 March 2019
doi: 10.3389/fimmu.2019.00394

The Relationship of NADPH Oxidases and Heme Peroxidases: Fallin' in and Out

Gábor Sirokmány[1,2]* *and Miklós Geiszt*[1,2]*

[1] Department of Physiology, Faculty of Medicine, Semmelweis University, Budapest, Hungary, [2] "Momentum" Peroxidase Enzyme Research Group of the Semmelweis University and the Hungarian Academy of Sciences, Budapest, Hungary

Peroxidase enzymes can oxidize a multitude of substrates in diverse biological processes. According to the latest phylogenetic analysis, there are four major heme peroxidase superfamilies. In this review, we focus on certain members of the cyclooxygenase-peroxidase superfamily (also labeled as animal heme peroxidases) and their connection to specific NADPH oxidase enzymes which provide H_2O_2 for the one- and two-electron oxidation of various peroxidase substrates. The family of NADPH oxidases is a group of enzymes dedicated to the production of superoxide and hydrogen peroxide. There is a handful of known and important physiological functions where one of the seven known human NADPH oxidases plays an essential role. In most of these functions NADPH oxidases provide H_2O_2 for specific heme peroxidases and the concerted action of the two enzymes is indispensable for the accomplishment of the biological function. We discuss human and other metazoan examples of such cooperation between oxidases and peroxidases and analyze the biological importance of their functional interaction. We also review those oxidases and peroxidases where this kind of partnership has not been identified yet.

Keywords: heme peroxidase, NADPH oxidase, hydrogen peroxide, reactive oxygen species, peroxidasin

OPEN ACCESS

Edited by:
Gabor Csanyi,
Augusta University, United States

Reviewed by:
Tohru Fukai,
Augusta University, United States
Patrick Pagano,
University of Pittsburgh, United States

***Correspondence:**
Gábor Sirokmány
sirokmany.gabor@med.semmelweis-univ.hu
Miklós Geiszt
geiszt.miklos@med.semmelweis-univ.hu

Specialty section:
This article was submitted to Inflammation, a section of the journal Frontiers in Immunology

Received: *08 October 2018*
Accepted: *14 February 2019*
Published: *05 March 2019*

Citation:
Sirokmány G and Geiszt M (2019) The Relationship of NADPH Oxidases and Heme Peroxidases: Fallin' in and Out. Front. Immunol. 10:394. doi: 10.3389/fimmu.2019.00394

INTRODUCTION

Heme peroxidases comprise a large number of heme-containing proteins. Families of these enzymes display distinct structural and biochemical properties and play a role in highly specialized biological processes. The numerous members of each of these families are expressed in all different kingdoms of life. Therefore, it had been recently suggested that the denomination of heme peroxidases should happen according to their characteristic enzymatic activities and structural properties instead of their animal, plant or fungal origin (1). The unique feature of the peroxidase-cyclooxygenase superfamily is the presence of a post-translationally modified heme group which is covalently linked to the peroxidase protein via two covalent bonds (2). Myeloperoxidase (MPO) is unique in this superfamily because of having three covalent linkages to the heme group.

The activity of these peroxidases results in oxidation of one-electron donors into the corresponding radical (AH in Reaction 1) or oxidation of halides or pseudohalides (two-electron donors) into hypohalous acids (HOX in Reaction 2) (3).

$$\text{Reaction1}: H_2O_2 + 2AH_2 \rightarrow 2H_2O + 2{\cdot}AH$$
$$\text{Reaction2}: H_2O_2 + H^+ + X^- \rightarrow H_2O + HOX$$

H_2O_2 is not only required for the generation of oxidants but it seems that it is also necessary to the autocatalytic activation of heme peroxidases during which process the heme-protein crosslink is reinforced (4).

Numerous biochemical processes can produce reactive oxygen species including hydrogen peroxide. The mitochondrial respiratory chain, several metabolic pathways, xanthine oxidase, monoamine oxidases, and the NADPH oxidases are all possible sources of H_2O_2 (5–7).

There are seven members of the Nox/Duox family of NADPH oxidases encoded in the human genome. In other species the number of NADPH oxidase homologs can vary greatly with only two isoforms present in *Caenorhabditis elegans*, five members in zebrafish, six in mouse and rat to name a few examples (8). The NADPH oxidases show important differences in tissue expression pattern and activation mechanism. Nox1, Nox2, Nox3, and Nox4 all require the membrane-bound $p22^{phox}$ protein to be able to produce ROS. Nox1, Nox2, and Nox3 also require different cytosolic factors to become active (9). However, Nox4 does not rely on cytosolic factors but is continuously active. Nox5, Duox1, and Duox2 are independent of $p22^{phox}$ and are primarily activated by intracellular Ca^{++}-signals. Interestingly, Duox proteins can be also classified as heme peroxidases although their peroxidase domain lacks a few critical amino acids that are required for the enzymatic activity of their N-terminal peroxidase domain (10). Dual oxidase (Duox) proteins also require the activity of maturation factors DuoxA1 or DuoxA2 for proper folding and membrane targeting (11).

Hydrogen peroxide is not always the primary oxidant product of NADPH oxidases. Nox2 for example generates mainly superoxide anion, which can be further converted into H_2O_2 in a dismutation reaction enhanced by superoxide dismutase (SOD) enzymes (12). SOD catalyzes the disproportionation of the free radical superoxide anion resulting in the generation of molecular oxygen and hydrogen peroxide (see in Reaction 3) (13).

$$\text{Reaction3}: 2O_2^- + 2H_3O^+ \rightarrow O_2 + \mathbf{H_2O_2} + 2H_2O$$

Certain members of the cyclooxygenase-peroxidase family rely specifically on hydrogen peroxide generated by an NADPH-oxidase. In these specific cases, the absence of the corresponding NADPH-oxidase cannot be supplemented by any other H_2O_2 sources. This closely intertwined mode of action suggests evolutionarily conserved cooperation between these heme peroxidases and NADPH-oxidases. Our aim was to collect and analyze all known examples of such coactions.

The natural beauty of these peroxidase-oxidase concurrences is literally highlighted by a chemiluminescent light emitted during intense activation of the phagocyte myeloperoxidase or the fertilized sea urchin egg's ovoperoxidase (14, 15).

LEUKOCYTE NOX2/MYELOPEROXIDASE SYSTEM

The prodigious increase in oxygen consumption of phagocytosing leukocytes was already described in 1933 by C.W. Baldridge and R.W. Gerard (16). During the following decades, it became clear that this oxygen consumption was not dependent on mitochondrial respiration but was necessary for the production of reactive oxygen species by a complex, multi-protein system that comprised of membrane-bound and cytosolic factors. Nox2 (formerly known as $gp91^{phox}$) contains 6 transmembrane helices and forms a membrane-bound complex with $p22^{phox}$. Whereas, there are 4 cytosolic factors that *in vivo* are all necessary for a fully activated oxidase complex: $p67^{phox}$, $p47^{phox}$, $p40^{phox}$, and the small GTPase Rac1 or Rac2 (9, 17). These cytosolic components are all able to rapidly translocate to the $gp91^{phox}$-$p22^{phox}$ complex upon activation of the phagocyte. The $gp91^{phox}$-$p22^{phox}$ complex is stored in the peroxidase negative subsets of the neutrophil granulocytes' granules which—upon activation—fuse with the phagosomal or plasma membrane. Compared to other Nox isoforms, the ROS producing capacity of the activated Nox2 system seems to be extremely high (18, 19) and this might ensure the potent antimicrobial function of this isoform.

Another line of research elucidated the biochemical activity of myeloperoxidase that was present in large quantities (5% of the total dry cell weight) in phagocytes and was able to turn H_2O_2 into microbicidal hypohalides like HOCl (20). Myeloperoxidase is stored mainly in the matrix of azurophilic granules of neutrophil granulocytes in a mature, dimeric form. The dimerization does not seem to affect the enzymatic activity of MPO but it is rather important for the stability and storage of the enzyme (21). In activated leukocytes, the granules can be released into the lumen of the forming phagosome or into the extracellular space around phagocytes (22, 23). The translocation of myeloperoxidase and Nox2 oxidase ($cytochrome_{b558}$ complex of Nox2 and $p22^{phox}$) from cytoplasmic granules and vesicles into the phagosomal lumen was demonstrated by different approaches including studies based on subcellular fractionation, fluorescent and electronmicroscopic analysis (24–27).

The above regulatory mechanisms, multi-component assembly, and compartmentalization ensure that in non-stimulated cells there is practically no hypohalide production. This can prevent that aggressive antimicrobial reactive oxygen products cause random tissue destruction in the host.

Notably, human phagocytes express about an order of magnitude higher amounts of MPO than mouse leukocytes which limit the interpretation of mouse data. However, to circumvent this problem mouse models expressing human MPO have been established (28, 29). These models became important also to study the role of MPO in the pathomechanism of atherosclerotic lesion formation, as human atherosclerotic lesions do contain MPO and its peroxidation products whereas mouse MPO is hardly detectable in macrophages of atherosclerotic plaques. The expression of human MPO in mouse macrophages was unanimously associated with increased atherosclerotic lesions in different studies. However, other

functional changes, like plasma lipoprotein and cholesterol levels showed more conflicting results, which might be explained by different transgenic systems used in different studies [i.e., bone marrow transplanted transgenic macrophages (28) or overall expression of the MPO transgene (29, 30)].

Similarly to the numerous other antimicrobial effector functions of phagocytes, dysregulation of superoxide production and myeloperoxidase activity can also contribute to the development of autoimmune diseases. Both the over activation or impairment of these processes can promote tissue damage associated with autoimmune conditions (31).

Furthermore, the lack of either Nox2 or MPO does result in immune deficiency disorder with substantially different characteristics and severity. In the absence of Nox2—or other components of the active phagocytic oxidase complex—a disease called chronic granulomatous disease (CGD) develops (32). CGD patients have largely increased susceptibility toward both bacterial and fungal infections. In contrast, many patients with loss of function mutations of MPO might have no obvious clinical symptoms or show an increased predisposition only toward fungal infections (caused mainly by *Candida albicans*) (33, 34). This phenotypic discrepancy might be explained in different ways. First, it is possible that the superoxide produced by Nox2 and/or its derivatives exert direct antimicrobial effects even without being converted into hypochlorous acid. Second, based on observations showing altered membrane potential changes and Ca^{++}-signals in CGD neutrophils it is possible to presume that altered intracellular ion concentrations might hamper also several other antimicrobial effector functions of these cells (35, 36).

EOSINOPHIL NOX2/EOSINOPHIL PEROXIDASE SYSTEM

Although the eosinophil peroxidase (EPO) and myeloperoxidase are highly homologous at the amino acid level their biochemical properties and biological role differ significantly. EPO binds its prosthetic group only via two covalent links and its spectral properties are more similar to that of LPO and TPO (2). Eosinophil granulocytes also express components of the Nox2 based superoxide-generating molecular machinery which provides H_2O_2 for EPO. Unlike MPO, EPO is not able to oxidize Cl^-, but it uses mainly Br^- and SCN^- to generate hypobromous acid and hypothiocyanous acid, respectively. Detection of protein bromotyrosination can be used as a marker of EPO mediated protein oxidation (37).

Eosinophil granulocytes exert their antimicrobial and antiparasitic activities extracellularly and EPO is also a secreted protein. Eosinophils also play a special role in the pathologies of allergic inflammatory diseases (38–40). Despite the essential host defense and inflammatory role of eosinophil granulocytes the lack of eosinophil peroxidase activity does not manifest in any obvious phenotype in humans and the diagnosis of EPO deficiency is usually an accidental clinical finding (41). In contrast, in allergic diseases, accumulation and hyperactivity of eosinophil granulocytes are associated with overproduction of oxidative substances which contributes to the pathology of these conditions. An especially interesting pathomechanism is the activation of endothelium-derived tissue factor by hypothiocyanous acid with the consequentially increased risk of thrombotic complications (42, 43).

DUOX2 AND THYROID PEROXIDASE IN THYROID HORMONE SYNTHESIS

The thyroid peroxidase (TPO) catalyzes the iodination of tyrosine residues of thyroglobulin (44, 45). This peroxidase has got a unique transmembrane domain through which it is located in the apical membrane of thyrocytes. Its heme-containing catalytic site faces the thyroglobulin containing follicular lumen. To produce active iodine radicals the thyrocytes take up iodide ion through the basolateral Na^+/I^- symporter and transport it to the lumen through pendrin or through other apically located anion transporters (46). H_2O_2 is produced by dual oxidase 2 (Duox2), an other apically located transmembrane NADPH oxidase enzyme. The pharmacological inhibition or loss of function mutations of I^- transporters, TPO or Duox2, and DuoxA2 all lead to insufficient thyroid hormone synthesis—i.e., hypothyreosis.

As we have no detailed structural insight into the molecular vicinity of the luminal site of the thyrocyte, it is difficult to explain how the produced, highly reactive iodine radicals can react selectively with tyrosine side chains of thyroglobulin without eliciting oxidative damage of other extracellular proteins. Co-immunoprecipitation studies revealed a molecular interaction between TPO and Duox2 in the membrane fractions of isolated thyroid tissue lysates and of transfected COS-7 cells as well (47). This close association can at least explain how leakage of H_2O_2 can be prevented.

In contrast to the Nox2/MPO system, the thyroid hormone synthesis is a rather continuous, steady process. Accordingly, the oxidase and peroxidase components are located in the same subcellular compartment. Interestingly, the thyroid expresses two dual oxidases, Duox1 and Duox2 (48), but the absence of Duox1 is not associated with hypothyreosis (49). Therefore, the exact function of Duox1 in the thyroid is still unknown. It is also quite enigmatic why the highly homologous Duox1 cannot compensate for the lack of Duox2 in the hormone synthesis process. One explanation might be that Duox1 localizes to another microdomain of the apical membrane. However, the lack of Duox1 specific antibodies that work in immunohistochemistry applications makes it difficult to prove this idea (50).

DUOX AND LACTOPEROXIDASE IN EXOCRINE GLANDS AND ON MUCOSAL SURFACES

Lactoperoxidase (LPO) has long been recognized as an antimicrobial enzyme present in various exocrine secretions like milk, saliva, and tear. In 2003 a detailed *in situ* hybridization

study identified Duox2 expression in major salivary ducts and on rectal epithelial cells and Duox1 expression in airway epithelial cells (58).

LPO can utilize I^- or SCN^- as substrates and the sodium/iodide transporter (NIS) plays an important role in transporting these anions through the epithelial cells. In the salivary glands LPO was expressed deep in the serous acini, NIS in the intercalated ducts and Duox2 in final ducts (58). This pattern of expression could ensure that the microbicide hypothiocyanous acid is formed only at later stages of secretion, just before entering the oral cavity.

In the airways, thiocyanate might be transported onto the epithelial surface via the cystic fibrosis transmembrane regulator CFTR (58–62). Decreased transport activity in cystic fibrosis patients might reduce the LPO mediated antimicrobial effects which might contribute to the high rate of pulmonary infections. Importantly microbes seem to be much more susceptible to HOSCN than mammalian cells probably because mammalian epithelial cells express high molecular weight thioredoxin reductase (TrxR) that can readily turn over HOSCN. In contrast, bacterial TrxR is strongly inhibited by HOSCN (62). This makes the Duox-LPO-HOSCN system much more adequate for continuous mucosal host defense functions than the more cytotoxic Nox2-MPO-HOCl system (63, 64).

C. ELEGANS DUAL OXIDASE 1 (BLI-3) AND HEME PEROXIDASES

The *Caenorhabditis elegans* NADPH oxidase, BLI-3 was described to be expressed in the hypodermal cells of *C. elegans* underlying the cuticle layer. The hypodermal cells play an essential role in the repeated synthesis of the cuticle (molting) during consecutive larval stages of the worm. RNAi knockdown of BLI-3 resulted in severe cuticle abnormalities. Di- and trityrosine crosslinks between cuticular collagen molecules were found to be significantly reduced in BLI-3 RNAi worms. The same study that described this phenotype also proposed that the BLI-3 peroxidase domain was responsible for the tyrosine crosslinks between cuticular collagens (65). However, later analysis revealed that the BLI-3 peroxidase domain lacks critical amino acids that are important for heme binding which makes its peroxidase activity doubtful. Accordingly, a reverse genetics RNAi screen approach identified the hypodermally expressed MLT-7 peroxidase that was responsible for collagen crosslinking (55). MLT-7 expression showed a cyclic pattern according to molting stages and its knockdown showed very similar phenotypes to BLI-3 knockdowns. It has been supposed that the enzymatically inactive BLI-3 peroxidase domain might function as a docking site for MLT-7 peroxidase domain thereby providing a spatial control of the peroxidase activity (55).

Another hypodermally localized heme peroxidase—SKPO-1—was also discovered by RNAi screening that was found to be important in maintaining normal cuticle phenotype. SKPO-1 was also claimed to play a role—along with BLI-3—in host defense against pathogenic bacteria (56, 66).

OVOPEROXIDASE AND URCHIN DUAL OXIDASE 1 IN THE SEA URCHIN FERTILIZATION MEMBRANE

In the sea urchin (*Strongylocentrotus purpuratus*) the fertilization of the egg elicits plasma membrane depolarization, cytosolic Ca^{++}-signal and a cortical reaction which involves degranulation of vesicles located below the egg's membrane surface (67). This results in the formation of a stiff, insoluble fertilization envelope (FE) which prevents the entry of other sperms (53). The active pool of the sea urchin oxidase is located in the egg's plasma membrane whereas the ovoperoxidase is tethered to the forming FE by a protein called proteoliaisin (54, 68). Bennett M. Shapiro and his coworkers gave a detailed description of this envelope formation, they isolated and characterized the ovoperoxidase enzyme that is released from the granules and is responsible for the crosslinking of protein tyrosyl residues in this hardened membrane. Another important feature of the secreted peroxidase is its spermicidal activity which means an additional defense mechanism against polyspermy. Although the source of H_2O_2 for these peroxidase mediated reactions were already addressed in the 1977 PNAS paper, the molecular identification of the urchin dual oxidase (Udx1) was accomplished almost three decades later (54). This process is also a prime example of how compartmentalization and inducible translocation can ensure a swift, robust, but tightly controlled oxidative burst and peroxidase activation.

Although it is challenging to find quantitatively comparable data about the ROS production of different NADPH oxidase systems, it seems that the respiratory burst in the sea urchin egg results in a H_2O_2 concentration of about 60 nM in the perivitelline space whereas in the phagosome of activated human neutrophil granulocytes the peroxide concentration is estimated to be in the micromolar range (54, 69). However, in the biological context of egg fertilization, this relatively lower rate of ROS production can still amply support the ovoperoxidase function.

NOX5 AND HEME PEROXIDASE 2 IN MOSQUITO ANTIPLASMODIAL IMMUNITY

A unique example has been identified in the midgut cells of Anopheles gambiae where the HPX2 heme peroxidase—in concert with Nox5 and nitric oxide synthase (NOS)—generates reactive nitrogen species (RNS) resulting in increased protein nitration. This process renders the Plasmodium ookinetes more susceptible to the Anopheles complement system which is the final effector mechanism against invading parasites (57) (see **Table 1**).

The same research group presented another mechanism in the Anopheles midgut where a Duox homolog cooperates with a secreted immunomodulatory epithelial peroxidase (IMPer) to form a dityrosine crosslinked matrix on the luminal surface. This matrix layer is supposed to separate the luminal microbiota and the epithelial immune system thereby subduing the immune activation and potential epithelial damage. On the other hand, Plasmodium parasites could proliferate more rapidly in the midgut lumen under these conditions (70).

TABLE 1 | An overview of the peroxidase-oxidase co-operations discussed in detail in this paper.

Peroxidase	Oxidase	Location	Function	Related anomaly or disease in the absence of oxidase/peroxidase function
MPO	Nox2	Neutrophil granulocytes, macrophages, peritoneal B lymphocytes	Production of antimicrobial hypochloric acid	Nox2: chronic granulomatous disease (CGD) (32) MPO: increased susceptibility to fungal infections (34)
EPO	Nox2	Eosinophil granulocytes	Production of antimicrobial hypobromous and hypothiocyanous acid	no evidence of disease (51)
TPO	Duox2	Thyroid gland	Oxidation of iodide ion during thyroid hormone synthesis	Duox2 or TPO: congenital hypothyreosis (52) (48) (44) (45)
LPO	Duox1, Duox2	Exocrin glands, mucosal surfaces	Production of antimicrobial hypothiocyanate and hypoiodide	?
Ovoperoxidase	Udx1	Plasmamembrane, subcortical granules, fertilization envelope	Crosslinking and subsequent hardening of matrix molecules in the fertilization membrane	Ovoperoxidase or Udx1: increased probability of polyspermy (53) (54)
MLT-7	BLI-3 (Ce-Duox1)	Hypodermis	Crosslinking of cuticle matrix molecules	BLI-3 or MLT7: developmental arrest, cuticle abnormalities (55)
SKPO-1	BLI-3 (Ce-Duox1)	Hypodermis	Maintaining normal cuticle, host defense	BLI-3 or SKPO-1: developmental arrest, susceptibility to Enterococcus infection (56)
HPX2	NOX5	Plasmodium infected Anopheles midgut epithelial cells	Nitration of Plasmodium ookinetes	Nox5 or HPX2: susceptibility to Plasmodium invasion (57)

NOX1, NOX3, AND NOX4 FUNCTION WITHOUT KNOWN PEROXIDASE PARTNERS

These three members of the NADPH oxidase family have not been linked to heme peroxidases in any known biological process yet. Nox1 is mainly expressed in the distal parts of the gastrointestinal tract, showing low expression levels in the ileum, and more robust levels in the colon epithelium (19, 71). In a glutathione peroxidase deficient animal model of spontaneous ileocolitis, it was shown to be involved in the pathogenesis of inflammatory bowel diseases (72). This and other potential physiological functions of Nox1 are reviewed in detail elsewhere (73). However, cooperation with a known heme peroxidase has not been described in the divergent actions of Nox1.

Nox3 is uniquely expressed in the inner ear (74). Although there are no published data about any connection to heme peroxidases in this organ, it is interesting to note that—according to the publicly available NCBI Unigene database—myeloperoxidase has got a surprisingly high expression level in the mouse inner ear. Whether there is any functional link between MPO and Nox3 in the inner ear remains to be investigated.

The Nox4 expression is more ubiquitous with the highest levels found in the kidney. Uniquely this oxidase is constitutively active. The exact intracellular localization of Nox4 is still dubious, however many independent literature data points toward the endoplasmic reticulum where Nox4 might contribute to the oxidative milieu of the ER (75–77). It would be a challenging task to pinpoint any specific Nox4-heme peroxidase functional interaction within this compartment.

PEROXIDASIN WITHOUT KNOWN OXIDASE PARTNER IN COLLAGEN IV CROSSLINKING

Peroxidasin (Pxdn) has been described as the specific enzyme catalyzing the formation of sulfilimine covalent crosslink of C-terminal NC1 domains between collagen IV protomers (78). This unique, evolutionarily conserved chemical bond might significantly affect the mechanical and biochemical properties of collagen IV containing extracellular matrix structures. However, using various NADPH-oxidase deficient mouse models, it has been recently shown *in vivo* that NADPH oxidases most probably do not provide H_2O_2 for this reaction. $P22^{phox}$ mutant, Nox4 deficient, Duox1 knockout, and Duoxa double knockout animals were all equally capable to crosslink NC1 domains as wild-type control animals (79). Lysyl oxidases which are also involved in collagen IV assembly were also ruled out as possible ROS sources (78). Therefore, the exact molecular identity of this reactions' ROS source is still unknown. It is also a puzzling question how the Pxdn mediated reaction is restricted only to the collagen IV NC1 amino acids and how it is ensured that the highly reactive HOBr is not attacking numerous neighboring matrix molecules (80). Identification of a specific ROS source might help explain the spatiotemporal control of redox modification.

CONCLUSION

Our review describes the functional cooperation between members of the peroxidase-cyclooxygenase family and NADPH oxidases in various biological settings. The deeper understanding of these processes might help identify novel biological targets of

oxidase and peroxidase products and improve our understanding of how these reactive oxidants can contribute to very specific, sophisticated physiological phenomena, or how they can trigger pathophysiological conditions.

AUTHOR CONTRIBUTIONS

All authors listed have made a substantial, direct and intellectual contribution to the work, and approved it for publication.

FUNDING

The research of the authors is supported by grants from the National Research, Development and Innovation Office (K119955, NVKP_16-1-2016-0039). The research was also financed by the Higher Education Institutional Excellence Programme of the Ministry of Human Capacities in Hungary, within the framework of the molecular biology thematic programme of the Semmelweis University. GS is a Bolyai fellowship holder of the Hungarian Academy of Science (BO/00504/18/5).

REFERENCES

1. Zamocky M, Jakopitsch C, Furtmüller PG, Dunand C, Obinger C. The peroxidase-cyclooxygenase superfamily: reconstructed evolution of critical enzymes of the innate immune system. *Proteins Struct Funct Genet.* (2008) 72:589–605. doi: 10.1002/prot.21950
2. Furtmüller PG, Zederbauer M, Jantschko W, Helm J, Bogner M, Jakopitsch C, et al. Active site structure and catalytic mechanisms of human peroxidases. *Arch Biochem Biophys.* (2006) 445:199–213. doi: 10.1016/j.abb.2005.09.017
3. Zámocký M, Hofbauer S, Schaffner I, Gasselhuber B, Nicolussi A, Soudi M, et al. Independent evolution of four heme peroxidase superfamilies. *Arch Biochem Biophys.* (2015) 574:108–19. doi: 10.1016/j.abb.2014.12.025
4. Fayadat L, Niccoli-Sire P, Lanet J, Franc JL. Role of heme in intracellular trafficking of thyroperoxidase and involvement of H2O2 generated at the apical surface of thyroid cells in autocatalytic covalent heme binding. *J Biol Chem.* (1999) 274:10533–8. doi: 10.1074/jbc.274.15.10533
5. Boveris A, Oshino N, Chance B. The cellular production of hydrogen peroxide. *Biochem J.* (1972) 128:617–30. doi: 10.1042/bj1280617
6. Knowles PF, Gibson JF, Pick FM, Bray RC. Electron-spin-resonance evidence for enzymic reduction of oxygen to a free radical, the superoxide ion. *Biochem J.* (1969) 111:53–8. doi: 10.1042/bj1110053
7. Edmondson D. Hydrogen peroxide produced by mitochondrial monoamine oxidase catalysis: biological implications. *Curr Pharm Des.* (2014) 20:155–60. doi: 10.2174/13816128113190990406
8. Kawahara BT, Quinn MT, Lambeth JD. Molecular evolution of the reactive oxygen-generating NADPH oxidase (Nox/Duox) family of enzymes. *BMC Evol Biol.* (2007) 7:1–21. doi: 10.1186/1471-2148-7-109
9. Brandes RP, Weissmann N, Schroder K. Nox family NADPH oxidases: molecular mechanisms of activation. *Free Radic Biol Med.* (2014) 76C:208–26. doi: 10.1016/j.freeradbiomed.2014.07.046
10. Meitzler JL, Ortiz De Montellano PR. *Caenorhabditis elegans* and human dual oxidase 1 (DUOX1) "Peroxidase" domains: insights into heme binding and catalytic activity. *J Biol Chem.* (2009) 284:18634–43. doi: 10.1074/jbc.M109.013581
11. Grasberger H, Refetoff S. Identification of the maturation factor for dual oxidase. Evolution of an eukaryotic operon equivalent. *J Biol Chem.* (2006) 281:18269–72. doi: 10.1074/jbc.C600095200
12. Rister M, Baehner RL. The alteration of superoxide dismutase, catalase, glutathione peroxidase, and NAD(P)H cytochrome C reductase in guinea pig polymorphonuclear leukocytes and alveolar macrophages during hyperoxia. *J Clin Invest.* (1976) 58:1174–84. doi: 10.1172/JCI108570
13. McCord JM, Fridovich I. Superoxide dismutase. An enzymic function for erythrocuprein (hemocuprein). *J Biol Chem.* (1969) 244:6049–55.
14. Foerder CA, Klebanoff SJ, Shapiro BM. Hydrogen peroxide production, chemiluminescence, and the respiratory burst of fertilization: interrelated events in early sea urchin development. *Proc Natl Acad Sci USA.* (1978) 75:3183–7. doi: 10.1073/pnas.75.7.3183
15. Allen RC, Stjernholm RL, Steele RH. Evidence for the generation of an electronic excitation state(s) in human polymorphonuclear leukocytes and its participation in bactericidal activity. *Biochem Biophys Res Commun.* (1972) 47:679–84. doi: 10.1016/0006-291X(72)90545-1
16. Gerard RW, Baldrige CW. The extra respiration of phagocytes. *Am J Physiol.* (1933) 103:235–6.
17. Sumimoto H, Miyano K, Takeya R. Molecular composition and regulation of the Nox family NAD(P)H oxidases. *Biochem Biophys Res Commun.* (2005) 338:677–86. doi: 10.1016/j.bbrc.2005.08.210
18. Björgvinsdóttir H, Zhen L, Dinauer MC. Cloning of murine gp91phox cDNA and functional expression in a human X-linked chronic granulomatous disease cell line. *Blood.* (1996) 87:2005–10.
19. Geiszt M, Lekstrom K, Brenner S, Hewitt SM, Dana R, Malech HL, et al. NAD(P)H oxidase 1, a product of differentiated colon epithelial cells, can partially replace glycoprotein 91phox in the regulated production of superoxide by phagocytes. *J Immunol.* (2003) 171:299–306. doi: 10.4049/jimmunol.171.1.299
20. Klebanoff SJ, Clem WH, Luebke RG. The peroxidase-thiocyanate-hydrogen peroxide antimicrobial system. *BBA Gen Subj.* (1966) 117:63–72. doi: 10.1016/0304-4165(66)90152-8
21. Banerjee S, Stampler J, Furtmüller PG, Obinger C. Conformational and thermal stability of mature dimeric human myeloperoxidase and a recombinant monomeric form from CHO cells. *Biochim Biophys Acta.* (2011) 1814:375–87. doi: 10.1016/j.bbapap.2010.09.015
22. Faurschou M, Borregaard N. Neutrophil granules and secretory vesicles in inflammation. *Microbes Infect.* (2003) 5:1317–27. doi: 10.1016/j.micinf.2003.09.008
23. Hansson M, Olsson I, Nauseef WM. Biosynthesis, processing, and sorting of human myeloperoxidase. (2006) 445:214–24. doi: 10.1016/j.abb.2005.08.009
24. Kjeldsen L, Sengeløv H, Lollike K, Nielsen MH, Borregaard N. Isolation and characterization of gelatinase granules from human neutrophils. *Blood.* (1994) 83:1640–9.
25. Casbon A-J, Allen L-AH, Dunn KW, Dinauer MC. Macrophage NADPH oxidase flavocytochrome b localizes to the plasma membrane and Rab11-positive recycling endosomes. *J Immunol.* (2009) 182:2325–39. doi: 10.4049/jimmunol.0803476
26. Moriguchi K. Independent trafficking of flavocytochrome b558 and myeloperoxidase to phagosomes during phagocytosis visualised by energy-filtering and energy-dispersive spectroscopy-scanning transmission electron microscopy. *J Microsc.* (2018) 269:338–45. doi: 10.1111/jmi.12620
27. Jesaitis AJ, Buescher ES, Harrison D, Quinn MT, Parkos CA, Livesey S, et al. Ultrastructural localization of cytochrome b in the membranes of resting and phagocytosing human granulocytes. *J Clin Invest.* (1990) 85:821–35. doi: 10.1172/JCI114509
28. McMillen TS, Heinecke JW, LeBoeuf RC. Expression of human myeloperoxidase by macrophages promotes atherosclerosis in mice. *Circulation.* (2005) 111:2798–804. doi: 10.1161/CIRCULATIONAHA.104.516278
29. Castellani LW, Chang JJ, Wang X, Lusis AJ, Reynolds WF. Transgenic mice express human MPO −463G/A alleles at atherosclerotic lesions, developing hyperlipidemia and obesity in −463G males. *J Lipid Res.* (2006) 47:1366–77. doi: 10.1194/jlr.M600005-JLR200
30. Kumar AP, Piedrafita FJ, Reynolds WF. Peroxisome proliferator-activated receptor γ Ligands regulate myeloperoxidase expression in macrophages by an estrogen-dependent mechanism involving

the−463GA promoter polymorphism. *J Biol Chem.* (2004) 279:8300–15. doi: 10.1074/jbc.M311625200
31. Németh T, Mócsai A, Lowell CA. Neutrophils in animal models of autoimmune disease. *Semin Immunol.* (2016) 28:174–86. doi: 10.1016/j.smim.2016.04.001
32. Baehner RL, Karnovsky ML. Deficiency of reduced nicotinamide-adenine dinucleotide oxidase in chronic granulomatous disease. *Science.* (1968) 162:1277–9. doi: 10.1126/science.162.3859.1277
33. Parry MF, Root RK, Metcalf JA, Delaney KK, Kaplow LS, Richar WJ. Myeloperoxidase deficiency. Prevalence and clinical significance. *Ann Intern Med.* (1981) 95:293–301. doi: 10.7326/0003-4819-95-3-293
34. Lehrer RI, Cline MJ. Leukocyte myeloperoxidase deficiency and disseminated candidiasis: the role of myeloperoxidase in resistance to Candida infection. *J Clin Invest.* (1969) 48:1478–88. doi: 10.1172/JCI106114
35. Geiszt M, Kapus A, Németh K, Farkas L, Ligeti E. Regulation of capacitative Ca2+ influx in human neutrophil granulocytes. Alterations in chronic granulomatous disease. *J Biol Chem.* (1997) 272:26471–8.
36. Geiszt M, Kapus A, Ligeti E. Chronic granulomatous disease: more than the lack of superoxide? *J Leukoc Biol.* (2001) 69:191–6. doi: 10.1189/jlb.69.2.191
37. Wu W, Chen Y, D'Avignon A, Hazen SL. 3-bromotyrosine and 3,5-dibromotyrosine are major products of protein oxidation by eosinophil peroxidase: potential markers for eosinophii- dependent tissue injury *in vivo*. *Biochemistry.* (1999) 38:3538–48.
38. Ramirez GA, Yacoub M-R, Ripa M, Mannina D, Cariddi A, Saporiti N, et al. Eosinophils from physiology to disease: a comprehensive review. *Biomed Res Int.* (2018) 2018:9095275. doi: 10.1155/2018/9095275
39. Cottin V, Bel E, Bottero P, Dalhoff K, Humbert M, Lazor R, et al. Respiratory manifestations of eosinophilic granulomatosis with polyangiitis (Churg-Strauss). *Eur Respir J.* (2016) 48:1429–41. doi: 10.1183/13993003.00097-2016
40. Tashkin DP, Wechsler ME. Role of eosinophils in airway inflammation of chronic obstructive pulmonary disease. *Int J Chron Obstruct Pulmon Dis.* (2018) 13:335–49. doi: 10.2147/COPD.S152291
41. Kutter D, Janecki J, Verstraeten L. Screening for total and partial eosinoperoxidase deficiency by flow cytometry: prevalence in a general population, pathology and genetic implications. *Redox Rep.* (2000) 5:225–8. doi: 10.1179/135100000101535663
42. Wu W, Samoszuk MK, Comhair SAA, Thomassen MJ, Farver CF, Dweik RA, et al. Eosinophils generate brominating oxidants in allergen-induced asthma. *J Clin Invest.* (2000) 105:1455–63. doi: 10.1172/JCI9702
43. Wang JG, Mahmud SA, Thompson JA, Geng JG, Key NS, Slungaard A. The principal eosinophil peroxidase product, HOSCN, is a uniquely potent phagocyte oxidant inducer of endothelial cell tissue factor activity: a potential mechanism for thrombosis in eosinophilic inflammatory states. *Blood.* (2006) 107:558–65. doi: 10.1182/blood-2005-05-2152
44. Magnusson RP, Chazenbalk GD, Gestautas J, Seto P, Filetti S, DeGroot LJ, et al. Molecular cloning of the complementary deoxyribonucleic acid for human thyroid peroxidase. *Mol Endocrinol.* (1987) 1:856–61. doi: 10.1210/mend-1-11-856
45. Kimura S, Kotani T, McBride OW, Umeki K, Hirai K, Nakayama T, et al. Human thyroid peroxidase: complete cDNA and protein sequence, chromosome mapping, and identification of two alternately spliced mRNAs. *Proc Natl Acad Sci USA*. (1987) 84:5555–9. doi: 10.1073/pnas.84.16.5555
46. Ravera S, Reyna-neyra A, Ferrandino G, Amzel LM, Carrasco N. The sodium/iodide symporter (NIS): molecular physiology and preclinical and clinical applications. *Annu Rev Physiol.* (2017) 79:261–89. doi: 10.1146/annurev-physiol-022516-034125
47. Song Y, Ruf J, Lothaire P, Dequanter D, Andry G, Willemse E, et al. Association of duoxes with thyroid peroxidase and its regulation in thyrocytes. *J Clin Endocrinol Metab.* (2010) 95:375–82. doi: 10.1210/jc.2009-1727
48. De Deken X, Wang D, Many MC, Costagliola S, Libert F, Vassart G, et al. Cloning of two human thyroid cDNAs encoding new members of the NADPH oxidase family. *J Biol Chem.* (2000) 275:23227–33. doi: 10.1074/jbc.M000916200
49. Donkó A, Ruisanchez E, Orient A, Enyedi B, Kapui R, Péterfi Z, et al. Urothelial cells produce hydrogen peroxide through the activation of Duox1. *Free Radic Biol Med.* (2010) 49:2040–8. doi: 10.1016/j.freeradbiomed.2010.09.027
50. Caillou B, Dupuy C, Lacroix L, Nocera M, Talbot M, Ohayon R, et al. Expression of reduced nicotinamide adenine dinucleotide phosphate oxidase (ThoX, LNOX, Duox) genes and proteins in human thyroid tissues. *J Clin Endocrinol Metab.* (2001) 86:3351–8. doi: 10.1210/jc.86.7.3351
51. Zabucchi G, Soranzo MR, Menegazzi R, Vecchio M, Knowles A, Piccinini C, et al. Eosinophil peroxidase deficiency: morphological and immunocytochemical studies of the eosinophil-specific granules. *Blood.* (1992) 80:2903–10.
52. Niepomniszcze H, Castells S, De Groot LJ, Refetoff S, Kim OS, Rapoport B, et al. Peroxidase defect in congenital goiter with complete organification block. *J Clin Endocrinol Metab.* (1973) 36:347–57. doi: 10.1210/jcem-36-2-347
53. Lafleur GJ, Horiuchi Y, Wessel GM. Sea urchin ovoperoxidase: oocyte-specific member of a heme-dependent peroxidase superfamily that functions in the block to polyspermy. *Mech Dev.* (1998) 70:77–89. doi: 10.1016/S0925-4773(97)00178-0
54. Wong JL, Créton R, Wessel GM. The oxidative burst at fertilization is dependent upon activation of the dual oxidase udx1. *Dev Cell.* (2004) 7:801–14. doi: 10.1016/j.devcel.2004.10.014
55. Thein MC, Winter AD, Stepek G, McCormack G, Stapleton G, Johnstone IL, et al. Combined extracellular matrix cross-linking activity of the peroxidase MLT-7 and the dual oxidase BLI-3 is critical for post-embryonic viability in *Caenorhabditis elegans*. *J Biol Chem.* (2009) 284:17549–63. doi: 10.1074/jbc.M900831200
56. Tiller GR, Garsin DA. The SKPO-1 peroxidase functions in the hypodermis to protect *Caenorhabditis elegans* from bacterial infection. *Genetics.* (2014) 197:515–26. doi: 10.1534/genetics.113.160606
57. Oliveira GDA, Lieberman J, Barillas-Mury C. Epithelial nitration by a peroxidase/NOX5 system mediates mosquito antiplasmodial immunity. *Science.* (2012) 335:856–9. doi: 10.1126/science.1209678
58. Geiszt M, Witta J, Baffi J, Lekstrom K, Leto TL. Dual oxidases represent novel hydrogen peroxide sources supporting mucosal surface host defense. *FASEB J.* (2003) 17:1502–4. doi: 10.1096/fj.02-1104fje
59. Fragoso MA, Fernandez V, Forteza R, Randell SH, Salathe M, Conner GE. Transcellular thiocyanate transport by human airway epithelia. *J Physiol.* (2004) 561(Pt. 1):183–94. doi: 10.1113/jphysiol.2004.071548
60. Lorentzen D, Durairaj L, Pezzulo AA, Nakano Y, Launspach J, Stoltz DA, et al. Concentration of the antibacterial precursor thiocyanate in cystic fibrosis airway secretions. *Free Radic Biol Med.* (2011) doi: 10.1016/j.freeradbiomed.2011.02.013
61. Moskwa P, Lorentzen D, Excoffon KJDA, Zabner J, McCray PB, Nauseef WM, et al. A novel host defense system of airways is defective in cystic fibrosis. *Am J Respir Crit Care Med.* (2007) 175:174–83. doi: 10.1164/rccm.200607-1029OC
62. Chandler JD, Nichols DP, Nick JA, Hondal RJ, Day BJ. Selective metabolism of hypothiocyanous acid by mammalian thioredoxin reductase promotes lung innate immunity and antioxidant defense. *J Biol Chem.* (2013) 288:18421–8. doi: 10.1074/jbc.M113.468090
63. Podrez EA, Abu-Soud HM, Hazen SL. Myeloperoxidase-generated oxidants and atherosclerosis. *Free Radic Biol Med.* (2000) 28:1717–25. doi: 10.1016/S0891-5849(00)00229-X
64. Ray RS, Katyal A. Myeloperoxidase: bridging the gap in neurodegeneration. *Neurosci Biobehav Rev.* (2016) 68:611–20. doi: 10.1016/j.neubiorev.2016.06.031
65. Edens WA, Sharling L, Cheng G, Shapira R, Kinkade JM, Lee T, et al. Tyrosine cross-linking of extracellular matrix is catalyzed by Duox, a multidomain oxidase/peroxidase with homology to the phagocyte oxidase subunit gp91phox. *J Cell Biol.* (2001) 154:879–92. doi: 10.1083/jcb.200103132
66. Chávez V, Mohri-Shiomi A, Garsin DA. Ce-Duox1/BLI-3 generates reactive oxygen species as a protective innate immune mechanism in *Caenorhabditis elegans*. *Infect Immun.* (2009) 77:4983–9. doi: 10.1128/IAI.00627-09
67. Veron M, Foerder C, Eddy EM, Shapiro BM. Sequential biochemical and morphological events during assembly of the fertilization membrane of the sea urchin. *Cell.* (1977) 10:321–8. doi: 10.1016/0092-8674(77)90226-4
68. Weidman PJ, Kay ES, Shapiro BM. Assembly of the sea urchin fertilization membrane: isolation of proteoliaisin, a calcium-dependent ovoperoxidase binding protein. *J Cell Biol.* (1985) 100:938–46. doi: 10.1083/jcb.100.3.938

69. Slauch JM. How does the oxidative burst of macrophages kill bacteria? Still an open question. *Mol Microbiol.* (2011) 80:580–3. doi: 10.1111/j.1365-2958.2011.07612.x
70. Kumar S, Molina-Cruz A, Gupta L, Rodrigues J, Barillas-Mury C. A peroxidase/dual oxidase system modulates midgut epithelial immunity in anopheles gambiae. *Science.* (2010) 327:1644–8. doi: 10.1126/science.1184008
71. Szanto I, Rubbia-Brandt L, Kiss P, Steger K, Banfi B, Kovari E, et al. Expression of NOX1, a superoxide-generating NADPH oxidase, in colon cancer and inflammatory bowel disease. *J Pathol.* (2005) 207:164–76. doi: 10.1002/path.1824
72. Esworthy RS, Kim BW, Chow J, Shen B, Doroshow JH, Chu FF. Nox1 causes ileocolitis in mice deficient in glutathione peroxidase-1 and−2. *Free Radic Biol Med.* (2014) 68:315–25. doi: 10.1016/j.freeradbiomed.2013.12.018
73. Sirokmány G, Donkó Á, Geiszt M. Nox/Duox family of NADPH oxidases: lessons from knockout mouse models. *Trends Pharmacol Sci.* (2016) 37:318–27. doi: 10.1016/j.tips.2016.01.006
74. Bánfi B, Malgrange B, Knisz J, Steger K, Dubois-Dauphin M, Krause KH. *J Biol Chem.* (2004) 279:46065–72. doi: 10.1074/jbc.M403046200
75. Prior KK, Wittig I, Leisegang MS, Groenendyk J, Weissmann N, Michalak M, et al. The endoplasmic reticulum chaperone calnexin is a NADPH oxidase NOX4 interacting protein. *J Biol Chem.* (2016) 291:7045–59. doi: 10.1074/jbc.M115.710772
76. Zana M, Péterfi Z, Kovács HA, Tóth ZE, Enyedi B, Morel F, et al. Interaction between p22phoxand Nox4 in the endoplasmic reticulum suggests a unique mechanism of NADPH oxidase complex formation. *Free Radic Biol Med.* (2018) 116:41–9. doi: 10.1016/j.freeradbiomed.2017.12.031
77. Amanso AM, Debbas V, Laurindo FRM. Proteasome inhibition represses unfolded protein response and Nox4, sensitizing vascular cells to endoplasmic reticulum stress-induced death. *PLoS ONE.* (2011) 6:e14591. doi: 10.1371/journal.pone.0014591
78. Bhave G, Cummings CF, Vanacore RM, Kumagai-Cresse C, Ero-Tolliver IA, Rafi M, et al. Peroxidasin forms sulfilimine chemical bonds using hypohalous acids in tissue genesis. *Nat Chem Biol.* (2012) doi: 10.1038/nchembio.1038
79. Sirokmány G, Kovács HA, Lázár E, Kónya K, Donkó Á, Enyedi B, et al. Peroxidasin-mediated crosslinking of collagen IV is independent of NADPH oxidases. *Redox Biol.* (2018) 16:314–21. doi: 10.1016/j.redox.2018.03.009.
80. Colon S, Page-McCaw P, Bhave G. Role of hypohalous acids in basement membrane homeostasis. *Antioxid Redox Signal.* (2017) 27:839–54. doi: 10.1089/ars.2017.7245

Conflict of Interest Statement: The authors declare that the research was conducted in the absence of any commercial or financial relationships that could be construed as a potential conflict of interest.

Advantages of publishing in Frontiers

OPEN ACCESS
Articles are free to read for greatest visibility and readership

FAST PUBLICATION
Around 90 days from submission to decision

HIGH QUALITY PEER-REVIEW
Rigorous, collaborative, and constructive peer-review

TRANSPARENT PEER-REVIEW
Editors and reviewers acknowledged by name on published articles

Frontiers
Avenue du Tribunal-Fédéral 34
1005 Lausanne | Switzerland

Visit us: www.frontiersin.org
Contact us: info@frontiersin.org | +41 21 510 17 00

REPRODUCIBILITY OF RESEARCH
Support open data and methods to enhance research reproducibility

DIGITAL PUBLISHING
Articles designed for optimal readership across devices

FOLLOW US
@frontiersin

IMPACT METRICS
Advanced article metrics track visibility across digital media

EXTENSIVE PROMOTION
Marketing and promotion of impactful research

LOOP RESEARCH NETWORK
Our network increases your article's readership